A THREE-DIMENSIONAL TURBULENT BOUNDARY LAYER UPSTREAM AND AROUND A JUNCTION VORTEX FLOW

by

John D. Menna

Dissertation submitted to the Faculty of the
Virginia Polytechnic Institute and State University
in partial fulfillment of the requirements for the degree of

DOCTOR OF PHILOSOPHY

in

Mechanical Engineering

APPROVED:

F. J. Pierce, Chairman	W. C. Thomas
H. L. Wood	W. E. Kohler
S. B. Thomason	T. E. Diller

May, 1984

Blacksburg, Virginia

A THREE-DIMENSIONAL TURBULENT BOUNDARY LAYER UPSTREAM AND AROUND A JUNCTION VORTEX FLOW

by

John D. Menna

(ABSTRACT)

A pressure-driven three-dimensional turbulent boundary layer flow upstream and around a junction vortex was experimentally studied and is offered for use as a benchmark flow for testing and evaluating the predictive ability of state-of-the-art three-dimensional turbulent boundary layer codes.

The pressure-driven flow and junction vortex system was generated by a streamlined cylinder placed normal to a flat surface. Measurements of wall static pressure, wall shear stress, mean velocity, and Reynolds stress tensor field are reported at several stations in the three-dimensional turbulent boundary layer region. Documentation of the flow edge conditions is provided as well as upstream initial conditions along a plane with measured mean velocity and Reynolds stress tensor to permit the testing of intermediate and higher order turbulence models.

Measurements of wall shear stress magnitude were made with a Preston tube and the wall shear stress directions were taken from an oil streak flow visualization. These results are compared with earlier direct force wall shear measurements of both magnitude and direction. Mean velocity magnitude and direction were measured with a single hot film probe. Measurements of the complete Reynolds stress tensor were carried out with three hot film x-array probes.

Supporting work includes: a wind tunnel calibration which examined the sensitivity and effects of spanwise nonuniformities and a two-dimensional momentum integral calculation along the tunnel center plane; the development of a calibration technique to determine individual sensor yaw characteristics in more complex probe geometries; and a generalized response analysis for a sensor with arbitrary orientation to the flow which allows for the use of an arbitrary yaw cooling law, allows for modest amounts of probe misalignment and yields a precise definition of matched sensors, geometric guidelines for constructing x-array probes, and a general mean velocity correction for turbulence where several existing formulas are compared. In addition, two popular cooling laws are studied, comparisons are made with other response equations, and an extensive discussion of the errors associated with the matched sensor approximations is given. Comparisons are made of several mean velocity measurements using different probes and redundant normal and shear stresses measured by the different x-array film probes, a single wire, and single film probe are compared.

ACKNOWLEDGEMENTS

I wish to express my sincere appreciation to Dr. Felix J. Pierce, my major advisor, for his invaluable contributions to my work, to my knowledge, and to my professional growth. His constant encouragement, guidance, and personal counsel helped me through the difficult times. I am thankful for having had the opportunity to work with him.

My appreciation and thanks are extended to Dr. T. E. Diller, Dr. W. E. Kohler, Dr. W. C. Thomas, Dr. S. B. Thomason, and Dr. H. L. Wood for serving on my advisory committee. I would also like to thank Mr. Joseph G. Marvin of the NASA, Ames Research Center for providing funding for this work and for his patience during the completion of the final manuscript.

I wish to thank Mr. David Fitts for his analyses of the tunnel calibration data and Mr. Christopher Pierce and Mr. Russell Lindsay for providing the much needed assistance in the data reduction phases of this work. C. L. Gray and the shop personnel, especially H. Smith, B. H. Shepherd, J. R. Lucas, and J. L. Cox are to be thanked for providing the technical support for the experimental hardware required in this study. A special thanks is given to Mrs. Neta Byerly who did an outstanding job of typing this manuscript. She provided invaluable clerical assistance and many helpful suggestions during the preparation of the final draft.

I wish to express my sincere appreciation to the Pierce family for their kindness and hospitality during the past five years, to my neighbors Mrs. Helen Morehead, Mr. Bill Kirchman, and Dr. Linda Leffel for

their support and encouragement, to Dr. John Teachman, Dr. Edgar Munday, and Miss Janet Hein for their friendship and to all the students, faculty, and staff who have made this effort an enjoyable experience. A special thanks goes to Mrs. Pat Ray for her love and support.

I express my heartfelt thanks and deepest appreciation to my family, whose unfaltering love and faith in me gave me the confidence and support to reach this level of achievement. Finally, I will always cherish my Grandmother, Mrs. Maria Caranci, who has been a great inspiration to me throughout my life. Though she did not live to see the completion of this work, her presence was always felt. To her, I dedicate this work.

TABLE OF CONTENTS

TABLE OF CONTENTS (Continued)

Page

TABLE OF CONTENTS (Continued)

TABLE OF CONTENTS (continued)

TABLE OF CONTENTS (continued)

LIST OF TABLES

LIST OF TABLES (continued)

LIST OF TABLES (continued)

LIST OF TABLES (continued)

LIST OF FIGURES

LIST OF FIGURES (continued)

LIST OF FIGURES (continued)

LIST OF FIGURES (continued)

LIST OF FIGURES (continued)

NOMENCLATURE

a_1	ratio of shear stress to turbulent kinetic energy (see Eq. 7.14)
a_1'	ratio of total resultant shear stress to turbulent kinetic energy
A, B_o	empirical constants in King's Law
$A^{\pm}, B^{\pm}, C^{\pm}$	sum and difference coefficients in sensor response equations
$A_I^{\pm}, B_I^{\pm}$	ideal sum and difference coefficients
B	$B_o f$
$\hat{B}, \hat{B}_o$	estimated values of B, B_o
C_f	skin friction coefficient, $\frac{2\ \tau_w}{\rho \overline{U}_{FS}^2}$
C_p	pressure coefficient, $\frac{2(p - p_{ATM})}{\rho \overline{U}_I^2}$
d	sensor diameter
e	fluctuating voltage
$\hat{e}_x, \hat{e}_y, \hat{e}_z$	unit vectors along the x,y,z axes
$\hat{e}_x^*, \hat{e}_y^*, \hat{e}_z^*$	unit vectors along x^*, y^*, z^* axes
E_o	voltage at zero flow conditions
$\overline{E}$	mean voltage
$f(\alpha, P)$	yaw cooling law function
Gr	Grashof number
h^2	pitch correction coefficient
k^2	yaw cooling law parameter (Hinze's Law)
$\hat{\ell}$	unit vector along the sensor
ℓ	mixing length
ℓ/d	sensor length to diameter ratio

ℓ_i, m_i, n_i, $i=1,2,3$	direction cosines
m	yaw cooling law parameter (Davies and Bruun's Law)
n	exponent in King's Law
$\hat{n}(t)$	instantaneous unit vector normal to the sensor
$\hat{N}$	unit vector normal to the sensor in the xyz coordinate system
$\hat{N}^*$	unit vector normal to the sensor in the $x^*y^*z^*$ coordinate system
P	general cooling law parameter
p	static pressure
p_{ATM}	atmospheric pressure
$\hat{q}(t)$	instantaneous velocity unit vector
$\underline{Q}(t)$	resultant instantaneous velocity vector
$R(Q,\theta)$	sensor response function
Re_d	Reynolds number based on sensor diameter
Re_{unit}	unit Reynolds number, $\frac{\overline{U}_I}{\nu}$
t	time
u,v,w	fluctuating velocity components in the x,y,z, directions
$\overline{U},\overline{V},\overline{W}$	mean velocity components in the x,y,z directions
U_N, U_T, U_{BN}	instantaneous normal, tangential, and binormal velocity components relative to the sensor
$\overline{U}_N$, $\overline{U}_T$, $\overline{U}_{BN}$	mean normal, tangential, and binormal velocity components relative to the sensor
$\overline{U}_\xi, \overline{U}_\eta, \overline{U}_\zeta$	mean velocity components in the ξ, η, ζ directions
u^*,v^*,w^*	fluctuating velocity components in the x^*,y^*,z^* directions
$\overline{U}^*,\overline{V}^*,\overline{W}^*$	mean velocity components in the x^*,y^*,z^* directions

u_1, u_2, u_3	fluctuating velocity components in the x_1, x_2, x_3 directions
$\overline{U}_1, \overline{U}_2, \overline{U}_3$	mean velocity components in the x_1, x_2, x_3 directions
$\overline{U}_I$	tunnel inlet throat velocity
$\overline{U}_{FS}$	local freestream velocity in the xyz system
$\overline{U}_{1,FS}$	local freestream velocity in the $x_1x_2x_3$ system
$\overline{U}_e$	mean effective cooling velocity
$\overline{U}_E^*$	mean velocity before turbulence correction
u_τ	friction velocity, $\sqrt{\tau_w/\rho}$
u^+, y^+	two-dimensional similarity variables
x, y, z	sensor cartesian coordinates
x^*, y^*, z^*	local streamline cartesian coordinates
x_1, x_2, x_3	laboratory cartesian coordinates
α	sensor yaw angle in sensor coordinate system
α^*	sensor yaw angle in local streamline coordinate system
β	local skew angle
β_w	limiting wall streamline direction
γ_x	sensor roll angle in sensor coordinate system
γ_x^*	sensor roll angle in local streamline coordinate system
δ, δ^*, θ	2D boundary layer thickness, displacement thickness, momentum thickness
ε	eddy viscosity
$\theta(t)$	instantaneous yaw angle
$\theta_\xi, \delta_\xi^*, \theta_{\xi\zeta}$	boundary layer thicknesses in curvilinear coordinates
μ	dynamic viscosity
ν	kinematic viscosity

ξ, η, ζ	freestream streamline coordinate system (orthogonal curvilinear coordinates)
ρ	density
τ_w	wall shear stress
$\overline{\psi}_y$, $\overline{\psi}_z^*$	yaw and pitch misalignment of the xyz coordinate system
ω	freestream streamline direction

I. INTRODUCTION

A. Motivation for a Standard Test Case

Historically, real progress in the field of fluid mechanics has always demanded the collaboration of theoretical and experimental efforts. Not since Prandtl's classic paper in 1907 has this relationship been more vital than in the study of three-dimensional turbulent boundary layer (3DTBL) flow for at least three reasons. First, the calculation of such a flow still relies heavily on empiricism to model the relentlessly complex and puzzling mechanisms involved in turbulent energy transport. Second, the number of experiments suitable for the evaluation of computational methods are few despite the significant technological advances in diagnostic and data acquisition capability over the past decade. Third, more information is needed to properly understand the physics involved.

The lack of well-documented flows suitable for use as standard test cases to guide both three-dimensional turbulence modeling and the development of computational methods was emphasized at the Stanford Conference on Complex Turbulent Flows [1]. Regardless of the class of flows, an evaluation of the experimentally studied flows showed an apparent shortage of standard test case-calibre documentation. Similar comments were made at the IUTAM conference [2] on 3DTBL flows in Berlin (1982) by Fernholz and Krause who stated, "The symposium has shown again that there exists few experiments which contain sufficient information for improving turbulence models". The recognized lack of complete documentation of the 3DTBL flow field coupled with an impetuosity generated by

a very rapid growth in computational fluid mechanics and computer capabilities has allowed and often required the computational fluid dynamicist, in solving turbulent flows, to make too many assumptions which could strongly influence the computed results. Clearly, the freedom and uncertainty in assuming such required information diminishes the objectivity of the computed solution and raises questions concerning the generality of the computational method itself.

B. The Turbulent Boundary Layer

In most applications involving the external surfaces of aircraft, ship hulls, turbine and compressor blades and in many internal geometric configurations such as channels, pipes, nozzles and diffusers, the flow field adjacent to a solid body as described by Prandtl can be divided into two regions: a very thin layer in proximity of the body where viscosity plays an essential role in the dynamics of the fluid motion and the remaining outer portion of the boundary layer where the effects of viscosity can be neglected. Prandtl's physical model resulted in a maximum degree of simplification of the well established Navier-Stokes equations. In view of the historical mathematical difficulties in solving these equations, Prandtl's work marked an epoch in the history of fluid mechanics which paved the way to solving many of the practical flow problems of today.

Turbulent boundary layer flows are classified as either two- or three-dimensional. This classification depicts only the mean flow features since strictly speaking, even the most two-dimensional flows have three-dimensional velocity fluctuations.

In 2DTBL flows, all the velocity vectors of a profile lie in a single plane and each of these profiles are mutually parallel throughout the flow field. A quasi-2DTBL or collateral 3DTBL flow is one in which the velocity directions coincide with the freestream direction at a given flow station but the planes containing the profiles are not parallel in the flow field. The main feature of a skewed 3DTBL that differentiates itself from the two previous cases is the deviation of the local boundary layer velocity direction from the freestream direction.

In most 3DTBL applications skewing of the boundary layer is initiated by two principal mechanisms: unbalanced pressure forces caused by curvature of the freestream streamlines or transverse skewing of the inner layers due to spanwise motion relative to the adjacent layers. Pressure-driven secondary flows are the most common and the majority of the published experiments fall into this category. Typical mean velocity profiles of a pressure-driven flow depicting unilateral and bilateral skewing are illustrated in Fig. 1.1. The boundary layer thickness, δ, is usually identified where $\overline{U}_{\xi} \cong \overline{U}_{FS}$. The edge of the boundary layer is rather arbitrary however, from an empirical point of view. The curvilinear $\xi\eta\zeta$ coordinate system is oriented in the usual fashion where the ξ and ζ axes lie on the bounding surface with the ξ direction tangent to the freestream streamline and the η direction normal to the $\xi\zeta$ plane. The $x_1x_2x_3$ system will be designated as the laboratory coordinate system. The limiting wall streamline angle, β_w, is also shown.

There are two methods available today for calculating turbulent boundary layer flows: the first involves an integrated form of the

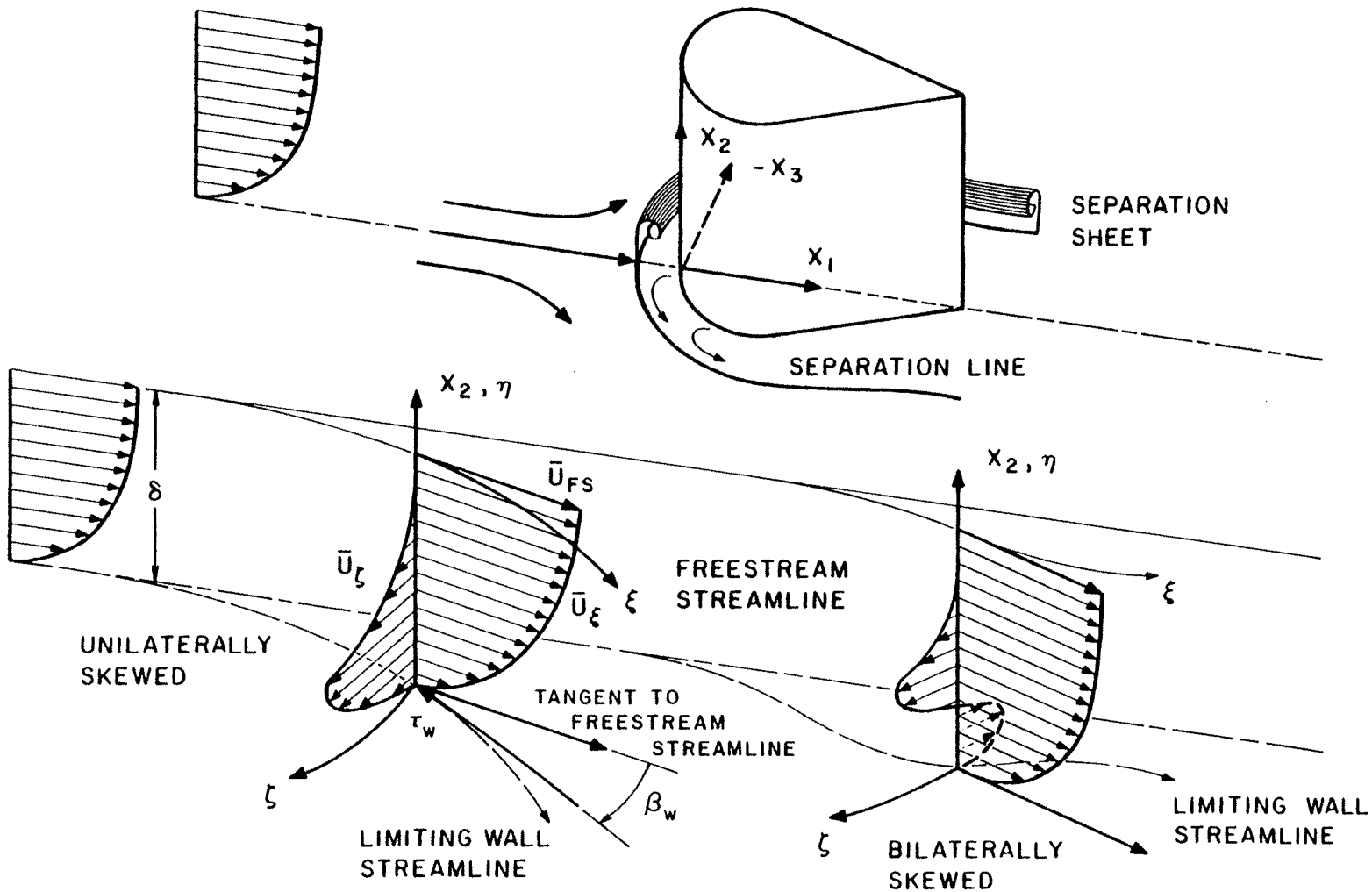

Figure 1.1 Typical Pressure-Drive 3DTBL Flow and Separated Region Generated by a Blunt Body Standing on a Flat Wall Showing Unilateral and Bilateral Skewing of the Boundary Layer

governing equations while the second attempts to solve the differential equations directly. Early attempts to calculate turbulent boundary layers in two dimensions were based on the momentum integral equation which can be traced to the work of von Karman in 1921. In essence, they are derived by using continuity to eliminate the U_2 velocity in the momentum equations followed by an integration of this new relation across the entire boundary layer (see Eq. 1.1). Consequently, the order of the resulting governing differential equations is reduced by one since the x_2 dependence disappears by the integration. For the case of a 3DTBL, the revised system is composed of two momentum integral equations which contain six unknown integral thickness terms and the two unknown compoments of the wall shear stress. A key advantage to this method is that only the gross behavior of the attendant profile representations are required to satisfy some prescribed boundary conditions and which do not have to satisfy the original differential equations. Although this approach is more convenient the details of the internal flow structure are lost due to the inherent global characterizations involved.

On the other hand, current computer technology has extended the practical limits of systemtic flow simulation to the point where current trends seem to indicate that differential formulation will replace the well served, integral techniques. With the differential method, finite difference or finite element discretization provides the resolution for studying the finer structures of the flow field. Furthermore, in solving the local differential equations, fewer assumptions are needed so that the computational methods are applicable to a wider range of

flows. However, a more detailed account of the initial and boundary conditions are required and these are generally lacking in nearly all of the 3DTBL experiments to date.

C. A Problem of Closure

From a theoretical point of view, the instantaneous time dependent Navier-Stokes equations represent the purest form of the governing equations available for computing turbulent flows. A direct solution of these equations however, is still beyond the current computational capabilities due to the high temporal and spacial resolution that is required to resolve the fine structures in practical turbulent flows which are unsteady in nature. An alternative was proposed by Reynolds as far back as 1880, who hypothesized that the randomly unsteady turbulent motions could be described by time averaged motions. To initiate this transformation, the instantaneous dependent variables are decomposed to mean and fluctuating components. Accordingly, for statistically stationary turbulence the Navier-Stokes equations can be re-written for an incompressible flow as

$$\frac{\partial \overline{U}_i}{\partial t} + \overline{U}_j \frac{\partial \overline{U}_i}{\partial x_j} = -\frac{1}{\rho}\frac{\partial \overline{P}}{\partial x_i} + \frac{\partial}{\partial x_j}\left(\nu \frac{\partial \overline{U}_i}{\partial x_j} - \overline{u_i u_j}\right) \qquad (1.1)$$

along with the continuity equation,

$$\frac{\partial \overline{U}_i}{\partial x_i} = 0 \quad . \qquad (1.2)$$

The mean momentum equations pose a more realistic problem from the standpoint of finding a solution since the inherently random time dependent turbulent motion is replaced by statistically equivalent mean turbulence quantities. In this context, unsteady turbulent flow refers to slower, often periodic mean velocity variations with time. That the time and length scales of the mean flow be large compared to those scales associated with the fluctuating velocities, is a restriction to bear in mind when studying complex flows that contain large eddies and high turbulence intensity as may be the case in separated regions of a turbulent flow.

The advantage gained by the mean momentum representation is at the expense of a well-defined system of equations. The time averaging procedure has introduced the additional unknown $\overline{u_i u_j}$ terms which form the well known Reynolds stress tensor. The turbulent or Reynolds stresses are the sole manifestation of the turbulent fluctuations. Interpreted physically as a bulk transport of x_i-momentum fluid through a plane normal to the x_j axis, they are revealed as an apparent increase in the stress of a fluid. Thus, the total stress is composed of the Newtonian viscous stresses of the average or mean flow plus apparent stresses. Actually, these $\overline{u_i u_j}$ terms originate from the nonlinear convective terms appearing on the left side of Eq. 1.1, but they behave as though they were added stress terms. Generally, the Reynolds stresses dominate in regions outside the viscous sub-layer and are therefore of great importance in predicting turbulent flows.

Unavoidably, one has to deal with the fundamental problem of closure as a result of the added six unique stresses appearing in the time

averaged momentum equations. A reduction in the number of unknown stresses is possible by applying Prandtl's boundary layer theory to Eq. 1.1.

For 3DTBLs that are thin or fairly thin as defined by Bradshaw [3], derivatives of velocity and turbulent stress within the boundary layer are small in the streamwise and cross-stream direction compared to derivatives normal to the solid boundary on which the boundary layer grows. In view of these approximations, an order of magnitude analysis on the quantities appearing in Eq. 1.1 yields the well-known turbulent boundary layer equations,

$$\bar{U}_1 \frac{\partial \bar{U}_1}{\partial x_1} + \bar{U}_2 \frac{\partial \bar{U}_1}{\partial x_2} + \bar{U}_3 \frac{\partial \bar{U}_1}{\partial x_3} = - \frac{1}{\rho} \frac{\partial \bar{P}}{\partial x_1} + \frac{\partial}{\partial x_2} \left(\nu \frac{\partial \bar{U}_1}{\partial x_2} - \overline{u_1 u_2} \right) \tag{1.3}$$

$$\bar{U}_1 \frac{\partial \bar{U}_3}{\partial x_1} + \bar{U}_2 \frac{\partial \bar{U}_3}{\partial x_2} + \bar{U}_3 \frac{\partial \bar{U}_3}{\partial x_3} = - \frac{1}{\rho} \frac{\partial \bar{P}}{\partial x_3} + \frac{\partial}{\partial x_2} \left(\nu \frac{\partial \bar{U}_3}{\partial x_2} - \overline{u_2 u_3} \right) \tag{1.4}$$

$$0 = - \frac{1}{\rho} \frac{\partial \bar{P}}{\partial x_2} . \tag{1.5}$$

Closure of this system including continuity (Eq. 1.2) still requires knowledge of the $\overline{u_1 u_2}$ and $\overline{u_2 u_3}$ shear stresses a priori. The former stress is the dominant shear stress in 2DTBL flows.

In addition to the apparent simplifications, the foregoing approximations have recast the governing equation from an elliptic nature to a parabolic set of equations. From a theoretical standpoint, one could hardly refer to both systems as similar, since their respective boundary condition requirements for obtaining a solution are different by nature. The elliptic or jury problem requires boundary conditions on all

upstream, lateral, and downstream surfaces whereas in the parabolic problem, boundary specifications on the downstream surfaces are not required.

During the past decade most of the efforts in calcuating 3D flows have focused on solving the 3DTBL equations. There are at least two reasons for this choice. First, the turbulence model(s) need only embrace two out of the six Reynolds stresses and secondly, the 3DTBL solution can be achieved with significantly lower requirements of computer time and storage than the elliptic case. While there is little doubt that the 3DTBL equations are a valid representation for a broad range of boundary layer flows found in practice, one must not loose sight of their limitations. In reality, the complete Reynolds stress tensor is involved in the cascade of energy flow predominately from the freestream to the near wall regions. In addition, a complex turbulent flow may not exhibit global parabolic behavior as in the case of separated 3DTBL flows where a strong parabolic flow upstream can transcend to a seemingly elliptic nature as the flow is overcome by an adverse pressure gradient. Near separation, a boundary layer solution has been shown to be inadequate in predicting the fluid motion [4].

Closure of the governing equations depends entirely upon the treatment of the Reynolds stresses. Owing to the extremely complex nature of turbulence, modeling has been inaccessible through purely mathematical theories. To date nearly all methods for calculating turbulent flows rely on semi-empirical models to resolve the turbulent stresses. A number of turbulence models have been proposed which range from simple algebraic models to very complex sets of equations requiring the solu-

tion of more than 20 differential equations. These include lower order eddy viscosity and mixing length models, intermediate order modeling using one and two differential equations involving the transport of kinetic energy, turbulent shear, dissipation, or even eddy viscosity, and higher order models involving greater numbers of such transport equations.

Of all the models available, the lower order algebraic or gradient transport models are the most convenient. The original idea can be traced to Boussinesq [6] who introduced the concept of an eddy viscosity. Analogous to the coefficient of viscosity, μ, in laminar flow, the eddy viscosity, ε, relates the apparent shear stress to the mean flow rate of strain. Unlike the absolute viscosity however, it is not a physical property of the fluid but varies with local flow conditions and geometry. More tangible properties of the eddy viscosity are found in Prandtl's mixing length hypothesis [7]. Viewed as the average distance over which the fluid exchanges momentum, the mixing length ℓ, resembles the mean free path in the kinetic theory of gases. The mixing length has been shown to vary strongly in proximity of the wall, vanishing at the wall.

A large number of turbulence models are linked to the mixing length concept. A simplified algebaric model for a 3DTBL, assuming an isotropic eddy viscosity, is

$$-\overline{u_1 u_2} = \varepsilon \frac{\partial \overline{U}_1}{\partial x_2} \tag{1.6}$$

$$-\overline{u_2 u_3} = \varepsilon \frac{\partial \overline{U}_3}{\partial x_2} \tag{1.7}$$

$$\varepsilon = \ell^2 \left\{ \left(\frac{\partial \overline{U}_1}{\partial x_2}\right)^2 + \left(\frac{\partial \overline{U}_3}{\partial x_2}\right)^2 \right\}^{1/2} . \qquad (1.8)$$

The mixing length distributions are determined by experiment from which empirical approximations are obtained in each of the three region of the boundary layer [9,10,11]. The inner region influence of the wall on the mixing length is usually treated by van Driest's damping factor [12].

Computational methods for 2DTBL flows using state-of-the-art mixing length or eddy viscosity models have performed well overall in predicting the mean velocity and stress distributions. It appears that current 3DTBL methods do not share in this success in predicting complex turbulent flows. Qualitative agreement with measurements of mean velocity or turbulence is often shown while consistent overall agreement is not. A reason often cited is the simplicity of the model due mainly to its neglect of convection and diffusion of the turbulence. One equation models are also subject to this criticism since they too rely on the mixing length model to complete closure of the governing equations.

In the development of more comprehensive models to handle the more representative processes of convection, diffusion, redistribution, etc., additional differential transport equations are required. These equations are often obtained by subjecting transport scalar quantities to conservation laws which themselves contain unknown transport phenonomon. Proper testing of the intermediate and higher qrder closure models involving kinetic energy or turbulent stress transport [13-15,17-19] requires initial energy and/or shear distributions as well as substantial turbulent field documentation to test, evaluate, and compare turbulence

models as a whole. While several experiments have documented mean velocity fields well, and a few have documented mean velocity and Reynolds stress fields, more often than not upstream and/or edge conditions necessary to initiate and sustain a computational solution are missing.

D. Scope of the Investigation

The need for more thoroughly documented 3DTBL flows is apparent. In this investigation, a pressure-driven 3DTBL flow upstream and around a junction vortex was experimentally studied and is offered for use as a standard test case or a benchmark flow for testing and evaluating the predictive ability of state-of-the-art 3DTBL codes.

The pressure-driven 3DTBL flow is generated by a streamlined cylinder placed normal to a flat surface. The total complex flow is characterized by different flow regions including a three-dimensional separated region and a body-wall junction vortex which wraps around the body as shown in Fig. 1.1. This same flow geometry was used by McAllister [27] in studying three-dimensional near-wall similarity. The documentation of the 3DTBL flow includes:

1) upstream initial conditions along a plane with measured
   a) mean velocity field,
   b) Reynolds stress tensor field including,
   c) the turbulent kinetic energy field;
2) freestream velocity or edge conditions measured from the initial plane extending downstream to the 3DTBL flow regions and wall static pressure field measurements;

3) measurements in the 3DTBL of

   a) mean velocity field,

   b) Reynolds stress tensor field,

   c) wall shear stress magnitude by a Preston tube,

   d) limiting wall streamline directions from oil streak flow visualizations, and

   e) earlier direct force wall shear measurements of both magnitude and direction.

These data should allow a good test of the predictive ability of any 3DTBL code. The specification of turbulence data on the initial plane should permit the testing of several intermediate and higher order turbulence models. The measured initial plane condition will circumvent having to perform any additional 2DTBL flow calculation to match some measured conditions at some downstream station to initiate a 3DTBL simulation. Further, the measured edge condition eliminates the need to assume a freestream potential flow to sustain the calculations.

A single hot film probe was used to measure the magnitude and direction of the mean velocity. Measurements of the complete Reynolds stress tensor were made with three hot film x-array probes used in a cross-flow mode. This particular probe configuration was used in place of the end-flow method because of the lower flow blockage it afforded. This configuration was especially suited for measurements in the neighborhood of flow separation and the junction vortex system. In a typical end-flow or parallel support system, the downstream supporting structure would most likely penetrate the separated regions while making

measurements near this area. Such an intrusion could significantly influence the behavior of the flow. From this point of view, the alternative configuration is believed to be less flow destructive but requires additional and more extensive calibrations. The vertical and slant x-array probes were specially designed to accommodate this perpendicular orientation with a minimum of aerodynamic interference for the probe's sensors.

In the development of this standard test case, a great emphasis was placed on the accuracy and precision of the mesaurements as well as the quality of the flow upstream of the body. Further, a thorough examination was made of response analyses and different cooling laws. Several comparisons of redundantly measured mean velocity and Reynolds stresses using different probes are reported.

As part of this overall effort, the following studies and comparisons were made:

1) A 2D wind tunnel calibration which involved,
   a) sensitivity studies of the spanwise nonuniformities to various upstream screen-filter cloth combinations,
   b) 2D momentum integral study along the tunnel centerline, and the
   c) effect of spanwise nonuniformities on the mean 3DTBL flow field.
2) Extensive studies on the repeatability in edge condition measurements, wall shear stresses, mean velocity and Reynolds stress profiles in the usptream and downstream regions of the flow were made.

3) An examination was made of the degree of symmetry in the initial and edge conditions, mean velocity field, and $\overline{uu}$ stress field.

4) A calibration technique was developed to determine the individual yaw characteristics of each sensor regardless of the probe configuration. This method replaced the conventional approach described by Jorgensen [49] which could not be applied to all the sensors used in this study. The cooling laws of Hinze [54], and Davies and Bruun [104] were studied using both linear and nonlinear response equations for each cooling law. The yaw parameters k^2 and m determined by this new method were compared to results obtained by a more conventional method.

5) A detailed hot wire/film analysis was developed for arbitrary sensor orientation to the flow which allows

   a) the correction of mean velocity for turbulence where comparisons were made to several existing correction formulas,

   b) misalignment of the sensor with the local streamline direction,

   c) the use of an arbitrary cooling law for calculating turbulence, and the

   d) the calculation of redundant stresses from the slant x-array.

e) The analysis yields a precise defintion of the conditions required for a matched sensors in an x-array probe, and also shows the effects of deviations from the matched sensor conditions.

f) Finally, the analysis yields geometric guidelines for constructing x-array probes.

6) The generalized response equation developed here was compared to the response equations of Bruun [57] and Champagne et al. [59].

7) Various sensor response sensitivity studies include,

a) sensitivity to flow misalignment,

b) Reynolds stress sensitivity to the cooling laws of Hinze [54], and Davies and Bruun [104], and

c) Reynolds stress sensitivity to sensor mismatch.

8) A comparison was made of redundant stresses measured by the slant x-array with those measured by the horizontal and vertical x-arrays.

9) A comparison of nine measurements of mean velocity was made using the various x-array probes and the single film probe, with and without turbulence correction.

10) Comparisons of x-array measured turbulent streamwise intensity were made with measurements from both a single hot film and a single hot wire probe.

11) Finally, comparisons of turbulent streamwise intensity obtained with and without linearizing circuitry were made.

II. LITERATURE SURVEYS

A. Review of Standard Test Cases for 3DTBL Flows

A large number of studies in the 3DTBL flow area appear in the literature. This discussion will be restricted mainly to the experiments which have been considered as test cases particularly for pressure-driven flows.

Fortunately there are several surveys [28-31] which provide extensive reviews of the large variety of pressure-driven and shear-driven 3DTBLs that have been considered to date. Johnston [28] provides a detailed list of over 80 experiments which involve a variety of external and internal flow geometries. These include: curved rectangular ducts, diffusers, and turbomachinery cascades, yawed plates, wings, cones, body junction flows, and the shear-driven flows of rotating bodies as well. Of all the available 3DTBL experiments only a few have reported Reynolds stress profiles. Johnston lists nine studies and Fernholz and Vagt [31] cite seven additional experiments. These experiments are summarized in Tables 2.1 and 2.2, and they include measuring techniques for the mean flow, the Reynolds stresses, and the wall shear stress fields.

Not all of the experiments listed in Tables 2.1 and 2.2 are suitable for testing 3DTBL calculation methods. Difficulties in finding well documented flows to serve as test cases were emphasized in the Stanford Conference on Complex Turbulent Flows in 1981 [1]. Of some sixteen candidate flows only four experiments were recommended to serve as standard test cases. They include the studies of van den Berg and Elsenaar [32,5] Bissonnette and Mellor [33,34], Dechow and Felsh

Table 2.1 Summary of 3DTBL Experiments with Turbulent Stress Profiles Compiled by Johnston [28]

Authors	Source and type of cross flow	Number of 3D profiles	Measurement method for Reynolds stress data (see text for description of methods)	Technique for mean field data
Bradshaw & Terrell (1969)	constant pressure yawed flow decaying to 2D; infinite yawed flat wall	5	Method II - hot wire probes of normal, slant and x-array to obtain $\overline{c_i c_j}$	pitot and twin tube (cobra type) probes for Q and γ
Johnston (1970)	strong $\partial p/\partial x$, growing from developed 2D layer; infinite swept step on wall	3	Method II - same as above except $\overline{q_i q_j}$ data obtained and reduced to $\overline{c_i c_j}$	same as above plus disk static probe to obtain p(y), and 2-hole cobra probe held on edge to obtain $\beta(y)$
Bissonnette & Mellor (1970,1974)	transverse wall motion, growing from 2D layer on cylinder	16	Method I - hot wires of normal and slant types with probe and prong axes normal to wall to obtain $\overline{c_i c_j}$, data given as $\overline{u^2}$, $\overline{v^2}$ (ref. system)	C and γ by hot wire probes
East (1973)	slightly favorable $\partial p/\partial x$, cross over profiles; delta wing at angle of attack	8	$(-\rho\overline{uv})$ and $(-\rho\overline{wv})$ from mean equations of motion using mean field data	3-hole impact tube (cobra type) for Q and γ
Lohmann (1973,1976)	see Bissonnette & Mellor	9	Method I - similar to Bissonnette and Mellor except probe stems held from downstream	C and γ by hot wire probes
Pierce & Duerson (1974)	layer on end wall of constant area rectangular curved duct	7	Method II - with cylindrical hot film probes of x-array to obtain $\overline{c_i c_j}$. Data reduced to $\overline{u^2}$, $\overline{v^2}$, $\overline{w^2}$, $\overline{uv}$, $\overline{wv}$, $\overline{wu}$ format (ref. system)	C and γ by hot film probes
Elsenaar & Boelsma (1974)	adverse chordwise pressure gradient due to 35° yawed wing to generate 'infinite' swept flow on flat wall with separation	10	Method II - hot wire probe of x-array to obtain $\overline{c_i c_j}$	Q, γ and β by 3-hole impact tube (cobra type)
Pierce & Ezekwe (1975)	strong $\partial p/\partial x$ impinging flow growing from developed 2D layer over flat wall	14	Method I - with cylindrical film sensors on probes	ditto Bissonnette and Mellor but with film sensors
Zimmerman & Abbott (1975)	constant pressure, slightly yawed profile decaying to 2D on flat yawed wall	11	Method III - instantaneous u, v, w by triaxial, 3-wire probe and analogue computer Data: $\overline{u^2}$, $\overline{v^2}$, $\overline{w^2}$, $\overline{uv}$, $\overline{wv}$, $\overline{wu}$, $\overline{k}$, $\overline{kv}$ (ref. system)	Q and γ by 3-hole impact probe (cobra type)

Table 2.2 Summary of Recent 3DTBL Experiments with Turbulent Stress Profiles Compiled by Fernholz and Vagt [31]

Authors	Source and type of cross flow	Number of 3-D profiles	Measurement method for Reynolds stress data and listing of data	Technique for mean field data and skin friction measurements	Maximum flow angle* Measuring method	y^+_{min}
Dechow, R. (1977)	Cylindrical body normal to the wall; pressure driven flow	14	Quarter square method, single and x-wires, stem parallel to the wall; method II $\overline{u'^2}, \overline{v'^2}, \overline{w'^2}, \overline{u'v'}, \overline{u'w'}, \overline{v'w'}$	Normal single hot wire; Preston probe; direction of skin friction with hot film probe	60^o x-wire	
Hebbar & Melnik (1976,1978)	Yawed flow decaying to 2-D; flat wall	9	Single rotated hot-wire probe. Probe protruding out of the wall; $\overline{u'^2}, \overline{w'^2}, \overline{u'w'}$; method I no continuous rotation	Normal hot wire; Preston probe; sublayer fence; hot film	22^o Bisector method	0.31
Chandrasekhara Swamy, N.V. et al. (1978)	20^o yawed flat plate at two angles of incidence; zero pressure gradient	more than 7	Normal single and x-wire probe; probe stem parallel or 3^o inclined towards the wall; method II $\overline{u'^2}, \overline{v'^2}, \overline{w'^2}, \overline{u'v'}, \overline{u'w'}, \overline{v'w'}$	Normal single hot-wire, Pitot probe; Preston probe	12^o 3-hole yaw probe	~30
Ezekwe, C. I., Pierce, F. J. McAllister, J. E. (1978)	Free-jet over a flat wall impinging against a back wall; OFF and on plane of symmetry	4	Rotating hot-film technique, straight and slanted hot-films; method I $\overline{u'^2}, \overline{v'^2}, \overline{w'^2}, \overline{u'v'}, \overline{u'w'}, \overline{v'w'}$	Straight hot film; no skin friction data	Rotating hot film	
De Grande, G. Hirsch, Ch. (1978)	60^o curved duct flow decaying along a straight extension; flat wall	140	Single rotated hot wire; single normal and slanted wire; probe protruding out of the wall; method I $\overline{u'^2}, \overline{v'^2}, \overline{w'^2}, \overline{u'v'}, \overline{u'w'}, \overline{v'w'}$	Normal single hot-wire; 3-hole probe; no skin friction measurements	28^o 3-hole probe Rotating hot-wire	<10 estimate
Muller & Krause (1979); Muller (1979)	Adverse chordwise pressure gradient due to inclined side wall and upper wall	21	Single normal, slanted wire, x-probe; stem parallel to the wall; method II $\overline{u'^2}, \overline{v'^2}, \overline{w'^2}, \overline{u'v'}, \overline{u'w'}, \overline{v'w'}$.	Normal single hot-wire; Preston probe	53^o Bisector method	
Fernholz & Vagt (1980)	Adverse pressure gradient, pressure driven circumferentially due to inclined back wall	24	Single normal, slanted and x-wire; probe stem normal to the wall $\overline{u'^2}, \overline{v'^2}, \overline{w'^2}, \overline{u'v'}, \overline{u'w'}, \overline{v'w'}$, u_τ-spectra; method I, with and without contin. rot.	Normal single hot-wire; Preston probe, surface fence	31^o modified rotating hot-wire	4

* against free stream direction

[35,36], and Lohmann [37] shown in Tables 2.1 and 2.2. The subcommittee also suggested that three other flows of Bradshaw and Terrell [38], Fernholz and Vagt [31], and Müller and Krause [39,40] might also be adopted with reservation since they were believed to be difficient in at least one essential aspect. The remaining flows were judged unsatisfactory due either to the lack of important measurements or because satisfactory flow quality had not been demonstrated. However, all 16 cases were expected to provide valuable information for turbulence modeling.

The experiments of Bissonnette [33,34] and Lohmann [37] are shear driven flows in which a developing 2DTBL axial flow over a stationary cylinder is suddenly skewed by the transverse motion of a rotating cylinder. The studies of van den Berg and Elsenaar [32,5] were made in a quasi two-dimensional turbulent boundary layer flow on a flat plate under infinite swept wing and adverse pressure gradient conditions. The external pressure field was induced by a suitably shaped body suspended above the plate which resulted in a 3DTBL with separation near the trailing edge. Measurements of mean velocity (magnitude and direction), Reynolds stress, and wall shear stress were obtained on the flat plate at 10 cordwise stations using a cobra probe, rotatable x-probe, and a Stanton type wall probe. The upstream station defines the initial conditions, while both the freestream velocities and wall static pressure measurements each specified the edge condition. Additional studies included: 1) comparisons of measured wall shear stress coefficients with those obtained from Clauser plots, 2) a momentum balance of the flow, 3) comparisons of mean velocity and direction using

wire and pressure probes, 4) comparison of turbulent shear stresses obtained by the half quadrant and full quadrant method and, 5) a detailed hot wire response and error analysis including the influences of sensor mismatch, probe malpositioning, and geometric imperfections. Their comprehensive treatment of this experiment exemplifies the thorough treatment of a test case.

The only work similar in some respects to the present study is that reported by Dechow and Felsh [35,36]. They investigated a pressure-driven 3DTBL generated by a similar streamlined cylinder mounted on a flat plate. This flow geometry produced substantial secondary flows and the body-floor junction supported a three-dimensional separated flow and horseshoe vortex system. Data was collected at 14 stations, 10 of which were located along a freestream streamline which extended from a nominally 2D upstream flow station to the separation line. They reported measurements of the mean velocity vector and the six Reynolds stresses made with a single wire and rotable x-probe, as well as of static pressure and wall shear stress from Preston tubes. The direction of the wall shear stress was evaluated from oil flow patterns, extrapolating the direction of mean velocity from values obtained close to the wall, and by a rotable flush mounted hot film probe. This is an excellent study, however, it provides initial condition data along a line rather than a plane and only limited edge condition data.

B. Hot Wire/Film Measurements in Turbulent Flows

Sensor Response

The difficulties of measuring a turbulent flow are due to the

random velocity fluctuations occurring over a wide range of frequencies. Since in the experimental documentation of such a flow both the mean velocity and turbulence fields are sought, the response characteristics of a hot wire/film requires detailed study.

The overall sensor response to a turbulent environment is easily observed by an oscilloscope time capture of the continuous constant temperature anemometer (CTA) output signal. The accurate translation of signals to local mean velocity and turbulent stresses requires a precise mathematical description of the sensor's response to the magnitude and direction of the instantaneous velocity. Due to the random nature of such flows, it is customary (and necessary) to rely on statistical methods of evaluation. Consistent with the Reynold's decomposition of the instantaneous velocity into a mean and fluctuating components, signal processing of instantaneous output voltage signatures from one or more sensors involves circuitry that can provide statistical information concerning the voltage fluctuations distributed about a mean value [41-47]. The tacit restriction of the statistical approach is the stationarity of the flow in question; that mean values including fluctuating quantities are statistically steady [48].

The signal processing equations that interpret the hot/wire film response are based on an effective cooling velocity. Many authors have chosen to use the formula proposed by Jorgensen [49] of the form

$$U_e = [U_N^2 + k^2 U_T^2 + h^2 U_{BN}^2]^{1/2} \qquad (2.1)$$

where U_N, U_T, and U_{BN} are the instantaneous normal, tangential, and

binormal velocity components, respectively. U_{BN} is perpendicular to the $U_N U_T$ plane. Coefficient k^2, is the yaw correction term which accounts for the tangential cooling velocity and the coefficient, h^2, is a pitch correction term which accounts for the sensor's sensitivity to rotation about its axis. For the limiting case of long sensors between widely spaced prongs, k=0 and h=1, the sensor is cooled strictly by normal components, and a simple cosine law is sufficient to describe the sensor's directional response to yaw. Due to the usual restrictions placed on the probe's size [50-53], however, commercial probe configurations possessing these ideal values for h and k are an exception rather than the rule. The pitch correction is usually not required for x-probes since the sensor's are calibrated and used in a stationary no pitch position.

The conventional approach of deriving the response equations involves a binomial series expansion, prior to time averaging, to deal with the nonlinear relations shown in Eq. 2.1. Ultimately, DC voltage levels and mean square AC voltage measurements are required to compute the local mean velocity and Reynolds stress fields. Unavoidably, truncation errors are introduced as a possible source of error. For low intensity flows (20-25%), it is sufficient to include only first order terms (order $(\frac{u}{U})$) in the series representation of Eq. (2.1) [54]. As a point of reference, a summary of typical streamwise turbulent intensity content occurring in turbulence flows is taken from Comte-Bellot [55]: $\sqrt{\frac{\overline{u^2}}{U^2}}$ is of the order of 0.05% in good wind tunnels, 0.2-2% in grid turbulence, 2-5% in wakes, 3-20% in boundary layers or pipe flows and over 20% in jets. For flows where velocity fluctuations are large,

higher order velocity correlations relative to the mean contribute significantly and more terms are needed in the root-expanded effective cooling velocity for the ultimate determination of meaningful flow field information [39,56-64]. Further, large fluctuations cause significant angular differences between the mean flow direction and instantaneous flow direction that are not present during calibrations usually performed in a very low intensity flow. Linearization of the hot wire/film nonlinear response signal offers some correction for the effects of large magnitude fluctuations [62,63], but essentially such errors still exist.

Correction of the mean velocity and Reynolds stresses is fundamentally possible in high intensity flows. For example, Rose [60], Müller [58], Klatt [64], Guitton [64] and Moussa and Eskinazi [65], show second order corrections of $\frac{\overline{vv}}{\overline{U}^2}$ and/or $\frac{\overline{ww}}{\overline{U}^2}$ for mean velocities measured with a normal sensor. Corrections for turbulent stresses involve velocity correlations higher than second order and are based either on an assumption concerning the distribution of the fluctuating velocity components i.e., Gaussian probability distribution [56,62,64,66], or else the higher order correlations are measured [56,58,62].

Rodi [67], Acrivlellis [68], Tutu and Chevray [66], have taken the novel approach which utilizes the squared output signal as a basis for obtaining the sensor's response in highly turbulent flows. Consequently, series expansions of Eq. 2.1 are not necessary and which in theory lifts the restrictions regarding the turbulent intensity level. Rodi's work in the two-dimensional flow of a round jet produced a program to

determine the normal and primary shear Reynolds stresses from linearized CTA output signals, applicable as long as the turbulent intensity was above 25%. His development however, does not allow for the evaluation of the streamwise mean velocity and normal stress separately. These quantities were separated by a return to conventional methods, namely, by using series expansions. Acrivlellis [68] presented a variation of this method which extended the application to include both low and high turbulent flows with no restrictions placed on the intensity level. The difficulty encountered by Rodi of determining $\overline{U}$ and $\overline{u^2}$ individually was apparently eliminated by including the DC reading of the squared AC voltage signal in his analysis. Acrivlellis [69,70] published two additional versions of this method: one which addressed the general problem of determining the time averaged velocity and all Reynolds stresses relative to a streamline based coordinate system and another, where a general analysis was performed in an inertial reference frame. While Acrivlellis's method initially overcomes the problems of the square root operation as shown in Eq. 2.1, it is believed to be based on an incorrect squared AC voltage response equation [71]. Thus, it remains to be seen whether this approach could justifiably replace the conventional method. Tutu and Chevray [66] use the squared signal approach to deal with the rectification of the signal by the sensor in high intensity flows. This error is separate from those errors arising from truncation of the square root series expansion.

Review of Competitive Methods

The resolution of the sensor's voltage response into mean velocity

and Reynolds stress components requires a closed system of equations with the unknown quantities equal to the number of response equations. This is achieved by collecting data from sensors at different angular positions selected partly for convenience but where sensor sensitivity to turbulent velocities is high and aerodynamic interference is negligible. There are essentially two methods found in the literature to measure turbulent flows: the so called rotating wire technique and a method which employs two or three stationary sensors mounted with a prescribed orientation for simultaneous processing of the data. In the first method data is collected at brief intervals as a single sensor is rotated about its probe stem which is usually perpendicular to the flow direction. Fujita and Kovasynay [122] developed the original method of using a continuously rotating, single wire ($\sim 2^{o}$/sec), to measure the Reynolds stresses of a fully developed pipe flow. The most widely used version of this method, however, combines a single slanting sensor (usually 45^{o} to the probe axis) and a single normal sensor to provide a complete documentation of a 3DTBL flow. This method has been used by Bissonnette [33], Pierce and Ezekwe [73], Lohmann [37], Siuru and Logan [74], Hoffmeister [75], and Grande and Kool [76].

Comparatively, the rotating sensor method offers a less complicated arrangement of sensor and supporting electronic equipment. An exact knowledge of the flow direction for probe positioning is not necessary and all the components of the mean velocity and all the turbulent stresses can be obtained for proper sensor positions. However, more extensive calibrations are required (e.g. Hoffmiester [75]) to obtain the directional characteristics of a rotating probe.

Although dual and triple sensor probes appear in the same category, differences in the methods of operation suggest that they be treated separately. Tri-axial probes represent the most recent stage of hot wire/film probe evolution and have proven to be a valuable research tool as shown by Frota and Moffat [77], Frota, Moffat, and Honami [78], Gaulier [79], Gourdon, Costes, and Domenech [80], Zank [81], Rey and Beguier [82], and Gorton and Lakshminarayana [83]. The most common triple sensor probe configurations employ three mutually perpendicular sensors. Lakshminarayana [84] provides an excellent survey of the literature for this method depicting typical probe configurations, and a general analysis is presented for orthogonal and non-orthogonal sensors arrangements. Data processing and instrumentation, along with the calibration techniques are also discussed. A detailed list of the possible sources of errors and corrections is presented for three sensor probes with this list generally applicable to all single and multi-sensor hot wire/film probe configurations as well.

Tri-axial probes offer a similar convenience to the single rotating sensor in that complete documentation of the local mean velocity and Reynolds stress tensor is possible with only one probe intrusion in the flow field. Likewise, only a crude a priori knowledge of the flow direction is necessary but a strong emphasis is placed on probe geometry for obtaining accurate results. A key advantage of this method is that measurements of higher order products of the voltage fluctuations are available for use in correcting lower order processing equations for high intensity flow applications. In addition, this method can provide third and fourth order velocity correlations, such as turbulent energy

with a fluctuating component, to facilitate higher order turbulence modeling.

Disadvantages include its dependence on a more extensive data acquisition system since three channels of output are available, and separate calibrations are required for three sensors. Since the sensors of a tri-axial probe are generally not identical and differences in bridge and other companion circuitry exists, a matching of the sensors' response is usually desirable [77]. Further, the larger probe will generally provide lower spacial resolution of the mesurements particularly in boundary layer regions near a solid surface.

The X-Array

Crossed sensor or x-array probes provide the most conventional means of obtaining the components of the Reynolds stress tensor. Data is processed from a sensor pair, which conceptually defines a plane, at fixed positions. In any one position measurement of a longitudinal and transverse intensity is possible along with the corresponding shear stress. Unlike the other competitive methods, a precise positioning of the sensor plane is required. Measurements obtained at four planar positions are sufficient to generate the complete Reynolds stress tensor. Thus, considerably more work can be involved in measuring the complete flow field and this method is often judged as undesirable for this reason. Although other methods have proven to be as effective in turbulence measurements, the present method is associated with a more extensive background of published literature [52,57,59,60,85-91] and documented success [32,34-36,39,58,92-94].

A geometrically perfect x-array in a horizontal xz plane can provide the $\overline{uu}$, $\overline{ww}$, and $\overline{uw}$ stresses. Similarily, a perfect vertical x-array in an xy plane will yield the $\overline{uu}$, $\overline{vv}$, and $\overline{uv}$ stresses where u, v, and w lie along the x,y, and z axes, respectively. The remaining $\overline{vw}$ shear stress can be obtained by a method attributed to Rodêt and used by Gessner [92]. It involves the combination of data measured at the two planar positions of a perfect slant x-array namely, $\pm 45^{o}$ to the vertical plane. These two positions differ by a 180^{o} rotation about the probe stem when the stem is perpendicular to flow direction. Thus, once the flow direction is known, four traverses of data have to be taken at each floor station to obtain all six components of the Reynolds stress tensor, with the acquisition of the $\overline{vw}$ stress as the primary purpose of the two slant x-array traverses.

Sensor response analyses are usually performed relative to a local streamline based coordinate system where the fluctuating velocities are superimposed on the streamwise mean flow vector. The line bisecting the angle formed by the sensing elements in the sensor plane is colinear with the local tangent to the mean local streamline. For flow situations where such alignment is not possible a complimentary sensor based reference frame is usually necessary [58,90,91] but this adds considerable complexity to the analysis due to the additional mean velocity component terms that must be included in the analysis.

To a lesser extent the x-array method shares some of the disadvantages associated with the tri-axial sensor class when compared to the single rotable wire technique. These include: 1) additional instrumentation to accommodate two channels of output, 2) probe size

with corresponding limits on spacial resolution, 3) possible aerodynamic interference of the sensing element and flow disturbance, 4) unique calibrations for velocity and directional characteristics, and 5) matching of two slightly different sensors. A key advantage of this method, stemming from the requirement that the flow direction be known with the probe aligned with this direction, is that the sensor calibrations can be restricted to a smaller neighborhood of the probe's operating position. This is usually not the case for the tri-axial probe method or the single wire method where sensor calibrations are usually performed over a wider range of angles to successfully account for probe displacement effects and tangential cooling effects. This would be especially important in flows where large skewing of the boundary exists. For this particular flow under investigation, skew angles of up to 30^{o} were measured.

C. Hot Wire/Film Probe Characteristics

Introduction

The interpretation of hot wire/film measurements in a turbulent flow depends on detailed knowledge of the heat loss from the sensors. For steady, uniform flow normal to a heated cylinder, thermal equilibrium requires that the power supplied be balanced by convection, conduction to the prongs, and radiative exchange between the sensor and its surroundings. For most applications in air, sensor operating temperatures ($<300^{o}C$) are such that radiation amounts to a very small percentage of the total heat loss and can be neglected [97]. Although the heat transfer is largely convective, incident flow on a finite

length sensor supported by prongs, gives rise to a complex three-dimensional flow and temperature gradients along the wire resulting in conduction heat loss to the prongs. This has made theoretical analysis difficult and practical application of the CTA more complicated. Despite the numerous studies found in the literature [97-101], no universal heat transfer law for heated cylindrical sensors has been reported.

For steady, incompressible, isothermal, continuum flow, theoretical and experimental research has shown the expression,

$$\overline{E}^2 = A + B_o \overline{U}_e^n \tag{2.2}$$

where

$$\overline{U}_e = \overline{U} f(\alpha, P) , \tag{2.3}$$

can be used to relate the CTA output voltage of electrically heated yawed cylinders to the flow. Other investigators such as Minner and Fox [102] and Elsenaar and Boelsma [32] have used polynominal representations and Gaulier [79] adds an extra term, $C\overline{U}_e$, to Eq. 2.2. Terms A, B_o, n, and P are empirical constants determined for each sensor configuration. The function f is referred to as the cooling law function and as written, describes only the yaw directional characteristics of the sensor. The parameter P represents any modification of the ideal cosine cooling law to correct for the tangential cooling velocity. The constants A and B_o generally depend on the thermal and fluid properties of the flow and thermal properties, resistance and aspect ratio of the sensor [54].

At zero incident flow, parameter A represents the sensor's heat loss by conduction and free convection. For sufficiently small wires however ($Gr \simeq 10^{-6}$ for 5μm diameter wire [54]) the heat loss will occur mostly by conduction through the air and through the prongs which suggests that heat loss at zero flow conditions will be largely independent of sensor orientation [97-99,103,104]. The value of A is usually taken to be the CTA output voltage reading at zero flow conditions with $A = E_o^2$ in Eq. 2.2.

Modification of King's Law

King [101] provided the general form of the Eq. 2.2. He described the convective heat transfer from an electrically heated wire as being linearly dependent on the square root of the velocity. Subsequent work by Collis and Williams [99] indicated a value of n of 0.45 for $0.02 < Re_d < 44$ and 0.51 for $44 < Re_d < 140$, where Re_d is the Reynolds number based on the wire diameter, d. They associated the change in n with the onset of vortex shedding from the cylinder defining $Re_d = 44$ as the critical Reynolds number. Since King's experiments were conducted at Reynolds numbers below this critical value, his value of n of 0.5 clearly differed from the results of Collis and Williams.

Since the work of King [101] and Collis and Williams [99] many different values for this exponent have been reported with consensus only on its qualitative behavior. Davies and Bruun [104], Elsner and Gundlach [105], Bruun [106], Kjellström and Hedberg [107], Rosenberg [108], and Davies [98] all show that the exponent will vary with velocity, decreasing steadily with increasing velocity. Table 2.3

Table 2.3. Comparison of Reported Values of Exponent n

Author	Flow Range $\bar{U}$[ms^{-1}] $\rho\bar{U}$[kg/m^{2}s]	Exponent	Sensor Identification
King [101]	$0.17 < \bar{U} < 9$ ($Re_d < 44$)	0.5	Platinum: Wire no. 1: $\ell/d \simeq 1516$[2] Wire no. 10: $\ell/d \simeq 1286$[2]
Collis, Williams [99]	$0.02 < Re_d < 44$ $44 < Re_d < 140$	0.45 0.51	Platinum, $2070 < \ell/d < 8660$
Davies [98]	$\sim 0 < \bar{U} < 30$	1.0 - 0.40	
Davies, Bruun [104]	$0.2 < \bar{U} < 160$	0.76 - 0.35	Tungsten, $\ell/d = 400$
Kjellström, Hedberg [107]	$47 < \rho\bar{U} < 128$ $27 < \rho\bar{U} < 165$ $33 < \rho\bar{U} < 165$ $55 < \rho\bar{U} < 187$	0.411 - 0.373 0.470 - 0.373 0.509 - 0.425 0.569 - 0.479	DISA 55A25 DISA 55A25 DISA 55A29[3] DISA 55A29[3]
Bruun [106]	$0.4 < \bar{U} < 150$	0.72 - 0.36	Tungsten, $\ell/d \simeq 400$
Rosenberg [108]	$40 < \rho\bar{U} < 240$	0.7 - 0.1[4,1]	Tungsten coated Au/w, $107 < \ell/d < 270$
Elsner, Gundlach [105]	$40 < \bar{U} < 160$	0.500 - 0.475[1]	DISA 55A22
Rasmussen, Larsen, Jorgensen [110]	$3 < \bar{U} < 15$	24 wires calibrated 17 had values from 0.40 - 0.45 with max=0.50, min=0.33	DISA wind vane with tri-axial probe [78]
Gourdon, Costes, Domenech [80]	$0.1 < \bar{U} < 2$	0.52, 0.55, 0.51 in water	DISA 55R91
Klatt [85]	$1 < \bar{U} < 40$ ($Re_d < 13$)	0.42-0.26	DISA x-probes with platinum coated tungsten wires, $\ell/d = 200$

1 taken from graphical results
2 based on length between potential terminals
3 inclined approximately 45°
4 These values were obtained from calibrations with constant static freestream temperature. Subsequent calibrations were performed with constant recovery temperature where

$$T_R = T_{ST} + r\frac{\bar{U}^2}{2C_p}$$

and r = recovery factor = 0.75. As a result, for the No. 8 designated wire, the range of n was collapsed to $0.30 < n < 0.55$.

summarizes the results reported by various authors. The apparent disagreement in the values of the exponent shown indicates that each probe should be calibrated in a velocity range representative of the particular flow of interest. Klatt [85] attributed differences in the exponent among the probes he tested to different amounts of dirt accumulation on the sensors and that values from clean probes tended to concentrate around 0.4.

The variations in the exponent with velocity have been addressed by Bruun [106], Elsner and Gundlach [105], and Kjellström and Hedberg [109]. Bruum shows that a constant value of n can be used in a considerable velocity interval. The limits of this interval, depended on the velocity, and were fixed by specifying a maximum allowable error in the estimated velocity, or as a second criterion, by a maximum allowable error in the estimated slope of the calibration curve (Eq. 2.2). Constants obtained at 30 ms^{-1}, for example, could be used in a velocity range $16 < \overline{U} < 48$ ms^{-1} with a maximum 1% uncertainty in estimated velocity and less than 5% uncertainty for turbulence intensities below 18%. Elsner and Gundlach treated a variable $n = n(\overline{U})$ and derived a logarithmic expression,

$$n = a - \frac{b\overline{U}}{\ln \overline{U}} + \frac{C}{\ln \overline{U}} . \qquad (2.4)$$

They concluded that neglecting the derivative $\frac{\partial n}{\partial \overline{U}}$ in the derivation of Eq. 2.4 resulted in extremely large errors in turbulent intensity (44.5% for the example they presented). Kjellström and Hedberg determine the slope of the calibration curve for each velocity interval and used a

least squares fit to obtain,

$$n = n_{AV} + K[(\rho\bar{U}) - (\rho\bar{U})_{AV}] \quad , \tag{2.5}$$

where $K = -0.0007782$. The term, n_{AV}, was estimated using a least squares fit of the data while $(\rho\bar{U})_{AV}$ was calculated as the logarithmic mean value for the data.

Directional Sensitivity

The basic construction of a hot wire/film probe consists of the sensor(s), prongs or needles to which a sensor of finite length is fastened, and a stem which encases and insulates the prongs that carry the electric signal through contact pins to the probe support. The supporting system can influence the local flow and the sensor's overall response to that flow. Numerous studies have addressed two major effects concerning the directional sensitivity of a sensor:

1) Deviation from the Cosine Law [49,57,58,86,100,103,104,106, 111-115], and
2) Influence of the probe support [57,106,116-120].

Deviation from the Cosine Law

The turbulent velocity correlations beyond the streamwise intensity are measured with sensor(s) yawed to the local flow direction. This requires knowledge of the directional characteristics of the sensors involved. For an infinitely long cylindrical sensor, only the normal velocity component cools the sensor [121] and thus, the cosine law can

be used. However for finite length sensors, the cosine law is inadequate [49,67,86,103,104,111-115] and calibrations are necessary to determine the yawed response of the sensor.

The deviation from the cosine law was studied in detail by Champagne et al. [113]. Temperature measurements were made with an infrared radiometer that revealed slight asymmetries in the temperature distribution along the wire when inclined 55^{o} to the flow. They concluded that the deviation from the cosine law is due to an increase in the convective heat loss attributed to the tangential velocity component.

The net effect of tangential cooling is manifested as an empirical modification of the cosine law to accurately describe the directional response of the sensor. Various models have been proposed by Hinze [54], Davies and Bruun [57,104], Fujita and Kovasnay [122], and Friehe and Schwarz [103].

Hinze gives

$$f(\alpha,k^2) = (\cos^2\alpha + k^2\sin^2\alpha)^{1/2} \quad , \quad 0.1 < k < 0.3; \tag{2.6}$$

Davies and Bruun give

$$f(\alpha,m) = \cos^m\alpha \quad , \quad 0.75 < m < 1.00; \tag{2.7}$$

Fujita and Kovasnay give

$$f(\alpha,\varepsilon) = \cos\alpha + \varepsilon(\cos\alpha - \cos 2\alpha) \quad , \quad 0.0 < \varepsilon < 0.05; \tag{2.8}$$

and Friehe and Schwarz give

$$f(\alpha,b) = [1-b(1 - \cos^{1/2}\alpha)]^2 \quad , \quad 0.7 < b < 1.0; \tag{2.9}$$

The most frequently used cooling laws appear to be those given in Eqs. 2.6 and 2.7 with the former used most often. Table 2.4 lists some of the values of k that have been reported in the literature for wire

Table 2.4 Comparison of Reported Values of k

Author	Velocity (ms^{-1})	Yaw Angle (deg)	ℓ/d	k	Support/Prong Orientation	Probe Identification
Hinze [54]				0.1-0.3		
Bruun [106]	1-60	20-80	400	0.1-0.4(5)	perpendicular	ISVR probe
Bruun [57]	5-60	45	600-200	0.0-0.22	parallel	ISVR probe
	5-60	45	600-200	0.22-0.43	perpendicular	ISVR probe
Webster [115]	4-6	0-360	1456-86	0.11-1.28 (0.02 ± 0.01)	perpendicular	Wallaston wires
Champagne et al. [113]	7-35	0- ± 60	600-200	0.0-0.230 ± 0.04	perpendicular	platinum
Kjellstrom, Hedberg [109]	11-113	35-55	220	$-0.011<k^2<0.0473$	parallel	DISA 55A25 DISA 55A29
Jorgensen [49]	10-30	0-90	250	0.1-0.4(5)	parallel	DISA 55F11
			250	0.1-0.6(5)		DISA 55F31
			18	0.1-0.6(5)		DISA 55F26 (Film)
Muller [58]	12-24	10-85	240	0.05-0.70(5)	parallel	DISA 55P61, X-array
Zank [81]	1-20	15-80	20	0.1-1.0(5)	-	Triaxial hot-film probe

5 Taken from graphical results

and film probes. Generally, the yaw coefficient, k, depends on ℓ/d ratio, velocity, yaw angle, and whether the supporting prongs are normal or parallel to the flow direction.

In summarizing some of the results, larger values of k are shown for a perpendicular support system than for the parallel support system. Bruun [57] and Champagne et al. [113] have shown k decreasing as ℓ/d ratio increases whereas Webster [115] found no such systematic dependence. The effect of isolating the sensor from its prongs on the value of k was shown by Jorgensen [49], who reported smaller values of k for a sensor with plated ends than from a sensor whose active length spanned the entire length between the prongs.

Kjellström and Hedberg's [109] describe the velocity dependence of k for their wire probes by the expression

$$k^2 = 0.0505 - 0.000415\ (\rho\overline{U}) \ , \tag{2.10}$$

while Rodi [67] reports the following values for k:

$$\begin{aligned} k &= 0.007\ (7.5 - \overline{U})^2 \quad && \text{for } \overline{U} \leq 7.5 \text{ m/s} \\ k &= 0 && \text{for } \overline{U} > 7.5 \text{ m/s.} \end{aligned} \tag{2.11}$$

Both Eqs. 2.10 and 2.11 describe k as decreasing with increasing velocity. Müller [58] presents graphical results which show both an increasing and decreasing behavior of k as velocity increases. However, no general dependence of a systematic nature can be made of these data. Müller's results further show an increasing-decreasing variation of k for increasing yaw angle. Jorgensen, on the other hand, shows k mostly decreasing with increasing values of yaw angle.

Comparisons of yaw parameters k and m are presented in Table 2.5 taken from Bruun [57]. Bruun was able to develop a relationship between

Table 2.5 Variations in the Yaw Parameters k and m with Velocity, ℓ/d, and Support Orientation, Bruun [57]

	Parallel support						Perpendicular support					
ℓ/d	200		400		600		200		400		600	
Vel(ms^{-1})	k	m	k	m	k	m	k	m	k	m	k	m
5	0.22	0.93	0.18	0.95	0.05	0.99	0.43	0.76	0.26	0.89	0.25	0.90
10	0.20	0.94	0.13	0.97	0.05	0.99	0.40	0.78	0.28	0.87	0.26	0.90
30	0.17	0.96	0.05	0.99	0	1.00	0.35	0.82	0.27	0.88	0.24	0.91
60	--	--	0	1.00	--	--	0.31	0.85	0.25	0.90	0.22	0.93

these two parameters by comparing two response equations: one using Eq. 2.7 as a cooling law, and the other using Eq. 2.6. He demonstrated that m was approximately equal to a term, A, of the form

$$A = \frac{\cos^2\alpha(1 - k^2)}{\cos^2\alpha(1 - k^2) + k^2} . \tag{2.12}$$

The use of this expression simplified the sensor response equations when compared to those of Champagne et al. [113] which included terms to fourth order in k.

Equation 2.12 can also be obtained by comparing the derivatives of Eq. 2.6 and 2.7 as follows. Identifying each cooling law by subscripts 1 and 2, respectively, gives

$$\frac{df_1}{f_1} = \frac{\cos\alpha \sin\alpha(k^2 - 1)}{f_1^2} d\alpha \tag{2.13}$$

and

$$\frac{df_2}{f_2} = - m\tan\alpha d\alpha . \tag{2.14}$$

Equating coefficients of $d\alpha$ and substituting Eq. 2.6 with the appropriate identity yields

$$- m\tan\alpha = \frac{\cos\alpha \sin\alpha(k^2 - 1)}{\cos^2\alpha + k^2(1 - \cos^2\alpha)} . \tag{2.15}$$

Solving for m, the expression becomes

$$m = \frac{\cos^2\alpha(1 - k^2)}{\cos^2\alpha(1 - k^2) + k^2} . \qquad (2.16)$$

Equation 2.16 is identical to Eq. 2.12 for A = m. Thus, the validity of this result depends on the degree of equivalence that exists in the relative change in f between the two cooling laws for pre-determined values of m and k.

Influence of Probe Support

Probe interference effects can cause errors in hot wire/film measurements whenever the flow direction relative to the sensor's supporting system at any time differs significantly from the position for which the probe was calibrated (the sensor itself being maintained at the same position). Such a difference in these directions usually occurs in high intensity flow or can occur if the probe is pitched to the flow during operation. The latter case is usually not identified with x-array probes since their orientation is usually fixed to the mean flow direction.

Such an effect is easily observed by rotating the probe about the sensor axis. For a normal wire, Hoole and Calvert [118] found that velocities were 20% greater when the probe was inclined $\pm 105^{o}$ to the flow direction. This behavior has largely been attributed to the aerodynamic displacement of the fluid caused by the presence of the supporting system: the acceleration of the fluid around the prongs and stem and the interaction of the wakes produced by these components result in increased heat loss. The former hypothesis is supported by the invisid flow analysis around two infinite cylinders by Gilmore [120] and Norman

[123]. Norman has shown that the wire senses a nonuniform normal velocity along its length, sensing higher values near the prongs. For the probe considered, this nonuniformity resulted in an average velocity 10% higher than the actual incident velocity.

Hoole and Calvert [118] and Gilmore [120] present corrections for the effects discussed above. The most widely used correction formula, following Gilmore, which accounts for both tangential cooling and the sensitivity of the sensor to pitch of it's supporting system is given by Jorgensen [49],

$$\overline{U}_e^2 = \overline{U}_N^2 + k^2\,\overline{U}_T^2 + h^2\,\overline{U}_{BN}^2 \quad . \tag{2.17}$$

Equation 2.17 assumed valid for the instantaneous flow was given as Eq. 2.1. Values of h are shown to lie between 1.0 and 1.2. Neglecting the pitch sensitivity resulted in relative errors between 5 to 12% for the probes used by Jorgensen.

III. EXPERIMENTAL PROGRAM - INSTRUMENTATION AND 3DTBL DIAGNOSTICS

A. Flow Geometry and Flow Field Identification

The pressure-driven 3DTBL flow was generated by a cylinder with a trailing edge placed normal to a flat plate floor. The teardrop shaped body was the same one used in McAllister's 3D near wall similarity studies [27,125] and is shown in Fig. 3.1. The cylinder has a leading edge diameter of nominally 12.7 cm (5.0 in.), is 22.9 cm (9.00 in.) high, and tapers to a sharp trailing edge with an overall length of 29.8 cm (11.75 in.).

This particular geometry produced large crossflow components under a wide range of skewing conditions in the 3DTBL as well as a three-dimensional separation and a junction vortex dominated flow region at the body-floor junction. The total complex flow as characterized by the different flow regions is shown in Fig. 3.2. In this study attention will focus on the pressure-driven 3DTBL flow upstream and around the body but excluding the separating flow.

The laboratory coordinate system for this flow system is also shown in Fig. 3.1. The coordinate system origin is on the floor at the body's leading edge. Positive x_1 is directed downstream, positive x_2 is directed upward from the tunnel floor, and x_3 is directed to form a right hand system (looking downstream, positive x_3 is directed to the right). Floor data stations are identified by an (x_1,x_3) pair of coordinates. Thus $x_1 < 0$ indicates floor stations upstream of the body, $x_1 > 0$ indicates stations downstream of the leading edge, and $x_3 < 0$ indicates stations to the left of the body when looking downstream.

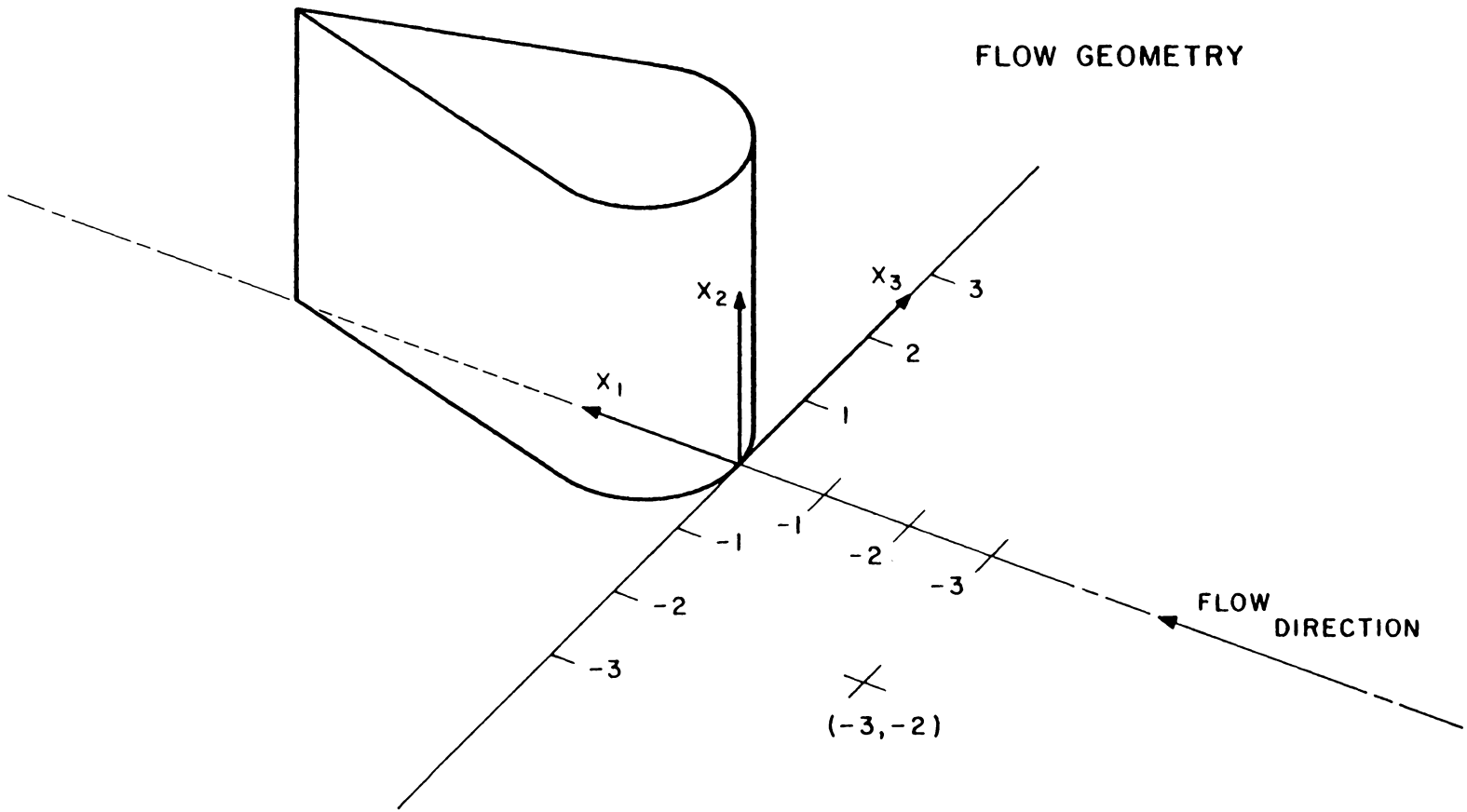

Figure 3.1 The Teardrop Body Used to Generate the Pressure-Driven Flow and Laboratory Coordinate System with Floor Station Identification

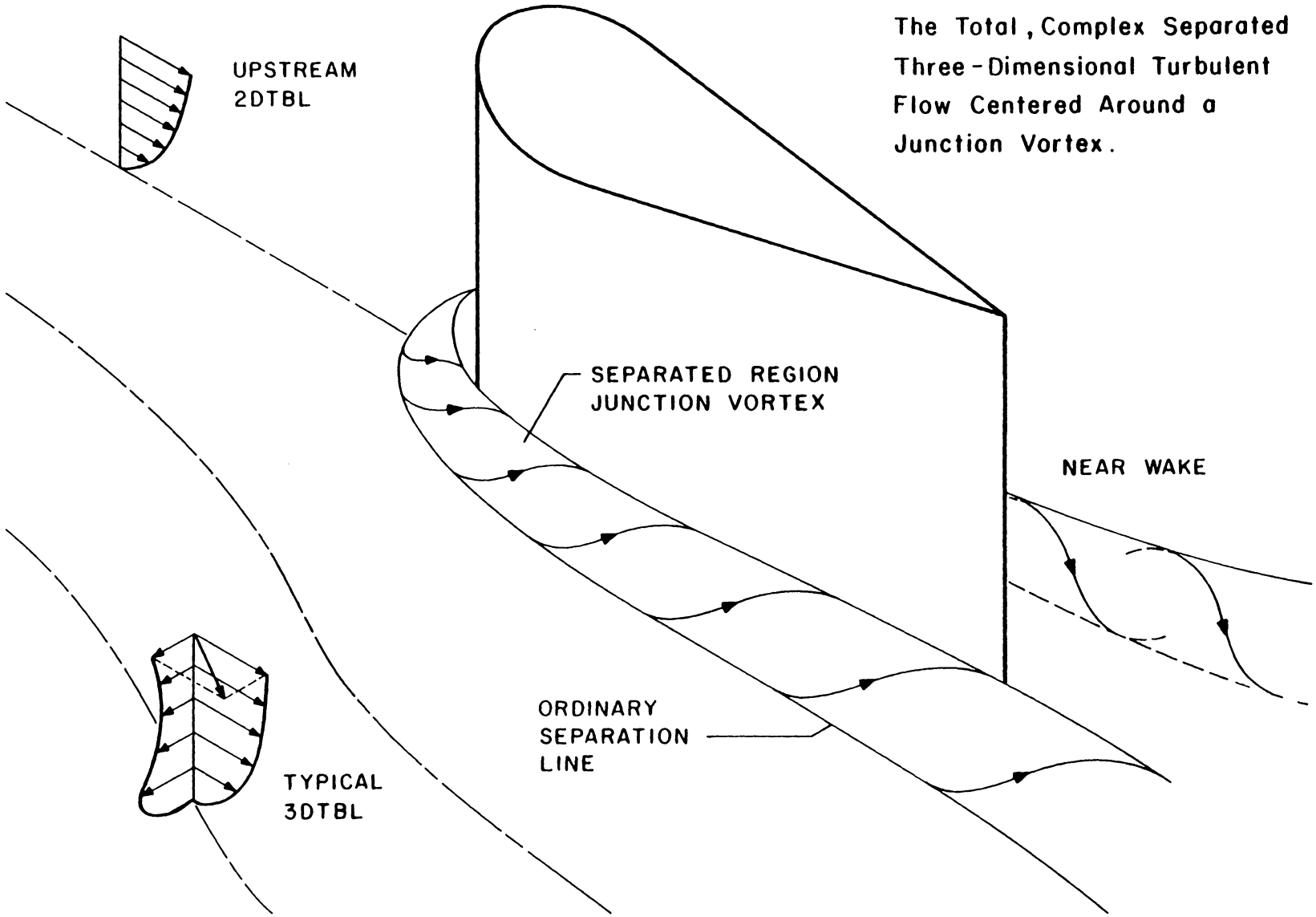

Figure 3.2 Characterization of the Total Complex Flow

Figure 3.3 shows a typical polar velocity plot depicting a flow station with unilateral skewing of the boundary layer where the usual definitions are used. The angle ω is the angle between the laboratory x_1-axis and the freestream velocity vector. Angle β is defined as the angle between the local velocity $\overline{U}$ and the freestream direction with β_w defined at the wall. In Fig. 3.3 all these angles are shown as positive.

B. Wind Tunnel Facility and Operating Conditions

Experiments were conducted in the open circuit, low speed, subsonic wind tunnel shown schematically in Fig. 3.4. This facility has a cross-sectional area of 0.61 by 0.91 m (2 by 3 ft) and provides a large potential core region with a boundary layer nominally four inches thick on the tunnel floor at the test section. The boundary layer growth on the tunnel walls imposed a slight favorable streamwise pressure gradient of approximately 5.66 Pa/m (2.50×10^{-4} psi/ft) on the nominal 2DTBL floor flow. At the tunnel operating speed, this amounted to an approximately 2% increase in the core velocity over the 4.88 m distance leading to the test section. The freestream turbulence intensity at the test section was measured at about 0.5%. The tunnel operates in a suction mode with the flow exhausting into room air.

Ambient air was drawn through a 2.44 by 3.66 m (12 by 8 ft) inlet plenum section which consists of a 0.64 cm (0.25 in.) filter cloth, a 16 by 18 mesh fiberglass screen (average open flow area ratio of 0.71), a matrix of 2.54 cm (1 in.) diameter by 15.24 cm (6 in.) mailing tubes, followed by three additional 16 by 18 mesh fiberglass screens, and a nozzle with a 16 to 1 contraction ratio designed for zero exit acceler-

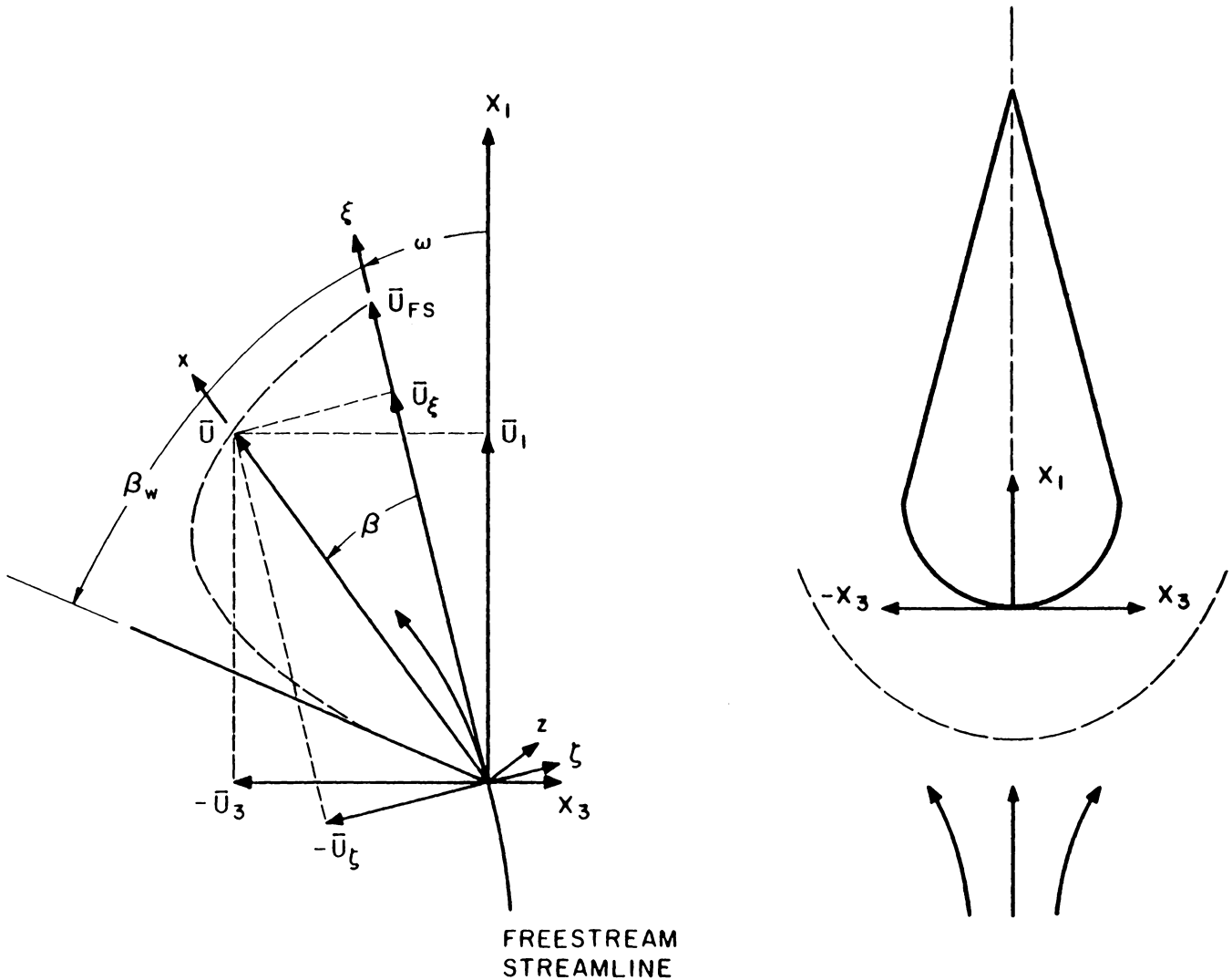

Figure 3.3 Polar Plot Illustrating the Nomenclature Employed

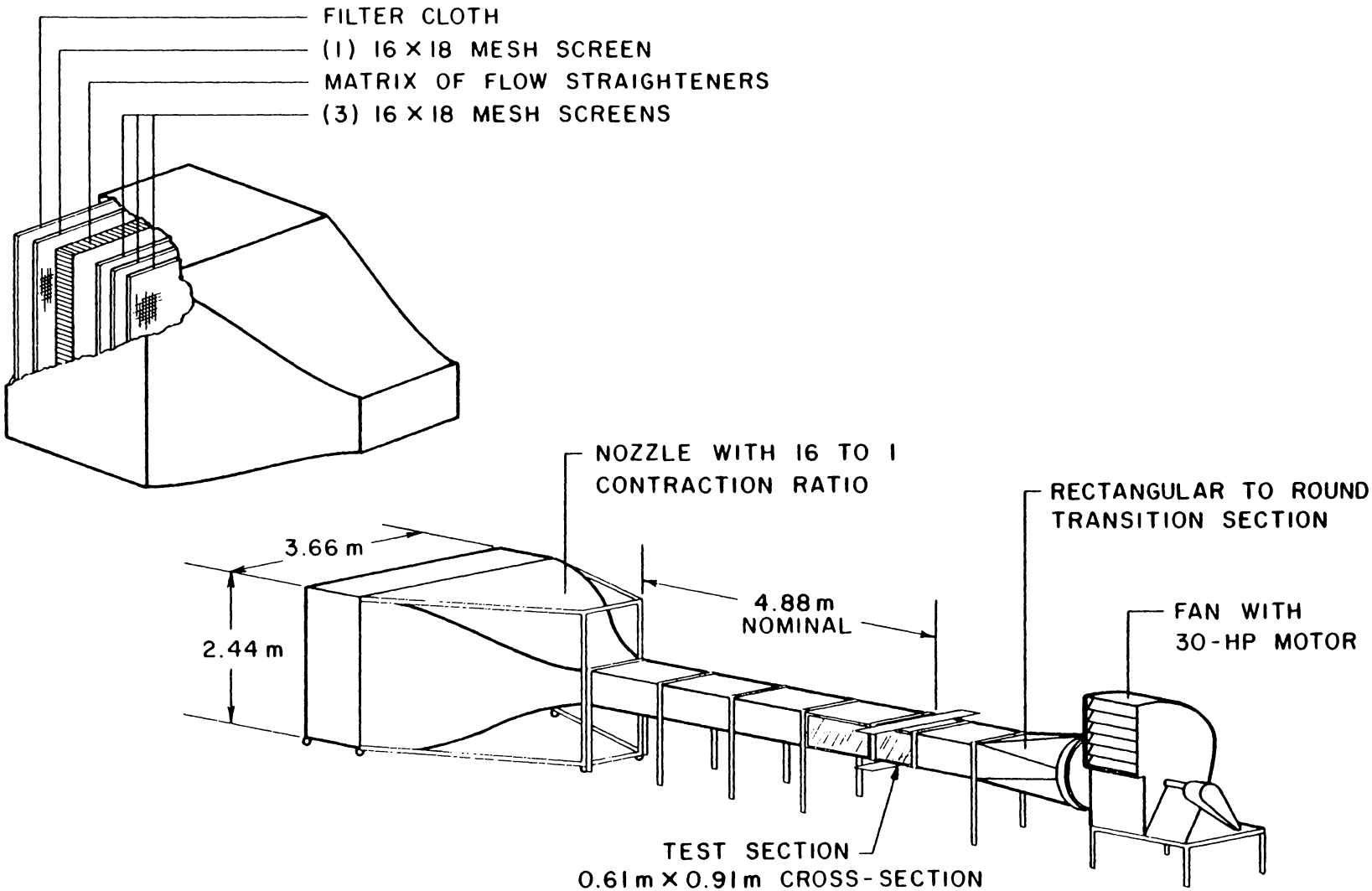

Figure 3.4 Schematic of Wind Tunnel Facility

ation before entering the tunnel. The boundary layer was tripped on all sides at the nozzle exit by small metal rods nominally 2.78 mm (7/64 in.) in diameter. The length of the rectangular channel leading to the test section reference plane is approximately 4.88 m (16 ft). The test section is followed by an additional 1.22 (4 ft) tunnel section which connects to a rectangular to round 3.44 (8 ft) transition piece leading to the centrifugal fan inlet.

The system is powered by a 30-horsepower motor coupled to a Twin City Fan and Blower Company BC-402 Centrifugal fan. The fan is isolated from the tunnel by a foam pad placed at the tunnel-fan junction. A louver mechanism located at the fan exit permitted adjustments of air-speeds up to about 25 m/s. To minimize any possible flow disturbances generated by the fan, two consecutive arrays of nominally 5.08 cm (2 in.) diameter by 15.24 cm (6 in.) cardboard mailing tubes were inserted next to the fan entrance.

The probes were mounted vertically by a traversing mechanism located on the roof of the tunnel. A unislide translational screw allowed for fine adjustments on the probe's vertical position within the boundary layer. Vertical displacements from the wall were measured by a Starrett long travel dial gauge to ± 0.25 mm (± 0.001 in.). Mating worm and spur gears allowed for rotation about the probe's vertical axis and a protractor with vernier scale permitted angular measurements to the nearest 0.2^{o}.

The tunnel was designed to accommodate a variety of diagnostic systems. The test section accommodated sliding floor and roof sections which allowed for lateral positioning of probes as well as the ability

to change these plates for the measurement of static pressure, wall shear stress, and mean velocity and turbulence. For the tunnel calibration experiments the 2.44 m (8 ft) length of the tunnel roof preceding the test section provided instrumentation access every 10.16 cm (4 in.) on the centerline and 10.16 cm (4 in.) intervals off the centerline. These ports provided for a reasonably thorough documentation of the upstream flow.

The tunnel is located in a 280 square meter (3000 ft^2) temperature-controlled laboratory. Since day to day variations in barometric pressure could not be controlled, similitude of the operating conditions was maintained by holding the unit Reynolds number at the tunnel inlet constant, with

$$Re_{unit} = \overline{U}_I / \nu = \text{constant} \qquad (3.1)$$

where $\overline{U}_I$ was measured in the freestream. A value of 1.34×10^6 m^{-1}, ± 0.5% was used throughout the experimental program. Nearly all the data were obtained at room temperatures in the range of 26 ± 1°C (79 ± 2°F). Temperature and barometric pressure uncertainites were taken to be ± 0.56°C (±1°F) and ± 0.254 mm (±0.01 in.) of mercury, respectively.

C. Positioning of the Teardrop Body

In the earlier near-wall similarity work of Pierce and McAllister [27,125], the difficulties in obtaining direct force wall shear measurements in a three-dimensional flow made it necessary to make all measurements at a fixed floor station while positioning the body. The extremes

in body motion were 20.3 cm (8 in.) in the transverse direction (relative to a 91.4 cm (36.0 in.) wide tunnel) and 30.5 cm (12.0 in.) in the longitudinal direction (relative to approximately 488 cm (192 in.) of floor upstream of the test section). In this earlier work, velocity profiles were taken over the local wall shear station ensuring self-consistent data as required for near-wall similarity studies.

In the context of a standard test case, not only must the data at each station be self-consistent but the entire flow field viewed collectively must be self-consistent as well. To accommodate the range of data stations reported in this study, some body motion was required. While a traverse repositioning of the probe in the transverse direction allowed all measurements to be made with the body on the tunnel centerline, a longitudinal movement along the centerline of up to 3.05 cm (12 in.) was necessary. The resulting uncertainty in the coordinates of a data station from both the transverse movement of the traverse mechanism and the longitudinal positioning of the body was estimated at ± 0.3 cm (0.125 in.).

The relatively long flow distance upstream of the test section resulted in a well developed boundary layer which changed very slowly with longitudinal distance within the test section. This was the rational behind allowing relatively modest longitudinal displacement of the body in this region of flow.

A study of the possible effects of longitudinal movement of the body on the mean flow was made. Figures 3.5-3.7 compare mean velocity profiles at stations (-7,0) and (-7,-8) to demonstrate the effects of moving the body 30.5 cm along the tunnel centerline in the test section

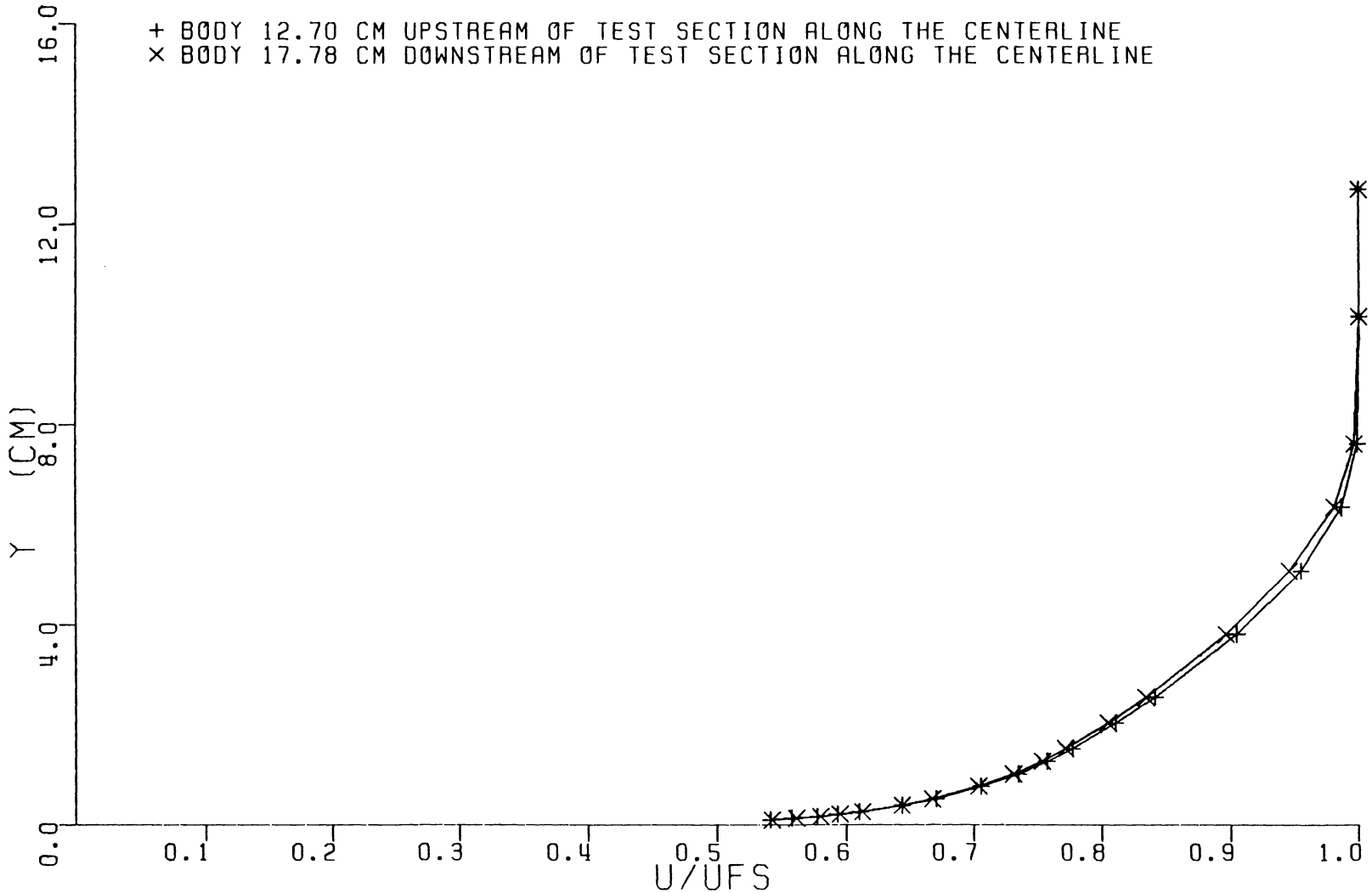

FIGURE 3.5. EFFECT OF BODY POSITION ON VELOCITY MAGNITUDE AT STATION (-7,-8)

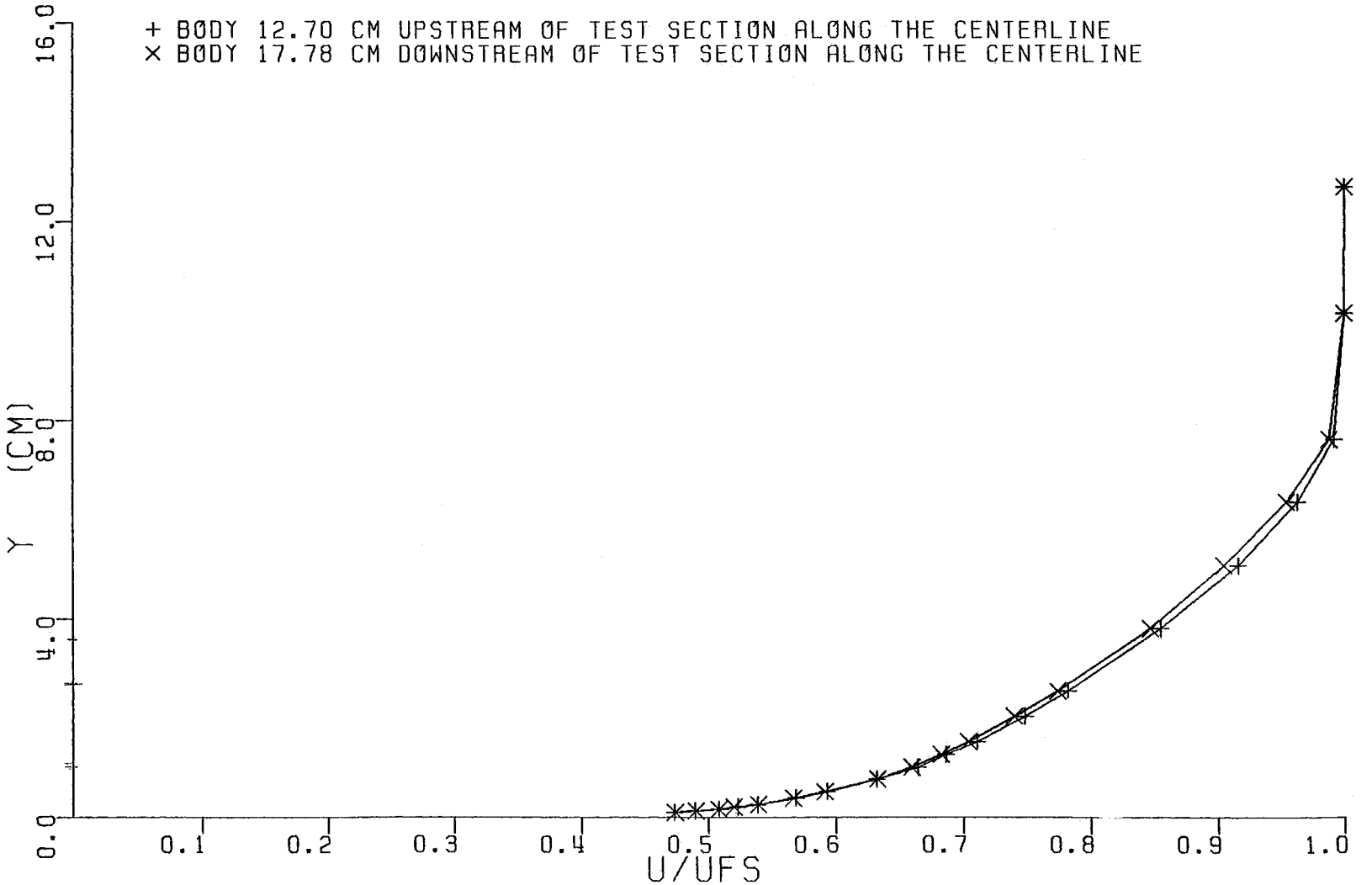

FIGURE 3.6. EFFECT OF BODY POSITION ON VELOCITY MAGNITUDE AT STATION (-7,0)

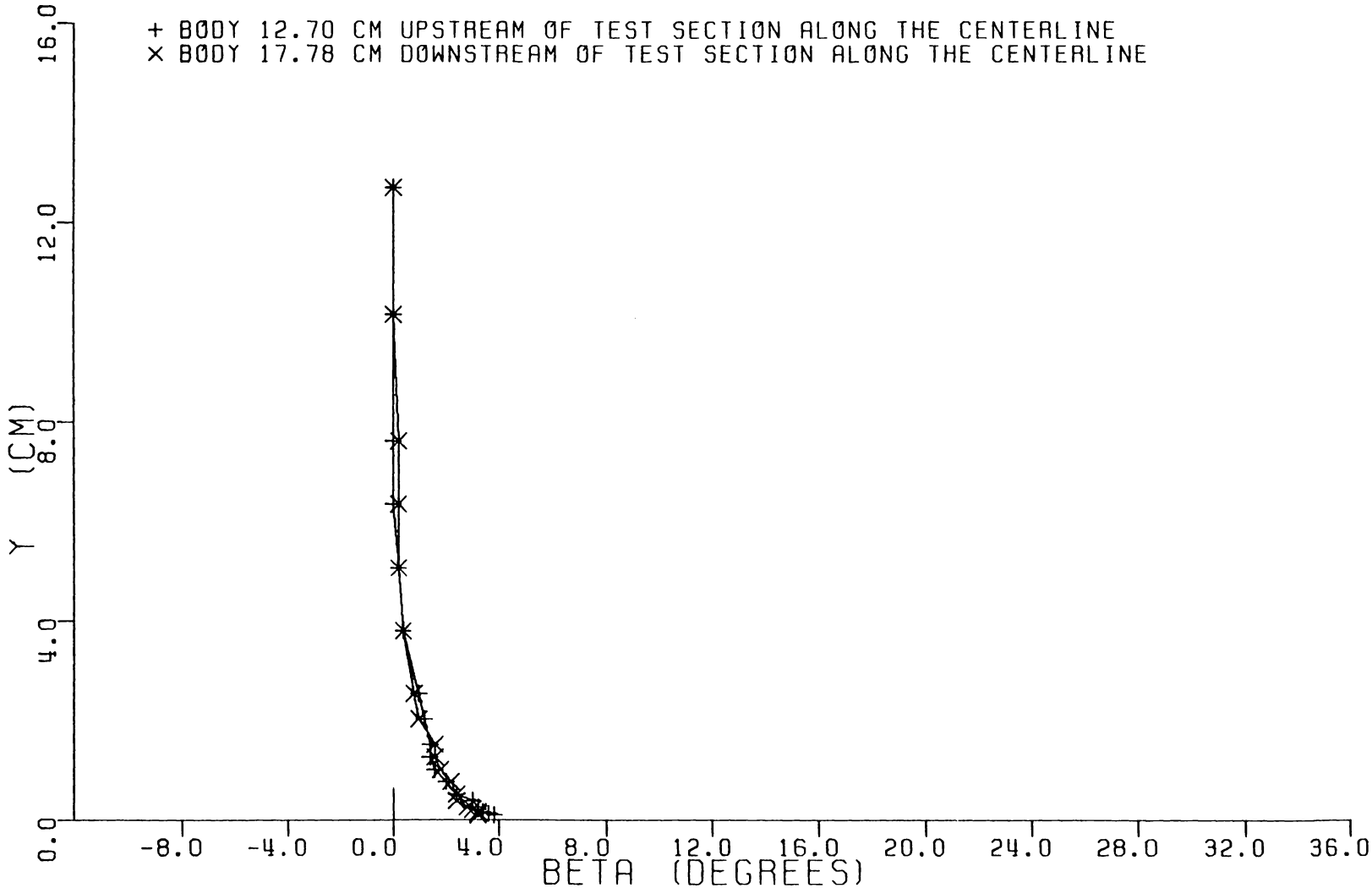

FIGURE 3.7. EFFECT OF BODY POSITION ON VELOCITY DIRECTION AT STATION (-7,-8)

region. These data were measured by a cobra probe with

1) the measuring station fixed at the center of the test section and the body positioned downstream of this point, and
2) the measuring station fixed 30.5 cm upstream of the center of the test section with the body positioned downstream of this point.

The results show very small differences in mean velocity magnitude and direction and suggest the longitudinal movements of the body up to 30.5 cm have a neglible influence on these 3DTBL flow measurements.

D. Data Stations

Initial Plane and Edge Conditions

The initial condition plane and data stations are shown in Fig. 3.8. The initial condition plane is located 24 inches upstream of the body's leading edge at x_1 = -24 in. Profiles of mean velocity and of the six Reynolds stresses were measured at floor stations (-24,8), (-24,0), (-24,-4), and (-24,-8). Repeated profiles of mean velocity were taken at stations (-24,-4) and (-24,-8).

The freestream velocity magnitude and direction was measured at 47 stations, 12.7 cm (5 in.) from the floor, beginning with the initial plane and extending downstream to the forward quadrant of the pressure-driven 3DTBL. In addition, 6 measurements of the edge condition were taken in the adjacent quadrant to check the degree of symmetry of the freestream field. These locations are also shown in Fig. 3.8. In establishing this edge condition two sets of data were obtained by two different methods. For the first set of data, both the magnitude and

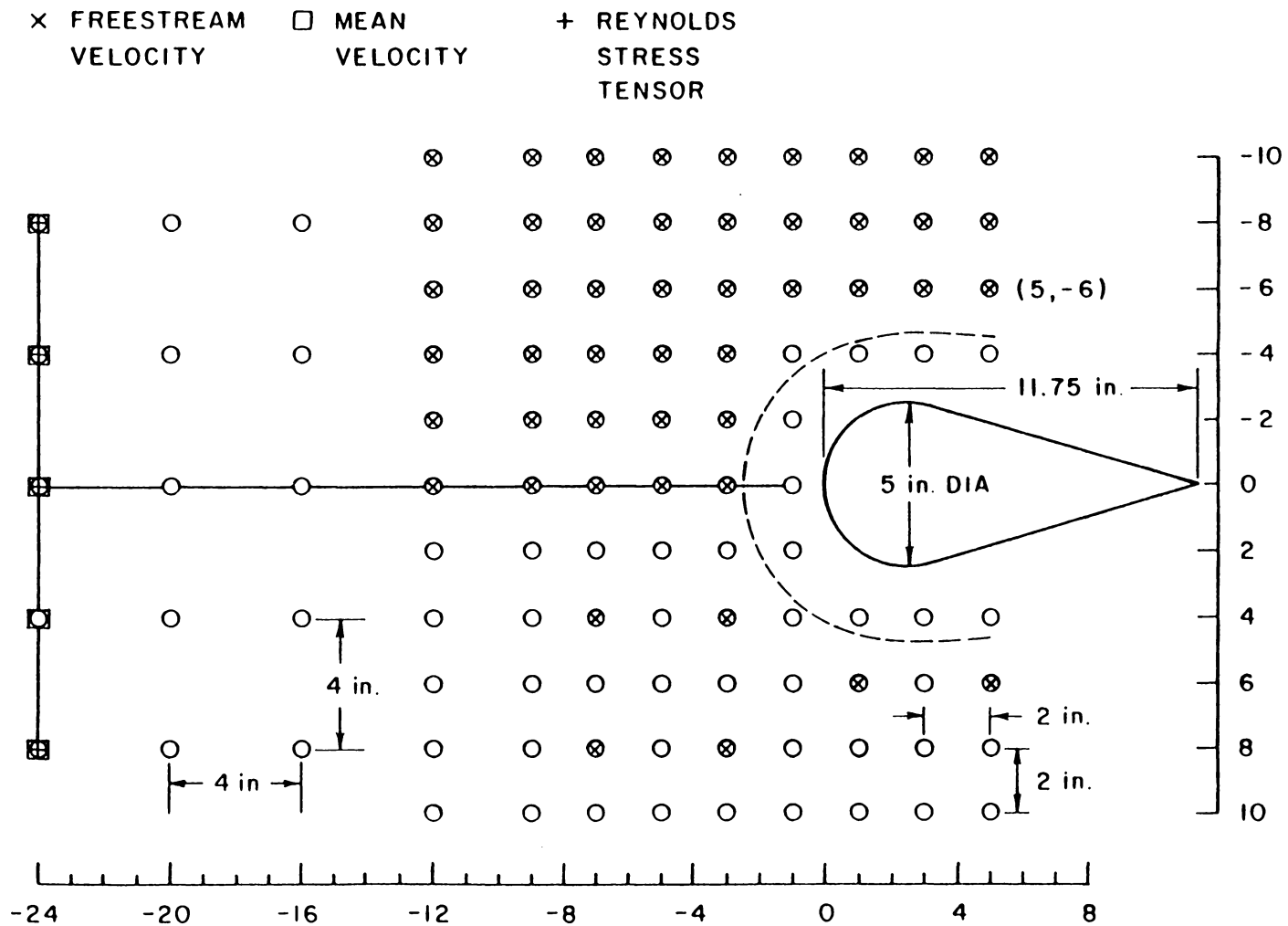

Figure 3.8 Wall Grid Illustrating the Initial Condition Plane and Edge Condition Data Stations

direction of the mean velocity were obtained with a single hot film. In the second set of measurements, a three-hole claw probe measured the flow angle and a Pitot-static probe measured the magnitude of the free-stream velocity. The results from both methods are compared in Chapter VII.

Three-Dimensional Turbulent Boundary Layer Flow Field

The 3DTBL mean velocity profile, Reynolds stress tensor, and wall shear measurement stations are shown in Fig. 3.9. Measurements of mean velocity and wall shear magnitude and direction were made at 15 stations. Six of these 15 mean velocity profiles were repeated and 8 repeated measurements of wall shear stress were also made. In addition, 3 mean velocity profiles at stations (-3,2), (-7,6), and (-7,8) were taken in the adjacent foreward quadrant of the flow to determine the degree of symmetry of the 3DTBL flow. Thus, a total of 24 3DTBL mean velocity profiles and 23 wall shear measurements are reported in all. The Preston tube results will be compared to the direct force wall shear measurements reported by Pierce and McAllister [27,125].

All six components of the Reynolds stress tensor were measured at 10 stations as indicated in Fig. 3.9. At two of these stations, (-3,-2) and (-7,-6), which were associated with large and small amounts of skewing, measurements of the complete stress tensor were repeated. The measurement of all the turbulent stresses required 4 traverses at each floor station combining the measurements of the horizontal x-array, the vertical x-array, and the two positions of the slant x-array. Each x-array allowed for the measurement of the $\overline{uu}$ stress and with the slant x-

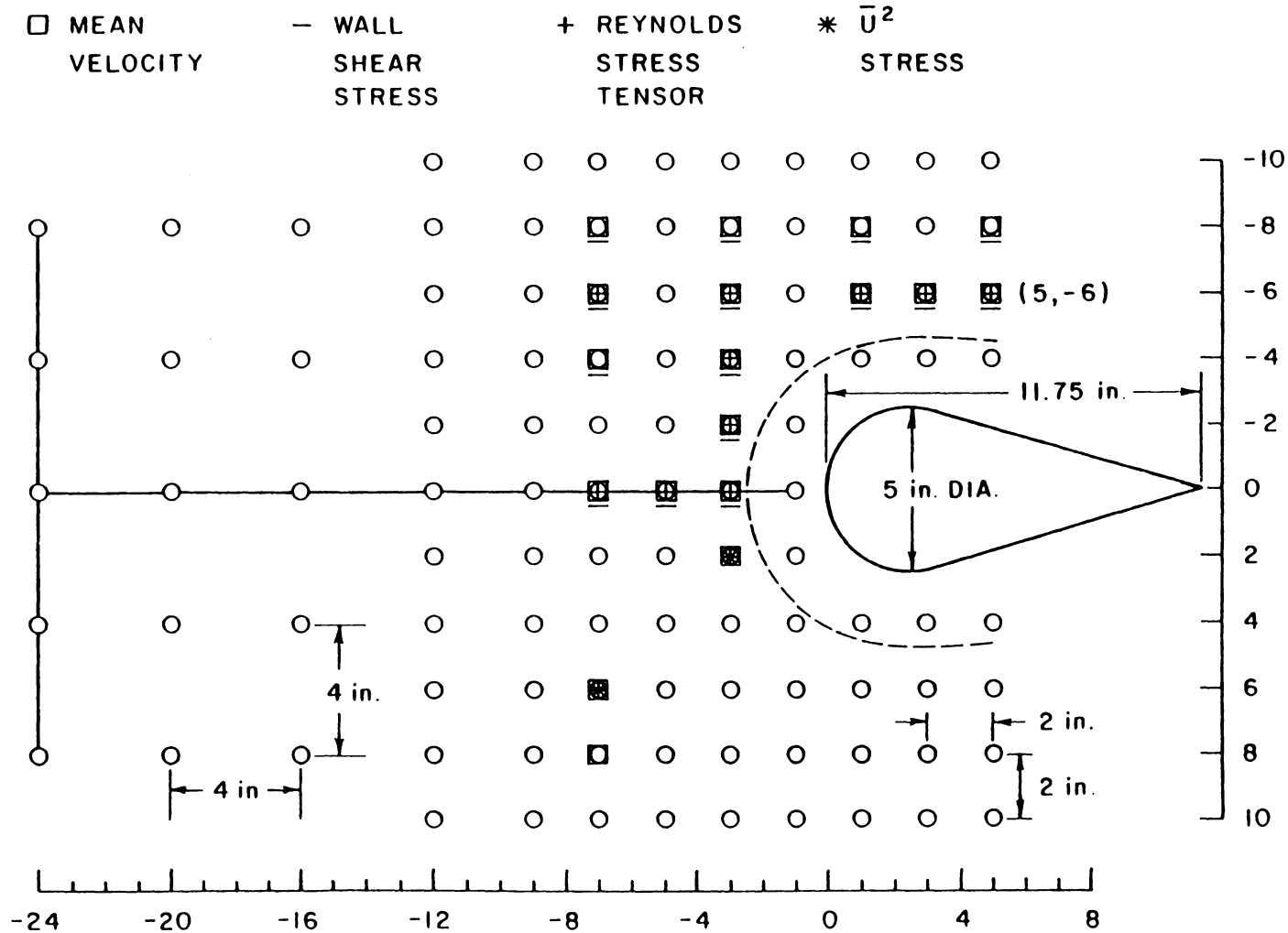

Figure 3.9 Wall Grid Illustrating the 3DTBL Mean Velocity, Wall Shear Stress, and Reynolds Stress Data Stations

array is was possible to obtain redundant shear stresses, $\overline{uv}$ and $\overline{uw}$, and the turbulent kinetic energy at each station. To check the level of symmetry present in the turbulent flow field, measurements of the $\overline{uu}$ stress were taken at stations (-3,2) and (-7,6). In addition to turbulence quantities, each x-array allowed for two measurements of local mean velocity magnitude (one from each sensor). Thus a total of 8 measurements of the mean velocity profiles were available in addition to the single film measurements at each station. A general mean velocity correction formula is derived in Chapter IV and was used to correct each mean velocity measurement for turbulence effects. While mean velocity turbulence corrections are usually neglected in a nominally low intensity flow as studied here, it was convenient to examine such corrections to gain an indication of their importance.

E. Instrumentation

A hot wire/film CTA was the heart of the data acquisition system used in measuring the 3DTBL flow. Despite its limitations, the CTA is still reguarded as the main diagnostic tool for turbulence measurements and provides the most exhaustively studied and probably the best means for measuring turbulent flows. With electronic compensation, both wires and films can obtain a flat response beyond the frequency content of typical turbulent flows. Detailed analysis and discussions concerning the operation of the CTA are presented in [41,46,50,55,126-130].

Mean velocity and turbulence quantities were measured with two channels of a DISA 55M modular CTA system [46]. Each channel was equipped with a 55M01 main unit, 55M10 standard bridge with a cable

compensation unit, and used in conjunction with a 55M25 linearizer [45]. A DISA 55B25 turbulence processor [43] provided a variety of signal combinations including $\overline{(e_a + e_b)^2}$, $\overline{(e_a - e_b)^2}$, and $\overline{(e_a + e_b)(e_a - e_b)}$ for x-array applications, with time constants of up to 100 seconds. These data were read from DANA series 5100 5 1/2 digital multimeters [132]. A DISA 55D35 RMS voltmeter [47] was used in parallel with the turbulence processor to continuously monitor and compare selected mean square signals from both channels. Mean (DC) voltage levels for each channel were measured with DISA 55D31 3 1/2 digit voltmeters [131] which also provided a wide range of time constants.

Linearized DC voltage levels generally ranged from 2-9 V and were taken with an instrument least count of 0.01 V. Nearly all these mean velocity data were obtained with a time constant of 30 seconds. The readability and stability of the measurements suggested an uncertainty of ± 0.04 V. Turbulence data were in the range of 0-1.5 V and were usually taken with the instrument least count of 0.001 V. These data were exposed to time constants of either 30 or 100 seconds depending on the stability of the reading where the uncertainty was estimated at ± 0.006 V. In the neighborhood of flow separation however, the uncertainty in the reading could be as high as ± 0.020 V.

Preston tube and pressure probe measurements were made with Datametrics model 1400 electronic manometers [133] with Gould Type 590 pressure transducers [134]. The electronic manometers were modified with damping circuits which provided a more stable reading. These units were calibrated periodically throughout the study using a Microtector

electronic point gage manometer manufactured by Dwyer Instruments Inc. which served as the laboratory pressure standard. The uncertainty in the pressure measurements was estimated at ± 0.051 mm (± 0.002 in.) of water.

F. Probe Geometry and Measuring Techniques

Introduction

Since the CTA bridge circuitry and compensating electronics are capable of measuring signals with very high frequency content, the practical upper limit of frequency response in the measuring system is set by the frequency response characteristics of sensing element. Typical sensors are either wire or film depending on the application.

Wire sensors are much smaller than film sensors, with wires usually 5 μm (0.0002 in.) in diameter, while films are typically 25 or 51 μm (0.001 or 0.002 in.) in diameter. Cylindrical films overcome some of the deficiencies of hot wires which are more suseptable to strain, breakage, and shifts in calibration due to environmental contamination. The larger films are more rugged and less sensitive to contamination than wires, and this feature is desirable when conducting experiments in large tunnels where the sensor is exposed to a flow for long periods of time. Films, however, exhibit inferior frequency response characteristics when compared to wires [127,129] and this is attributed to the substrate or backing material in the film sensor [130]. While wires are identified with a flatter response curve extending to higher frequencies, an extensive study by Taslin, Kline, and Moffat [87] has shown that 51 μm diameter cylindrical films in x-arrays gave Reynolds

stress values within 2% of 5 μm diameter x-array wire probes. This small error was accepted in favor of the strength and stability of the cylindrical film sensor. The performance of the 51 μm diameter film sensors used in this study was compared with that of a 4 μm diameter wire at stations (-3,-2) and (-7,-6). The results are presented in Chapter VII.

Hot Film Probes

Three hot film x-array probes and a single hot film probe were used to measure the Reynolds stress and mean velocity fields, respectively. A standard TSI model 1240-20 horizontal x-array and a standard TSI model 1210-20 single film probe were used along with a TSI model 1241BA-20 vertical and model 1240AG-20 slant x-array probes. The latter two arrays were specially designed to accommodate a perpendicular probe support orientation to the flow with a minimum of aerodynamic interference of the sensing elements. Two TSI 1240-20 horizontal x-arrays were used due to damage inadvertently inflicted on the first probe during a profile run.

The x-array probes are pictured in Figs. 3.10-3.12. The sensing elements are standard -20 films consisting of platinum coated quartz cylinders with a nominal diameter of 51 μm (0.002 in.) and a length-to-diameter-ratio of about 20 based on an active length of 1.02 mm (0.040 in.). For the vertical and slant x-arrays, the prong tips were bent to ensure a clear line of sight for each sensor, freeing the sensors of interference from any of the sensors' supporting material. The measured specifications of probe geometry are given in Table 3.1 with the spacial

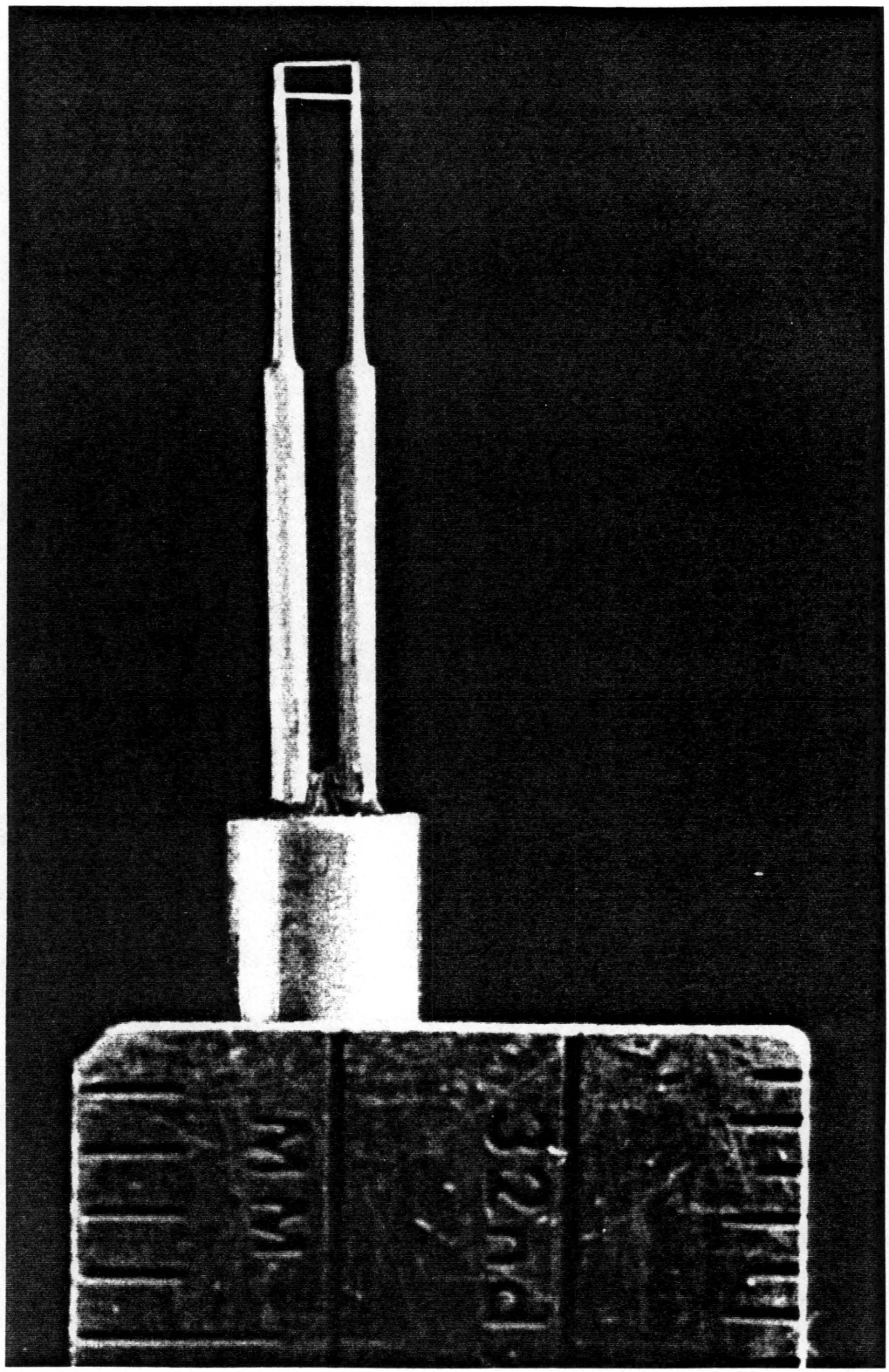

Figure 3.10 The Horizontal X-Array Probe

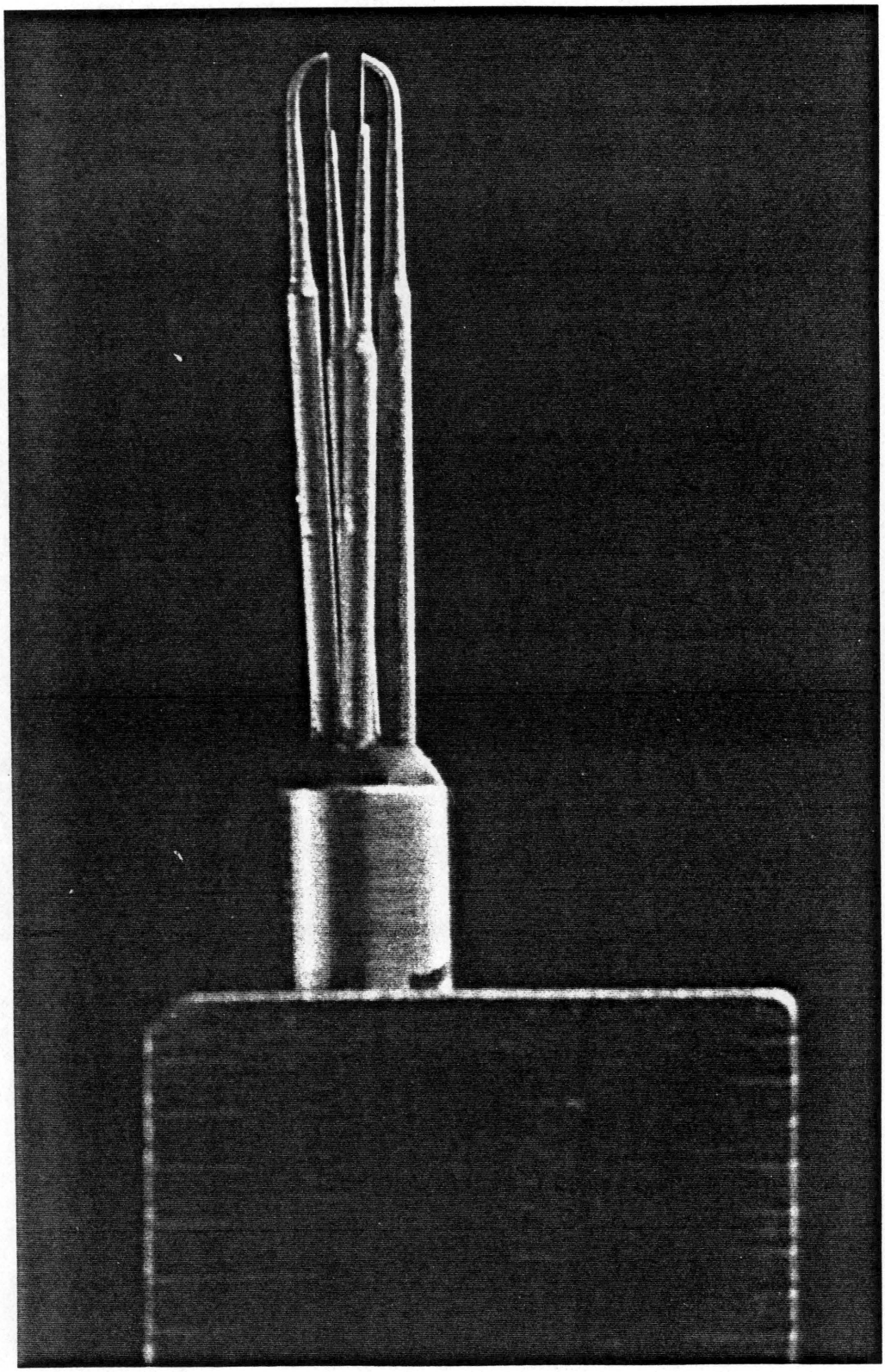

Figure 3.11 The Vertical X-Array Probe

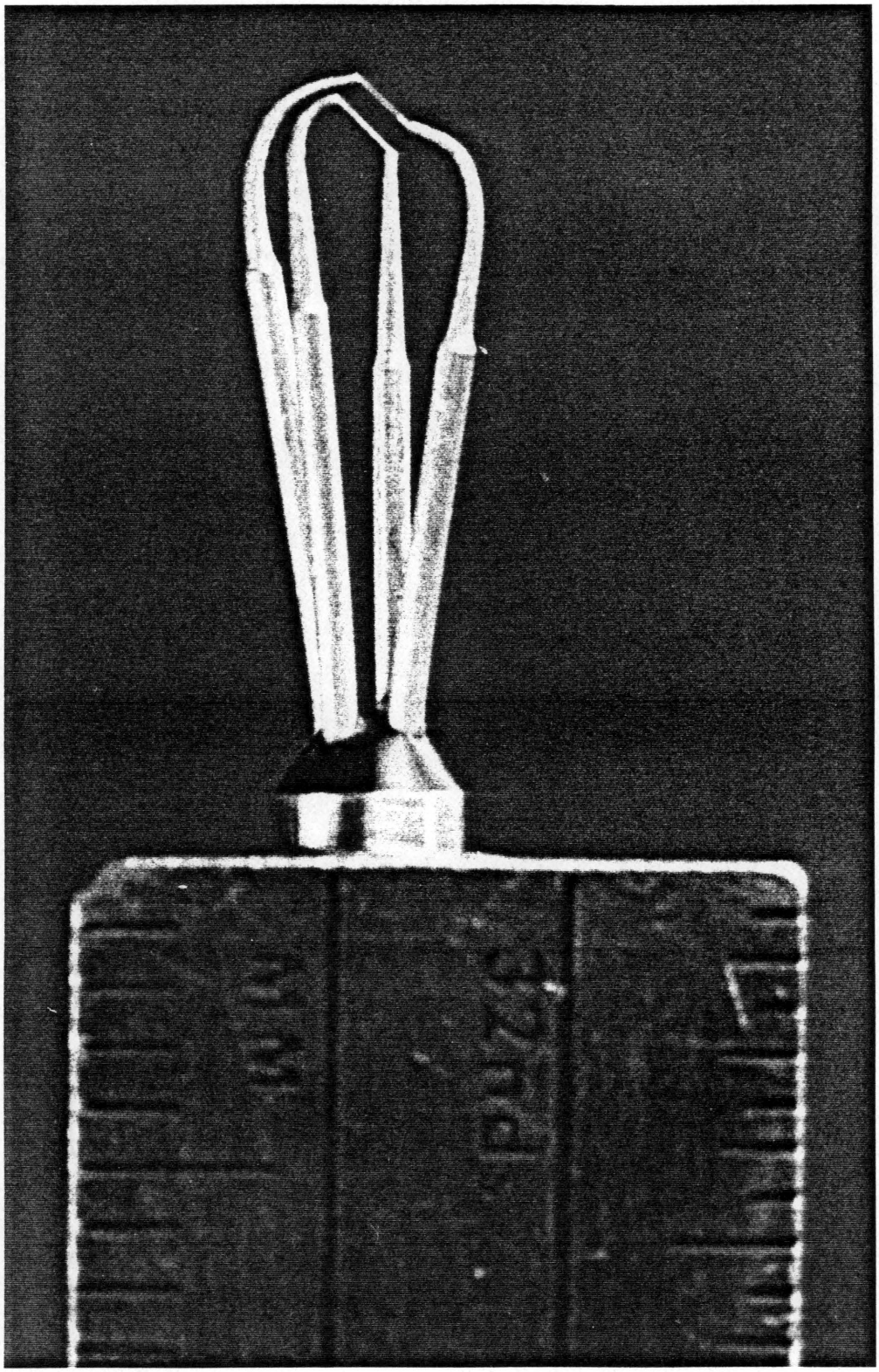

Figure 3.12 The Slant X-Array Probe

Table 3.1 Measured Values of Probe Geometry for the Various X-Arrays

X-Array	$(\gamma_x, \alpha)^*$, Degrees		c^{**}, mm
	Sensor a	Sensor b	
Horizontal, Probe 1	(90.0,44.5)	(-90.0,44.5)	0.289
Horizontal, Probe 2	(90.0,45.0)	(-90.0,45.0)	0.270
Vertical	(3.0,43.0)	(-180.0,42.0)	0.734
Slant, Position 1	(45.0,45.0)	(-135.0, 45.0)	0.664
Slant, Position 2	(135.0,45.0)	(-45.0,45.0)	0.664

* Uncertainty estimated at ± 0.5^o for each angle.

** Vertical distance from probe tip to assumed point of measurement. Uncertainty estimated at ± 0.02 mm.

definitions defined in Fig. 3.13. Sensor geometry is defined in the sensor xyz coordinate system as shown in Fig. 3.13 where x, y, and z axes are directed in the $\overline{U}$, $\overline{V}$, and $\overline{W}$ velocity component directions and form a right-handed coordinate system. Both the sensor xyz and local streamline $x^*y^*z^*$ systems shown in Fig. 4.1 will be discussed in detail in Chapter IV. Deviations from geometrically perfect construction and the effects of such imperfections on the computed Reynolds stress tensor will also be discussed in Chapter IV. The point of measurement was taken to be at the geometric center of the x-configuration at a distance midway between the planes of the sensors.

To study the effects of self-induced turbulence by the probe due to vortex shedding or vibration of the probe components, each probe was checked in the flow. It was important to determine if these disturbances, which could occur in the frequency range of the turbulent flow, would have a significant effect on the turbulence measurements. The components of a probe which could induce such flow disturbances are the probe stem and support, prongs, and the sensor. For the typical component diameters used by the probes, the shedding frequencies, based on the Strouhal number, were found to range between 1 to 100 KHz, approximately.

An experiment was devised in which the output voltage signal from an individual sensor was fed directly to a FFT analyzer and monitored simultaneously on an oscilloscope. With the probe in its operating position the sensors were tested in two flow regions of the wind tunnel flow: a) the low intensity potential core in the freestream and b) the 2DTBL flow region. The frequency spectrum showed no significant con-

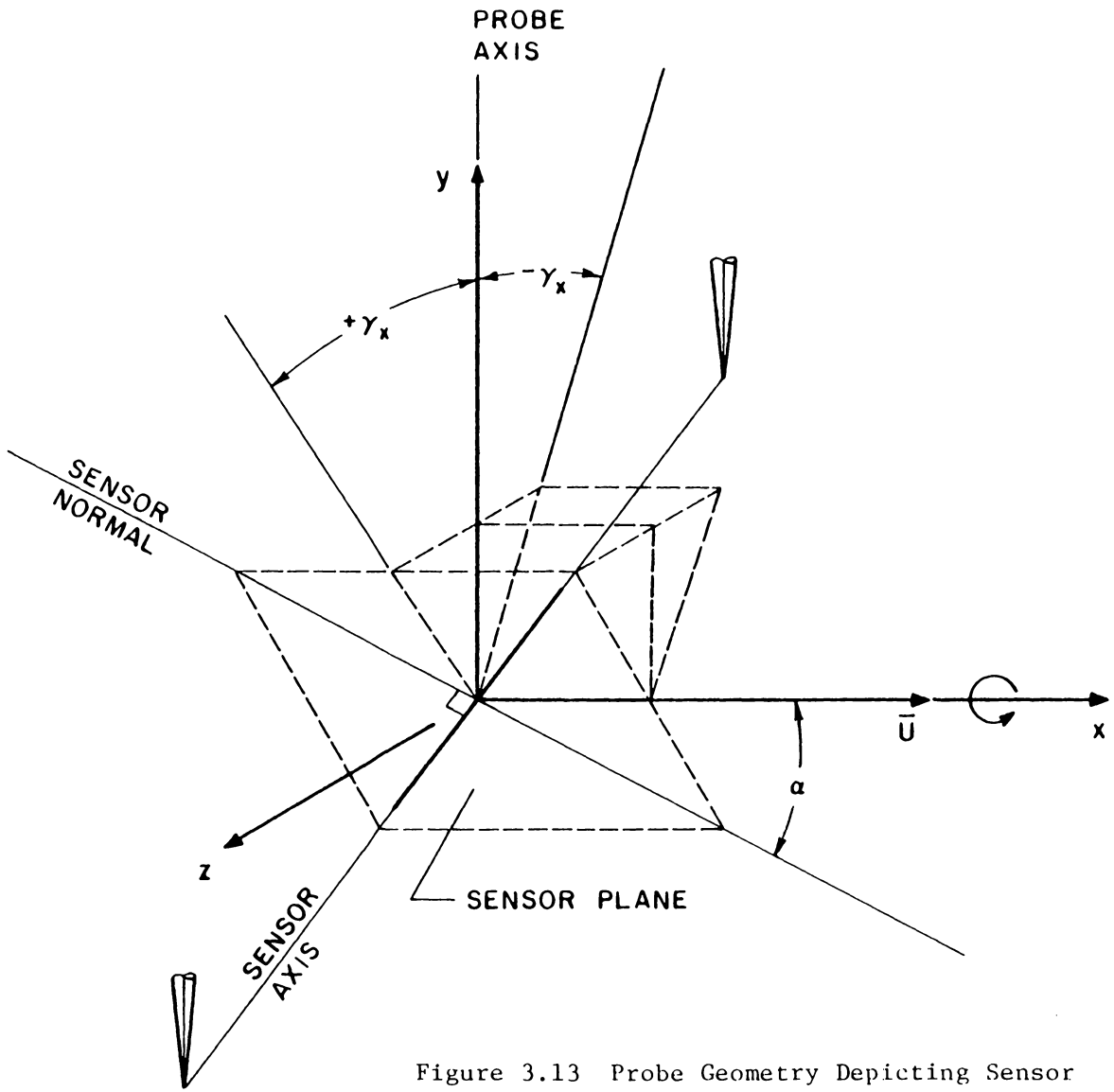

Figure 3.13 Probe Geometry Depicting Sensor Plane Orientation

tributions at frequencies identified with the probe components. The magnitude of the turbulent stresses in the freestream measured by the various probes was of the order identified with the freestream turbulence level of the tunnel flow itself. Thus, it is believed that any self-induced flow disturbances that might have been present were sufficiently small so as to have no significant effect on the turbulent boundary layer measurements.

Positioning of the Probe from the Wall

A method was developed to consistently position the probe from the wall without contacting the wall and damaging the hot film probe. A highly polished aluminum block of known height was placed on the tunnel floor directly under the probe's tip. A carefully positioned horizontal-vertical cathetometer with a 10-power eyepiece was used to establish a reference line of known distance from the wall by aligning a horizontal reticle line with the top edge of the block. The block was removed and the probe lowered until the needle tip appeared to touch the horizontal reference line. In developing this technique, probe position was verified at least 60 times, using a dummy probe that sensed wall contact through an electric circuit. The uncertainty in locating the wall by this method was estimated at ± 0.051 mm (± 0.002 in.) with 20/1 odds. Since the size of the tunnel and magnitude of volume flow rate created sufficient suction to slightly displace the roof and floor of the tunnel, the reference line was determined with the tunnel turned on and the body in place for all the profiles taken.

Close proximity to a solid boundary can affect any diagnostic probe. The smaller size of a single sensor probe gives it a better spacial resolution than for x-arrays and is less effected by the local velocity gradients. Nevertheless, all the measurements made in the vicinity of the wall were expected to be influenced by the local velocity gradients to some degree. The reader is referred to Gessner and Moller [51], and Sandborn [53] for discussions concerning the effects of velocity gradients on the response of sensors.

An additional effect on heated cylinders near a wall has been identified by Wills [135] and Oka and Kostic [136]. This effect is caused by the presence of the cooler wall surface and results in an increased heat loss and hence a larger cooling velocity perceived by the sensor. Such an effect is usually identified for heated sensors below a value of $y^+ \simeq 10$. In the present study, the smallest distance from the wall corresponded to a value of $y^+ \simeq 30$ and hence no correction of this kind was necessary.

Flow Direction and Probe Alignment

Flow angles in planes parallel to the tunnel floor (yaw) were measured with a single hot film probe using the bisector method. The bisector method is similiar to the rotated wire technique [137] which in principle can be used to determine the relative mean flow direction. The basic method has been used by Müller [39,58], Pierce and Duerson [93,94], and Vagt and Fernholz [137] to measure turbulent flows. Vagt and Fernholz report that the bisector method can be used in flow regions not to close to the wall where the turbulence level is below 20%.

At a fixed distance y from the wall, the local flow direction was taken to be the mean of two protractor readings where for each measurement the sensor lies on opposite sides of the parallel position. The first reading was obtained with the sensor offset approximately 20^{o}. The second position was found by rotating the probe across the parallel position until an equal voltage was indicated on the voltmeter. The mean voltage level could be determined accurately by electronically integrating the signal over time with time constants of up to 100 seconds. This procedure assumes symmetic flow-angle characteristics of the sensor and this was verified for the single film used. Repeated measurements suggested a yaw angle uncertainty of $\pm$ 0.5^{o}.

The bisector found when the two signals from the sensor were equal was interpreted as the local mean yaw angle and which defined the local orientation of the sensor coordinate system as shown in Fig. 3.14. As will be discussed in Chapter IV, the $x^{*}y^{*}z^{*}$ coordinate system is the local streamline system and in this case it differs from the sensor xyz system, shown in Fig. 3.13, through the pitch angle, $\overline{\psi}_{z}^{*}$, measured in the vertical plane. The situation as shown in Fig. 3.14 amounts to a partial alignment of the probe with the flow due to the existence of small $\overline{V}$ ($\overline{U}_{2}$) components of velocity within the 3DTBL flow. The possible effects of pitch angle and turbulence on the flow angle measurement are analyzed in Appendix D.

After measuring the yaw distribution throughout the 3DTBL flow, the magnitude of the mean velocities and Reynolds stresses were measured with the probes aligned with these local yaw directions as shown in Fig. 3.14. Thus, the $\overline{W}$ components vanish by definition and measurements

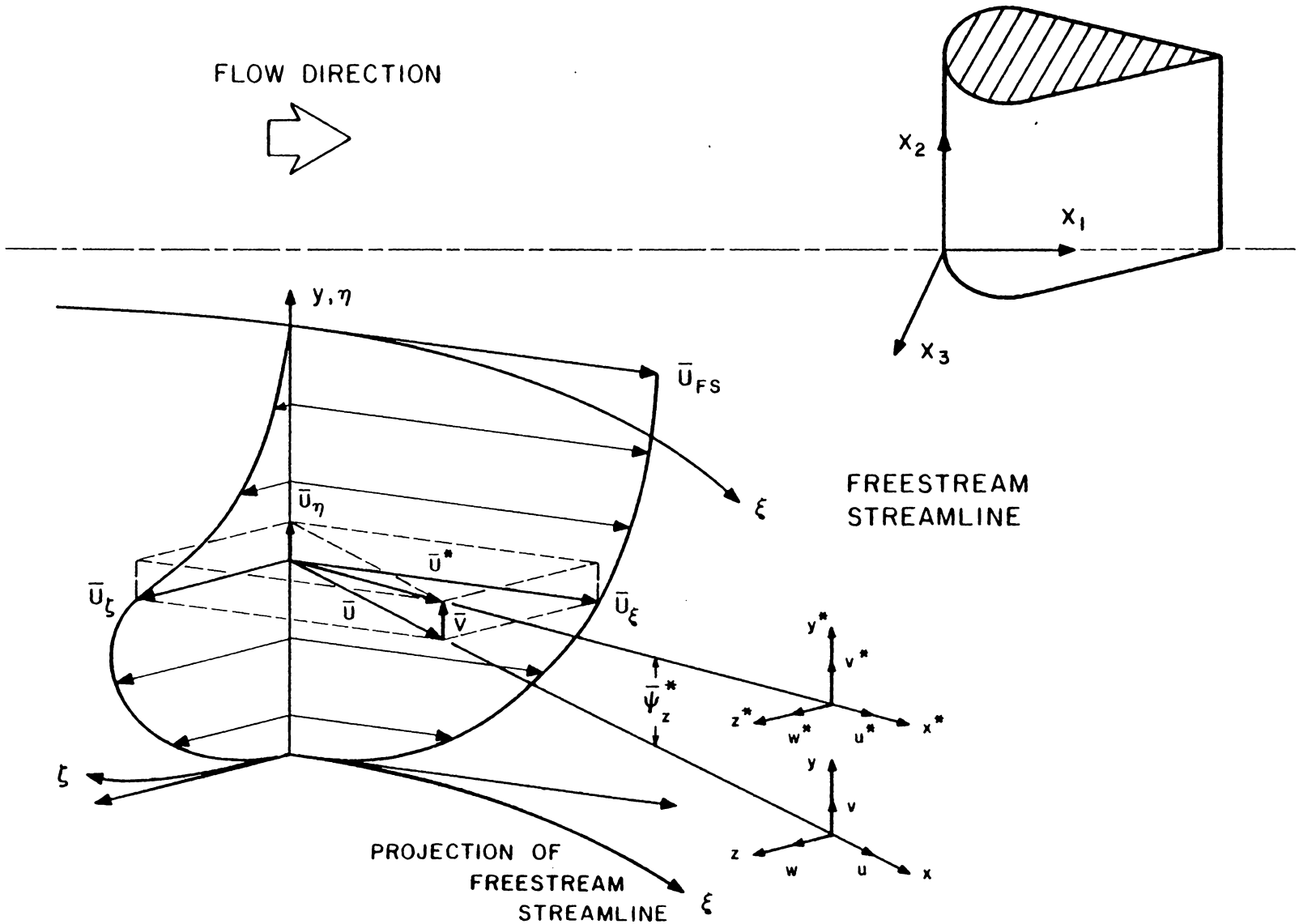

Figure 3.14 Partial Misalignment of the Sensor Coordinate System to the Local Streamline Coordinate System Resulting from $\bar{V}$ Components of Velocity

of the two remaining components, $\overline{U}$ and $\overline{V}$, were made. The pitch angle $\overline{\psi}_z^*$ and hence $\overline{V}$ was obtained by using the calibrated sensor sensitivities of the vertical x-array as in Müller [39,58]. In Chapter IV, a generalized sensor response analysis is derived in a misaligned sensor coordinate system which accounts for modest amounts of $\overline{V}$ in calculating the turbulent stresses and also corrects mean velocity magnitudes for these flow pitch effects.

Probe Calibration Procedures and Traversing

The mean velocity profiles measured by the single film ranged from y of 0.051 to 12.7 cm (0.020 to 5.00 in.). Measurements of turbulent stress and mean velocity using the x-arrays ranged from 0.127 cm near the wall to 12.7 cm (0.05 to 5.00 in.) where the smallest distance from the wall was dictated by the physical size of the probe. As stated earlier, the measuring point was assumed to be at the geometric center of the x-array. Changes in local skew within the probes measuring volume were ignored, that is, the probe measuring volume was assumed to see a locally, collateral flow.

Static velocity calibrations were performed on the sensors of each probe in the potential core of the tunnel 2D flow before and after each traverse was taken. With the probe in its operating position, the output signals from each channel were initially linearized over the velocity range identified with the particular data station, with the velocity sensitivities adjusted to give equal slopes of the sensor calibration curves. Both the initial and final calibration data were used simultaneously, by a least squares algorithm, in estimating a

velocity calibration curve for the entire profile run. The combined processing of these data gave scatter usually to within 1% RMS about the estimated line. Data sessions typically lasted from 4-12 hours with each profile requiring approximately 4 hours to complete. The final calibration served as a means of detecting and quantifying the amount drift that may have occurred during the profile run. With the laboratory temperature held essentially constant and continuous operation of the instruments, electronic drift was usually not a problem. The linearizers did however appear to be somewhat sensitive to small changes in the ambient conditions. Whenever any detected drift was judged unacceptable, measured by a corresponding change in the sensors' velocity calibration, the profile was repeated.

A detailed yaw calibration study was made and is presented in Chapter V. A method is developed to replace the conventional calibration method for hot wire/film probes so that individual sensor yaw calibrations could be made on the more complex probe geometries. In addition, the two popular cooling laws of Hinze [54] (Eq. 2.6) and Davies and Bruun [104] (Eq. 2.7) are studied in Chapter V from the standpoint of turbulence data reduction and the mean velocity corrections for turbulence and results are compared in Chapter VII. The standard test case results will use Hinze's law which appears to be used in most of the turbulence studies reported.

G. Preston Tube Measurements

The use of indirect wall shear diagnostic devices such as Preston tubes to infer wall shear stress in three-dimensional flows, assumes a

priori the validity of the two-dimensional similarity law in a three-dimensional flow. The calibration of a Preston tube is in effect dependent on the two-dimensional near-wall similarity law and thus ignores the confirmed vector character of the near-wall flow in three dimensions. While nearly all indirect devices reported to date, that have been used to measure wall shear in three-dimensional flows, rely on two-dimensional calibrations, it is only recently through the work of Pierce and McAllister [27,125] that any support for this common approach has been provided.

As stated earlier, the work of Pierce and McAllister [27,125] was centered around the 3DTBL flow generated by the same flow geometry as used in the present study. In attempting to resolve the more fundamental question of three-dimensional near-wall similarity, they made direct force wall shear measurements of both magnitude and direction accompanied by extensive measurements of mean velocity field and the wall pressure field. Using a unique, omnidirectional floating element mechanical shear meter, direct wall shear measurements were made in the 2DTBL tunnel flow where excellent agreement was obtained with a variety of direct and indirect two-dimensional wall shear diagnostic devices and techniques. A total of 10 near-wall similarity models proposed in the literature for 3DTBL flows were tested under various skew conditions.

For modestly skewed profiles with an approximate upper limit of 15-20^{o} as well as on the plane of symmetry, Pierce and McAllister's [27,125] results indicate that the Clauser chart type of approach could give the magnitude of the local wall shear stress to within 5-10% of the values obtained by the direct force shear meter. They further suggest

that indirect devices such as Preston tubes, which are not highly sensitive to yaw angles, could give reasonably good approximations of the magnitude of the wall shear stress in modestly skewed flows using a two-dimensional calibration. The indirect devices however, would be relatively poor in indicating the local wall shear stress or limiting wall streamline direction due to their insensitivity to yaw. Pierce and McAllister suggest that for modestly skewed flows, the combination of an indirect device such as a Preston tube with a well established flow visualization technique could do a reasonably satisfactory job in mapping a wall shear field.

Measurements of wall shear stress magnitude were made with one of the Preston tubes used by Pierce and McAllister [27,125] in their two-dimensional flow studies. The Preston tube used in this study consisted of a 0.457 mm (0.018 in.) OD stainless steel tube mounted on a 12.7 cm (5 in.) diameter aluminum disk with the tube opening at the center of the disk. The opening of the tube was hand crafted in order to insure a smooth, round entrance free of burrs. Static pressure taps were located 0.635 and 1.27 cm (0.25 and 0.50 in.) from the tube opening on a line perpendicular to the tube axis. To account for the cross-stream pressure gradients present in this flow, the static pressure was measured at both ports and a first order (linear) static pressure correction was used to calculate the dynamic pressure at the tube opening. The Preston tube center was placed at an angle obtained from a linear interpolaton between the limiting wall streamline direction, taken from an oil streak flow visualization, and the measured flow direction nearest to the wall at y = 0.51 mm (0.020 in.). The limiting wall streamline visualizations

were made with titanium dioxide particles suspended in a diesel fuel-mineral oil mix.

IV. SENSOR RESPONSE

A. Sensor Response Analysis in a Three-Dimensional Turbulent Flow - Preliminary Remarks

A response analysis is presented for a sensor placed arbitrarily in a three-dimensional turbulent boundary layer flow of modest intensity where no restrictions are placed on the mathematical form of the cooling law. Response equations of a sensor pair are combined to form the response of each of the three probes used in this study. Initially, the sensing elements are treated as having unique velocity and directional characteristics as in Elsenaar and Boelsma [32]. It will be shown that while sensors of equal velocity and directional characteristics are necessary for obtaining stresses from the slant x-array, these are not necessary for the horizontal and vertical x-array measured stresses. Provisions are also made for small amounts of probe misalignment with the flow as discussed in Bruun [90] and Müller [58]. In addition, a more precise definition of matched sensors is given as well as geometric guidelines for constructing x-array probes. It will be shown that electronic matching of the signal levels of two sensors is necessary but not sufficient for obtaining the conventional matched sensor response equations. Further, a geometrically perfect, matched slant x-array alone can yield the turbulent kinetic energy and all the Reynolds shear stresses. Finally, a general mean velocity correction for turbulence effects is present.

The sensor's directional response to yaw is represented by the function, $f(\alpha,P)$ where α is the angle between local the mean velocity vector and the normal to the sensor in the plane defined by the mean velocity and the sensor, and P represents a yaw parameter associated with a specific cooling law. The case of a yaw dependent parameter will be considered as in

$$P = P(\alpha) \, . \tag{4.1}$$

Strictly speaking, Eq. 4.1 implies that the yaw cooling law be represented as depending on α alone. However, it will be convenient to show the parameter P dependence which can itself depend on α. As stated in Chapter II this parameter, for example k^2, has also been shown to vary with velocity but this dependence will not be treated in the derivation of the response equations.

The following analysis makes use of the knowledge and insight that various authors [33,51,52,57,59,60,85,90] have contributed to the literature.

B. Description of Coordinate Systems

Figure 4.1 illustrates the two local Cartesian systems used in this analysis. The conventional $x^*y^*z^*$ system with unit vectors $\hat{e}^*_x$, $\hat{e}^*_y$ and $\hat{e}^*_z$, is a local streamline system where the x^*-axis is aligned with the local tangent to the local mean flow streamline. For this orientation, the magnitude of the instantaneous velocity vector is

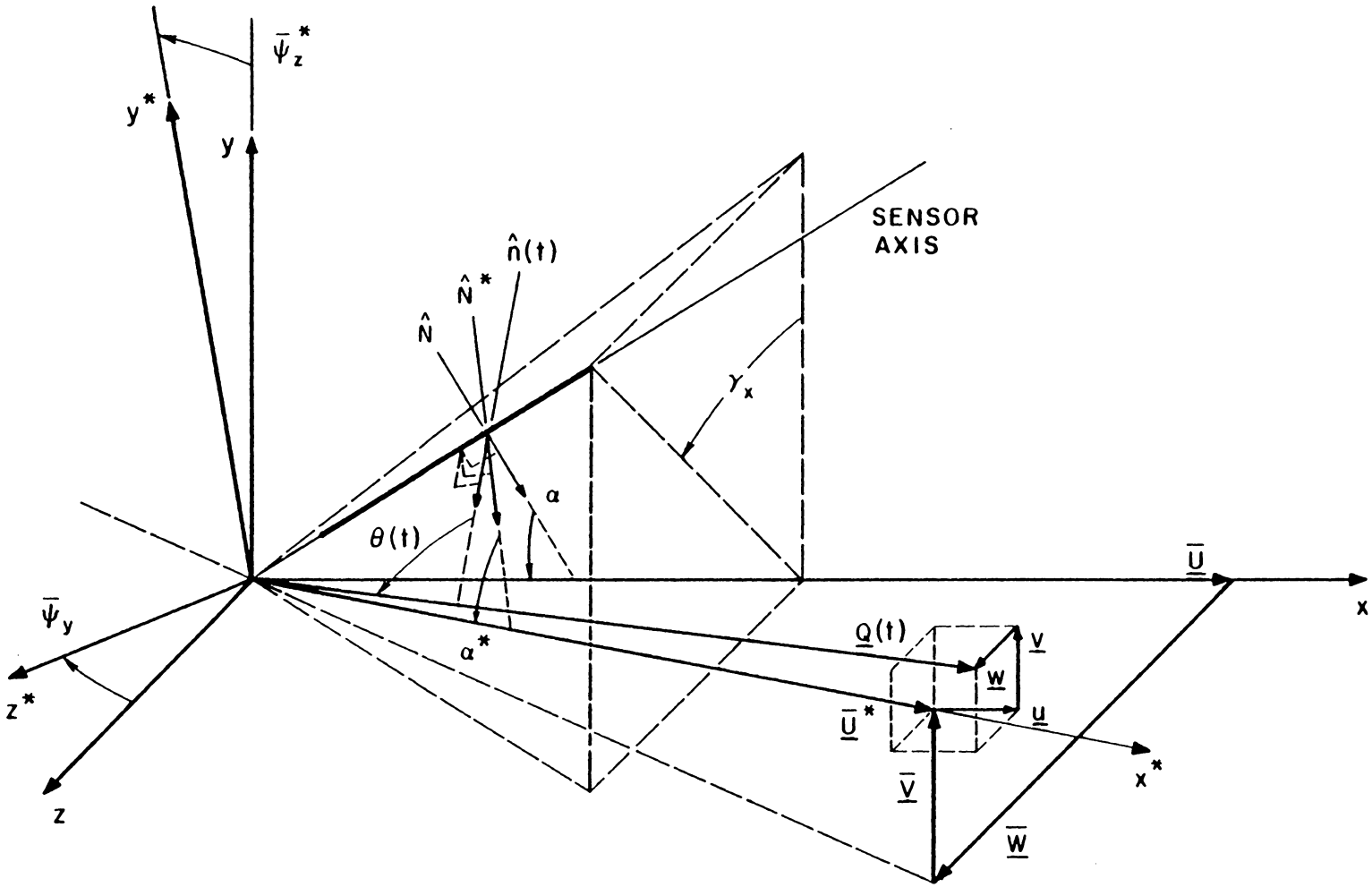

Figure 4.1 Definitions of the Local Streamline and Sensor Coordinate Systems Employed

composed of a time averaged velocity component, $\overline{U}^*$, and fluctuations, u^*, v^*, w^*, in the form

$$|\underline{Q}(t)| = [(\overline{U}^* + u^*)^2 + v^{*2} + w^{*2}]^{1/2} \tag{4.2}$$

where the instantaneous velocity is

$$\underline{Q}(t) = (\overline{U}^* + u^*)\, \hat{e}_x^* + v^* \hat{e}_y^* + w^* \hat{e}_z^* . \tag{4.3}$$

The sensor is fixed to the xyz system which has the corresponding $\hat{e}_x$, $\hat{e}_y$, and $\hat{e}_z$ unit vectors. Probe geometry is specified in this xyz reference frame. This arrangement accommodates possible probe spatial misalignment with the local flow direction through the angles $\overline{\psi}_y$ and $\overline{\psi}_z^*$. These represent rotations about the y and z^* axis, respectively, as shown in Fig. 4.2. Describing the instantaneous velocity in the sensor xyz system requires three mean velocity components, $\overline{U}$, $\overline{V}$, $\overline{W}$, and corresponding u, v, w fluctuations as in

$$\underline{Q}\ (t) = (\overline{U} + u)\, \hat{e}_x + (\overline{V} + v)\, \hat{e}_y + (\overline{W} + w)\, \hat{e}_z \tag{4.4}$$

with magnitude

$$|\underline{Q}(t)| = [\overline{U} + u)^2 + (\overline{V} + v)^2 + (\overline{W} + w)^2]^{1/2} . \tag{4.5}$$

All the angles defined in Figs. 4.1 and 4.2 are shown as positive. Angles $\overline{\psi}_y$ and $\overline{\psi}_z^*$ indicate yaw and pitch, respectively, of the

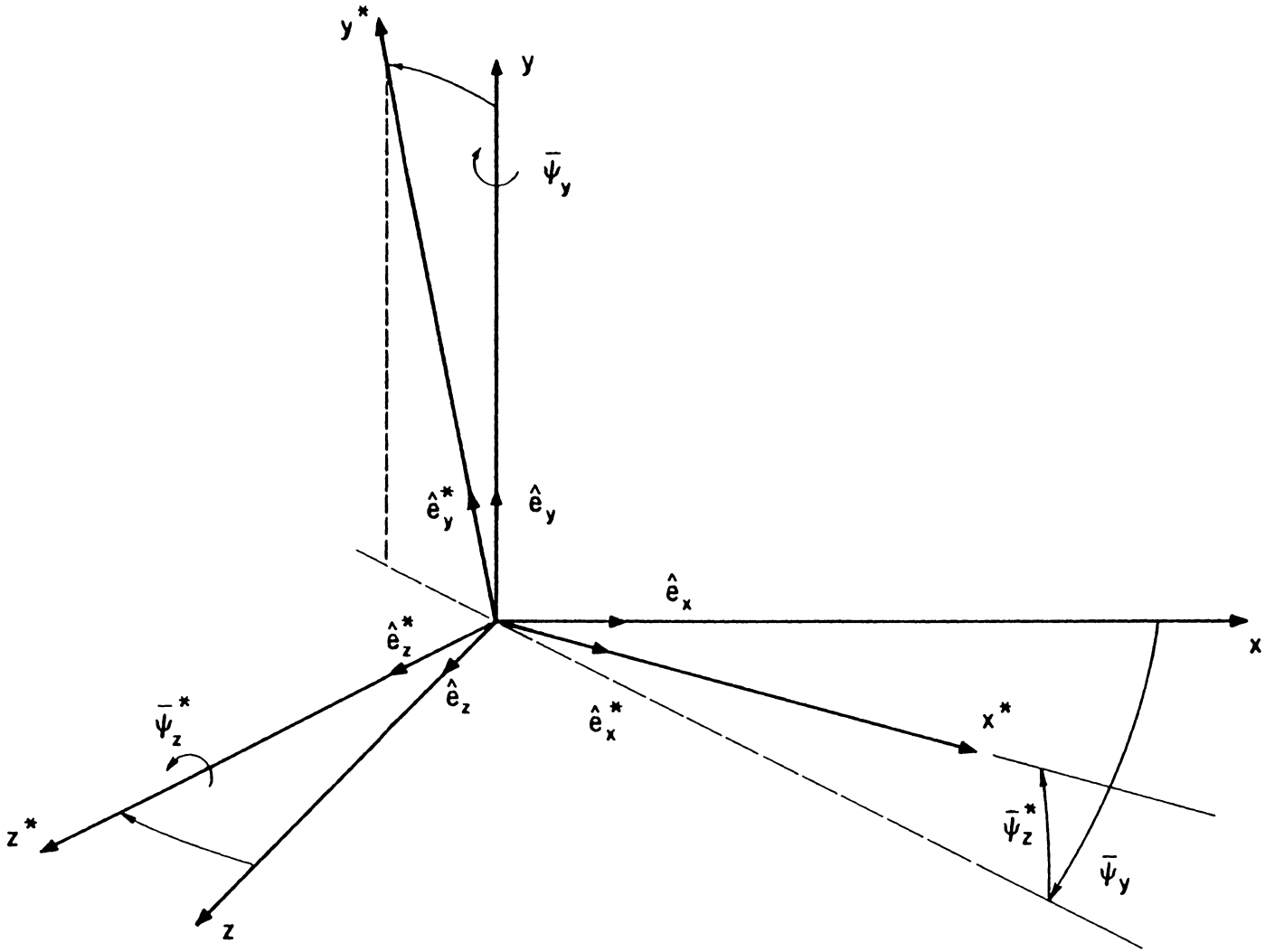

Figure 4.2 Orientation of the Sensor Coordinate System to the Local Streamline Coordinate System

sensor coordinate system relative to the local flow or $x^*y^*z^*$ system where

$$0 \leq |\overline{\psi}_y| < \pi/2$$

and

$$0 \leq |\overline{\psi}^*_z| < \pi/2 \ .$$

These are related to the mean velocity components by

$$\frac{\overline{U}}{\overline{U}^*} = \cos \overline{\psi}^*_z \cos \overline{\psi}_y \ , \tag{4.6}$$

$$\frac{\overline{V}}{\overline{U}^*} = \sin \overline{\psi}^*_z, \tag{4.7}$$

and

$$\frac{\overline{W}}{\overline{U}^*} = \cos \overline{\psi}^*_z \sin \overline{\psi}_y \ . \tag{4.8}$$

Summing the squares of Eqs. 4.6-4.8 yields

$$\overline{U}^* = [\overline{U}^2 + \overline{V}^2 + \overline{W}^2]^{1/2} \ . \tag{4.9}$$

For the case of perfect positioning of the probe, the local streamline and sensor coordinate systems coincide, hence

$$\overline{\psi}_z^* = \overline{\psi}_y = 0 \ , \tag{4.10}$$

with $\overline{V} = \overline{W} = 0$ and $\overline{U} = \overline{U}^*$.

In turbulence studies one uses statistical means to describe the instantaneous fluid motion. To facilitate this approach, it is helpful to distinguish between an instantaneous plane and a mean plane with each plane being associated with their own unit normal vector. In Fig. 4.1, $\hat{n}(t)$ represents a unit vector, normal to the sensor, lying in the instantaneous plane which contains the instantaneous velocity vector and the sensor. The instantaneous yaw angle in this plane, defined on the interval

$$0 \leq \theta(t) < \pi/2 \ , \tag{4.11}$$

is the angle between $\hat{n}(t)$ and the instantaneous velocity vector. The unit vector, $\hat{N}^*$, is normal to the sensor in the mean plane formed by the x^*-axis ($\overline{U}^*$) and the sensor. The angle α^* is a mean sensor yaw angle defined in this mean plane on the interval

$$0 \leq \alpha^* < \pi/2. \tag{4.12}$$

With misalignment, a mean plane can be identified with the sensor xyz system and defined by the x-axis ($\overline{U}$) and the sensor, where $\hat{N}$ is the unit normal vector. Angle α is the angle between the x-axis ($\overline{U}$) and the sensor normal, $\hat{N}$, defined on the same interval as α^*. The various probe configurations, which are arranged in this xyz coordinate system,

are fixed by one specification of α and γ_x, where γ_x represents rotation or roll about the x-axis.

The tensor transformations from the streamline based system to the sensor reference frame (and visa versa) require the direction cosines defined in the familiar notation

	x^*	y^*	z^*
x	ℓ_1	m_1	n_1
y	ℓ_2	m_2	n_2
z	ℓ_3	m_3	n_3

(4.13)

Referring to Fig. 4.2, this becomes

	x^*	y^*	z^*
x	$\cos \bar{\psi}^*_z \cos \bar{\psi}_y$	$- \sin \bar{\psi}^*_z \cos \bar{\psi}_y$	$- \sin \bar{\psi}_y$
y	$\sin \bar{\psi}^*_z$	$\cos \bar{\psi}^*_z$	0
z	$\cos \bar{\psi}^*_z \sin \bar{\psi}_y$	$- \sin \bar{\psi}^*_z \sin \bar{\psi}_y$	$\cos \bar{\psi}_y$

(4.14)

Thus the coordinate systems described above are related by the vector transformation

$$\begin{vmatrix} \hat{e}^*_x \\ \hat{e}^*_y \\ \hat{e}^*_z \end{vmatrix} = \begin{vmatrix} \ell_1 & \ell_2 & \ell_3 \\ m_1 & m_2 & m_3 \\ n_1 & n_2 & n_3 \end{vmatrix} \begin{vmatrix} \hat{e}_x \\ \hat{e}_y \\ \hat{e}_z \end{vmatrix} \tag{4.15}$$

and the inverse transform

$$\begin{vmatrix} \hat{e}_x \\ \hat{e}_y \\ \hat{e}_z \end{vmatrix} = \begin{vmatrix} \ell_1 & m_1 & n_1 \\ \ell_2 & m_2 & n_2 \\ \ell_3 & m_3 & n_3 \end{vmatrix} \begin{vmatrix} \hat{e}^*_x \\ \hat{e}^*_y \\ \hat{e}^*_z \end{vmatrix} . \tag{4.16}$$

The Reynolds stress tensor, obtained in a particular coordinate system can be transformed to any other coordinate system by a tensor transformation. The derivations are straight-forward and the reader is referred to Ugural and Fenster [138] for a complete derivation. From the appropriate definitions given in Eq. 4.14, the Reynolds stress tensor transformation from the xyz to the $x^*y^*z^*$ system is

$$\begin{vmatrix} \overline{uu} & \overline{vu} & \overline{wu} \\ \overline{uv} & \overline{vv} & \overline{wv} \\ \overline{uw} & \overline{vw} & \overline{ww} \end{vmatrix}^* = \begin{vmatrix} \ell_1 & m_1 & n_1 \\ \ell_2 & m_2 & n_2 \\ \ell_3 & m_3 & n_3 \end{vmatrix} \begin{vmatrix} \ell_1 & \ell_2 & \ell_3 \\ m_1 & m_2 & m_3 \\ n_1 & n_2 & n_3 \end{vmatrix} \begin{vmatrix} \overline{uu} & \overline{vu} & \overline{wu} \\ \overline{uv} & \overline{vv} & \overline{wv} \\ \overline{uw} & \overline{vw} & \overline{ww} \end{vmatrix} , \tag{4.17}$$

and by symmetry,

$$\begin{aligned} \overline{vu} &= \overline{uv} \\ \overline{wu} &= \overline{uw} \\ \overline{wv} &= \overline{vw} . \end{aligned} \tag{4.18}$$

The sensor points in the direction of a unit vector, $\hat{\ell}$, defined in the sensor coordinate system as

$$\hat{\ell}\ (\alpha,\ \gamma_x) = \sin\ \alpha\ \hat{e}_x + \cos\ \alpha \cos\ \gamma_x\ \hat{e}_y + \cos\ \alpha \sin\ \gamma_x\ \hat{e}_z \qquad (4.19)$$

and in the local streamline system as

$$\hat{\ell}(\alpha^*,\ \gamma_x^*) = \sin\ \alpha^*\ \hat{e}_x^* + \cos\ \alpha^*\ \cos\ \gamma_x^*\ \hat{e}_y^* + \cos\ \alpha^*\ \sin\ \gamma_x^*\ \hat{e}_z^*. \qquad (4.20)$$

Using Eq. 4.16, Eq. 4.19 can be re-written as

$$\begin{aligned}\hat{\ell}(\alpha,\gamma_x) = [&\sin\ \alpha \cos\ \bar{\psi}_z^* \cos\ \bar{\psi}_y + \cos\ \alpha \cos\ \gamma_x \sin\ \bar{\psi}_z^* \\ &+ \cos\ \alpha \sin\ \gamma_x \cos\ \bar{\psi}_z^* \sin\ \bar{\psi}_y]\ \hat{e}_x^* + [-\sin\ \alpha \sin\ \bar{\psi}_z^* \cos\ \bar{\psi}_y \\ &+ \cos\ \alpha \cos\ \gamma_x \cos\ \bar{\psi}_z^* - \cos\ \alpha \sin\ \gamma_x \sin\ \bar{\psi}_z^* \sin\ \bar{\psi}_y]\ \hat{e}_y^* \\ &+ [-\sin\ \alpha \sin\ \bar{\psi}_y + \cos\ \alpha \sin\ \gamma_x \cos\ \bar{\psi}_y]\ \hat{e}_z^*\ . \qquad (4.21)\end{aligned}$$

Referring to Eq. 4.20, the following indentities are noted for later use:

$$\begin{aligned}\sin\ \alpha^* = &\sin\ \alpha \cos\ \bar{\psi}_z^* \cos\ \bar{\psi}_y + \cos\ \alpha \cos\ \gamma_x \sin\ \bar{\psi}_z^* \qquad (4.22) \\ &+ \cos\ \alpha \sin\ \gamma_x \cos\ \bar{\psi}_z^* \sin\ \bar{\psi}_y\ ,\end{aligned}$$

$$\cos \alpha^* \cos \gamma_x^* = - \sin \alpha \sin \bar{\psi}_z^* \cos \bar{\psi}_y + \cos \alpha \cos \gamma_x \cos \bar{\psi}_z^*$$

$$- \cos \alpha \sin \gamma_x \sin \bar{\psi}_z^* \sin \bar{\psi}_y \, , \tag{4.23}$$

$$\cos \alpha^* \sin \gamma_x^* = - \sin \alpha \sin \bar{\psi}_y + \cos \alpha \sin \gamma_x \cos \bar{\psi}_y \, . \tag{4.24}$$

C. Sensor Response Analysis

The following derivation will be performed in the sensor xyz coordinate system misaligned by the angular displacements $\bar{\psi}_y$ and $\bar{\psi}_z^*$. In deriving the response equation, it is assumed that the sensing element responds to only the local flow, sees instantaneous but uniform components, and responds to the frequency content of the flow correctly.

The sensor responds to the magnitude and direction of the instantaneous velocity vector. The function

$$R = R(Q, \theta) \tag{4.25}$$

will represent the general time dependence of the sensor to the variables Q and θ for both the nonlinear and linearized CTA signals. Q is the magnitude of the instantaneous velocity vector and θ has been defined as the instantaneous yaw angle between $\underline{Q}$ and the unit normal to the sensor, $\hat{n}(t)$, in the instantaneous plane.

Inasmuch as instantaneous angles are difficult to obtain, consider a Taylor series expansion of Eq. 4.25 in the two independent variables,

Q and θ, about the points $\overline{U}$ and α, respectively, where

$$R(Q,\theta) = R(\overline{U},\alpha) + (Q - \overline{U})\, R_Q\,(\overline{U},\alpha) + (\theta - \alpha)\, R_\theta\,(\overline{U},\alpha)$$

$$+ \frac{1}{2}\{(\theta - \overline{U})^2\, R_{QQ}\,(\overline{U},\alpha) + 2(Q - \overline{U})(\theta - \alpha)\, R_{Q\theta}\,(\overline{U},\alpha)$$

$$+ (\theta - \alpha)^2 R_{\theta\theta}\,(\overline{U},\alpha)\} + \frac{1}{6}\{(Q - \overline{U})^3\, R_{QQQ}\,(\overline{U},\alpha)$$

$$+ 3(Q - \overline{U})^2 (\theta - \alpha)\, R_{QQ\theta}\,(\overline{U},\alpha) + 3(Q - \overline{U})(\theta - \alpha)^2\, R_{Q\theta\theta}\,(\overline{U},\alpha)$$

$$+ (\theta - \alpha)^3 R_{\theta\theta\theta}\,(\overline{U},\alpha)\} + \ldots . \qquad (4.26)$$

An advantage is gained by linearizing the CTA signal and this is easily shown by considering the nonlinear case first. For signals obtained directly from the CTA, it is customary to express

$$R(Q,\theta) = E_o^2 + B_o\{Qf(\theta,P(\theta))\}^n . \qquad (4.27)$$

The term in the braces is the instantaneous effective cooling velocity and the function $f(\theta,P(\theta))$ incorporates the directional properties of the sensing element. Successive differentiations of Eq. 4.27 yields

$$R_Q = B_o n\, \{Qf\}^n/Q ,$$

$$R_{QQ} = B_o n\,(n - 1)\, \{Qf\}^n/Q^2 ,$$

$$R_\theta = B_o n\ Q\{Qf\}^{n-1}\ f_\theta\ ,$$

$$R_{\theta\theta} = B_o nQ\ [Q(n-1)\{Qf\}^{n-1} f_\theta^2 + \{Qf\}^{n-1}\ f_{\theta\theta}]\ ,$$

and

$$R_{Q\theta} = B_o n^2\ \{Qf\}^{n-1}\ f_\theta\ , \tag{4.28}$$

and upon substituting into Eq. 4.26 gives, to second order,

$$R(Q,\theta) = E_o^2 + B_o\ \{\bar{U}f(\alpha,P(\alpha))\}^n + \frac{B_o n}{\bar{U}}\ (Q-\bar{U})\ \{\bar{U}f(\alpha,P(\alpha))\}^n$$

$$+ B_o n\bar{U}\ (\theta-\alpha)\ \{\bar{U}f(\alpha,P(\alpha))\}^{n-1}\ f'(\alpha,P(\alpha))$$

$$+ \frac{1}{2}\frac{B_o n(n-1)}{\bar{U}^2}\ (Q-\bar{U})^2\ \{\bar{U}f(\alpha,P(\alpha))\}^n + B_o n^2\ (Q-\bar{U})\ (\theta-\alpha)\cdot$$

$$\{\bar{U}f(\alpha,P(\alpha))\}^{n-1} f'(\alpha,P(\alpha)) + \frac{1}{2} B_o n\bar{U}(\theta-\alpha)^2\ [\bar{U}(n-1)\cdot$$

$$\{\bar{U}f(\alpha,P(\alpha))\}^{n-2}\ f'^2(\alpha,P(\alpha)) + \{\bar{U}f(\alpha,P(\alpha))\}^{n-1}\ f''(\alpha,P(\alpha))] + \cdots\ .$$

(4.29)

The prime denotes derivatives with respect to α. The next step would involve replacing the quantities $(Q-\bar{U})$ and $(\theta-\alpha)$ with those derived in Appendix A. It is exident that using the nonlinear response model in Eq. 4.27 would involve very tedious algebraic manipulations especially

in high intensity flows where additional higher order terms are necessarily retained.

A mathematical advantage is gained by linearizing the output signal. Using $R(Q,\theta)$ to denote the linearized signal and E_o and B_o in Eq. 4.27 as linearized constants, the linearized version is of the form

$$R(Q,\theta) = E_o + B_o Q\, f(\theta,P(\theta)) \,, \tag{4.30}$$

where the repeated terms E_o and B_o in Eqs. 4.87 and 4.30 are not equal. As noted by Bissonnette [15], second and higher order derivatives of R with respect to Q in Eq. 4.26 such as R_{QQ}, R_{QQQ}, $R_{QQ\theta}$, ..., will vanish and which results in higher order truncation errors. Substituting the successive derivatives of Eq. 4.30 into Eq. 4.26 and simplifying gives

$$R(Q,\theta) = E_o + B_o Q f(\alpha,P(\alpha)) + B_o Q(\theta - \alpha) f'(\alpha,P(\alpha))$$

$$+ \frac{1}{2} B_o\, Q(\theta - \alpha)^2\, f''(\alpha,P(\alpha)) + O(\theta - \alpha)^3 + \cdots \,. \tag{4.31}$$

(An identical result can be obtained by replacing E_o^2 with E_o and setting n=1 in Eq. 4.29.) The mathematical advantage gained by linearizing the signal is a less complicated response equation with high order truncation errors in $(Q - \bar{U})$. If one were to assume a velocity dependent P and/or n, additional derivatives would appear in both Eqs. 4.29 and 4.31 which would in themselves present even greater difficulties.

Substituting the expressions for Q, $Q(\theta - \alpha)$, and $Q(\theta - \alpha)^2$ given in Appendices A and B along with Eqs. 4.6 - 4.8 in Eq. 4.31, and non-dimensionalizing by the local mean velocity, $\bar{U}^*$, yields the expanded form

$$\frac{R(Q,\theta) - E_o}{B_o \bar{U}^*} = f(\alpha,P(\alpha)) + S_o + \frac{u}{\bar{U}^*}\{f(\alpha,P(\alpha)) + S_u\}$$

$$+ \frac{v}{\bar{U}^*}\{f'(\alpha,P(\alpha)) \cos \gamma_x + S_v\} + \frac{w}{\bar{U}^*}\{f'(\alpha,P(\alpha)) \sin \gamma_x + S_w\}$$

$$+ \frac{uu}{\bar{U}^{*2}}\{S_{uu}\} + \frac{vv}{\bar{U}^{*2}}\{\frac{1}{2} f(\alpha,P(\alpha)) - \frac{1}{2} f'(\alpha,P(\alpha)) \cdot$$

$$[\tan \alpha - \cos^2 \gamma_x \tan \alpha] + \frac{1}{2} f''(\alpha,P(\alpha)) \cos^2 \gamma_x + S_{vv}\}$$

$$+ \frac{ww}{\bar{U}^{*2}}\{\frac{1}{2} f(\alpha,P(\alpha)) - \frac{1}{2} f'(\alpha,P(\alpha))[\tan \alpha - \sin^2 \gamma_x \tan \alpha]$$

$$+ \frac{1}{2} f''(\alpha,P(\alpha)) \sin^2 \gamma_x + S_{ww}\}$$

$$+ \frac{uv}{\bar{U}^{*2}}\{S_{uv}\} + \frac{uw}{\bar{U}^{*2}}\{S_{uw}\} + \frac{vw}{\bar{U}^{*2}}\{\cos \gamma_x \sin \gamma_x \cdot$$

$$[f'(\alpha,P(\alpha)) \tan \alpha + f''(\alpha,P(\alpha))] + S_{vw}\}, \qquad (4.32)$$

where

$$S_o = f'\{b_o + \frac{1}{2} b_o^2 \tan\alpha + b_o^3 [\frac{1}{2}\tan^2\alpha + \frac{1}{6}]$$

$$+ b_o^4 [\frac{5}{8}\tan^3\alpha + \frac{5}{24}\tan\alpha] + b_o^5 [\frac{7}{8}\tan^4\alpha + \frac{7}{24}\tan^2\alpha]\}$$

$$+ \frac{1}{2} f''\{b_o^2 + b_o^3 \tan\alpha + b_o^4 [\frac{5}{4}\tan^2\alpha + \frac{1}{3}] + b_o^5 [\frac{7}{4}\tan^3\alpha + \frac{7}{12}\tan\alpha]$$

$$+ b_o^6 [\frac{21}{8}\tan^4\alpha + \frac{23}{24}\tan^2\alpha + \frac{1}{36}]\}\ , \qquad (4.33)$$

$$S_u = f\{\cos\bar{\psi}_z^* \cos\bar{\psi}_y - 1\} + f'\{C_1^u + \frac{1}{2}\tan\alpha\, C_2^u + [\frac{1}{2}\tan^2\alpha + \frac{1}{6}]C_3^u$$

$$+ [\frac{5}{8}\tan^3\alpha + \frac{5}{24}\tan\alpha]C_4^u + [\frac{7}{8}\tan^4\alpha + \frac{7}{24}\tan^2\alpha]\, C_5^u\}$$

$$+ \frac{1}{2} f''\{C_2^u + \tan\alpha\, C_3^u + [\frac{5}{4}\tan^2\alpha + \frac{1}{3}]C_4^u + [\frac{7}{4}\tan^3\alpha + \frac{7}{12}\tan\alpha]C_5^u$$

$$+ [\frac{21}{8}\tan^4\alpha + \frac{23}{24}\tan^2\alpha + \frac{1}{36}]\, C_6^u\}\ , \qquad (4.34)$$

$$S_v = f\sin\bar{\psi}_z^* + f'\{-\tan\alpha\sin\bar{\psi}_z^* + \frac{1}{2}\tan\alpha\, C_2^v + [\frac{1}{2}\tan^2\alpha + \frac{1}{6}]\, C_3^v$$

$$+ [\frac{5}{8}\tan^3\alpha + \frac{5}{24}\tan\alpha]\, C_4^v + [\frac{7}{8}\tan^4\alpha + \frac{7}{24}\tan^2\alpha]\, C_5^v\}$$

$$+ \frac{1}{2} f''\{C_2^v + \tan\alpha\, C_3^v + [\frac{5}{4}\tan^2\alpha + \frac{1}{3}]\, C_4^v + [\frac{7}{4}\tan^3\alpha + \frac{7}{12}\tan\alpha]\, C_5^v$$

$$+ [\frac{21}{8}\tan^4\alpha + \frac{23}{24}\tan^2\alpha + \frac{1}{36}]\, C_6^v\}\ , \qquad (4.35)$$

$$S_w = f \cos \bar{\psi}_z^* \sin \bar{\psi}_y + f' \{-\tan \alpha \cos \bar{\psi}_z^* \sin \bar{\psi}_y + \tfrac{1}{2} \tan \alpha C_2^w +$$

$$+ [\tfrac{1}{2} \tan^2 \alpha + \tfrac{1}{6}] C_3^w + [\tfrac{5}{8} \tan^3 \alpha + \tfrac{5}{24} \tan \alpha] C_4^w$$

$$+ [\tfrac{7}{8} \tan^4 \alpha + \tfrac{7}{24} \tan^2 \alpha] C_5^w\} + \tfrac{1}{2} f'' \{C_2^w + \tan \alpha C_3^w + [\tfrac{5}{4} \tan^2 \alpha + \tfrac{1}{3}] C_4^w$$

$$+ [\tfrac{7}{4} \tan^3 \alpha + \tfrac{7}{12} \tan \alpha] C_5^w + [\tfrac{21}{8} \tan^4 \alpha + \tfrac{23}{24} \tan^2 \alpha + \tfrac{1}{36}] C_6^w\}, \quad (4.36)$$

$$S_{uu} = \tfrac{1}{2} f(1 - \cos^2 \bar{\psi}_z^* \cos^2 \bar{\psi}_y) + f' \{C_1^{uu} + \tfrac{1}{2} \tan \alpha C_2^{uu}$$

$$+ [\tfrac{1}{2} \tan^2 \alpha + \tfrac{1}{6}] C_3^{uu} + [\tfrac{5}{8} \tan^3 \alpha + \tfrac{5}{24} \tan \alpha] C_4^{uu}$$

$$+ [\tfrac{7}{8} \tan^4 \alpha + \tfrac{7}{24} \tan^2 \alpha] C_5^{uu}\} + \tfrac{1}{2} f'' \{C_2^{uu} + \tan \alpha C_3^{uu}$$

$$+ [\tfrac{5}{4} \tan^2 \alpha + \tfrac{1}{3}] C_4^{uu} + [\tfrac{7}{4} \tan^3 \alpha + \tfrac{7}{12} \tan \alpha] C_5^{uu}$$

$$+ [\tfrac{7}{2} \tan^4 \alpha + \tfrac{23}{24} \tan^2 \alpha + \tfrac{1}{36}] C_6^{uu}\}, \quad (4.37)$$

$$S_{vv} = -\tfrac{1}{2} f \sin^2 \bar{\psi}_z^* + f' \{[\tfrac{1}{2} \tan \alpha \sin^2 \bar{\psi}_z^*]$$

$$+ \tfrac{1}{2} \tan \alpha [\tan^2 \alpha \sin^2 \bar{\psi}_z^* - 2 \cos \gamma_x \tan \alpha \sin \bar{\psi}_z^*$$

$$+2 b_o b_{vv} - 2 b_o b_v \sin \bar{\psi}_z^* - \frac{b_o^2}{2} (1 - 3 \sin^2 \bar{\psi}_z^*)] + [\tfrac{1}{2} \tan^2 \alpha + \tfrac{1}{6}] C_3^{vv} +$$

$$+ \left[\frac{5}{8}\tan^3\alpha + \frac{5}{24}\tan\alpha\right] C_4^{vv} + \left[\frac{7}{8}\tan^4\alpha + \frac{7}{24}\tan^2\alpha\right] C_5^{vv} \}$$

$$+ \frac{1}{2} f'' \{[\tan^2\alpha \sin^2 \overrightarrow{\psi}_z^* - 2\cos\gamma_x \tan\alpha \sin \overrightarrow{\psi}_z^*$$

$$+ 2b_o b_{vv} - 2b_o b_v \sin \overrightarrow{\psi}_z^* - \frac{b_o^2}{2}(1 + 3\sin^2 \overrightarrow{\psi}_z^*)] + \tan\alpha\, C_3^{vv}$$

$$+ \left[\frac{5}{4}\tan^2\alpha + \frac{1}{3}\right] C_4^{vv} + \left[\frac{7}{4}\tan^3\alpha + \frac{7}{12}\tan\alpha\right] C_5^{vv}$$

$$+ \left[\frac{21}{8}\tan^4\alpha + \frac{23}{24}\tan^2\alpha + \frac{1}{36}\right] C_6^{vv} \}\,, \qquad (4.38)$$

$$S_{ww} = -\frac{1}{2} f (\cos \overrightarrow{\psi}_z^* \sin \overline{\psi}_y)^2 + f' \{[\frac{1}{2}\tan\alpha(\cos \overrightarrow{\psi}_z^* \sin \overline{\psi}_y)^2]$$

$$+ \frac{1}{2}\tan\alpha\, [\tan^2\alpha(\cos \overrightarrow{\psi}_z^* \sin \overline{\psi}_y)^2 - 2\sin\gamma_x \tan\alpha \cos \overrightarrow{\psi}_z^* \sin \overline{\psi}_y$$

$$+ 2\, b_o b_{ww} - 2b_o b_w \cos \overrightarrow{\psi}_z^* \sin \overline{\psi}_y - \frac{b_o^2}{2}(1 - 3(\cos \overrightarrow{\psi}_z^* \sin \overline{\psi}_y)^2]$$

$$+ \left[\frac{1}{2}\tan^2\alpha + \frac{1}{6}\right] C_3^{ww} + \left[\frac{5}{8}\tan^3\alpha + \frac{5}{24}\tan\alpha\right] C_4^{ww}$$

$$+ \left[\frac{7}{8}\tan^4\alpha + \frac{7}{24}\tan^2\alpha\right] C_4^{ww} \} + \frac{1}{2} f'' \{[\tan^2\alpha\, (\cos \overrightarrow{\psi}_z^* \sin \overline{\psi}_y)^2$$

$$- 2\sin\gamma_x \tan\alpha \cos \overrightarrow{\psi}_z^* \sin \overline{\psi}_y + 2b_o b_{ww} - 2b_o b_w \cos \overrightarrow{\psi}_z^* \sin \overline{\psi}_y$$

$$- \frac{b_o^2}{2}(1 + 3(\cos \overrightarrow{\psi}_z^* \sin \overline{\psi}_y)^2)] + \tan\alpha\, C_3^{ww} + \left[\frac{5}{4}\tan^2\alpha + \frac{1}{3}\right] C_4^{ww}$$

$$+ \left[\frac{7}{4}\tan^3\alpha + \frac{7}{12}\tan\alpha\right] C_5^{ww} + \left[\frac{21}{8}\tan^4\alpha + \frac{23}{24}\tan^2\alpha + \frac{1}{36}\right] C_6^{ww}, \quad (4.39)$$

$$S_{uv} = -f\{\cos\bar{\psi}_z^*\cos\bar{\psi}_y\sin\bar{\psi}_z^*\} + f'\{C_1^{uv} + \frac{1}{2}\tan\alpha\, C_2^{uv}$$

$$+ \left[\frac{1}{2}\tan^2\alpha + \frac{1}{6}\right] C_3^{uv} + \left[\frac{5}{8}\tan^3\alpha + \frac{5}{24}\tan\alpha\right] C_4^{uv} + \left[\frac{7}{8}\tan^4\alpha\right.$$

$$\left. + \frac{7}{24}\tan^2\alpha\right] C_5^{uv}\} + \frac{1}{2} f''\{C_2^{uv} + \tan\alpha\, C_3^{uv} + \left[\frac{5}{4}\tan^2\alpha + \frac{1}{3}\right] C_4^{uv}$$

$$+ \left[\frac{7}{4}\tan^3\alpha + \frac{7}{12}\tan\alpha\right] C_5^{uv}$$

$$+ \left[\frac{21}{8}\tan^4\alpha + \frac{23}{24}\tan^2\alpha + \frac{1}{36}\right] C_6^{uv}\}, \quad (4.40)$$

$$S_{uw} = -f\{\cos^2\bar{\psi}_z^*\cos\bar{\psi}_y\sin\bar{\psi}_y\} + f'\{C_1^{uw} + \frac{1}{2}\tan\alpha\, C_2^{uw}$$

$$+ \left[\frac{1}{2}\tan^2\alpha + \frac{1}{6}\right] C_3^{uw} + \left[\frac{5}{8}\tan^3\alpha + \frac{5}{24}\tan\alpha\right] C_4^{uw}$$

$$+ \left[\frac{7}{8}\tan^4\alpha + \frac{7}{24}\tan^2\alpha\right] C_5^{uw}\} + \frac{1}{2} f''\{C_2^{uw} + \tan\alpha\, C_3^{uw}$$

$$+ \left[\frac{5}{4}\tan^2\alpha + \frac{1}{3}\right] C_4^{uw} + \left[\frac{7}{4}\tan^3\alpha + \frac{7}{12}\tan\alpha\right] C_5^{uw}$$

$$+ \left[\frac{21}{8}\tan^4\alpha + \frac{23}{24}\tan^2\alpha + \frac{1}{36}\right] C_6^{uw}\}, \quad (4.41)$$

$$S_{vw} = - f\{\cos \bar{\psi}_z^* \sin \bar{\psi}_y^* \sin \bar{\psi}_z^*\} + f'\{b_{vw} + \frac{1}{2} \tan \alpha [2b_o b_{vw}$$

$$- 2 \sin \gamma_x \tan \alpha \sin \bar{\psi}_z^* - 2 \cos \gamma_x \tan \alpha \cos \bar{\psi}_z^* \sin \bar{\psi}_y$$

$$+ 2 \tan^2 \alpha \sin \bar{\psi}_z^* \cos \bar{\psi}_z^* \sin \bar{\psi}_y - 2 b_o b_v \cos \bar{\psi}_z^* \sin \bar{\psi}_y$$

$$- 2b_o b_w \sin \bar{\psi}_z^* + 3b_o^2 \sin \bar{\psi}_z^* \cos \bar{\psi}_z^* \sin \bar{\psi}_y]$$

$$+ [\frac{1}{2} \tan^2 \alpha + \frac{1}{6}] C_3^{vw} + [\frac{5}{8} \tan^3 \alpha + \frac{5}{24} \tan \alpha] C_4^{vw}$$

$$+ [\frac{7}{8} \tan^4 \alpha + \frac{7}{24} \tan^2 \alpha] C_5^{vw}\}$$

$$+ \frac{1}{2} f''\{[2b_o b_{vw} - 2 \sin \gamma_x \tan \alpha \sin \bar{\psi}_z^*$$

$$- 2 \cos \gamma_x \tan \alpha \cos \bar{\psi}_z^* \sin \bar{\psi}_y + 2 \tan^2 \alpha \sin \bar{\psi}_z^* \cos \bar{\psi}_z^* \sin \bar{\psi}_y$$

$$- 2 b_o b_v \cos \bar{\psi}_z^* \sin \bar{\psi}_y - 2b_o b_w \sin \bar{\psi}_z^* + 3b_o^2 \sin \bar{\psi}_z^* \cdot$$

$$\cos \bar{\psi}_z^* \sin \bar{\psi}_y] + \tan \alpha C_3^{vw} + [\frac{5}{4} \tan^2 \alpha + \frac{1}{3}] C_4^{vw}$$

$$+ [\frac{7}{4} \tan^3 \alpha + \frac{7}{12} \tan \alpha] C_5^{vw} + [\frac{21}{8} \tan^4 \alpha$$

$$+ \frac{23}{24} \tan^2 \alpha + \frac{1}{36}] C_6^{vw}\} \cdot \qquad (4.42)$$

The C terms appearing in Eqs. 4.32 - 4.42 are defined in Appendix A and depend on mean velocity components, probe geometry and sensor orientation in the sensor xyz coordinate system. When sensor alignment with the flow is assumed

$$S_o = S_u = S_v = S_w = S_{uu} = S_{vv} = S_{ww} = S_{uv} = S_{uw} = S_{vw} = 0 \, . \quad (4.43)$$

The response equations, Eqs. 4.32 - 4.42, are compared to equations given by Bruun [57] and Champagne et al. [59] in Appendix C for an aligned sensor. In addition, an evaluation of Eqs. 4.32 - 4.42 is performed in Appendix E by testing the response of a misaligned vertical x-array.

D. Determination of the Mean Velocity

For a linearized response, the instantaneous voltage signal, R = E(t) in Eq. 4.25 and the time averaging of Eq. 4.32 yields

$$\frac{\overline{E}(t) - E_o}{B_o \overline{U}^*} = f + S_o + \frac{\overline{uu}}{\overline{U}^{*2}} \{S_{uu}\} + \frac{\overline{vv}}{\overline{U}^{*2}} \left\{ \frac{1}{2} f - \frac{1}{2} f' (\tan \alpha - \cos^2 \gamma_x \tan \alpha) \right.$$

$$\left. + \frac{1}{2} f'' \cos^2 \gamma_x + S_{vv} \right\} + \frac{\overline{ww}}{\overline{U}^{*2}} \left\{ \frac{1}{2} f - \frac{1}{2} f' (\tan \alpha - \sin^2 \gamma_x \tan \alpha) \right.$$

$$\left. + \frac{1}{2} f'' \sin^2 \gamma_x + S_{ww} \right\} + \frac{\overline{uv}}{\overline{U}^{*2}} \{S_{uv}\} + \frac{\overline{uw}}{\overline{U}^{*2}} \{S_{uw}\}$$

$$+ \frac{\overline{vw}}{\overline{U}^{*2}} \{\cos \gamma_x \sin \gamma_x (f' \tan \alpha + f'') + S_{vw}\} \, . \quad (4.44)$$

Equation 4.44 can be arranged to give a general mean velocity correction formula for turbulence effects. Let $\overline{U}^*$ represent the true velocity and $\overline{U}^*_E$ denote the estimated mean velocity neglecting the contribution of the turbulence quantities where

$$\frac{\overline{E} - E_o}{B_o \overline{U}^*_E} = f + S_o \, . \tag{4.45}$$

Dividing Eq. 4.44 by Eq. 4.45 yields

$$\frac{\overline{U}^*_E}{\overline{U}^*} = 1 + [f + S_o]^{-1} \left[\frac{\overline{uu}}{\overline{U}^{*2}} \{\,\}_{uu} + \frac{\overline{vv}}{\overline{U}^{*2}} \{\,\}_{vv} + \frac{\overline{ww}}{\overline{U}^{*2}} \{\,\}_{ww} \right.$$

$$\left. + \frac{\overline{uv}}{\overline{U}^{*2}} \{\,\}_{uv} + \frac{\overline{uw}}{\overline{U}^{*2}} \{\,\}_{uw} + \frac{\overline{vw}}{\overline{U}^{*2}} \{\,\}_{vw}\right] \tag{4.46}$$

where for convenience, the subscripted brace pairs represent the corresponding coefficients of the velocity product terms found in Eq. 4.44. The only unknown term in Eq. 4.46 is $\overline{U}^*$ since presumably, $\overline{U}^*_E$, the turbulent stresses, probe geometry, calibration constants and the degree of misalignment are all known. An iterative technique would usually be employed to determine $\overline{U}^*$. To obtain a more convenient form of Eq. 4.46, consider the quadratic form

$$\left(\frac{\overline{U}^*}{\overline{U}^*_E}\right)^2 - \left(\frac{\overline{U}^*}{\overline{U}^*_E}\right) + [f + S_o]^{-1} \left[\frac{\overline{uu}}{\overline{U}^{*2}_E} \{\,\}_{uu} + \frac{\overline{vv}}{\overline{U}^{*2}_E} \{\,\}_{vv} \right.$$

$$\left. + \frac{\overline{ww}}{\overline{U}^{*2}_E} \{\,\}_{ww} + \frac{\overline{uv}}{\overline{U}^{*2}_E} \{\,\}_{uv} + \frac{\overline{uw}}{\overline{U}^{*2}_E} \{\,\}_{uw} + \frac{\overline{vw}}{\overline{U}^{*2}_E} \{\,\}_{vw}\right] = 0$$

which can be solved to give

$$\frac{\overline{U}^*}{\overline{U}_E^*} = \frac{1}{2}\left\{1 + \left[1 - 4\left[f + S_o\right]^{-1}\left[\frac{\overline{uu}}{\overline{U}_E^{*2}}\left\{\ \right\}_{uu} + \frac{\overline{vv}}{\overline{U}_E^{*2}}\left\{\ \right\}_{vv}\right.\right.\right.$$

$$\left.\left.\left. + \frac{\overline{ww}}{\overline{U}_E^{*2}}\left\{\ \right\}_{ww} + \frac{\overline{uv}}{\overline{U}_E^{*2}}\left\{\ \right\}_{uv} + \frac{\overline{uw}}{\overline{U}_E^{*2}}\left\{\ \right\}_{uw} + \frac{\overline{vw}}{\overline{U}_E^{*2}}\left\{\ \right\}_{vw}\right]\right]^{1/2}\right\} . \qquad (4.47)$$

The plus sign was chosen since as $\overline{uu}, \ldots, \overline{vw} \to 0$, $\overline{U}_E^*$ becomes $\overline{U}^*$. Expanding the square root term in Eq. 4.47 yields

$$\frac{\overline{U}^*}{\overline{U}_E^*} \hat{=} 1 - \left[f + S_o\right]^{-1}\left[\frac{\overline{uu}}{\overline{U}_E^{*2}}\left\{\ \right\}_{uu} + \frac{\overline{vv}}{\overline{U}_E^{*2}}\left\{\ \right\}_{vv}\right.$$

$$\left. + \frac{\overline{ww}}{\overline{U}_E^{*2}}\left\{\ \right\}_{ww} + \frac{\overline{uv}}{\overline{U}_E^{*2}}\left\{\ \right\}_{uv} + \frac{\overline{uw}}{\overline{U}_E^{*2}}\left\{\ \right\}_{uw} + \frac{\overline{vw}}{\overline{U}_E^{*2}}\left\{\ \right\}_{vw}\right] , \qquad (4.48)$$

which represnts a more convenient form since the true mean velocity, $\overline{U}^*$, can be computed directly to $0\left(\frac{(\overline{uu})^2}{\overline{U}_E^{*4}}\right)$.

For comparison purposes, consider a vertical sensor normal to the flow where $\gamma_x = 0$ and $\alpha = 0$. For this geometry, Eq. 4.46 becomes

$$\frac{\overline{U}_E}{\overline{U}} = 1 + \frac{1}{2}\frac{\overline{vv}}{\overline{U}^2}\left\{1 + f''\left(0, P(0)\right)\right\} + \frac{1}{2}\frac{\overline{ww}}{\overline{U}^2} . \qquad (4.49)$$

Since for these conditions the sensor is aligned with the flow, the superscript star notation has been omitted. For this case f and f' are equal to 1 and 0, respectively, regardless of the cooling law function

used. For f", the cooling law proposed by Hinze (Eq. 2.6) is used with k assumed constant, which gives

$$f(\alpha,k^2) = \{\cos^2 \alpha + k^2 \sin^2 \alpha\}^{1/2} , \tag{4.50}$$

$$f'(\alpha,k^2) = f(\alpha,k^2) \left\{ \frac{(k^2 - 1) \tan \alpha}{1 + k^2 \tan^2 \alpha} \right\} , \tag{4.51}$$

$$f''(\alpha,k^2) = f(\alpha,k^2) \left\{ \frac{(k^2 - 1) + (k^2 - k^4) \tan^4 \alpha}{(1 + k^2 \tan^2 \alpha)^2} \right\} . \tag{4.52}$$

For the conditions above, Eq. 4.49 becomes

$$\frac{\overline{U}_E}{\overline{U}} = 1 + \frac{k^2}{2} \frac{\overline{vv}}{\overline{U}^2} + \frac{1}{2} \frac{\overline{ww}}{\overline{U}^2} . \tag{4.53}$$

For the same assumptions, the correction following Eq. 4.48 is

$$\frac{\overline{U}}{\overline{U}_E} = 1 - \frac{k^2}{2} \frac{\overline{vv}}{\overline{U}_E^2} - \frac{1}{2} \frac{\overline{ww}}{\overline{U}_E^2} . \tag{4.54}$$

A summary of correction formulas reported by other authors follows:

Klatt [64]

$$\frac{\overline{U}_E}{\overline{U}} = 1 + \frac{K^2}{2} \frac{\overline{ww}}{\overline{U}^2} \tag{4.55}$$

where K is a sensitivity coefficient greater than unity to account for the influence of the binormal velocity component; Rose [60]

$$\frac{\overline{U}}{\overline{U}_E} = 1 - \frac{1}{2} \frac{\overline{ww}}{\overline{U}_E^2} \quad ; \tag{4.56}$$

Moussa and Eskinazi [65]

$$\frac{\overline{U}_E}{\overline{U}} = 1 + \frac{k^2}{2}\frac{\overline{vv}}{\overline{U}^2} + \frac{1}{2}\frac{\overline{ww}}{\overline{U}^2} \; ; \qquad (4.57)$$

Muller [58]

$$\frac{\overline{U}_E}{\overline{U}} = 1 + k^2\frac{\overline{vv}}{\overline{U}^2} + \frac{1}{2}\frac{\overline{ww}}{\overline{U}^2} \; . \qquad (4.58)$$

Equation 4.46 gives results that are consistent with expressions reported by other investigators and will serve as a basis for correcting the mean velocity measured by a sensor placed arbitrarily in a 3DTBL flow. The velocity measured by each sensor of the three x-arrays used in this study was corrected using Eq. 4.48 and the results are presented in Chapter VII.

E. General X-Array Response Equations

The earlier results can be used to develop a general and comprehensive set of equations for obtaining the turbulent stresses from an x-array probe. The resulting equations are based on the sum and difference combinations of the voltage fluctuations measured by two sensors placed in a prescribed plane.

The sensor's response to velocity fluctuations is obtained by substracting the mean response (Eq. 4.44) from the instantaneous response (Eq. 4.32). This gives

$$\frac{E(t) - \bar{E}}{B_o \bar{U}^*} = \frac{u}{\bar{U}^*}\{f + S_u\} + \frac{v}{\bar{U}^*}\{f' \cos \gamma_x + S_v\}$$

$$+ \frac{w}{\bar{U}^*}\{f' \sin \gamma_x + S_w\} + \{\frac{\overline{uu}}{\bar{U}^{*2}} - \frac{\overline{uu}}{\bar{U}^{*2}}\}\{S_{uu}\} + \frac{1}{2}\{\frac{\overline{vv}}{\bar{U}^{*2}} - \frac{\overline{vv}}{\bar{U}^{*2}}\} \cdot$$

$$\{f - f' \tan \alpha \sin^2 \gamma_x + f'' \cos^2 \gamma_x + S_{vv}\}$$

$$+ \frac{1}{2}\{\frac{\overline{ww}}{\bar{U}^{*2}} - \frac{\overline{ww}}{\bar{U}^{*2}}\}\{f - f' \tan \alpha \cos^2 \gamma_x + f'' \sin^2 \gamma_x + S_{vv}\}$$

$$+ \{\frac{\overline{uv}}{\bar{U}^{*2}} - \frac{\overline{uv}}{\bar{U}^{*2}}\}\{S_{uv}\} + \{\frac{\overline{uw}}{\bar{U}^{*2}} - \frac{\overline{uw}}{\bar{U}^{*2}}\}\{S_{uw}\}$$

$$+ \{\frac{\overline{vw}}{\bar{U}^{*2}} - \frac{\overline{vw}}{\bar{U}^{*2}}\}\{\cos \gamma_x \sin \gamma_x [f' \tan \alpha + f''] + S_{vw}\} . \qquad (4.59)$$

Consider two sensors, a and b, located in a plane denoted by i. With $e(t) = E(t) - \bar{E}$, the response equations according to Eq. 4.59 become, to first order,

$$e_{a,i} = B_{o,a,i}\{u [f_{a,i} + S_{u,a,i}] + v [f'_{a,i} \cos \gamma_{x,a,i} + S_{v,a,i}]$$

$$+ w [f'_{a,i} \sin \gamma_{x,a,i} + S_{w,a,i}]\} \qquad (4.60)$$

and

$$e_{b,i} = B_{o,b,i}\{u [f_{b,i} + S_{u,b,i}] + v [f'_{b,i} \cos \gamma_{x,b,i} + S_{v,b,i}]$$

$$+ w [f'_{b,i} \sin \gamma_{x,b,i} + S_{w,b,i}]\} , \qquad (4.61)$$

where the compact notation

$$f_{a,i} = f(\alpha_{a,i}, P_a(\alpha_{a,i})) \tag{4.62}$$

and

$$f_{b,i} = f(\alpha_{b,i}, P_b(\alpha_{b,i})) \tag{4.63}$$

have been used for convenience with similar representations implied by the other subscripted symbols. Forming the sum and difference combinations of Eqs. 4.60 and 4.61 yields

$$(e_{a,i} + e_{b,i}) = (e_a + e_b)_i = A_i^+ u + B_i^+ v + C_i^+ w \tag{4.64}$$

and

$$(e_{a,i} - e_{b,i}) = (e_a - e_b)_i = A_i^- u + B_i^- v + C_i^- w \tag{4.65}$$

with considerable simplification resulting from the notation used where:

$$A_i^{\pm} = B_{o,a,i}[f_{a,i} + S_{u,a,i}] \pm B_{o,b,i}[f_{b,i} + S_{u,b,i}], \tag{4.66}$$

$$B_i^{\pm} = B_{o,a,i}[f'_{a,i} \cos \gamma_{x,a,i} + S_{v,a,i}]$$

$$\pm B_{o,b,i}[f'_{b,i} \cos \gamma_{x,b,i} + S_{v,b,i}], \tag{4.67}$$

$$C_i^{\pm} = B_{o,a,i}[f'_{a,i} \sin \gamma_{x,a,i} + S_{w,a,i}]$$

$$\pm B_{o,b,i}[f'_{b,i} \sin \gamma_{x,b,i} + S_{w,b,i}]. \tag{4.68}$$

Squaring Eqs. 4.64 and 4.65 separately, multiplying them together and time averaging, yields the three equations of interest, namely

$$\overline{(e_a + e_b)_i^2} = A_i^{+2}\,\overline{uu} + B_i^{+2}\,\overline{vv} + C_2^{+2}\,\overline{ww} + 2A_i^{+}B_i^{+}\,\overline{uv}$$

$$+ 2A_i^{+}C_i^{+}\,\overline{uw} + 2B_i^{+}C_i^{+}\,\overline{vw}\,, \tag{4.69}$$

$$\overline{(e_a - e_b)_i^2} = A_i^{-2}\,\overline{uu} + B_i^{-2}\,\overline{vv} + C_i^{-2}\,\overline{ww} + 2A_i^{-}B_i^{-}\,\overline{uv}$$

$$+ 2A_i^{-}C_i^{-}\,\overline{uw} + 2B_i^{-}C_i^{-}\,\overline{vw}\,, \tag{4.70}$$

and

$$\overline{(e_a + e_b)(e_a - e_b)_i} = A_i^{+}A_i^{-}\,\overline{uu} + B_i^{+}B_i^{-}\,\overline{vv} + C_i^{+}C_i^{-}\,\overline{ww}$$

$$+ (A_i^{+}B_i^{-} + A_i^{-}B_i^{+})\,\overline{uv} + (A_i^{+}C_i^{-} + A_i^{-}C_i^{+})\,\overline{uw}$$

$$+ (B_i^{+}C_i^{-} + B_i^{-}C_i^{+})\,\overline{vw}. \tag{4.71}$$

In any position i, the two sensors, their imaginary normal vectors, and the x-axis can be viewed as all lying in the same plane. This re-

striction follows from the concept of the x-probe. As a result, $\gamma_{x,a}$ and $\gamma_{x,b}$ are constrained by

$$(\gamma_{x,a} - \gamma_{x,b}) = \pi \ , \tag{4.72}$$

where in general

$$0 \leq \gamma_{x,a} \leq \pi \tag{4.73}$$

and

$$-\pi \leq \gamma_{x,b} \leq 0 \ . \tag{4.74}$$

To show this, consider the sensor xyz coordinate system with unit vector, $\hat{\ell}$, describing the sensor's direction as given by Eq. 4.19 as

$$\hat{\ell} = \sin \alpha \, \hat{e}_x + \cos \alpha \cos \gamma_x \, \hat{e}_y + \cos \alpha \sin \gamma_x \, \hat{e}_z \ . \tag{4.19}$$

For the plane defined by the x-array containing the unit vectors $\hat{\ell}_a$ and $\hat{\ell}_b$,

$$\hat{\ell}_b \cdot (\hat{\ell}_a \times \hat{e}_x) = 0 \tag{4.75}$$

is required. Substituting the expressions for the unit vectors of sensors a and b after Eq. 4.19 into Eq. 4.75 and performing the required operations yields

$$\sin (\gamma_{x,a} - \gamma_{x,b}) = 0 \tag{4.76}$$

from which

$$(\gamma_{x,a} - \gamma_{x,b}) = n\pi \ , \ n = 0,1,2,3,\ldots \ , \tag{4.77}$$

which completes the proof. For the x-array, the value n = 1 is sufficient as other values are not relevant to the specification of the sensor geometry.

Unless otherwise specified, the following response analysis will be presented in an aligned sensor system, that is, with the sensor and local coordinate systems coincident.

The Response of the Horizontal X-Array

The horizontal x-array (hx) lies in a plane that is parallel to the xz plane. Measurements obtained from this spatial arrangement will provide the $\overline{uu}$, $\overline{ww}$, and $\overline{uw}$ stresses. For a geometrically perfect hx-array,

$$\gamma_{x,a} = \pi/2 \tag{4.78}$$

and

$$\gamma_{x,b} = -\pi/2 \ . \tag{4.79}$$

The subscript i has been omitted from the notation for this single plane operation. Thus from Eq. 4.67, one finds

$$B^{+} = B^{-} = 0 \,, \tag{4.80}$$

which transforms Eqs. 4.69-4.71 to the simultaneous system

$$\left|\begin{array}{c} \overline{(e_a + e_b)^2} \\ \overline{(e_a - e_b)^2} \\ \overline{(e_a + e_b)(e_a - e_b)} \end{array}\right| = \left|\begin{array}{ccc} A^{+2} & C^{+2} & 2A^{+}C^{+} \\ A^{-2} & C^{-2} & 2A^{-}C^{-} \\ A^{+}A^{-} & C^{+}C^{-} & A^{+}C^{-} + A^{-}C^{+} \end{array}\right| \left|\begin{array}{c} \overline{uu} \\ \overline{ww} \\ \overline{uw} \end{array}\right| \,. \tag{4.81}$$

At this point, the assumption of a geometrically perfect probe is emphasized inasmuch as a tilted sensor plane would involve the remaining stresses appearing in Eqs. 4.67-4.71. These added terms would result in an ill-defined system of 3 equations and 6 unknown turbulent stresses.

Matched Sensors

The coefficient matrix of the hx-array, given by Eq. 4.81, consists of all possible sensor sensitivities to the $\overline{uu}$, $\overline{ww}$, and $\overline{uw}$ stresses. It accounts for unique sensor yaw angles, velocity calibrations, and directional characteristics of each sensor in the sensor pair. It is further noted that each computed stress is functionally dependent on all three mean voltage combinations appearing on the left side of Eq. 4.81. Such a dependence is also shown by Elsenaar and Boelsma [32]. This general treatment is necessary to fully understand the response of the x-array to a turbulent flow and will provide greater insight into the so-called matched sensor assumption. This assumption will be discussed in detail

for the horizontal x-array and the discussion is applicable to the vertical and slant x-arrays as well.

The most widely used form of the processing equations for x-arrays are for "matched" sensors. For the hx-array, these equations can be represented by

$$\overline{(e_a + e_b)^2} \propto \overline{u^2} , \tag{4.82}$$

$$\overline{e_a - e_b}^2 \propto \overline{w^2} , \tag{4.83}$$

and

$$\overline{(e_a + e_b)(e_a - e_b)} \propto \overline{uw} . \tag{4.84}$$

Equations 4.82 - 4.84 result from Eq. 4.81 when

$$A^- = C^+ = 0 , \tag{4.85}$$

which alters Eq. 4.81 to the simpler form

$$\begin{vmatrix} \overline{(e_a + e_b)^2} \\ \overline{(e_a - e_b)^2} \\ \overline{(e_a + e_b)(e_a - e_b)} \end{vmatrix} = \begin{vmatrix} A^{+2} & 0 & 0 \\ 0 & C^{-2} & 0 \\ 0 & 0 & A^+C^- \end{vmatrix} \begin{vmatrix} \overline{uu} \\ \overline{ww} \\ \overline{uw} \end{vmatrix} . \tag{4.86}$$

The content of the coefficient matrix in Eq. 4.86 is given in Eqs. 4.66 and 4.68 as

$$A^{+2} = 4B_o^2 f^2 , \tag{4.87}$$

$$C^{-2} = 4B_o^2 f'^2 , \tag{4.88}$$

and

$$A^{+}C^{-} = 4B_o^2 f f' . \tag{4.89}$$

Applying Hinze's [54] cooling law function (Eqs. 4.50 and 4.51) for $\alpha = \frac{\pi}{4}$ yields

$$A^{+2} = 4\left(B_o f(\tfrac{\pi}{4}, k^2)\right)^2 , \tag{4.90}$$

$$C^{-2} = 4\left(B_o f(\tfrac{\pi}{4}, k^2)\right)^2 \left(\frac{k^2 - 1}{k^2 + 1}\right)^2 , \tag{4.91}$$

and

$$A^{+}C^{-} = 4\left(B_o f(\tfrac{\pi}{4}, k^2)\right)^2 \left(\frac{k^2 - 1}{k^2 + 1}\right) . \tag{4.92}$$

Equations 4.90-4.92 are typical results that have been reported by others for a similar probe [35,52,58,59,92,93]. A closer look reveals that this simplified version of Eq. 4.81, which results from Eq. 4.85, assumes that both

$$B_{o,a} f(\alpha_a, P_a(\alpha_a)) = B_{o,b} f(\alpha_b, P_b(\alpha_b)) \tag{4.93}$$

and

$$B_{o,a}\, f'(\alpha_a, P_a(\alpha_a)) = B_{o,b}\, f'(\alpha_b, P_b(\alpha_b)) \tag{4.94}$$

are satisfied simultaneously where Eq. 4.93 yields $A^- = 0$ and Eq. 4.94 yields $C^+ = 0$. Equation 4.93 can be re-written as

$$B_a(\alpha_a) = B_b(\alpha_b) , \tag{4.95}$$

which is more readily recognized as an equivalence of the sensors' velocity sensitivities at a fixed position since $B_a(\alpha_a)$ and $B_b(\alpha_b)$ represent the slopes of the velocity calibration curves at α_a and α_b for sensors a and b, respectively. The equalities given by Eq. 4.93 and 4.94 are clearly valid when

$$B_{o,a} = B_{o,b} , \tag{4.96}$$

$$\alpha_a = \alpha_b , \tag{4.97}$$

and

$$P_a(\alpha) = P_b(\alpha) \tag{4.98}$$

are met. Thus Eq. 4.96 - 4.98 are the most stringent conditions that are necessary to obtain a matched sensor response assumed by the con-

ventional processing equations given by Eqs. 4.82-4.84. It is noted that Eq. 4.98 is due solely to deviations from the ideal cosine law. In practice, Eq. 4.96 is attainable by manipulating linearizer gain settings or controlling overheat, while Eq. 4.97 is easily satisfied by properly adjusting the position of the probe. The parameter, $P(\alpha)$, however will be unique to each sensor, although the general forms for a sensor pair are usually chosen to be similar. It is most desirable that sensors have equal yaw characteristics thereby satisfying Eq. 4.98. However, such an ideal situation is usually not found in practice and hence, Eq. 4.98 is not easily satisfied, as shown in Tables 5.2 and 5.3 for the case of constant k^2. Moreover, when aerodynamic interference between a sensor and its supporting material prohibits yaw calibration in a required angular range, one must impose the assumption given by Eq. 4.98. The usual definition of matched sensors seems to ignore the role of the yawed response of a sensor explicit in Eqs. 4.93 and 4.94 in matching the sensors. It must be emphasized that both equations are shown as necessary and sufficient to have properly "matched" sensors. It will be shown in Chapter VII that significant errors in the turbulent stresses can result when the conventional response equations are used to reduce turbulence data obtained from unmatched sensors.

As noted earlier, it is possible to force A^- to a zero value, thereby satisfying Eq. 4.93, (or 4.95) simply by adjusting gain settings or sensor overheat so that the slope of the calibration curve of sensor a at position α_a is equal to the corresponding slope of sensor b at position α_b. This coefficent matrix,

$$\begin{vmatrix} A^{+2} & C^{+2} & 2A^{+}C^{+} \\ 0 & C^{-2} & 0 \\ 0 & C^{+}C^{-} & A^{+}C^{-} \end{vmatrix}, \tag{4.99}$$

represents a more realistic "quasi-matched" sensor condition.

As an example, consider an hx-array with the sensors having unique yaw characteristics. For convenience the cooling law (and its first derivative) of Davies and Bruun [104] is used. For the case of constant m,

$$f(\alpha,m) = \cos^{m}\alpha \tag{4.100}$$

and

$$f'(\alpha,m) = - f\ m \tan \alpha\ . \tag{4.101}$$

If the gain settings are adjusted so that Eq. 4.93 is satisfied then the sensors are quasi-matched. Introducing Eq. 4.101 into Eq. 4.94, one obtains for quasi-matched sensors

$$m_a \tan \alpha_a = m_b \tan \alpha_b, \tag{4.102}$$

which in general is not satisfied unless adjustments of the yaw angles α_a and α_b can be made. This can be shown by letting, $m_a = m$, $m_b = m + \Delta m$, $\alpha_a = \alpha + \Delta\alpha$, and $\alpha_b = \alpha - \Delta\alpha$, where Δm and $\Delta\alpha$ represent the asymmetries in m and α, respectively, between

the two sensors. With these definitions, Eq. 4.102 becomes

$$\frac{\Delta m}{m} = \frac{\tan\ (\alpha + \Delta\alpha)}{\tan\ (\alpha - \Delta\alpha)} - 1\ . \qquad (4.103)$$

For $\alpha = \pi/4$ and a range of $\Delta\alpha$ values, the corresponding relative errors in m are calculated from Eq. 4.103:

$\Delta\alpha$, deg.	$\Delta m/m$
0	0.00
2	0.15
5	0.42
10	1.04 .

These results show that despite differences in m, which prevent a direct match in sensors yaw characteristics, a balancing of Eq. 4.102 (and thus Eq. 4.94) is possible by rotating the x-plane. The new values of α_a and α_b (e.g. 47^o and 43^o, respectively, for a 15% difference in m) would replace the old value of $\alpha = 45^o$ in the response equations and the newly computed stresses would be relative to the adjusted sensor coordinate system. In practice, such an adjustment may not always be possible due to limitations of the traversing mechanism.

Summarizing, the sensors of a perfect hx-array are matched when they are correctly positioned (Eq. 4.97), and have identical velocity and yaw characteristics (Eqs. 4.96 and 4.98). Collectively these conditions satisfy Eqs. 4.93 and 4.94 which in turn gives the system shown in Eq. 4.86. Complete "matching" is possible by electronic adjustments

and repositioning the x-plane such that Eq. 4.93 and 4.94 are satisfied. The latter adjustment will depend on the rotational capabilities of the transversing mechanism in positioning the probe.

The Response of the Vertical X-Array

The vertical x-array (vx) lies in a vertical plane and provides the $\overline{uu}$, $\overline{vv}$ and $\overline{uv}$ stresses. The geomtrically perfect probe is formed when

$$\gamma_{x,a} = 0 \tag{4.104}$$

and

$$\gamma_{x,b} = -\pi , \tag{4.105}$$

which gives

$$C^{+} = C^{-} = 0 \tag{4.106}$$

in Eqs. 4.69-4.71. The earlier analysis and discussion presented for the hx-array directly applies to this configuration when C^{+}_{-} is replaced by B^{+}_{-}. Similar to Eq. 4.81, the general matrix form is

$$\begin{vmatrix} \overline{(e_a + e_b)^2} \\ \overline{(e_a - e_b)^2} \\ \overline{(e_a + e_b)(e_a - e_b)} \end{vmatrix} = \begin{vmatrix} A^{+2} & B^{+2} & 2A^{+}B^{+} \\ A^{-2} & B^{-2} & 2A^{-}B^{-} \\ A^{+}A^{-} & B^{+}B^{-} & A^{+}B^{-} + A^{-}B^{+} \end{vmatrix} \begin{vmatrix} \overline{uu} \\ \overline{vv} \\ \overline{uv} \end{vmatrix} , \tag{4.107}$$

which can be solved to give two normal and primary shear stresses associated with two-dimensional flows. For matched sensors, Eq. 4.107 becomes

$$\begin{vmatrix} \overline{(e_a + e_b)^2} \\ \overline{(e_a - e_b)^2} \\ \overline{(e_a + e_b)(e_a - e_b)} \end{vmatrix} = \begin{vmatrix} A^{+2} & 0 & 0 \\ 0 & B^{-2} & 0 \\ 0 & 0 & B^{-}A^{+} \end{vmatrix} \begin{vmatrix} \overline{uu} \\ \overline{vv} \\ \overline{uv} \end{vmatrix} . \tag{4.108}$$

In this case Eqs. 4.93 and 4.94 give

$$A^{-} = B^{+} = 0 \tag{4.109}$$

after Eqs. 4.66 and 4.67. The "quasi-matched" form of the coefficient matrix

$$\begin{vmatrix} A^{+2} & B^{+2} & 2A^{+}B^{+} \\ 0 & B^{-2} & 0 \\ 0 & B^{+}B^{-} & A^{+}B^{-} \end{vmatrix} \tag{4.110}$$

is obtained by electronically matching the signal voltage levels of the sensors.

The Response of the Slant X-Array

The slant x-array (sx) is usually employed for the sole purpose of measuring the remaining $\overline{vw}$ shear stress. In the earlier analysis in

both the horizontal and vertical planes, the coefficients of this $\overline{vw}$ stress vanish, preventing the measurement of this combination of fluctuating velocities. Data is required at two intermediate positions, namely

$$0 < \gamma_{x,a,1} < \frac{\pi}{2} \tag{4.111}$$

and

$$-\pi < \gamma_{x,b,1} < -\frac{\pi}{2} \tag{4.112}$$

for position 1, and in the second position

$$\frac{\pi}{2} < \gamma_{x,a,2} < \pi \tag{4.113}$$

and

$$-\frac{\pi}{2} < \gamma_{x,b,2} < 0 \, . \tag{4.114}$$

Referring to Eqs. 4.69-4.71 for i = 1,2, the response equations are written in their most general form as

$$\begin{vmatrix} P_1^2 \\ M_1^2 \\ P_1M_1 \\ P_2^2 \\ M_2^2 \\ P_2M_2 \end{vmatrix} = \begin{vmatrix} A_1^{+2} & B_1^{+2} & C_1^{+2} & 2A_1^+B_1^+ & 2A_1^+C_1^+ & 2B_1^+C_1^+ \\ A_1^{-2} & B_1^{-2} & C_1^{-2} & 2A_1^-B_1^- & 2A_1^-C_1^- & 2B_1^-C_1^- \\ A_1^+A_1^- & B_1^+B_1^- & C_1^+C_1^- & A_1^+B_1^-+A_1^-B_1^+ & A_1^+C_1^-+A_1^-C_1^+ & B_1^+C_1^-+B_1^-C_1^+ \\ A_2^{+2} & B_2^{+2} & C_2^{+2} & 2A_2^+B_2^+ & 2A_2^+C_2^+ & 2B_2^+C_2^+ \\ A_2^{-2} & B_2^{-2} & C_2^{-2} & 2A_2^-B_2^- & 2A_2^-C_2^- & 2B_2^-C_2^- \\ A_2^+A_2^- & B_2^+B_2^- & C_2^+C_2^- & A_2^+B_2^-+A_2^-B_2^+ & A_2^+C_2^-+A_2^-C_2^+ & B_2^+C_2^-+B_2^-C_2^+ \end{vmatrix} \begin{vmatrix} \overline{uu} \\ \overline{vv} \\ \overline{ww} \\ \overline{uv} \\ \overline{uw} \\ \overline{vw} \end{vmatrix} . \tag{4.115}$$

For compactness, symbols P and M represent the plus (sum) and minus (difference) voltages. In principal, all six Reynold's stresses can be computed by the system presented in Eq. 4.115 provided that the coefficient matrix is non-singular. Ironically, the sx-array with matched sensors results in a singular coefficient matrix and sensitivity studies have shown that modest deviations from the matched sensor conditions do not adequately neutralize the singularity to expect meaningful results. Nevertheless, the demonstrated potential of the sx-array to generate the complete Reynolds stress tensor should not be ignored since this alternative would significantly reduce the efforts involved in the x-array method as a whole. For example, finding suitable sensor plane locations and appropriate gain settings that can provide adequate "mismatch" may produce a well defined system of equations.

Development of the Perfect Slant X-Array with Matched Sensors

The geometrically perfect slant x-array resembles a plane that is inclined 45^{o} to the xz (or xy) plane in each position. Position 1 is defined by the sensors positions

$$\gamma_{x,a,1} = \frac{\pi}{4} \tag{4.116}$$

and

$$\gamma_{x,b,1} = -\frac{3\pi}{4} , \tag{4.117}$$

and for position 2

$$\gamma_{x,a,2} = \frac{3\pi}{4} \tag{4.118}$$

and

$$\gamma_{x,b,2} = -\frac{\pi}{4} . \tag{4.119}$$

For a sx-array probe with supporting prongs normal to the flow direction, postion 2 is obtained by a 180^{o} rotation about the probe's axis from position 1.

Consider the case of matched sensors in each plane. The conditions of Eqs. 4.93 and 4.94 together with Eqs. 4.66-44.68 and 4.72 result in

$$A_i^- = B_i^+ = C_i^+ = 0 , \qquad i = 1,2 , \tag{4.120}$$

which produces the sparse version of the system given in Eq. 4.115

$$\begin{vmatrix} P_1^2 \\ M_1^2 \\ P_1 M_1 \\ P_2^2 \\ M_2^2 \\ P_2 M_2 \end{vmatrix} = \begin{vmatrix} A_1^{+2} & 0 & 0 & 0 & 0 & 0 \\ 0 & B_1^{-2} & C_1^{-2} & 0 & 0 & -2B_1^- C_1^- \\ 0 & 0 & 0 & A_1^+ B_1^- & A_1^+ C_1^- & 0 \\ A_2^{+2} & 0 & 0 & 0 & 0 & 0 \\ 0 & B_2^{-2} & C_2^{-2} & 0 & 0 & -2B_2^- C_2^- \\ 0 & 0 & 0 & A_2^+ B_2^- & A_2^+ C_2^- & 0 \end{vmatrix} \begin{vmatrix} \overline{uu} \\ \overline{vv} \\ \overline{ww} \\ \overline{uv} \\ \overline{uw} \\ \overline{vw} \end{vmatrix} \tag{4.121}$$

where the element components

$$A_1^+ = 2\, B_{o,1}\, f_1 \,, \tag{4.122}$$

$$A_2^+ = 2\, B_{o,2}\, f_2 \,, \tag{4.123}$$

$$B_1^- = 2\, B_{o,1}\, f_1^{'} \cos \gamma_{x,a,1} \,, \tag{4.124}$$

$$B_2^- = 2\, B_{o,2}\, f_2^{'} \cos \gamma_{x,a,2} \,, \tag{4.125}$$

$$C_1^- = 2\, B_{o,1}\, f_1^{'} \sin \gamma_{x,a,1} \,, \tag{4.126}$$

and

$$C_2^- = 2\, B_{o,2}\, f_2'\, \sin\, \gamma_{x,a,2} \,. \tag{4.127}$$

For the match sensor case, the subscripted a and b notations are not necessary and are excluded in the statements above. By inspection, the 6 x 6 coefficient matrix is singular which prevents a unique and meaningful solution to the general problem. However, an alternative solution is possible which will yield the desired $\overline{vw}$ stress along with other 'redundant' stresses. This approach involves a decomposition of the unknown stresses to their fluctuating velocity components. Prior to time averaging, the system shown in Eq. 4.121 can be reduced to six equations by straight-forward multiplications. These are

$$P_1^2 = A_1^{+2}\, u^2 \,, \tag{4.128}$$

$$M_1^2 = (B_1^- v + C_1^- w)^2 \,, \tag{4.129}$$

$$P_1 M_1 = A_1^+ u(B_1^- v + C_1^- w) \,, \tag{4.130}$$

$$P_2^2 = A_2^{+2}\, u^2 \,, \tag{4.131}$$

$$M_2^2 = (B_2^- v + C_2^- w)^2 \,, \tag{4.132}$$

and

$$P_2 M_2 = A_2^+ u(B_2^- v + C_2^- w) \,. \tag{4.133}$$

Proceeding with the problem of determining the $\overline{vw}$ stress, Eqs. 4.129 and 4.132 can be solved simultaneously to yield the following expressions for v and w:

$$v = \frac{\bar{C}_2 M_1 - \bar{C}_1 M_2}{\bar{B}_1 \bar{C}_2 - \bar{B}_2 \bar{C}_1} , \tag{4.134}$$

$$w = \frac{\bar{B}_1 M_2 - \bar{B}_2 M_1}{\bar{B}_1 \bar{C}_2 - \bar{B}_2 \bar{C}_1} . \tag{4.135}$$

Forming the vw product and time averaging,

$$\overline{vw} = \frac{\overline{M_1 M_2} (\bar{B}_1 \bar{C}_2 + \bar{B}_2 \bar{C}_1) - \bar{B}_2 \bar{C}_2 \overline{M_1^2} - \bar{B}_1 \bar{C}_1 \overline{M_2^2}}{(\bar{B}_1 \bar{C}_2 - \bar{B}_2 \bar{C}_1)^2} . \tag{4.136}$$

The term $\overline{M_1 M_2}$, namely $\overline{(e_a + e_b)_1 (e_a - e_b)_2}$, involves the simultaneous processing of signals from two positions. This measurement is temporally impossible to make without digital or analog recorders. Such measurements are not usually associated with x-probe systems and fortunately they are not necessary if the coefficient $(\bar{B}_1 \bar{C}_2 + \bar{B}_2 \bar{C}_1)$ vanishes. To determine the necessary conditions for this to occur, Eqs. 4.72 and 4.124-4.127 are used. For sensor a

$$4 B_{o,1} B_{o,2} f_1' f_2' \{\sin \gamma_{x,a,2} \cos \gamma_{x,a,1} + \sin \gamma_{x,a,1} \cos \gamma_{x,a,2}\} = 0 ,$$

which can be simplified to give

$$\sin (\gamma_{x,a,1} + \gamma_{x,a,2}) = 0 \tag{4.137}$$

since in general $f_1' \neq f_2' \neq 0$. Equation 4.137 implies

$$\gamma_{x,a,1} + \gamma_{x,a,2} = n\pi, \quad n = 0,1,2,3, \ \ldots \ .$$

For typical sx-array operation

$$\gamma_{x,a,1} + \gamma_{x,a,2} = \pi \tag{4.138}$$

is chosen. A similar expression for sensor b can be written as

$$\gamma_{x,b,1} + \gamma_{x,b,2} = -\pi \ . \tag{4.139}$$

The necessary conditions given by equations 4.138 and 4.139 are geometric and play a role similar to Eq. 4.72 insofar as they impose the spacial limitations on the relative locations of the sensor planes. According to these restrictions, Eqs. 4.136 becomes

$$\overline{vw} = \frac{-\bar{B}_1 \bar{C}_1 \overline{M_2^2} - \bar{B}_2 \bar{C}_2 \overline{M_1^2}}{(\bar{B}_1 \bar{C}_2 - \bar{B}_2 \bar{C}_1)^2} \tag{4.140}$$

and Eqs. 4.122-4.127 can be written in terms of $\gamma_{x,a,1}$ as

$$A_1^+ = 2 B_{o,1} f_1 \ , \tag{4.141}$$

$$A_2^+ = 2 B_{o,2} f_2 \ , \tag{4.142}$$

$$\bar{B_1} = 2\, B_{o,1}\, f_1'\, \cos\, \gamma_{x,a,1}\,, \tag{4.143}$$

$$\bar{B_2} = -\,2\, B_{o,2}\, f_2'\, \cos\, \gamma_{x,a,1}\,, \tag{4.144}$$

$$\bar{C_1} = 2\, B_{o,1}\, f_1'\, \sin\, \gamma_{x,a,1}\,, \tag{4.145}$$

and

$$\bar{C_2} = 2\, B_{o,2}\, f_2'\, \sin\, \gamma_{x,a,1}\,. \tag{4.146}$$

Three simplifications of Eq. 4.140 which stem from idealizations of probe operation are noted. The first case results from the perfect probe geometry given in Eqs. 4.116-4.119. In this case, $\gamma_{x,a,1} = \frac{\pi}{4}$ and Eqs. 4.138 and 4.139 are satisfied. Referring to Eqs. 4.143-4.146,

$$\bar{B_1} = \bar{C_1}\,, \tag{4.147}$$

$$\bar{B_2} = -\,\bar{C_2}\,, \tag{4.148}$$

and consequently Eq. 4.140 becomes

$$\overline{vw} = \frac{\bar{B_2}\,\overline{M_1^2} - B_1^{-2}\,\overline{M_2^2}}{4 B_2^{-2}\, B_1^{-2}}\,. \tag{4.149}$$

The second case occurs when

$$B_{o,1}\, f_1 = B_{o,2}\, f_2 \tag{4.150}$$

and

$$B_{o,1}\, f_1' = B_{o,2}\, f_2' \,, \tag{4.151}$$

which essentially matches the sensor characteristics of the first position with the second. In this case of matched positions

$$\bar{B_2} = -\bar{B_1} \tag{4.152}$$

and

$$\bar{C_2} = \bar{C_1} \tag{4.153}$$

which further reduces Eq. 4.140 to

$$\overline{vw} = \frac{\overline{M_1^2} - \overline{M_2^2}}{4\bar{B_1}\bar{C_1}} \,. \tag{4.154}$$

Equations 4.150 and 4.151 resemble the conditions given as necessary for matched sensors. Equation 4.150 can be easily satisfied by electronic matching techniques. If no differences in the yaw characteristics of sensor pair exist between the two positions, then Eq. 4.151 is valid. However, such differences can occur as indicated in Tables 5.2 and 5.3 where differences in the values of the cooling law parameter, k^2, are shown.

The last version of Eq. 4.140 incorporates both geometrically perfect probe and matched position features. In this case,

$$B_1^- = -B_2^- = C_1^- = C_2^- \tag{4.155}$$

and the resulting equation becomes

$$\overline{vw} = \frac{\overline{(e_a - e_b)_1^2} - \overline{(e_a - e_b)_2^2}}{8\, B_o^2\, f'^2} . \tag{4.156}$$

This form is most often used to determine the $\overline{vw}$ stress [32,35,41,52,58,92,93].

Summarizing, the remaining $\overline{vw}$ stress requires the intermediate positions provided by the sx-array. Sensor plane locations 45^o to the horizontal plane (Eqs. 4.116-4.119), matched sensors in each position (Eqs. 4.93 and 4.94), and matched positions (Eqs. 4.150 and 4.151) represent the ideal situation. However, successful measurement of the $\overline{vw}$ shear stress can be made with only

1) matched sensors in each position,

2) $\gamma_{x,a,i} - \gamma_{x,b,i} = \pi$, $i = 1,2$, (Eq. 4.72)

3) $\gamma_{x,a,1} + \gamma_{x,a,2} = \pi$, (Eq. 4.138)

$\gamma_{x,b,1} + \gamma_{x,b,2} = -\pi$. (Eq. 4.139)

Calculation of Redundant Normal Stresses

As a result of the reduced system of response equations given by Eqs. 4.128-4.133 additional normal stresses can be obtained from the sx-array. These include the $\overline{uu}$ and a combination of the $\overline{vv}$ and $\overline{ww}$ normal stresses. The $\overline{uu}$ stress is obtained by solving either Eqs. 4.128 or 4.131 where

$$\overline{uu} = \frac{P_1^2}{A_1^{+2}} = \frac{P_2^2}{A_2^{+2}} . \tag{4.157}$$

Equations 4.129 and 4.132, which were involved in obtaining the $\overline{vw}$ shear stress, can provide a linear combination of the $\overline{vv}$ and $\overline{ww}$ normal stresses. Squaring Eq. 4.134 and 4.135, and time averaging gives

$$\overline{vv} = \frac{C_2^{-2}\,\overline{M_1^2} + C_1^{-2}\,\overline{M_2^2} - 2C_1^- C_2^-\,\overline{M_1 M_2}}{(B_1^- C_2^- - B_2^- C_1^-)^2} \tag{4.158}$$

and

$$\overline{ww} = \frac{B_2^{-2}\,\overline{M_1^2} + B_1^{-2}\,\overline{M_2^2} - 2\,B_1^- B_2^-\,\overline{M_1 M_2}}{(B_1^- C_2^- - B_2^- C_1^-)^2} . \tag{4.159}$$

As was the case for the $\overline{vw}$ stress, the term $\overline{M_1 M_2}$ in Eq. 4.136 is an unknown term and thus $\overline{vv}$ and $\overline{ww}$ cannot be computed separately. This is not surprising since Eqs. 4.129 and 4.132 viewed as a system of 2 equations has 3 unknown stresses $\overline{vv}$, $\overline{ww}$, and $\overline{vw}$. Useful information is provided, however, by a geometrically perfect sx-array since for this case the coefficients of $\overline{M_1 M_2}$ in Eqs. 4.158 and 4.159 are equal and

opposite in sign. Thus, a sum will remove the $\overline{M_1 M_2}$ term leaving

$$\overline{vv} + \overline{ww} = \frac{B_2^{-2}\,\overline{M_1^2} + B_1^{-2}\,\overline{M_2^2}}{4\,B_2^{-2}\,B_1^{-2}} \,. \tag{4.160}$$

Matched positions for a geometrically perfect probe provides the simplest expression

$$\overline{vv} + \overline{ww} = \frac{\overline{(e_a - e_b)_1^2} + \overline{(e_a - e_b)_2^2}}{4\,B_o^2\,f'^2} \,. \tag{4.161}$$

The turbulent kinetic energy can be computed by combining Eqs. 4.157 and 4.160 for

$$TKE = \frac{\overline{uu} + \overline{vv} + \overline{ww}}{2} = \frac{1}{4}\frac{P_1^2}{A_1^{+2}} + \frac{1}{4}\frac{P_2^2}{A_2^{+2}} + \frac{1}{4}\frac{B_2^{-2}\,\overline{M_1^2} + B_1^{-2}\,\overline{M_2^2}}{B_2^{-2}\,B_1^{-2}} \tag{4.162}$$

where an arithmetic average of $\overline{uu}$ is used.

Calculation of Redundant Shear Stresses

Redundant $\overline{uv}$ and $\overline{uw}$ shear stresses are also available from the sx-array. Since both unknown quantities appear in Eqs. 4.130 and 4.133, the system can be solved simultaneously to give

$$\overline{uv} = \frac{A_2^+ C_2^- \overline{P_1 M_1} - A_1^+ C_1^- \overline{P_2 M_2}}{A_1^+ A_2^+ B_1^- C_2^- - A_2^+ A_1^+ B_2^- C_1^-} \tag{4.163}$$

and

$$\overline{uw} = \frac{A_1^+ B_1^- \overline{P_2 M_2} - A_2^+ B_2^- \overline{P_1 M_1}}{A_1^+ A_2^+ B_1^- C_2^- - A_2^+ A_1^+ B_2^- C_1^-} \,. \tag{4.164}$$

As was the case for the $\overline{vw}$ stress, the following variations are considered. First, for the case of a perfect probe arrangement these expressions become

$$\overline{uv} = \frac{A_2^+ B_2^- \overline{P_1 M_1} + A_2^+ B_1^- \overline{P_2 M_2}}{2 A_1^+ A_2^+ B_1^- B_2^-} \tag{4.165}$$

and

$$\overline{uw} = \frac{A_2^+ B_2^- \overline{P_1 M_1} - A_1^+ B_1^- \overline{P_2 M_2}}{2 A_1^+ A_2^+ B_1^- B_2^-} . \tag{4.166}$$

Next, for matched positions, one obtains

$$\overline{uv} = \frac{\overline{P_1 M_1} - \overline{P_2 M_2}}{2 A_1^+ B_1^-} \tag{4.167}$$

and

$$\overline{uw} = \frac{\overline{P_1 M_1} + \overline{P_2 M_2}}{2 A_1^+ C_1^-} . \tag{4.168}$$

When both conditions are satisfied Eqs. 4.163 and 4.164 give the most convenient forms

$$\overline{uv} = \frac{\overline{(e_a + e_b)(e_a - e_b)_1} - \overline{(e_a + e_b)(e_a - e_b)_2}}{4\sqrt{2}\, B_o^2\, ff'} \tag{4.169}$$

and

$$\overline{uw} = \frac{\overline{(e_a + e_b)(e_a - e_b)_1} + \overline{(e_a + e_b)(e_a - e_b)_2}}{4\sqrt{2}\, B_o^2\, ff'} . \qquad (4.170)$$

Some Fictitious Stresses

Consider a geometrically perfect probe where Eqs. 4.147 and 4.148 apply. Substituting these expressions into Eqs. 4.129 and 4.132 and time averaging gives

$$\overline{(v + w)^2} = \frac{\overline{(e_a - e_b)_1^2}}{2\, B_{o,1}^2\, f_1'^2} \qquad (4.171)$$

and

$$\overline{(v - w)^2} = \frac{\overline{(e_a - e_b)_2^2}}{2B_{o,2}^2\, f_2'^2} . \qquad (4.172)$$

Both equations resemble Eq. 4.83 and each quantity can be viewed as a transverse normal stress in their respective planes. In this context, these fictitious stresses are similar to the $\overline{ww}$ and $\overline{vv}$ stresses in the horizontal and vertical x-array planes, respectively.

In a similar fashion, fictitious shear stresses are computed from Eqs. 4.130 and 4.133 where

$$\overline{u(v + w)} = \frac{\overline{(e_a + e_b)(e_a - e_b)_1}}{2\sqrt{2}\, B_{o,1}^2\, f_1\, f_1'} \qquad (4.173)$$

and

$$\overline{u(v - w)} = -\frac{\overline{(e_a + e_b)(e_a - e_b)_2}}{2\sqrt{2}\, B_{o,2}^2\, f_2\, f_2'} , \qquad (4.174)$$

which are similar in form to Eq. 4.84. These quantities are identified as fictitious shear stresses in the 45^{o} planes and resemble the $\overline{uw}$ and $\overline{uv}$ shear stresses in the horizontal and vertical planes.

Summary

The interpretation of signals from x-arrays, which use sum and difference combinations of sensor response equations as a basis for obtaining turbulent stresses, demands careful study. A detailed knowledge of the consequences of non-ideal probe response is necessary to guide in the construction and use of the x-arrays.

In a prescribed plane, matched sensors requires not only equal slopes of the velocity calibration curves (Eq. 4.93) but also an equivalence in the sensors' directional characteristics (Eq. 4.94). Electronically matching the velocity calibration curves gives a partial or 'quasi' matching of the sensors which simplifies the system of response equations. The only asymmetries that remain for quasi-matched sensors are in the yaw characteristics due mainly to differences in the yaw parameter. Adjustments of the sensor yaw angle can compensate for a yaw parameter asymmetry provided, of course, that such adjustments can be made. This correction would require individual sensor calibrations to determine their unique yaw parameters since knowledge of the relative differences in these parameters is required to successfully compensate for this asymmetry through a yaw angle correction as was demonstrated by the example presented.

The horizontal and vertical x-arrays do not require the matched sensor assumptions and hence require none of these remedial adjustments if the systems shown in Eqs. 4.81 and 4.107 are used to compute their stresses. On the other hand, the slant x-array requires the complete set of matched sensor assumptions which are necessary to obtain the $\overline{vw}$ stress. It is possible to extend the utility of this probe to measure the $\overline{uv}$ and $\overline{uw}$ shear stresses and the turbulent kinetic energy in addition to the usual $\overline{uu}$ and $\overline{vw}$ stresses. These results are summarized in Table 4.1. It is noted that matched sensors in each position is the first and foremost requirement. Second, and equally important for the $\overline{vw}$ stress is the correct relative location of the sensor planes. Any further refinements or assumptions such as perfect probe geometry and/or matched positions simplify the resulting response equations. The redundant stresses of the slant x-array are compared to the stresses measured by horizontal x- and vertical x-arrays, and the effects of yaw parameter asymmetries on the calculation of these stresses are studied in Chapter VII.

Table 4.1 Summary of Stresses Measured by the Slant X-Array with Matched Sensors in Each Position

	Planar Location $\gamma_{x,a,i} - \gamma_{x,b,i} = \pi$	$\overline{uu}$	$\overline{(v+w)^2}$	$\overline{u(v+w)}$	$\overline{(v-w)^2}$	$\overline{u(v-w)}$	$\overline{vv}+\overline{ww}$	$\overline{uv}$	$\overline{uw}$	$\overline{vw}$
a)	Position 1 $0 < \gamma_{x,a,i} < \frac{\pi}{2}$ $-\pi < \gamma_{x,b,1} < -\frac{\pi}{2}$	X								
b)	Position 2 $\frac{\pi}{2} < \gamma_{x,a,2} < \pi$ $-\frac{\pi}{2} < \gamma_{x,b,2} < 0$	X								
c)	a) and b)	X						X	X	
d)	a) and b) with $\gamma_{x,a,1} + \gamma_{x,a,2} = \pi$ $\gamma_{x,b,1} + \gamma_{x,b,2} = -\pi$	X						X	X	X
e)	a), b), and c) with $\gamma_{x,a,1} = -\frac{\pi}{4}$ (perfect probe geometry)	X	X	X	X	X	X	X	X	X

V. CALIBRATION

A. Introduction

This chapter is devoted to individual sensor calibrations. Following the usual practice, static calibrations were performed and these are assumed valid in describing the sensor's dynamic response to a turbulent flow. Under certain conditions however, this assumption is not valid and dynamic calibrations are necessary [50,130,139,140].

The exponent, n, is central to the problem of determining the sensor's response to the flow and much attention has been devoted to its study. As discussed in Chapter II, there seems to be no quantitative agreement on the value of n. The exponent has been shown to vary considerably with velocity. Bruun [106] showed, however, that a constant value of n could be used over a substantial velocity interval with reasonably good results. A velocity dependent exponent in response analyses can complicate the processing equations in the form of additional partial derivatives of n with respect to velocity. Signal linearization can correct for a velocity dependence but at the expense of more tedious and time consuming calibrations, and additional circuitry is usually required to handle this dependence. The sensor calibration can be further complicated by a yaw dependent exponent [103,141] although considerably less attention has been given to this type of behavior.

The cooling law coefficient k appearing in Eq. 2.6 also depends on velocity and yaw angle as discussed earlier. The generalized form of the response equation given in Eq. 4.32 accounts for a yaw dependent

cooling law parameter since this parameter appears implicitly in the functions of f, f', f'', etc. A velocity dependent parameter would, however, require more complex derivatives of the cooling law function. This dependence was not considered in the response analysis presented in Chapter IV.

The differences in the values of the exponent n and the yaw coefficient k among the various studies listed in Tables 2.3 and 2.4 suggests that such values are unique to a particular probe and therefore, separate calibrations are necessary for each sensor. The most popular and more conventional yaw calibration method as used by Jorgensen [49] and Müller [58] requires that mean voltage measurements be made with the sensor placed normal to a constant velocity flow. It is tacitly assumed that the incident flow is not influenced by the presence of any upstream probe components such as prongs or other sensors at this normal position or any other position of the calibration. Thus, the utility of this conventional approach depends on whether each sensor when placed normal to the flow can experience a pure flow.

The aerodynamic related disturbances, discussed in Chapter II, that may be encountered by the sensor during the calibration can be identified with probe positions that differ substantially from the intended point of measurement. Regardless of the probe configuration however, it is essential that the sensors experience a pure flow at the intended operating position if meaningful results are to be expected. Such effects are more likely to occur during the calibration of multi-element probes (which inherently require additional probe material and have more complex geometries than for single sensor probes) whose sensors are

supported by prongs that are oriented perpendicular to the flow as in Figs. 3.10-3.12, than for a parallel supporting system which lies downstream of the sensing element. The former configuration can result in a more restricted angular range of positions in which a meaningful calibration can be made. The upper sensor of the horizontal x-array viewed in Fig. 3.10, for example, when place normal to the flow experiences the wake of the prong that lies directly upstream and which supports the lower sensor. Such disturbances are not encountered by either sensor at the operating position i.e., when each sensor is yawed approximately 45^{o} to the flow. For this probe, a conventional calibration of the upper sensor would not provide results of the quality that is required for turbulent stress measurements due primarily to the unknown influence of the upstream prong. If the sensors are 'identical' then a calibration of the lower sensor alone is sufficient. In view of the difficulties involved in producing such a probe however, matched sensors by the strict definition, are usually not found in practice. As discussed in Chapter IV, matched sensors required an equality of the sensors' sensitivities to velocity and similar yaw characteristics as well. Together, these conditions resulted in a maximum simplification of the x-arrays response equations. One could approach this ideal situation by satisfying the first condition via an electronic matching procedure such as discussed in Gessner [92] and Frota and Moffat [77], but this alone is not sufficient to reach the state of completely matched sensors. Any further attempts of matching the sensors would require a priori knowledge of the yaw characteristics of each sensor. One must recognize that when probe calibrations are based on this assumption, an additional

source of error in turbulence measurements may be introduced. The uncertainty in the measurement for this case would be difficult to estimate quantitatively due to the unknown deviation of the sensors actual yaw characteristics from the ideal, matched sensor case.

Thus, the conventional method as described by Jorgensen [49] cannot be viewed as a general approach for obtaining a meaningful calibration of all the sensors of a given probe. A more generalized method was developed that would allow for an individual calibration of each sensor on any yaw angle interval, preferably in the neighborhood of the actual point of measurement and where the sensor's preception of the flow is uninfluenced by other probe components. The present method provides the means of obtaining a unique result for each sensor regardless of the probe construction. Furthermore, a more localized calibration can be made on the sensor in the vicinity of the point where the actual measurements will occur.

The present method relies on the method of least squares to estimate the calibration constants and is similar to the procedure described in Hoffmeister [75]. This method will be applied to both the nonlinear and linearized responses given in Eq. 4.27 and 4.30, respectively, where n in Eq. 4.27 is assumed constant. In essence, a calibration curve is obtained at several positions in a selected, yaw interval. This generates a family of curves in the neighborhood of the point of interest. These curves will serve as the basis for determining the yaw parameter k^2. The unique results obtained for each sensor are required in the response equations derived in Chapter IV.

This method differs from the one used by Jorgensen [49] in that 1) measurements with the sensor normal to the flow direction are not required and 2) the entire calibration curve, which covers a velocity range, is involved in determining the yaw parameter rather than at a particular incident velocity. The results from both methods are compared using the cooling law functions suggested by Hinze [57] and Davies an Bruun [104] given in Eqs. 2.6 and 2.7, respectively. For the purpose of comparison, a yaw dependent coefficient k is considered assuming a linear variation for k^2. Such behavior is more likely to occur for applications which require a wider range of sensor yaw angles.

In presenting both the present and conventional calibration methods, it is assumed that the sensor is immersed in a uniform flow of negligible turbulent intensity. The calibrations are performed in the $x^*y^*z^*$ coordinate system shown in Fig. 4.1 and can be viewed as fixed to the calibration wind tunnel. Throughout the calibration the angles $\bar{\psi}_y$ and $\bar{\psi}_z^*$ also shown in Fig. 4.1, which had been previously associated with a misaligned sensor (xyz) coordinate system will be identified with yaw angular displacements of the x-array from the actual point of measurement.

B. Positioning of the Sensor Plane

In an ideal freestream environment, no fluctuations of velocity are present and the nonlinear response of a sensor yawed to this flow can be written as

$$\bar{E}^2 - A = \{B_o \bar{U}^* f(\alpha^*, P(\alpha^*))\}^n . \qquad (5.1)$$

If linearizers are used, then the linearized resonse is given by

$$\bar{E} - A = B_o \bar{U}^* f(\alpha^*, P(\alpha^*)) \tag{5.2}$$

where, as noted earlier, the AB_o pairs in Eqs. 5.1 and 5.2 are not equal. X-array calibrations that determine the individual yaw characteristics of the sensor pair require that measurements be made at distinct yaw locations, α^*, in the plane of the sensors which also contains the mean velocity vector $\underline{\bar{U}}^*$ as defined in Chapter IV. Yaw rotations of this plane will generally involve a combination of the rotational components $\bar{\psi}_y$ and $\bar{\psi}_z^*$. Referring to Fig. 4.1, the scalar triple product

$$\{\hat{\ell} \times \hat{e}_x\} \cdot \hat{e}_x^* = 0 \tag{5.3}$$

guarantees that the selected yaw locations will lie in the mean plane containing the mean velocity vector. By performing the required operations, Eq. 5.3 becomes

$$\cos \gamma_x \sin \bar{\psi}_y = \sin \gamma_x \tan \bar{\psi}_z^* , \tag{5.4}$$

which, for a given sensor, represents an equation of constraint on $\bar{\psi}_z^*$ and $\bar{\psi}_y$. The locus of points, α^*, representing the yaw angle locations during the calibration are generated by satisfying Eqs. 5.4 and 4.22 simultaneously. To assist in this discussion, Eq. 4.22 is repeated below:

$$\sin \alpha^* = \sin \alpha \cos \bar{\psi}_z^* \cos \bar{\psi}_y + \cos \alpha \cos \gamma_x \sin \bar{\psi}_z^* \qquad (4.22)$$

$$+ \cos \alpha \sin \gamma_x \cos \bar{\psi}_z^* \sin \bar{\psi}_y \, .$$

As an example, consider Fig. 4.1 for the case of a geometrically perfect vertical x-array previously defined by the values $\gamma_{x,a} = 0$ and $\gamma_{x,b} = -\pi$. In addition, let $\alpha_a = \alpha_b = \alpha_o$ in Eq. 4.22. Using these values, Eq. 5.4 gives $\bar{\psi}_y = 0$ for each sensor and Eq. 4.22 becomes

$$\sin \alpha_a^* = \sin (\alpha_o + \bar{\psi}_z^*) \qquad (5.5)$$

for sensor a and

$$\sin \alpha_b^* = \sin (\alpha_o - \bar{\psi}_z^*) \qquad (5.6)$$

for sensor b. For this case, the positioning of the sensor plane requires a rotation about the z^* axis which is perpendicular to the vertical plane of the sensors.

C. Determination of the Yaw Cooling Law Parameter

The following discussion summarizes the procedure used to determine the unique yaw parameters k^2 and m given in Eqs. 2.6 and 2.7, respectively. The nonlinear version of the present method will be presented first.

To facilitate this least squares approach, Eq. 5.1 is rewritten as

$$\bar{E}^2 = A + B(\alpha) \bar{U}^n \qquad (5.7)$$

where

$$B(\alpha) = B_o f(\alpha,P)^n, \tag{5.8}$$

and A, B_o, and n are assumed constant. For convenience the * notation has been omitted. For a range of velocities and yaw angles, Eq. 5.7 represents a family of response curves with the sensor's directional characteristics contained in the single term, $B(\alpha)$. Note that Eq. 5.7 is an alternate form of Eq. 2.2. For the case of a sensor normal to the flow, the effective cooling velocity is the incident flow velocity and by definition

$$B(0) = B_o. \tag{5.9}$$

To gain the best estimate of any yaw parameter P for a restricted range of yaw angles or a restricted yaw interval, the first step is to determine the optimum values of A, B, and n, shown in Eq. 5.7, at each yaw position on the interval. The method of least squares requires the minimization of

$$\phi_j = \sum_{i=1}^{M} (\tilde{\bar{E}}^2_{i,j} - \hat{A}_j - \hat{B}_j \bar{U}_i^{\hat{n}_j})^2, \tag{5.10}$$

where $\tilde{\bar{E}}_{i,j}$, i = 1, 2, ..., M are the measured mean voltage responses to the velocities $\bar{U}_i$ and $\hat{A}_j$, $\hat{B}_j$, and $\hat{n}_j$ are the estimated values of A_j, B_j and n_j, respectively, at the position α_j. For a range of α_j positions,

the parameter P can be estimated using Eq. 5.8 by minimizing

$$\psi = \sum_{j=1}^{N} \left(\tilde{\hat{B}}_j - \hat{B}_o \, f(\alpha_j, \hat{P})^{\tilde{\hat{n}}_j}\right)^2 \tag{5.11}$$

where j = 1, 2, ..., N. The terms $\tilde{\hat{B}}$ and $\tilde{\hat{n}}$ appearing in Eq. 5.11 are the estimates $\hat{B}$ and $\hat{n}$ found by minimizing Eq. 5.10. The tilde is used to distinguish these values, determined a priori, from the present estimates $\hat{B}_o$ and $\hat{P}$.

Equations 5.10 and 5.11 provide the means of obtaining a unique yaw parameter on any appropriate yaw interval $[\alpha_1, \alpha_N]$ by allowing a piecewise construction of the function $B(\alpha)$ from the discrete estimates $\hat{B}_j$. The value of $B_o = B(0)$ is inferred from Eq. 5.11 without actually calibrating the sensor at $\alpha = 0$.

The present method can be refined to give better results by addressing the possible variations of A, n, and P with yaw angle. The less systematic curve to curve variations in A and n can be treated simply by using the arithmetic averages

$$\bar{n} = \frac{1}{N} \sum_{j=1}^{N} \hat{n}_j \tag{5.12}$$

and

$$\bar{A} = \frac{1}{N} \sum_{j=1}^{N} \hat{A}_j \tag{5.13}$$

in Eq. 5.11. Any large residual errors of the cooling law $f(\alpha_j, \hat{P})$ would most likely be identified with the small differences in the exponent

with yaw rather than the small variations in A. Further, since a constant yaw parameter may not always give a reasonable curve fit of the data over the desired yaw interval, it may be necessary to allow P to vary with yaw angle. The present method allows for this flexibility in the specification of the parameter. For example, the linear relation

$$P = a_o + a_1 \alpha \tag{5.14}$$

was used in Eq. 5.11 for comparison and which required the estimation of the constants a_o and a_1.

The present method can be easily adapted to the linearized response given in Eq. 5.1 by setting n = 1 and substituting $\bar{E}$ for $\bar{E}^2$ in Eqs. 5.10 and 5.11. This gives,

$$\phi_j = \sum_{i=1}^{M} (\tilde{\bar{E}}_{i,j} - \hat{A}_j - \hat{B}_j \bar{U}_i)^2 \tag{5.15}$$

and

$$\psi = \sum_{j=1}^{N} (\tilde{\hat{B}}_j - \hat{B}_o f(\alpha_j, \hat{P}))^2 \tag{5.16}$$

where $\hat{A}$, $\hat{B}$, and $\hat{B}_o$ will be associated with the linearized response. It is believed that the present method can be applied to any of the existing cooling laws such as given in Eqs. 2.6 - 2.9. The first two laws were chosen for this study.

The conventional method as described by Jorgensen [14] for determining k^2 in Eq. 2.6, requires that measurements be made at two posi-

tions. In the first position the sensor is normal to the flow. The second position is arbitrary and will depend on the particular application. If the second position is denoted by α_j, then an average yaw parameter is found on the interval $[0, \alpha_j]$. For the nonlinear mean response given by Eq. 5.7, an equation can be written for each position as

$$B(0) = \frac{\overline{E}^2(\overline{U},0) - A}{\overline{U}^n} \tag{5.17}$$

and

$$B(\alpha_j) = \frac{\overline{E}^2(U,\alpha_j) - A}{\overline{U}^n} . \tag{5.18}$$

Dividing the second equation by the first and introducing Eq. 5.8 yields

$$\frac{f(\alpha_j,P)}{f(0,P)} = \left\{ \frac{\overline{E}^2(\overline{U},\alpha_j) - A}{\overline{E}^2(\overline{U},0) - A} \right\}^{1/n} \tag{5.19}$$

where $f(0,P) = 1$. Employing the Hinze [54] law and solving for k^2 gives

$$k^2_{\alpha_j} = \frac{\left(\frac{\overline{E}^2(\overline{U},\alpha_j) - A}{\overline{E}^2(\overline{U},0) - A} \right)^{2/n} - \cos^2 \alpha_j}{\sin^2 \alpha_j} . \tag{5.20}$$

The corresponding equation for the linear case is

$$k^2_{\alpha_j} = \frac{\left(\frac{\overline{E}(\overline{U},\alpha_j) - A}{\overline{E}(\overline{U},0) - A} \right)^{2} - \cos^2 \alpha_j}{\sin^2 \alpha_j} . \tag{5.21}$$

Equations similar to Eqs. 5.20 and 5.21 can be derived for the Davies and Bruun [104] law. For the nonlinear case one obtains

$$m = \frac{\ell n \left\{ \dfrac{\overline{E}^2(\overline{U}, \alpha_j) - A}{\overline{E}^2(\overline{U}, 0) - A} \right\}}{n \ \ell n \{\cos \alpha_j\}}, \qquad \alpha_j \neq \pi/2 \tag{5.22}$$

and for the linearized response

$$m = \frac{\ell n \left\{ \dfrac{\overline{E}(\overline{U}, \alpha_j) - A}{\overline{E}(\overline{U}, 0) - A} \right\}}{\ell n \{\cos \alpha_j\}}, \qquad \alpha_j \neq \pi/2 \ . \tag{5.23}$$

D. Experimental Arrangement and Procedure

The calibrations were conducted in a rectangular jet of low turbulence intensity. This calibration facility consisted of an inlet settling chamber covered on four sides with filters, an adjustable louver assembly, a 10 horsepower fan followed by a diffuser, plenum, and nozzle with a 9 to 1 contraction ratio. The nozzle discharged to a 25.4 x 35.6 cm (10 x 14 in.) channel section that exhausted into room air. The diffuser housed an array of cardboard mailing tubes placed between two series of screens to minimize any possible swirl generated by the fan and to ensure a low intensity core in the channel section. This facility provided a large, uniform core for calibrating the hot film probes in air at speeds ranging from 5 to 40 m/s.

The tests were performed at the exit of the channel section with the probes entering the flow from the top. The probe support was mounted on a calibration stand which permitted rotation about the probe's axis ($\bar{\psi}_y$) and also allowed for the inclination of the probe body ($\bar{\psi}_z^*$) over a wide range of angular positions. Angles of probe rotation were read from a dial vernier scaled to a least count of 0.1^o but repeated measurements suggested an angular uncertainty of $\pm 0.5^o$ in the positioning of the probe relative to the flow direction. The uncertainty in the angle of inclination was estimated from the scales least count to be 0.5^o and this value of uncertainty was confirmed in repeated measurements.

Velocity measurements were made with a standard Pitot-static probe mounted adjacent to the hot film probes. The dynamic pressure was sensed by a Gould type 590 transducer with the companion Datametrics model 1400 electronic manometer. The pressure measurement was made on the range of the instrument, 25.4 μm (0.001 in.) with an estimated uncertainty of ±0.051 mm (±0.002 in.) of water.

Measurements of the sensor's nonlinear and linearized mean voltage responses were made with the DISA hot wire/film CTA system. Additional DANA model 5100 digital multimeters were used with the DISA digital voltmeters to obtain a simultaneous reading of both responses. The data ranged from 2 to 10 volts and was taken with a least count of 0.01 V. The uncertainty in the mean voltage measurement based on the stability of a time averaged reading was estimated at 0.02 V.

Each sensor was cleaned before any data was taken. The probes were calibrated prior to measuring in the 3DTBL flow and several of these

calibrations were repeated. Most of the sensors were re-calibrated at the end of the 3DTBL experiment with the exception of the hx-array. Due to sensor damage that was inadvertently inflicted during a profile run, two different hx-array probes were used and calibrated only before the measurements were taken. The standard procedures, as described by DISA [46], were used in determining the probe resistances, adjusting the overheat ratio, and balancing the bridge. These adjustments were carried out very carefully for each individual sensor in each application. The sensor's operating resistances were set to the values recommended by TSI for their probes which gave operating temperatures of nominally 250°C. During a standard square wave test, the bridge adjustments were fine-tuned so that the frequency responses of the sensor pair appeared identical when viewed on an oscilloscope. The square wave test cut-off frequency was estimated in the 30-40 kHz range in all cases.

During the intial phase of the calibration, the probe was rotated about its axis from a reference point to its operating position. This position, designated by $(\bar{\psi}_y, \bar{\psi}_z^*) = (0,0)$, was checked using a high-powered cathetometer to ensure that the probe was in fact at the intended position of operation. In this position, the CTA signal from each sensor was linearized generally to within a 1% RMS residual error about the estimated line. The linearization occurred over flow velocities ranging from 5 to 30 ms^{-1}. Yawing of the sensor from the operating position generally required two rotations of the probe namely, $(\bar{\psi}_y, \bar{\psi}_z^*)$, obtained by solving Eqs. 4.22 and 5.4. The sensor calibrations were made over a wide range of yaw angles ranging from 0-90°, concentrating in a neighborhood of the probe's operating position of

nominally 45±15°. In this range, data was collected in 2 to 3° increment, with larger increments of 5 to 10° used for yaw angles outside this range.

E. Results and Discussion

Figures 5.1-5.8 show two sets of typical calibration results using the nonlinear sensor response given by Eq. 5.7 and Hinze's [54] law with coefficient k^2. Each set is composed of four plots which include the curve fits of the nonlinear calibration data to the form of Eq. 5.10, a plot of the residual errors of the family of estimated curves, the estimated cooling law function obtained by Eq. 5.11, and a plot of the relative errors in predicting the flow velocity from a yawed sensor using the estimated value of k^2. The lower sensor (sensor a) of the hx-array shown, was calibrated in the yaw interval of nominally 35° to 55°.

The differences between the two sets of results described above lie in the treatment of constants n and A. The effect of small variations in the exponent n with yaw angle, on the sensor's directional characteristics, is seen by comparing the estimated cooling laws given in Figs. 5.3 and 5.7 where the ideal cosine law is included on each plot for comparison purposes. In the first set of results, Figs. 5.1-5.4, k^2 (shown as A0) is based on the family of curves shown in Fig. 5.1 where three parameters A, B_o, and n are determined for each curve. In the second set of results, Figs. 5.5-5.8, k^2 is determined using the average values of n and A defined by Eqs. 5.12 and 5.13, respectively and only one parameter, B_o, is estimated for each calibration curve. A significant improvement in the quality of the cooling law curve fit is gained

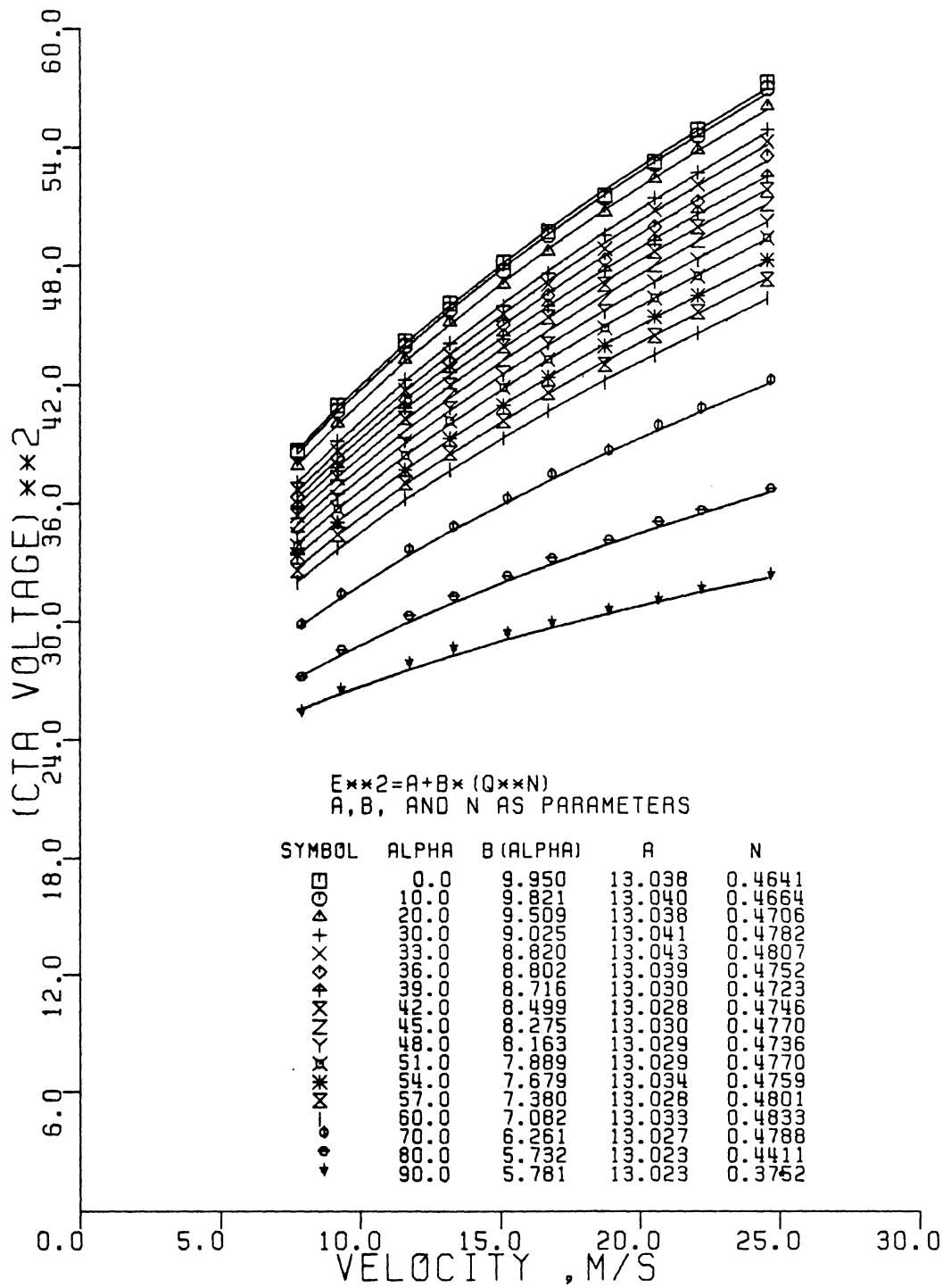

Figure 5.1 Typical Velocity Calibration Results Using the Nonlinear Response with Three Parameters, B, A, and n, Estimated

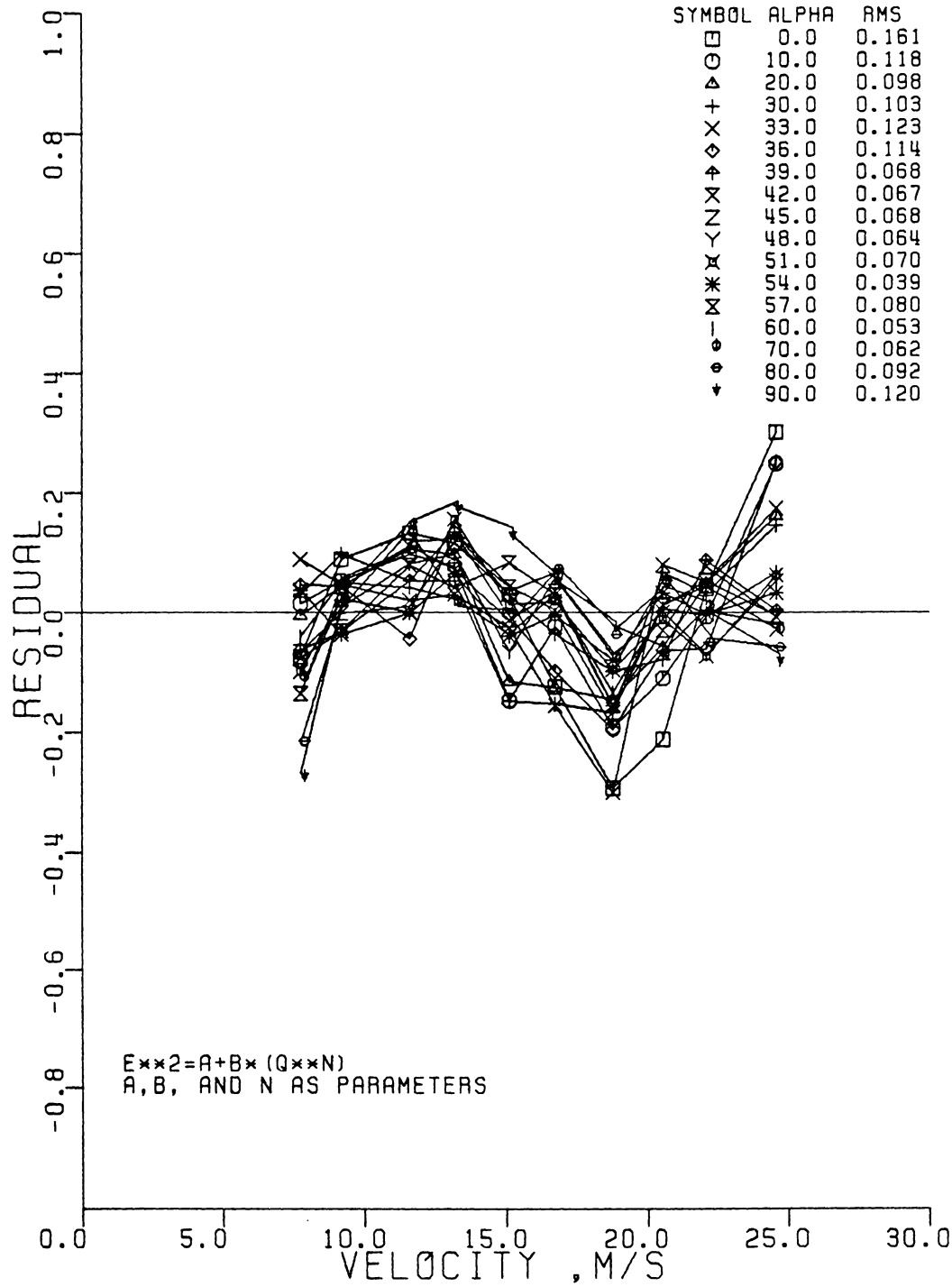

Figure 5.2 Residual Errors in the Estimated Nonlinear Response Curves for the Three Parameter Case

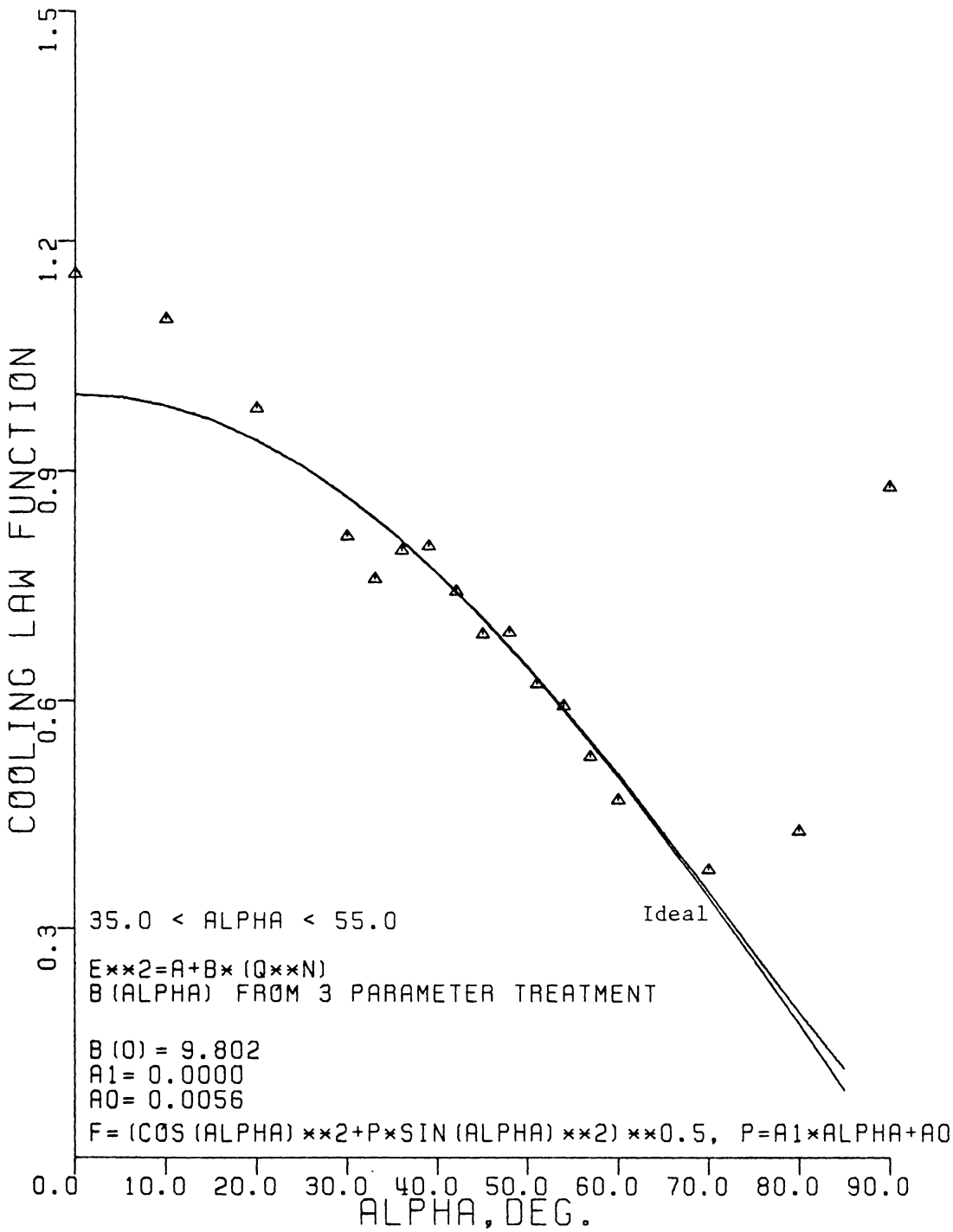

Figure 5.3 Cooling Law Estimated from the Family of Nonlinear Response Curves of the Three Parameter Case on the Yaw Interval of Nominally [35°, 55°]

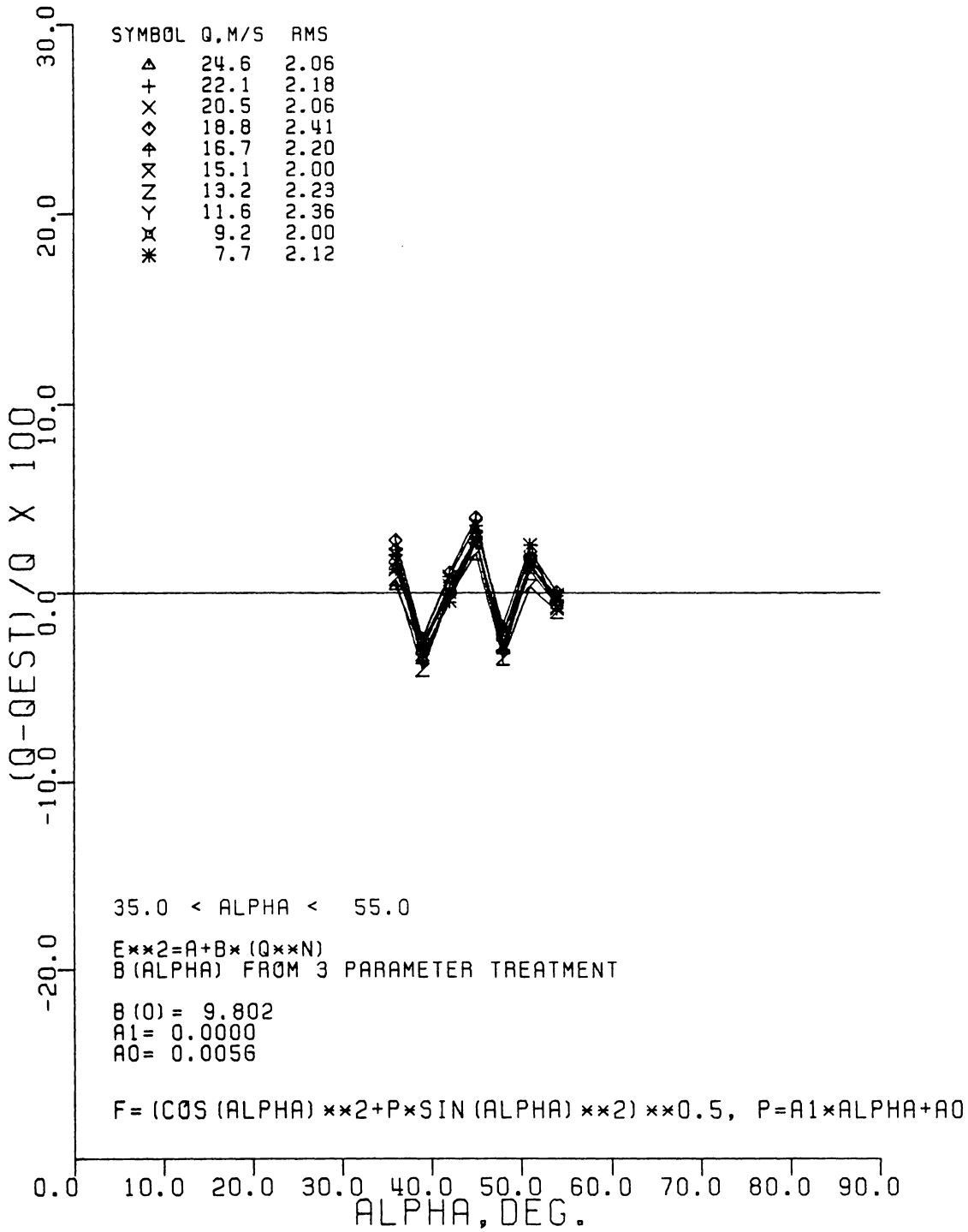

Figure 5.4 Relative Errors in the Estimated Velocities for a Nonlinear Response Using k^2 from the Three Parameter Case

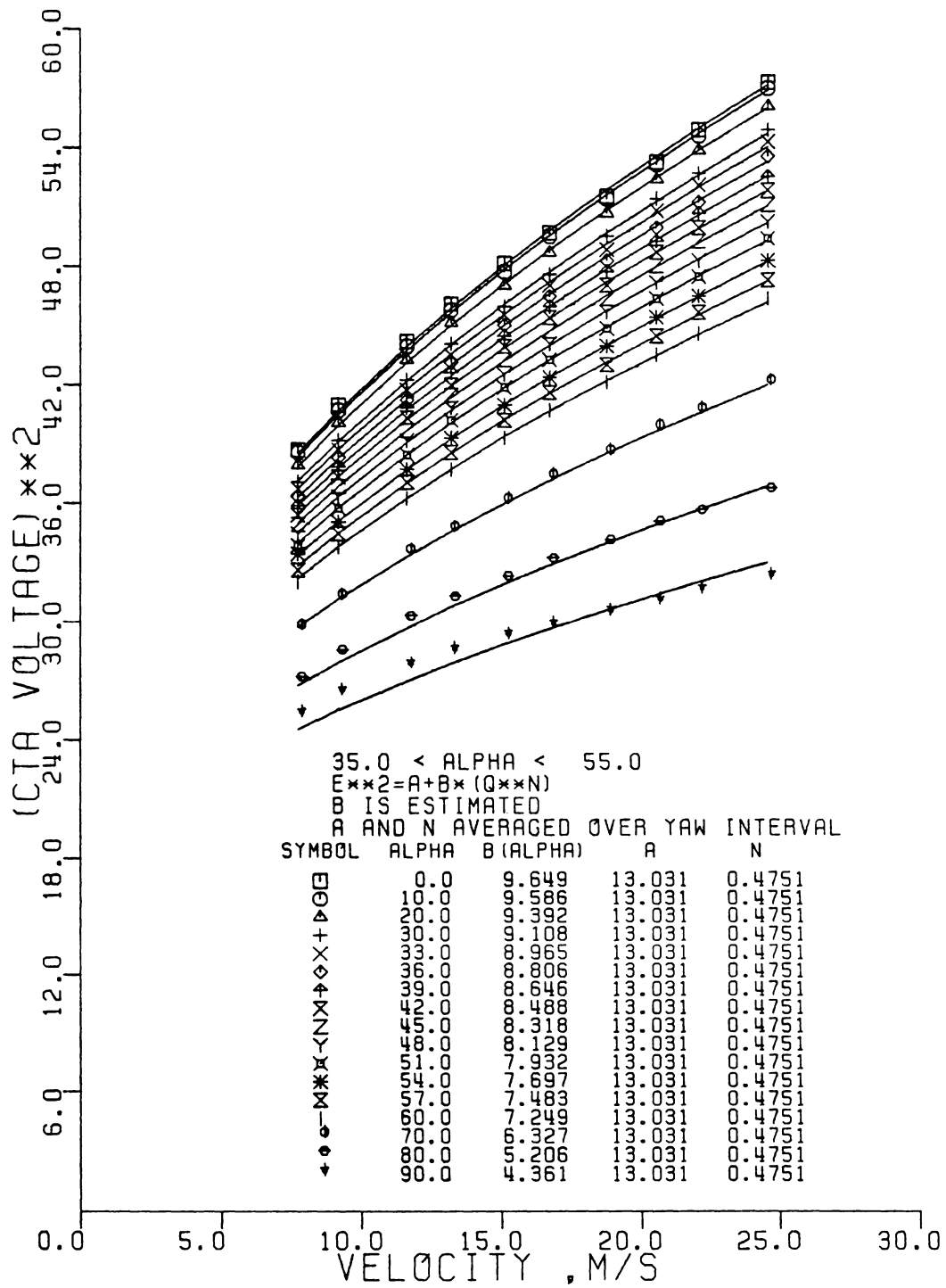

Figure 5.5 Typical Velocity Calibration Results Using the Nonlinear Response with One Parameter, B, Estimated

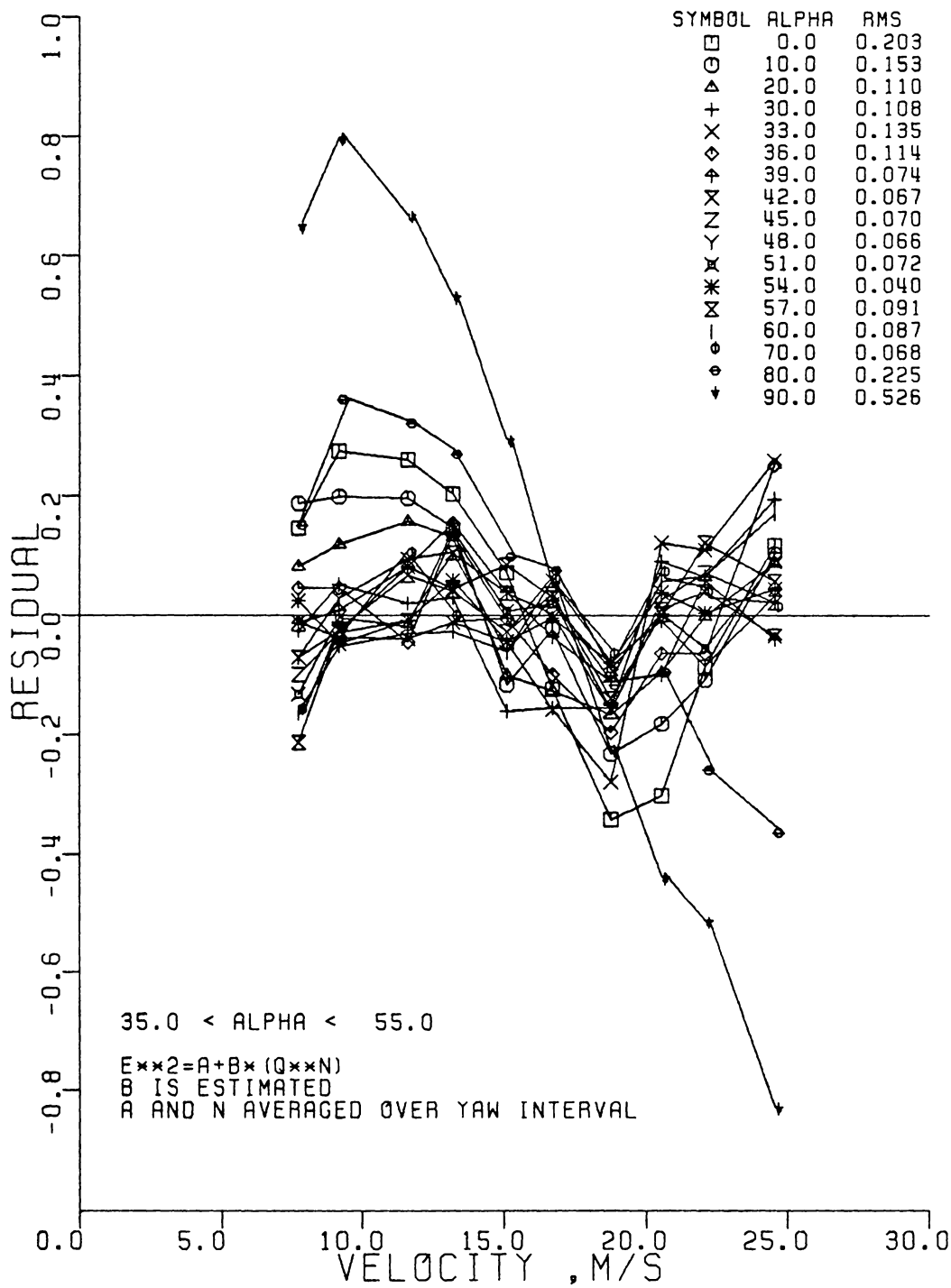

Figure 5.6 Residual Errors in the Estimated Nonlinear Response Curves for the One Parameter Case

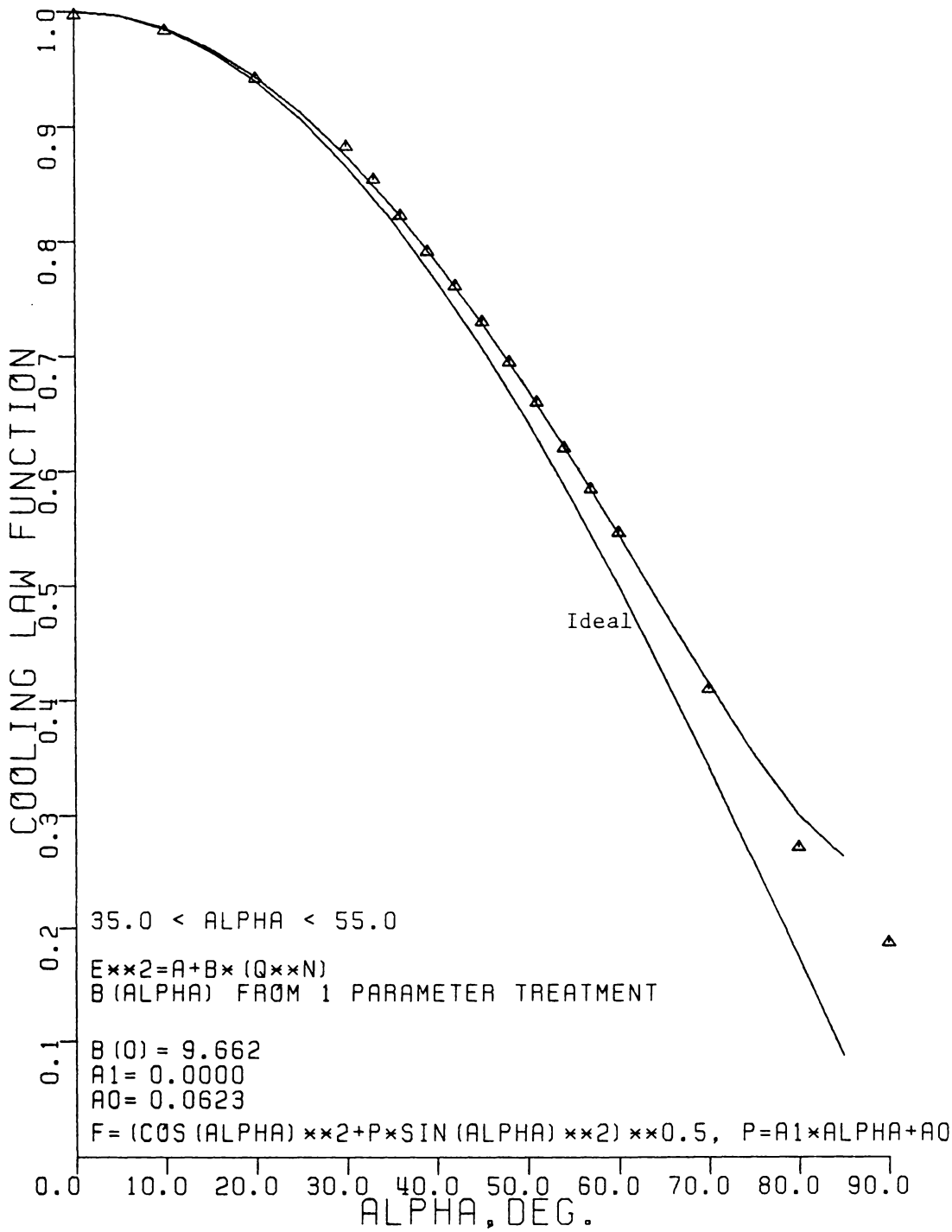

Figure 5.7 Cooling Law Estimated from the Family of Nonlinear Response Curves of the One Parameter Case on the Yaw Interval of Nominally [35^{o}, 55^{o}]

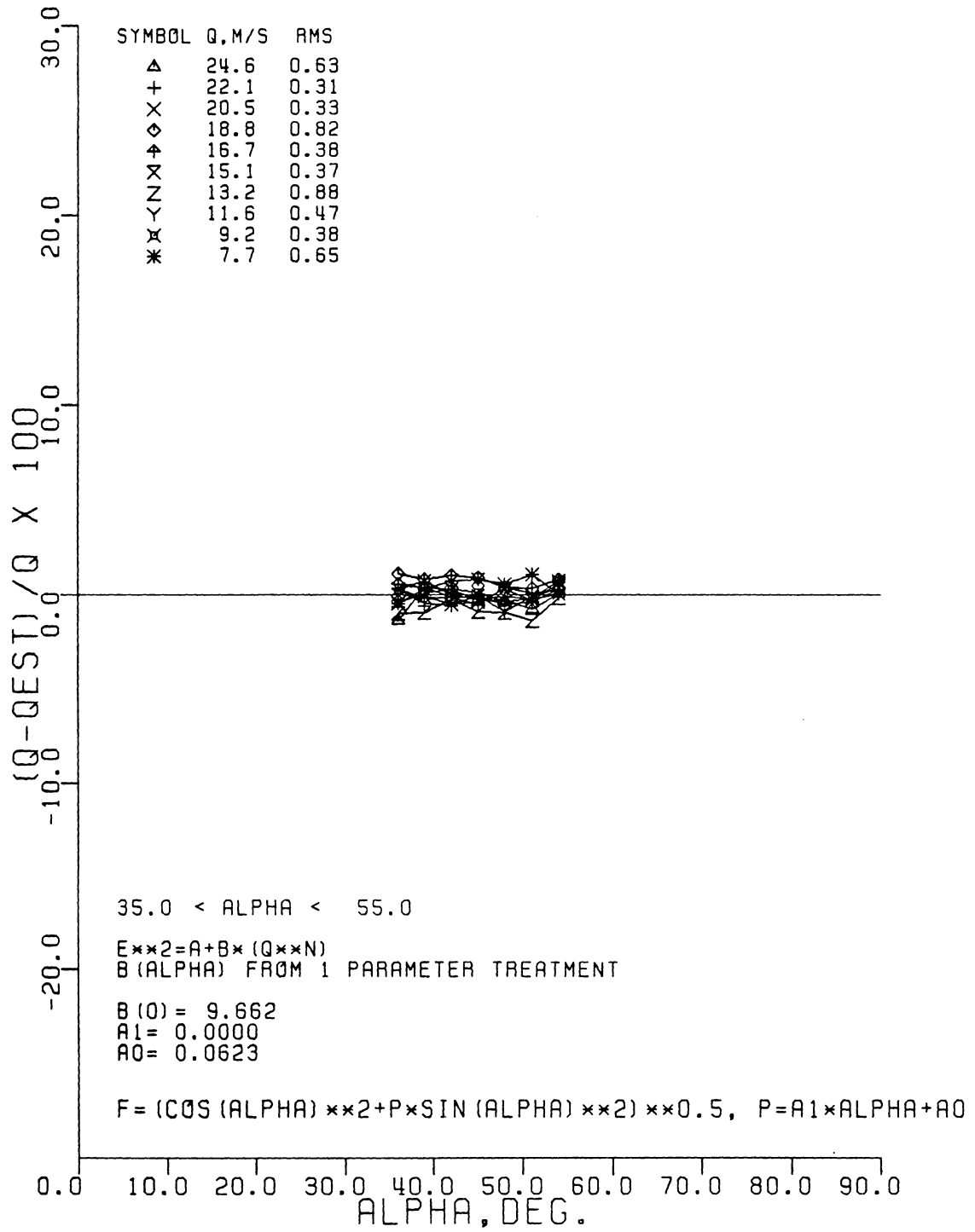

Figure 5.8 Relative Errors in the Estimated Velocities for a Nonlinear Response Using k^2 from the One Parameter Case

by the one parameter treatment. This is shown by comparing Figs. 5.3 and 5.7. While the three parameter treatment gives acceptable and generally slightly better fits for the individual velocity calibration curves than the one parameter treatment, it produces larger, more systematic errors in velocity as shown in Fig. 5.4 and values of $f(0,k^2) > 1$ as shown in Fig. 5.3. The validity of the assumed constant values of n and A is supported by a less than 1% RMS relative error in the estimated velocity over the yaw interval considered in Fig. 5.8.

The inability of the three parameter method to predict the velocity as well as the one parameter method is identified with the small variations in the values of the exponent n with yaw rather than with variations in parameter A with yaw. As shown in Fig. 5.1, A remains essentially constant throughout the entire yaw interval. The fact that small variations in n, of the order of magnitude shown in Fig. 5.1, can cause such a large effect on the estimated cooling law function is further supported by Figs. 5.9-5.12 which show sensor calibration results using the linearized response. These results indicate that, for the degree of linearization achieved in Fig. 5.9 and quantified in Fig. 5.10, the value of k^2 obtained for the linear case assuming two parameters (A and B) is consistent with the values obtained for the nonlinear case when averaged values of n and A were used, despite the small differences in A shown in Fig. 5.9. In the linearized approach, the exponent does not appear explicitly in the minimization of Eq. 5.16 and consequently the estimation of f and hence k^2 does not directly depend on n. It is only through the linearization process via the applied transfer function, which gives the slope of the linearized response curve, that the expo-

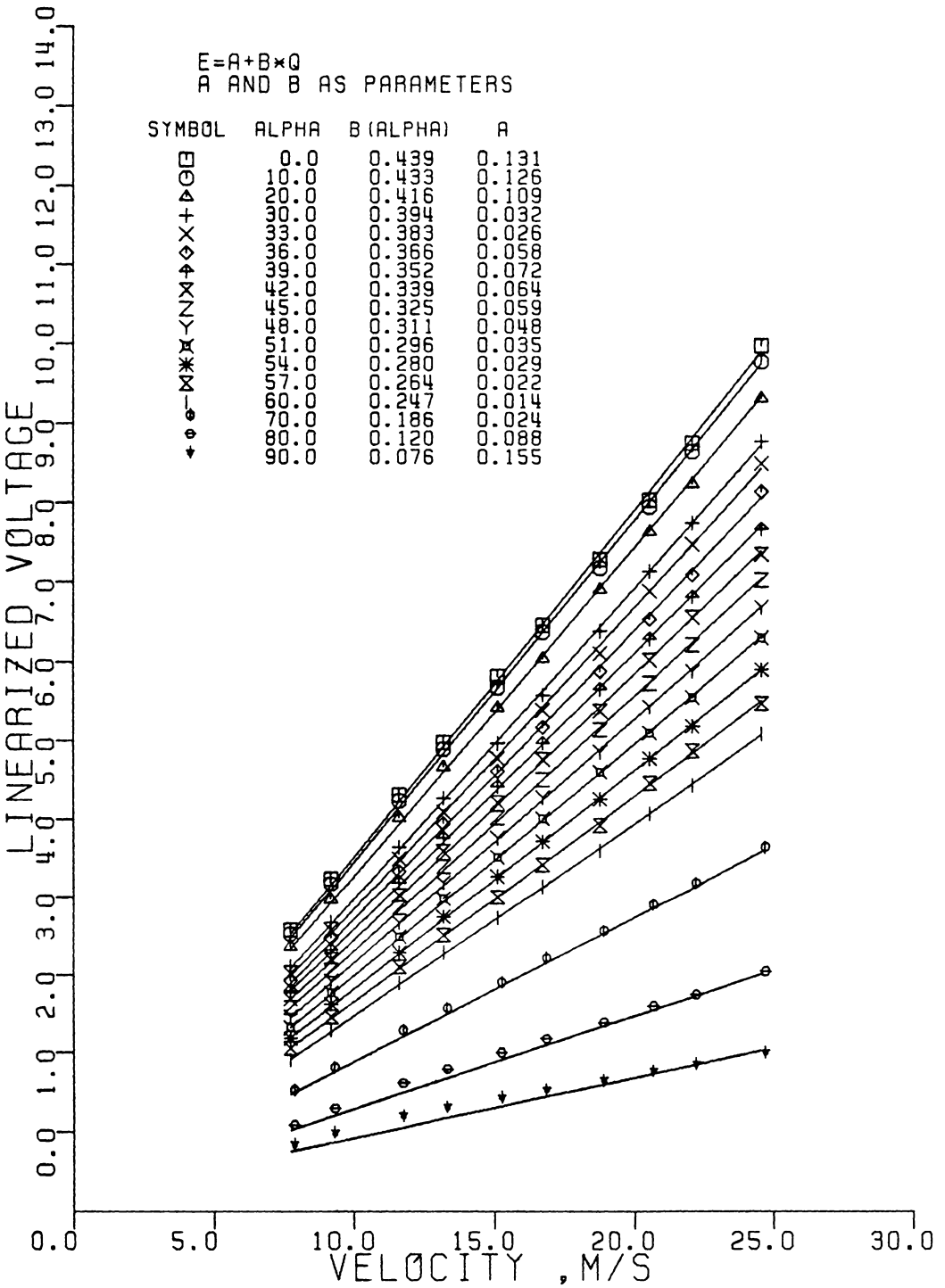

Figure 5.9 Typical Velocity Calibration Results Using the Linear Response with Two Parameters, B and A, Estimated

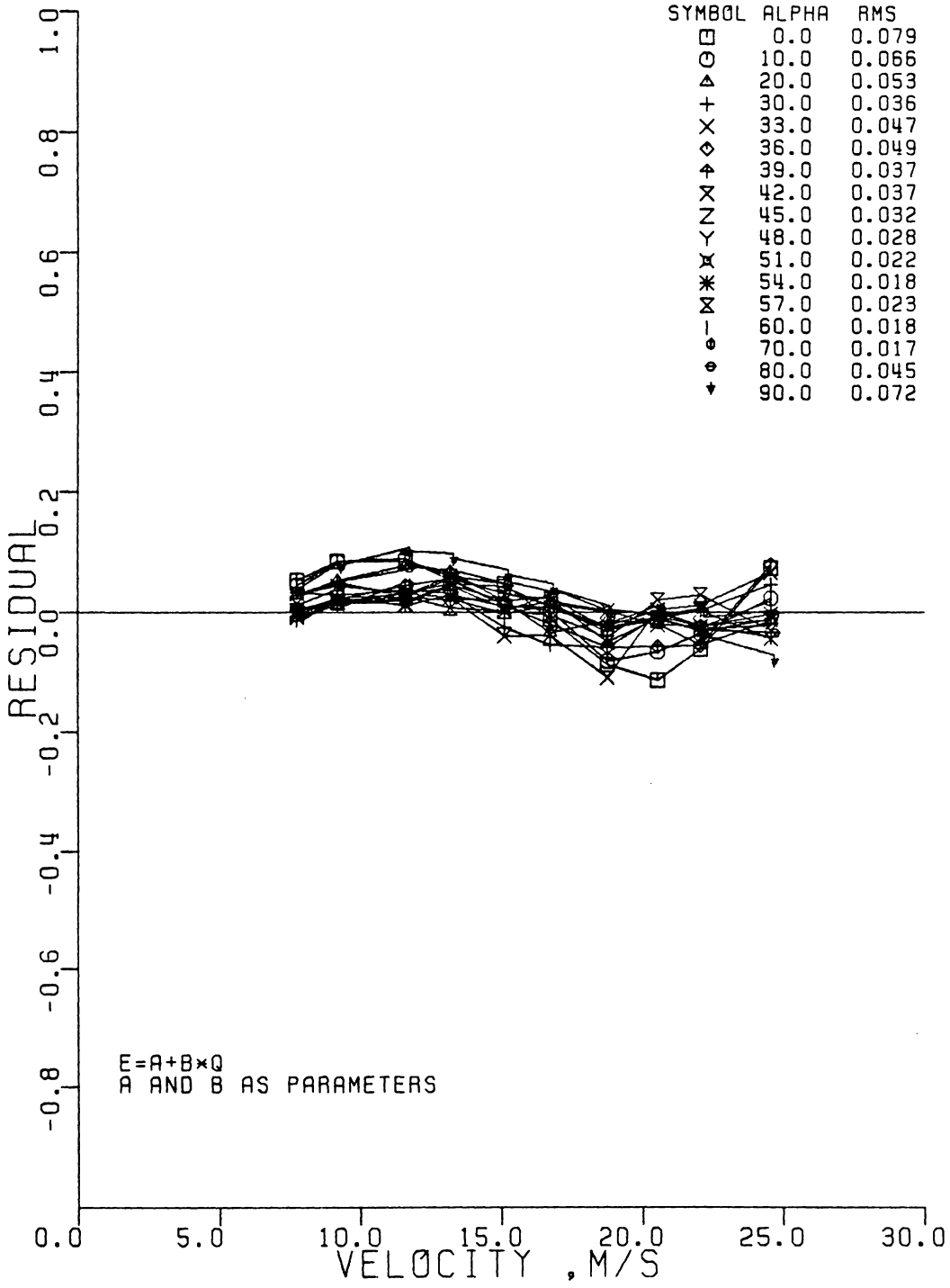

Figure 5.10 Residual Errors in the Estimated Linear Response Curves for the Two Parameter Case

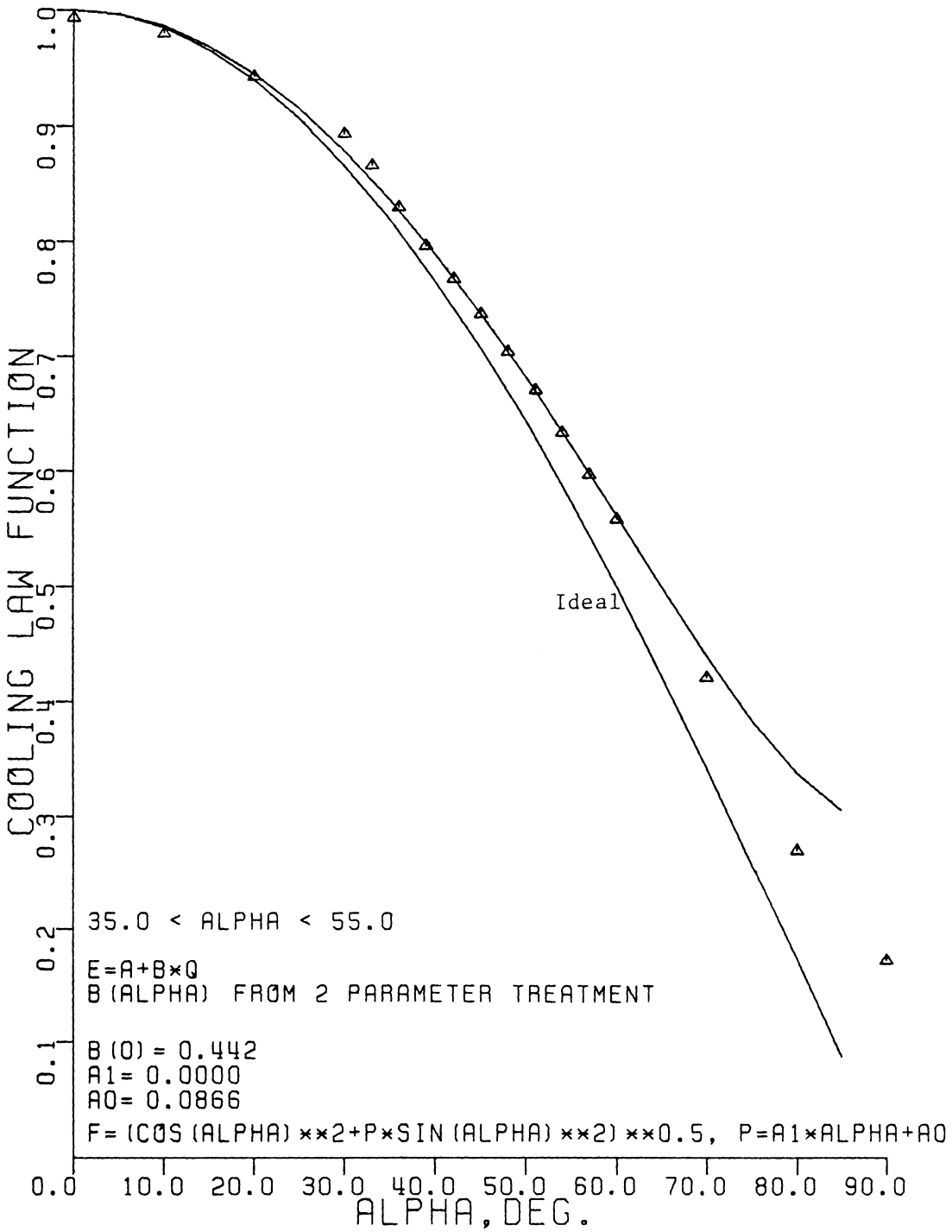

Figure 5.11 Cooling Law Estimated from the Family of Linear Response Curves of the Two Parameter Case on the Yaw Interval of Nominally [35^{o},55^{o}]

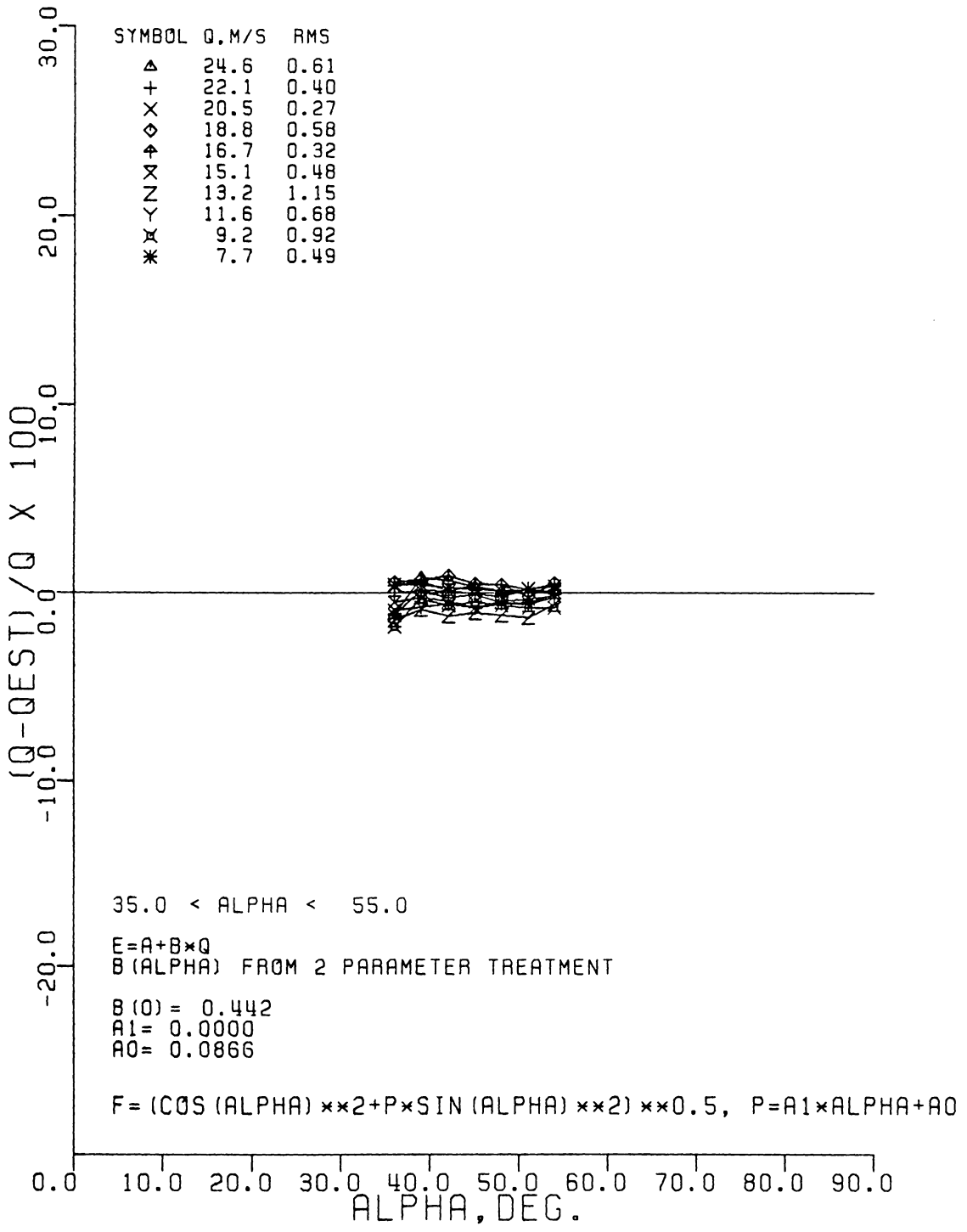

Figure 5.12 Relative Errors in the Estimated Velocities for a Linear Response Using k^2 from the Two Parameter Case

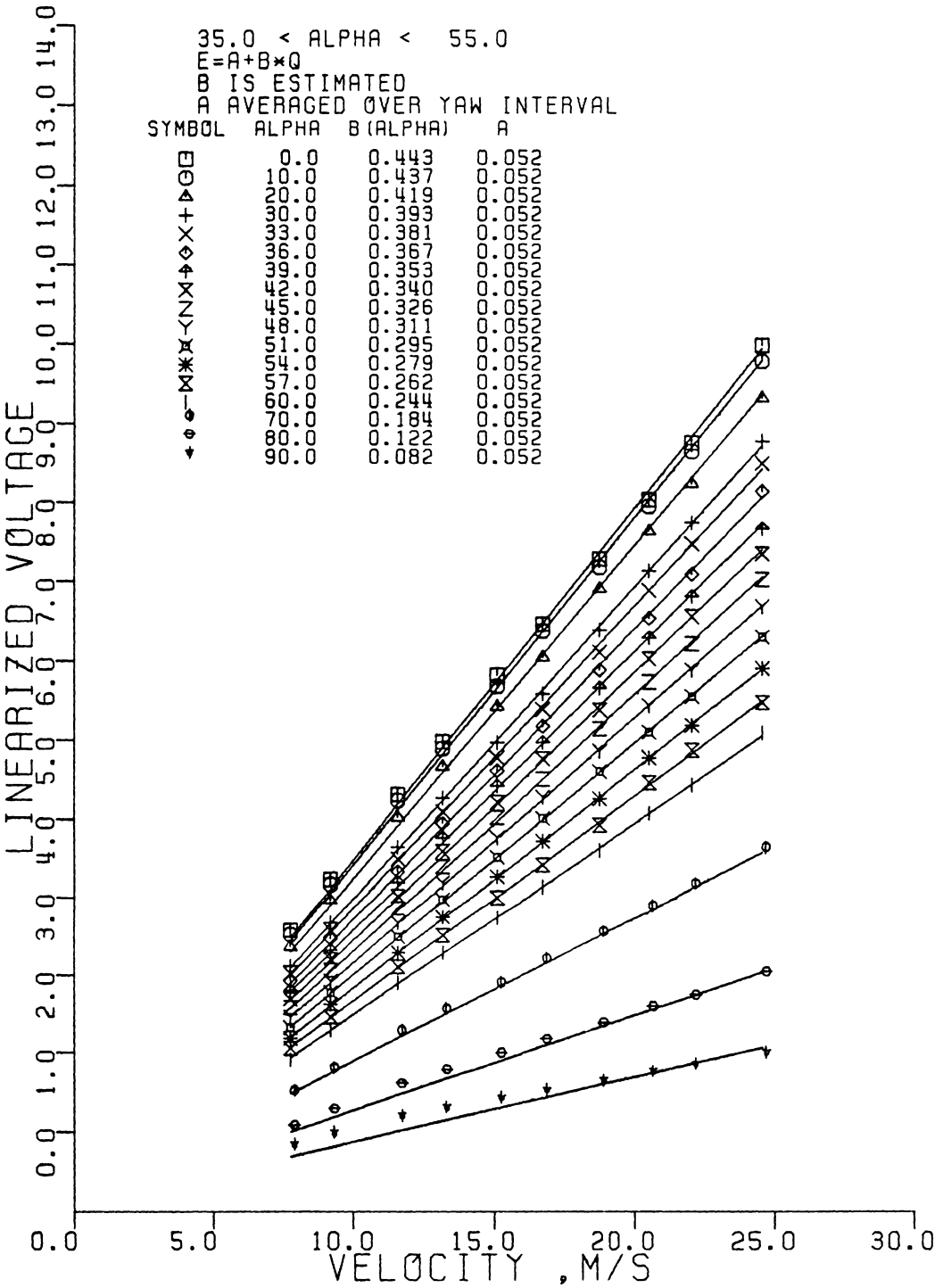

Figure 5.13 Typical Velocity Calibration Results Using the Linear Response with One Parameter, B, Estimated

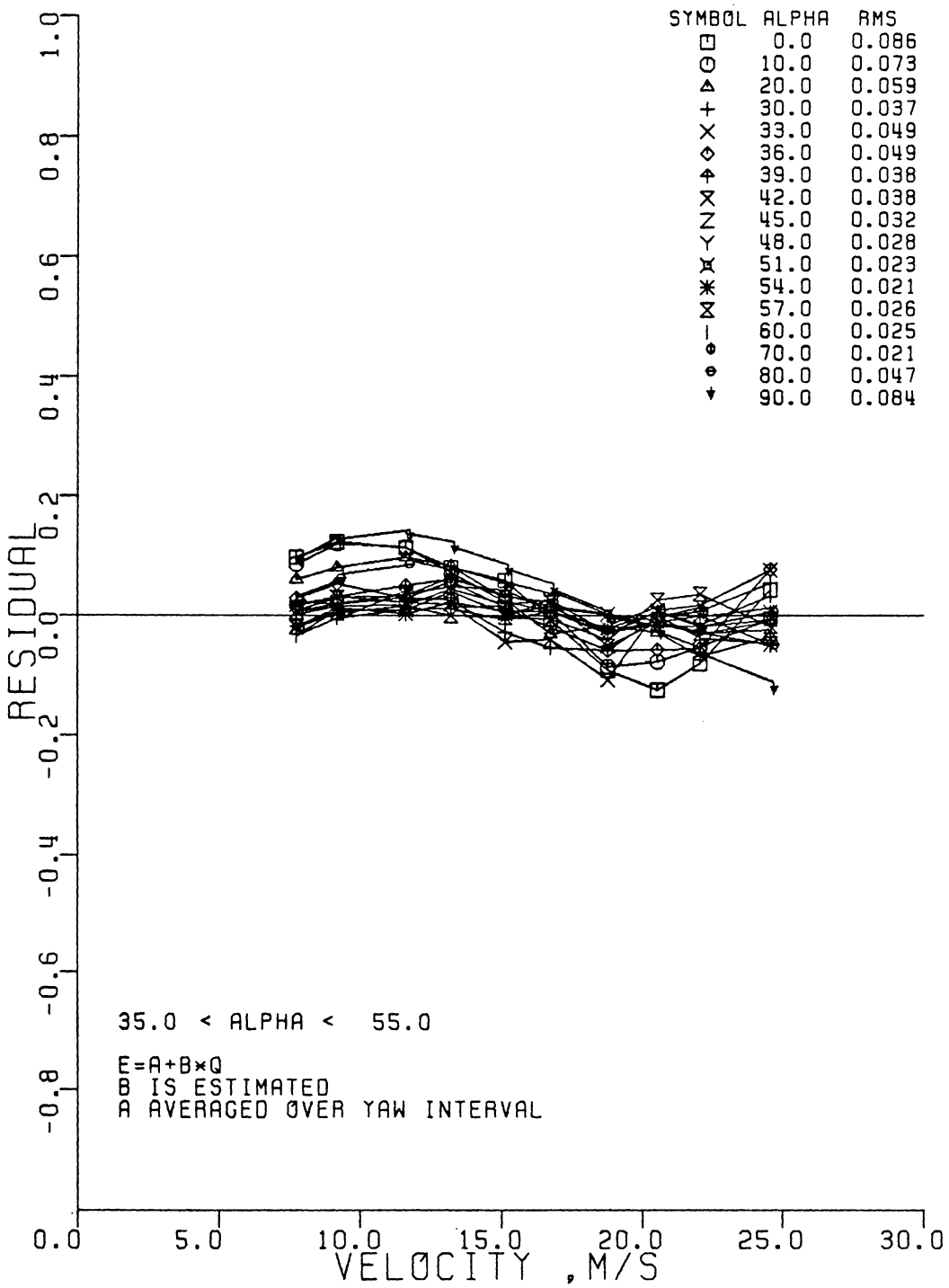

Figure 5.14 Residual Errors in the Estimated Linear Response Curves for the One Parameter Case

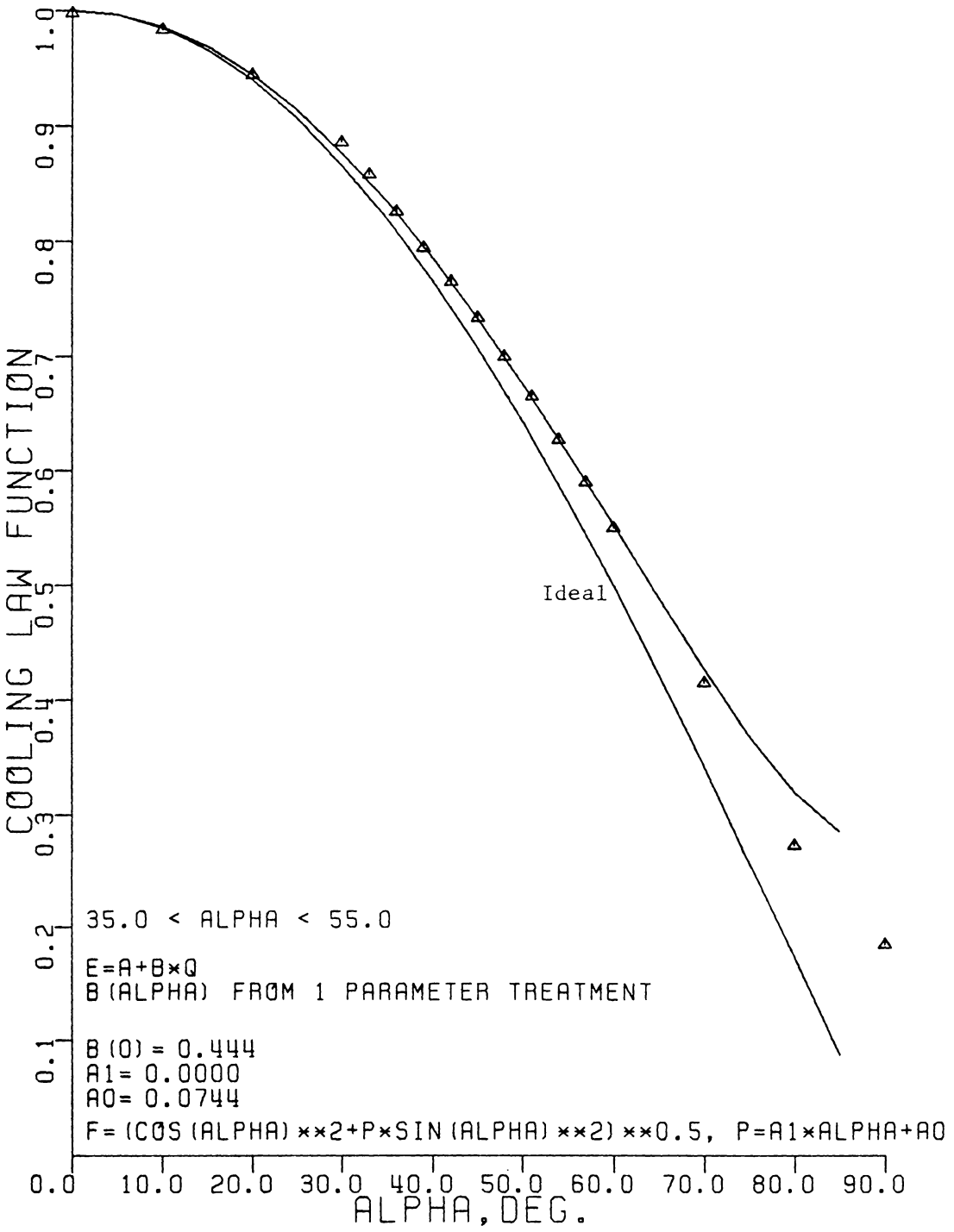

Figure 5.15 Cooling Law Estimated from the Family of Linear Response Curves of the One Parameter Case on the Yaw Interval of Nominally [35^{o},55^{o}]

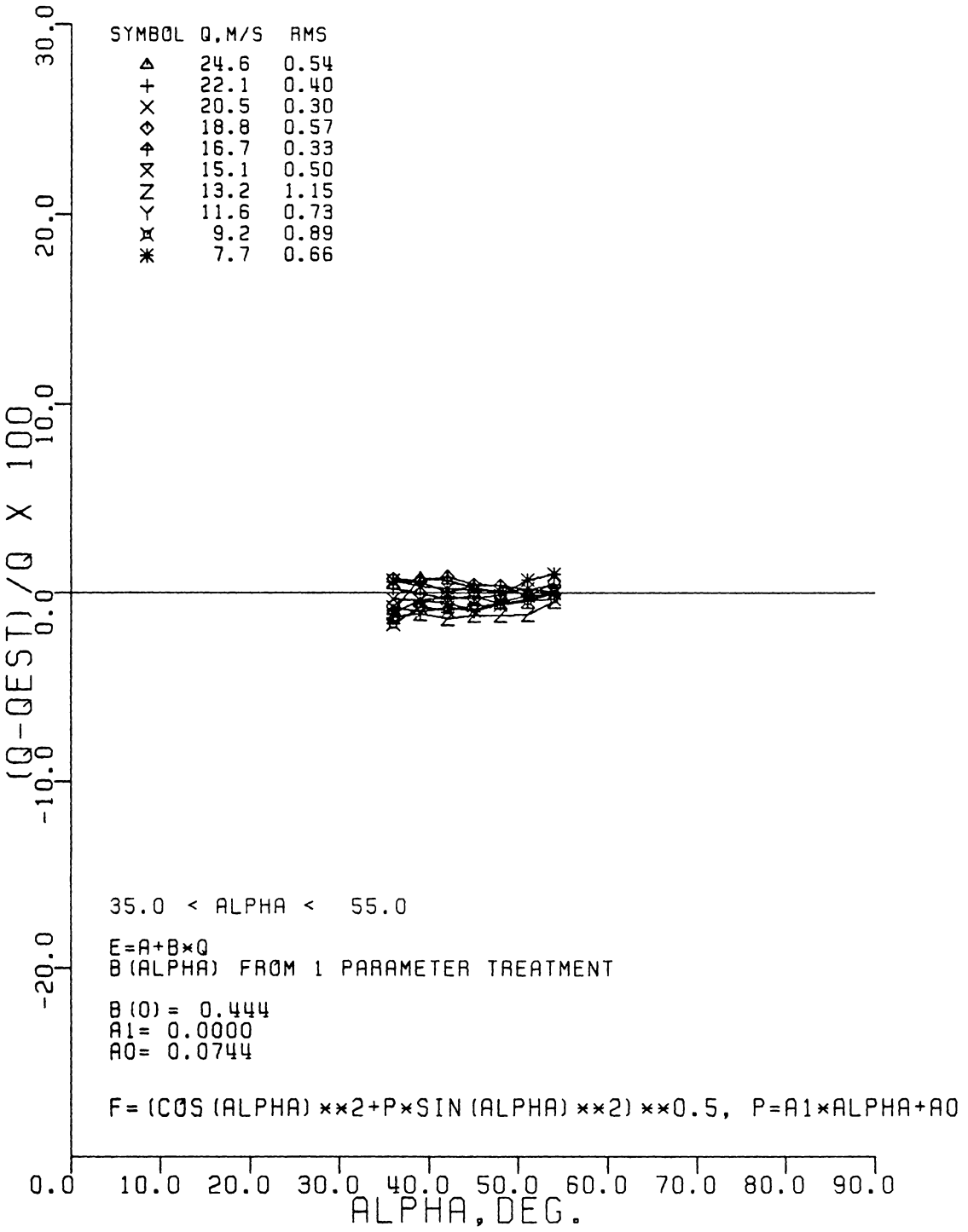

Figure 5.16 Relative Errors in the Estimated Velocitites for a Linear Response Using k^2 from the One Parameter Case

nent is involved. This role of n for the linearized case removes any explicit dependence of k^2 on n. Therefore, one can say that the linearized approach gives results that are less sensitive to the small variation in the exponent that may occur with yaw angle. The estimated cooling law functions between the one parameter treatment of the nonlinear response shown in Fig. 5.7 and both the two parameter and one parameter treatment of the linearized response shown in Figs. 5.11 and 5.15, respectively, show good agreement despite the somewhat larger differences in their k^2 values. The one parameter treatment for the linearized response which uses an averaged value of A, usually gave results that were in better agreement with the results using the one parameter, nonlinear response.

The values of the exponents ranged from approximately 0.43-0.60 over the yaw interval of nominally $[0^o,80^o]$ and from 0.47-0.56 in the restricted yaw interval of nominally $[35^o,55^o]$ for the sensors calibrated. These values are consistent with the constant values reported by the various authors shown in Table 2.3. As discussed in Chapter II, the constant A in the nonlinear response Eq. 5.1 represents a sensor's heat loss at zero incident flow. At this no net flow condition, A is usually taken to be the square of the CTA voltage reading with $A = E_o^2$. It is worth noting that the estimated values of E_o obtained by the present method were essentially equal to the measured value of E_o for nearly all the sensors calibrated for the velocity range considered.

In addition to estimating the cooling law parameter, the present method via Eq. 5.11 or 5.16 determines the constant B_o. Assuming that a given cooling law is valid in describing the sensor's yaw character-

istics over any range of yaw angles, the present method would be expected to give consistent results when comparing $\hat{B}_o$, inferred from a restricted yaw interval, with $\hat{B}(0)$ found by a direct calibration of the sensor at $\alpha = 0$. Ideally both procedures should give the same result. Such a comparison is made in Table 5.1 where the ratio $\hat{B}_o/\hat{B}(0)$ is compared for the lower sensor's of the two hx-arrays used in this study. The values of $\hat{B}_o$ are inferred from the calibrations made in the yaw interval of nominally $[35^o, 55^o]$. The cooling laws suggested by Hinze [54] and Davies and Bruun [104] are compared for both the nonlinear and linearized responses presented earlier. The good agreement shown between the inferred and actual values of B_o strongly supports the validity of the more localized yaw calibrations proposed, which do not necessarily depend on measurements made with the sensor normal to the flow direction as does the more conventional method used by Jorgensen [49]. As shown in Table 5.1 better agreement is obtained for the linearized response regardless ofwhether average values of A and n were used in estimating $\hat{B}_o$. Both the cooling laws tested give similar results. The results from the upper sensor (sensor b) of the hx-array shown in Fig. 5.17 could not be used in such a comparison since a direct calibration of the sensor at $\alpha = 0$ would be influenced by the upstream prong. In this case neither cooling law function would be a valid representation of the effective cooling of the sensor in the neighborhood of $\alpha = 0$.

Table 5.2 summarizes the yaw calibration results of the sensor pairs in the three probe configurations used in this study. Values of k^2, f_1, f_1' and f_1'' for both the linear and nonlinear responses are presented. The values of k^2 listed are in the range of the values

Table 5.1 Comparison of $\hat{B}_o/\hat{B}(0)$ Ratio Using Two Cooling Laws for the Linear and Nonlinear Responses. $\hat{B}_o$ Inferred from the Yaw Interval $[35^o, 55^o]$; $\hat{B}(0)$ Estimated from Calibration at $\alpha = 0$.

$$f_1(\alpha,k^2) = (\cos^2\alpha + k^2\sin^2\alpha)^{1/2} \qquad f_2(\alpha,m) = (\cos\alpha)^m$$

	$B_o^{(1)}/\hat{B}(0)$	$\hat{B}_o^{(2)}/\hat{B}(0)$	$\hat{B}_o^{(1)}/\hat{B}(0)$	$\hat{B}^{(2)}/\hat{B}(0)$
hx-array, Probe 1 (Lower Sensor)	1.002(1.014)*	1.011(0.970)	0.991(1.027)	1.000(0.965)
hx-array, Probe 2 (Lower Sensor)	1.007(0.985)	1.011(0.971)	0.991(0.985)	1.000(0.966)

* linear (nonlinear)

(1) B_o inferred from Eq. 5.16 (5.11) using A (A and n) estimated for each calibration curve in the yaw interval $[35^o, 55^o]$

(2) B_o inferred from Eq. 5.16 (5.11) using values $\bar{A}$ ($\bar{A}$ and $\bar{n}$) averaged over the yaw interval $[35^o, 55^o]$

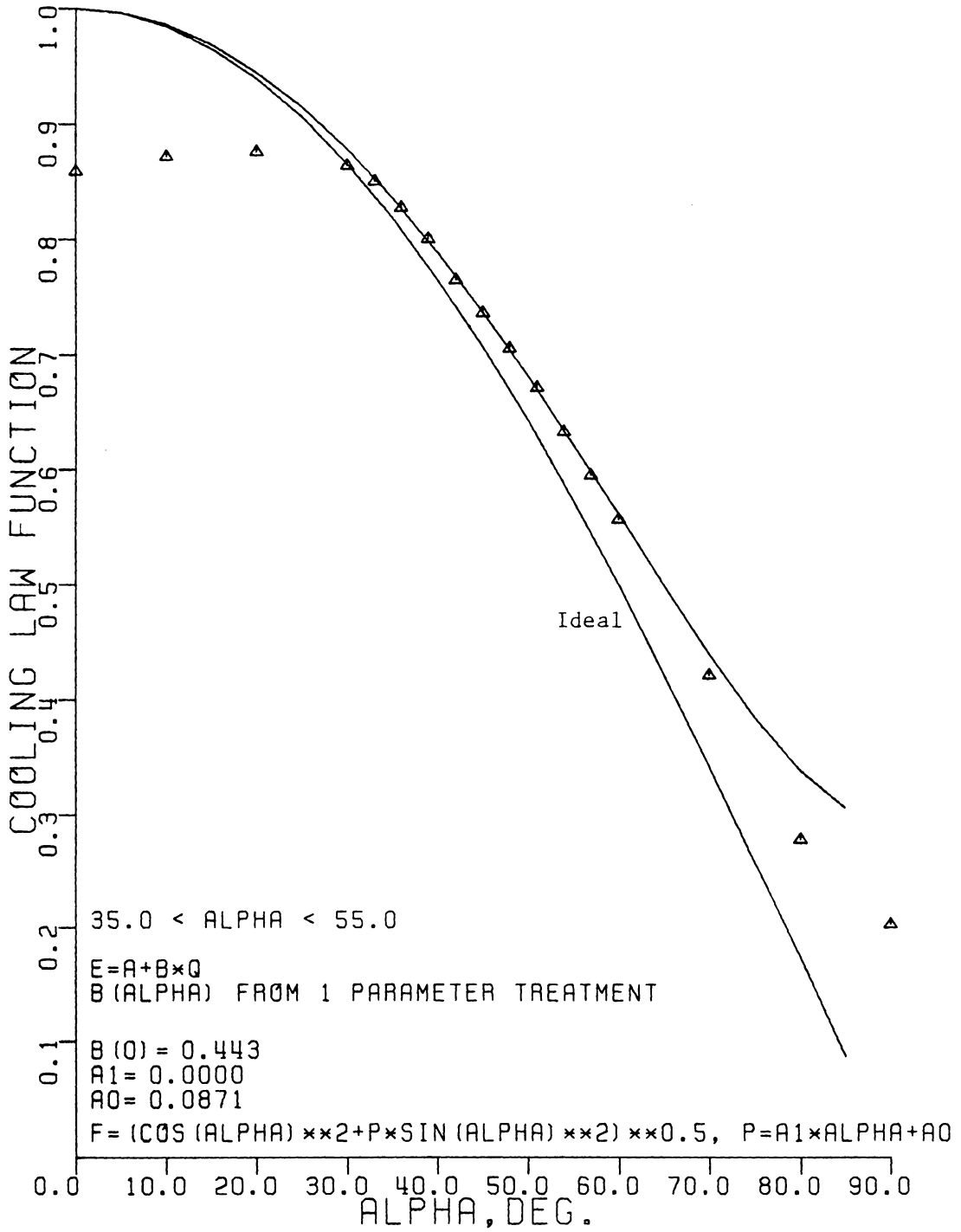

Figure 5.17 Influence of an Upstream Prong on a Calibration Near $\alpha = 0, k^2$ Estimated on the Interval of Nominally $[35^{\circ}, 55^{\circ}]$

Table 5.2 Individual Sensor Yaw Characteristics at the Probes' Operating Position after Hinze [54] for the Linear and Nonlinear Responses. $f_1(\alpha_o,k^2) = (\cos^2\alpha_o + k^2\sin^2\alpha_o)^{1/2}$, k^2 Estimated on the Interval of Nominally [35°,55°].

Probe Calibration Run	k^2		f_1		f_1'		f_1''	
	Sensor a	Sensor b	Sensor a	Sensor b	Sensor a	Sensor b	Sensor a	Sensor b
HX-Array, Probe 1 (I)	0.067(0.062)*	0.092(0.089)	0.736(0.734)	0.744(0.743)	-0.634(-0.639)	-0.610(-0.613)	-0.569(-0.578)	-0.521(-0.526)
HX-Array, Probe 2 (I)	0.074(0.062)	0.087(0.091)	0.733(0.729)	0.737(0.739)	-0.631(-0.643)	-0.619(-0.615)	-0.544(-0.568)	-0.520(-0.512)
VX-Array (I)	0.114(0.096)	0.024(0.013)	0.767(0.761)	0.750(0.747)	-0.577(-0.593)	-0.647(-0.657)	-0.514(-0.544)	-0.694(-0.715)
VX-Array (R)	0.113(0.097)	-0.009(-0.016)	0.766(0.762)	0.741(0.738)	-0.578(-0.591)	-0.677(-0.685)	-0.516(-0.542)	-0.762(-0.779)
VX-Array (F)	(0.106)	(0.008)	(0.764)	(0.746)	(-0.584)	(-0.661)	(-0.528)	(-0.725)
SX-Array, Position 1 (I)	0.055(0.059)	0.120(0.115)	0.726(0.728)	0.748(0.747)	-0.651(-0.646)	-0.588(-0.593)	-0.583(-0.574)	-0.462(-0.471)
SX-Array, Position 2 (I)	0.088(0.081)	0.122(0.112)	0.738(0.735)	0.749(0.746)	-0.619(-0.625)	-0.586(-0.595)	-0.519(-0.531)	-0.459(-0.475)
SX-Array, Position 1 (R)	(0.053)	(0.087)	(0.726)	(0.737)	(-0.653)	(-0.619)	(-0.587)	(-0.520)
SX-Array, Position 1 (F)	(0.054)	(0.095)	(0.726)	(0.740)	(-0.652)	(-0.611)	(-0.586)	(-0.505)
SX-Array, Position 2 (F)	(0.084)	(0.118)	(0.736)	(0.748)	(-0.622)	(-0.590)	(-0.526)	(-0.466)

* linear (nonlinear)

(I) Initial calibration prior to 3DTBL flow measurements

(R) Repeated initial calibration

(F) Final calibration at the completion of the 3DTBL flow experiment

Table 5.3 Individual Sensor Yaw Characteristics at the Probes' Operating Position after Davies and Bruun [104] for the Linear and Nonlinear Responses. $f_2(\alpha_o, m) = (\cos \alpha_o)^m$, m Estimated on the Interval of Nominally [35°, 55°].

Probe Calibration Run	m		f_2		f_2'		f_2''	
	Sensor a	Sensor b	Sensor a	Sensor b	Sensor a	Sensor b	Sensor a	Sensor b
HX-Array, Probe 1 (I)	0.872(0.881)*	0.827(0.831)	0.745(0.743)	0.756(0.755)	-0.638(-0.643)	-0.614(-0.617)	-0.730(-0.729)	-0.730(-0.730)
HX-Array, Probe 2 (I)	0.856(0.878)	0.834(0.826)	0.743(0.738)	0.749(0.751)	-0.636(-0.647)	-0.625(-0.621)	-0.728(-0.727)	-0.728(-0.728)
VX-Array (I)	0.794(0.824)	0.954(0.973)	0.780(0.773)	0.753(0.749)	-0.578(-0.594)	-0.647(-0.656)	-0.730(-0.734)	-0.746(-0.745)
VX Array (R)	0.790(0.817)	1.014(1.030)	0.781(0.775)	0.740(0.737)	-0.575(-0.590)	-0.676(-0.683)	-0.730(-0.733)	-0.742(-0.740)
VX-Array (F)	(0.802)	(0.979)	(0.778)	(0.748)	(-0.582)	(-0.659)	(-0.731)	(-0.745)
SX-Array, Position 1 (I)	0.898(0.890)	0.774(0.784)	0.733(0.735)	0.765(0.762)	-0.658(-0.654)	-0.592(-0.597)	-0.725(-0.726)	-0.726(-0.727)
SX-Array, Position 2 (I)	0.829(0.841)	0.778(0.794)	0.750(0.747)	0.764(0.759)	-0.622(-0.628)	-0.594(-0.603)	-0.728(-0.728)	-0.726(-0.727)
SX-Array, Position 1 (R)	(0.902)	(0.831)	(0.732)	(0.750)	(-0.660)	(-0.623)	(-0.725)	(-0.728)
SX-Array, Position 1 (F)	(0.899)	(0.817)	(0.732)	(0.754)	(-0.659)	(-0.615)	(-0.725)	(-0.728)
SX-Array, Position 2 (F)	(0.836)	(0.788)	(0.748)	(0.761)	(-0.626)	(-0.599)	(-0.728)	(-0.727)

* linear (nonlinear)

(I) Initial calibration prior to 3DTBL flow measurements

(R) Repeated initial calibration

(F) Final calibration at the completion of the 3DTBL flow experiment

reported by different authors in Table 2.4 although most of these values are for sensors having larger ℓ/d ratios. Reasonably good agreement in the values of the cooling law function and its derivatives between the two different responses treated here is shown despite the larger differences in the values of k^2. In view of the differences in the signal processing and equations used in estimating k^2 (Eqs. 5.1 and 5.2) between the two responses, the variations in k^2 between the linear and nonlinear cases are considered to lie within reasonable limits. The values of k^2 obtained with signal linearization were used in calculating the turbulent stresses.

In the sensor response equations derived in Chapter IV, the mean velocity and turbulence quantities depended on the functions f, f', and f'' with the cooling law parameter P contained in these terms. Hence, for this more general representation, it is proper to study the effects of variations in the yaw parameter on the values of the cooling law function and its derivatives. The results given in Table 5.2 show a low insensitivity for f_1 to relatively large differences in k^2 while values of f_1' and f_1'' demonstrate a greater sensitivity to such differences that seems to increase with the successive derivatives of f_1. For example, sensor a of the vertical x-array gave relative differences in f_1, f_1', and f_1'', between the linear and nonlinear cases, of 1, 3, and 6% respectively, for roughly a 16% change in k^2. When the Davies and Bruun [104] law was used to describe the sensors yaw characteristics, different trends were found. The values pertaining to this cooling law are given in Table 5.3 where similiar comparisons are made as in Table 5.2. The values of m for both the linear and nonlinear cases vary not

nearly as much as the parameter k^2. Furthermore, the net effect of these smaller differences propagating into f_2 and its derivaties is a more uniform sensitivity of f_2, f_2', and f_2'' to changes in m than for the case using k^2. In comparing similiar results for sensor a of the vertical-array given in the example above, one finds a 1, 3, and 1% variation in magnitude of f_2, f_2', and f_2'' between the linear and nonlinear cases for an approximately 4% change in m.

It is noted that while the values of f and f' calculated from the two cooling laws gives similar results, considerable differences in the values of f'' are found. The results are consistent in that they generally show slightly larger values for f and f' of up to 2% higher and substantially larger values of f", as much as 40% and higher, when using the Davies and Bruun law as opposed to Hinze's law. Such large differences are due to the different generic forms of the functions themselves. This point is easily verified by considering Eqs. 5.21 and 5.23 which are used by the more conventional calibration method to determine values of k^2 and m, respectively. Clearly, m is undefined at $\alpha = \pi/2$ whereas Eq. 5.21 will give finite values of k^2 at $a = \pi/2$. Since this amount of yaw corresponds to the sensor lying parallel to the flow direction and the usual operating position lies sufficiently far from this parallel position in practice, this feature does not discredit the Davies and Bruun law but merely points out a difference between the two cooling law functions.

It is difficult to justify the use of one law over the other since there appears to be no physical basis to guide in such a choice. Both cooling laws involve empiricism that is needed to correct for the effect

of tangential cooling of the sensor as shown in Fig. 5.15, for example, which demonstrates the inadequacy of the ideal cosine law. Under certain conditions, both laws can be considered as being equivalent from a mathematical standpoint as indicated by Eq. 2.16. In view of the calibration results presented, both laws were able to accurately predict the flow velocity usually to within 1% RMS when k^2 and m were determined by the present method in the neighborhood of the operating position and for the range of velocities considered.

Of primary concern, however, is to what extent the discrepancies in the corresponding characteristics between the two laws, especially in f", will effect the turbulence results in general. Since the higher level derivatives appear in combination with higher order velocity correlations, it is reasonable to neglect terms involving f" for the case of low to modest intensity flows. For this case both laws, as shown in Tables 5.2 and 5.3, give reasonably equivalent values of f and f' and hence the remaining differences are not as critical.

An advantage gained in formulating a sensor's response to turbulence in terms of the cooling law function and its derivaties rather than the more common approach is that the explicit dependence of the response to the cooling law and its first and second derivatives becomes clear. In the latter approach, when a specific cooling law is introduced early, the response equation is written in terms of the cooling law parameter. While the dependence of the response equation on cooling law parameter may be clear, the importance of the effect of the parameter on the derivaties of the cooling law function are usually lost. The identification of the errors of a response equation to the deriv-

atives of an assumed cooling law can indicate where emphasis is required in extracting these parameters from experimentally measured yaw data. Further advantages in using the generalized cooling law function approach are discussed in Appendix C. For this study, the more popular law of Hinze [54] was used in reducing the mean velocity and turbulence data. In high intensity flows, where higher order terms cannot be neglected, the large differences in f'' between the two laws would be of major concern in choosing the more 'correct' cooling law.

Tables 5.2 and 5.3 also show repeated calibration runs for the various sensors including a final (F) calibration performed at the end of the 3DTBL flow experiment. These results suggest that any contamination or other change in the sensors, which may have occurred during the experiment, was not substantial so as to have caused a significant change in the sensors directional characteristics. It is further noted that the yaw characteristics found for each sensor pair are generally not matched and which in fact show considerable differences in the values of f'. This justifies the need to incorporate sensor mismatch in the response analysis derived in Chapter IV. The effect of this probe asymmetry will be discussed in Chapter VII. Small differences in the yaw characteristics between the two positions of the sx-array are also noted and may be attributed to the different aerodynamic displacement effects as discussed in Chapter II.

An uncertainty analysis was performed on one sensor from each of the three different probes used. A Kline and McClintock [142] approach was used as a basis for determining the most probable error in determining the cooling law parameter using the present method with a linearized

response. The yaw parameters k^2 and m were found to be essentially dependent on the uncertainty in the yaw angle and the degree of linearization achieved at the beginning of each calibration run. The partial derivatives with respect to these variables were formed numerically as suggested by Moffat [143]. In the yaw interval of nominally $[35^o, 55^o]$, the absolute uncertainty in k^2 ranged from 0.004 to 0.009 (20/1 odds) and 0.007 to 0.017 (20/1 odds) for the parameter m.

For the purpose of comparison, the calibration data was reduced by a conventional approach where both cooling laws were used. At a given velocity, a value of $f(\alpha_j, k^2)$ was determined for each $[0, \alpha_j]$ subinterval using Eqs. 5.20-5.23 where α_j ranged from 0 to 80^o. A constant value of k^2 was estimated for the interval $[0, 60^o]$ using the method of least squares. Typical results obtained with the lower sensor of the hx-array (Probe 2) are shown in Figs. 5.18-5.21 where a linearized response is used. The values of k^2 and m, each listed as A0 in Figs. 5.18 and 5.20, are consistent with the values shown in Tables 5.2 and 5.3. Figures 5.19 and 5.21 show a distribution of k^2 and m values, respectively, on the yaw interval $[0^o, 80^o]$. These parameter variations with yaw angle can be incorporated in the estimation algorithm in the form given by Eq. 5.14, for example. Several calibration runs were reduced assuming this linear model using the present method. For the magnitude of the variations in k^2 and m shown in Figs. 5.19 and 5.21, curve fits of f similiar to the constant parameter case were obtained when the parameters were allowed to vary linearly with yaw. The RMS residual error of the estimated cooling law function was used as the basis for comparing these two cases. Thus, the assumption of constant k^2 or m over the interval

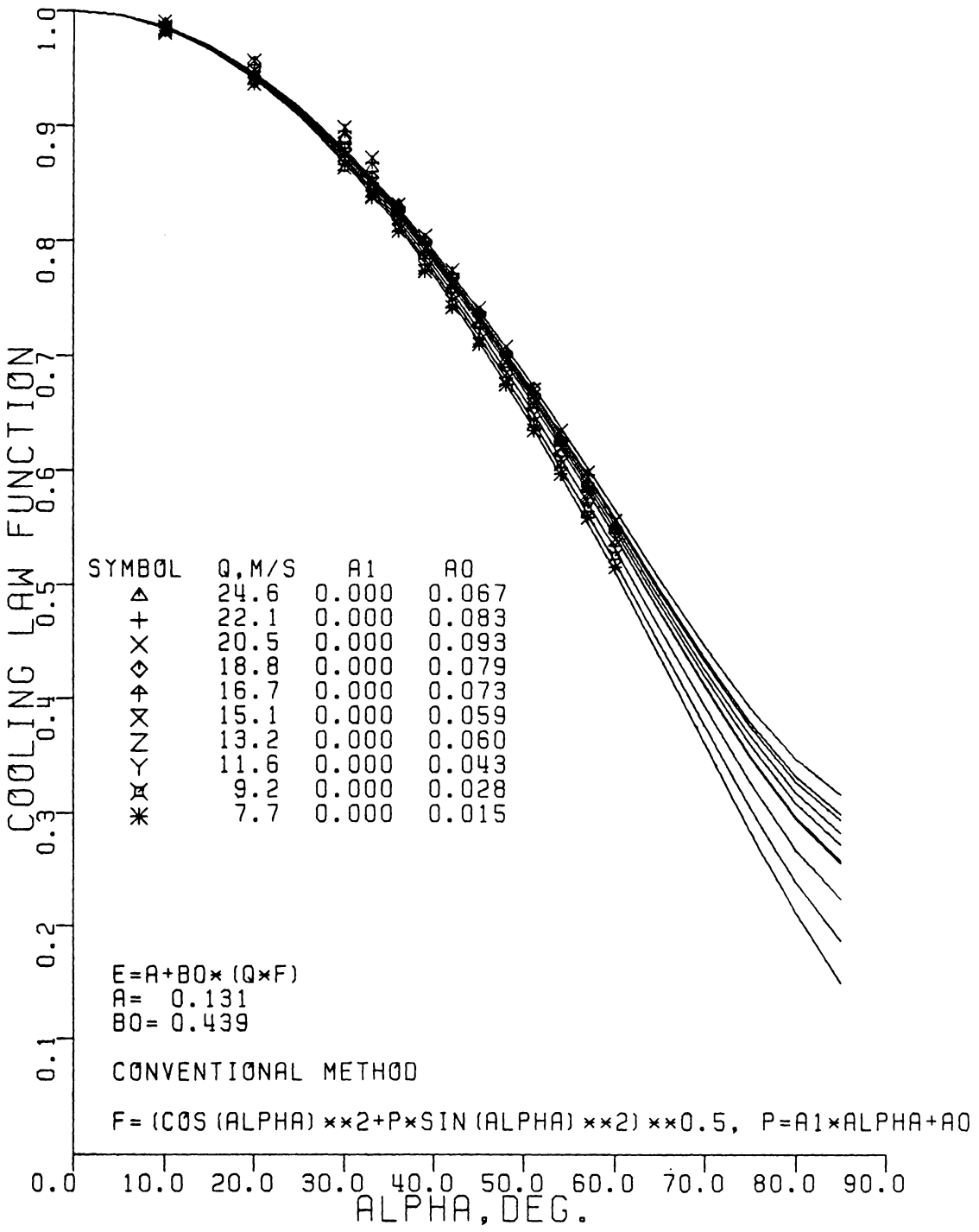

Figure 5.18 Sensor Calibration by a Conventional Approach Using Hinze's [54] Law

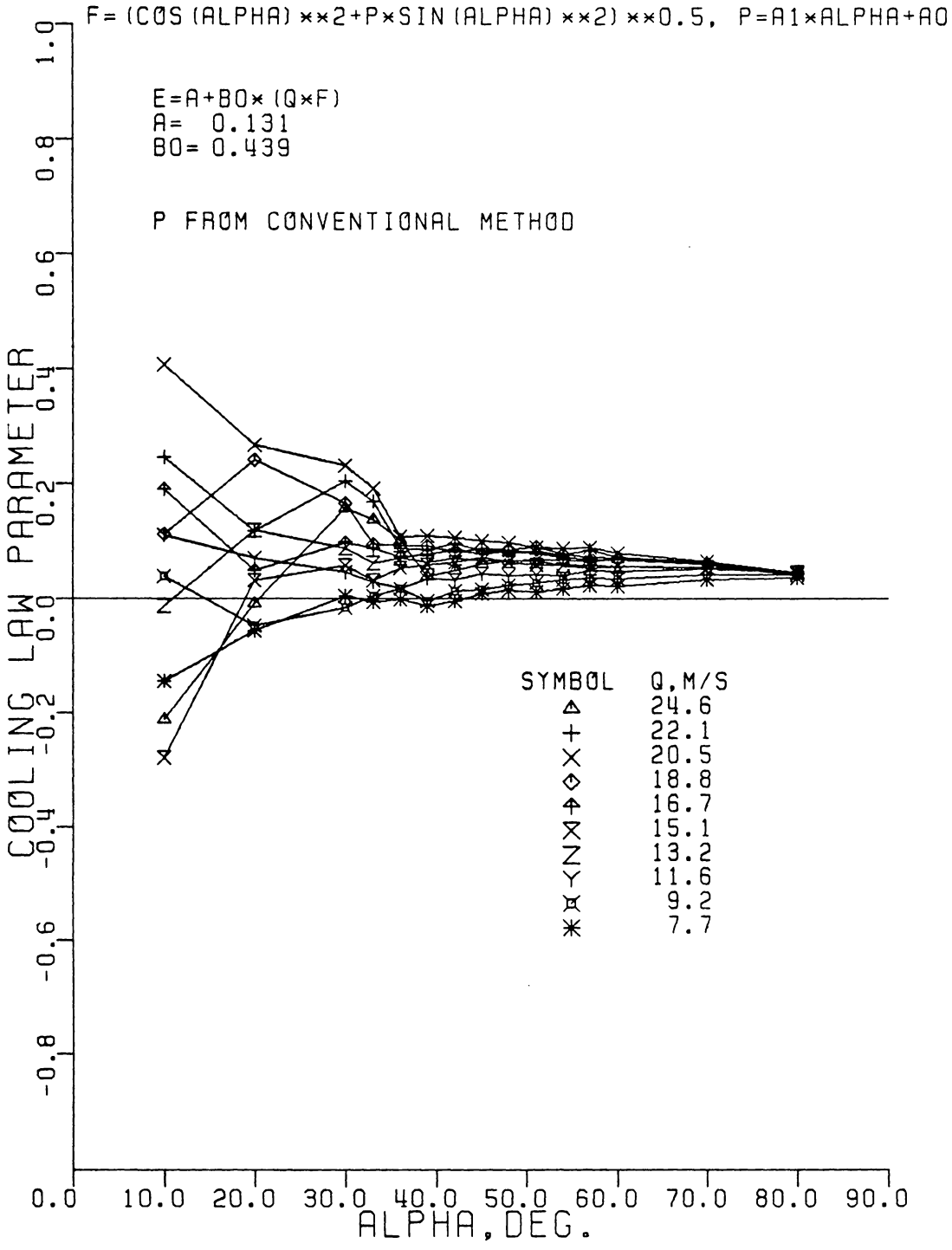

Figure 5.19 Variations of Parameter k^2 with Yaw for Different Velocities

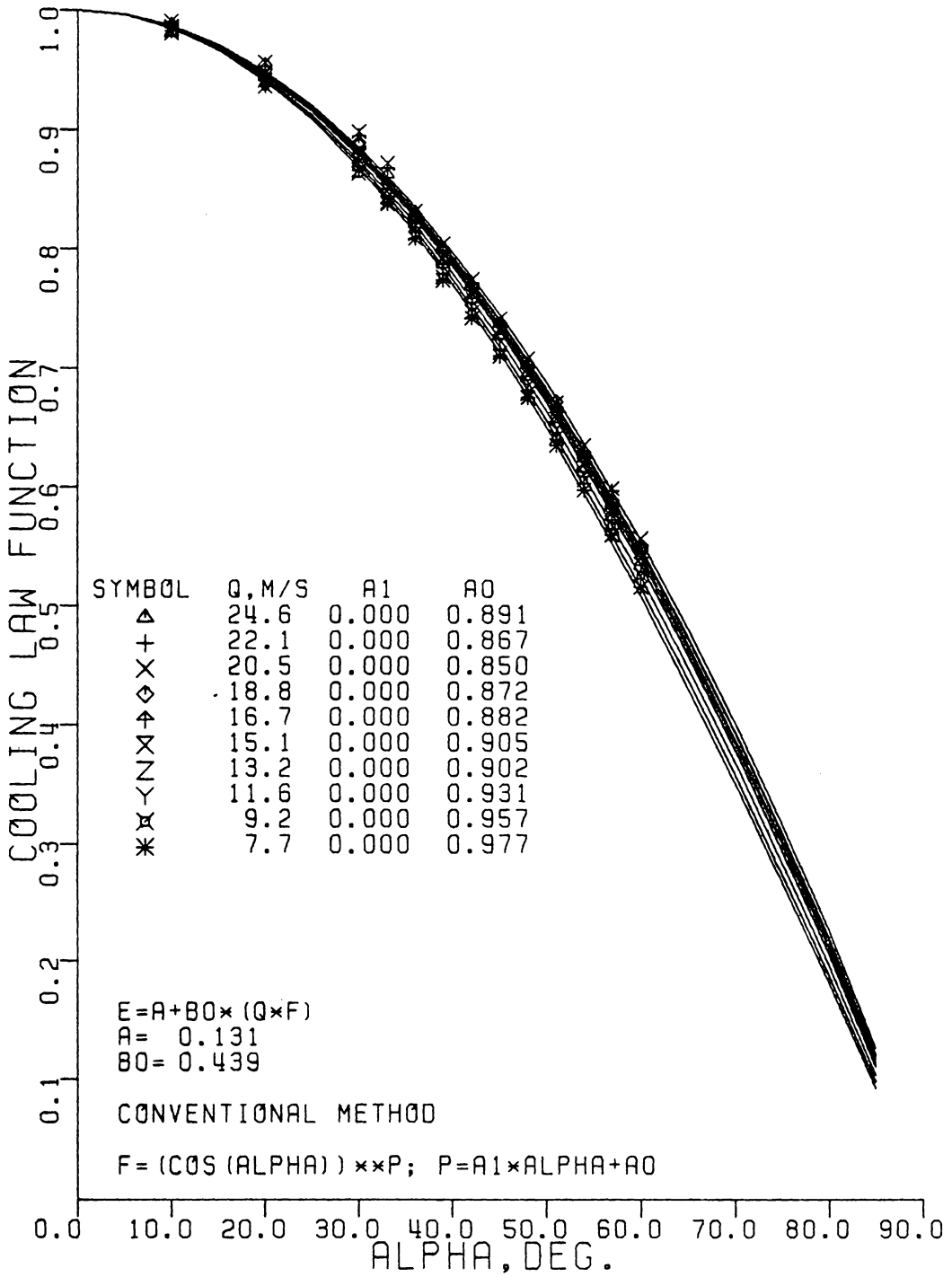

Figure 5.20 Sensor Calibration by a Conventional Approach Using Davies and Bruun's [104] Law

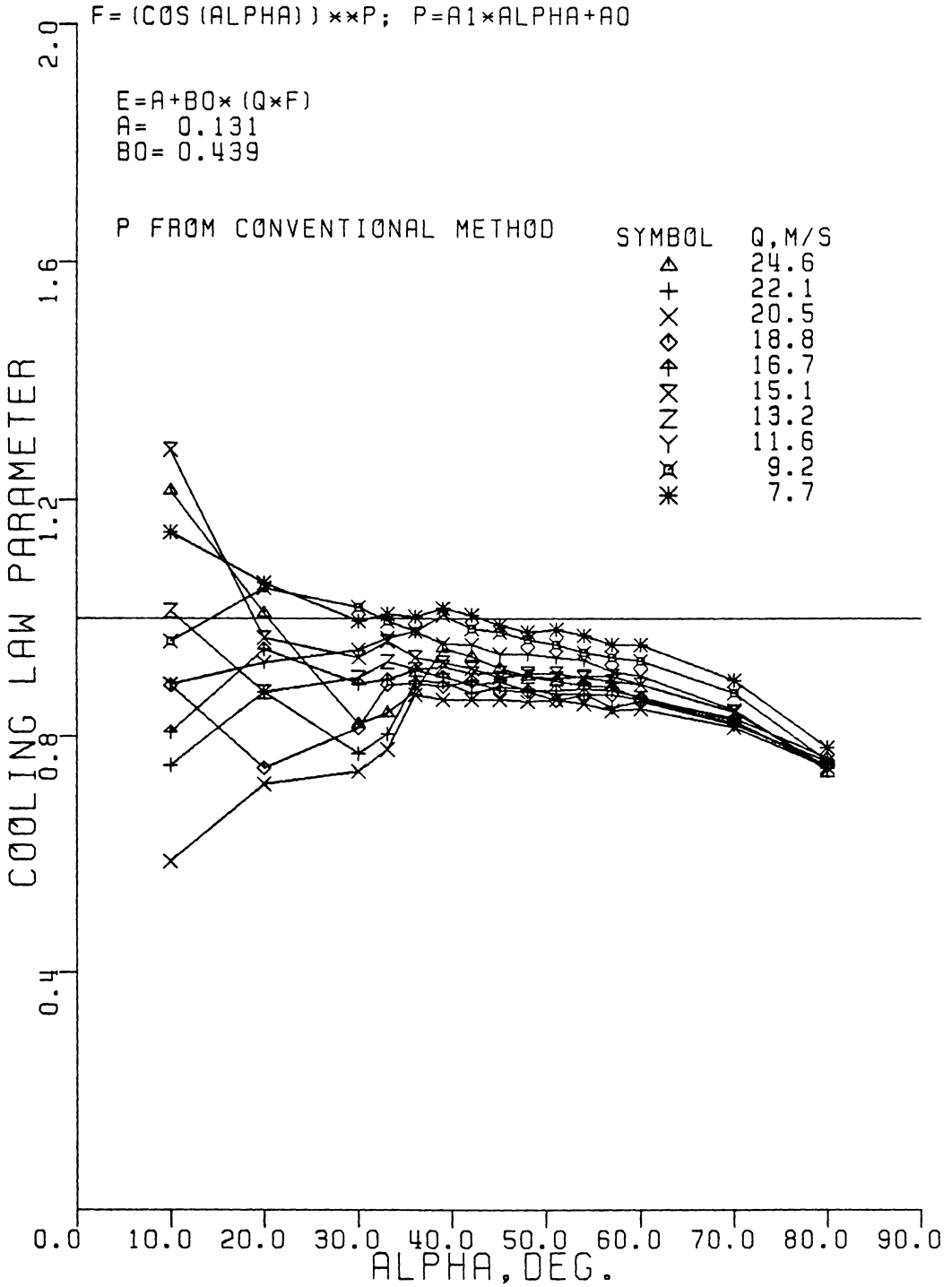

Figure 5.21 Variations of Parameter m with Yaw for Different Velocities

$[35^{o}, 55^{o}]$ was sufficient in describing the yaw characteristics of the sensors studied.

The more convention method, by nature, is able to show the velocity dependence of the yaw parameter since a parameter can be found at each incident velocity. The variations of the yaw parameters k^2 and m with velocity, also shown in Figs. 5.18 and 5.20, are not of the order of magnitude that would be identified as causing significant errors in the turbulence results. That a constant value of the yaw parameter can be used for the velocity range encountered in this study is strongly supported by the results in Figs. 5.15 and 5.16 which indicate a very good curve fit of the yaw data giving a high degree of accuracy in predicting the flow velocity in the range of about 7-25 ms^{-1}.

The yaw calibration results obtained by the present method are consistent with values obtained by the conventional approach. In the present method, the entire calibration curve is used to determine the sensor's yaw characteristics whereas the conventional method, which requires considerably less data, relies on measurements made at a single velocity. Since in measuring turbulent flows, the sensor is exposed to a range of velocities continuously, (although usually quite smaller in magnitude), due to the contribution of the instantaneous fluctuating velocity components, the present method is believed to be more suitable.

VI. TWO-DIMENSIONAL FLOW STUDIES

A. Introduction

The wind tunnel facility used in this study was calibrated to define, improve, and assess the quality of the tunnel flow, and to determine the effects of confirmed transverse nonuniformities on the pressure-driven 3DTBL flow.

From a computational standpoint, it is important that a standard test case flow be based on a high quality upstream flow since the computation of such a flow depends on the initial or upstream flow conditions. The ideal upstream flow is one that is two-dimensional and uniform across an initial plane but uniform 2D tunnel flows are difficult to produce in practice. In reality, the flow through the tunnel is more likely to experience spanwise nonuniformities to at least some degree. While transverse variations in the flow are generally not reported, it appears that whenever such transverse variations are carefully sought out, they have been confirmed to exist in nominally two-dimensional flows. Any spanwise nonuniformities of mean velocity and/or turbulence properties can add ambiguity in specifying the initial conditions and such ambiguities must be resolved by the computational fluid dynamicist.

An accurate and definitive documentation of the initial conditions is therefore essential since the computation of the 3DTBL flow depends on these initial conditions. Considerable attention was given to the tunnel flow to determine the two-dimensionality of the flow and the effects of upstream spanwise nonuniformities on the downstream 3DTBL

flow. One would expect a strong downstream three-dimensional flow to overpower any asymmetries or other effects arising from any weak upstream transverse variations.

B. Spanwise Nonuniformities

The large scale, low speed, low turbulence level wind tunnel that was evaluated is shown in Fig. 3.4 and described in Chapter III. The principal variable reported on here is the screen arrangement located near the entrance of the contraction nozzle. For this tunnel configuration, this inlet section consists of a 0.635 cm (0.25 in.) filter pad, a 16 x 18 mesh fiberglass screen with an average open flow area ratio β of 0.71, a matrix of 2.54 cm (1 in.) diameter of 15.24 cm (6 in.) long mailing tubes, followed by three additional 16 x 18 mesh fiberglass screens. It has been reported by several investigators [50,144-149] that screens can minimize spanwise nonuniformities (and reduce the turbulence level in the flow). On the other hand, it has also been reported that screens can contribute to such nonuniformities when a nonuniform mesh or two small an open flow area ratio ($\beta < 0.57$) is used.

The inlet tunnel configuration reported by Pierce and McAllister [125] consisted of four aluminum screens downstream of the mailing tubes with no upstream screen. The test section spanwise variation in mean velocity for this arrangement is shown in Fig. 6.1. The replacement of the aluminum screens with the fiberglass screens provided the opportunity to study the nature of spanwise nonuniformities more closely and

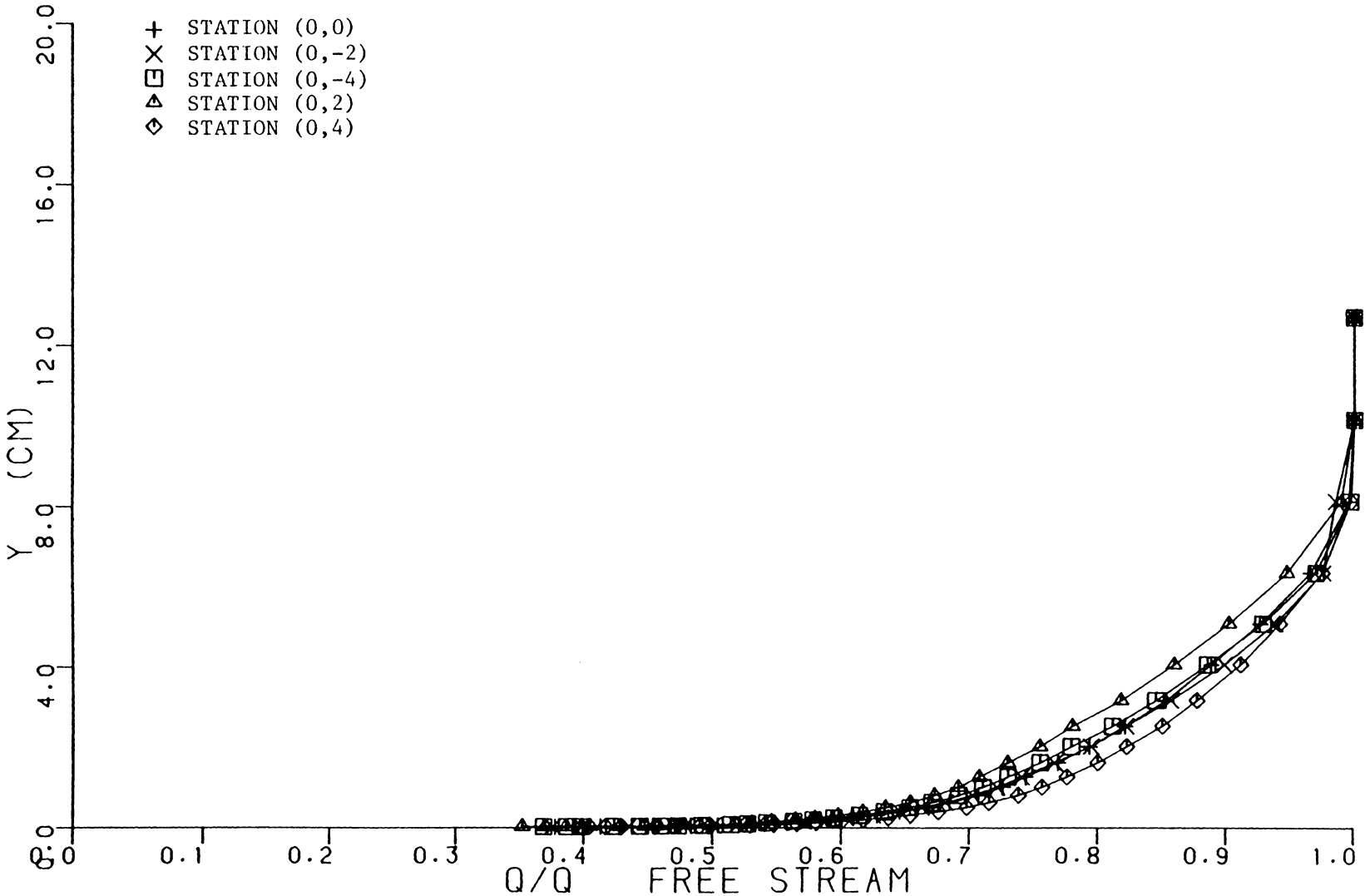

Figure 6.1 Spanwise Nonuniformity in Mean Velocity Across the Test Section as Reported by Pierce and McAllister [125]

compare the 3DTBL flow following to two different upstream transverse variation conditions.

The fiberglass screens offered a more uniform grid than the older aluminum screens. Due to the large cross-sectional area at the inlet to the contraction nozzle, three 1.22 by 2.44 m (4 by 8 ft) sections were sewn together to accommodate the 3.66 by 2.44 m (12 by 8 ft) inlet section. Each screen was hung to give two horizontal seams per screen. The horizontal seams were placed so that no seam followed directly behind the other. Several combinations of screens with and without the filter cloth were tested.

Measurements of mean velocity and local flow angle were obtained with the same gooseneck cobra probe used by Pierce and McAllister [125]. In order to document the effect of each of the inlet screen modifications on the spanwise nonuniformity, mean velocity data were taken across the test section at three vertical positions, x_2 = 0.0254, 2.54, and 19.1 cm (0.010, 1.000, and 7.500 inches) for the spanwise position x_3 ranging from -20.32 to +20.32 (-8 to +8 inches) in 5.08 cm (two inches) intervals. The vertical position x_2 = 0.0254 cm corresponds to the probe lying on the wall and x_2 = 19.1 cm corresponds to the freestream. Depending on the proximity of the cobra probe to the wall, static pressure was measured either by a wall static pressure tap or a pitot-static probe in the freestream.

Figure 6.2 shows typical spanwise variations of the local velocity for various inlet plenum screen configurations for x_2 = 2.54 cm. The quantity $(\overline{U}_{x_3}/\overline{U}_o - 1)$ is plotted versus x_3 where $\overline{U}_{x_3}$ is the mean velocity at a given x_3 location and $\overline{U}_o$ is the mean velocity at x_3 = 0.

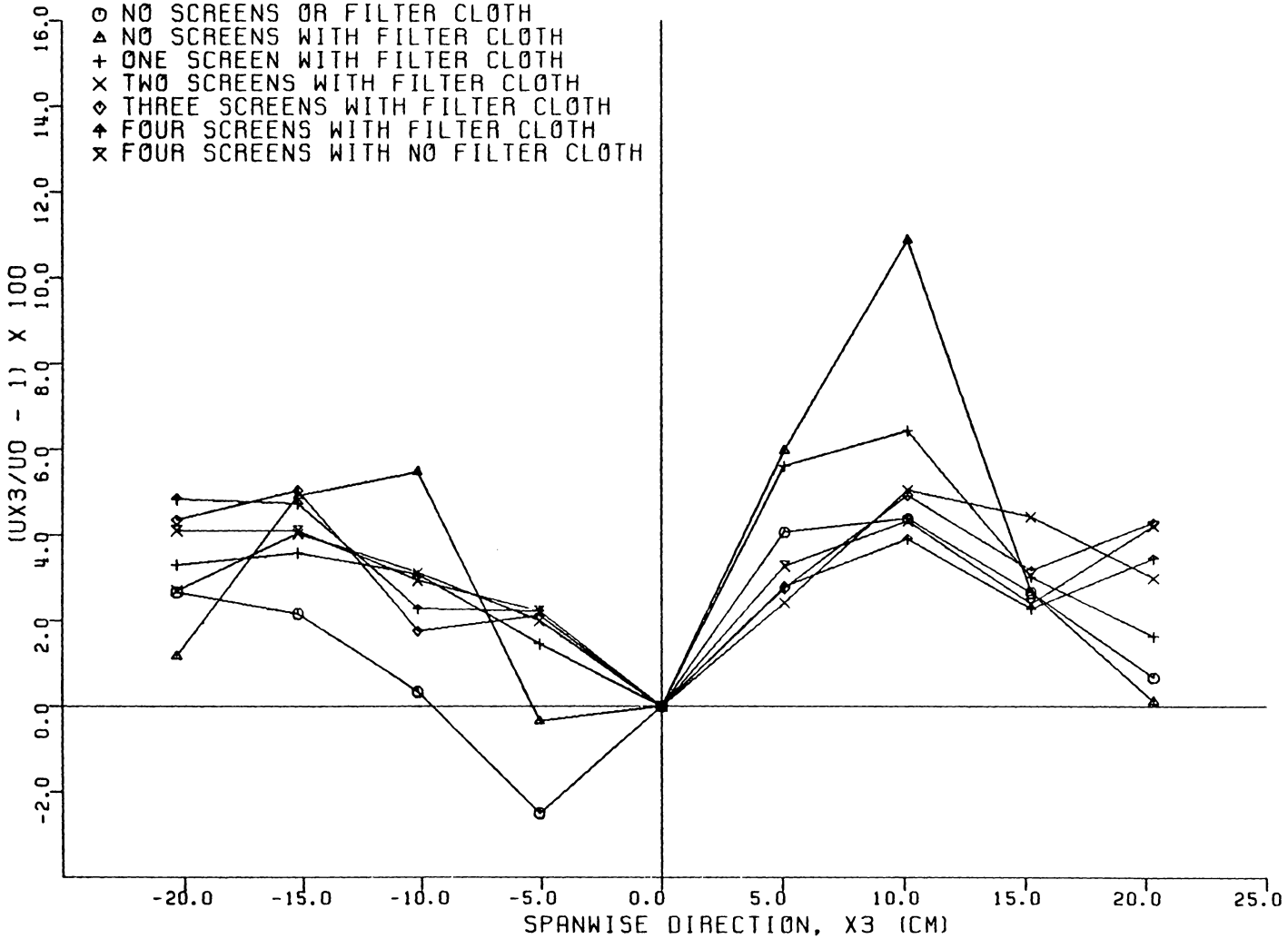

FIGURE 6.2. EFFECT OF UPSTREAM SCREEN-FILTER CLOTH CONFIGURATION ON THE SPANWISE NONUNIFORMITY IN MEAN VELOCITY ACROSS TEST SECTION, 2.54 CM FROM THE WALL

Slightly larger transverse variations, similiar in shape, were found at x_2 = 0.0254 cm. It is also noted that the freestream velocity variations were less than 1% for all combinations of screens and filter cloth tested. Furthermore, the static pressure was essentially constant across the test section for the present configuration shown in Fig. 3.4. As illustrated in Fig. 6.2, the filter cloth added nonuniformity to the flow while, and as expected, the screens acted to reduce it. Small but consistent changes were also noted in the local direction of the nominally two-dimensional flow with these various screen/filter combinations. Although the filter cloth added a considerable amount of spanwise nonuniformity to the flow, it acted as a damper that essentially eliminated any large pressure fluctuations in the tunnel. The filter cloth was also effective in removing airborne particles from the flow and significantly reduced the amount of contamination of the hot-film probes used extensively in this study.

The freestream turbulence level was measured by a single hot-film probe placed normal to the flow. As shown in Fig. 6.3, the filter cloth reduced the freestream turbulence to a value slightly below 0.5%. The screens appear to have had no significant effect in further reducing the freestream turbulence level.

The spanwise variations which remained are consistent in magnitude with those reported by de Brederode and Bradshaw [144], de Bray [145], Bradshaw [146], Furuya and Osaka [147], Furuya et. al. [148], and Favre and Gaviglio [149] in their carefully documented work. Table 6.1 compares skin friction coefficients for the former and present transverse variations which are shown in Figs. 6.1 and 6.8 for mean velocity. The

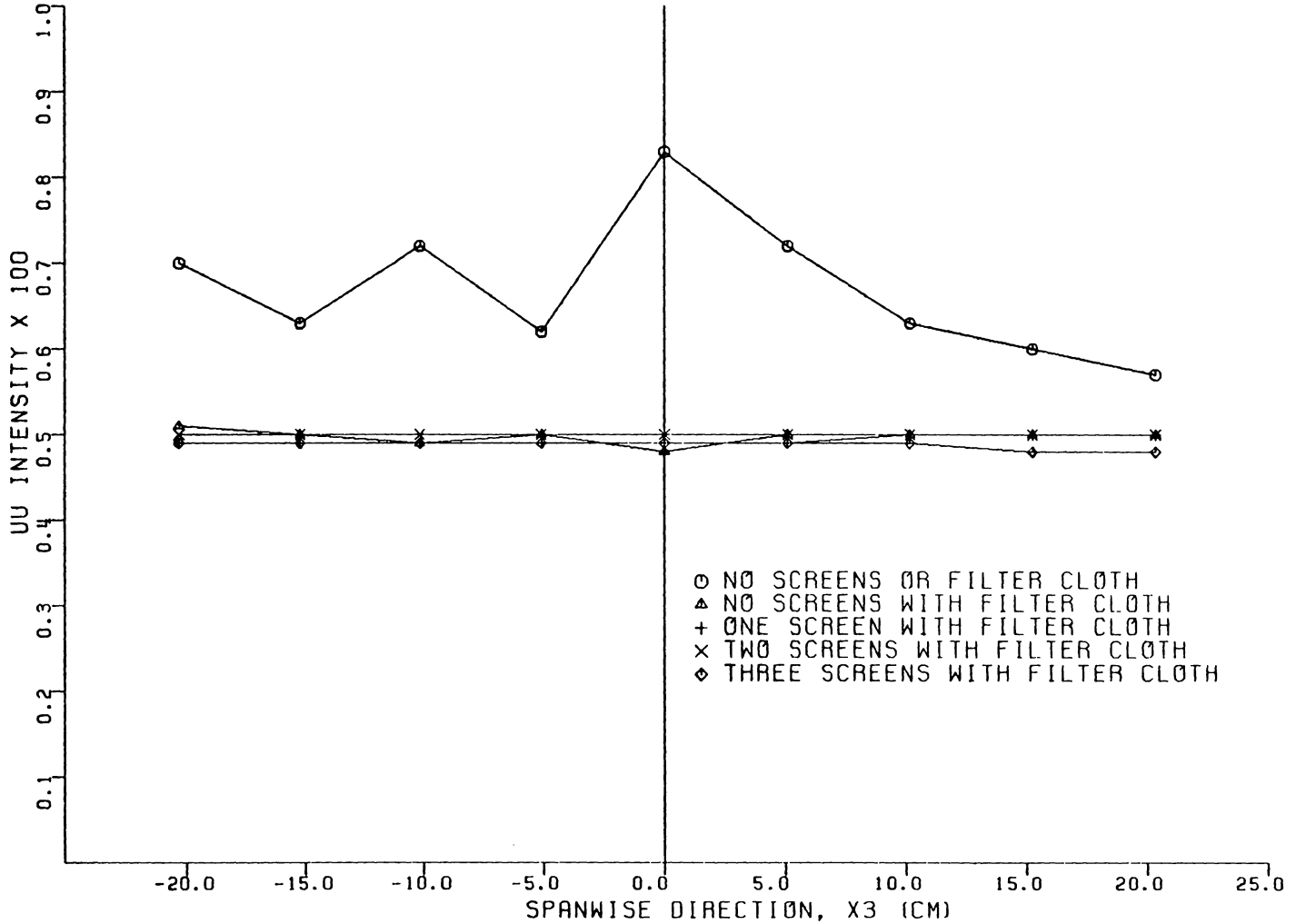

FIGURE 6.3. EFFECT OF UPSTREAM SCREEN-FILTER CLOTH CONFIGURATION ON THE SPANWISE NONUNIFORMITY IN FREESTREAM UU INTENSITY ACROSS THE TEST SECTION

Table 6.1 Comparison of Test Section Spanwise Nonuniformity in Skin Friction Coefficient between the Former and Present Inlet Screen Configurations

Station	Former Inlet Tunnel Configuration*	Present Inlet Tunnel Configuration*
(0,8)		2.66
(0,4)	2.74	2.52
(0,2)	2.31	2.64
(0,0)	2.54	2.42
(0.-2)	2.53	2.55
(0,-4)	2.46	2.50
(0,-8)		2.62

*Value skin friction coefficient ($C_f \times 10^3$) obtained from the Ludwieg-Tillmann correlation.

tabulated wall shear values were obtained from the Lugwieg-Tillmann correlation.

To study the effects of different spanwise nonuniformities on the 3DTBL flow, the profiles of mean velocity were measured at stations (-7,0) and (-7,-8). Figures 6.4a and 6.4b show these results obtained under the two different upstream conditions. These particular stations would seem to be least affected by the generally strong 3D flow imposed by the body and hence more likely influenced by the upstream flow conditions. The agreement and repeatability in these mean flow profiles suggest that the different spanwise variations confirmed in Figs. 6.1 and 6.8, each due to a different inlet filter/screen configuration, did not appear to significantly influence the downstream, three-dimensional flow generated by the teardrop body.

C. Wind Tunnel Two-Dimensionality

To further study the two-dimensionality of the tunnel flow, mean velocity and flow angle profiles were taken along three planes: a far field transverse plane located 2.44 m (8 ft) upstream of the test section on 10.16 cm (4 in.) intervals, the tunnel centerline plane on 30.48 cm (12 in.) intervals up to the test section, as well as the plane that extends across the test section on 5.08 to 10.16 cm (2 to 4 in.) intervals. These stations are shown in Fig. 6.5 where the same numbering system that identifies the 3D stations is used to identify these 2D data stations. Figures 6.6 and 6.8 show the spanwise nonuniformities of mean velocity at the upstream and downstream transverse planes. These results indicate that spanwise nonuniformities are increased as the up-

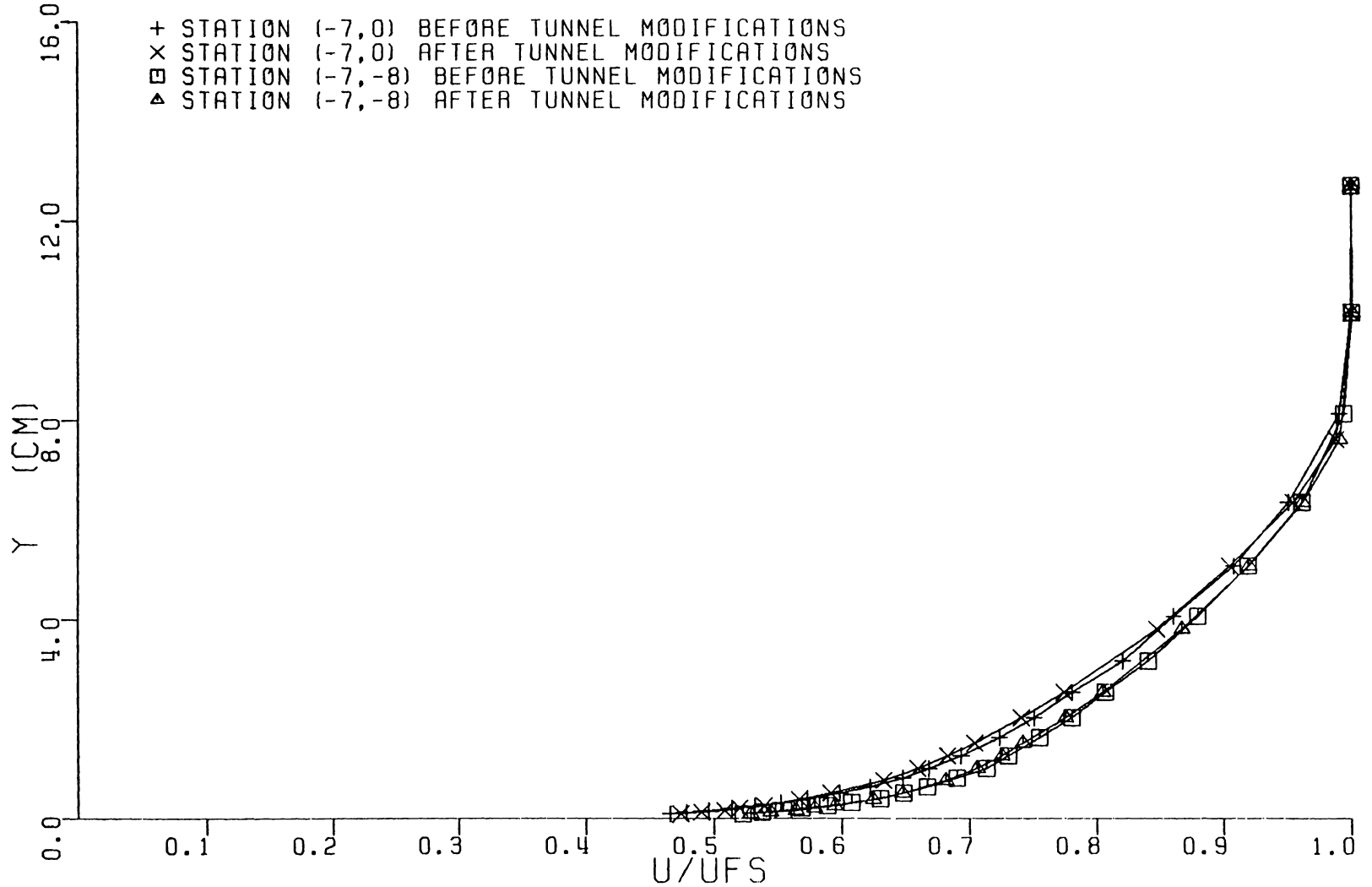

FIGURE 6.4A. EFFECT OF SPANWISE NONUNIFORMITIY ON 3DTBL MEAN FLOW

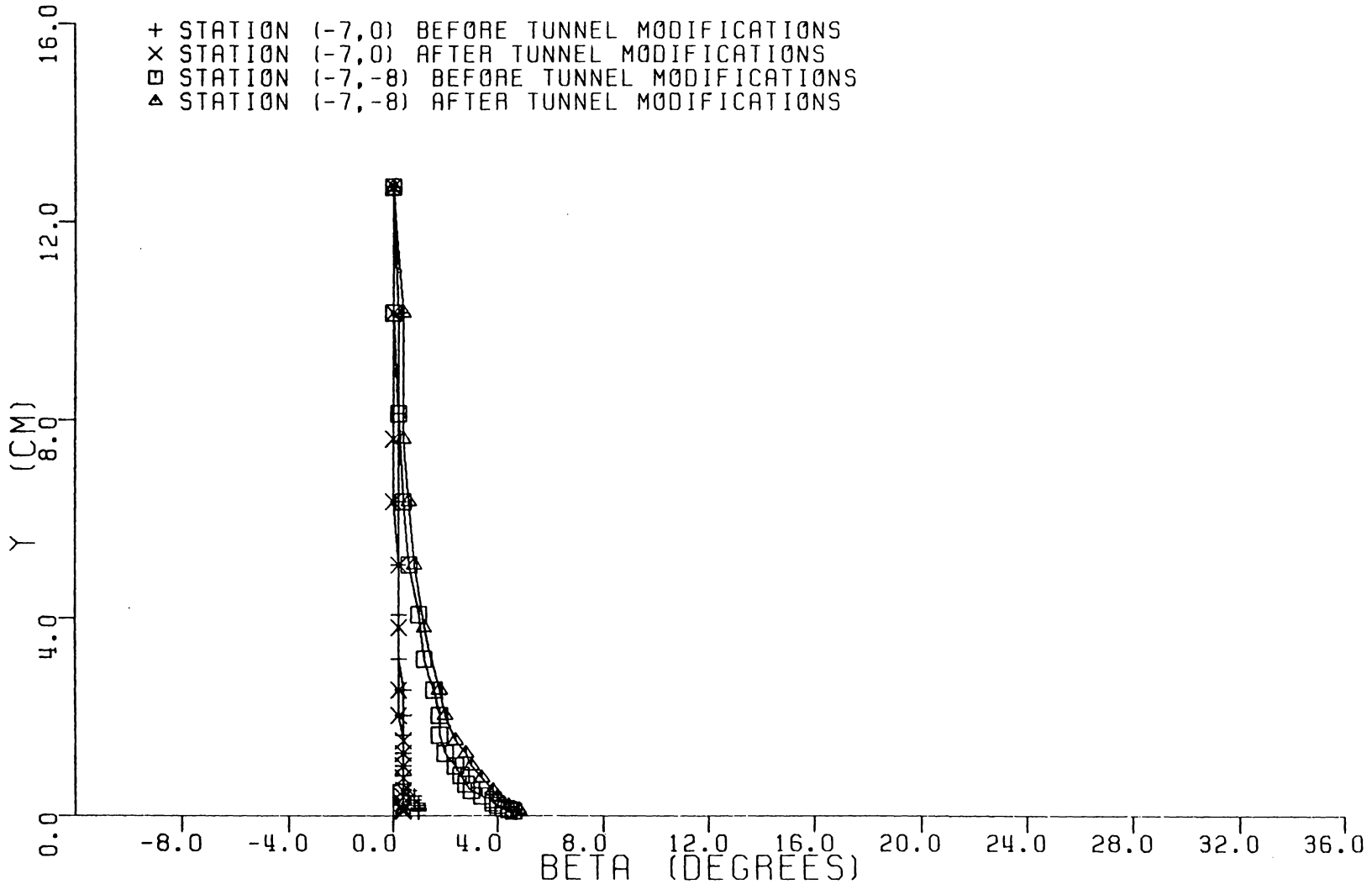

FIGURE 6.4B. EFFECT OF SPANWISE NONUNIFORMITIY ON 3DTBL MEAN FLOW

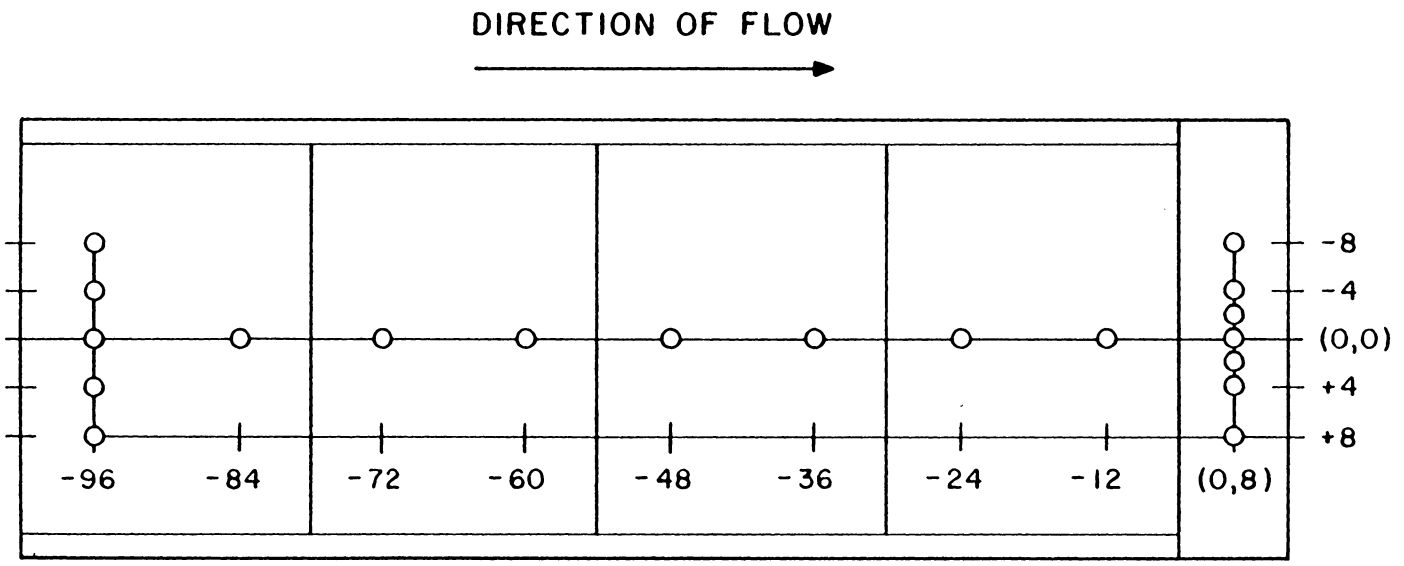

Figure 6.5 Location of Data Stations for the Two-Dimensional Flow Studies

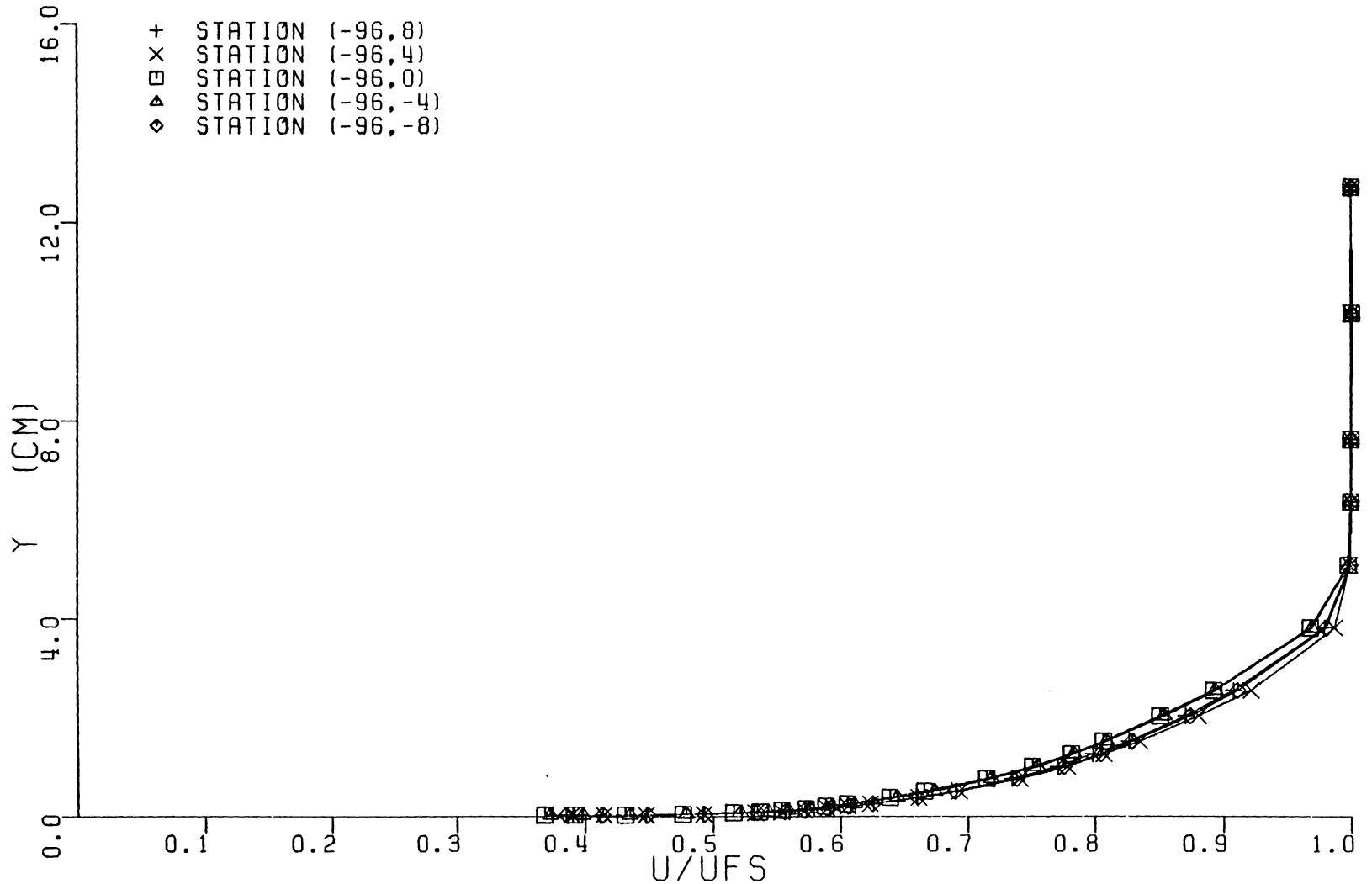

FIGURE 6.6. FAR FIELD SPANWISE NONUNIFORMITY IN MEAN VELOCITY

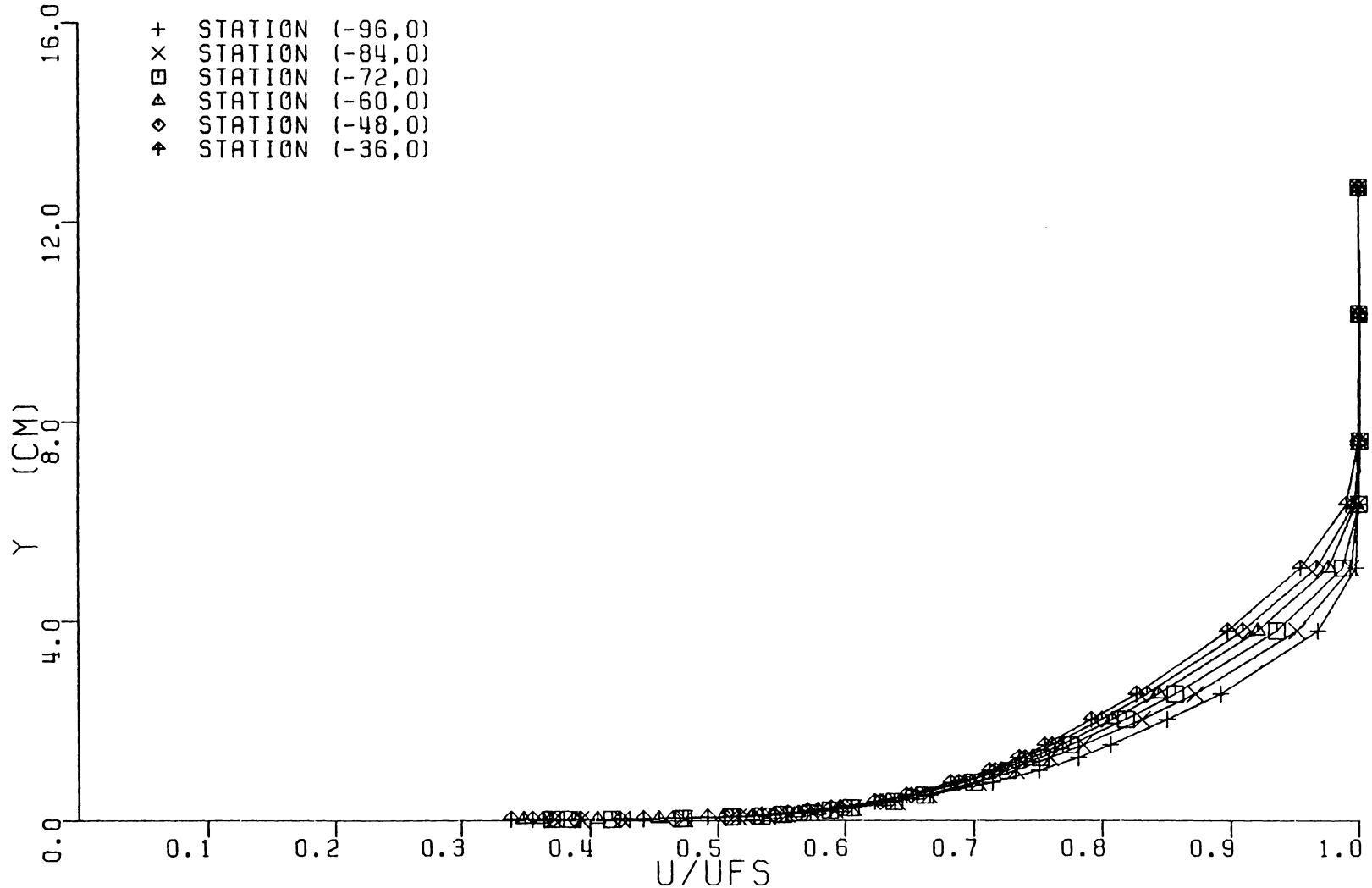

FIGURE 6.7A. TWO-DIMENSIONAL MEAN VELOCITY PROFILES ALONG THE TUNNEL CENTERLINE

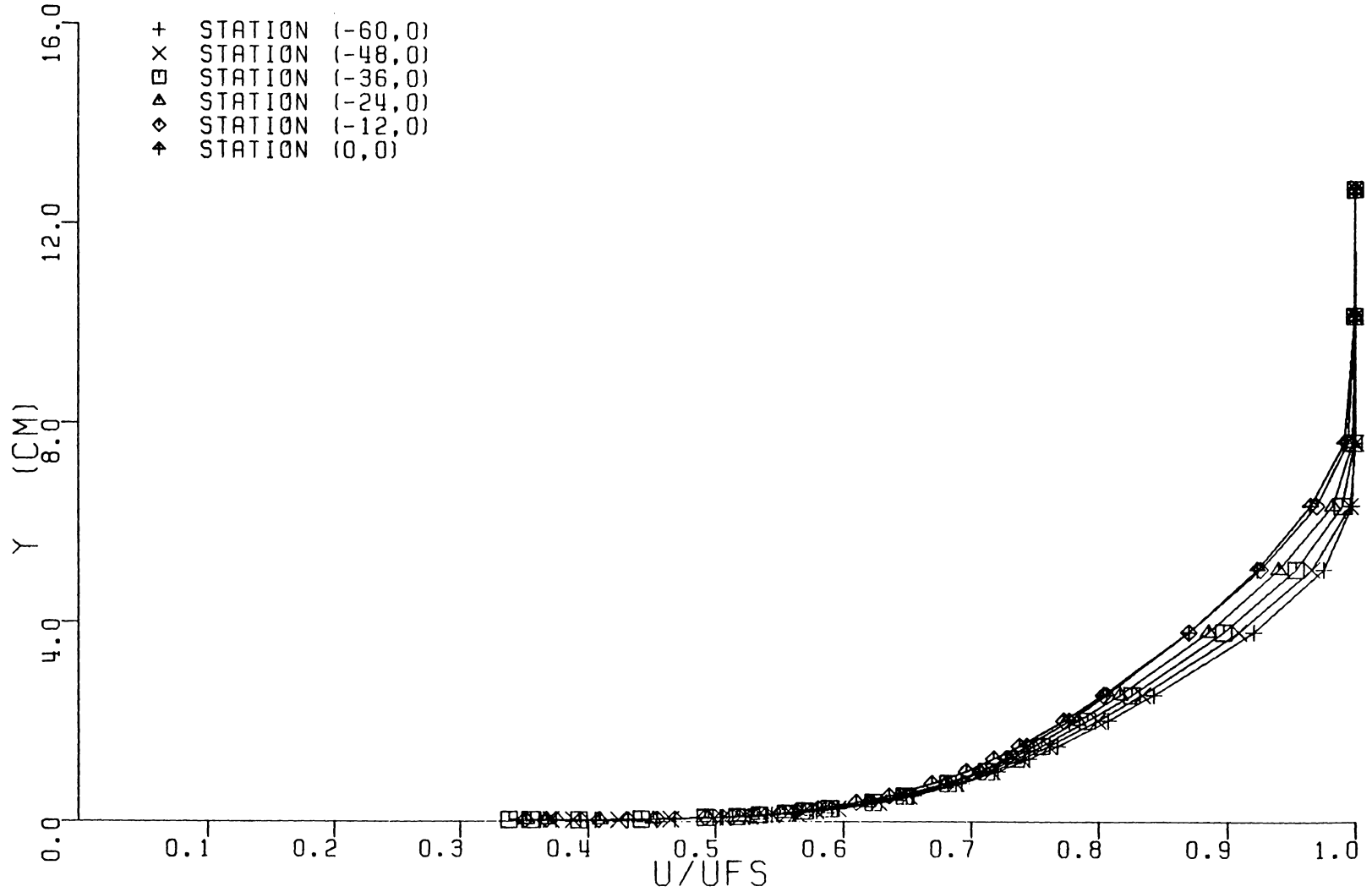

FIGURE 6.7B. TWO-DIMENSIONAL MEAN VELOCITY PROFILES ALONG THE TUNNEL CENTERLINE

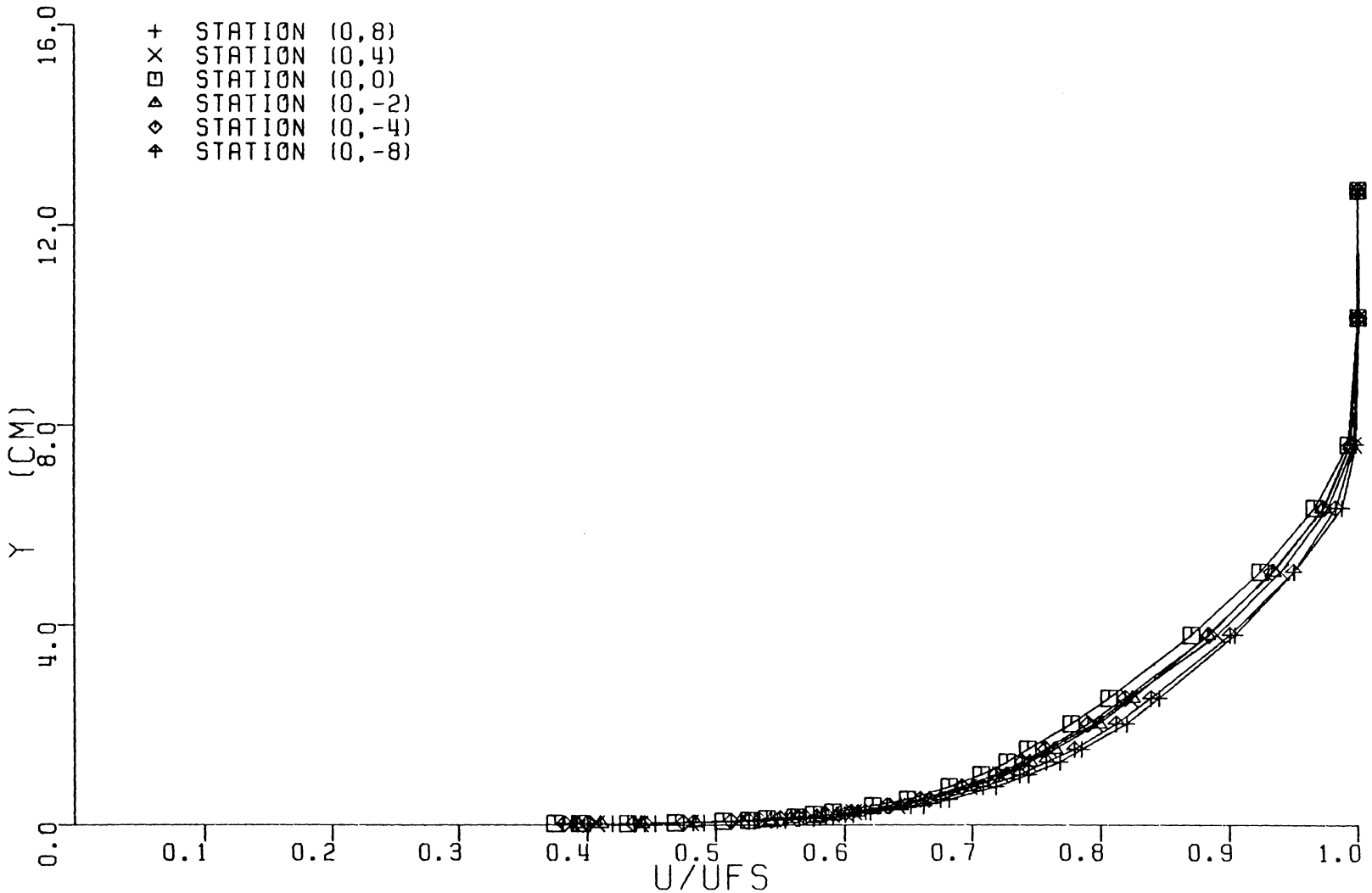

FIGURE 6.8. SPANWISE NONUNIFORMITY IN MEAN VELOCITY ALONG THE TEST SECTION

stream flow progresses to the test section. The 2D near wall similarity plots along these two planes are presented in Figs. 6.9 and 6.11 and the tunnel centerline profiles are shown in Figs. 6.7a and 6.7b with the corresponding similarity plots given in Figs. 6.10a and 6.10b.

The flow conditions and boundary layer parameters for these 2D surveys are listed in Table 6.2. A comparison of the skin friction coefficients is given in Table 6.3 where wall shear values, inferred from the Law of the Wall using the similarity constants of Coles [151], NPL [152], and Patel [153], are compared to the values obtained from the skin friction correlations of Ludwieg and Tillmann, Coles, and White given in White [154]. The results show considerable disagreement in the values of C_f among the various methods themselves although similar trends are found in each of the methods appearing in Table 6.3. Across the upstream and test section planes, the results are consistent in that they indicate a ± 3% spanwise variation in C_f about the mean value with the centerline values typicaly 4-6% lower. These results seem to indicate a defect in streamwise momentum near the wall which appears consistent with the migration of low momentum fluid as would occur with small convergence of the flow. This inflow of low momentum fluid toward the centerline would tend to give higher centerline values of the momentum and displacement thicknesses as is shown in Table 6.2. A small convergence of this tunnel flow was quantified in the following momentum integral study.

As a means of detecting possible 3D behavior of the flow, not apparent in the results presented thus far, a momentum balance was performed. This involved integrating the 2D momentum integral equation

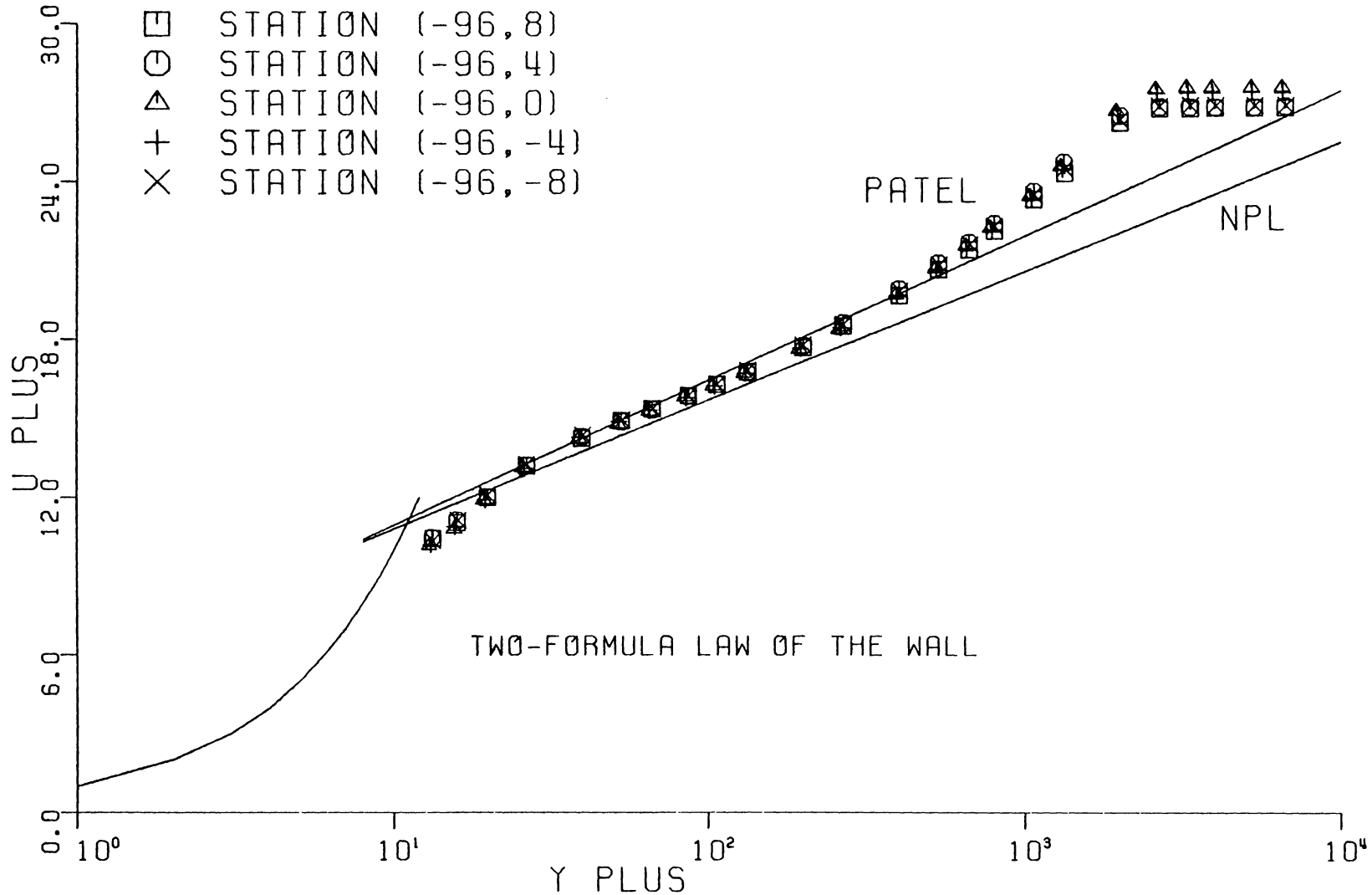

FIGURE 6.9. TWO-DIMENSIONAL SIMILARITY ACROSS THE FAR FIELD PLANE

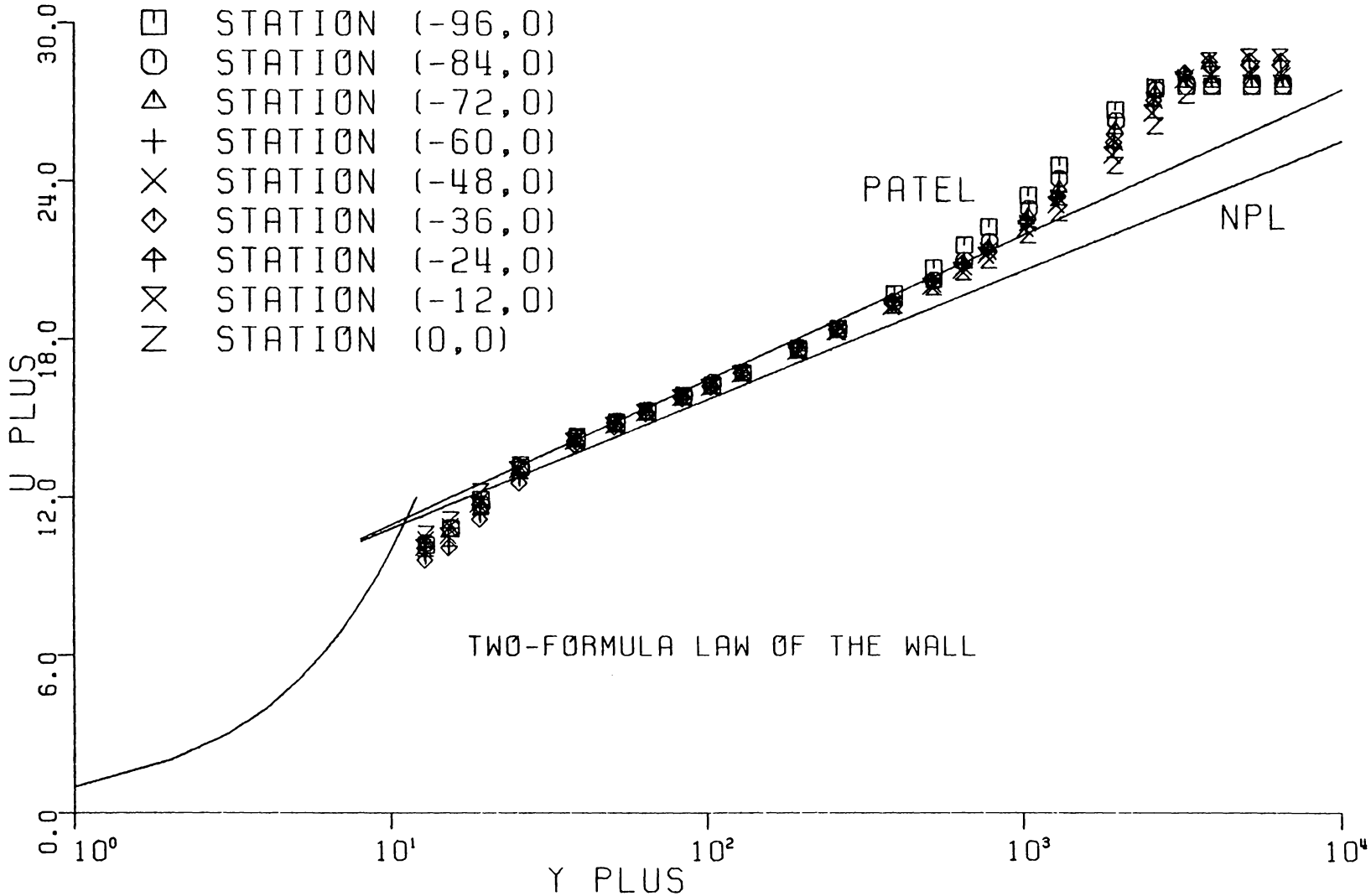

FIGURE 6.10. TWO-DIMENSIONAL SIMILARITY ALONG THE TUNNEL CENTERLINE

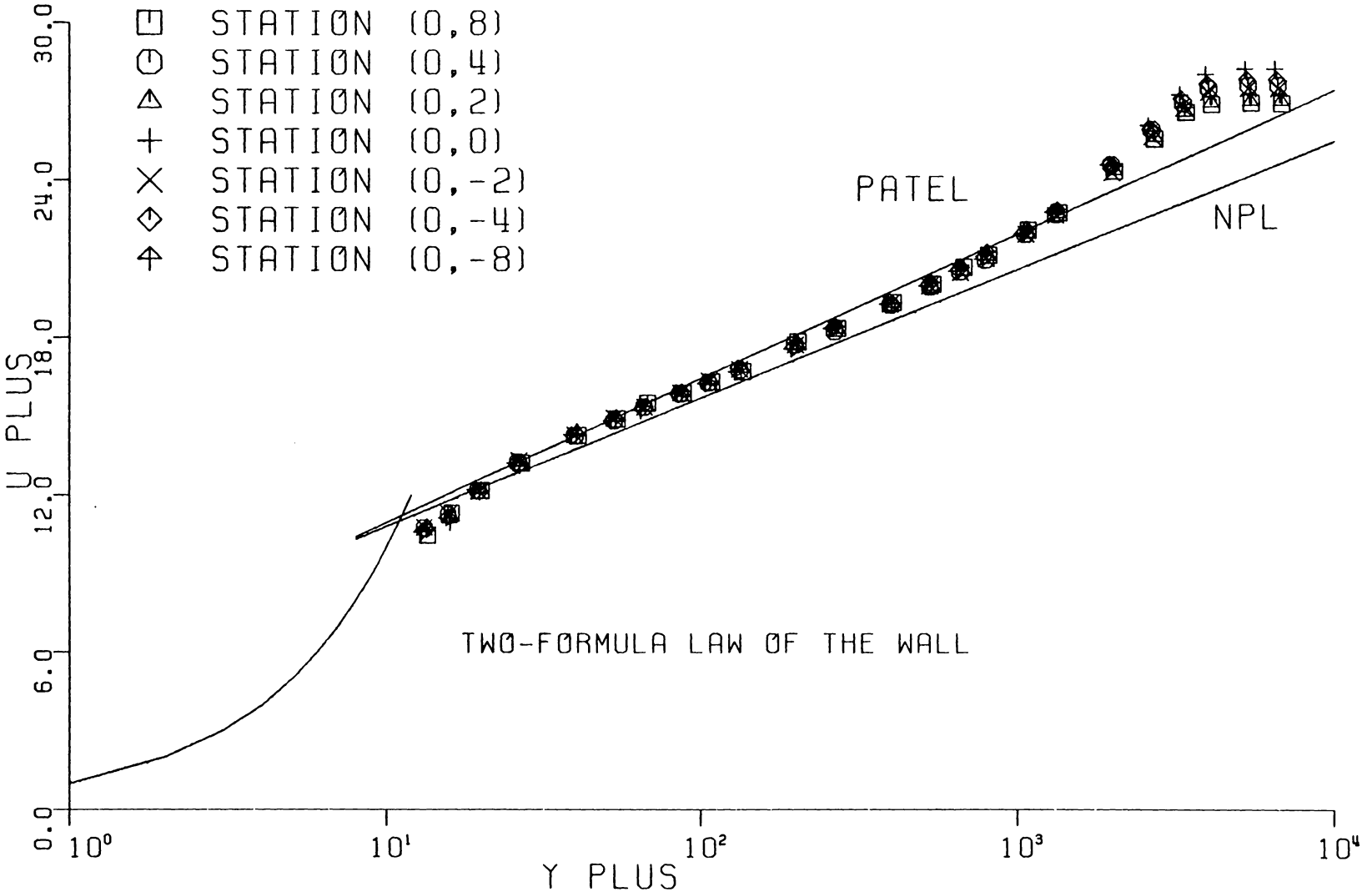

FIGURE 6.11. TWO-DIMENSIONAL SIMILARITY ACROSS THE TEST SECTION PLANE

Table 6.2 Flow Conditions and Boundary Layer Parameters for the Nominally 2D Tunnel Flow Field

Station	Re_{unit}	ν	ρ	$\overline{U}_{FS}$	δ^*	θ
	($m^{-1} \times 10^{-6}$)	($m^2s^{-1} \times 10^5$)	(kgm^{-3})	(ms^{-1})	(cm)	(cm)
			Far Field Plane			
(-96,8)	1.34	1.69	1.09	23.8	0.667	0.493
(-96,4)	1.34	1.69	1.09	22.6	0.632	0.466
(-96,0)	1.34	1.69	1.09	22.7	0.743	0.543
(-96,-4)	1.34	1.67	1.10	23.6	0.728	0.533
(-96,-8)	1.34	1.65	1.11	22.1	0.655	0.484
			Centerline Plane			
(-96,0)	1.34	1.69	1.09	22.7	0.743	0.543
(-84,0)	1.34	1.65	1.11	22.1	0.817	0.598
(-72,0)	1.33	1.68	1.10	23.8	0.873	0.641
(-60,0)	1.34	1.69	1.09	24.1	0.942	0.692
(-48,0)	1.33	1.68	1.10	23.9	0.985	0.725
(-36,0)	1.34	1.69	1.10	24.2	1.05	0.774
(-24,0)	1.34	1.69	1.10	24.3	1.11	0.822
(-12,0)	1.34	1.67	1.10	24.0	1.21	0.893
(0,0)	1.34	1.67	1.10	24.1	1.20	0.898
			Test Section Plane			
(0,8)	1.34	1.67	1.10	24.1	0.960	0.734
(0,4)	1.34	1.67	1.10	24.1	1.08	0.816
(0,2)	1.34	1.68	1.10	24.1	0.979	0.747
(0,0)	1.34	1.67	1.10	24.1	1.20	0.898
(0,-2)	1.34	1.67	1.10	24.2	1.10	0.834
(0,-4)	1.34	1.67	1.10	24.1	1.12	0.844
(0,-8)	1.34	1.67	1.10	24.0	1.00	0.762

Table 6.3 Comparison of Skin Friction Distribution for the Tunnel Flow; $C_f = 2\tau_w/\rho \bar{U}_{FS}^2 \times 10^3$

Station	Spalding Formula[1]	Spalding Formula[2]	Spalding Formula[3]	Ludwieg-Tillmann[4]	White[5]	Coles[6]
			Far Field Plane			
(-96,8)	2.78	2.82	3.02	2.79	2.56	2.72
(-96,4)	2.77	2.81	3.01	2.81	2.57	2.74
(-96,0)	2.62	2.66	2.84	2.65	2.42	2.58
(-96,-4)	2.66	2.70	2.89	2.67	2.45	2.61
(-96,-8)	2.77	2.81	3.00	2.80	2.56	2.73
			Centerline Plane			
(-96,0)	2.62	2.66	2.84	2.65	2.42	2.58
(-84,0)	2.63	2.67	2.85	2.59	2.38	2.53
(-72,0)	2.61	2.65	2.83	2.55	2.35	2.50
(-60,0)	2.54	2.58	2.75	2.50	2.31	2.46
(-48,0)	2.53	2.57	2.75	2.48	2.30	2.44
(-36,0)	2.48	2.51	2.68	2.44	2.26	2.41
(-24,0)	2.46	2.50	2.66	2.42	2.25	2.40
(-12,0)	2.42	2.46	2.62	2.36	2.21	2.35
(0,0)	2.50	2.54	2.71	2.42	2.27	2.42
			Test Section Plane			
(0,8)	2.75	2.79	2.98	2.66	2.50	2.66
(0,4)	2.61	2.65	2.83	2.52	2.37	2.52
(0,2)	2.73	2.77	2.96	2.64	2.48	2.63
(0,0)	2.50	2.54	2.71	2.42	2.27	2.42
(0,-2)	2.64	2.68	2.87	2.55	2.40	2.55
(0,-4)	2.58	2.62	2.80	2.50	2.34	2.49
(0,-8)	2.69	2.73	2.92	2.62	2.45	2.61

[1] Third order Formula using Patel's Constants, (K,C) = (0.42, 5.45)

[2] Third order Formula using Coles Constants; (K,C) = (0.41, 5.0)

[3] Third order Formula using NPL Staff Constants, (K,C) = (0.47, 5.45)

[4] $C_f = 0.246\ Re_\theta^{-0.268} \times 10^{-0.678H}$ [104]

[5] $C_f = 0.228\ e^{-1.37H} \times \log (Re_\theta)^{-(1.753 + 0.283H)}$ [104]

[6] $C_f = 0.3\ e^{-1.33H} \times \log (Re_\theta)^{-(1.74 + 0.31H)}$ [104]

along a streamwise plane and comparing the left-hand side of the equation (PL) with the right-hand side (PR). This 2D PL-PR method was used at the Stanford Conference in 1968 to determine the quality of the numerous 2D candidate flows. Fitts [155] performed a PL-PR balance on this 2D flow for the centerline stations shown in Fig. 6.5. These results are presented in Table 6.4 which compare PR values calculated from the skin friction coefficients inferred from the different pairs of the law of the wall constants. Figure 6.12 shows the PL and PR_3 balance as an assessment of two-dimensionality of the tunnel flow. Irrespective of the small differences found in the PR values of Table 6.4, all the results are consistent in that they indicate slight deviations from a purely two-dimensional flow. The differences are of the order of magnitude quantified by de Brederode and Bradshaw [144] as not sufficiently large to identify with tunnel sidewall interference. That small amounts of three-dimensionality may exist even in the most carefully controlled two-dimensional flow is not surprising in view of the difficulties involved in constructing such an ideal flow situation. Several other investigations [144-146] have reported similar deviations from a nominally 2DTBL flow.

From the standpoint of the standard test case, it was desirable to quantify the amount of secondary flow that might exist in this flow field. Assuming a center-plane of symmetry, the flow was examined by Fitts [155] for the case of a: a) collateral converging/diverging, and b) skewed converging/diverging flow along the centerline. For any plane of symmetry flow, it is convenient to express the momentum integral equation in curvilinear coordinates. According to Pierce [156],

Table 6.4 PL and PR for Centerline Two-Dimensional Flow: A Comparison Using Friction Velocities Inferred from Different Law of the Wall Constants

Station	x, in.	PL	PR_1	PR_2	PR_3	ΔPL	ΔPR_1	ΔPR_2	ΔPR_3
(0,0)	0	0.0	0.0	0.0	0.0				
						0.111	0.080	0.075	0.074
(-12,0)	12	0.111	0.080	0.075	0.074				
						0.091	0.080	0.075	0.074
(-24,0)	24	0.202	0.160	0.150	0.148				
						0.106	0.080	0.074	0.073
(-36,0)	36	0.308	0.240	0.225	0.221				
						0.074	0.079	0.074	0.073
(-48,0)	48	0.382	0.319	0.298	0.294				
						0.106	0.078	0.073	0.072
(-60,0)	60	0.489	0.397	0.372	0.366				
						0.107	0.077	0.072	0.071
(-72,0)	72	0.595	0.474	0.444	0.438				
						0.150	0.077	0.072	0.071
(-84,0)	84	0.745	0.551	0.516	0.508				
						0.025	0.078	0.073	0.072
(-96,0)	96	0.770	0.629	0.589	0.580				

1 - Coles (151) Constants

2 - NPL Staff (152) Constants

3 - Patel (153) Constants

Conversion factor

1 in. = 2.54 cm

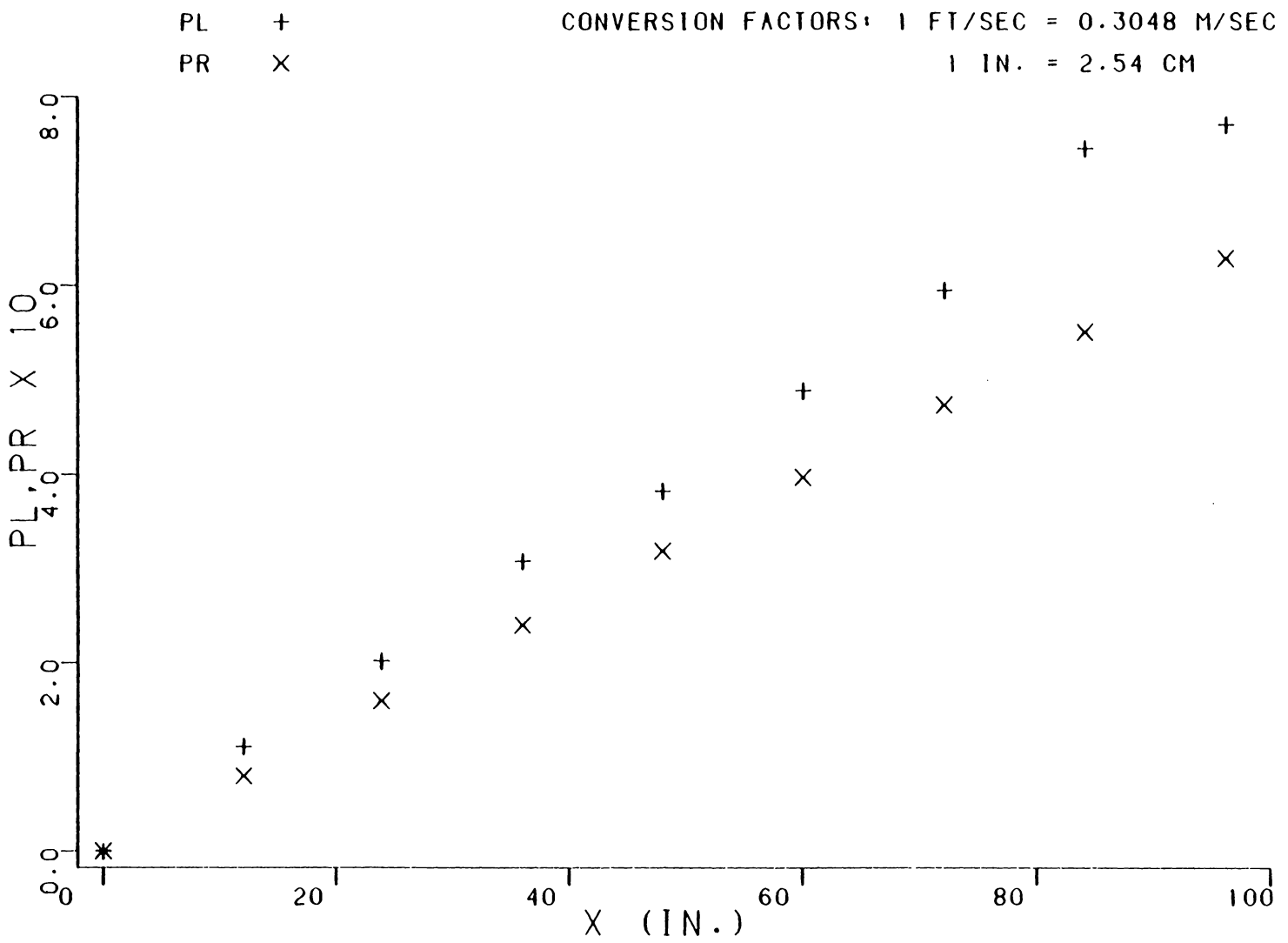

Figure 6.12 Momentum Balance for the Upstream, Nominally Two-Dimensional Flow Along the Tunnel Centerline

$$\frac{\partial \theta_\xi}{\partial \xi} + \frac{(2\theta_\xi + \delta_\xi^*)}{Q}\frac{\partial Q}{\partial \xi} + \frac{1}{h_3}\frac{\partial \theta_{\xi\zeta}}{\partial \zeta} + \frac{\theta_\xi}{h_3}\frac{\partial \omega}{\partial \zeta} = \frac{\tau_{o_x}}{\rho Q^2} \qquad (6.1)$$

where θ_ξ, δ_ξ^*, and $\theta_{\xi\zeta}$ are the boundary layer parameters and h_3 is the metric in the transverse direction for the curvilinear set. The angle ω is the angle between the freestream direction and the x_1 direction. On the plane of symmetry $\delta_\xi^* = \delta_1$, $\theta_\xi = \theta_{11}$ and $\frac{\partial}{\partial \xi} = \frac{\partial}{\partial x}$. The third and fourth terms in Eq. 6.1 are additional to the two-dimensional momentum integral equation. The term $\frac{1}{h_3}\frac{\partial \theta_{\xi\zeta}}{\partial \zeta}$ is a result of skewing of the boundary layer and the term $\frac{\theta_\xi}{h_3}\frac{\partial \omega}{\partial \zeta}$ is associated with the spreading of the freestream streamlines. For collateral flow the former term vanishes and the latter term alone results from any small amounts of three-dimensionality along the tunnel centerline.

Fitts [155] tested a variety of cases of possible converging/diverging of the freestream streamlines for both collateral and skewed plane of symmetry flows and concluded:

i) the dominant effect was a result of slight convergence of the freestream streamlines rather than skewing of the velocity profiles, and

ii) the momentum integral balance is very sensitive to small amounts of three-dimensionality in a nominally two-dimensional flow.

Assuming a collateral plane of symmetry flow, Fitts determined the rate, $\frac{\partial \omega}{\partial z}$, of convergence ($\frac{\partial \omega}{\partial z} < 0$) or divergence ($\frac{\partial \omega}{\partial z} > 0$) present at each interval along the centerline. These results, shown in Table 6.5, indicate both a converging and diverging behavior at the center plane,

Table 6.5 Average Convergence/Divergence for Assumed Collateral Plane of Symmetry Flow

$x_i - x_{i+1}$, in.	$\frac{\partial \omega}{\partial z}$, $\frac{\text{deg.}}{\text{in.}}$
0 - 12	- 1/7.1
12 - 24	- 1/23
24 - 36	- 1/9.8
36 - 48	1/58
48 - 60	- 1/11
60 - 72	- 1/11
72 - 84	- 1/4.7
84 - 96	1/6.8

Conversion factor

1 in. = 2.54 cm

tending more towards convergence. An overall best PL-PR balance of this flow was repeated assuming a constant freestream convergence of 0.33 deg/mm (1/12 deg/in.) at each measurement station. This assumed convergence is quantified in the results of Table 6.6 and Fig. 6.13 which shows excellent PL-PR agreement for an assumed convergence rate of only $1/12^{o}$ per inch in the transverse direction. This assumed small amount of convergence was too small to verify by measurement but in effect, could be seen in the behavior of C_f, δ^*, and θ along the upstream and test section planes as noted earlier.

The small amount of convergence assumed present along the tunnel centerline could be identified with the tunnel side-wall boundary layers. To some extent this slight convergence is the price paid for having a 10.16-12.70 cm (4-5 in.) thick boundary layer in the test section and an acceptable trade off considering the advantages in measuring in such a thick layer. It was judged that these small amounts of convergence in the flow are not a significant deviation for a nominally 2D flow condition.

Table 6.6 PL and PR for the Upstream Assumed Collateral Plane of Symmetry Flow. Assumes Freestream Convergence = 1/12 deg./in.

Station	PL	PR
(0,0)	0.0	0.0
(-12,0)	0.093	0.080
(-24,0)	0.164	0.160
(-36,0)	0.248	0.240
(-48,0)	0.299	0.319
(-60,0)	0.380	0.397
(-72,0)	0.461	0.474
(-84,0)	0.582	0.551
(-96,0)	0.577	0.629

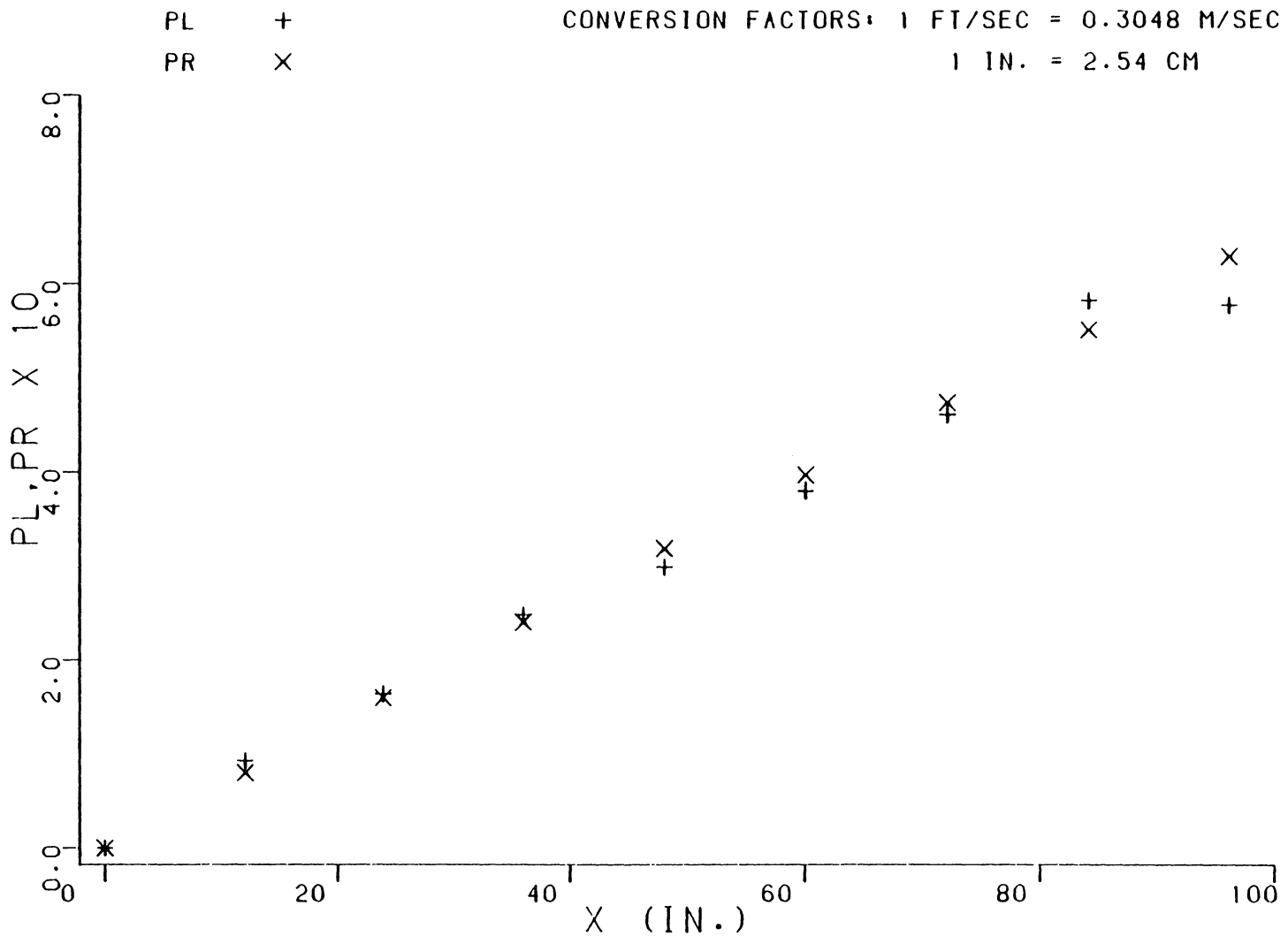

Figure 6.13 PL-PR Momentum Balance for the Upstream, Nominally Two-Dimensional Flow Assuming a Collateral Plane of Symmetry Flow with a 1/12 deg/in. Freestream Convergence

VII. STANDARD TEST CASE RESULTS AND DISCUSSIONS

A. Mean Velocity Field

The mean velocity profiles of the standard test case 3DTBL flow are presented in Figs. 7.1-7.17. These results consist of profiles of the three mean velocity components in the laboratory $x_1x_2x_3$ coordinate system, nondimensionalized by the local freestream velocity, and the usual polar plots of the mean velocity field.

The $\overline{U}_1$ and $\overline{U}_3$ profiles in Figs. 7.1-7.6 are presented on the six planes depicted in Figs. 3.8 and 3.9: the initial condition plane, the plane of symmetry, the two longitudinal planes, ($x_3 = -6$ and $x_3 = -8$), located 15.24 and 20.32 cm (6 and 8 in.) from the plane of symmetry, and the two transverse planes, ($x_1 = -3$ and $x_1 = -7$), located 7.62 and 17.78 cm (3 and 7 in.) forward the body's leading edge. The mean velocity measurements of magnitude $\overline{U}$ and direction β relative to the local freestream direction were made in the sensor xyz coordinate system (see Fig. 3.3) with the single film probe and were transformed to give the $\overline{U}_1$ and $\overline{U}_3$ components in the laboratory coordinate system. The results are tabulated in Appendix F with the tunnel operating conditions and fluid properties listed as well. None of the velocities given in Appendix F have been corrected for turbulence effects. The velocities corrected for turbulence are tabulated with the Reynolds stress results in Appendix G.

The mean velocity profiles along the initial condition plane are shown in Fig. 7.1. Transverse variations in mean velocity of 4-6% are shown which were of the order of magnitude measured along the test sec-

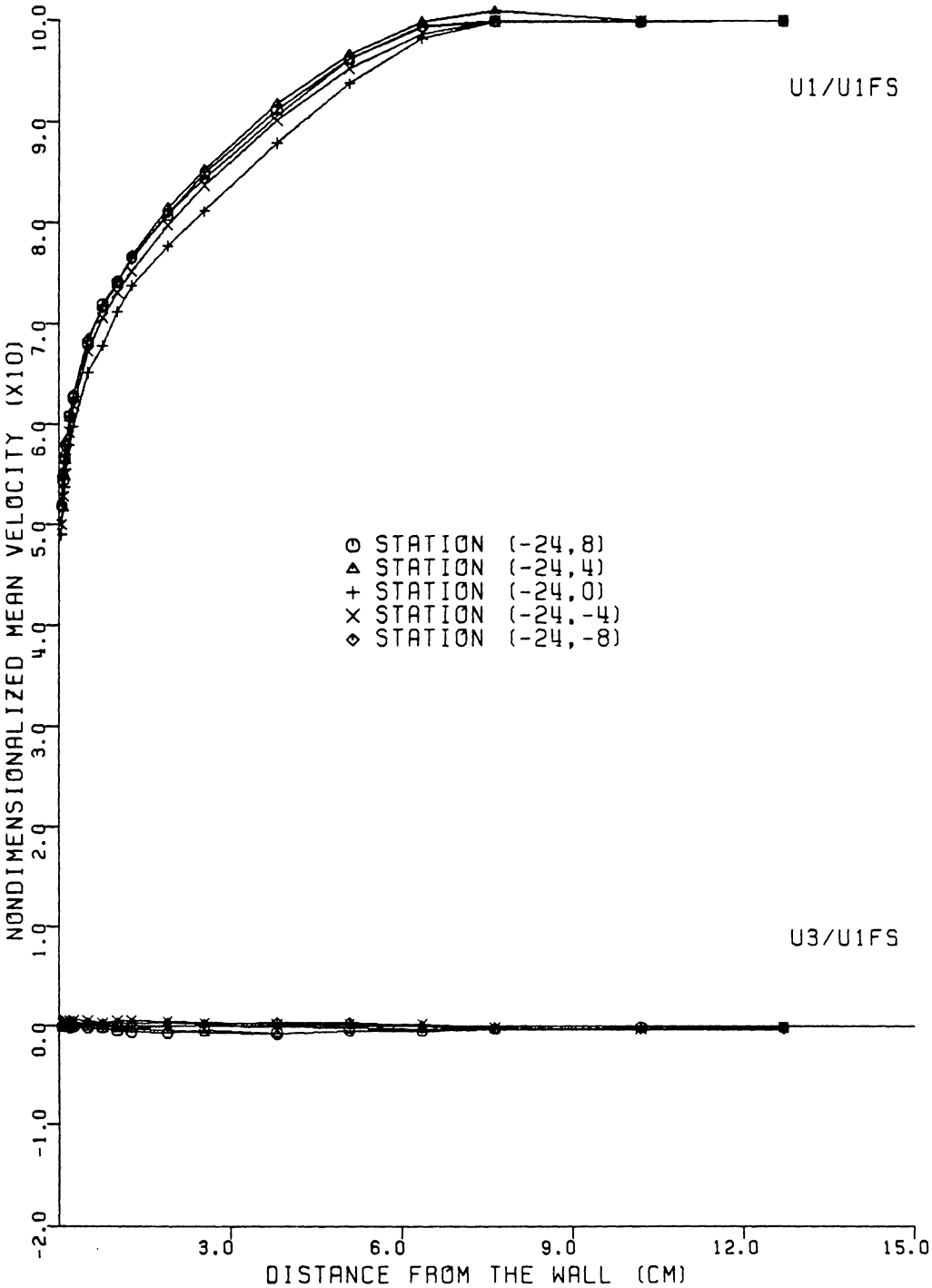

FIGURE 7.1. MEAN VELOCITY PROFILES ALONG THE INITIAL CONDITION PLANE

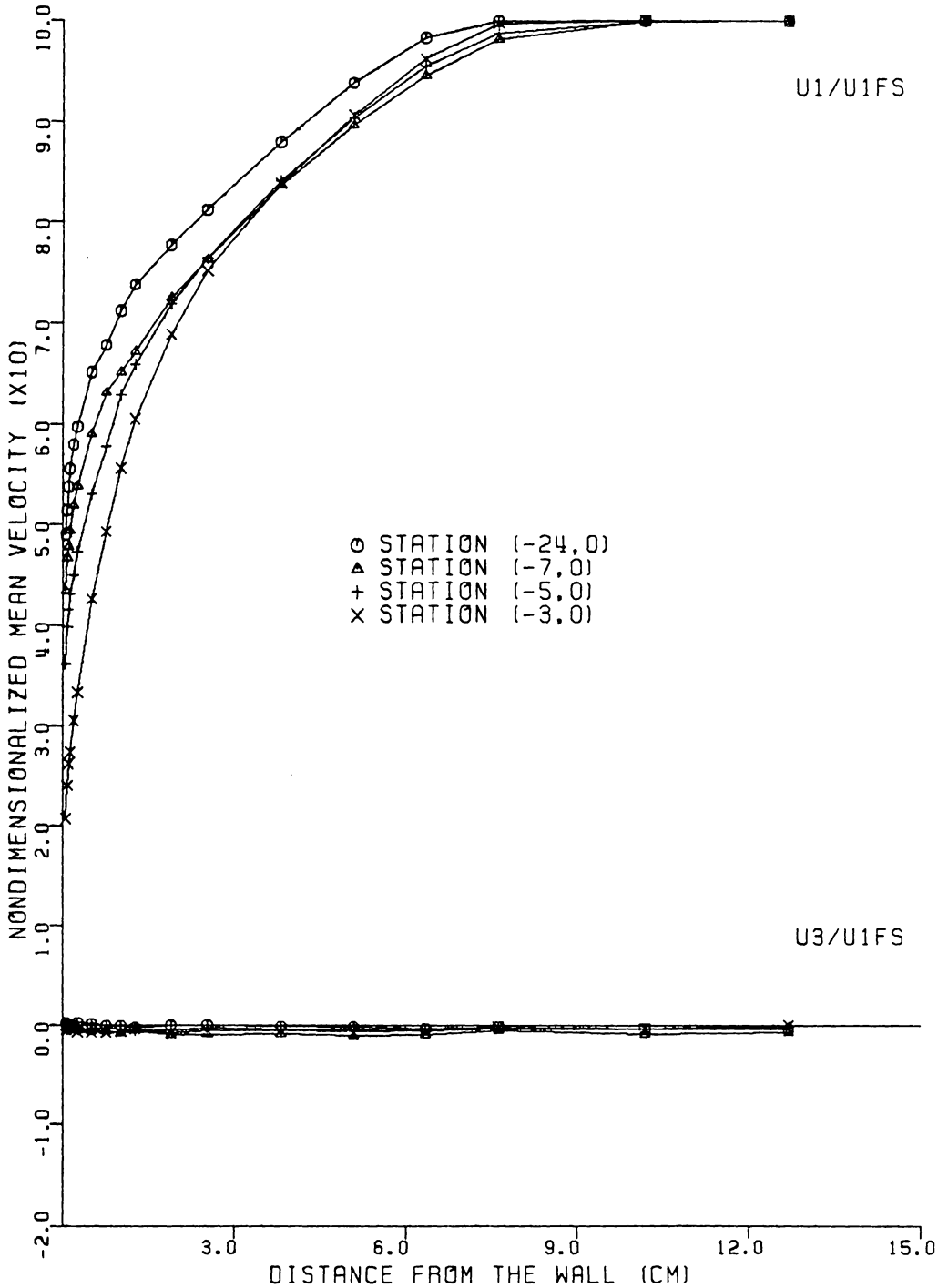

FIGURE 7.2. MEAN VELOCITY PROFILES ALONG THE PLANE OF SYMMETRY

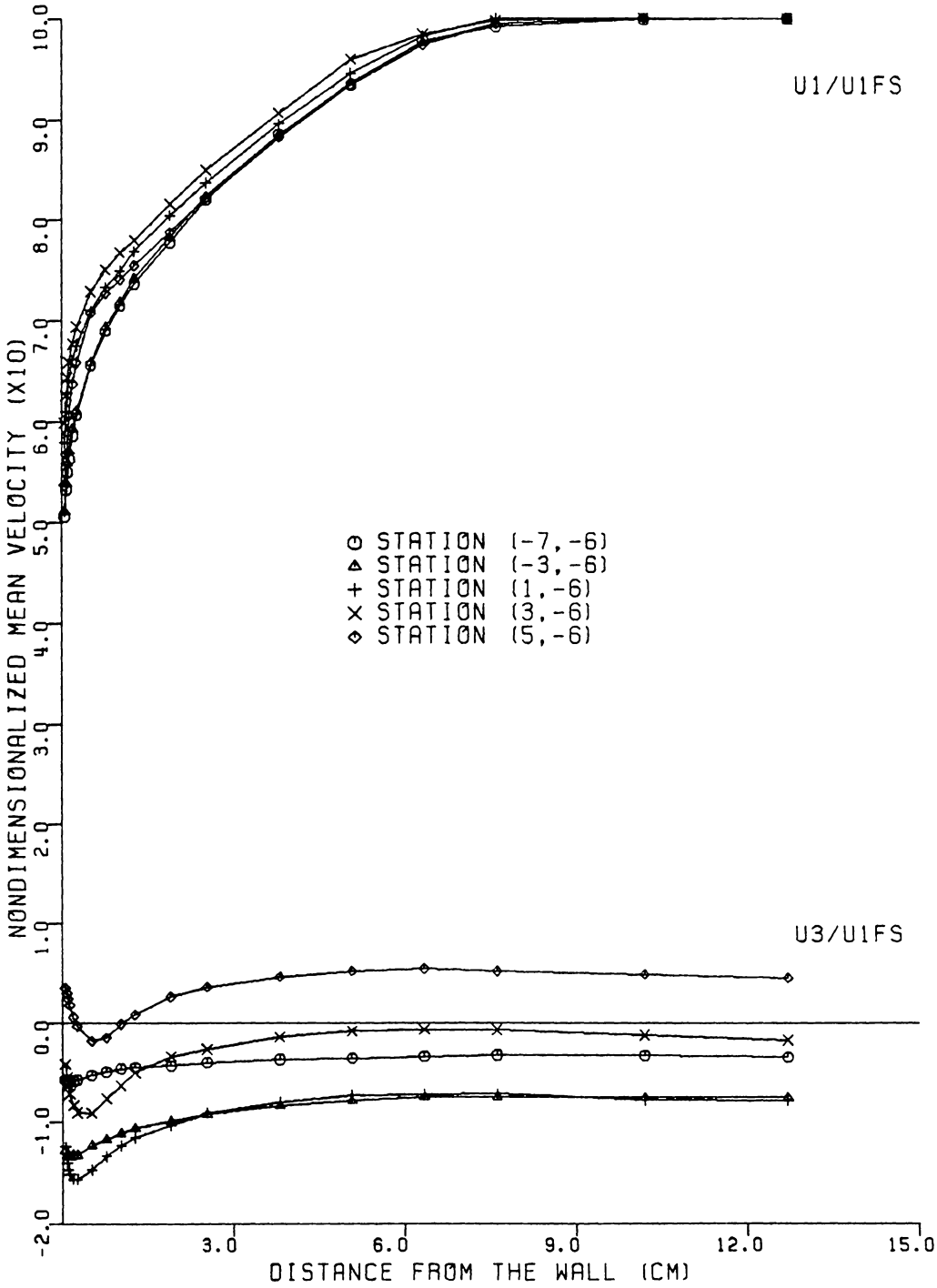

FIGURE 7.3. MEAN VELOCITY PROFILES ALONG THE PLANE X3=-6

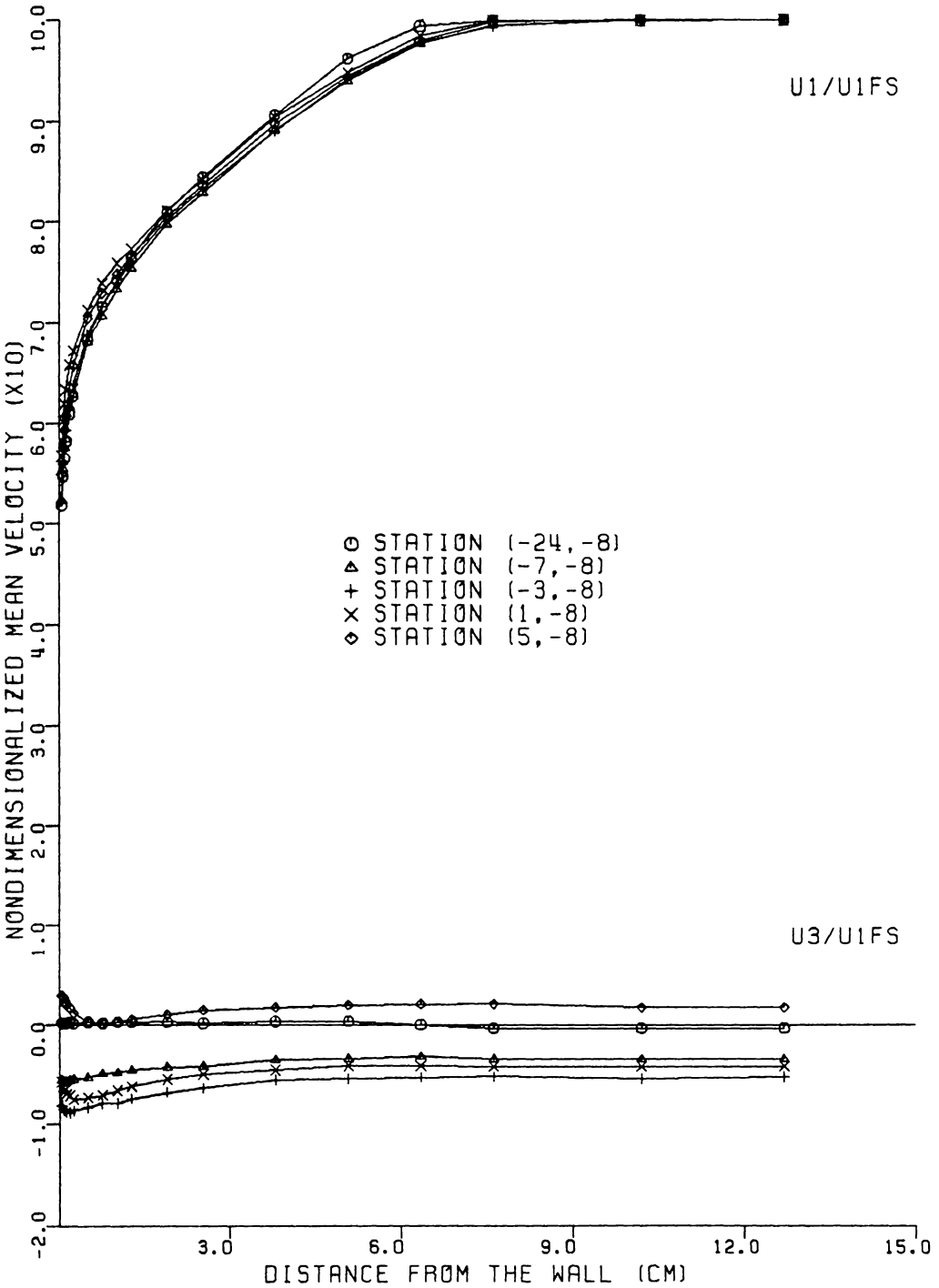

FIGURE 7.4. MEAN VELOCITY PROFILES ALONG THE PLANE X3=-8

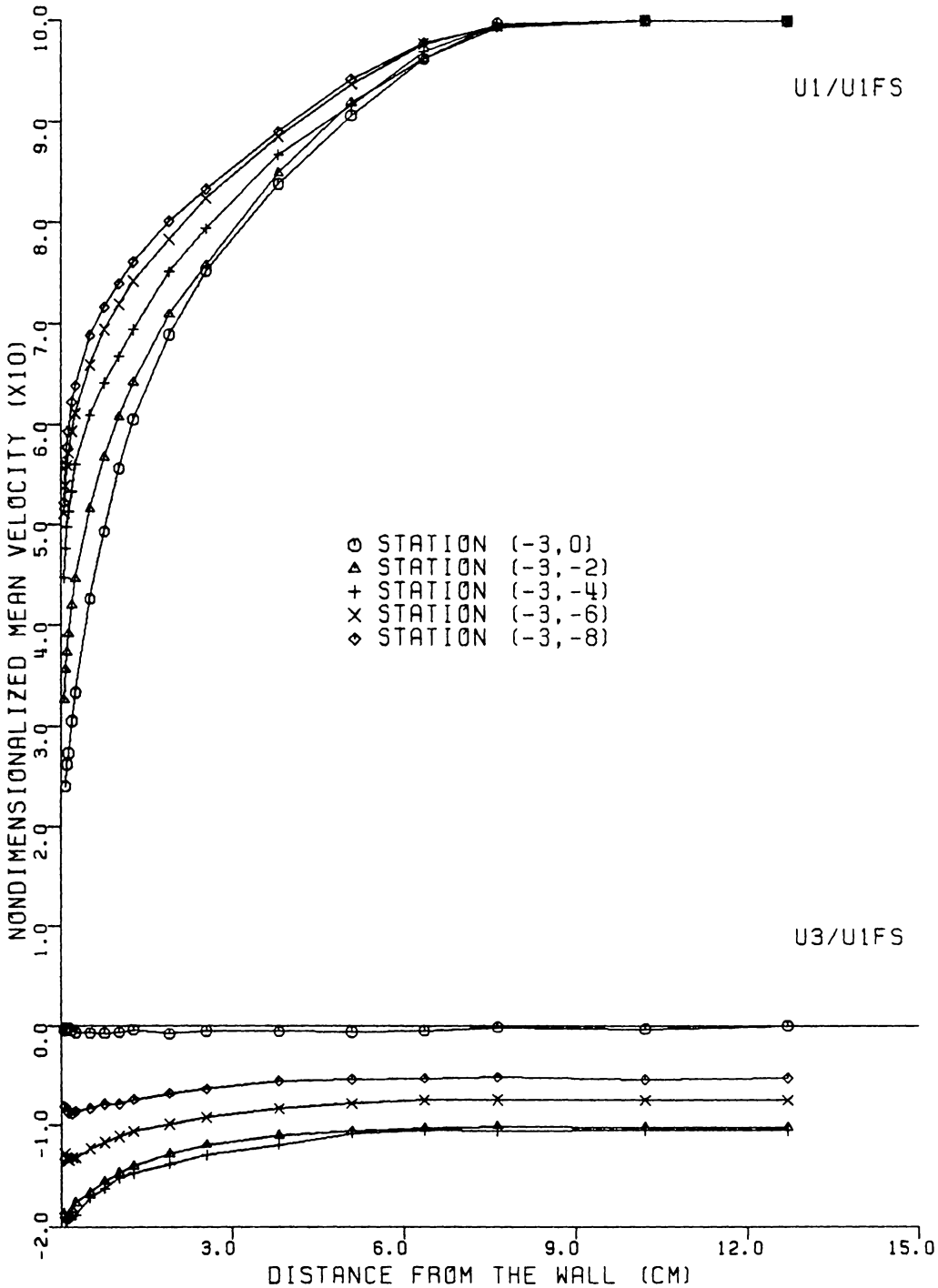

FIGURE 7.5. MEAN VELOCITY PROFILES ALONG THE PLANE X1=-3
STATION (-3,0)

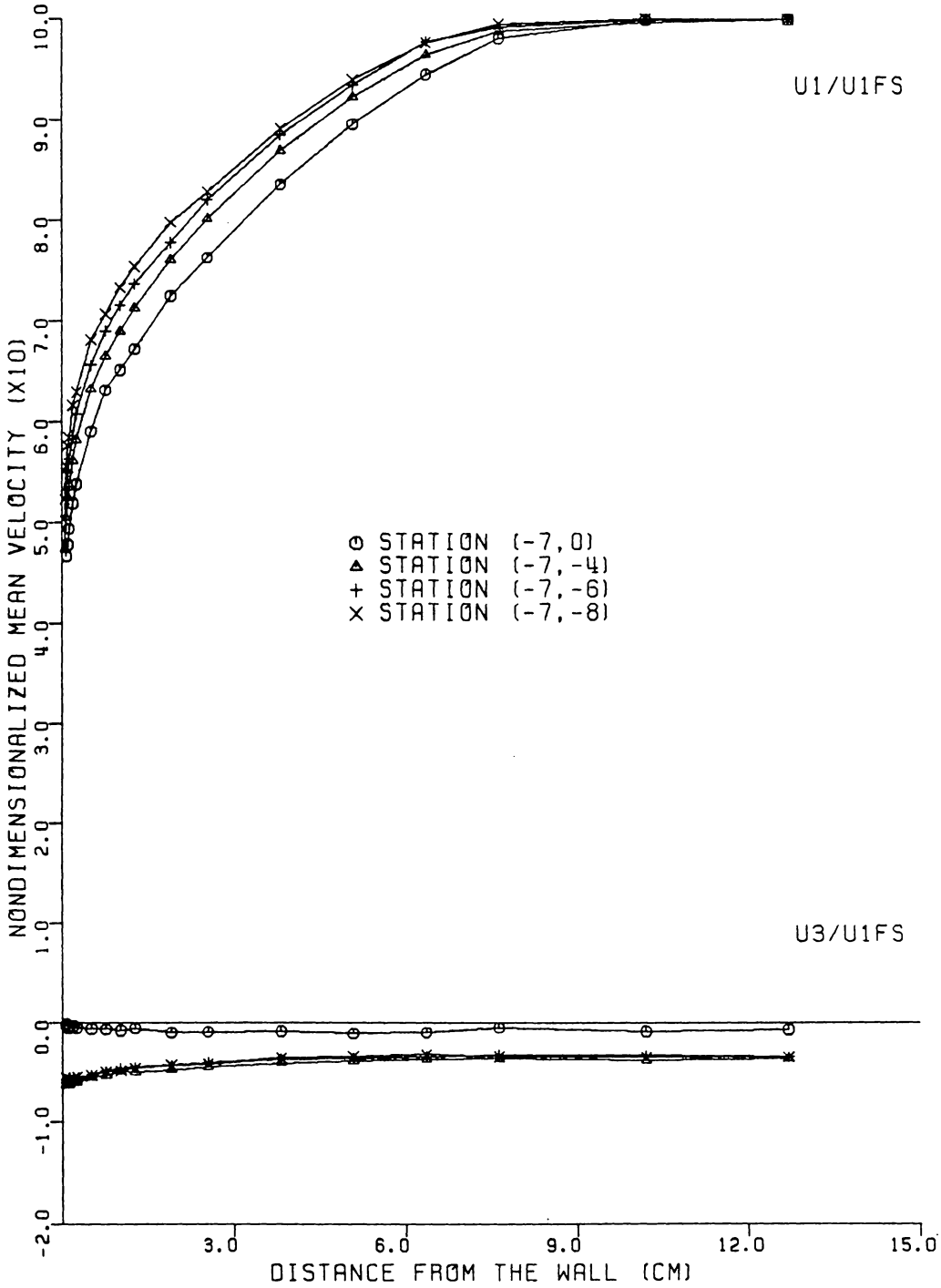

FIGURE 7.6. MEAN VELOCITY PROFILES ALONG THE PLANE X1=-7
STATION (-7,0)

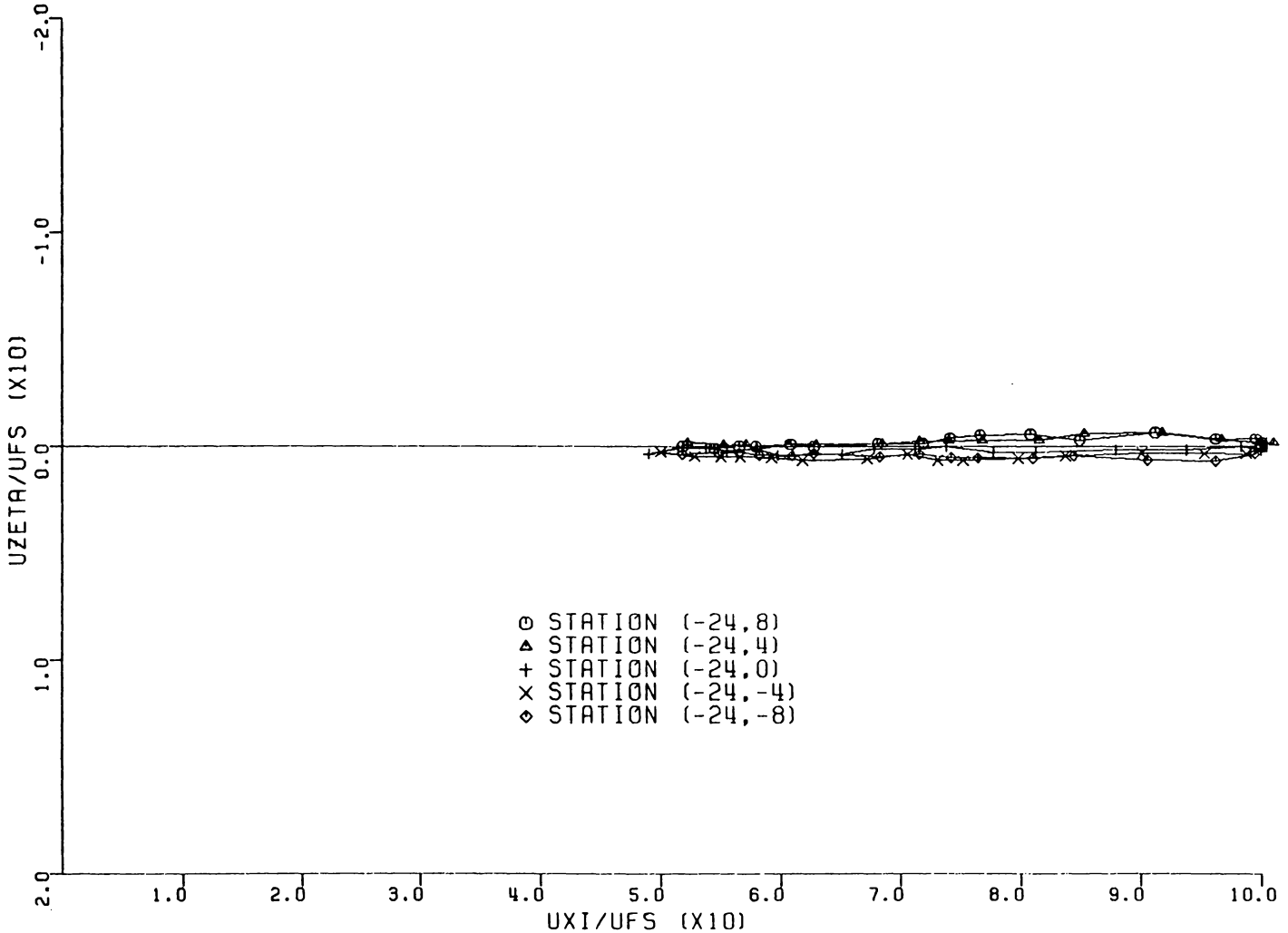

FIGURE 7.7. POLAR PLOT OF THE PROFILES ALONG THE INITIAL CONDITION PLANE

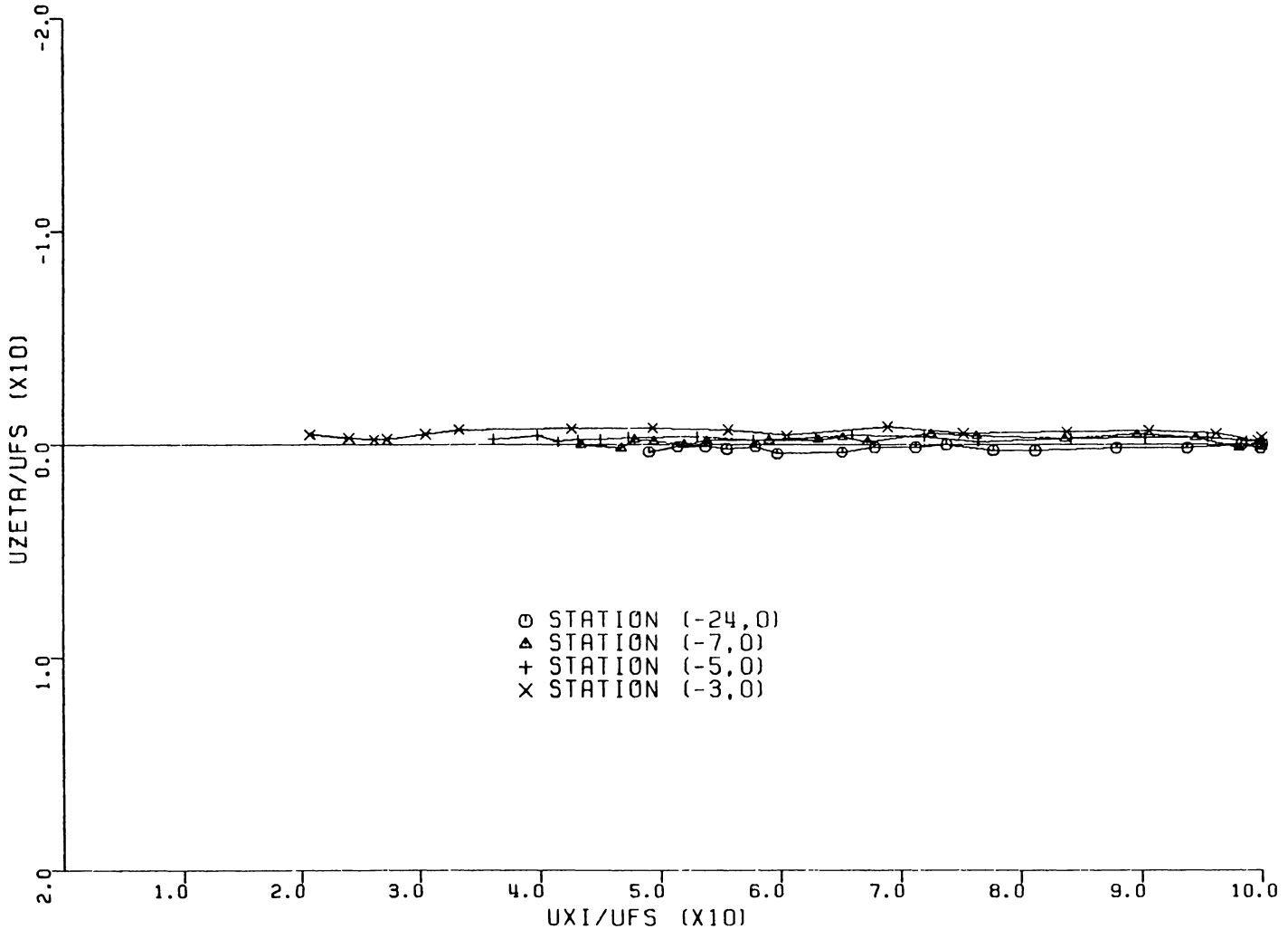

FIGURE 7.8. POLAR PLOT OF THE PROFILES ALONG THE PLANE OF SYMMETRY

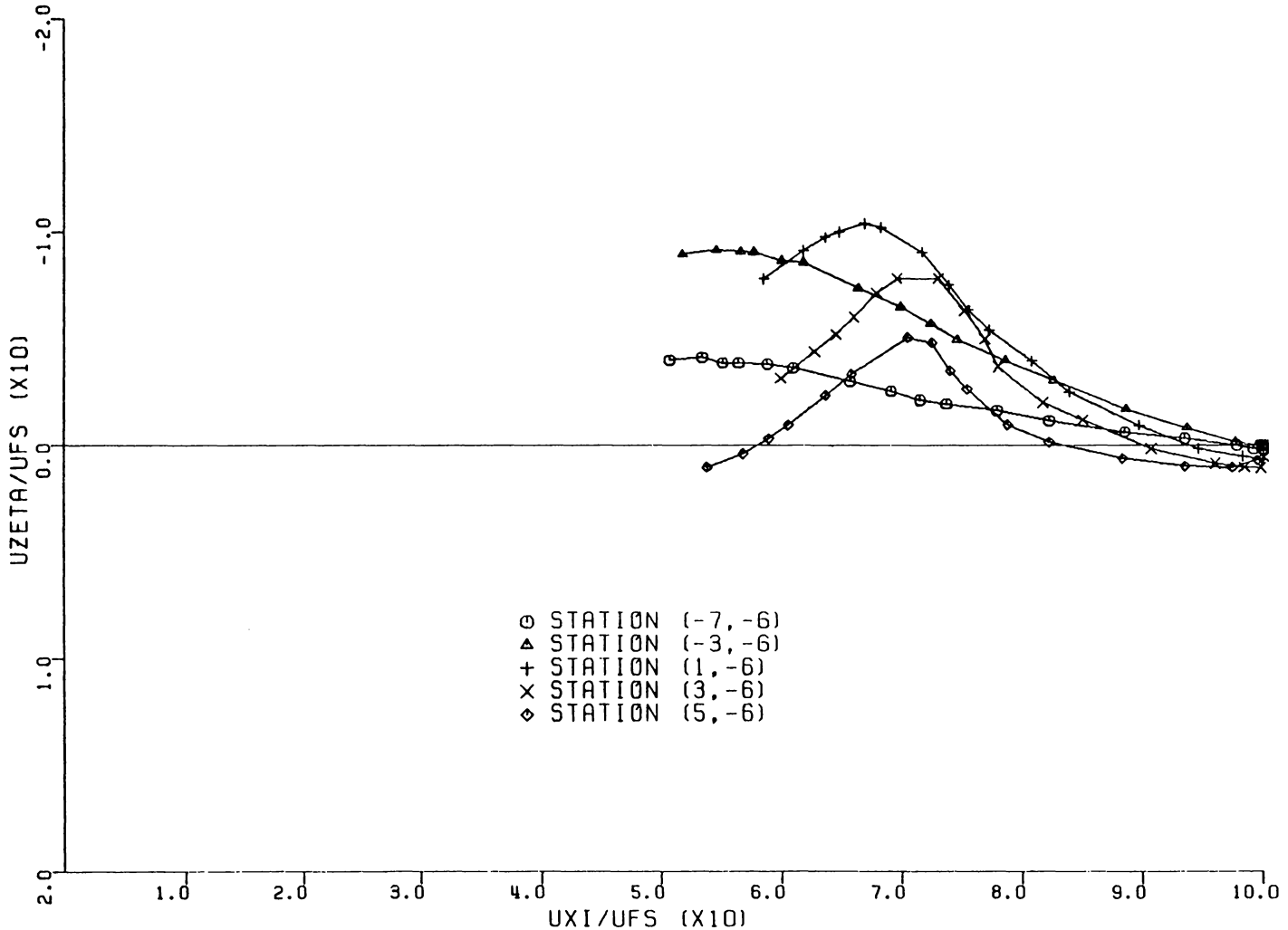

FIGURE 7.9. POLAR PLOT OF THE PROFILES ALONG THE X3=-6 PLANE

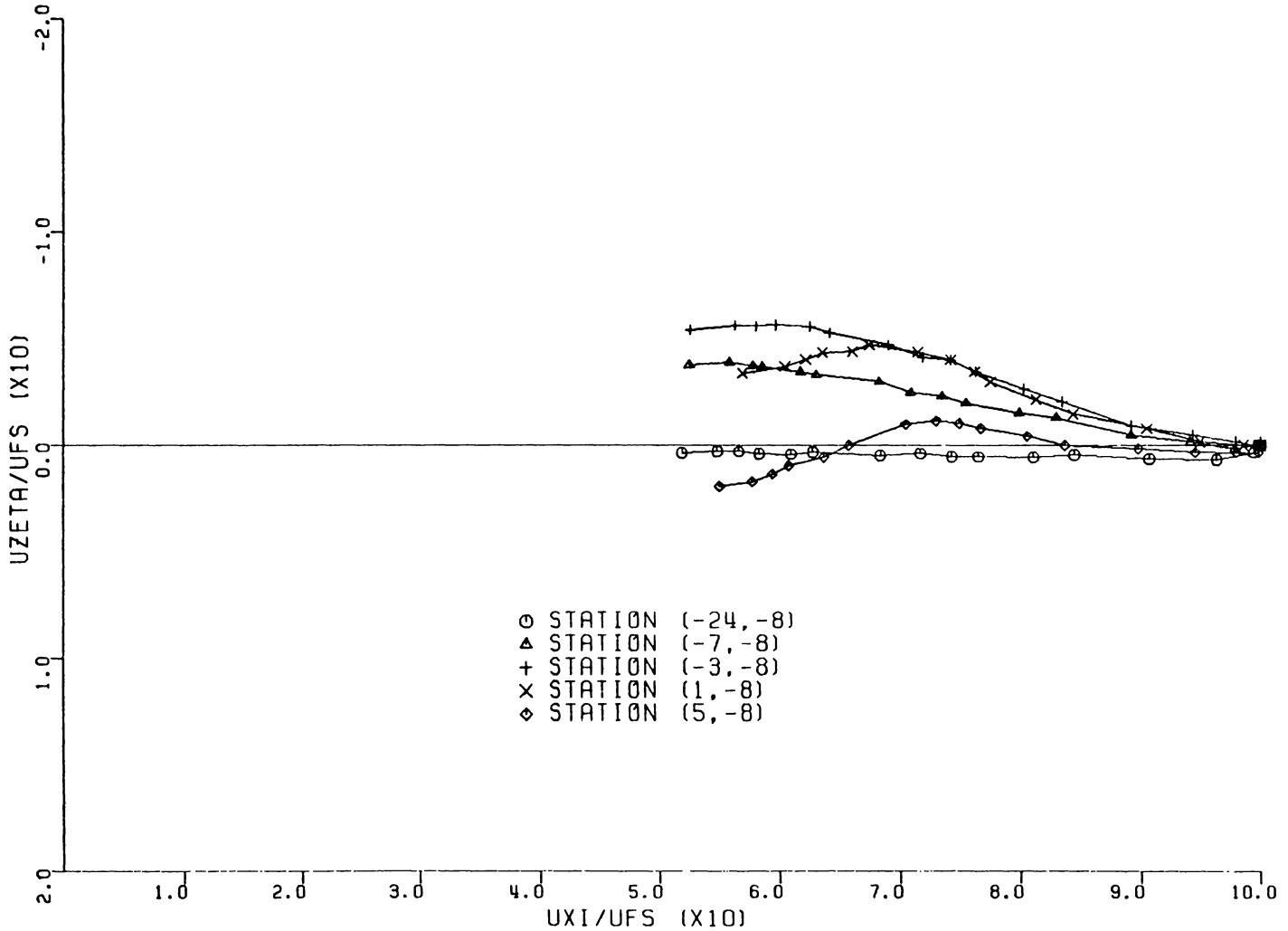

FIGURE 7.10. POLAR PLOT OF THE PROFILES ALONG THE X3=-8 PLANE

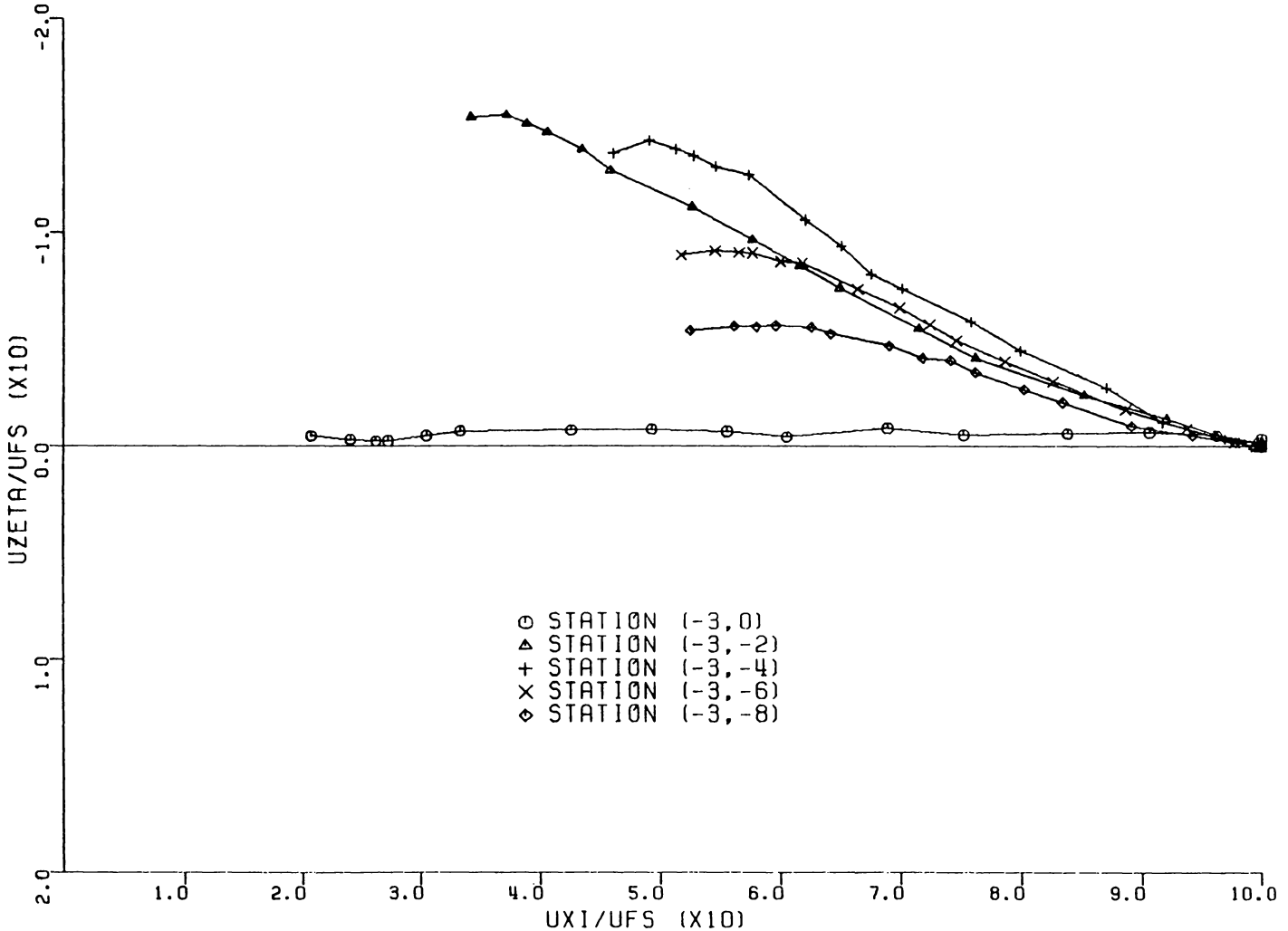

FIGURE 7.11. POLAR PLOT OF THE PROFILES ALONG THE X1=-3 PLANE

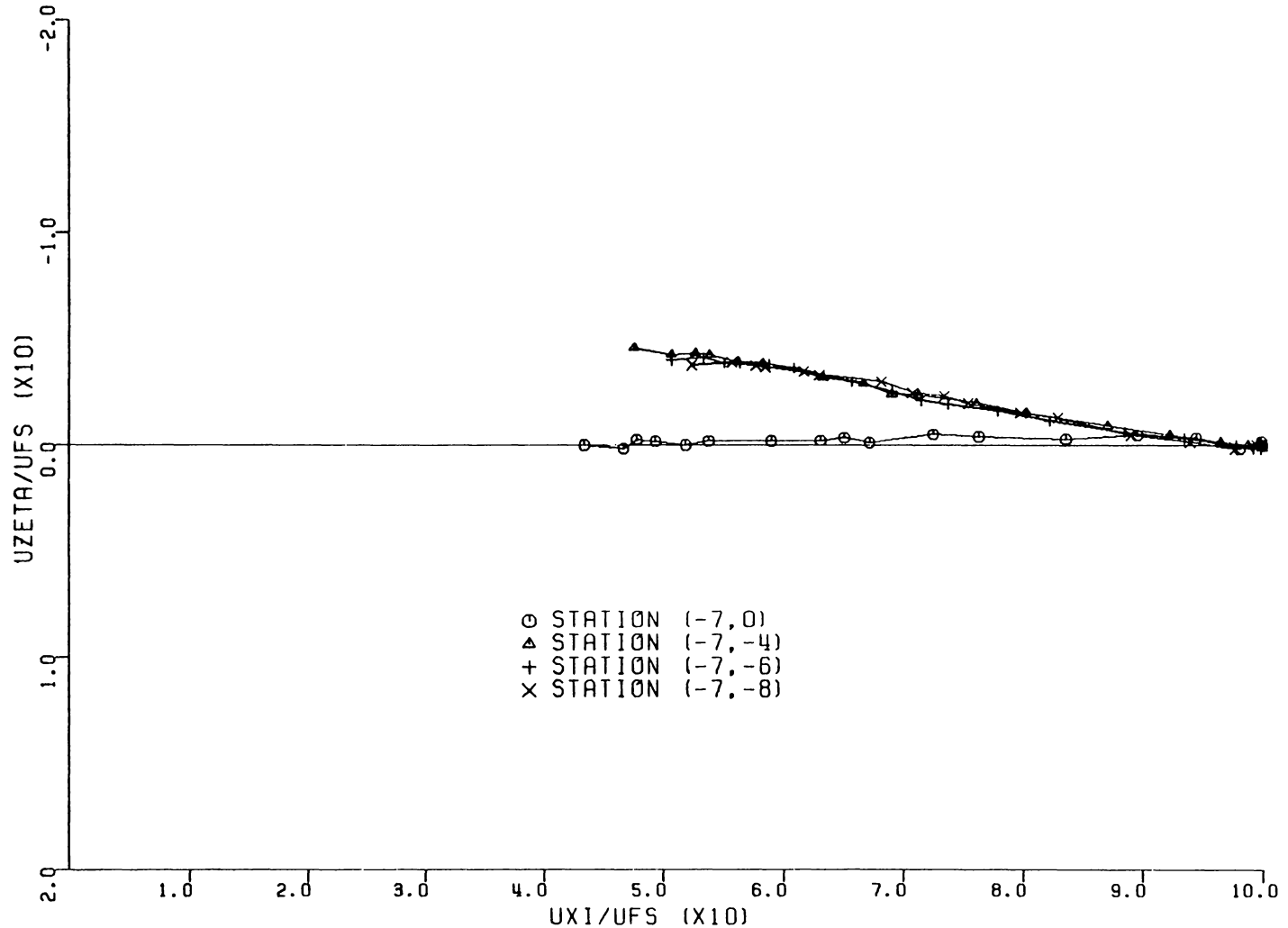

FIGURE 7.12. POLAR PLOT OF THE PROFILES ALONG THE X1=-7 PLANE

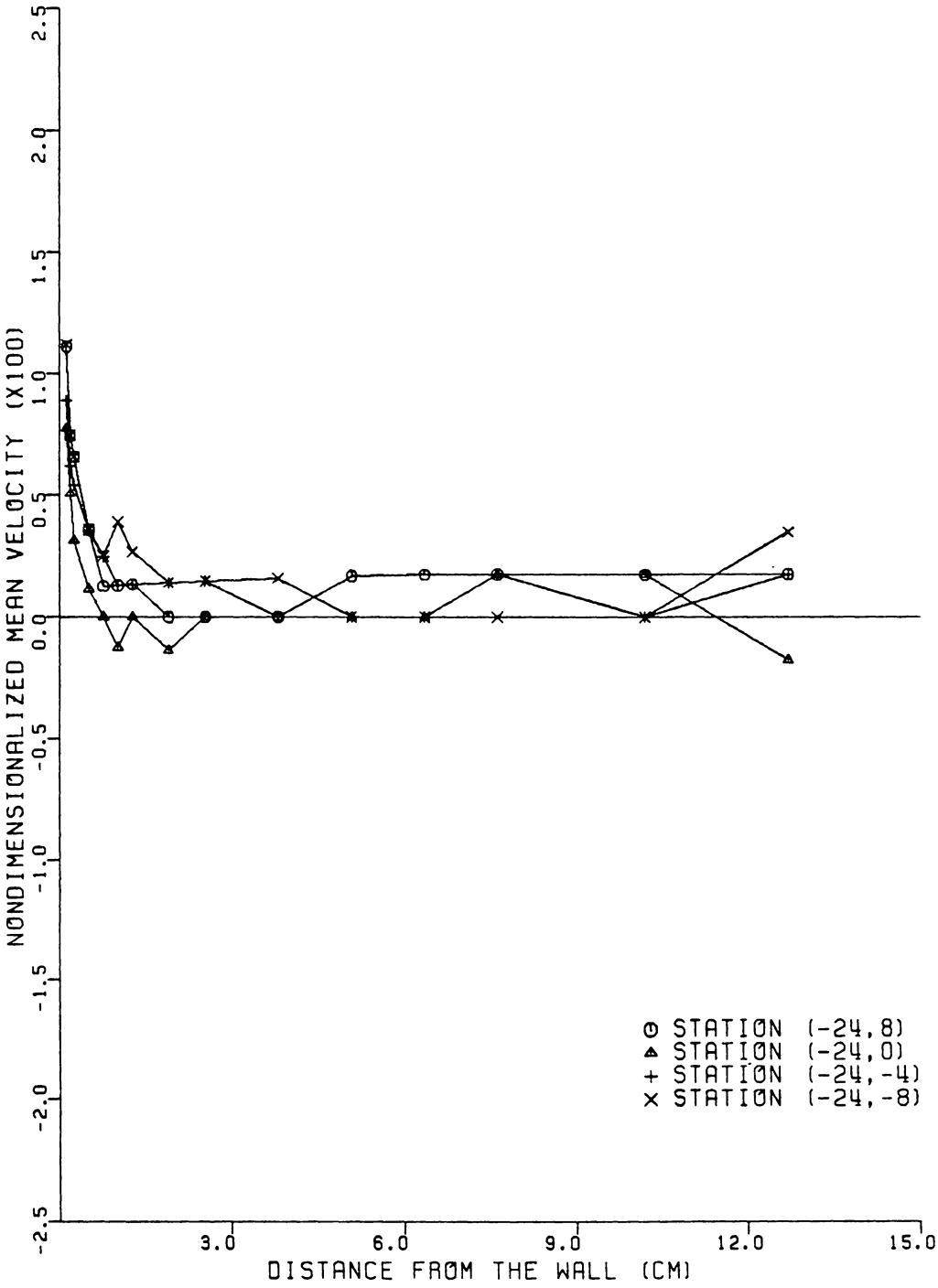

FIGURE 7.13. U2/U1FS MEAN VELOCITY PROFILES ALONG THE INITIAL CONDITION PLANE

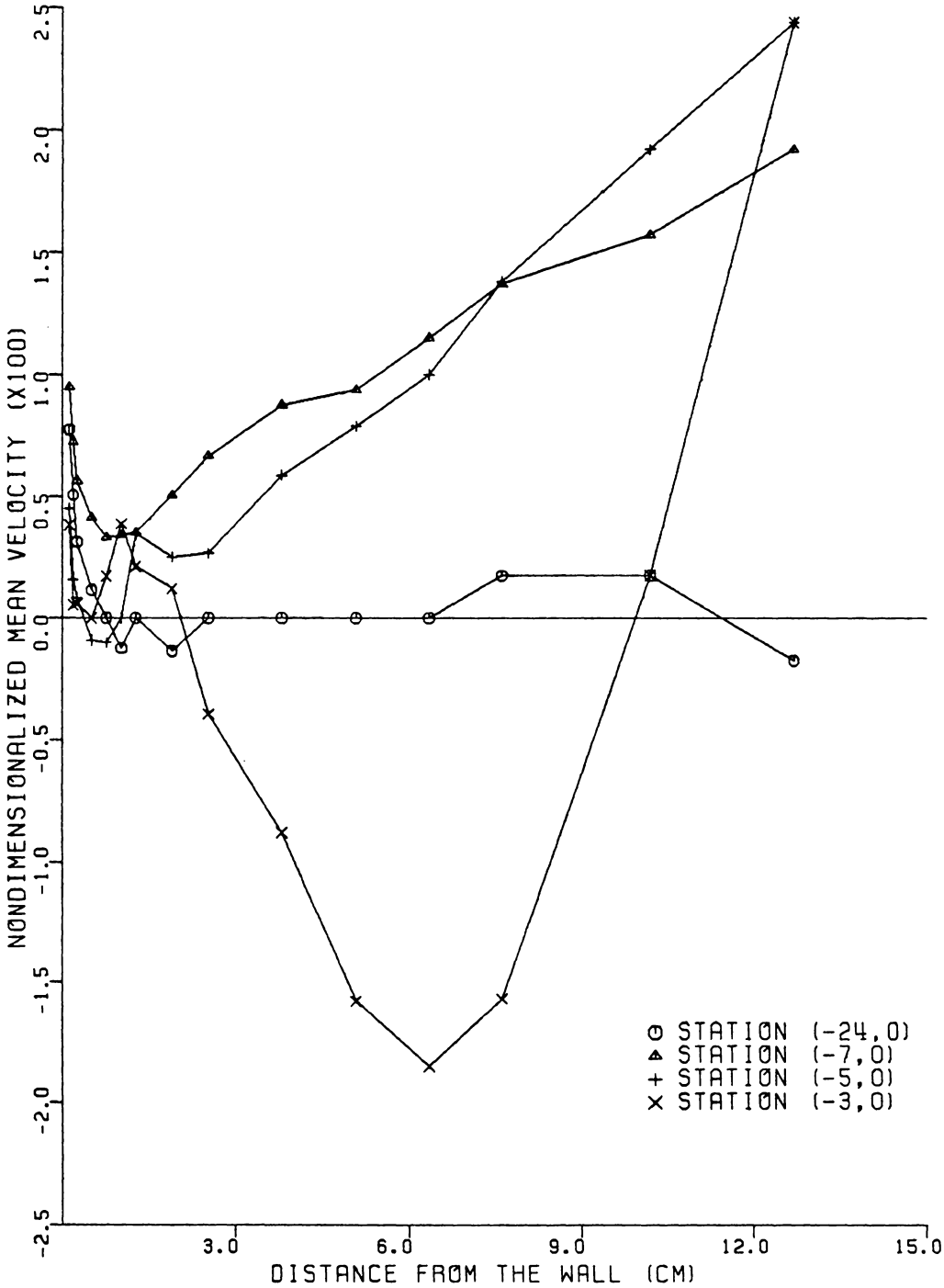

FIGURE 7.14. U2/U1FS MEAN VELOCITY PROFILES ALONG THE PLANE OF SYMMETRY

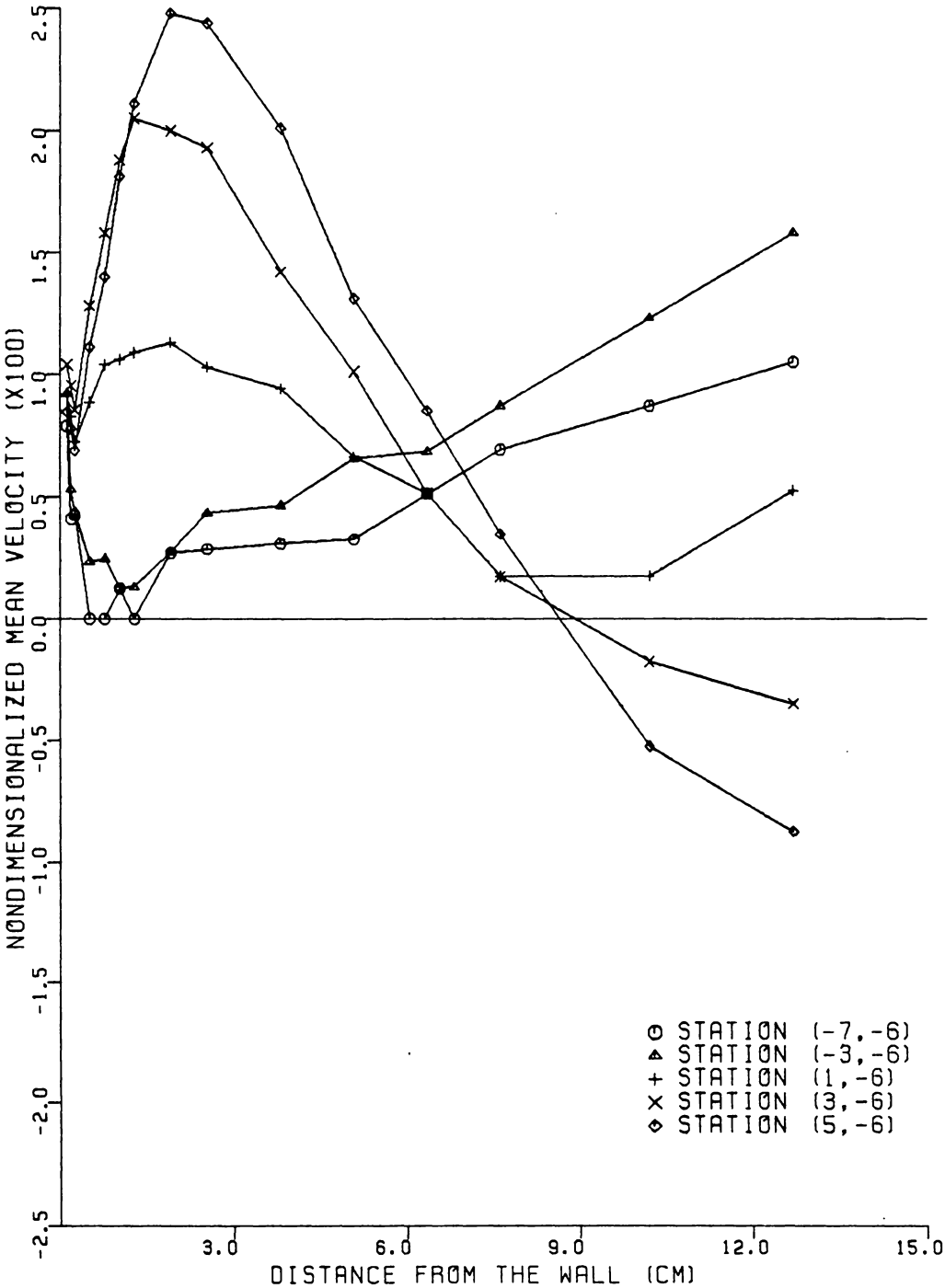

FIGURE 7.15. U2/U1FS MEAN VELOCITY PROFILES ALONG THE PLANE X3=-6

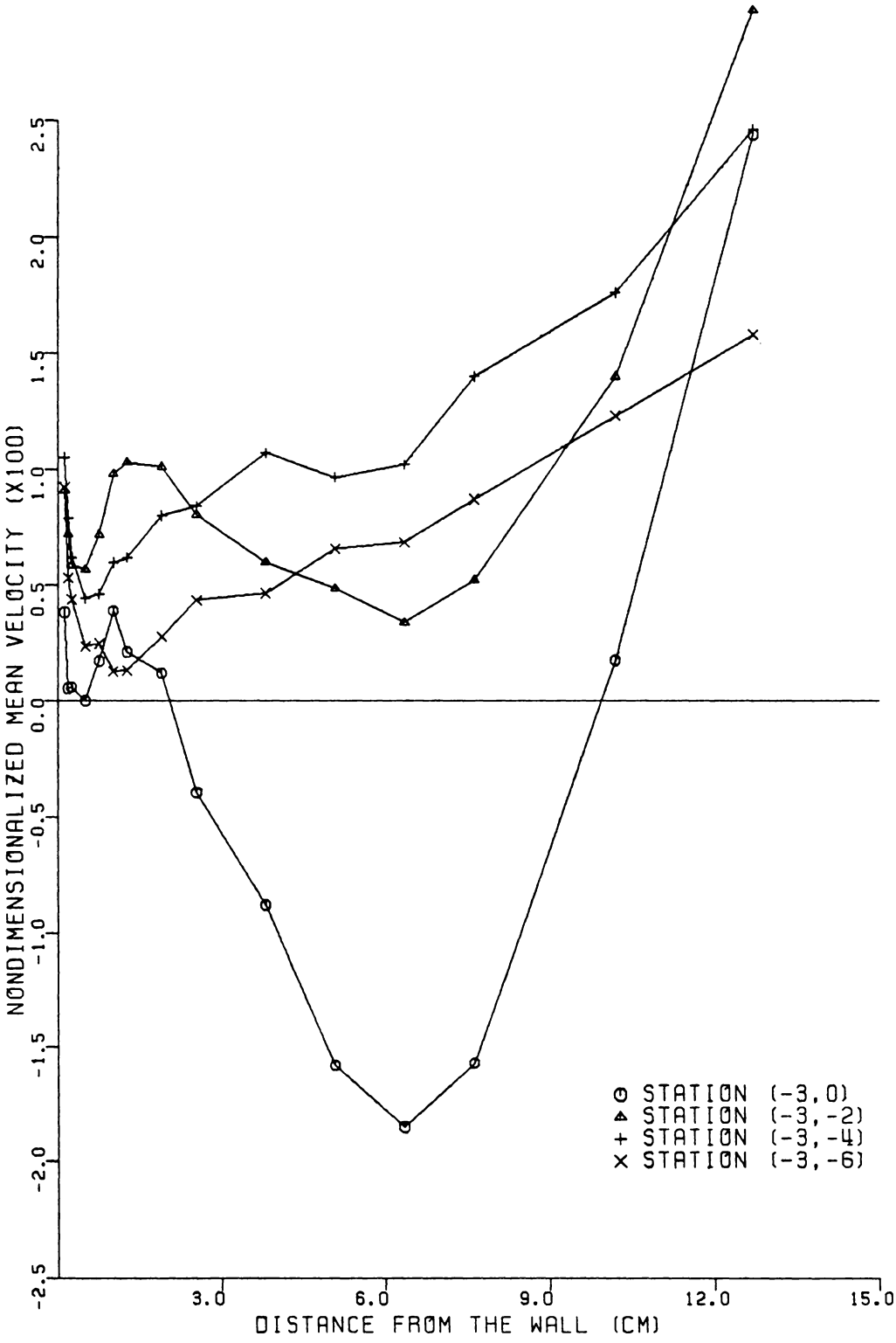

FIGURE 7.16. U2/U1FS MEAN VELOCITY PROFILES ALONG THE PLANE X1=-3

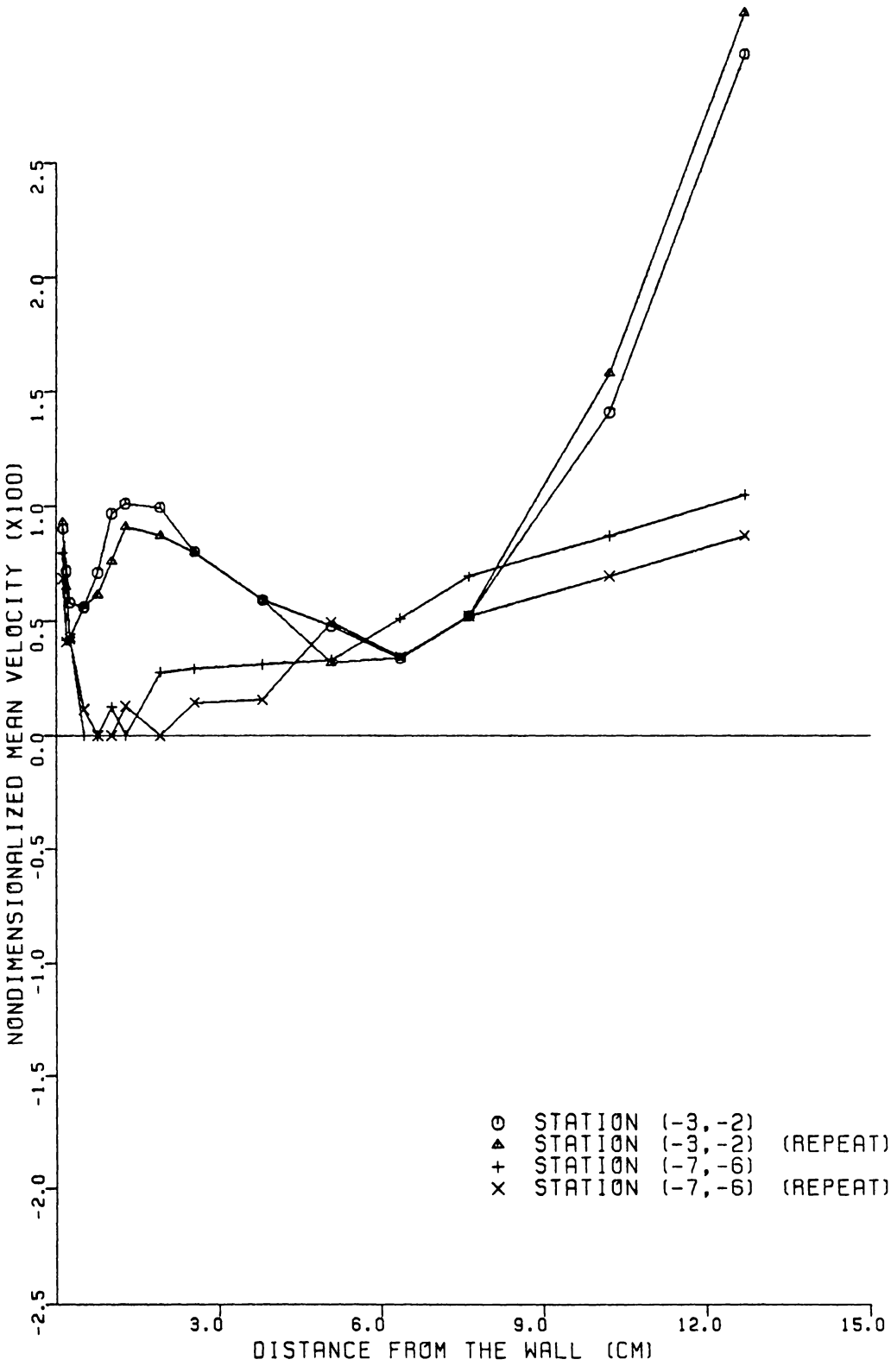

FIGURE 7.17. REPEATABILITY IN THE U2 VELOCITY COMPONENT

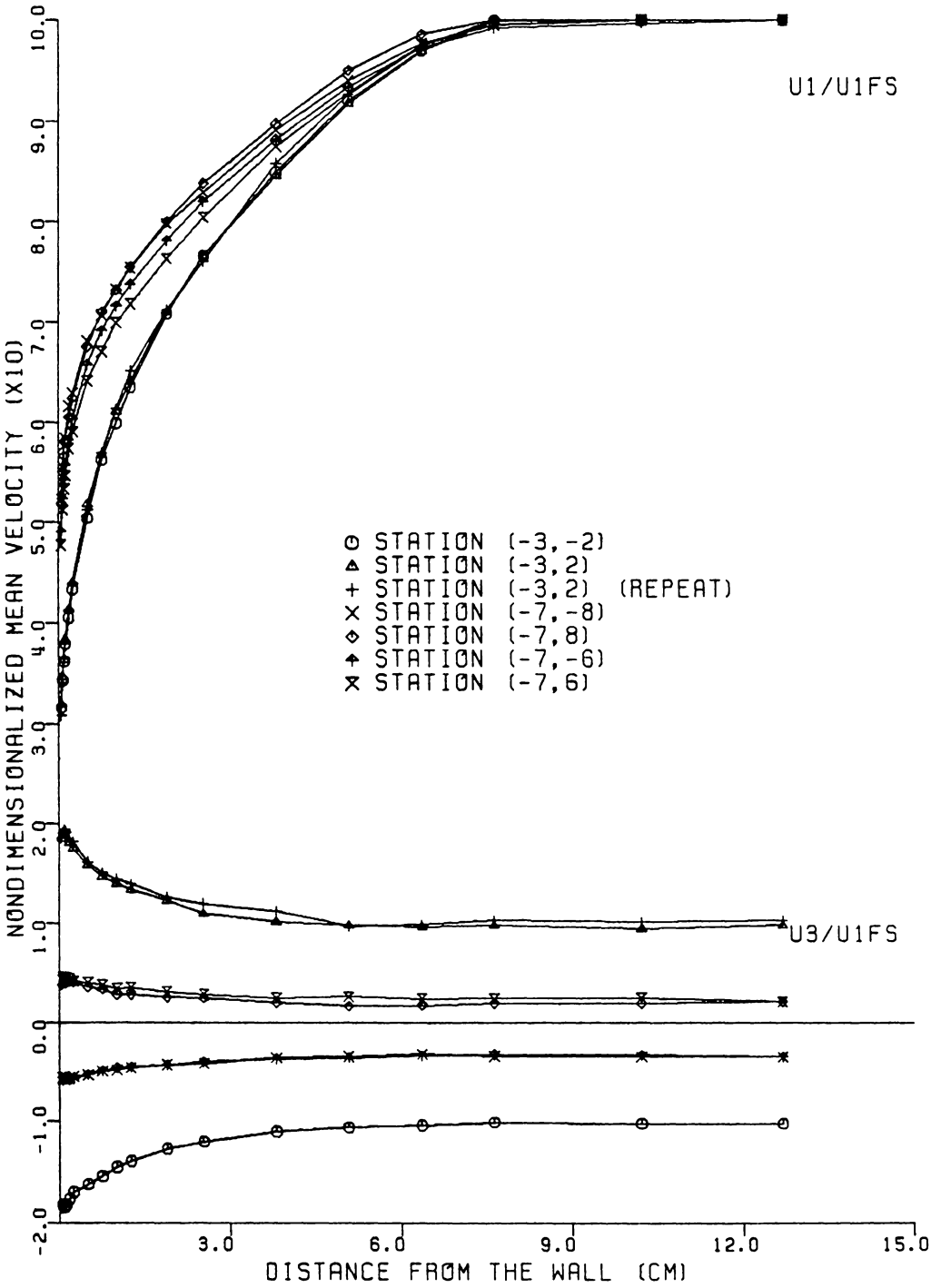

FIGURE 7.18. SYMMETRY IN MEAN VELOCITY OF THE 3DTBL FLOW

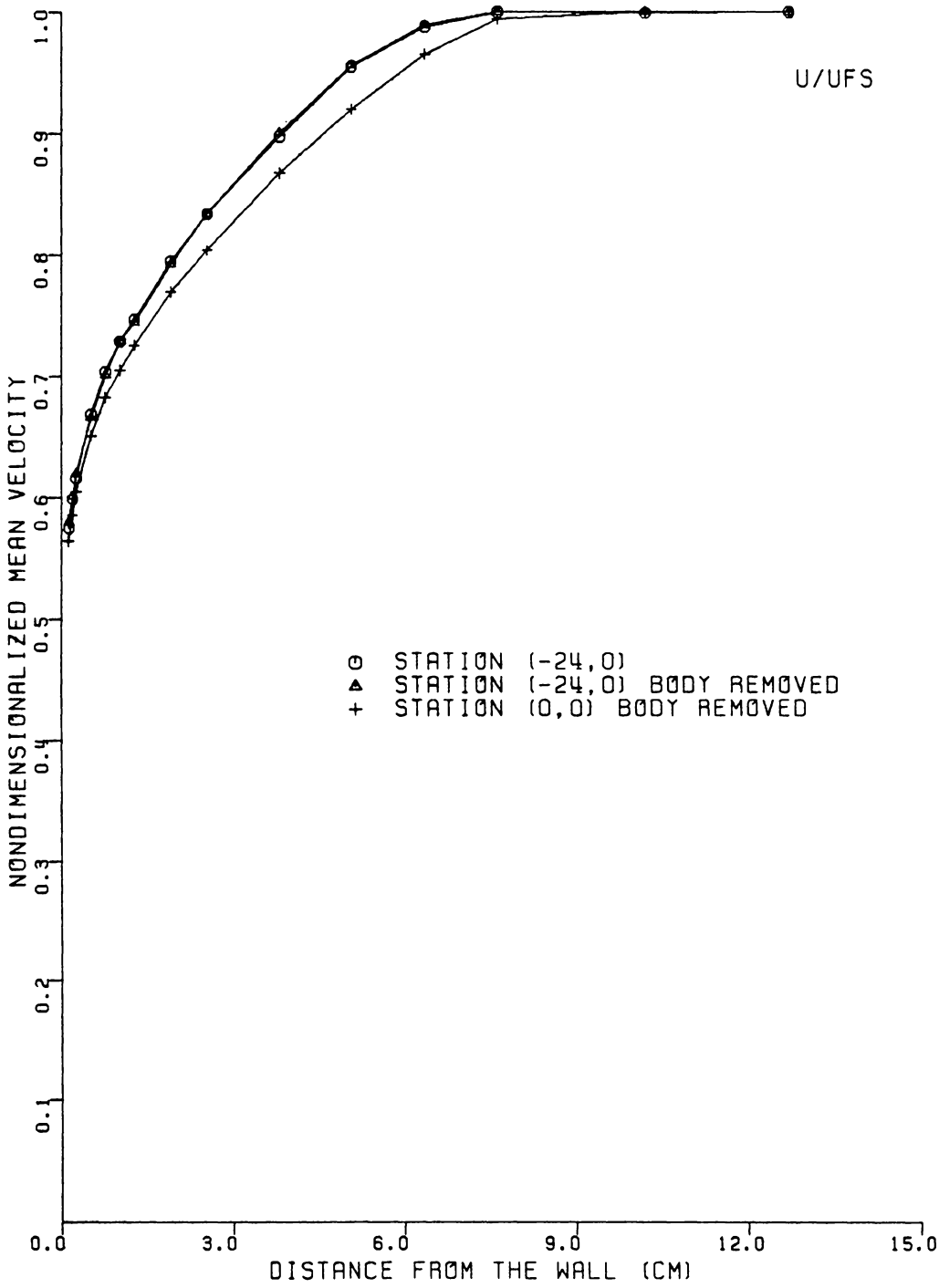

FIGURE 7.19. EFFECT OF THE BODY ON THE INITIAL CONDITION MEAN VELOCITY PROFILES

tion as was discussed in Chapter VI. This amount of nonuniformity in the mean velocity was confirmed to exist in the nominally two-dimensional flow and was of the order quantified by other investigators [144-149] in carefully studied nominally two-dimensional flows.

In comparison, the largest deviation of these upstream mean velocity profiles occured at station (-24,0), located on the plane of symmetry. The smaller magnitudes of mean velocity measured at this station were not believed to be an effect of the body, being 61 cm (24 in.) directly downstream. This is shown in Fig. 7.19 where mean velocity profiles were taken with the vx-array at station (-24,0), with and without the body in the tunnel flow. These results show no apparent effect of the body on the (-24,0) upstream initial condition velocity profile. It appears that the nonuniformities in the initial velocity profiles were characteristic of the tunnel itself. A similar study was made to determine the influence of the body on the initial condition turbulent stress field. These turbulence results will be presented in a later section. Figure 7.18 also shows the mean velocity profile at the center of the test section (61 cm or 24 in. downstream of the initial plane) for comparison.

In nominally two-dimensional flows the usual procedure is to assume zero transverse velocities, rather than to seek these out. Figures 7.1 and 7.7 show the very small amounts of $\overline{U}_3$ components of velocity that were measured along the initial condition plane. These values are typically within the experimental uncertainty of the velocity measurements and were judged negligible in the nominally 2D upstream flow. Similar results are shown in the plane of symmetry flow in Figs. 7.2 and

7.8. The systematic broadening of the $\overline{U}_1$ profiles along this plane is identified with the effect of the pressure gradient on the flow approaching separation.

For the flow upstream of the body's leading edge and off the plane of symmetry, the results indicate monotone increasing skew toward the wall within the boundary layer. Downstream of the leading edge monotone decreasing and increasing skew is shown. The two longitudinal planes x_3 = -15.24 and -20.32 cm (-6 and -8 in.) show mainly unilateral skewing, with only small amounts of bilateral skewing of the boundary layer. The profiles along these planes are plotted in Figs. 7.3 and 7.4. The bilaterally skewed stations (5,-8) and (5,-6) are more readily identified in Figs. 7.9 and 7.10 by their s-shaped curves. It is noted that stations (1,-6), (3,-6), (5,-6) and (5,-8) also show a slight bilateral turning of the velocity vectors in the outer regions of the boundary layer. Bilateral skewing is usually identified with the flow nearest the wall. The bilateral skewing in the outer portions of these profiles may be due to the finite body height or the presence of the junction vortex as it wraps around the body and develops downstream.

A range of unilaterally skewed profiles, across the transverse plane 7.62 cm (3 in.) upstream of the leading edge of the body, is shown in Figs. 7.5 and 7.11. The larger amounts of secondary flow found at station (-3,-2), -5.08 cm (-2 in.) from the plane of symmetry, could be identified with an approximately 30° of skewing near the wall. It is noted that nearly constant skewing of the boundary layer occurs along the transverse plane x_1 = -17.78 cm (-7 in.) from the leading edge of the plane of symmetry as shown in Figs. 7.6 and 7.12.

Figures 7.13-7.16 show the vertical, $\overline{U}_2$, velocity profiles measured along the initial condition plane, the plane of symmetry, the longitudinal plane x_3 = -15.24 cm (-6 in.) and the transverse plane 7.62 cm (3 in.) upstream of the body's leading edge. These profiles are tabulated with the Reynolds stress results in Appendix G.

The $\overline{U}_2$ components of velocity were measured with the vx-array. The vx-array, being very sensitive to changes in velocity alignment in the vertical plane, was very effective in detecting small amounts of upwash or downwash in the flow. With the probe aligned to the local yaw direction ($\overline{\psi}_y = 0$), the pitch angle $\overline{\psi}_z^*$ was obtained by utilizing the combined mean linearized response of the sensor pair. According to Eq. 5.2, one can write

$$\overline{U}^* = \frac{\overline{E}_a(\overline{U}^*, \alpha_a^*) - A_a}{B_{o,a}\, f(\alpha_a^*, P_a)} \tag{7.1}$$

for sensor a and

$$\overline{U}^* = \frac{\overline{E}_b(\overline{U}^*, \alpha_b^*) - A_b}{B_{o,b}\, f(\alpha_b^*, P_b)} \tag{7.2}$$

for sensor b. Combining Eqs. 7.1 and 7.2 yields

$$\frac{f(\alpha_b^*, P_b)}{f(\alpha_a^*, P_a)} = \frac{B_{o,a}\, \overline{E}_b(\overline{U}^*, \alpha_b^*) - A_b}{B_{o,b}\, \overline{E}_a(\overline{U}^*, \alpha_a^*) - A_a} \tag{7.3}$$

which can be used with Eq. 4.22 for each sensor with $\overline{\psi}_y = 0$ to determine the value of $\overline{\psi}_z^*$. For a geometrically perfect vx-array with $\alpha = \frac{\pi}{4}$, for example, Eq. 4.22 gives

$$\alpha_a^* = \frac{\pi}{4} + \overline{\psi}_z^* \tag{7.4}$$

and

$$\alpha_b^* = \frac{\pi}{4} - \overline{\psi}_z^* \ . \tag{7.5}$$

In the results presented in Figs. 7.13-7.16, Hinze's [54] cooling law was used in Eq. 7.3 and a root search algorithm was employed to determine $\overline{\psi}_z^*$. The $\overline{U}_2$ velocity was calculated directly from Eq. 4.7.

The results show small but systematic $\overline{U}_2$ velocity variations throughout the 3DTBL flow region. The values plotted corresponded to only an approximately ± 0 to 2^o of pitch in the flow relative to the wall. That such small, systematic variations of the vertical velocity component could be accurately measured in the 3DTBL flow is supported by the high degree of repeatability shown in Fig. 7.17 at stations (-3,-2) and (-7,-6) where relatively large and small amounts of skewing of the 3DTBL occurred. Across the initial condition plane, where less systematic behavior is shown, the values of $\overline{U}_2$ are essentially zero but tending toward small positive values. Close to the wall, the results show a monotonically increasing $\overline{U}_2$ component as the wall is approached. This type of behavior is shown consistently throughout the 3DTBL flow and might possibly be due to the probe interfering with the local flow in the wall region. It would be difficult to give any definitive explanation for this behavior without a more detailed investigation of the possible mechanisms involved. It is noted however that 1) the effects

are confined to regions close to the wall and decrease quickly with distance from the wall and 2) such effects are more likely due to the probe interfering with the flow near the wall rather than an influence of normal velocity gradients since each sensor of the vx-array would be exposed to the same vertical velocity gradient.

At the floor stations upstream of the body's leading edge, excluding station (-3,0) near separation, the results show the $\overline{U}_2$ velocity component to be positive and generally monotone increasing. This appears consistent with an increasing boundary layer thickness with fluid displaced away from the wall. Figure 7.14 shows a larger outflow of fluid occurring as the boundary layer approaches separation along the plane of symmetry.

Close to the point of separation at station (-3,0) (see Fig. 3.9), both a downwash and upwash within the boundary layer is shown which may be identified with the nature of the flow in the neighborhood of the separated region and the junction vortex. This separation system also appears to influence the flow to some degree at (-3,-2). At this point, one can only speculate on the influence the vortex system may have on the adjacent 3DTBL flow. It must be emphasized that while some of the characteristics of the 3DTBL mean flow field may be identified with the junction vortex via the behavior of the $\overline{U}_2$ velocity profiles, these effects documented here are very small.

On the x_3 = -15.24 plane (15.24 cm or 6 in. from the plane of symmetry) Fig. 7.15 shows the developing $\overline{U}_2$ profiles which change in shape with distance along this plane. At stations (-7,-6) and (-3,-6) the results show a monotone increasing $\overline{U}_2$ component of velocity (ex-

cluding the inner layers near the wall), indicating flow leaving the boundary layer. This develops into an increasing and decreasing variation leading to flow into the boundary layer at station (5,-6).

Figure 7.18 shows the degree of symmetry in mean velocity profiles taken in the adjacent forward quadrant of the 3DTBL flow. At the extreme flow stations (-3,-2) and (-7,-8) which are located relatively close to and far from the body, the flow shows a very high degree of symmetry. The flow is shown to be less symmetric at station (-7,-6) but the 2-3% asymmetry in the mean velocity shown is still considered reasonable.

Mean Velocity Comparisons

A total of 9 mean velocity measurements were available at each y location: two velocity magnitudes (one from each sensor) from each of the four traverses required to measure the complete Reynolds stress tensor and one measurement with the single film probe. A comparison of all of these measurements were made at each station, with each velocity magnitude corrected for turbulence using Eq. 4.48, but neglecting the higher order effects of any small misalignment of the probe. Typical results are shown in Figs. 7.20-7.22 at stations (-3,-2), (-7,-6), and (5,-6). In these results, an arithmetic average of the two velocity magnitudes measured by each sensor of the given x-array probe is used. A comparison of the 9 individual mean velocity measurements, at each y location, is made in Tables 7.1-7.3. The results show very good agreement in the mean velocity magnitudes measured by the different probes. These results not only show consistency among the various probe measure-

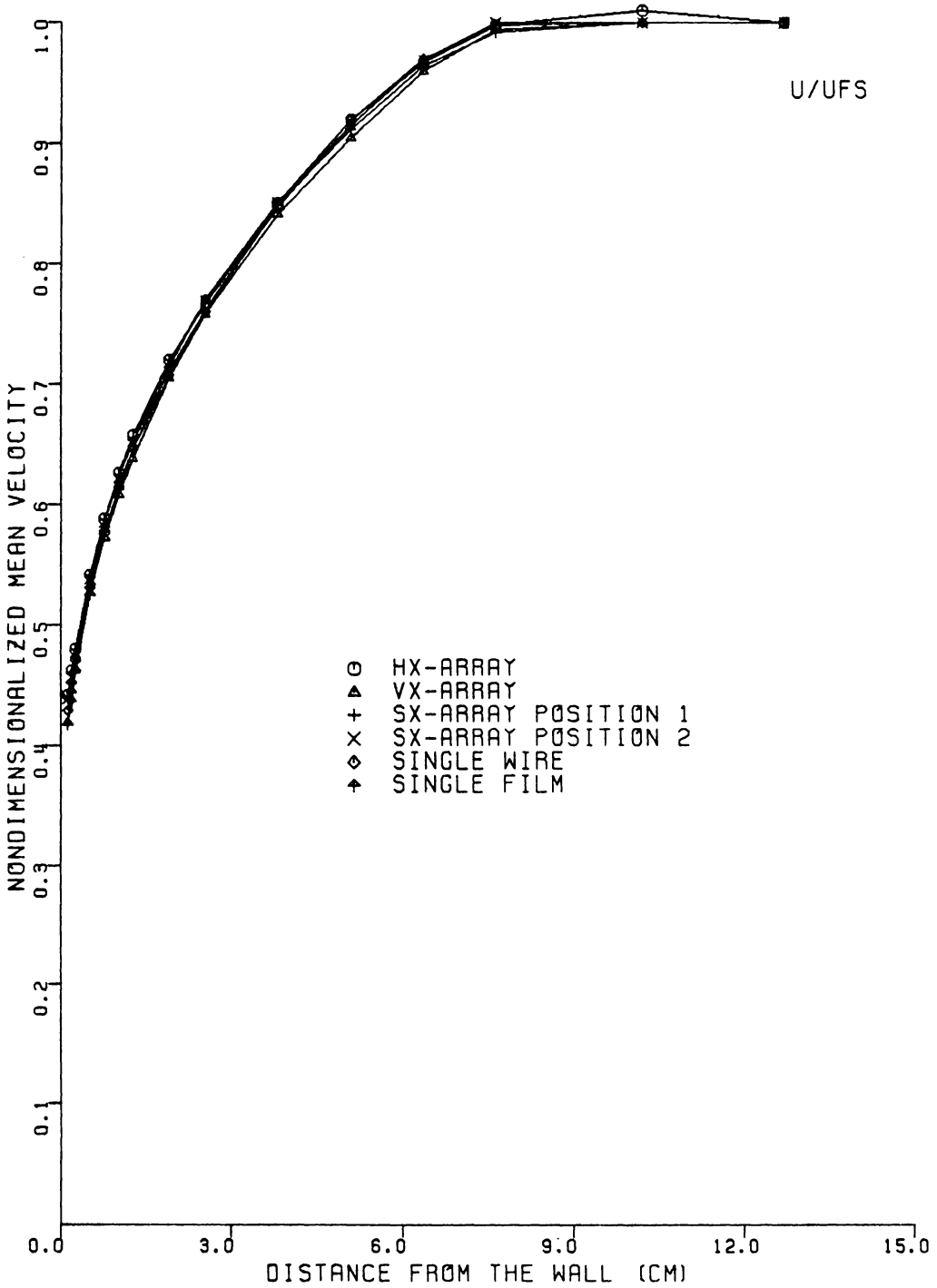

FIGURE 7.20. COMPARISON OF MEAN VELOCITY FROM DIFFERENT PROBES AT STATION (-3,-2)

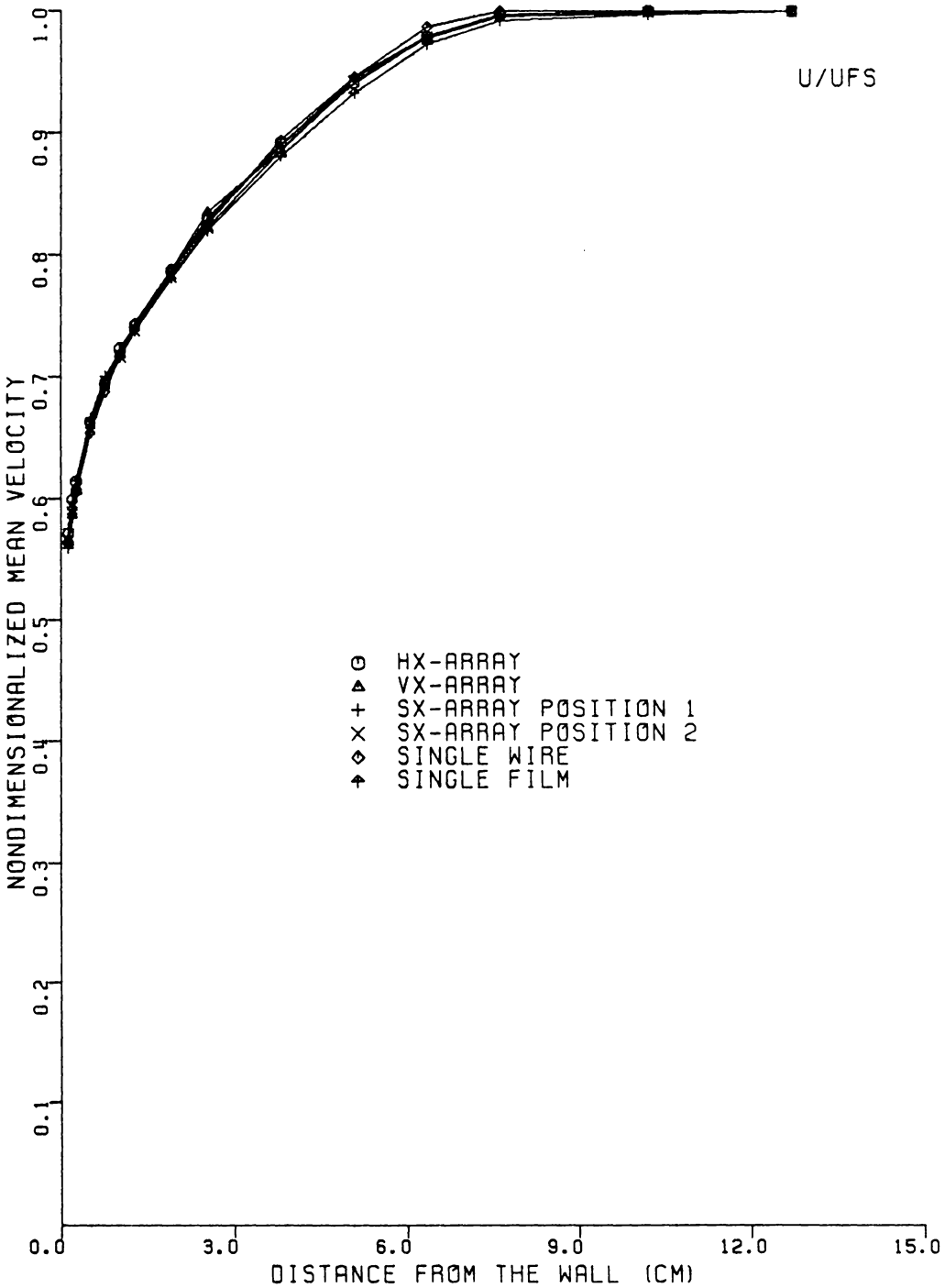

FIGURE 7.21. COMPARISON OF MEAN VELOCITY FROM DIFFERENT PROBES AT STATION (-7,-6)

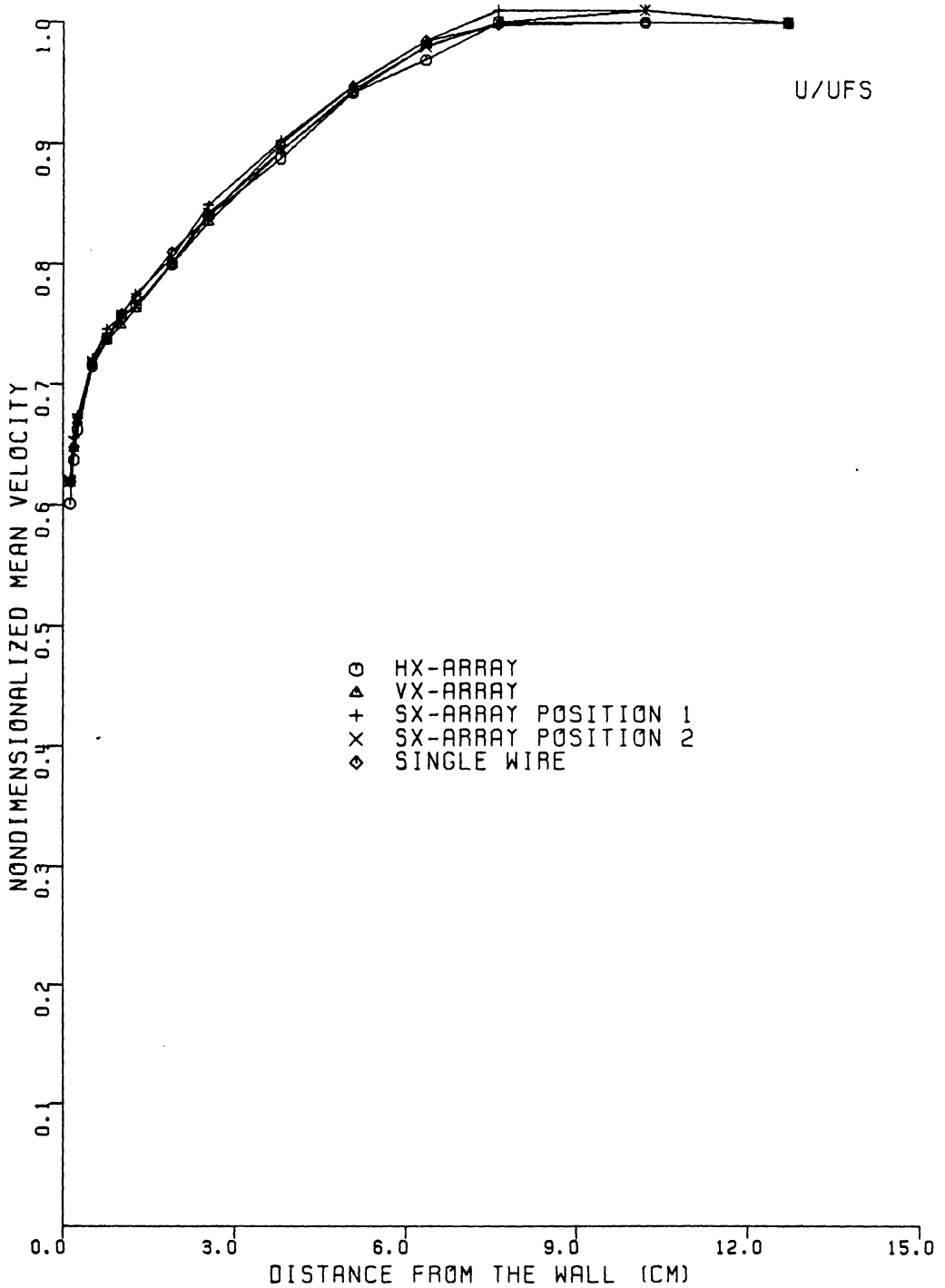

FIGURE 7.22. COMPARISON OF MEAN VELOCITY FROM DIFFERENT PROBES AT STATION (5,-6)

TABLE 7.1. COMPARISON OF CORRECTED AND UNCORRECTED MEAN VELOCITIES AT STATION (-3,0)

CORRECTED MEAN VELOCITY (M/S), UC - SENSOR A

Y	HX		VX		SX1		SX2		SINGLE FILM	
(CM)	UC/U	UC	UC/U	UC	UC/U	UC	UC/U	UC	UC/U	UC
0.127	0.979	5.2	0.959	5.2	0.972	5.6	0.967	5.2	0.991	5.3
0.190	0.980	5.9	0.965	5.8	0.975	6.3	0.971	5.8	0.991	5.9
0.254	0.981	6.5	0.969	6.3	0.977	6.8	0.975	6.4	0.991	6.4
0.508	0.987	8.4	0.980	8.1	0.984	8.7	0.983	8.3	0.993	8.2
0.762	0.989	9.7	0.986	9.3	0.988	10.2	0.987	9.4	0.995	9.5
1.016	0.992	10.8	0.989	10.4	0.991	11.3	0.990	10.5	0.996	10.8
1.270	0.993	11.6	0.991	11.0	0.992	12.2	0.992	11.3	0.997	11.7
1.905	0.995	13.2	0.993	12.5	0.994	13.6	0.994	12.9	0.998	13.4
2.540	0.996	14.3	0.995	13.9	0.996	14.7	0.995	14.1	0.998	14.6
3.810	0.997	16.3	0.997	15.8	0.997	16.9	0.997	16.2	0.999	16.3
5.080	0.998	17.8	0.998	17.3	0.998	18.2	0.998	17.7	0.999	17.6
6.350	0.999	18.8	0.999	18.3	0.999	19.2	0.999	18.8	1.000	18.7
7.620	1.000	19.6	1.000	19.2	1.000	19.9	1.000	19.6	1.000	19.4
10.160	1.000	19.9	1.000	19.4	1.000	20.0	1.000	19.8	1.000	19.5
12.700	1.000	19.8	1.000	19.4	1.000	19.7	1.000	19.6	1.000	19.4

CORRECTED MEAN VELOCITY (M/S), UC - SENSOR B

Y	HX		VX		SX1		SX2		SINGLE FILM	
(CM)	UC/U	UC	UC/U	UC	UC/U	UC	UC/U	UC	UC/U	UC
0.127	0.982	5.8	0.961	5.2	0.974	6.0	0.971	5.6	0.991	5.3
0.190	0.982	6.4	0.966	5.8	0.977	6.6	0.974	6.2	0.991	5.9
0.254	0.983	7.0	0.970	6.3	0.978	7.1	0.977	6.9	0.991	6.4
0.508	0.987	8.8	0.981	8.1	0.984	8.7	0.984	8.7	0.993	8.2
0.762	0.990	10.1	0.987	9.4	0.988	10.0	0.988	9.7	0.995	9.5
1.016	0.992	11.2	0.990	10.4	0.990	11.0	0.990	10.9	0.996	10.8
1.270	0.993	11.7	0.991	11.0	0.991	11.6	0.992	11.5	0.997	11.7
1.905	0.995	13.4	0.994	12.5	0.994	13.0	0.994	13.3	0.998	13.4
2.540	0.996	14.4	0.995	13.9	0.995	14.1	0.996	14.4	0.998	14.6
3.810	0.997	16.4	0.997	15.8	0.997	16.2	0.997	16.5	0.999	16.3
5.080	0.998	17.8	0.998	17.3	0.998	17.7	0.998	17.8	0.999	17.6
6.350	0.999	18.8	0.999	18.4	0.999	18.7	0.999	18.9	1.000	18.7
7.620	1.000	19.5	1.000	19.2	1.000	19.3	1.000	19.5	1.000	19.4
10.160	1.000	19.8	1.000	19.5	1.000	19.7	1.000	19.6	1.000	19.5
12.700	1.000	19.6	1.000	19.4	1.000	19.7	1.000	19.5	1.000	19.4

TABLE 7.1. CONTINUED

CORRECTED MEAN VELOCITY (M/S), UC - SENSORS A & B (AVERAGED)

Y	HX		VX		SX1		SX2		SINGLE FILM	
(CM)	UC/U	UC	UC/U	UC	UC/U	UC	UC/U	UC	UC/U	UC
0.127	0.980	5.5	0.960	5.2	0.973	5.8	0.969	5.4	0.991	5.3
0.190	0.981	6.1	0.966	5.8	0.976	6.5	0.972	6.0	0.991	5.9
0.254	0.982	6.8	0.970	6.3	0.978	7.0	0.976	6.7	0.991	6.4
0.508	0.987	8.6	0.981	8.1	0.984	8.7	0.984	8.5	0.993	8.2
0.762	0.990	9.9	0.986	9.3	0.988	10.1	0.987	9.6	0.995	9.5
1.016	0.992	11.0	0.989	10.4	0.990	11.1	0.990	10.7	0.996	10.8
1.270	0.993	11.7	0.991	11.0	0.992	11.9	0.992	11.4	0.997	11.7
1.905	0.995	13.3	0.993	12.5	0.994	13.3	0.994	13.1	0.998	13.4
2.540	0.996	14.3	0.995	13.9	0.995	14.4	0.996	14.3	0.998	14.6
3.810	0.997	16.3	0.997	15.8	0.997	16.6	0.997	16.3	0.999	16.3
5.080	0.998	17.8	0.998	17.3	0.998	17.9	0.998	17.8	0.999	17.6
6.350	0.999	18.8	0.999	18.4	0.999	19.0	0.999	18.8	1.000	18.7
7.620	1.000	19.6	1.000	19.2	1.000	19.6	1.000	19.5	1.000	19.4
10.160	1.000	19.9	1.000	19.5	1.000	19.8	1.000	19.7	1.000	19.5
12.700	1.000	19.7	1.000	19.4	1.000	19.7	1.000	19.5	1.000	19.4

TABLE 7.2. COMPARISON OF CORRECTED AND UNCORRECTED MEAN VELOCITIES AT STATION (-3,-2)

CORRECTED MEAN VELOCITY (M/S), UC - SENSOR A

Y	HX		VX		SX1		SX2		SINGLE FILM	
(CM)	UC/U	UC	UC/U	UC	UC/U	UC	UC/U	UC	UC/U	UC
0.127	0.991	9.0	0.977	8.8	0.984	9.1	0.984	8.9	0.997	9.0
0.190	0.991	9.5	0.980	9.3	0.984	9.6	0.986	9.4	0.996	9.6
0.254	0.991	10.0	0.982	9.7	0.986	10.1	0.987	9.8	0.996	10.0
0.508	0.992	11.3	0.987	11.0	0.988	11.4	0.990	11.1	0.997	11.3
0.762	0.993	12.3	0.990	12.0	0.991	12.4	0.992	12.0	0.997	12.3
1.016	0.994	13.1	0.991	12.8	0.992	13.2	0.993	12.8	0.997	13.0
1.270	0.995	13.8	0.993	13.4	0.993	13.8	0.994	13.5	0.998	13.7
1.905	0.996	15.2	0.995	14.8	0.995	15.1	0.995	14.8	0.998	15.1
2.540	0.997	16.1	0.996	15.9	0.996	16.1	0.996	15.9	0.998	16.0
3.810	0.998	17.9	0.997	17.7	0.998	18.0	0.998	17.6	0.999	17.9
5.080	0.999	19.4	0.998	19.0	0.999	19.2	0.999	19.0	0.999	19.3
6.350	0.999	20.3	0.999	20.2	0.999	20.3	0.999	20.1	1.000	20.2
7.620	1.000	21.0	1.000	20.9	1.000	20.8	1.000	20.8	1.000	20.9
10.160	1.000	21.2	1.000	21.1	1.000	21.1	1.000	20.9	1.000	21.0
12.700	1.000	21.1	1.000	21.0	1.000	20.9	1.000	20.8	1.000	21.0

CORRECTED MEAN VELOCITY (M/S), UC - SENSOR B

Y	HX		VX		SX1		SX2		SINGLE FILM	
(CM)	UC/U	UC	UC/U	UC	UC/U	UC	UC/U	UC	UC/U	UC
0.127	0.992	9.5	0.978	8.8	0.984	9.3	0.984	9.2	0.997	9.0
0.190	0.991	9.8	0.980	9.4	0.984	9.8	0.985	9.5	0.996	9.6
0.254	0.991	10.2	0.983	9.7	0.985	10.1	0.987	9.9	0.996	10.0
0.508	0.992	11.4	0.988	11.1	0.989	11.4	0.990	11.2	0.997	11.3
0.762	0.993	12.4	0.990	12.0	0.991	12.4	0.992	12.1	0.997	12.3
1.016	0.994	13.2	0.992	12.8	0.992	13.1	0.993	12.9	0.997	13.0
1.270	0.995	13.8	0.993	13.4	0.993	13.7	0.994	13.5	0.998	13.7
1.905	0.996	15.0	0.995	14.8	0.995	14.9	0.995	14.8	0.998	15.1
2.540	0.997	16.0	0.996	15.9	0.996	16.0	0.996	15.8	0.998	16.0
3.810	0.998	17.8	0.998	17.7	0.997	17.8	0.998	17.5	0.999	17.9
5.080	0.999	19.3	0.999	19.0	0.998	19.2	0.998	18.9	0.999	19.3
6.350	0.999	20.3	0.999	20.1	0.999	20.3	0.999	19.9	1.000	20.2
7.620	1.000	20.9	1.000	20.9	1.000	21.0	1.000	20.5	1.000	20.9
10.160	1.000	21.0	1.000	21.1	1.000	21.3	1.000	20.6	1.000	21.0
12.700	1.000	20.9	1.000	21.0	1.000	21.2	1.000	20.5	1.000	21.0

TABLE 7.2. CONTINUED

CORRECTED MEAN VELOCITY (M/S), UC - SENSORS A & B (AVERAGED)

Y	HX		VX		SX1		SX2		SINGLE FILM	
(CM)	UC/U	UC	UC/U	UC	UC/U	UC	UC/U	UC	UC/U	UC
0.127	0.992	9.3	0.977	8.8	0.984	9.2	0.984	9.1	0.997	9.0
0.190	0.991	9.7	0.980	9.4	0.984	9.7	0.985	9.4	0.996	9.6
0.254	0.991	10.1	0.982	9.7	0.986	10.1	0.987	9.8	0.996	10.0
0.508	0.992	11.4	0.987	11.1	0.989	11.4	0.990	11.1	0.997	11.3
0.762	0.993	12.3	0.990	12.0	0.991	12.4	0.992	12.1	0.997	12.3
1.016	0.994	13.1	0.992	12.8	0.992	13.1	0.993	12.8	0.997	13.0
1.270	0.995	13.8	0.993	13.4	0.993	13.8	0.994	13.5	0.998	13.7
1.905	0.996	15.1	0.995	14.8	0.995	15.0	0.995	14.8	0.998	15.1
2.540	0.997	16.1	0.996	15.9	0.996	16.0	0.996	15.9	0.998	16.0
3.810	0.998	17.8	0.997	17.7	0.997	17.9	0.998	17.6	0.999	17.9
5.080	0.999	19.3	0.998	19.0	0.998	19.2	0.999	18.9	0.999	19.3
6.350	0.999	20.3	0.999	20.2	0.999	20.3	0.999	20.0	1.000	20.2
7.620	1.000	20.9	1.000	20.9	1.000	20.9	1.000	20.6	1.000	20.9
10.160	1.000	21.1	1.000	21.1	1.000	21.2	1.000	20.7	1.000	21.0
12.700	1.000	21.0	1.000	21.0	1.000	21.1	1.000	20.6	1.000	21.0

TABLE 7.3. COMPARISON OF CORRECTED AND UNCORRECTED MEAN VELOCITIES AT STATION (-7,-6)

CORRECTED MEAN VELOCITY (M/S), UC - SENSOR A

Y	HX		VX		SX1		SX2		SINGLE FILM	
(CM)	UC/U	UC	UC/U	UC	UC/U	UC	UC/U	UC	UC/U	UC
0.127	0.996	13.0	0.993	13.3	0.995	13.3	0.994	13.1	0.998	13.4
0.190	0.996	13.8	0.994	13.9	0.995	13.9	0.995	13.7	0.998	14.0
0.254	0.996	14.2	0.994	14.3	0.995	14.4	0.995	14.2	0.998	14.5
0.508	0.997	15.5	0.995	15.6	0.996	15.6	0.996	15.4	0.998	15.6
0.762	0.997	16.3	0.996	16.3	0.996	16.5	0.996	16.2	0.999	16.4
1.016	0.997	17.0	0.996	16.9	0.996	17.0	0.997	16.8	0.999	17.0
1.270	0.997	17.4	0.997	17.5	0.997	17.4	0.997	17.4	0.999	17.5
1.905	0.998	18.5	0.997	18.5	0.997	18.5	0.997	18.4	0.999	18.5
2.540	0.998	19.5	0.998	19.6	0.998	19.5	0.998	19.4	0.999	19.5
3.810	0.999	21.0	0.998	20.8	0.998	21.0	0.999	20.9	0.999	21.0
5.080	0.999	22.2	0.999	22.2	0.999	22.2	0.999	22.2	1.000	22.2
6.350	1.000	23.0	1.000	23.0	1.000	23.0	1.000	23.1	1.000	23.2
7.620	1.000	23.4	1.000	23.4	1.000	23.5	1.000	23.5	1.000	23.6
10.160	1.000	23.6	1.000	23.5	1.000	23.5	1.000	23.6	1.000	23.7
12.700	1.000	23.5	1.000	23.5	1.000	23.5	1.000	23.6	1.000	23.8

CORRECTED MEAN VELOCITY (M/S), UC - SENSOR B

Y	HX		VX		SX1		SX2		SINGLE FILM	
(CM)	UC/U	UC	UC/U	UC	UC/U	UC	UC/U	UC	UC/U	UC
0.127	0.996	13.9	0.993	13.3	0.995	13.8	0.994	13.6	0.998	13.4
0.190	0.997	14.4	0.994	14.0	0.995	14.2	0.995	14.1	0.998	14.0
0.254	0.997	14.7	0.994	14.3	0.995	14.6	0.995	14.5	0.998	14.5
0.508	0.997	15.7	0.995	15.6	0.996	15.7	0.996	15.5	0.998	15.6
0.762	0.997	16.5	0.996	16.4	0.996	16.5	0.996	16.3	0.999	16.4
1.016	0.997	17.1	0.996	16.9	0.996	17.0	0.996	16.9	0.999	17.0
1.270	0.997	17.5	0.997	17.5	0.997	17.5	0.997	17.4	0.999	17.5
1.905	0.998	18.6	0.997	18.5	0.997	18.5	0.997	18.5	0.999	18.5
2.540	0.998	19.5	0.998	19.6	0.998	19.5	0.998	19.4	0.999	19.5
3.810	0.999	21.0	0.998	20.8	0.998	21.0	0.998	20.9	0.999	21.0
5.080	0.999	22.2	0.999	22.2	0.999	22.4	0.999	22.2	1.000	22.2
6.350	1.000	23.1	1.000	23.0	1.000	23.1	1.000	23.0	1.000	23.2
7.620	1.000	23.5	1.000	23.4	1.000	23.5	1.000	23.5	1.000	23.6
10.160	1.000	23.6	1.000	23.4	1.000	23.6	1.000	23.5	1.000	23.7
12.700	1.000	23.6	1.000	23.5	1.000	23.6	1.000	23.5	1.000	23.8

TABLE 7.3. CONTINUED

CORRECTED MEAN VELOCITY (M/S), UC - SENSORS A & B (AVERAGED)

Y	HX		VX		SX1		SX2		SINGLE FILM	
(CM)	UC/U	UC	UC/U	UC	UC/U	UC	UC/U	UC	UC/U	UC
0.127	0.996	13.4	0.993	13.3	0.995	13.6	0.994	13.3	0.998	13.4
0.190	0.996	14.1	0.994	13.9	0.995	14.1	0.995	13.9	0.998	14.0
0.254	0.996	14.5	0.994	14.3	0.995	14.5	0.995	14.3	0.998	14.5
0.508	0.997	15.6	0.995	15.6	0.996	15.7	0.996	15.5	0.998	15.6
0.762	0.997	16.4	0.996	16.4	0.996	16.5	0.996	16.3	0.999	16.4
1.016	0.997	17.0	0.996	16.9	0.996	17.0	0.997	16.9	0.999	17.0
1.270	0.997	17.5	0.997	17.5	0.997	17.5	0.997	17.4	0.999	17.5
1.905	0.998	18.6	0.997	18.5	0.997	18.5	0.997	18.4	0.999	18.5
2.540	0.998	19.5	0.998	19.6	0.998	19.5	0.998	19.4	0.999	19.5
3.810	0.999	21.0	0.998	20.8	0.998	21.0	0.999	20.9	0.999	21.0
5.080	0.999	22.2	0.999	22.2	0.999	22.3	0.999	22.2	1.000	22.2
6.350	1.000	23.1	1.000	23.0	1.000	23.1	1.000	23.1	1.000	23.2
7.620	1.000	23.5	1.000	23.4	1.000	23.5	1.000	23.5	1.000	23.6
10.160	1.000	23.6	1.000	23.4	1.000	23.5	1.000	23.6	1.000	23.7
12.700	1.000	23.6	1.000	23.5	1.000	23.6	1.000	23.6	1.000	23.8

ments but also establishes a high degree of credibility for the measurements themselves by the high level of repeatability that is shown.

Turbulence Corrections Using Hinze's Law

The effects of the turbulence on the magnitude of the mean velocity are shown in Tables 7.1-7.3 for stations (-3,0), (-3,-2) and (-7,-6) where the corrected and uncorrected velocities are compared for the individual sensors. The magnitude of the correction depends on the orientation of the sensor to the flow. The vx-array, being more sensitive to the generally larger $\overline{ww}$ intensities, required the largest correction, while the velocities measured by the hx-array and single film probe operating normal to the flow were least affected by these corrections. The remaining probe configurations required corrections that fell systematically between these two cases. These results show an effect of the turbulence on the x-array mean velocity measurements that decreases monotonically with increasing roll angle (γ_x) of the sensor plane. It must be emphasized that no generalization should be made here since turbulence corrections depend on the individual flow field.

Just upstream of the point of separation at station (-3,0) where the turbulence intensity level reached approximately 40% near the wall, the mean velocities were corrected by approximately 4, 3, and 2%, as shown in Table 7.1, for the vertical, slant, and horizontal x-array probes, respectively. At this same station, the correction for the single film velocities was only approximately 1%. The results in Table 7.3 for station (-7,-6) show the uncorrected velocities to lie within 1% of the corrected values for all the probes listed. For this station the

maximum turbulence intensity level (based on the local mean velocity) was of the order of 20%.

Turbulence Correction Using Davies and Bruun's Law

As noted earlier, Hinze's [54] cooling law was used in Eq. 4.48 to determine the corrected velocities given in Tables 7.1-7.3. In the sensor calibrations presented in Chapter V, the cooling laws suggested by Hinze [54] and Davies and Bruun [104] were tested. While both laws were expected to give consistent results, significant differences in the value of f" were found, which raised serious questions concerning the overall effect of these differences on the turbulence-related results. The differences in the turbulence correction, which involves f", between these two popular cooling laws, are shown in the corrected velocities at station (-3,0) in Table 7.4. Tables 7.1 with 7.4 show only small differences in the corrected velocities between the two laws, with Davies and Bruun's law giving slightly smaller corrections.

B. Edge Conditions and Wall Static Pressure Distribution

The edge condition for the standard test case flow was obtained in the freestream at the locations shown in Fig. 3.8. As described earlier, two complete sets of freestream data were taken. The freestream mean velocity results of magnitude and direction by the single film and by the Pitot static and 3-hole yaw probes are tabulated in Tables 7.5 and 7.6 where the mean velocity magnitudes are nondimensionalized by the tunnel inlet throat velocity, $\overline{U}_I$. The results show good agreement overall between the methods used. The uncertainty in the edge condition

TABLE 7.4. COMPARISON OF CORRECTED AND UNCORRECTED MEAN VELOCITIES AT STATION (-3,0) USING DAVIES AND BRUUN'S LAW (104)

CORRECTED MEAN VELOCITY (M/S), UC - SENSOR A

Y	HX		VX		SX1		SX2		SINGLE FILM	
(CM)	UC/U	UC	UC/U	UC	UC/U	UC	UC/U	UC	UC/U	UC
0.127	0.983	5.3	0.961	5.2	0.974	5.6	0.971	5.2	0.990	5.3
0.190	0.983	5.9	0.967	5.8	0.977	6.3	0.974	5.8	0.990	5.9
0.254	0.984	6.5	0.971	6.3	0.979	6.9	0.978	6.5	0.991	6.4
0.508	0.988	8.4	0.982	8.1	0.985	8.7	0.985	8.3	0.993	8.2
0.762	0.991	9.7	0.987	9.3	0.989	10.2	0.989	9.4	0.995	9.5
1.016	0.993	10.9	0.990	10.4	0.991	11.3	0.991	10.5	0.996	10.8
1.270	0.994	11.6	0.991	11.0	0.993	12.2	0.993	11.3	0.996	11.7
1.905	0.995	13.2	0.994	12.5	0.995	13.6	0.995	12.9	0.997	13.4
2.540	0.996	14.3	0.995	13.9	0.996	14.8	0.996	14.1	0.998	14.6
3.810	0.998	16.3	0.997	15.8	0.997	16.9	0.998	16.2	0.999	16.3
5.080	0.999	17.8	0.998	17.3	0.999	18.2	0.999	17.7	0.999	17.6
6.350	0.999	18.8	0.999	18.4	0.999	19.2	0.999	18.8	1.000	18.7
7.620	1.000	19.6	1.000	19.2	1.000	19.9	1.000	19.6	1.000	19.4
10.160	1.000	19.9	1.000	19.4	1.000	20.0	1.000	19.8	1.000	19.5
12.700	1.000	19.8	1.000	19.4	1.000	19.7	1.000	19.6	1.000	19.4

CORRECTED MEAN VELOCITY (M/S), UC - SENSOR B

Y	HX		VX		SX1		SX2		SINGLE FILM	
(CM)	UC/U	UC	UC/U	UC	UC/U	UC	UC/U	UC	UC/U	UC
0.127	0.986	5.8	0.961	5.2	0.978	6.0	0.975	5.7	0.990	5.3
0.190	0.986	6.4	0.966	5.8	0.980	6.6	0.978	6.2	0.990	5.9
0.254	0.987	7.1	0.970	6.3	0.981	7.1	0.981	6.9	0.991	6.4
0.508	0.990	8.8	0.981	8.1	0.986	8.7	0.987	8.7	0.993	8.2
0.762	0.991	10.1	0.987	9.4	0.989	10.0	0.990	9.8	0.995	9.5
1.016	0.993	11.2	0.990	10.4	0.991	11.0	0.992	10.9	0.996	10.8
1.270	0.994	11.7	0.991	11.0	0.993	11.6	0.993	11.5	0.996	11.7
1.905	0.995	13.4	0.994	12.5	0.994	13.0	0.995	13.3	0.997	13.4
2.540	0.996	14.4	0.995	13.9	0.996	14.1	0.996	14.4	0.998	14.6
3.810	0.998	16.4	0.997	15.8	0.997	16.2	0.998	16.5	0.999	16.3
5.080	0.999	17.8	0.998	17.3	0.998	17.7	0.999	17.9	0.999	17.6
6.350	0.999	18.8	0.999	18.4	0.999	18.7	0.999	18.9	1.000	18.7
7.620	1.000	19.5	1.000	19.2	1.000	19.3	1.000	19.5	1.000	19.4
10.160	1.000	19.8	1.000	19.5	1.000	19.7	1.000	19.6	1.000	19.5
12.700	1.000	19.6	1.000	19.4	1.000	19.7	1.000	19.5	1.000	19.4

TABLE 7.4. CONTINUED

CORRECTED MEAN VELOCITY (M/S), UC - SENSORS A & B (AVERAGED)

Y	HX		VX		SX1		SX2		SINGLE FILM	
(CM)	UC/U	UC	UC/U	UC	UC/U	UC	UC/U	UC	UC/U	UC
0.127	0.985	5.5	0.961	5.2	0.976	5.8	0.973	5.4	0.990	5.3
0.190	0.985	6.2	0.967	5.8	0.978	6.5	0.976	6.0	0.990	5.9
0.254	0.986	6.8	0.971	6.3	0.980	7.0	0.979	6.7	0.991	6.4
0.508	0.989	8.6	0.982	8.1	0.986	8.7	0.986	8.5	0.993	8.2
0.762	0.991	9.9	0.987	9.4	0.989	10.1	0.989	9.6	0.995	9.5
1.016	0.993	11.0	0.990	10.4	0.991	11.1	0.992	10.7	0.996	10.8
1.270	0.994	11.7	0.991	11.0	0.993	11.9	0.993	11.4	0.996	11.7
1.905	0.995	13.3	0.994	12.5	0.995	13.3	0.995	13.1	0.997	13.4
2.540	0.996	14.3	0.995	13.9	0.996	14.4	0.996	14.3	0.998	14.6
3.810	0.998	16.4	0.997	15.8	0.997	16.6	0.998	16.3	0.999	16.3
5.080	0.999	17.8	0.998	17.3	0.998	17.9	0.999	17.8	0.999	17.6
6.350	0.999	18.8	0.999	18.4	0.999	19.0	0.999	18.9	1.000	18.7
7.620	1.000	19.6	1.000	19.2	1.000	19.6	1.000	19.5	1.000	19.4
10.160	1.000	19.9	1.000	19.5	1.000	19.8	1.000	19.7	1.000	19.5
12.700	1.000	19.7	1.000	19.4	1.000	19.7	1.000	19.5	1.000	19.4

Table 7.5 Flow Angle (ω) Edge Conditions* for the Teardrop 3DTBL Flow Measured by a Single Hot Film Probe and a Standard 3-Hole Yaw Probe. $Re_{unit} = 1.34 \times 10^6\ m^{-1}$.

Station	Single Film (Deg)	3-Hole Probe (Deg)	Station	Single Film (Deg)	3-Hole Probe (Deg)
(-24,8)	(0.1)**		(-5,0)	0.1(0.1)	0.0
(-24,4)	(0.1)		(-5,-2)	2.2	2.2
(-24,0)	(0.2)		(-5,-4)	2.9	3.2
(-24,-4)	(0.1)		(-5,-6)	2.7	2.8
(-24,-8)	(0.2)		(-5,-8)	2.0	2.0
(-12,0)	0.1	0.2	(-5,-10)	1.5	1.6
(-12,-2)	0.2	0.4	(-3,0)	0.0(0.0)	0.0
(-12,-4)	0.4	0.4	(-3,-2)	5.9(5.8)	5.8
(-12,-6)	0.5	0.6	(-3,-4)	5.9(6.0)	5.8
(-12,-8)	0.5	0.6	(-3,-6)	4.0(4.3)	4.2
(-12,-10)	0.5	0.6	(-3,-8)	2.6(3.0)	2.6
(-9,0)	0.1	0.0	(-3,-10)	1.6	1.8
(-9,-2)	0.5	0.6	(-1,-6)	5.3	5.4
(-9,-4)	0.9	1.0	(-1,-8)	2.8	3.0
(-9,-6)	1.0	1.2	(-1,-10)	1.6	1.6
(-9,-8)	0.9	1.0	(1,-6)	4.3(4.5)	4.4
(-9,-10)	0.8	1.0	(1,-8)	2.1(2.4)	2.0
(-7,0)	0.0(0.4)	0.2	(1,-10)	1.2	1.2
(-7,-2)	1.1	1.2	(3,-6)	0.6(1.0)	0.6
(-7,-4)	1.7(2.1)	1.6	(3,-8)	0.5	0.6
(-7,-6)	1.8(2.0)	1.8	(3,-10)	0.3	0.4
(-7,-8)	1.4(2.0)	1.4	(5,-6)	-2.9(-2.6)	-2.8
(-7,-10)	1.1	1.2	(5,-8)	-1.2(-1.0)	-1.2
			(5,-10)	-0.6	-0.4

* Measured at y = 12.7 cm

** From 3DTBL mean velocity profiles measured with a single hot film probe.

Table 7.6 Mean Velocity Edge Condition* for the Teardrop 3DTBL Flow Measured by a Single Hot Film and a Standard Pitot Static Probe. $Re_{unit} = 1.34 \times 10^6\ m^{-1}$, $\overline{U}_I = 22.4\ ms^{-1}$.

Station	Single Film	Pitot Static Probe	Station	Single Film	Pitot Static Probe
(-24,8)	(1.08)**		(-5,0)	0.98(-.98)	0.99
(-24,4)	(1.07)		(-5,-2)	1.00	1.00
(-24,0)	(1.08)		(-5,-4)	1.04	1.03
(-24,-4)	(1.08)		(-5,-6)	1.07	1.05
(-24,-8)	(1.08)		(-5,-8)	1.08	1.07
(-12,0)	1.06	1.06	(-5,-10)	1.08	1.08
(-12,-2)	1.05	1.06	(-3,0)	0.89(-.86)	0.91
(-12,-4)	1.06	1.06	(-3,-2)	0.94(0.93)	0.95
(-12,-6)	1.06	1.06	(-3,-4)	1.02(1.02)	1.02
(-12,-8)	1.07	1.07	(-3,-6)	1.07(1.07)	1.06
(-12,-10)	1.07	1.07	(-3,-8)	1.09(1.10)	1.08
(-9,0)	1.04	1.05	(-3,-10)	1.10	1.09
(-9,-2)	1.04	1.05	(-1,-6)	1.12	1.10
(-9,-4)	1.05	1.05	(-1,-8)	1.12	1.10
(-9,-6)	1.06	1.06	(-1,-10)	1.11	1.10
(-9,-8)	1.07	1.07	(1,-6)	1.19(1.19)	1.16
(-9,-10)	1.07	1.07	(1,-8)	1.15(1.16)	1.13
(-7,0)	1.01(1.01)	1.02	(1,-10)	1.12	1.12
(-7,-2)	1.02	1.03	(3,-6)	1.23(1.22)	1.21
(-7,-4)	1.04	1.04	(3,-8)	1.16	1.15
(-7,-6)	1.06(1.06)	1.06	(3,-10)	1.14	1.13
(-7,-8)	1.07(1.06)	1.07	(5,-6)	1.20(1.18)	1.19
(-7,10)	1.08	1.08	(5,-8)	1.15(1.16)	1.15
			(5,-10)	1.13	1.13

* $\overline{U}_{FS}$ measured at y = 12.7 cm and nondimensionalized by the tunnel inlet throat velocity, $\overline{U}_I$.

** From 3DTBL mean velocity profiles measured with a single hot film probe.

was estimated at ± 0.5° for the flow angle measurements and ± 0.5% for the mean velocity magnitudes. For comparison, the freestream measurements made at the end of each single film mean velocity traverses are included. These mean velocity profiles were obtained before any other profiles were taken and the two sets of edge condition data were taken after all the 3DTBL profiles were measured. The agreement shown between the edge conditions obtain at the beginning and at the end of the experiment suggests stable and repeatable tunnel flow conditions. The symmetry of the freestream flow is shown in Table 7.7. The small variations in these results are within the range of experimental uncertainty.

The wall static pressure field results are presented in Appendix H. Table H1 lists pressure coefficients defined by

$$C_p = \frac{p - p_{ATM}}{\frac{1}{2} \rho \overline{U}_I^2} \tag{7.6}$$

where p is the local wall static pressure and p_{ATM} is the barometric pressure. The C_p results tabulated in Appendix H were used by McAllister [27] to obtain the wall static pressure gradient map in the forward half of the teardrop 3DTBL flow. Wall static pressure measurements were taken on a 1.27 cm (0.5 in.) grid which spanned ± 25.4 cm (± 10 in.) laterally from the plane of symmetry, beginning 17.78 cm (7 in.) upstream of the body, and extending 30.48 cm (12 in.) longitudinally to 12.7 cm (5 in.) downstream of the body's leading edge. Figure H1, taken from McAllister, shows these wall static pressure gradient results. In this figure floor stations were designated by a letter-number pair.

Table 7.7 Symmetry in Edge Condition of the Teardrop Flow Measured by a Single Hot Film Probe. $Re_{unit} = 1.34 \times 10^6\ m^{-1}$, $\overline{U}_I = 22.7\ ms^{-1}$.

Station	$\overline{U}_{FS}/\overline{U}_I$	ω, deg.
(-3,-4)	1.02	5.9
(-3,4)	1.02	-5.3
(-7,-4)	1.04	1.7
(-7,4)	1.03	-1.1
(1,-6)	1.19	4.3
(1,6)	1.18	-3.7
(5,-6)	1.20	-2.9
(5,6)	1.19	3.0
(-3,-8)	1.09	2.6
(-3,8)	1.09	-2.3
(7,-8)	1.07	1.4
(-7,8)	1.06	-1.3

Letters beginning with A on the centerline of the body, corresponded to columns at one-inch intervals towards the right of the centerline when looking upstream as shown in Fig. H1. The numbers represented the distance in inches along a column, measured positive upstream of the body's leading edge beginning with zero at the leading edge. Negative numbers indicated stations downstream of the leading edge. Thus, stations C3 and G7 in Fig. H1 correspond to stations (-3,-2) and (-7,-6), respectively in Fig. 3.9.

The wall static pressure field as reported by McAllister [27] in Fig. H1 should be viewed with some caution when used with the results of this study. This is due to a small amount of transverse positioning of the body that was necessary to accommodate the wide range of wall static pressure data stations required for his study. The transverse body displacement for these wall static pressure measurements was much less than that required for McAllister's direct force wall shear measurements. McAllister's results show very good symmetry in the pressure gradient field and this is taken as a good indication that the overall wall static pressure field was not strongly affected by this modest transverse body displacement. The results in Fig. H1 shows only modest differences in the pressure gradient field at the extreme stations furthest from the body. Some comparisons between McAllister's wall static pressure results and the Preston tube static pressures could be made at a few stations. At these stations, the results showed agreement generally to within ± 1%. Since no transverse body positioning was necessary for this study, this agreement further suggests that

McAllister's small transverse body displacement did not significantly affect the wall static pressure at the stations compared.

C. Wall Shear Stress Distribution

The wall shear stress measurements by the Preston tube were taken the floor stations shown in Fig. 3.9. The results are tabulated in Table 7.8 as skin friction coefficients where

$$C_f = \frac{\tau_w}{\frac{1}{2} \rho \bar{U}_{FS}^2} . \qquad (7.7)$$

While it is universal practice to nondimensionalize the wall shear stress using a freestream mean velocity in two-dimensional flows, it is also common to extend this practice in three-dimensional flows as well. One should recognize the differences in this nondimensional form for these two cases since, unlike typical two-dimensional flows, the freestream direction in a three-dimensional flow can be skewed relative to the wall shear direction. In particular, Eq. 7.7 does not assume collateral wall shear and freestream mean velocity vectors.

The wall shear stress magnitudes were obtained from Patel's (1965) calibration equations.

$$y^* = 0.5x^* + 0.037 , \qquad x^* < 2.9 , \qquad (7.8)$$

$$y^* = 0.8287 - 0.1381\, x^* + 0.1437\, x^{*2} - 0.006\, x^{*3} , \qquad 2.9 \leq x^* < 5.60 , \qquad (7.9)$$

Table 7.8 Flow Conditions, Skin Friction Coefficients, and Limiting Wall Streamline and Freestream Field Results for the Teardrop 3DTBL Flow

Station	Re_{unit}	ν	ρ	$\overline{U}_{FS}$	ω	$C_f^{(1)}$	$(\beta_w + \omega)^{(2)}$	$(\beta_1 + \omega)^{(3)}$
	$(m^{-1}x10^{-6})$	$(m^2s^{-1}x10^5)$	(kgm^{-3})	(ms^{-1})	(Deg)	$(x10^3)$	(Deg)	(Deg)
(-24,8)	1.34	1.67	1.10	24.1	0.1			0.1
(-24,4)	1.34	1.67	1.10	24.0	0.1			0.3
(-24,0)	1.34	1.67	1.10	24.1	0.2			-0.2
(-24,-4)	1.34	1.67	1.10	24.1	0.1			-0.2
(-24,-8)	1.34	1.67	1.10	24.1	0.2			-0.2
(-7,0)	1.34	1.67	1.10	22.5	0.4	1.94	0.5	-0.4
(-5,0)	1.34	1.66	1.11	21.7	0.1	1.54		0.5
(-3,0)	1.34	1.68	1.10	19.4	0.0	0.71		1.3
(-3,-2)	1.34	1.68	1.10	21.0	5.8	1.57	47.0	30.0
(-7,-4)	1.34	1.68	1.10	23.1	2.1	2.19	10.0	7.6
(-3,-4)	1.34	1.68	1.10	23.0	6.0	2.37	31.5	22.6
(-7,-6)	1.34	1.68	1.10	23.8	2.0	2.36	10.5	6.5
(-3,-6)	1.34	1.67	1.10	23.9	4.3	2.58	16.5	14.1
(1,-6)	1.34	1.67	1.10	26.7	4.5	3.19	5.5	12.1
(3,-6)	1.34	1.68	1.10	27.5	1.0	3.13	-4.0	4.0
(5,-6)	1.34	1.67	1.10	26.5	-2.6	2.58	-10.5	-3.7
(-7,-8)	1.34	1.68	1.10	23.9	2.0	2.42	7.0	6.1
(-3,-8)	1.34	1.67	1.10	24.6	3.0	2.62	9.0	8.9
(1,-8)	1.34	1.67	1.10	25.9	2.4	2.90	4.0	5.8
(5,-8)	1.34	1.67	1.10	26.0	-1.0	2.72	-7.0	-3.0

(1) Measured with a 0.457 mm (0.018 in.) OD Preston Tube.
(2) β_w obtained from oil streak wall flow visualizations [125].
(3) β_1 measured at y = 0.508 mm by a single hot film probe.

$$x^* = y^* + 2 \log_{10}(1.95\, y^* + 4.10), \quad 5.6 \leq x^* < 7.6 , \qquad (7.10)$$

where

$$x^* = \log_{10} \left(\frac{\Delta P\, D^2}{4\, \rho\, \nu^2}\right)$$

$$y^* = \log_{10} \left(\frac{\tau_w\, D^2}{4\, \rho\, \nu^2}\right)$$

ΔP = Dynamic Pressure = $P_o - P$

D = Preston Tube Outer Diameter.

The variables x^* and y^* are not to be confused with the x and y directions of the local streamline coordinate system described in Chapter IV. For this study the values of x^* fell within the range identified with Eq. 7.9.

The Preston tube arrangement used in measuring wall shear stress magnitudes was described in Chapter III. The two static pressure taps located 0.635 and 1.27 cm (0.25 and 0.50 in.) to the left of the tube opening, when looking downstream, allowed for a correction of the static pressure to account for the cross-stream pressure gradients. The dynamic pressure at the tube opening was calculated using a first order Taylor series approximation,

$$\Delta P = (P_o - P_{1/4}) + (P_{1/2} - P_{1/4}) \qquad (7.11)$$

where $P_{1/4}$ and $P_{1/2}$ were the static pressures measured 1/4 and 1/2 inches, respectively, from the tube opening. Table 7.9 shows the wall shear stress results with and without the pressure gradient correction. The corrected wall shear values were usually within 4% of the uncorrected values. However, as might be expected, larger corrections were required at floor stations closer to the body and the junction vortex. An extreme case is shown at station (-3,-2) where the wall shear stress was changed approximately 13% by the correction. The largest correction, of the order of 20%, is shown at station (-3,0) which was believed to lie within 1 cm of the nominal flow separation line as seen in wall flow visualizations. At the floor stations upstream of the transverse plane, x_1 = 2.54 cm (-1 in.), the results show lower corrected magnitudes of the wall shear stress. This appears to be consistent with the rising transverse pressure toward the center-line of the body, as shown in Fig. H1, and would tend to give a lower dynamic pressure reading at the Preston tube opening. Downstream of this plane, where the transverse pressure gradient changes direction, the corrected values are higher indicating a rising transverse pressure outward from the body.

The local wall shear stress directions were taken from an oil streak limiting wall streamline pattern and are tabulated in Table 7.8. These are the same oil streak directions reported by Pierce and McAllister [125] which were compared to direct force wall shear directions. Their results showed excellent agreement between the two methods.

Table 7.9 A Comparison of Wall Shear Stress Measurements by the Omnidirectional Wall Shear Meter and a 0.457 mm OD Preston Tube at a Nominal $Re_{unit} = 1.34 \times 10^6\ m^{-1}$

Station	Wall Shear Meter [27] (Pa)	Preston Tube (Pa)	Preston Tube (corrected) (Pa)
(-7,0)	0.56	0.56(0.55)*	0.55(0.54)
(-5,0)	0.40	0.42(0.42)	(0.41)
(-3,0)	0.07	0.20(0.20)	(0.16)
(-3,-2)	0.51	0.47	0.41
(-7,-4)	0.63	0.66(0.67)	0.65(0.65)
(-3,-4)	0.76	0.73(0.71)	0.70(0.68)
(-7,-6)	0.73	0.74	0.73
(-3,-6)	0.87	0.83(0.83)	0.82(0.83)
(1,-6)	1.20	1.17	1.21
(3,-6)	1.28	1.19(1.21)	1.24(1.26)
(5,-6)	1.11	0.96(0.96)	1.00(1.00)
(-7,-8)	0.78	0.77	0.77
(-3,-8)	0.88	0.86	0.86
(1,-8)	1.04	1.02	1.04
(5,-8)	0.99	0.97	0.99

* ( ) Repeated measurements.

The wall shear measurement was assumed to occur at the center of the Preston tube. The Preston tube was aligned with the velocity direction that one could identify with the vertical displacement equal to the radius of the tube. This direction was found by a linear interpolation between the oil streak limiting wall streamline direction and the measured flow direction nearest to the wall.

As shown in Table 7.8, the nearest wall velocity direction can differ significantly from the local oil streak or wall shear stress direction. These results are consistent with those of Pierce and McAllister [27,125], and indicate that the velocity vector generally changes direction continuously to the wall in a pressure-driven flow.

While it has been common practice to infer wall shear stress magnitudes in 3D flows from indirect devices that use 2D calibrations, such as given by Eqs. 7.8-7.10, it is only recently that any quantitative support for this approach has been provided. As discussed earlier, Pierce and McAllister's [27,125] results indicated that for modestly skewed flows, the combination of an indirect device, such as a Preston tube, and a proven wall flow visualization technique to indicate the limiting wall streamline direction, could do an adequate job of mapping the wall shear field. The excellent agreement between both the direct force wall shear directions and the oil streak directions of Pierce and McAllister given in Table 7.8 established a high credibility to the oil stream method for determining the local wall shear directions.

The Preston tube, being relatively poor in sensing flow direction, could not do an adequate job of measuring these wall shear directions. However, this feature is desirable since it allows a wider margin of

error for aligning the tube to the limiting wall flow directions. This latitude in positioning the tube was expected to substantially reduce the stress magnitude errors associated with small amounts of tube misalignment from the local wall flow direction. Table 7.10 shows some yaw sensitivity results of the 0.457 mm (0.018 in.) OD Preston tube that were obtained at station (-3,-2) in close proximity to the separated region and where a substantial cross-stream pressure gradient was found. Both the corrected and uncorrected values of C_f are shown in these results which, as noted earlier, differ by approximately 13% at this particular station. Prior to correction, the results show a monotone increasing and decreasing asymmetric variation about the aligned position. This amounts to a 2-5% error in C_f for a $\pm$ 2.5^o tube misalignment. The corrected C_f results indicate similiar errors for a $\pm$ 2.5^o tube misalignment. Assuming that the yaw sensitivity of the Preston was in fact symmetric, one could identify the asymmetric behavior in the uncorrected data with the relatively large cross-stream pressure gradient that were present at station (-3,-2). Support for the claim is provided by the C_f results, corrected by Eq. 7.11, which gives a nearly symmetric tube sensitivity for the range of yaw angles considered. In view of the relatively large cross-stream pressure gradient occuring at this floor station, the results also suggest that the first order static pressure corrections using Eq. 7.11 adequately accounted for the effects of these pressure gradients on the Preston tube measurements.

Comparisons with Earlier Work

Table 7.9 also compares Pierce and McAllister's [27,125] direct

Table 7.10 Yaw Angle Sensitivity of a 0.457 mm (0.018 in.) OD Preston Tube Showing the Effect of Large Cross-Stream Pressure Gradient Correction

Yaw Angle (Deg)	$C_f x 10^3$	$C_f x 10^3$ (Corrected)
10.0	1.79	1.54
5.0	1.82	1.57
2.5	1.89	1.64
0.0	1.81	1.57
-2.5	1.85	1.63
-5.0	1.80	1.56
-10.0	1.74	1.53

force wall shear magnitudes with the Preston tube results of this study. The uncorrected wall shear values fall generally within 10% of the direct force measurements while the corrected measurements gave somewhat better agreement, being within 8% of the direct force measurements. The largest differences occur at stations (-3,-2), (-3,0) and (5,-6) which probably indicate the effect of the junction vortex region on the wall shear measurements. The repeated wall shear measurements are also shown in Table 7.9. Seven of the 8 repeated measurements show repeatability to within 2% with the remaining measurement repeatable to within approximately 3% at station (-3,-4). The uncertainties in the Preston tube measurements in two-dimensional flows have been addressed in the near-wall similarity studies of Pierce and McAllister.

The direct force wall shear results of Pierce and McAllister [27,125] shown in Table 7.9 should be used with caution with the results of this study due to the different methods used in positioning the body in the tunnel. As noted in Chapter III, the difficulties in obtaining direct-force wall shear measurements made it necessary to make all measurements at a fixed floor station with the body positioned relative to this station. Each velocity profile was taken with a claw probe over the local wall shear station ensuring self-consistent profiles as required for near wall similarity studies. The differences in the methods used in positioning the body between the earlier near-wall studies and the present study amounted to a maximum 20.32 cm (8 in.) transverse displacement of the body from the tunnel centerline in the former study, with no such transverse motion required of the body in the present study. The reasonably good agreement in the direct force and Preston

tube measurements shown in Table 7.9 suggests no apparent large effects from these transverse displacements of the body on the wall shear stress distribution. Even at the outermost stations where the body was located 20.32 cm (8 in.) from the tunnel centerline for the direct force measurements, good agreement between the former shear meter and current Preston tube measurements is shown.

Figures 7.23a and 7.23b compares some mean velocity results of the present study with those reported by McAllister [27]. The results are shown at stations (-3,-2) and (-7,-8) where the data was obtained using both methods of positioning the body namely, with and without a transverse body displacement from the tunnel centerline. In addition, a single film traverse is compared to that of a claw probe at station (-7,-8) in the standard test case flow where the body remained on the tunnel centerline. The results show good agreement in the mean velocity magnitude and direction when the same method was used to position the body. The single film and claw probe profiles, compared for this study, are also in good agreement.

It appears however, that the lateral displacement of the body does change the 3DTBL velocity field to some degree. The results indicate an approximately 4-5% difference in the profiles at stations (-3,-2) and (-7,-8) with transverse body movement. From these comparisons it appears that the body positioning method used by Pierce and McAllister [27,125) had a lesser effect on the wall shear stress field than on the local mean velocity field. It would appear that Pierce and McAllister's wall shear stress values can be used with the present flow field with a modest increase in uncertaintly as suggested in Table 7.9.

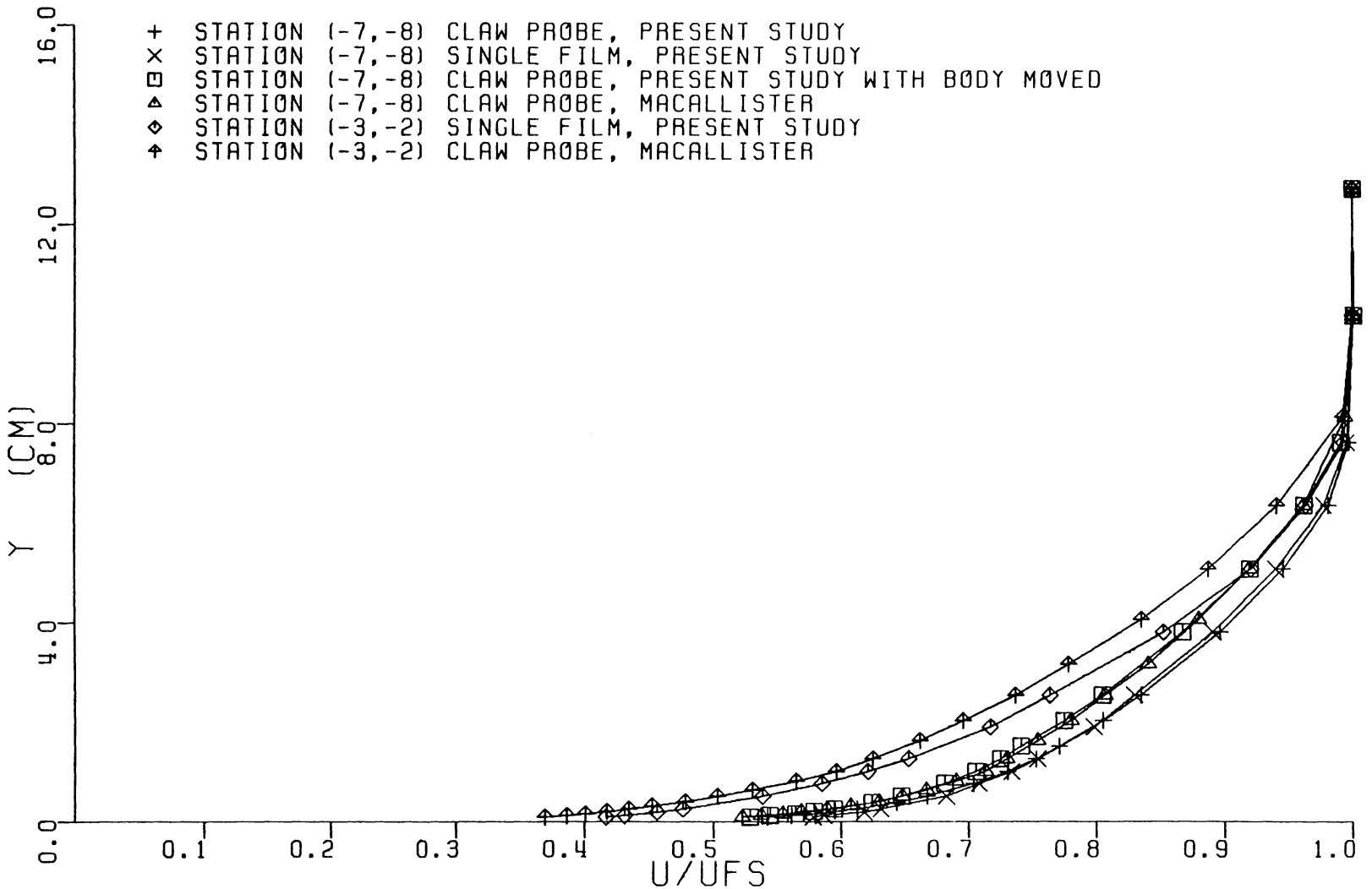

FIGURE 7.23A.COMPARISON OF MEAN VELOCITY MAGNITUDE WITH MCALLISTER'S(27) RESULTS

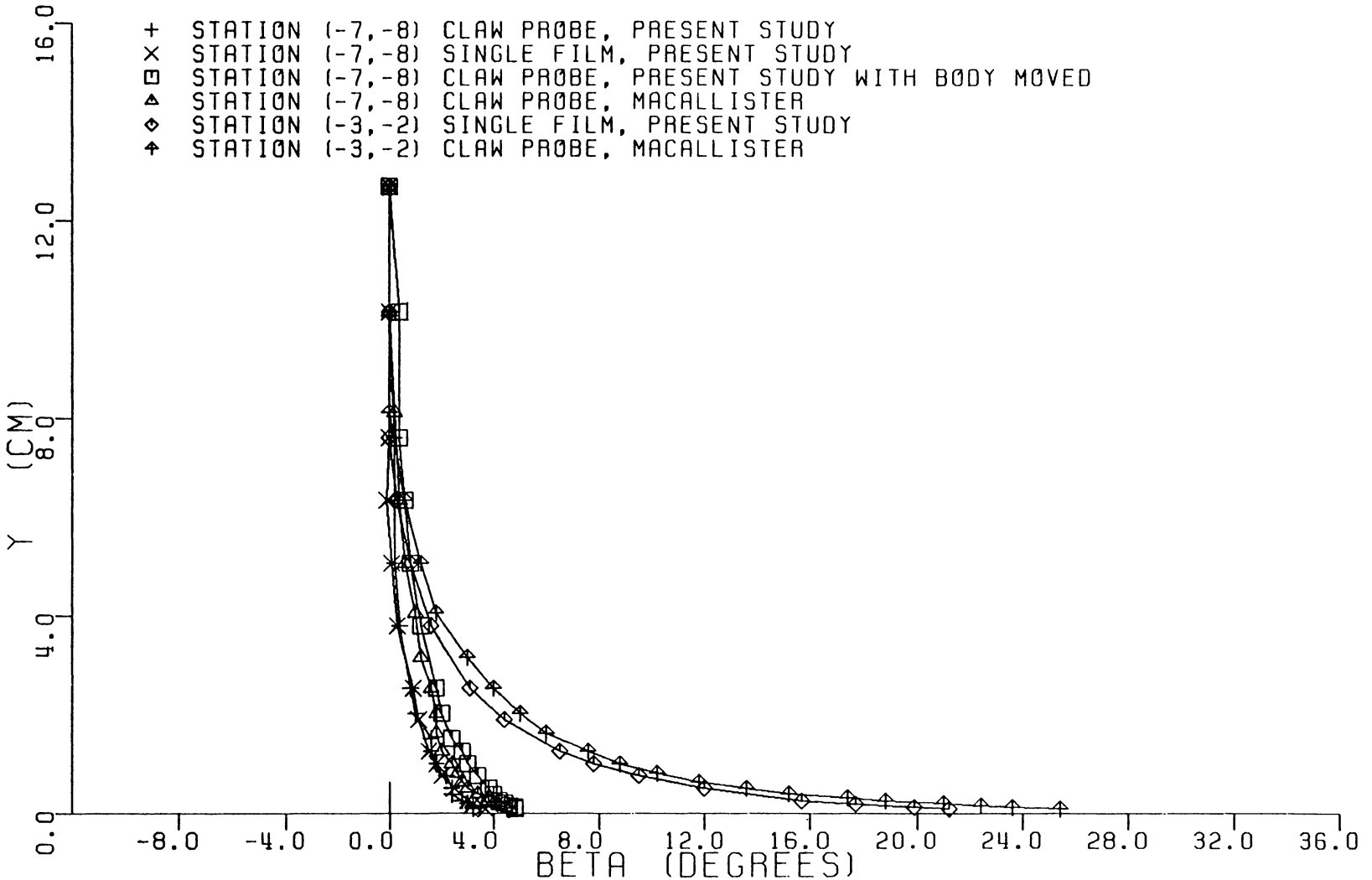

FIGURE 7.23B.COMPARISON OF MEAN VELOCITY DIRECTION WITH MCALLISTER'S(27) RESULTS

The 3DTBL mean flow, as characterized by the results presented, develops from a collateral nominally 2D upstream flow as a result of the curvature of the freestream streamlines. The collateral character of the flow quickly changes when significant curvature of the freestream streamlines begins. The 3DTBL flow is characterized by a turning of the local velocity vectors within the boundary layer. Approximately 6.4 cm (2.5 in.) downstream of the body's leading edge, the freestream flow appears to experience an inflection in response to the contour of the body as the body tapers, and this appears to initiate the small bilateral skewing of the inner layers reported earlier. In addition to skewing of the boundary layer, the blockage effect of the body standing on the wall results in steep adverse pressure gradients along the plane of symmetry. The boundary layer progresses into this region of adverse pressure gradient as it approaches the leading edge of the body resulting in flow separation ahead of the leading edge and a junction vortex which wraps itself around the body. The characteristics of this separation vortex and freestream flow in close proximity of the body are presently being studied in further work in this complex 3D turbulent flow.

D. Turbulence Results

Preliminary Remarks

The Reynolds stress results are shown in Figs. 7.24-7.34. At each floor station, the complete stress tensor is presented in the laboratory $x_1x_2x_3$ coordinate system, nondimensionalized by the local freestream velocity. The different probes that measured the turbulent stresses

usually gave slightly different magnitudes of the local mean velocity. For consistency, the local freestream velocity measured by the single film probe was used to nondimensionalize the Reynolds stresses.

Generally, it was not possible to obtain the single film and x-array data simultaneously and hence, in nondimensionalizing the Reynolds stresses, it was necessary to correct the single film data to the x-array measuring conditions to account for typical day to day variations in the fluid properties. Since similitude of the tunnel flow conditions was maintained by holding the unit Reynolds number constant at the tunnel inlet, one could correct the single film local freestream velocity measurements to the turbulent stress measuring conditions by assuming similitude and using the unit Reynolds number

$$\frac{\overline{U}_{FS,F}}{\nu_F} = \frac{\overline{U}_{FS,X}}{\nu_X}$$

where $\overline{U}_{FS,F}$ is the local freestream velocity measured by the single film in the flow having kinematic viscosity ν_F and $\overline{U}_{FS,X}$ is the local freestream velocity that would have been measured by the single film under given x-array measuring conditions namely, in the flow with kinematic viscosity ν_X. The corrected ratio of turbulent stress to local freestream velocity was obtained by

$$\frac{\overline{u_i u_j}}{\overline{U}_{FS,X}} = \frac{\overline{u_i u_j}}{\overline{U}_{FS,F}} \left(\frac{\nu_F}{\nu_S}\right)^2 , \quad i,j = 1, 2, 3 . \tag{7.12}$$

The variations in the kinematic viscosity of the fluid were generally within ± 0.5%. These small variations in the kinematic viscosity usu-

ally resulted in small changes in the corrected turbulent stress ratios. It is noted however, that the correction was more important for the nondimensionalized $\overline{vw}$ stress which in some cases was changed by as much as 10%. This was due to the data reduction procedure where the $\overline{vw}$ stress was calculated from two separate sx-array traverses. While corrections to the individual sx-array traverse results were of the order of those for the other x-probes, the $\overline{vw}$ stress required differences in these sx-array results. This increased the effect of the small sx-array changes in the calculated $\overline{vw}$ values.

The turbulence measurements were made using a linearized bridge output for each channel. The linearizers were adjusted to give equal slopes of the sensors calibration curves resulting in a 'quasi-matched' sensor condition as defined in Chapter IV. The measurements were made in the sensor xyz coordinate system aligned to the local flow yaw direction as shown in Fig. 3.14. For negligible amounts of $\overline{V}$ (or $\overline{U}_2$) components of velocity, the sensor coordinate system can be viewed as the local streamline system.

Results are tabulated in Appendix G in both the sensor xyz system and the laboratory $x_1x_2x_3$ system. The xyz and $x_1x_2x_3$ systems were related through the yaw angles β and ω defined in Fig. 3.3. The stress tensors in the xyz system were transformed to the $x_1x_2x_3$ system by the tensor transformation equations given by Eq. 4.17 with $x_1x_2x_3$ replacing $x^*y^*z^*$, $\overline{\psi}^*_z = 0$, and the angle sum $(\beta + \omega)$ used in place of $\overline{\psi}_y$.

In the standard test case results tabulated in Appendix G, the mean velocities measured by the single film are listed with the $\overline{uu}$, $\overline{uw}$, and $\overline{ww}$ stresses by the hx-array, the $\overline{uv}$ and $\overline{vv}$ stresses by

the vx-array and the $\overline{vw}$ stresses taken from the sx-array. The stress data measured by the hx- and vx-arrays were reduced using the general form of the response equations given in Eq. 4.81 and 4.107 where no matched sensor assumption was made. Equation 4.140 was used to calculate the $\overline{vw}$ stresses. As discussed in Chapter IV, matched sensors were necessary for obtaining this shear stress from the sx-array traverses. Since the sensors were quasi-matched, the strength of this assumption depended on the magnitude of the probe asymmetries found in the sensor's yaw characteristics that were inherent in the probe. Differences in the sensors' yaw parameters and the small differences that may have resulted after curve fitting the sensors' velocity calibration data were treated arithmetically by using average values for B, f, and f' in Eq. 4.140. Hinze's [54] cooling law was used in the response equations given above where the small amounts of $\overline{V}$ velocity components in the flow were taken into account.

Reynolds Stress Tensor Results

The Reynolds stress tensor results on the initial condition plane are shown in Fig. 7.24. The Reynolds stress profiles across this plane are reasonably uniform overall indicating a ±5% nonuniformity about the mean values. Since transverse variations in the turbulent stresses in a nominally 2D flow are generally not reported, it is difficult to compare these nonuniformities with other experimental results.

As was the case in the transverse nonuniformities in mean velocity reported earlier, the variations in the Reynolds stresses shown in Fig. 7.24 were identified with the small variations in the nominally 2D

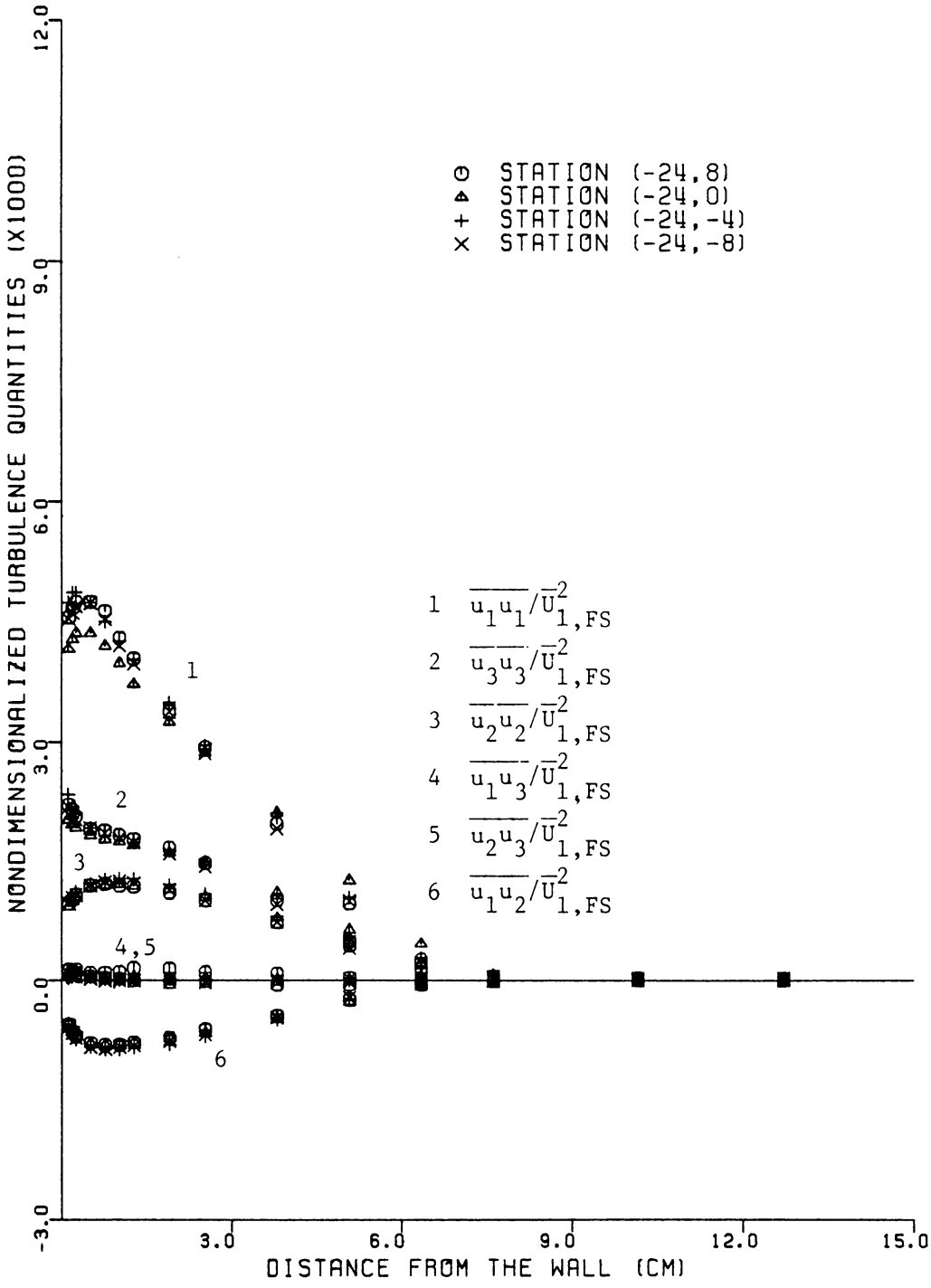

FIGURE 7.24. REYNOLDS STRESS TENSOR ALONG THE INITIAL CONDITION PLANE

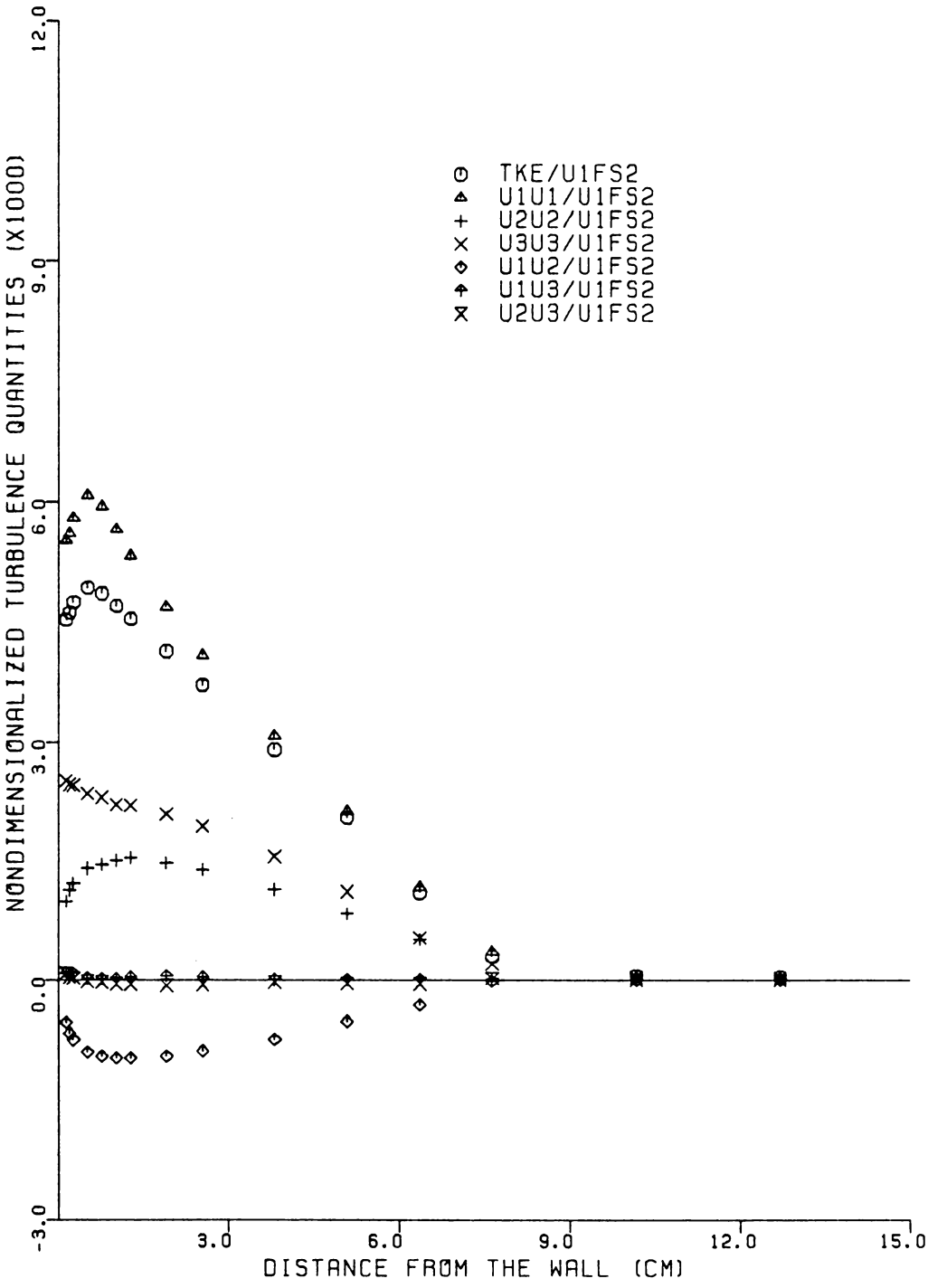

FIGURE 7.25. REYNOLDS STRESS TENSOR AND TURBULENT KINETIC ENERGY AT STATION (-7,0)

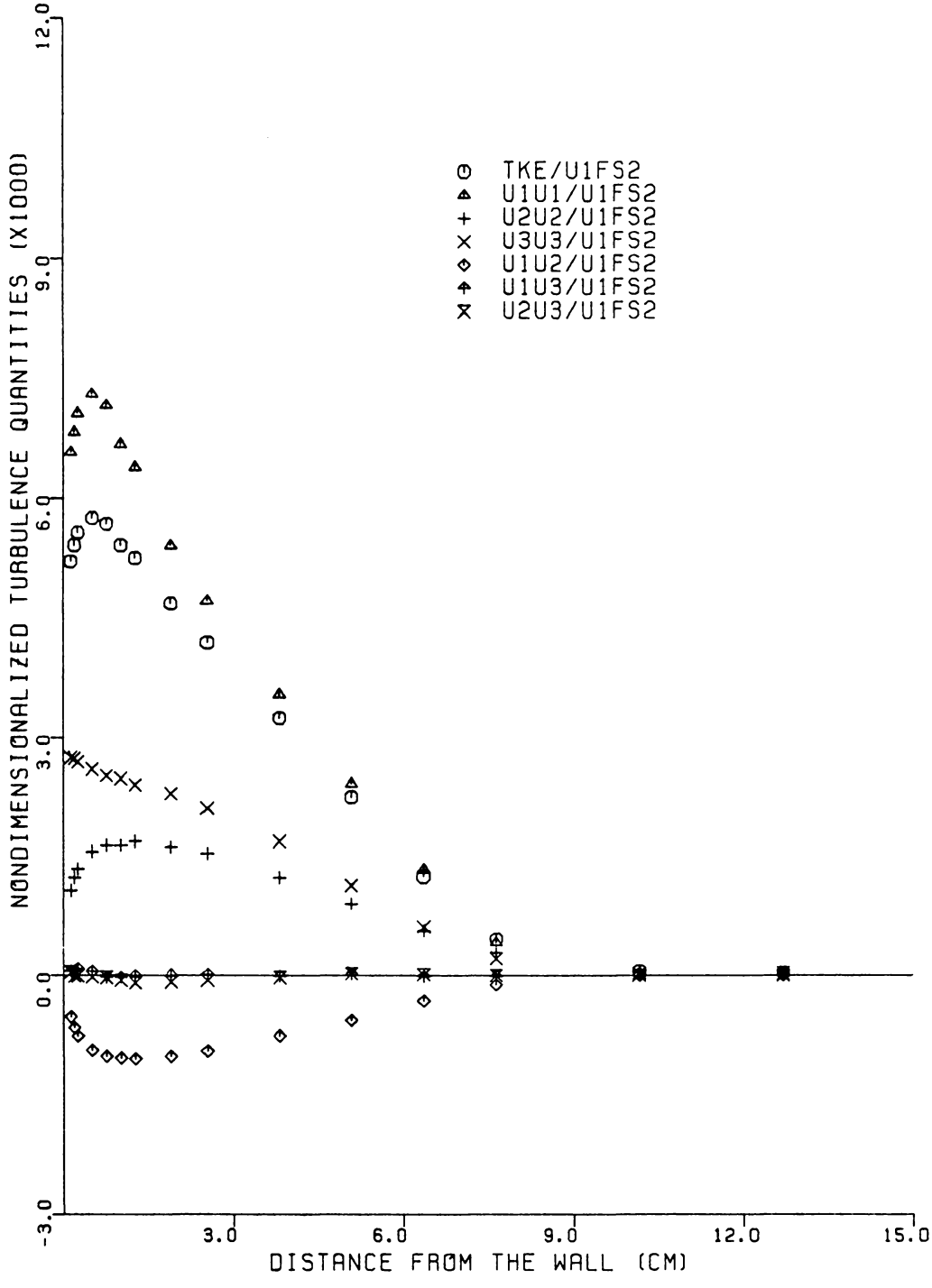

FIGURE 7.26. REYNOLDS STRESS TENSOR AND TURBULENT KINETIC ENERGY AT STATION (-5,0)

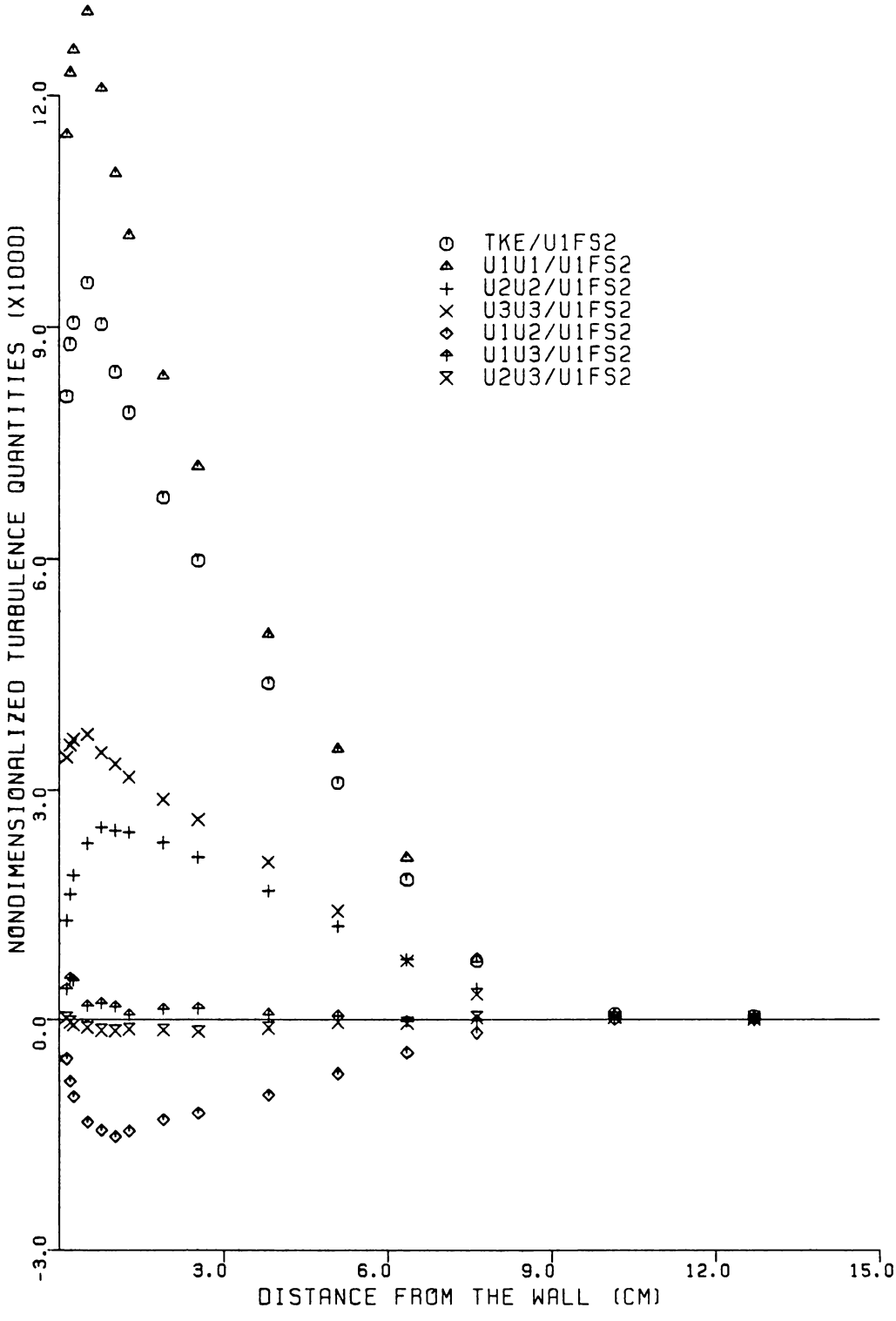

FIGURE 7.27. REYNOLDS STRESS TENSOR AND TURBULENT KINETIC ENERGY AT STATION (-3,0)

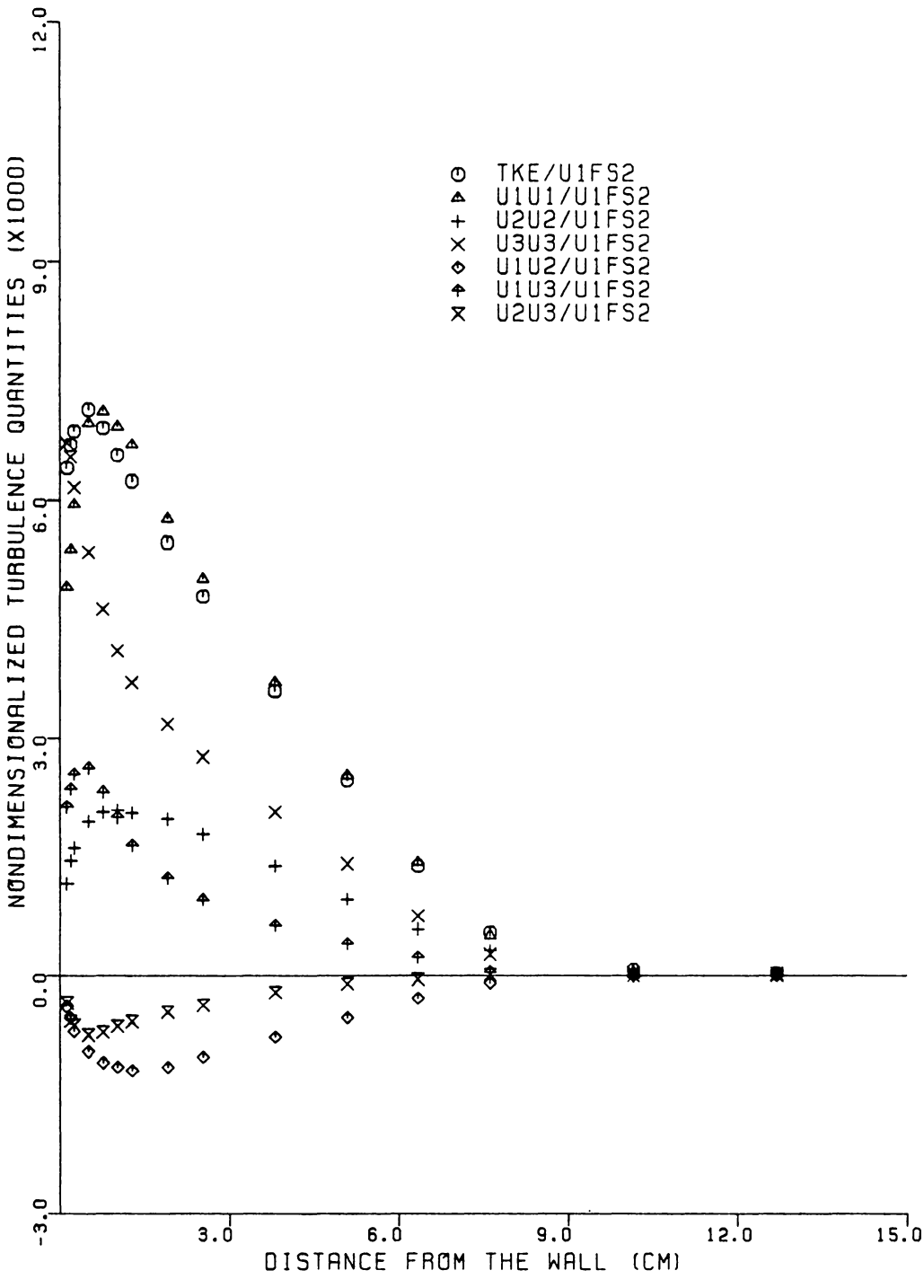

FIGURE 7.28. REYNOLDS STRESS TENSOR AND TURBULENT KINETIC ENERGY AT STATION (-3,-2)

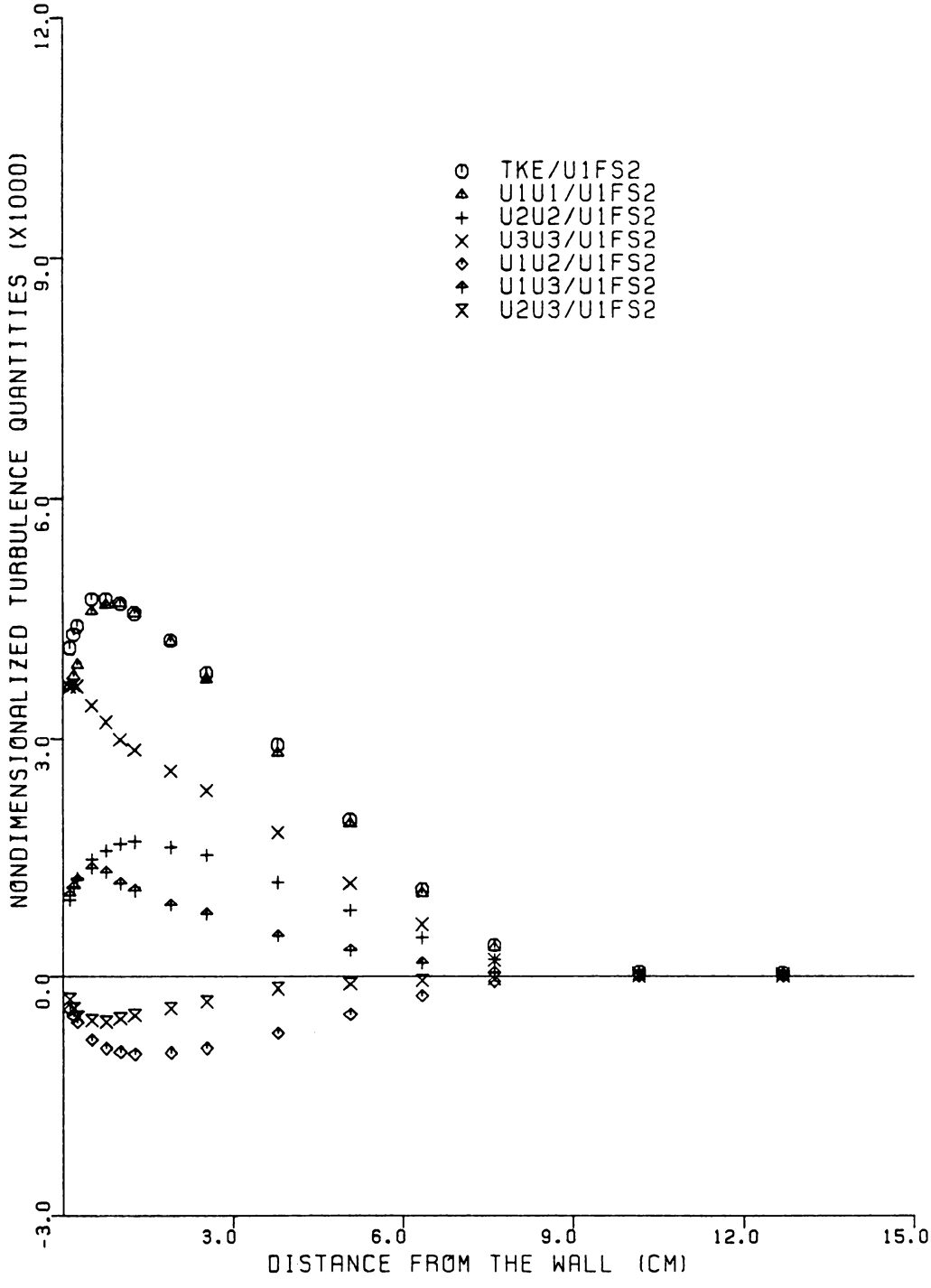

FIGURE 7.29. REYNOLDS STRESS TENSOR AND TURBULENT KINETIC ENERGY AT STATION (-3,-4)

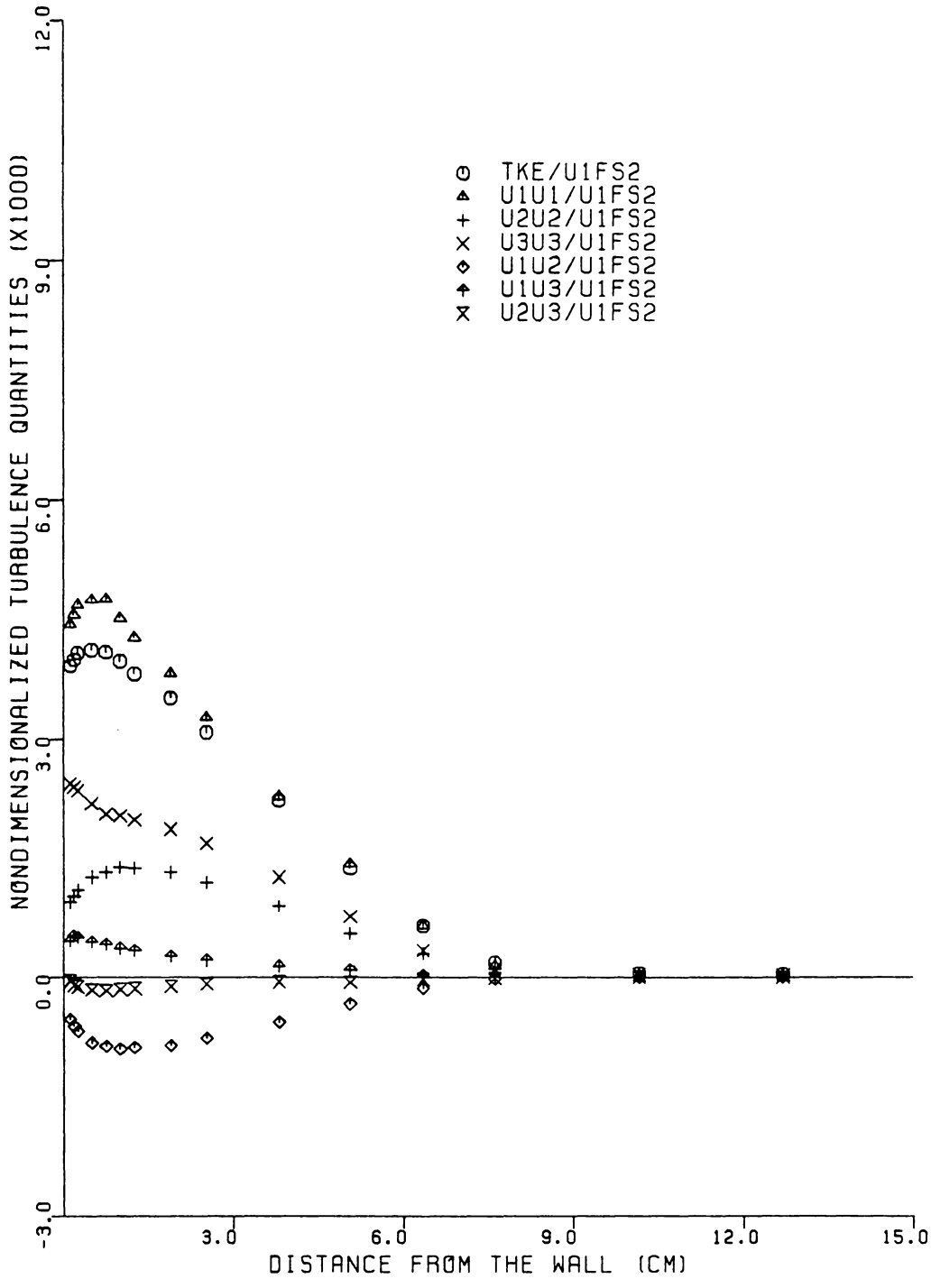

FIGURE 7.30. REYNOLDS STRESS TENSOR AND TURBULENT KINETIC ENERGY AT STATION (-7,-6)

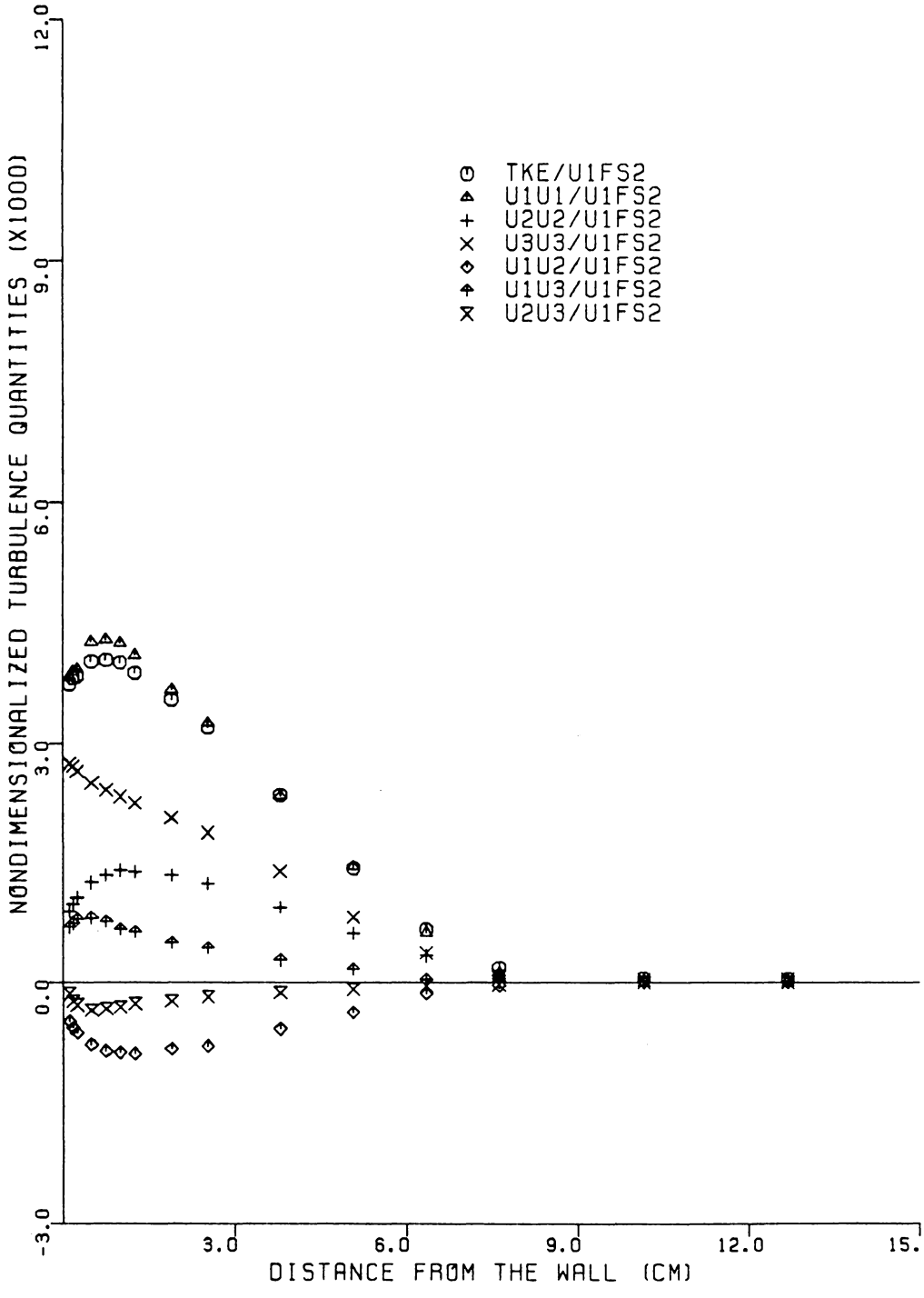

FIGURE 7.31. REYNOLDS STRESS TENSOR AND TURBULENT KINETIC ENERGY AT STATION (-3,-6)

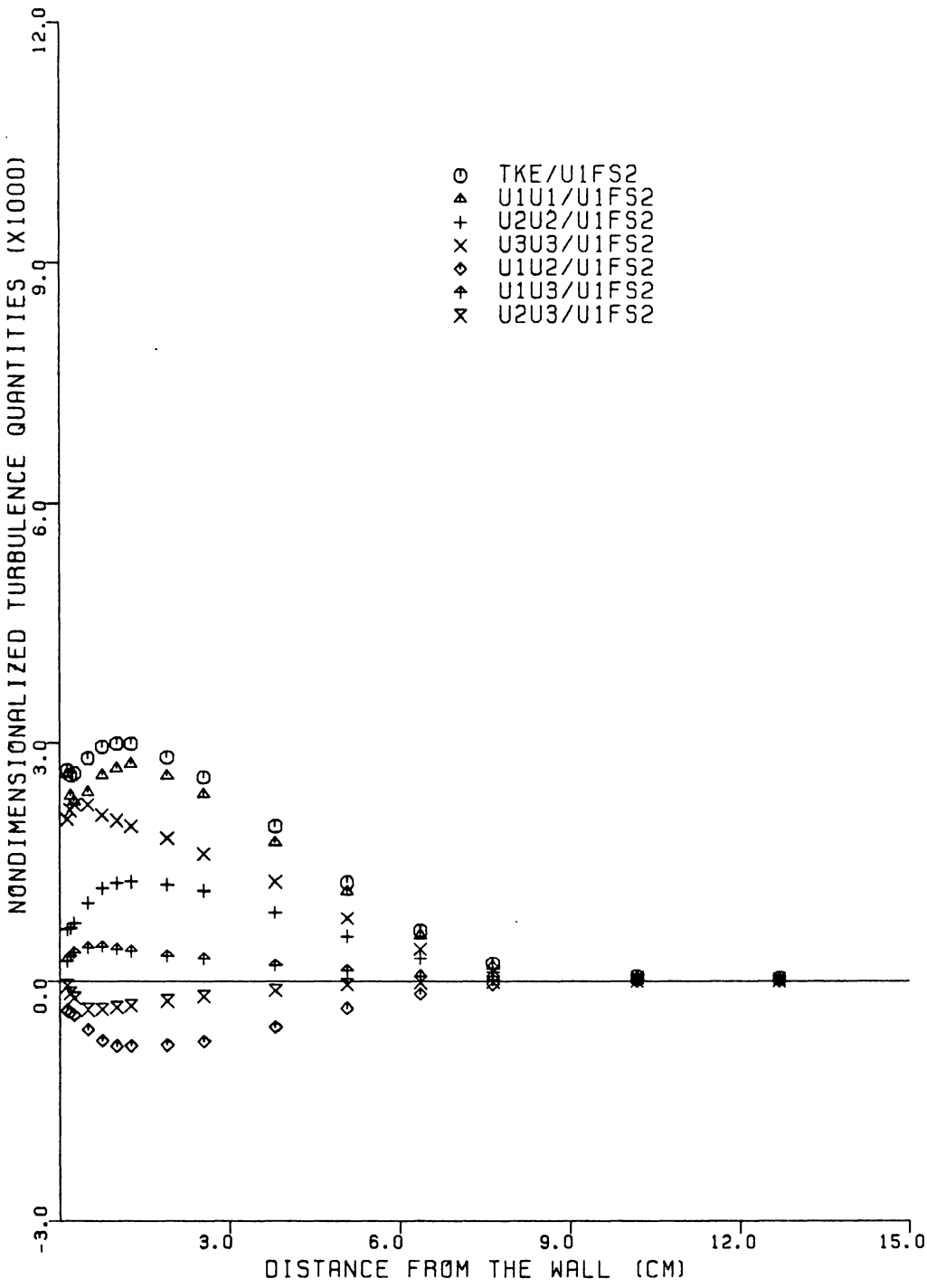

FIGURE 7.32. REYNOLDS STRESS TENSOR AND TURBULENT KINETIC ENERGY AT STATION (1,-6)

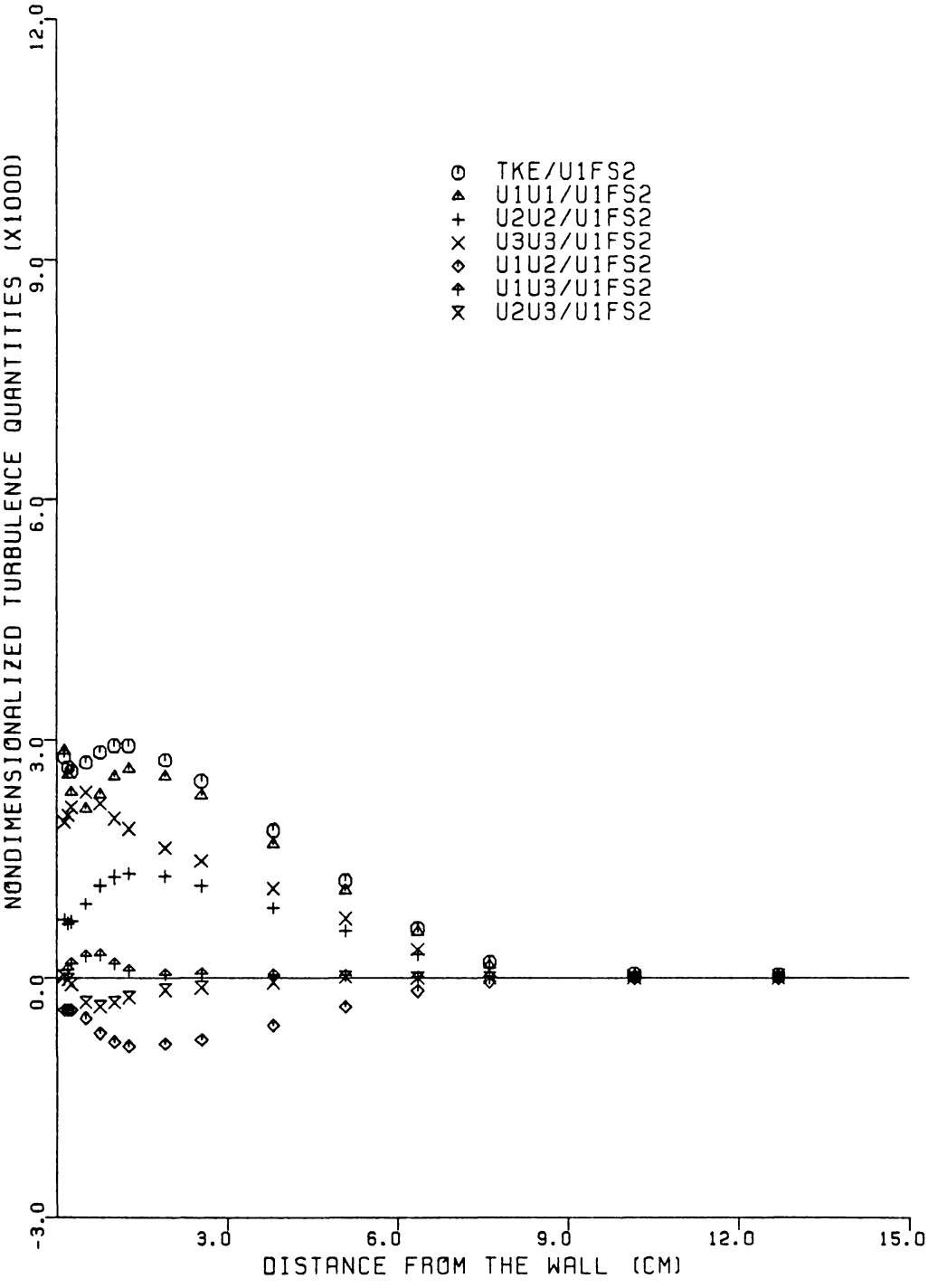

FIGURE 7.33. REYNOLDS STRESS TENSOR AND TURBULENT KINETIC ENERGY AT STATION (3,-6)

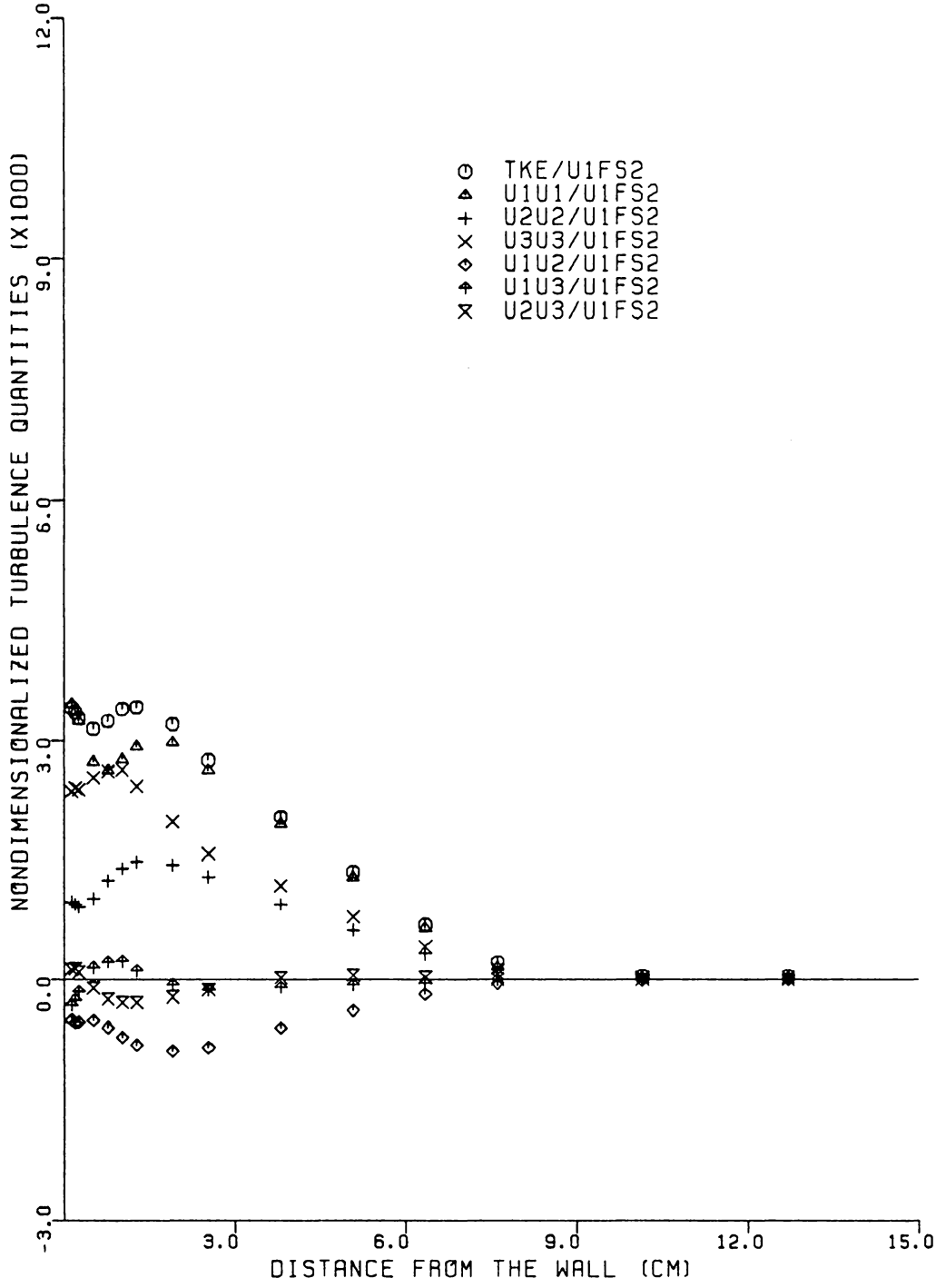

FIGURE 7.34. REYNOLDS STRESS TENSOR AND TURBULENT KINETIC ENERGY AT STATION (5,-6)

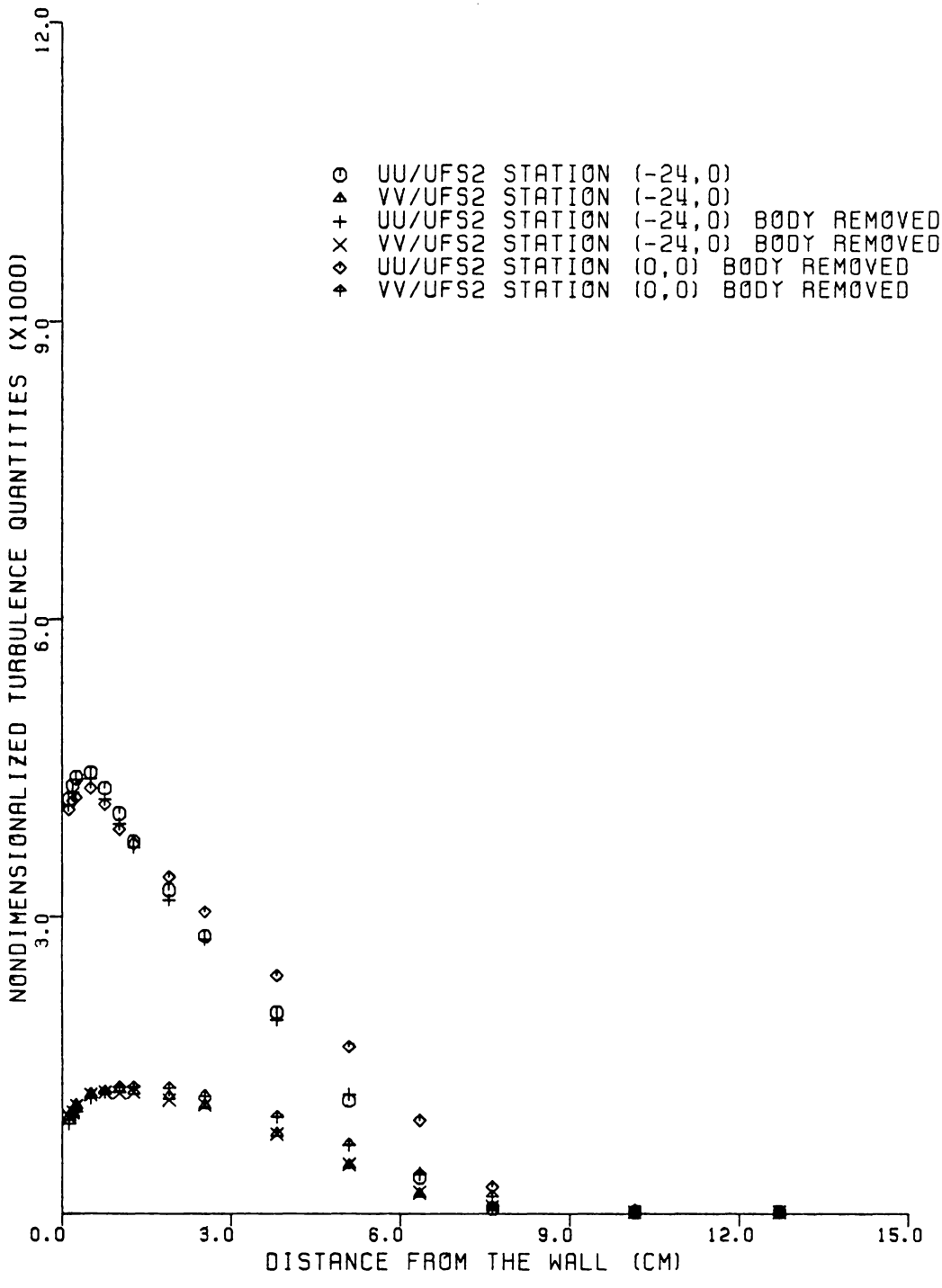

FIGURE 7.35A. EFFECT OF THE BODY ON THE INITIAL CONDITION UU AND VV STRESSES

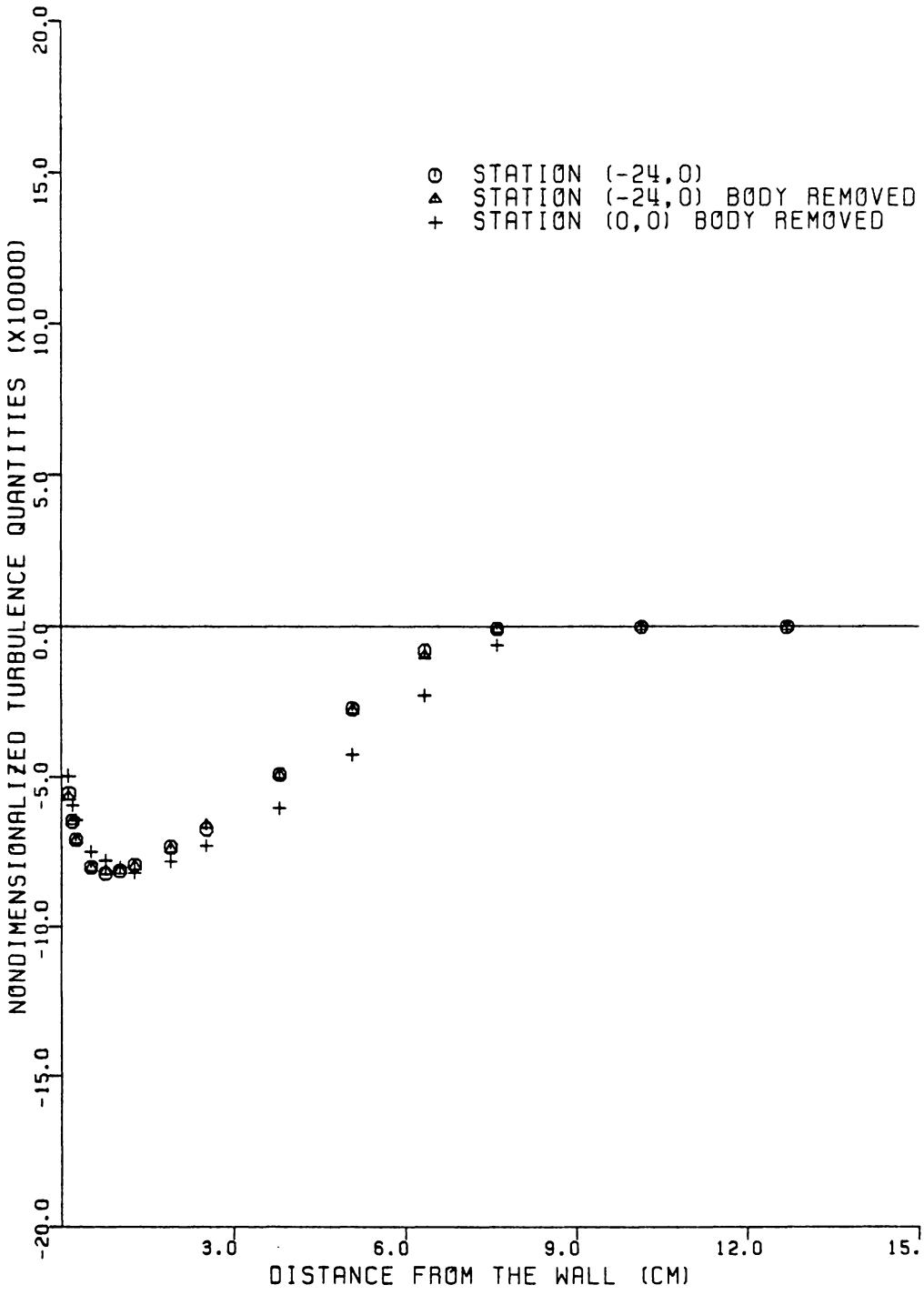

FIGURE 7.358. EFFECT OF THE BODY ON THE INITIAL CONDITION UV STRESS

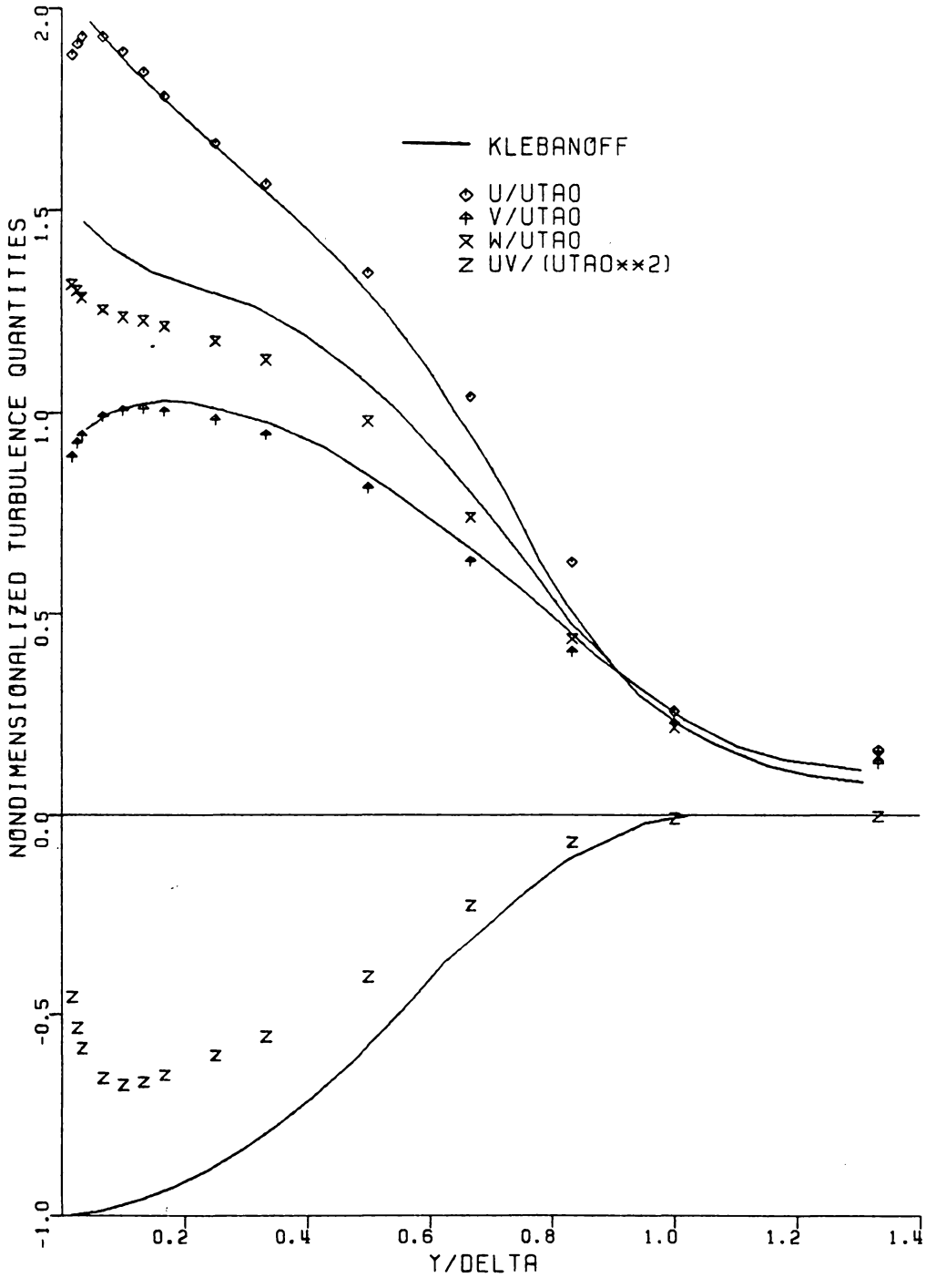

FIGURE 7.36A. COMPARISON OF UPSTREAM INITIAL CONDITION STRESSES AT STATION (-24,0) WITH KLEBANOFF'S (22) DATA

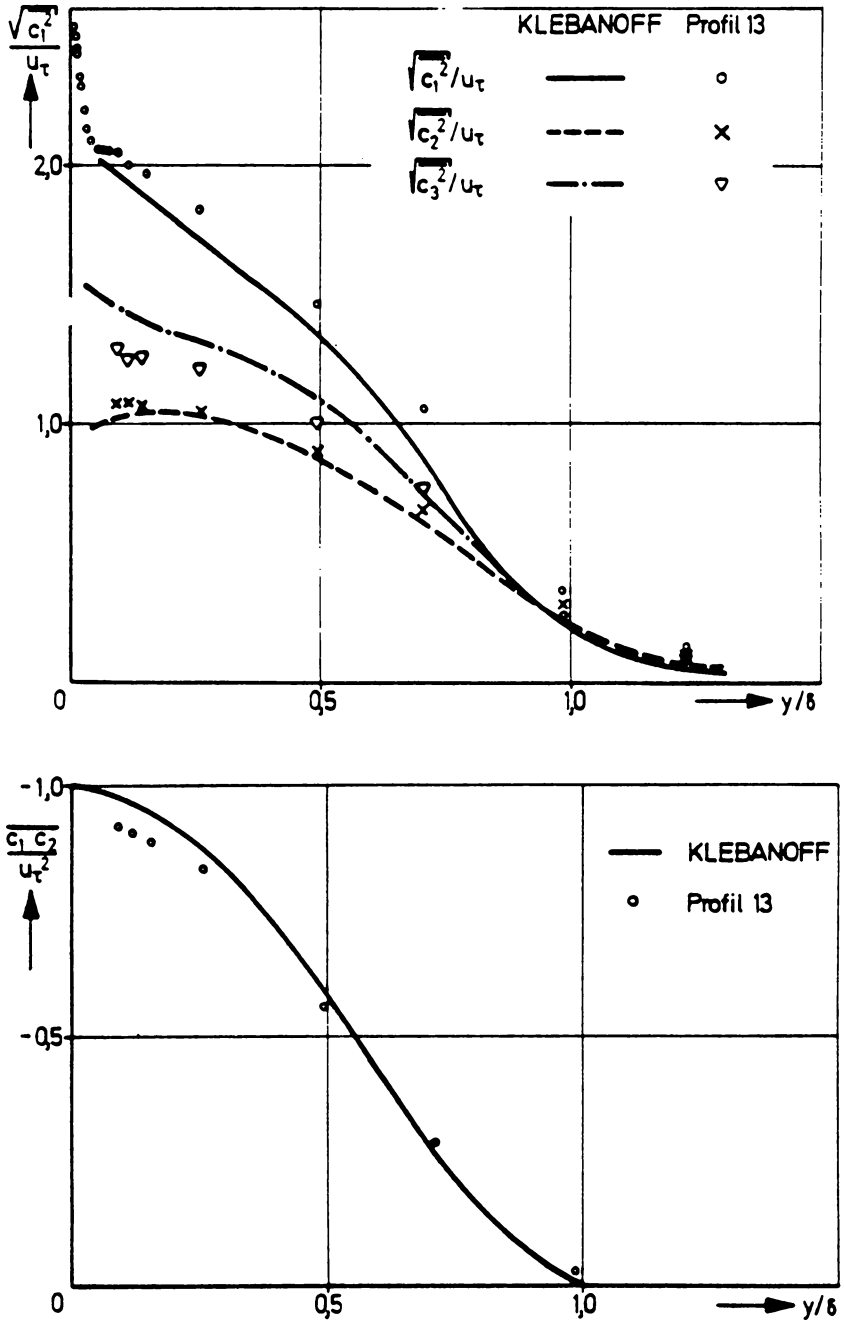

Figure 7.36b The Dechow [35] Comparisons with the Klebanoff [22] Data

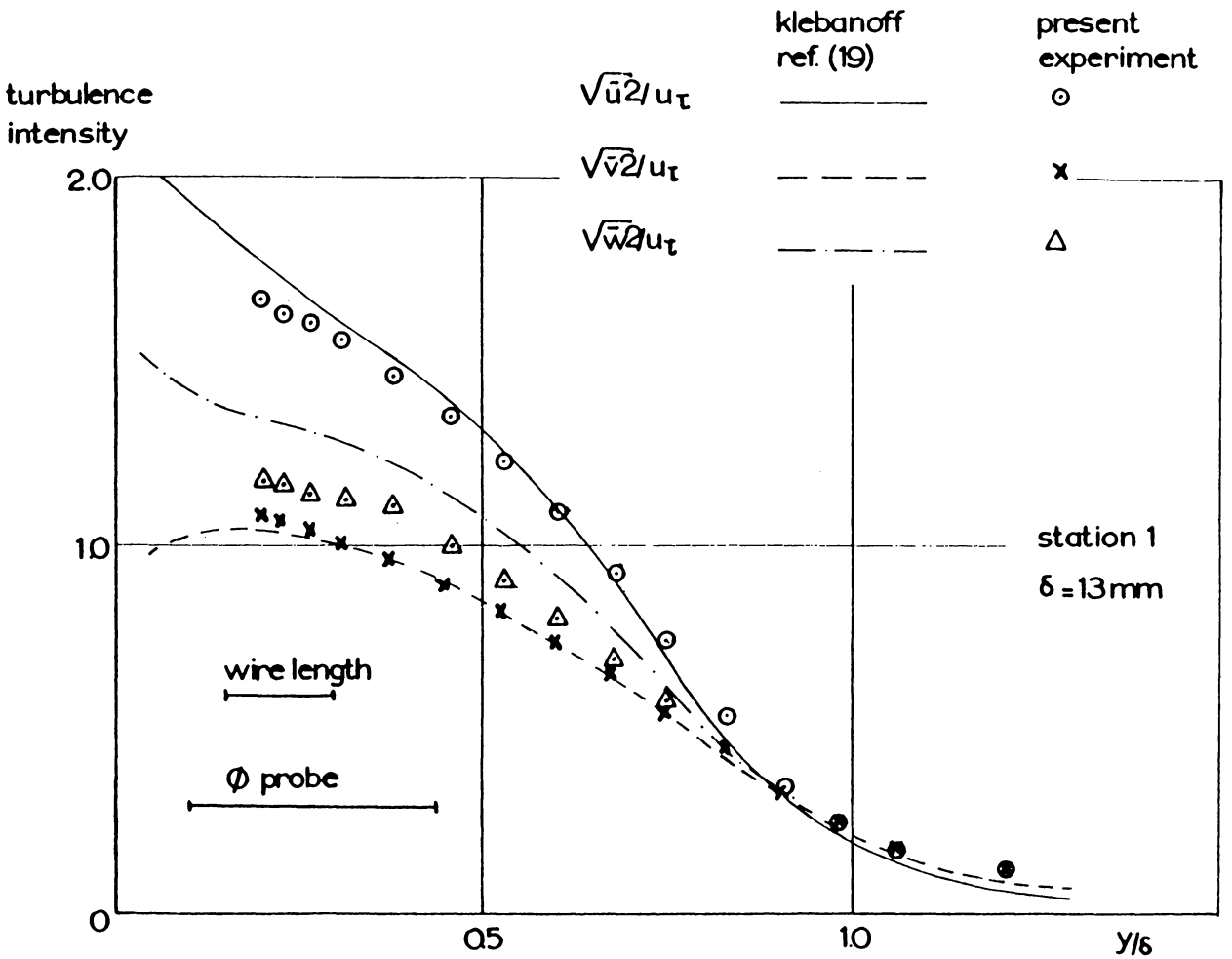

Figure 7.36c The Elsenaar and Boelsma [32] Comparisons with the Klebanoff [22] Data

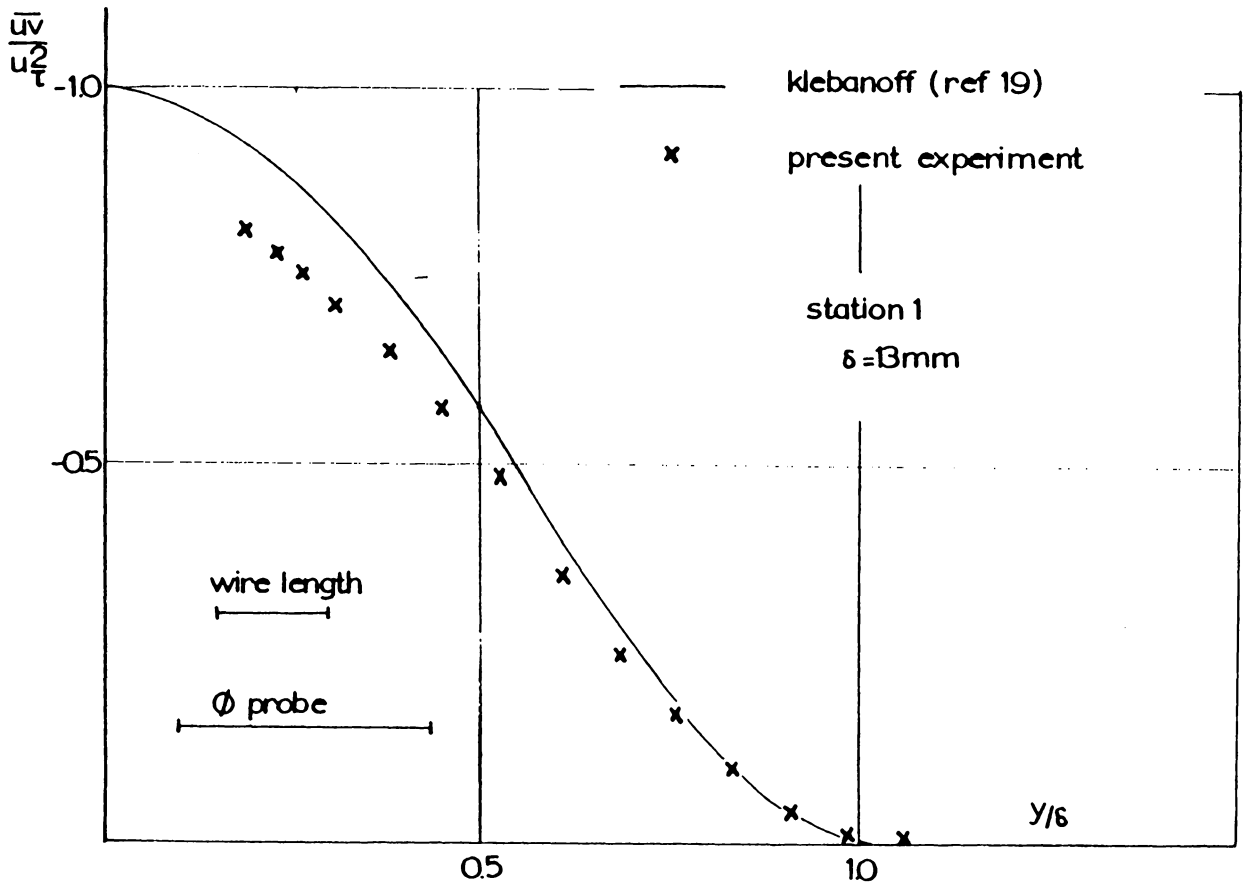

Figure 7.36d The Elsenaar and Boelsma [32] Comparisons with the Klebanoff [22] Data (continued)

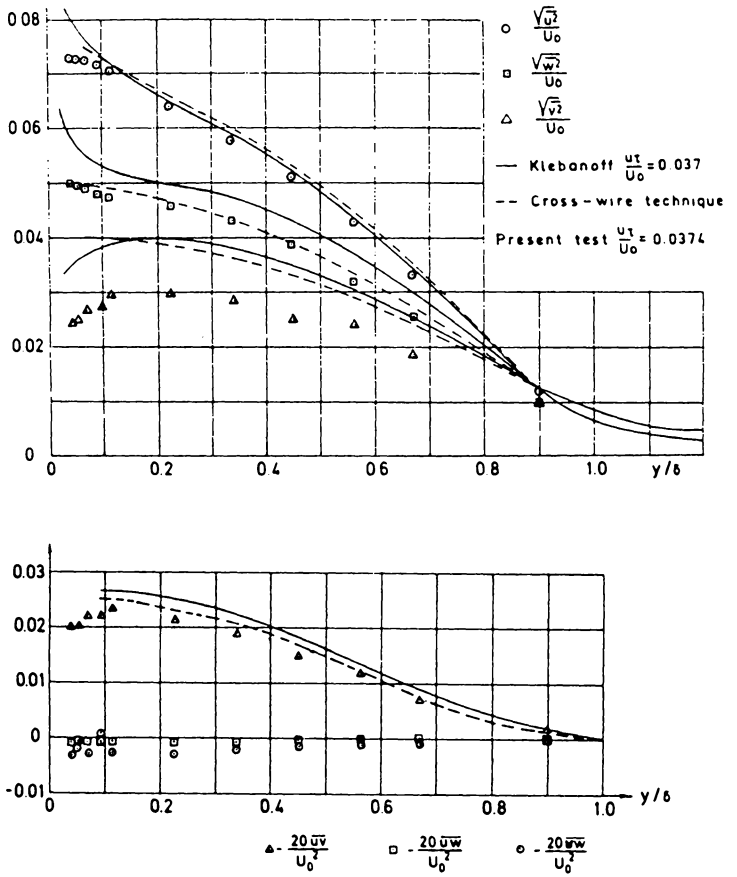

Figure 7.36e The Löfdahl and Larsson [25] Comparisons with the Klebanoff [22] Data

tunnel flow rather than an influence of the body approximately 61 cm (24 in.) downstream of the initial condition plane. This is supported by the results in Figs. 7.35a and 7.35b which show $\overline{uu}$, $\overline{uv}$, and $\overline{vv}$ stress profiles at the initial condition centerline station (-24,0) that were taken with and without the body in the tunnel flow. These results suggest no apparent effect of the body on the upstream initial condition stresses. As reported earlier, this was also the case for the initial condition mean velocities in Fig. 7.1. Thus, the results in Figs. 7.19, 7.35a, and 7.35b suggest that the initial condition plane was sufficiently far upstream so as to show no measurable influence of the downstream pressure-driven 3DTBL flow.

Figures 7.35a and 7.35b also show the nominally 2D stress profiles 61 cm (24 in.) downstream of the initial condition plane at the center of the test section plane (station (0,0) with the body removed). The slightly different shapes of these 2D stress profiles and the 2D mean velocity profiles shown in Fig. 7.19 between the initial condition and test section stations indicates a developing 2DTBL along the centerline that changes gradually with longitudinal distance within a approximately 61 cm (24 in.) tunnel section. As noted in Chapter III, the boundary layer growth on the tunnel walls imposed a slight favorable pressure gradient on this nominally 2DTBL floor flow.

The upstream initial condition flow at station (-24,0) was compared with Klebanoff's [22] flat plate boundary layer data. The results are shown in Fig. 7.36a where the $\overline{uu}$, $\overline{vv}$, $\overline{ww}$, and $\overline{uv}$ stresses, nondimensionalized by the friction velocity $u_\tau = \sqrt{\tau_w/\rho}$, are compared. Reasonably good agreement exists between the $\overline{uu}$ and $\overline{vv}$ stresses with poorer agree-

ment for the $\overline{ww}$ and $\overline{uv}$ stresses. The present $\overline{ww}$ and $\overline{uv}$ stresses are considerably lower in magnitude than Klebanoff's values. In addition to magnitude, the shapes of the $\overline{uv}$ profiles near the wall appear to be different. Klebanoff's results indicate a blunt profile shape near the wall with the peak stress occurring almost at the wall. The present results indicate a peak $\overline{uv}$ stress occurring further away from the wall.

Differences between the upstream 2DTBL shear distribution and the often cited results of Klebanoff [22] are somewhat unsettling. The question is one of what degree of universality should be assigned to Klebanoff's results and whether all 2DTBL flows should be characterized by (nearly) identical profiles.

These differences were carefully considered. The well documented and thorough study of Taslin, Kline, and Moffat [87] shows clearly that for lower speed incompressible flows, the larger film type probes such as cones and wedges do in fact show relatively poor agreement with hot wires in normal stress or turbulent intensity measurements. However, their detailed comparisons show normal and shear stresses measured by -20 hot film sensors as an x-array probe to be within 2% of the values measured by similar hot wire probes, with these film values below the wire values as expected. The x-array sensors used in this study were all -20 films and the same models of the DISA hot wire/film instrumentation system was used in both studies. The only difference between the two systems was in the probes' mode of operation. In this study the probes were designed for operation in the cross-flow mode rather than in an end flow mode as used by Taslin et al. The cross-flow mode was

better suited for measurements near flow separation and the junction vortex system.

As noted earlier, the CTA bridge frequency response was optimized very carefully for each individual sensor in each application. Typical cutoff frequencies as suggested by the wave form response to the square wave input was in the 30-40 kHz range for all cases.

The differences in magnitude and in shape of the $\overline{uv}$ stress profiles between these two nominally 2DTBL flows is not clear. The differences shown here are well outside the range of experimental uncertainty that could be identified with the present results. Furthermore, in the critical examinations made of the methods used in measuring/reducing the turbulence data in this study, several comparisons were made among redundant stresses measured by the three -20 film x-arrays used here and a single wire probe with generally good agreement among these values. Results of redundantly measured values of the TKE, and the $\overline{uv}$ and $\overline{uw}$ stresses all show a high degree of agreement among the -20 x-array probes for matched sensors. In particular, there is also a good degree of agreement in the $\overline{uu}$ normal stress as measured by each of the -20 film x-array probes and the values of a single wire.

The $\overline{uu}$ and $\overline{vv}$ normal stresses by the vertical x-array in Fig. 7.36a are in very good agreement with Klebanoff's values. It seems unreasonable to assume that this same vertical x-array would provide inconsistent values of the $\overline{uv}$ stress. After careful consideration, the reported stress values are taken to be the correct values. It would be reassuring and it is recommended that comparative stress measurements of the complete stress tensor be made with wire sensor probes in the up-

stream 2DTBL flow and at selected stations in the 3DTBL flow region. Such measurements are in progress in a parallel investigation.

While it has been common practice to compare other nominally 2D flows to the Klebanoff [22] data, a survey of the literature revealed that such comparisons show various degrees of disagreement in the Reynolds stress distributions. A few of these comparisons are shown in Figs. 7.36b - 7.36e. These results indicate better agreement in the $\overline{uu}$ stress overall while various levels of agreement are shown for the remaining stresses. It appears that the overall best agreement is shown by Dechow [35]. Elsenaar and Boelsma [32] attribute part of the differences in their data to probe interference and the limitation due to the finite sensor length. The results of Lofdahl and Larsson [26] show the $\overline{uv}$ stress tending to approach the kind of behavior that is shown in this study. Their results indicate the $\overline{uv}$ profile peak occurring further away from the wall with the $\overline{uv}$ values slightly decreasing towards the wall.

The apparent lack of similarity among the flows shown here may be a result of differences in the usptream flow conditions including differences in upstream turbulence levels in the boundary layer where surfaces are usually artifically roughened to achieve a suitably developed 2DTBL flow. At this point, it is not clear what may be considered an acceptable level of agreement among nominally 2DTBL turbulence profiles. From a computational point of view, this suggests that a measured upstream initial condition of a particular flow be used to initiate a calculation of that particular flow.

The turbulence measurements in the 3DTBL flow were taken at the floor stations shown in Fig. 3.9 and the results are shown in Figs. 7.25-7.34. In these results, profiles of the complete Reynolds stress tensor and turbulent kinetic energy

$$TKE = \frac{1}{2}\left(\overline{u_1u_1} + \overline{u_2u_2} + \overline{u_3u_3}\right) \tag{7.13}$$

are shown at each station. At the outer regions of the boundary layer, the turbulent stress profiles tended to converge simultaneously, decreasing monotonically in value towards the freestream. The freestream turbulence intensity was slightly less than 0.6%. In the boundary layer, the turbulence intensity levels (based on the local mean velocity) were usually below 20% except at station (-3,0) near flow separation where the intensity reached as high as 40% near the wall.

The 3DTBL Reynolds stress field shown in Figs. 7.25-7.34, develops from a collateral, nominally 2D upstream turbulent flow. Except for a few stations, the $\overline{u_1u_2}$ stresses are shown throughout the flow to be similiar in qualitative behavior to the $\overline{u_1u_2}$ stresses in the upstream nominally 2D flow. The $\overline{u_1u_2}$ stress is also shown to dominate turbulent shear at stations identified with collateral or near collateral flow such as along the initial condition plane (Fig. 7.24) and the plane of symmetry (Figs. 7.25-7.27). Along these planes, the results generally show very small magnitudes of the $\overline{u_1u_3}$ and $\overline{u_2u_3}$ shear stresses typically within the experimental uncertainty of the stress measurements. A growth in magnitude of the $\overline{u_1u_3}$ and $\overline{u_2u_3}$ stresses occurs off the plane of symmetry as the secondary flow develops in response to the transverse

pressure gradients following freestream streamline curvature. In regions of relatively large cross-flow, such as measured at stations (-3,-2) and (-3,-4), substantial $\overline{u_1u_3}$ shear stresses are found, up to and exceeding the $\overline{u_1u_2}$ stresses in absolute value. Considerable $\overline{u_2u_3}$ stresses are also shown in these highly skewed flow regions but as shown in Figs. 7.28 and 7.29 they are smaller in magnitude than the other shear stresses at these stations.

Along the plane of symmetry, the boundary layer encounters a steep adverse pressure gradient before separating ahead of the leading edge of the body. Prior to separation, there is a monotone increase in the normal stresses along this plane with the $\overline{u_1u_1}$ stress increasing most rapidly as shown in Figs. 7.25-7.27. The growth in this normal stress dominates and results in the increase in the TKE magnitudes that is shown along the plane of symmetry. The opposite trend in the TKE profiles is shown along the upstream portion of the lateral plane x_3 = -15.24 cm (-6 in.), parallel to the plane of symmetry. From station (-7,-6) to station (1,-6) the results in Figs. 7.30-7.32 indicate a reduction in the TKE magnitudes which appears to be in response to the decrease in the $\overline{u_1u_1}$ stresses within the boundary layers. It is noted that in this region of flow, the boundary layer encounters a favorable longitudinal pressure gradient as indicated in McAllister's [27] results (Fig. H1) along the G column. Downstream of station (1,-6) where the body begins to taper to the trailing edge, the flow experiences an adverse pressure gradient and the results indicate a slight increase in the TKE magnitudes.

In Figs. 7.30-7.34, a noticeable difference in the shapes of the Reynolds stress profiles between the upstream and downstream flows on the x_3 = -15.24 cm (-6 in.) plane is shown. Upstream of the body's leading edge, the profiles are similiar in shape to other upstream station profiles where one peak in the stress profiles occurs. Downstream of the leading edge, these peaks are shown to move away from the wall with a second, smaller local maximum or minimum (depending on the stress) appearing near the wall in nearly all of the Reynolds stress profiles. This type of behavior is most evident at station (5,-6). The results in Fig. 7.34 indicate that the location of the second extremum generally falls within the region where turning of the mean velocity vectors from the wall changed from monotone increasing to monotone decreasing. In Table G14, this transition is shown to occur between approximately 1/4 and 1 cm from the wall. It is noted that in this neighborhood, the $\overline{u_1u_3}$ and $\overline{u_2u_3}$ shear stresses change sign as shown in Fig. 7.34. It appears that the change in shape of the turbulent stress profiles which first appears at station (1,-6) is related to the direction of the transverse pressure gradient. This is indicated in McAllister's [27] results in Fig. H1 which show a reversal of the transverse component of the pressure gradient vector which occurs between stations (-1,-6) and (1,-6).

Symmetry of the turbulent stress field was examined by looking at the local streamwise normal stress in the sensor coordinate system, viz. $\overline{uu}$. The degree of symmetry in the $\overline{uu}$ stress was checked in the adjacent forward quadrant of the teardrop flow at stations (-7,6) and (-3,2) using a single stationary film normal to the flow direction. The

results are shown in Fig. 7.37 where a good degree of symmetry is shown at both stations. Also shown in Fig. 7.37 is one repeated profile at station (-3,2). These results suggest that the small amount of asymmetry shown within the flow was real.

Shear/TKE Ratios

The ratio of turbulent shear stress to turbulent kinetic energy is an important quantity used in some of the popular boundary layer closure models [13-15]. The common practice is to assume a constant value of 0.15 for this ratio in calculating turbulent flows, although it is generally known to be a function of position, y/δ, within the boundary layer.

In this study two shear/TKE ratios were considered. In the first case, this parameter was defined as the total resultant shear stress divided by twice the TKE where

$$a_1' = \frac{[(\overline{u_1u_2})^2 + (\overline{u_1u_3})^2 + (\overline{u_2u_3})^2]^{1/2}}{\overline{u_1u_1} + \overline{u_2u_2} + \overline{u_3u_3}} . \qquad (7.14)$$

These results are presented in Fig. 7.38. In the second case, only the $\overline{u_1u_2}$ and $\overline{u_2u_3}$ shear stresses were used with

$$a_1 = \frac{[(\overline{u_1u_2})^2 + (\overline{u_2u_3})^2]^{1/2}}{\overline{u_1u_1} + \overline{u_2u_2} + \overline{u_3u_3}} \qquad (7.15)$$

and these results are shown in Fig. 7.39.

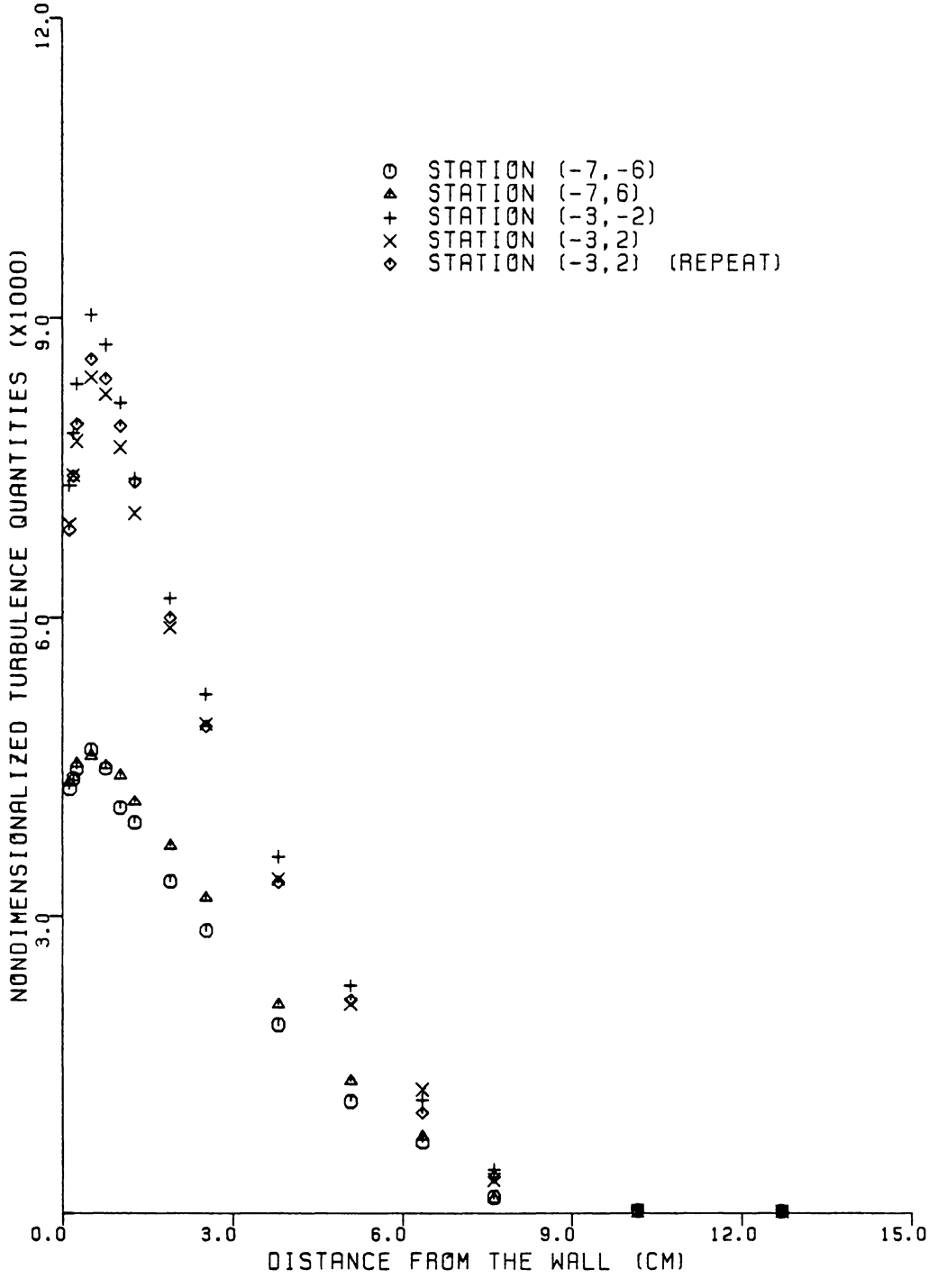

FIGURE 7.37. SYMMETRY IN UU STRESS OF 3DTBL FLOW

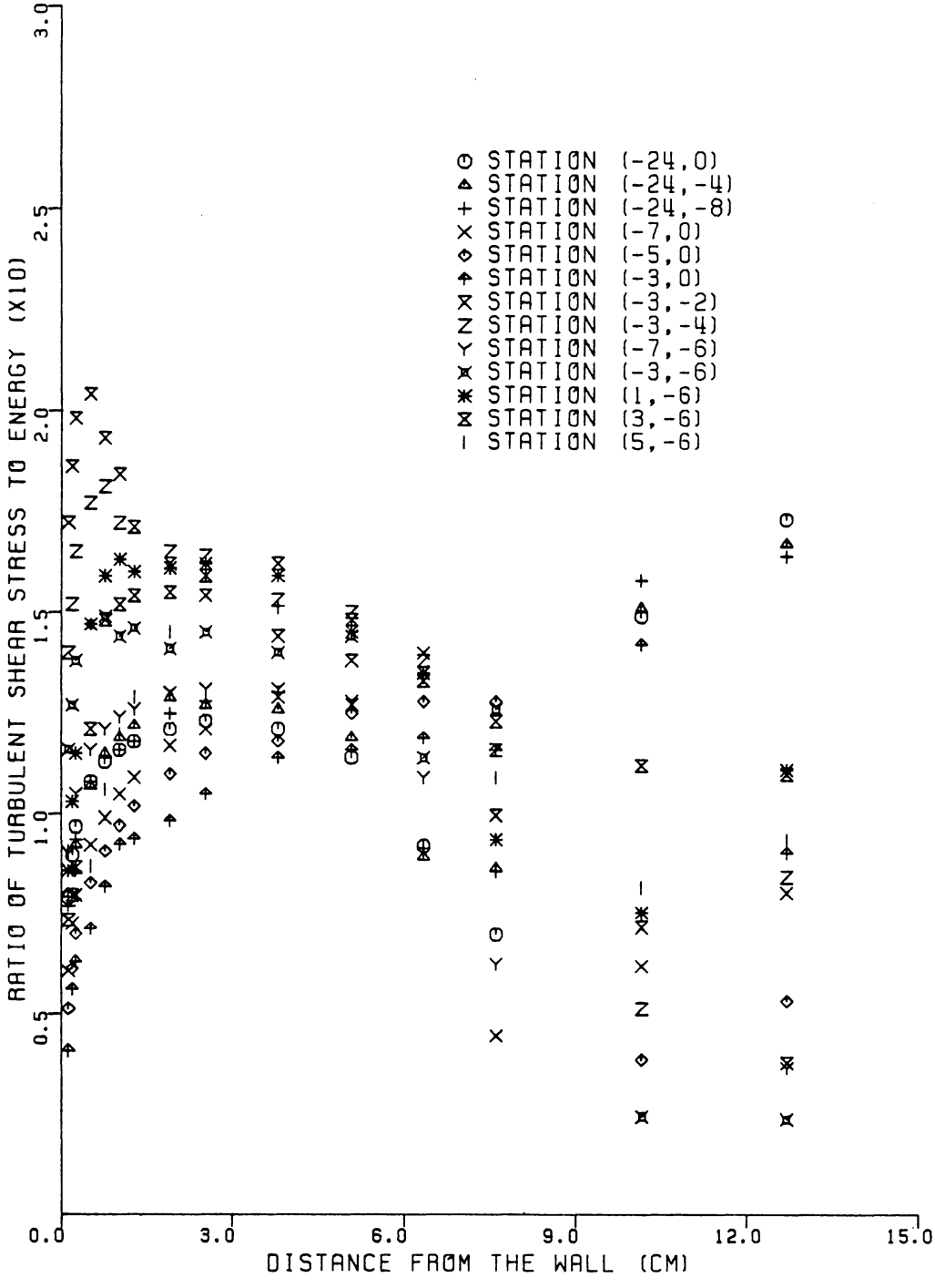

FIGURE 7.38. RATIO OF TOTAL SHEAR STRESS TO TURBULENT KINETIC ENERGY FOR THE 3DTBL FLOW

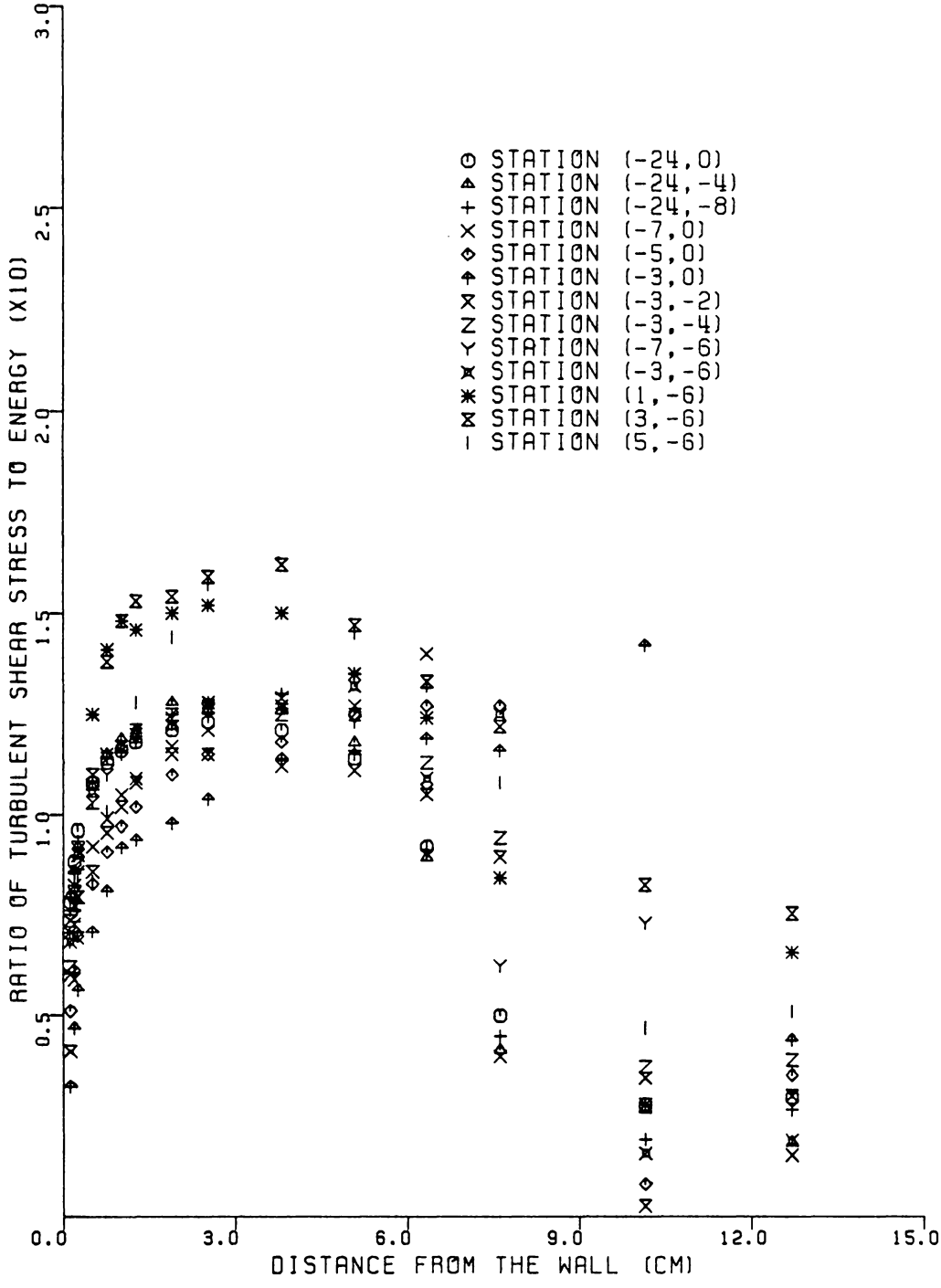

FIGURE 7.39. RATIO OF SHEAR STRESS TO TURBULENT KINETIC ENERGY FOR THE 3DTBL FLOW USING TWO SHEAR STRESSES

Figure 7.38 shows the values of a_1' ranging from 0.05 to 0.2 near the wall, which tend to converge to values between 0.11-0.15 near the center of the boundary layer. These results appear to be consistent in magnitude with those reported by Dechow [35]. A divergence in magnitude of a_1' near the outer regions of the boundary layer is shown which can be attributed to noise in the data due to the very small turbulence levels that were measured near the freestream. The higher values near the wall occurred in regions identified with relatively large secondary flow. The lower values near the wall occurred on the plane of symmetry where there is a monotone decrease in a_1' as the flow approaches separation. The larger TKE magnitudes reported earlier along this plane would tend to give smaller a_1' ratios reported here. In this sense, these results are consistent in that a growth in the TKE would result in a reduction in the shear/TKE ratio as shown.

Figure 7.39 shows the shear stress-kinetic energy ratio distribution neglecting the $\overline{u_1 u_3}$ shear stress as defined in Eq. 7.15. These results indicate a monotone increasing ratio from near the wall through the 3DTBL that reaches magnitudes of 0.10-0.15 before dropping off at the outer edge of the boundary layer. These results tend to agree with those reported by Elsenaar and Boelsma [32] and Dechow [35]. As in Fig. 7.38, the smallest ratio values occurred along the plane of symmetry. It is noted that the shear/TKE ratios were not nearly as large at stations (-3,-2) and (-3,-4) off the plane of symmetry when the $\overline{u_1 u_3}$ stress were neglected. The largest magnitudes occurred along the x_3 = -15.24 cm (-6 in.) plane (parallel to the plane of symmetry) at stations

(1,-6), (3,-6) and (5,-6) which were noticeably higher than the values shown in other regions of the flow.

E. Alternate Methods for Measuring/Reducing Turbulence Data

Preliminary Remarks

The response equations derived in Chapter IV provided the opportunity to study different methods of obtaining turbulent stresses. The generality of these equations allows 1) the use of several of the existing yaw cooling laws for calculating the turbulent stresses, 2) the detailed study of the matched sensor approximations, and 3) the study of different methods for measuring normal and shear stresses. In this section some of these methods for measuring/reducing turbulence data are compared. In particular, the Reynolds stress tensor results are compared using Hinze's [54] and Davies and Bruun's [104] laws, a comparison is made of $\overline{uu}$ normal stresses measured by the various probes used in this study, the redundant $\overline{uv}$, $\overline{uw}$, and the TKE by the sx-array are compared to those of the hx- and vx-arrays, and a comparison is made of Reynolds stresses by the hx- and vx-arrays with and without assuming matched sensors. While it is common practice to assume matched sensors when measuring turbulent flows with x-arrays, the results will show that considerable errors can result when this assumption is used. In addition, hot wire and hot film measurements of $\overline{uu}$ stress are compared and a comparison is made of the $\overline{uu}$ stress obtained with and without linearizers.

The comparisons are made at stations (-3,-2) and (-7,-6) which encompassed extreme features of the flow for a more severe test of the

methods. As noted earlier, the former station was located relatively close to the body where relatively large skewing of the boundary layer occurred. In contrast, the latter station was located considerably further upstream and further away from the body where substantially smaller amounts of skewing were found. Quantitative evaluation of the methods was based on the measurements taken in the lower 2/3 of the boundary layer where the sizeable magnitudes of stress were found. This allowed for a meaningful comparison of the methods considered. The results of these comparisons are presented in the sensor coordinate system.

Cooling Law Comparisons

Figures 7.40-7.41 compares the two complete Reynolds stress tensors at the (-3,-2) and (-7,-6) locations, using Hinze's [54] cooling law and the Davies and Bruun's [104] law. The yaw parameters for these laws are listed in Tables 5.2 and 5.3 with the corresponding values of f, f', and f" as well. The results show excellent agreement in all the stresses for the two cooling laws considered. Davies and Bruun's law gives consistently higher stresses by 1-2% for nearly all the stresses, with the exception of the $\overline{vw}$ stress which were approximately 3-5% higher.

These results further indicate that Hinze [54] and Davies and Bruun's [104] cooling laws can be considered as nearly equivalent in calculating Reynolds stress tensors. It must be noted however that the second derivative, f", of the cooling law was not involved in computing these stresses since the higher order velocity correlations containing f" in the response equations were neglected for this flow. As noted in

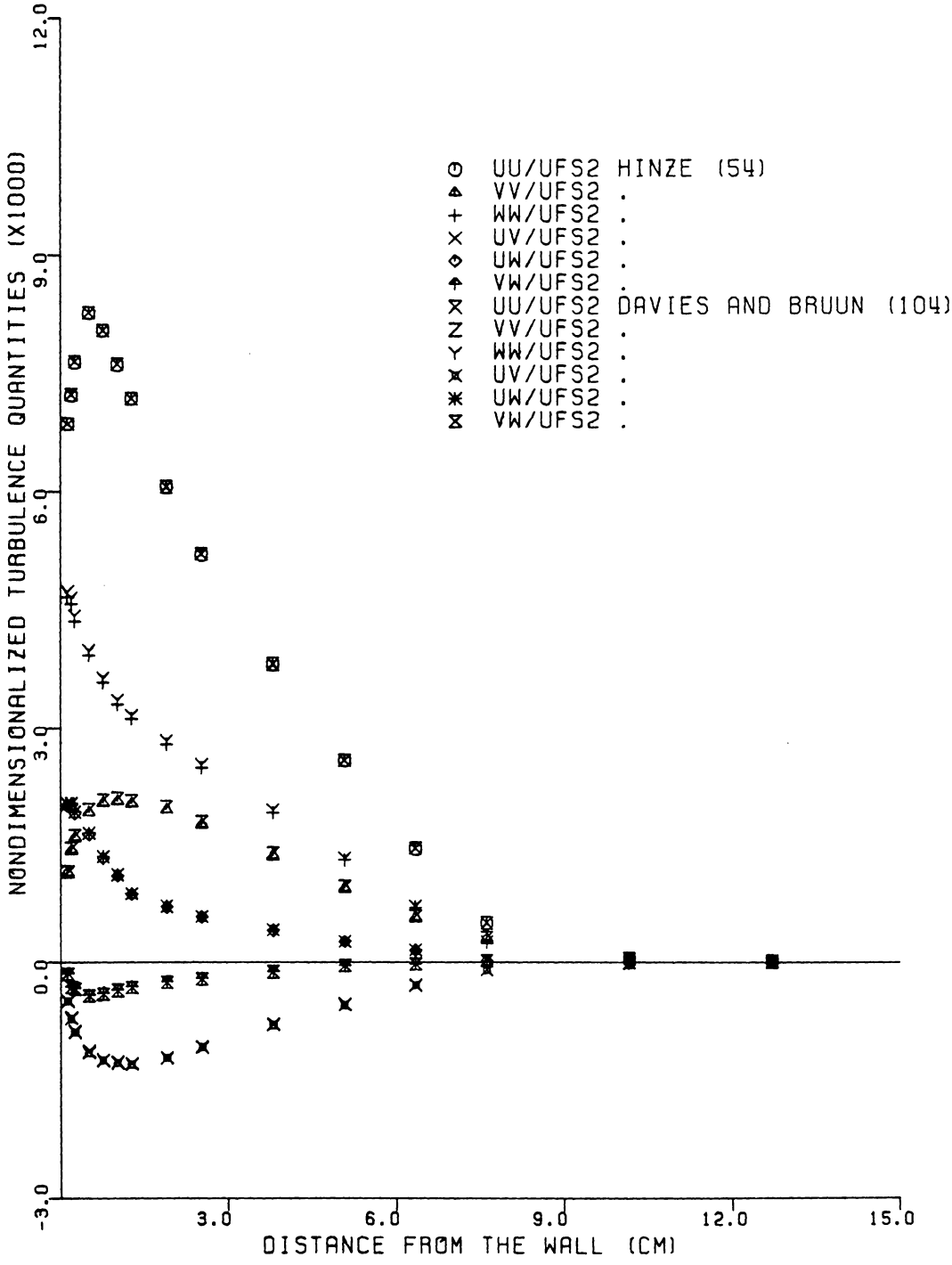

FIGURE 7.40. COMPARISON OF REYNOLDS STRESS TENSOR USING TWO COOLING LAWS AT STATION (-3,-2)

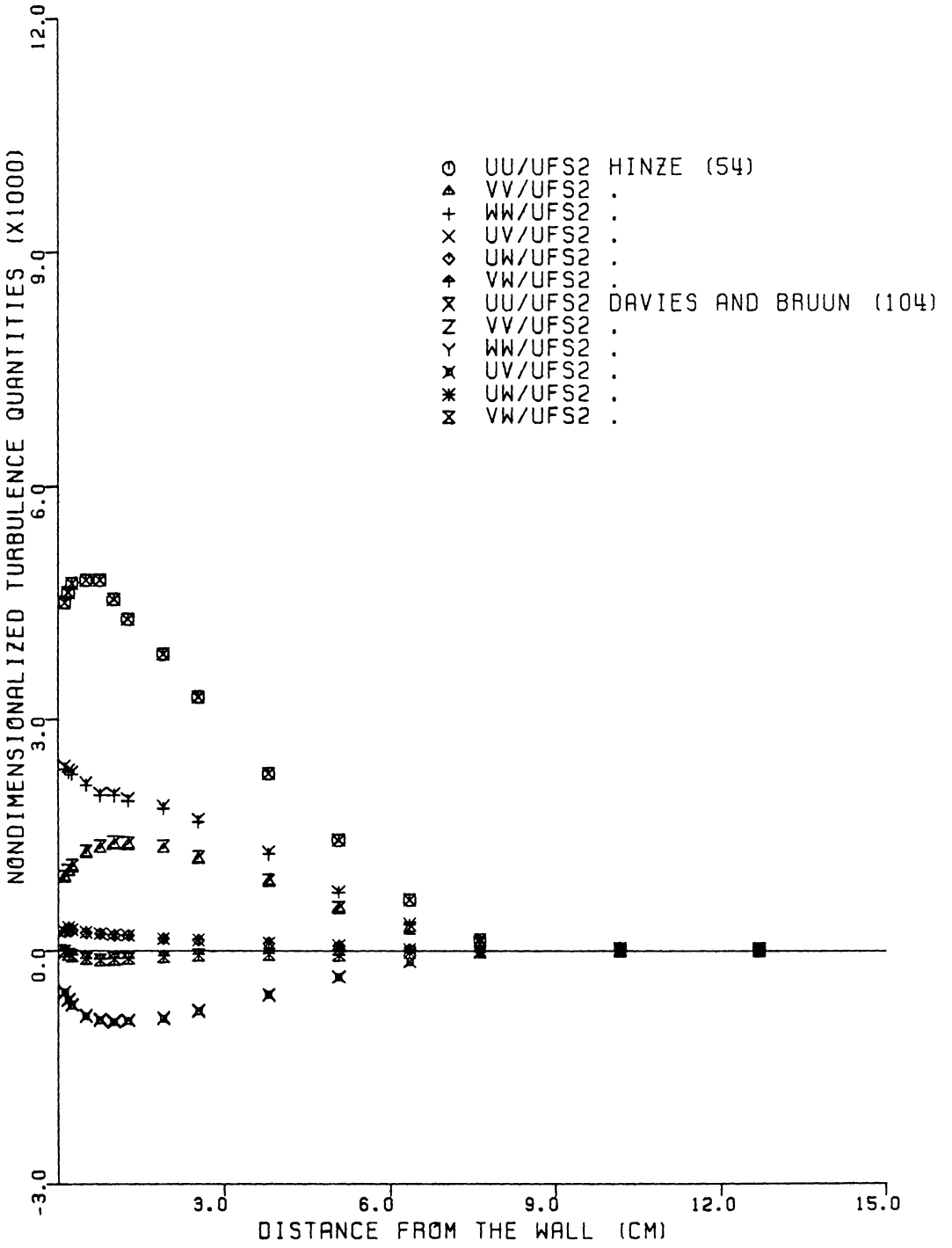

FIGURE 7.41. COMPARISON OF REYNOLDS STRESS TENSOR USING TWO COOLING LAWS AT STATION (-7,-6)

Chapter V, the most significant difference between these two laws is in the magnitude of the second derivative f" as shown in Tables 5.2 and 5.3.

Redundant Stresses

Figures 7.42 and 7.43 compare the redundant $\overline{uu}$ stresses and TKE profiles with those of the hx- and vx-arrays reported earlier. In these results, the $\overline{uu}$ stresses measured during each sx-array traverse are included and are identified by the Position 1 and Postion 2 designations shown in these figures. The results show very good agreement in the TKE profiles between the hx-, vx-array and the sx-array measurements at both stations. These results also show an approximately ± 2.5% variation in $\overline{uu}$ stress at station (-7,-6) and an approximately 5 to 7% variation at station (-3,-2) with the vx-array giving the largest stress magnitudes.

The redundant shear stresses by the sx-array are compared to the hx- and vx-array results in Figs. 7.44 and 7.45. The $\overline{uw}$ stress profiles by the hx- and sx-arrays are shown to be in good agreement while larger, more significant differences in the $\overline{uv}$ stresses between the vx- and sx-array measurements are shown. A large part of the difference can be accounted for in the matched sensor approximations as quantified in the following section.

Matched Versus Unmatched Sensors

As discussed in Chapter IV, the hx- and vx-arrays did not require the matched sensor assumptions if the systems given in Eq. 4.81 and

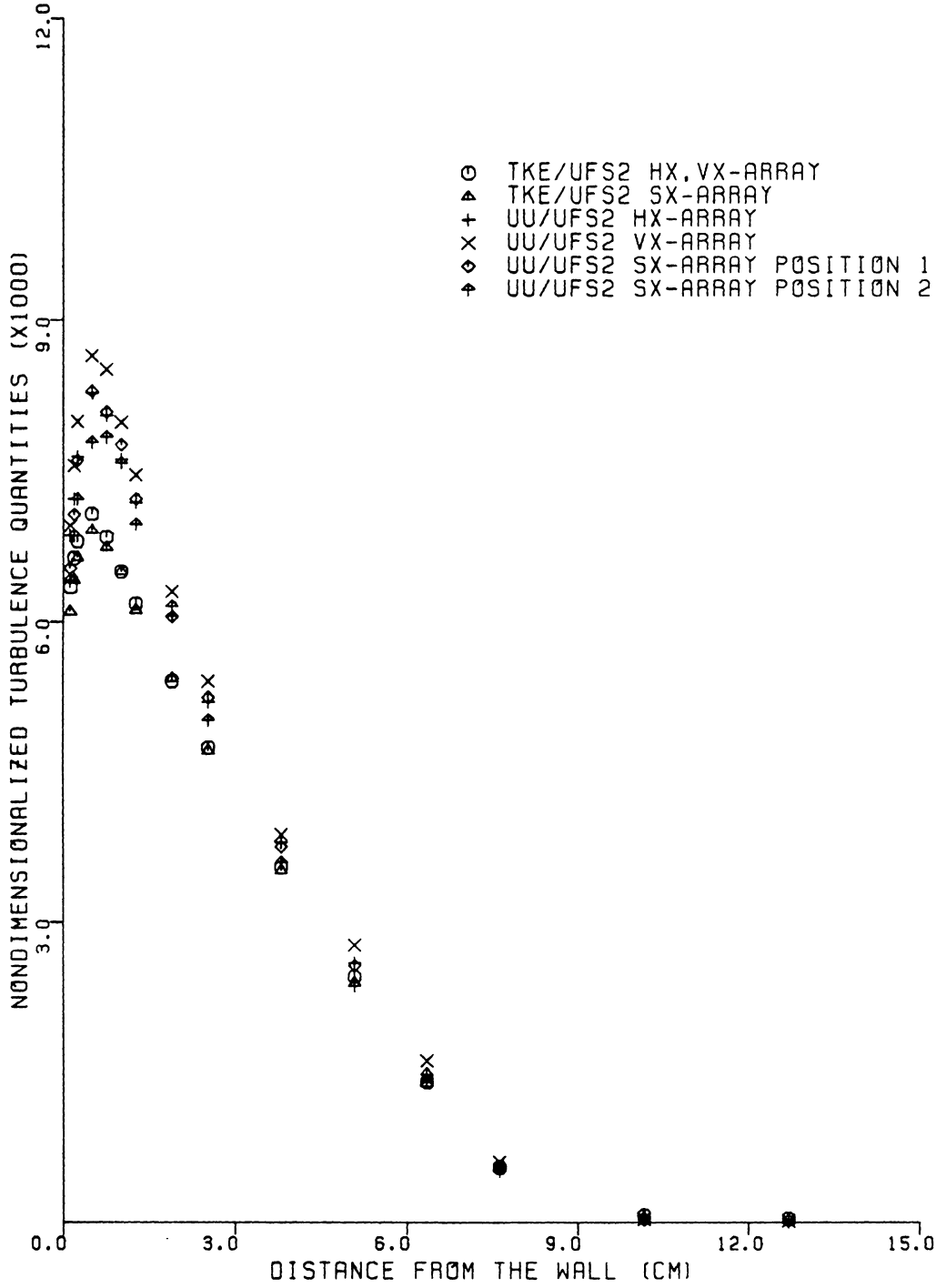

FIGURE 7.42. COMPARISON OF UU STRESS AND TURBULENT KINETIC ENERGY MEASUREMENTS AT STATION (-3,-2)

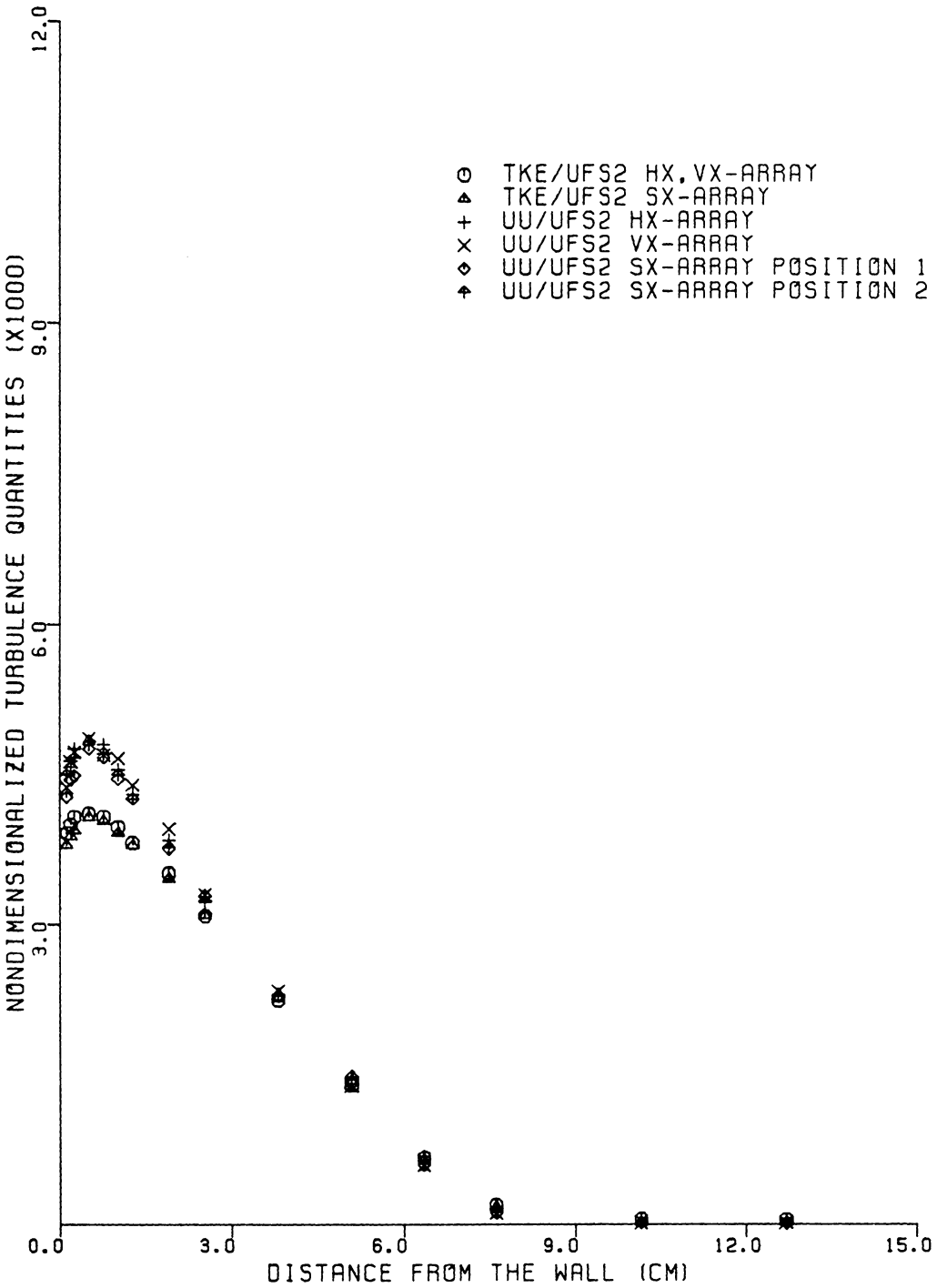

FIGURE 7.43. COMPARISON OF UU STRESS AND TURBULENT KINETIC ENERGY MEASUREMENTS AT STATION (-7,-6)

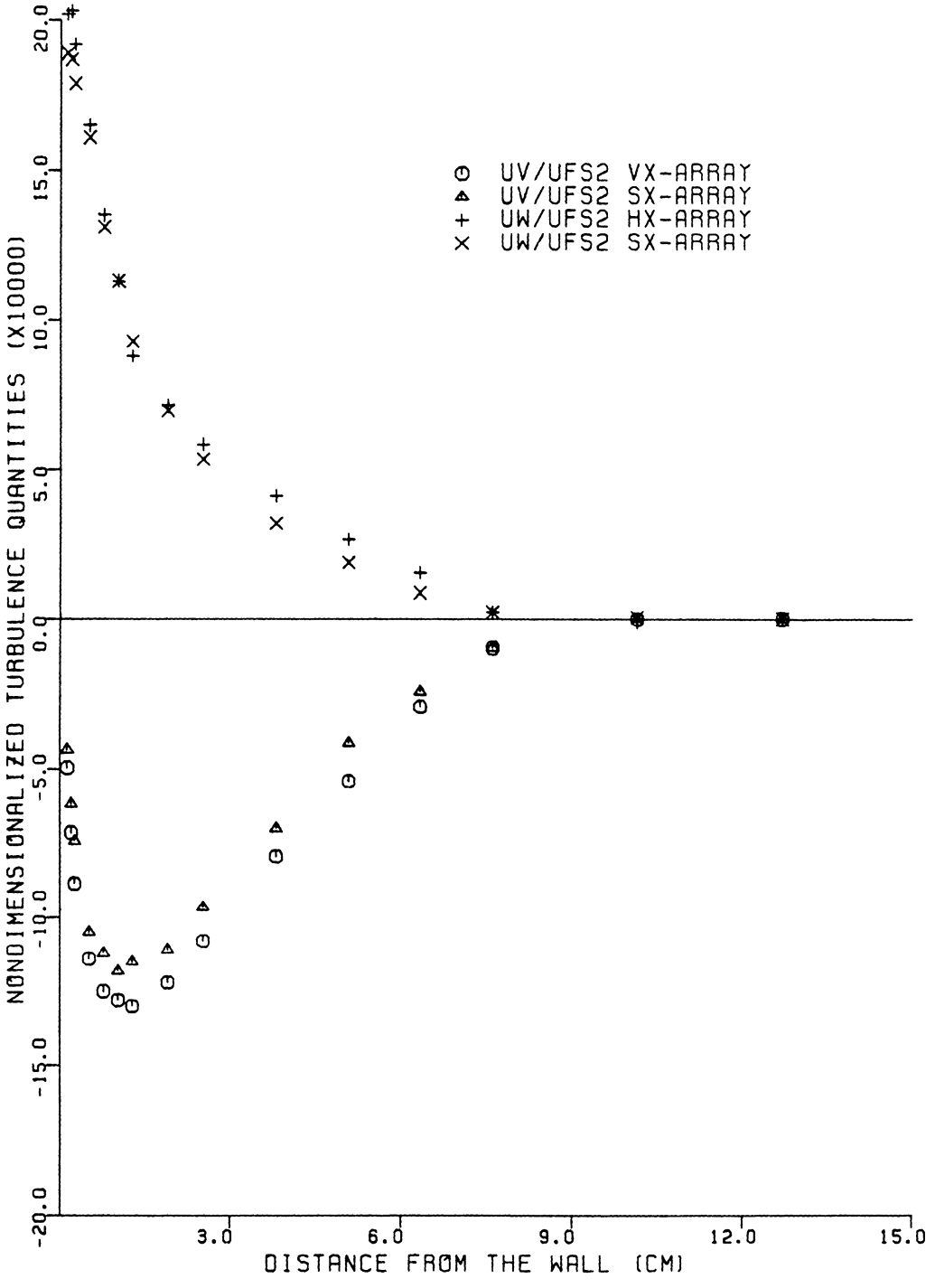

FIGURE 7.44. COMPARISON OF SHEAR STRESS MEASUREMENTS AT STATION (-3,-2)

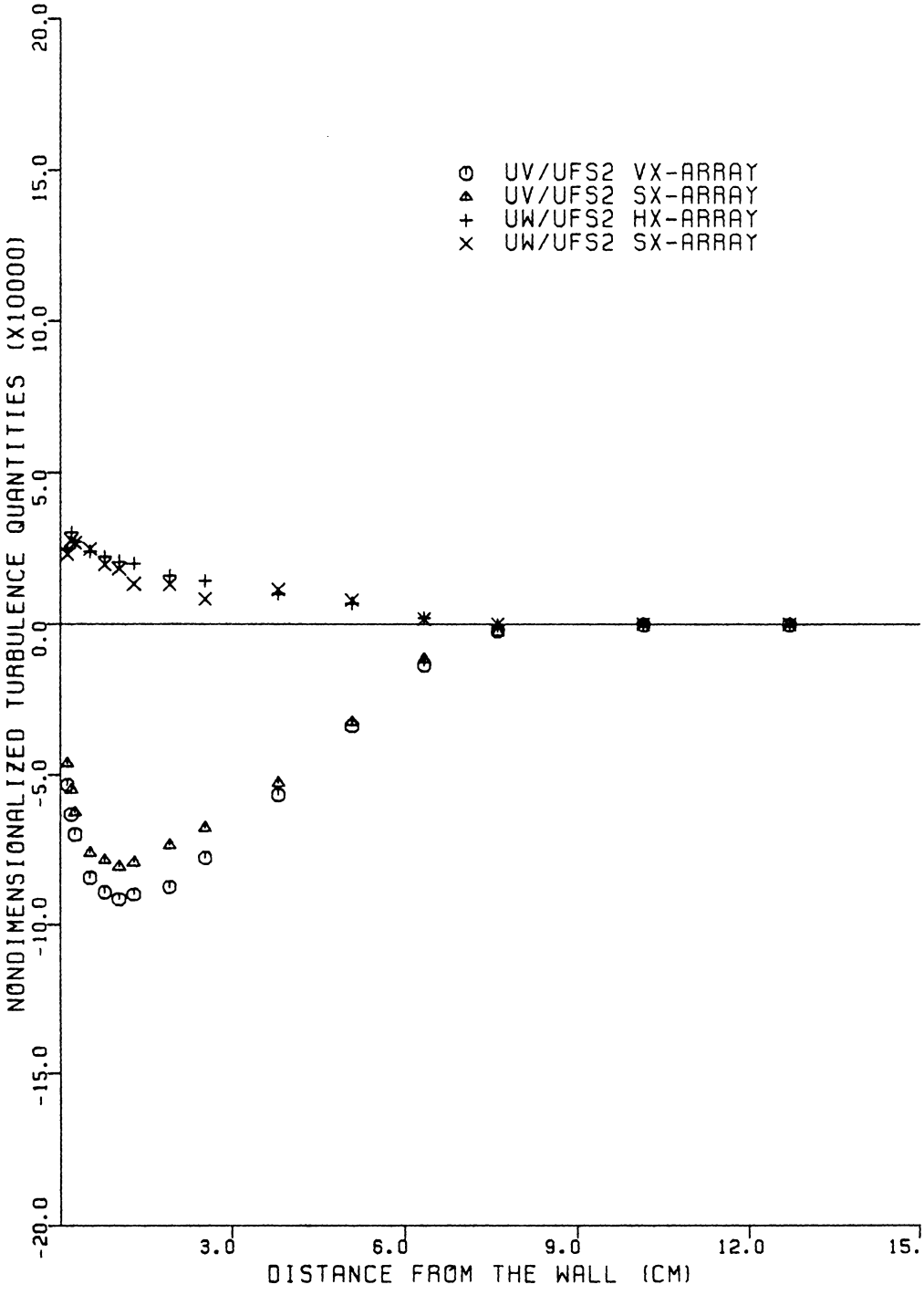

FIGURE 7.45. COMPARISON OF SHEAR STRESS MEASUREMENTS AT STATION (-7,-6)

4.107 were used to compute their stresses. Matching of the two velocity calibration curves of the x-array gave a partial matching of the sensors which resulted in a more simplified version of the sensors' response as given in Eqs. 4.86 and 4.108. Thus, the only differences or asymmetries between the two sensors that remained after this matching were in the directional or yaw characteristics of the sensors. Such asymmetries, due mainly to differences in k^2 with corresponding differences in f and f', were confirmed to exist to at least some degree for the probes calibrated and could be taken into account in the hx- and vx-array quasi-matched sensor response equations derived in Chapter IV.

The sx-array response equations were based on the complete set of matched sensor assumptions which were necessary to obtain the $\overline{vw}$ stress. Differences in the velocity sensitivities of the two sensors at the probe's operating position could be corrected by electronically matching the slopes of the velocity calibration curves. However, asymmetries in the sensors' yaw parameters could not be properly corrected. In this case, average values were used. Thus, for the reasons given above, the hx- and vx-arrays can be viewed as giving a more accurate measurement of normal and $\overline{uv}$ and $\overline{uw}$ stresses. The accuracy of the sx-array stresses would depend on the magnitude of the asymmetries or mismatch in the sensors' yaw parameters. In the results that follow, an unmatched array will mean the existence of asymmetries in the sensors' yaw parameter only.

To study the effect of a matched sensor assumption on the computed normal and $\overline{uw}$ and $\overline{uv}$ shear stresses, the turbulence data by the hx- and vx-arrays were reduced using average values for all the sensor param-

eters. Since the sensors' velocity sensivities were matched electronically a priori, the differences between the matched and unmatched probe results would be largely due to asymmetries in k^2. Using these average values in effect artificially matches the sensors from a mathematical standpoint resulting in the system of equations of the form given by Eqs. 4.86 and 4.108.

The results of this matching technique are presented in Figs. 7.46 and 7.47 for the normal stresses and Figs. 7.48 and 7.49 for the shear stresses. At both stations, the $\overline{uu}$ and $\overline{ww}$ stresses assuming matched sensors were generally within 1% of the unmatched case for an approximately 1 and 4% difference in the hx-array values of f and f', respectively (relative to sensor a values). At station (-3,-2), the $\overline{uw}$ stresses were generally within 3-7% of the unmatched case while at station (-7,-6), where $\overline{uw}$ stresses were considerably smaller, the change was more than twice this amount with matched sensors giving 15-20% lower values. For the matched vx-array, an approximately -2 and -12% difference in f and f' resulted in $\overline{vv}$ stresses generally within 1% of the unmatched case while the $\overline{uv}$ stresses were aproximately 10% lower at both stations.

These results show the shear stresses being much more sensitive to the yaw parameter asymmetries than the normal stresses. The TKE results shown in Figs. 7.42 and 7.43 appear to be consistent with these normal stress results in that the necessarily matched sx-array gave TKE values close to the unmatched hx-, vx-values. Such effects of sensor yaw asymmetries on the normal and shear stresses can be explained as follows. The normal stress coefficients A^{+2} and B^{-2} or C^{-2} appear as

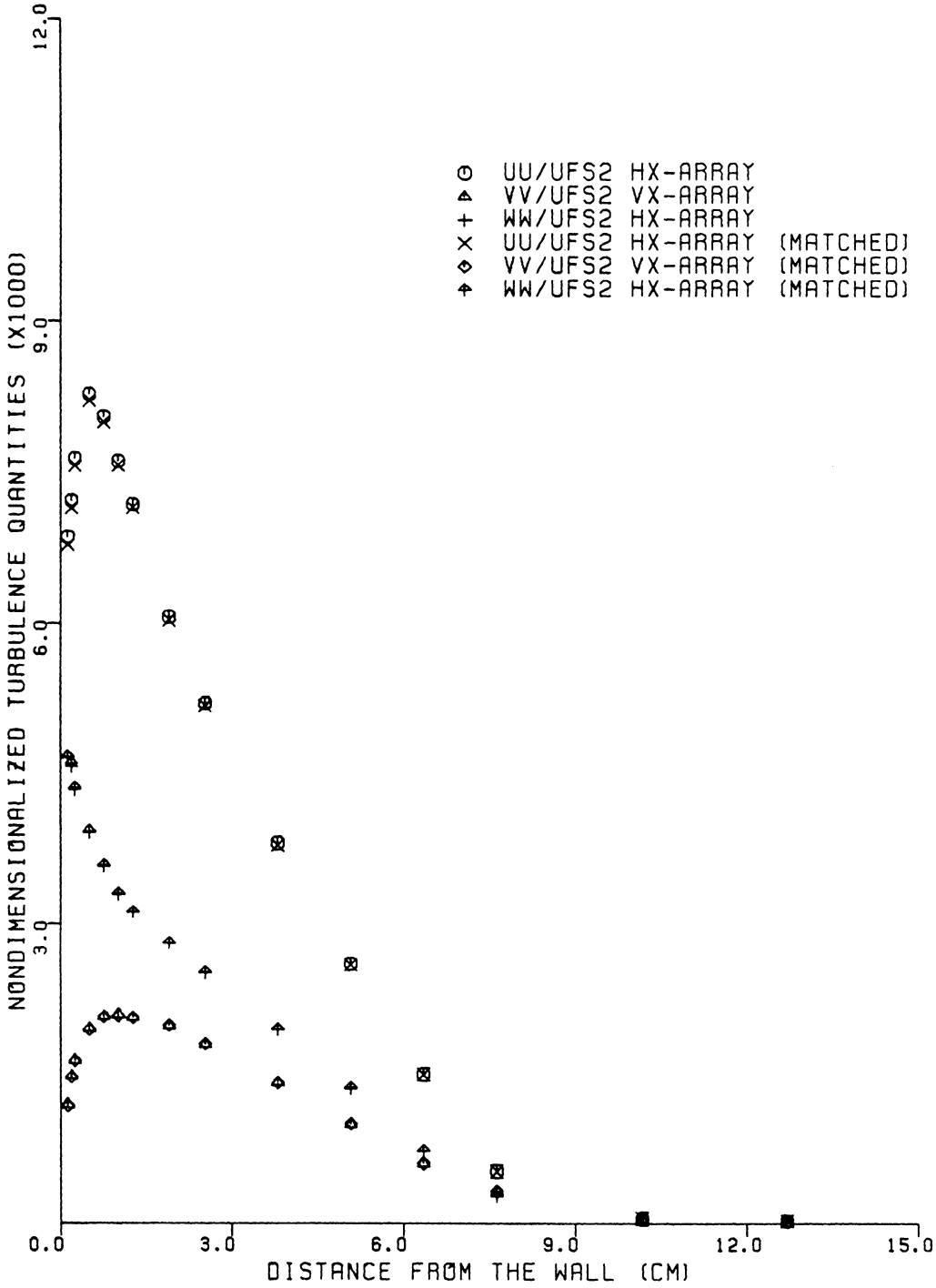

FIGURE 7.46. COMPARISON OF NORMAL STRESS FOR MATCHED AND UNMATCHED SENSORS AT STATION (-3,-2)

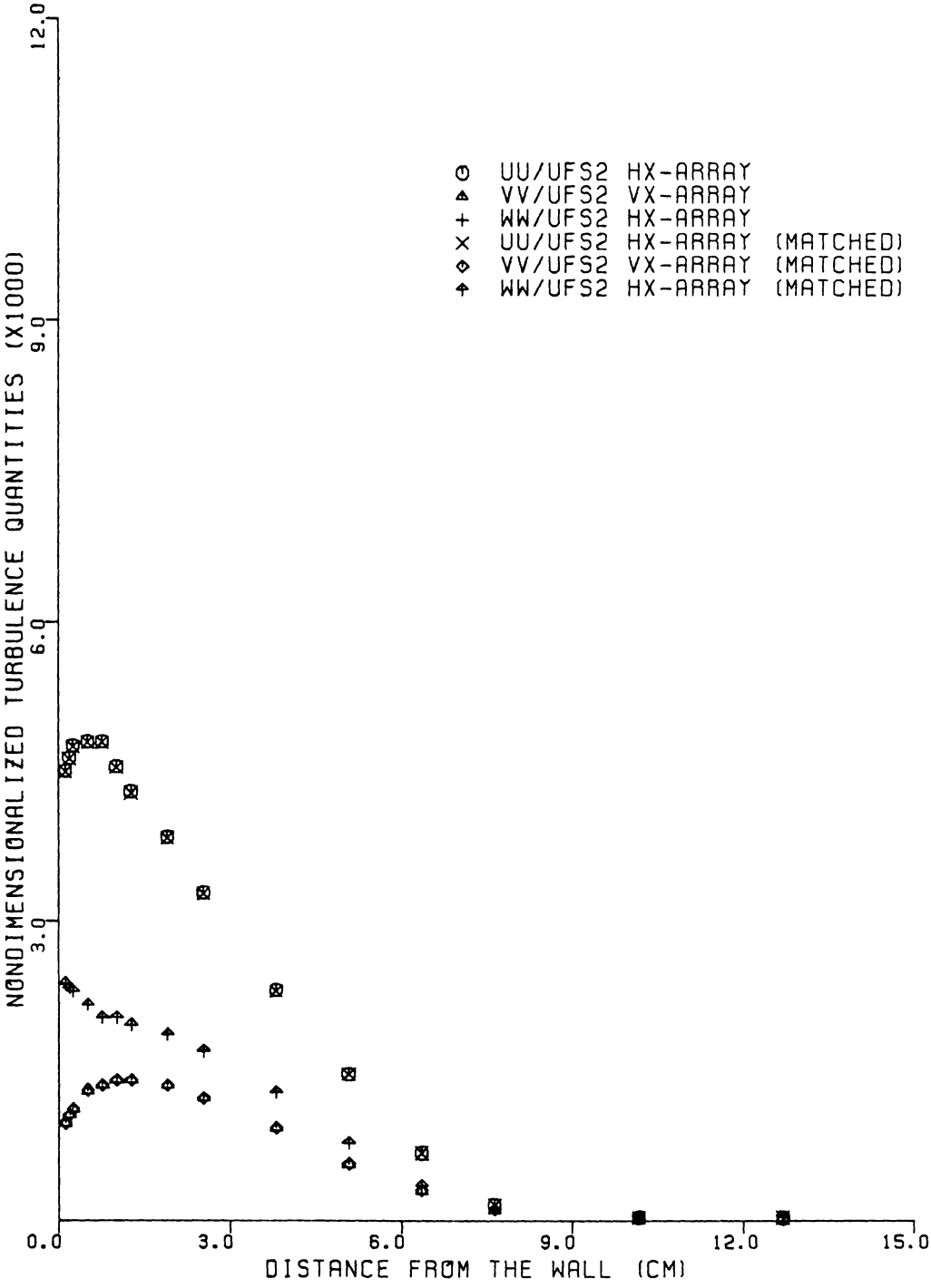

FIGURE 7.47. COMPARISON OF NORMAL STRESS FOR MATCHED AND UNMATCHED SENSORS AT STATION (-7,-6)

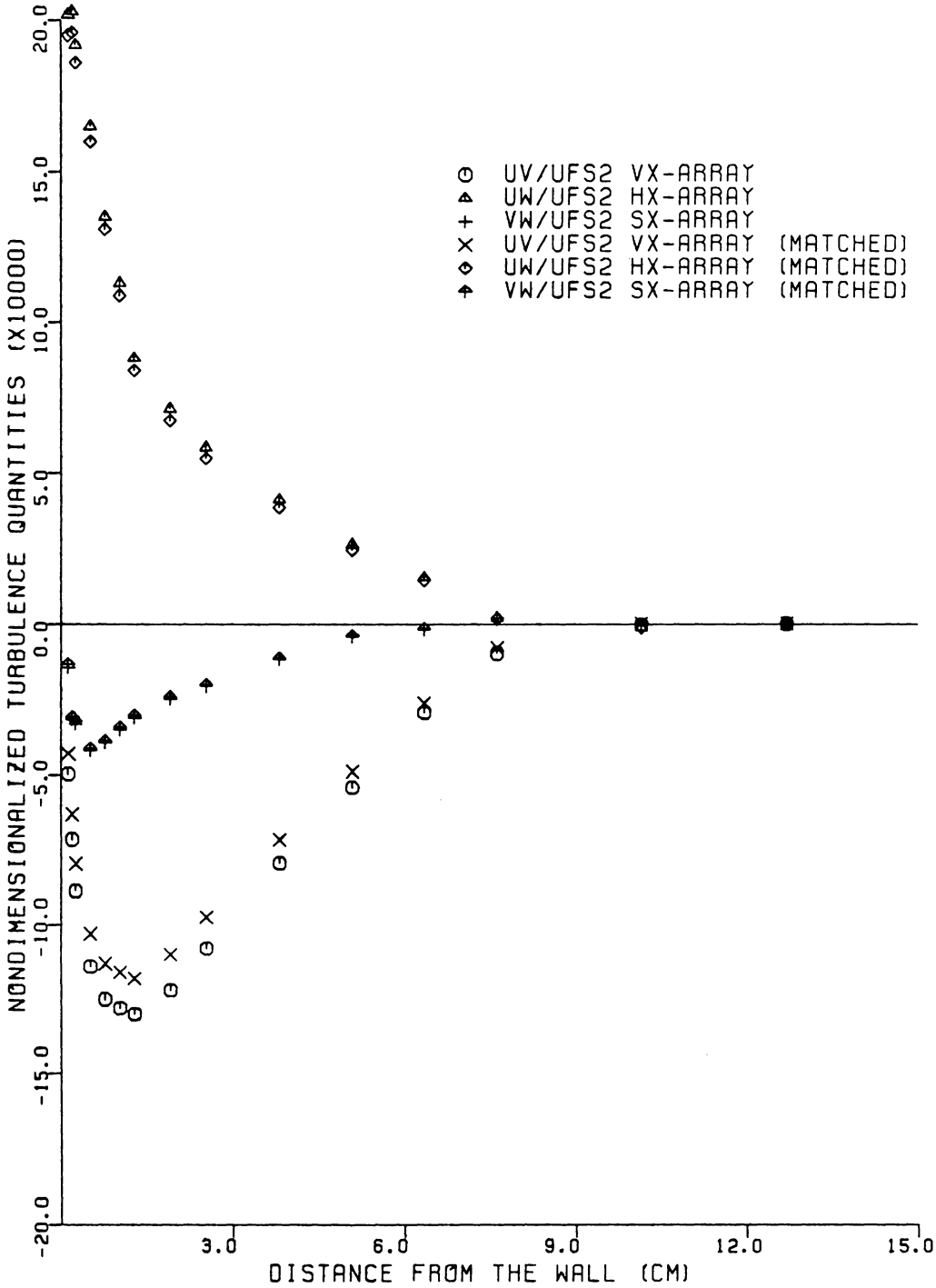

FIGURE 7.48. COMPARISON OF SHEAR STRESS FOR MATCHED AND UNMATCHED SENSORS AT STATION (-3,-2)

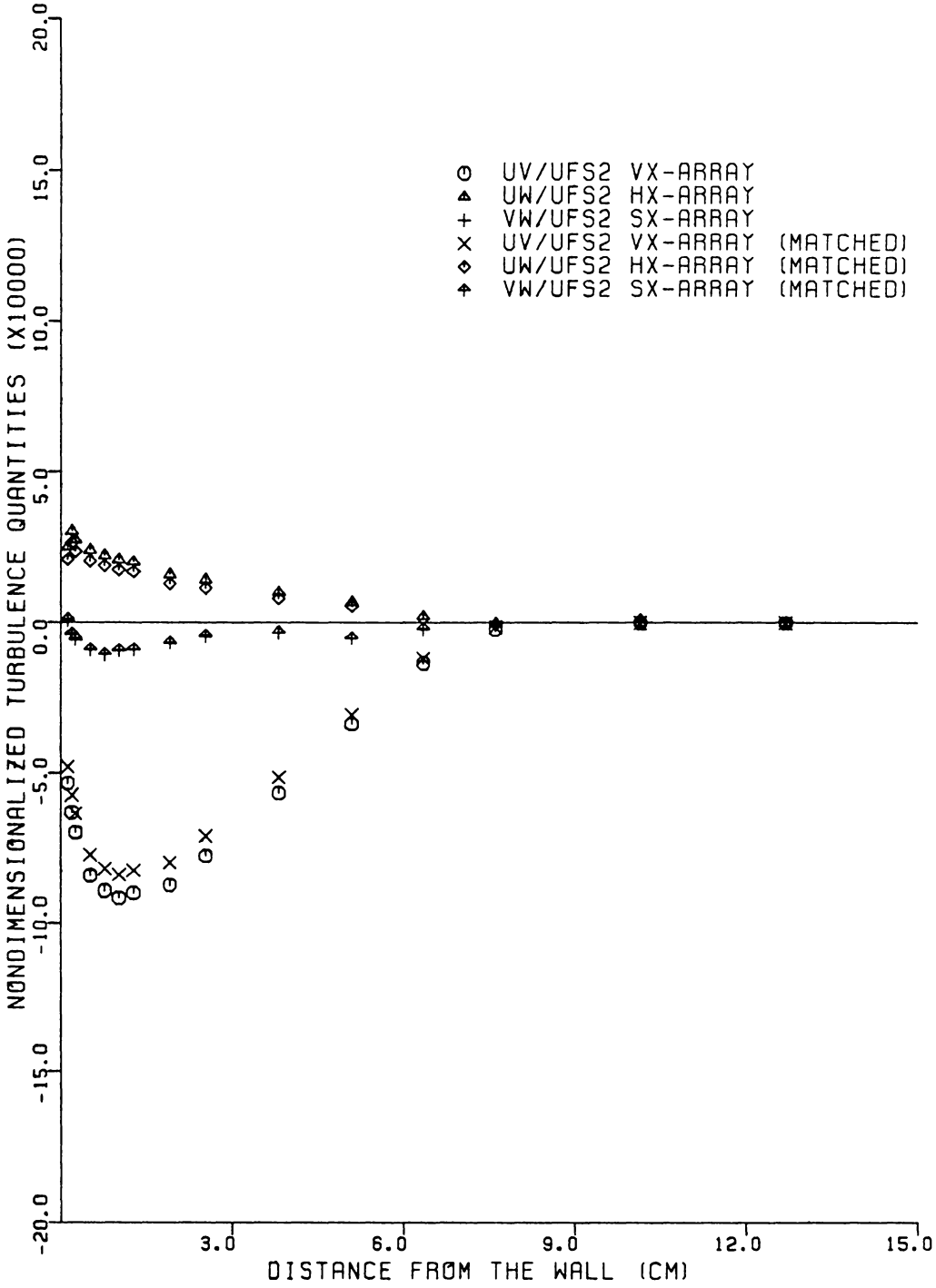

FIGURE 7.49. COMPARISON OF SHEAR STRESS FOR MATCHED AND UNMATCHED SENSORS AT STATION (-7,-6)

diagonally dominant terms in the probe's response coefficient matrix (Eqs. 4.81 and 4.107). The probe's response to the normal stresses via $\overline{(e_a + e_b)^2}$ and $\overline{(e_a - e_b)^2}$ are largely determined by these coefficients which, for unmatched sensors, are usually among considerably smaller terms that arise from differences in f and f' such as A^{-2} and B^{+2} or C^{+2}. The shear stresses, being usually smaller in magnitude, are more affected by the contributions of the subsidiary 'asymmetric' terms involving the larger voltage sum squared and difference squared terms. Thus, using the matched sensor response equations for sensors that are not really matched in parameter k^2 can cause significant errors in the computed shear stresses as shown here. The resulting effect on both the normal and shear stresses of artificially matching unmatched sensors will ultimately depend not only on the magnitude of the sensor asymmetries but also on the relative magnitude of the normal and shear stresses themselves.

It would appear that the differences in the $\overline{uw}$ and $\overline{uv}$ stresses, shown in Figs. 7.44, 7.45, 7.48, and 7.49 between the unmatched hx- and vx-arrays and matched sx-array are due largely to the effect of yaw parameter asymmetries on the matched sensor approximations. This is most evident in Figs. 7.50 and 7.51 which directly compare the results from matched x-array probes where very good agreement is shown in each probe pair results. These results suggest a kind of similarity among the probes' matched sensor response equations even though each system of equations does not give the true response of the probe. Strictly speaking, a precise description of such a response requires all three voltage fluctuation combinations as discussed in Chapter IV and as shown in

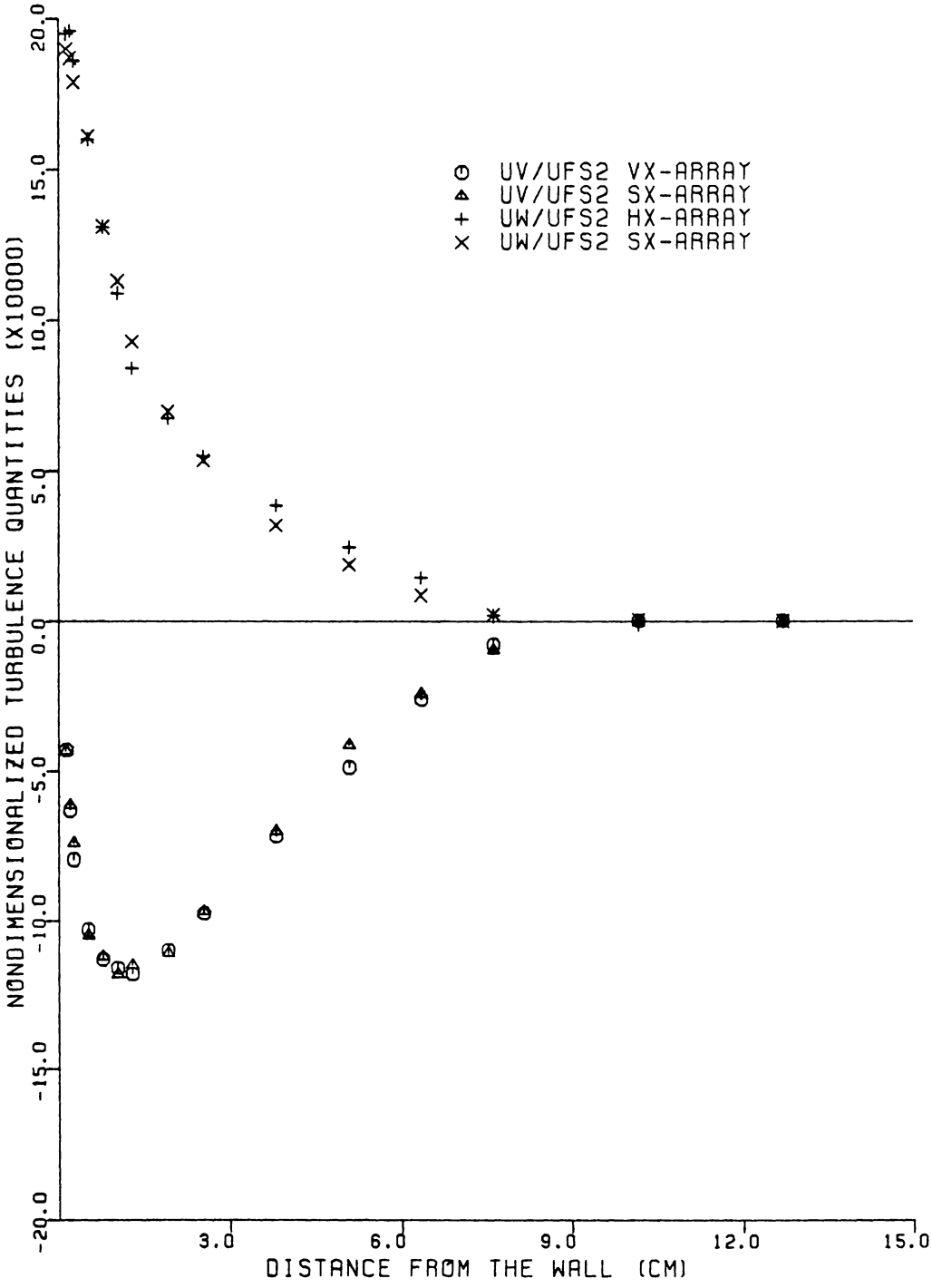

FIGURE 7.50. COMPARISON OF SHEAR STRESS BETWEEN MATCHED SENSOR PROBES AT STATION (-3,-2)

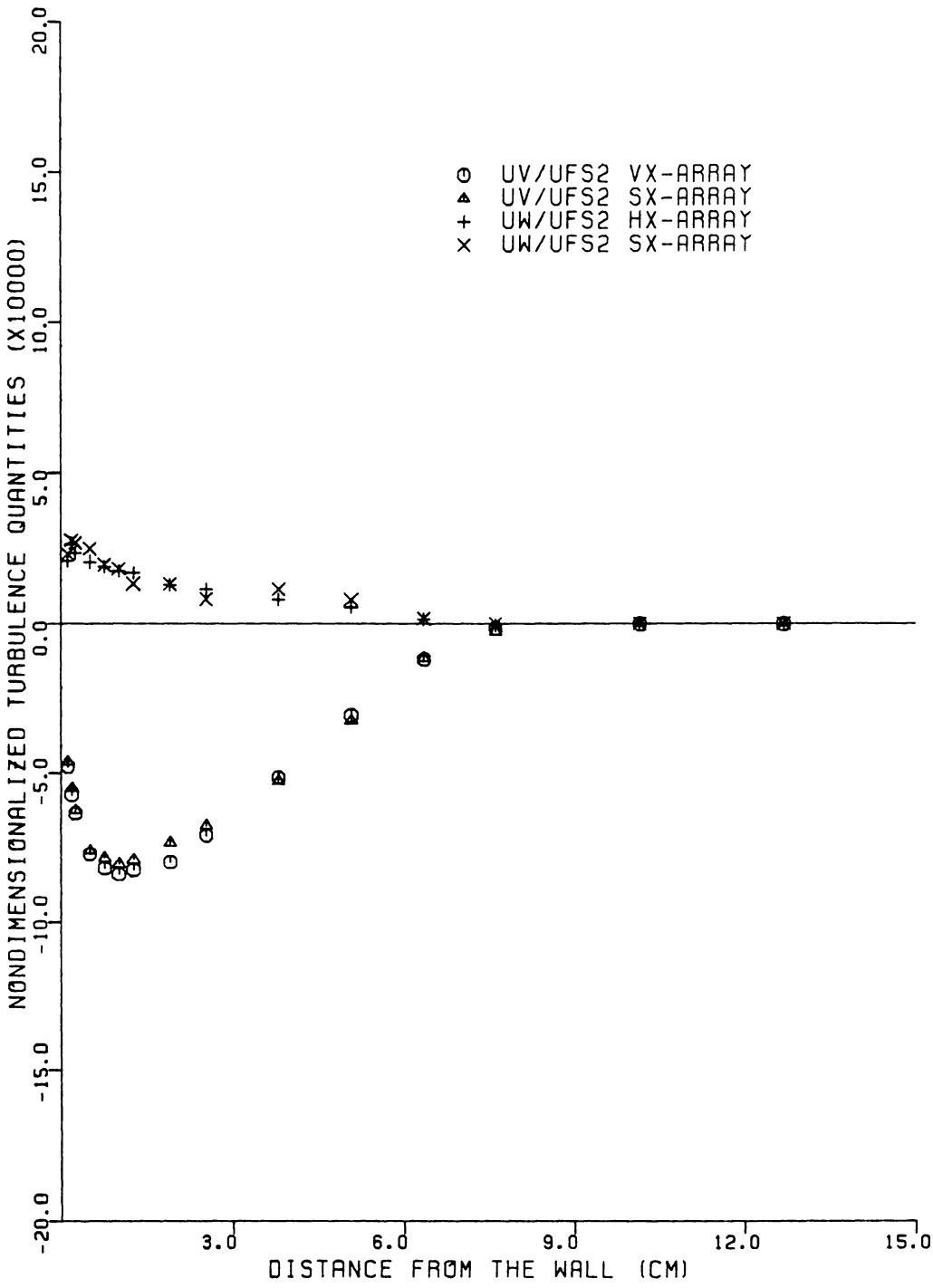

FIGURE 7.51. COMPARISON OF SHEAR STRESS BETWEEN MATCHED SENSOR PROBES AT STATION (-7,-6)

Elsenaar and Boelsma [32]. It would appear that for the flow conditions at stations (-3,-2) and (-7,-6), the sx-array can give a reasonably good approximation of the $\overline{uv}$ and $\overline{uw}$ shear stresses as well as the TKE reported earlier comparable to those of the matched hx- and vx-arrays. However, one must recognize that considerable errors in shear stress may result from the matched sensor assumptions as shown in Figs. 7.48 and 7.49. Smaller errors are noted for the normal stresses as shown in Figs. 7.46 and 7.47. The accuracy of the matched sensor results would depend on the magnitude of sensor asymmetries and also on the relative magnitudes of the turbulent stresses themselves. The use of the more exact, unmatched hx- and vx-array response equations requires individual sensor calibrations to determine the unique yaw parameters but would give a more accurate measurement of the $\overline{uv}$ and $\overline{uw}$ stresses and TKE. The results presented in this study were based on individual sensor calibrations to provide the best accuracy in the hx- and vx-array measurements.

Film Versus Wires

Hot wire and hot film measurements of the $\overline{uu}$ stress are compared in Figs. 7.52 and 7.53. In these results, the x-array values reported earlier are compared to 51 μm (0.002 in.) dia. single film and 4 μm (0.00015 in.) dia. single wire measurements made normal to the flow direction. One repeated wire profile is also shown in the comparison. Figure 7.52 shows that at station (-3,-2) the wire measurements generally fall within the 5 to 7% range of scatter of the film x-array measurements. Figure 7.53 shows that at station (-7,-6) the wire gave

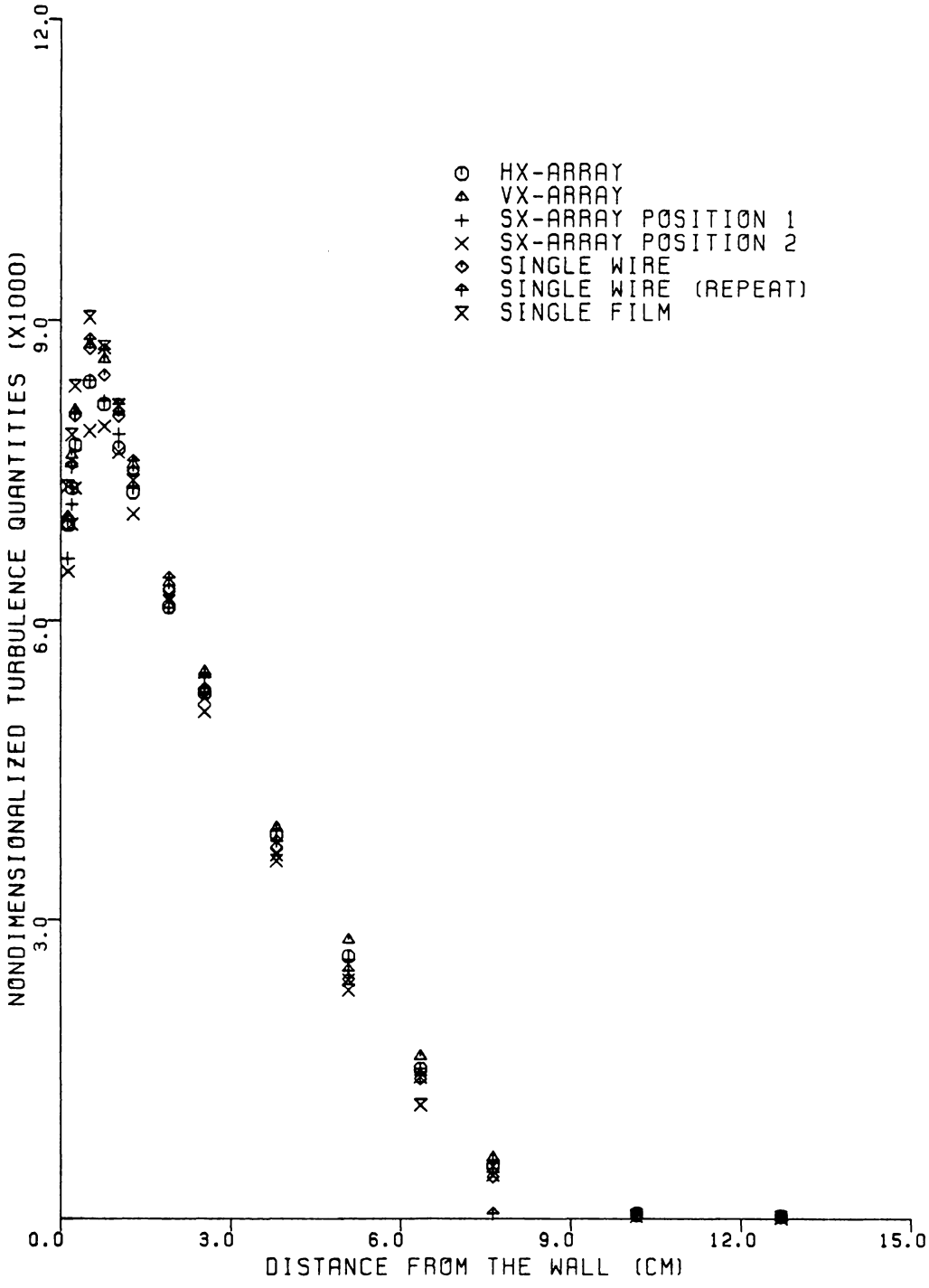

FIGURE 7.52. COMPARISON OF UU STRESS MEASURED BY FILM AND WIRE PROBES AT STATION (-3,-2)

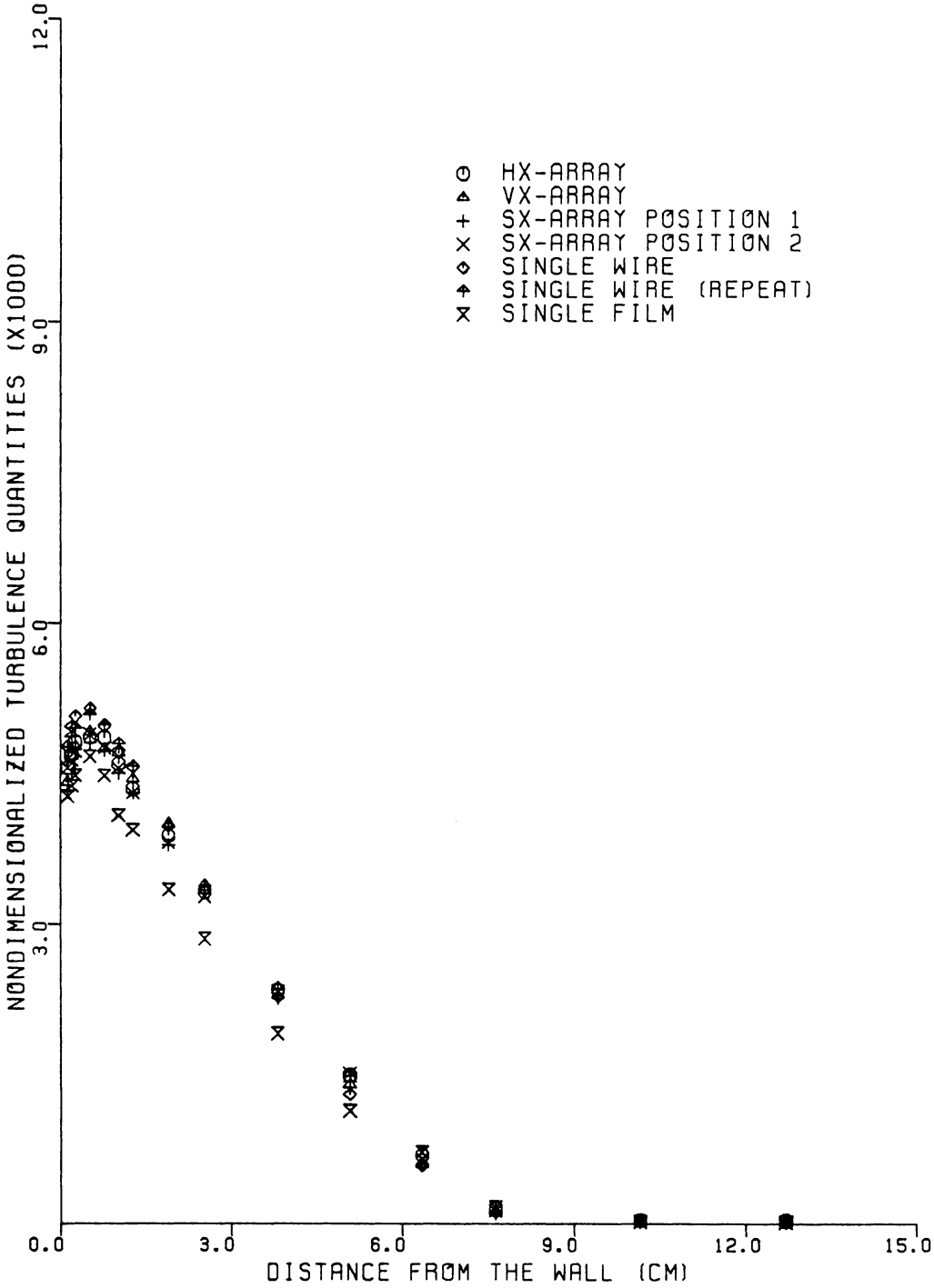

FIGURE 7.53. COMPARISON OF UU STRESS MEASURED BY FILM AND WIRE PROBES AT STATION (-7,-6)

values typically 5% higher than the x-array measured $\overline{uu}$ stresses. For the extreme flow conditions of station (-3,-2), it is noted that the film gave values typically within 4% of the wire with the film values higher at the wall and lower at the outer edge compared to the wire. At station (-7,-6) the single film $\overline{uu}$ stresses were typically 10-20% lower than those of the single wire sensor and 5-15% lower than the film x-array values. For similiar 51 μm diameter films in x-array probes the results of Taslin, Kline, and Moffat [87] suggest only slightly lower normal and shear stresses of the order of 2%. The reasons for the larger differences shown here between the single wire and the single film measurements at station (-7,-6) are not clear.

Linear Versus Nonlinear Response

Single film $\overline{uu}$ stress measurements with and without the use of a linearizer are shown in Fig. 7.54 with one repeated profile. At both stations these results show reasonably good agreement, typically within ± 2%. As noted in Chapter IV, the linearized response gave higher order truncation errors in the Taylor series expansion. From this point of view, good signal linearization would be desirable in high intensity flows.

F. Repeatability, Errors, and Estimates of Uncertainty

Repeatability

Repeatability is an indication of consistency in measured results and is important in estimating uncertainty in experimental work. Several repeated measurements of edge condition, wall shear stress, as well

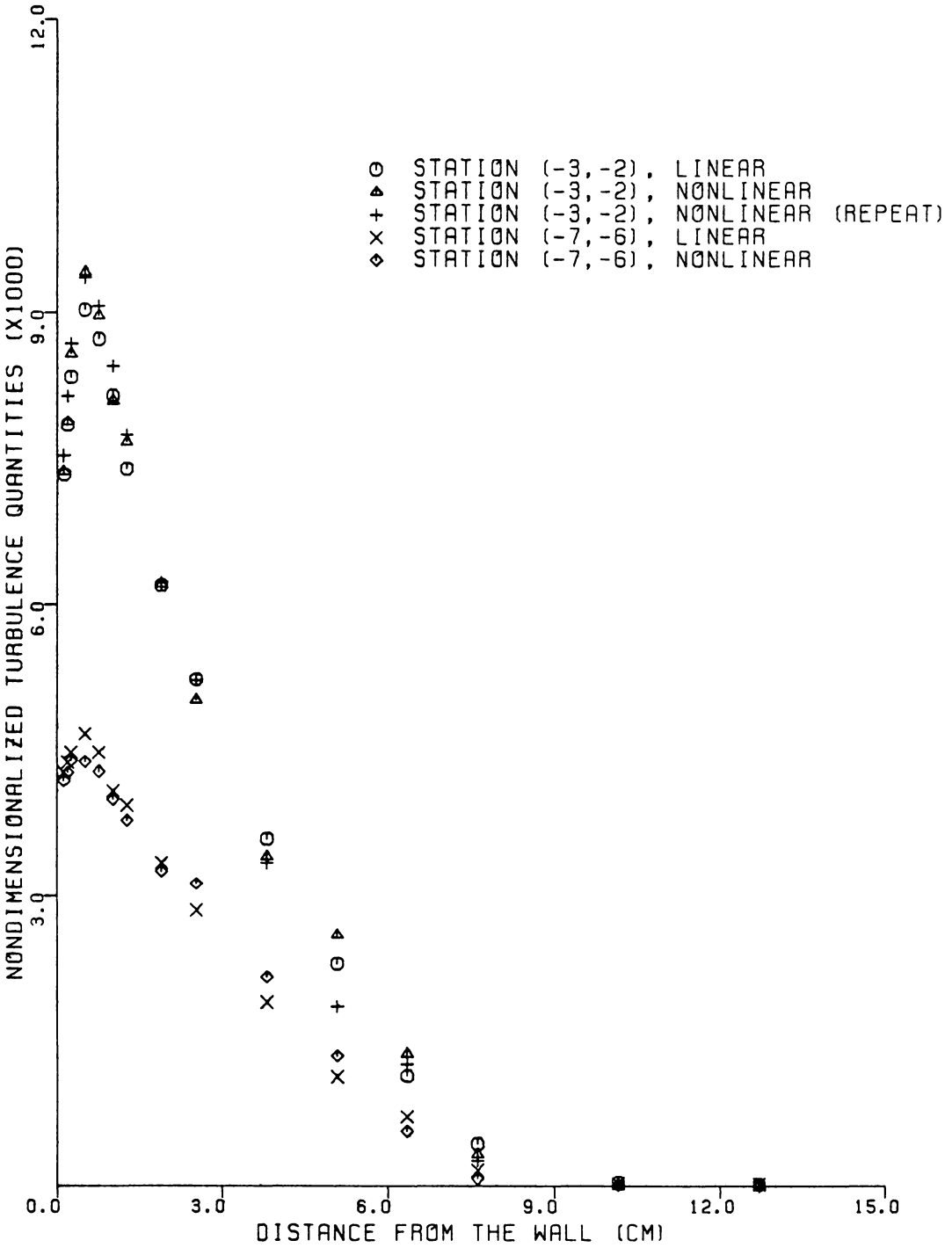

FIGURE 7.54. COMPARISON OF UU STRESS BY A SINGLE FILM WITH AND WITHOUT LINEARIZER

as several repeated mean velocity and Reynolds stress profiles in the upstream and downstream regions of the flow were taken in a detailed examination of this 3DTBL flow. The edge condition and wall shear stress results were reported earlier in this chapter.

Repeatability in mean velocity in the upstream and downstream regions of the flow is shown in Figs. 7.55-7.57. The results show good repeatability in the $\overline{U}_1$ and $\overline{U}_3$ profiles with the repeated measurements typically within ±1% of the initial values. The flow angle (yaw) measurements involved in transforming the mean velocity from the sensor coordinate system to the laboratory system were generally repeatable to within ±0.5°. As discussed in Chapter III, frequent velocity calibrations were performed throughout the experiment. The uncertainty in these calibrations in predicting mean velocity was estimated at ±0.5%. A consistent and good degree of linearization would tend to correct for any fixed errors that could be identified with the velocity measurements.

Figures 7.58-7.59 show the repeatability of the complete Reynolds stress tensor at stations (-3,-2) and (-7,-6). It is noted that each repeated set of the six stress components required the usual 4 traverses by the x-arrays. Hence, a total of 8 traverses were actually repeated between the stations. Generally, the results show good repeatability of the Reynolds stress tensor at both stations. Generally, these stresses were repeatable to within ±3% to 4% in the lower 2/3 of the boundary layer where significant values were measured.

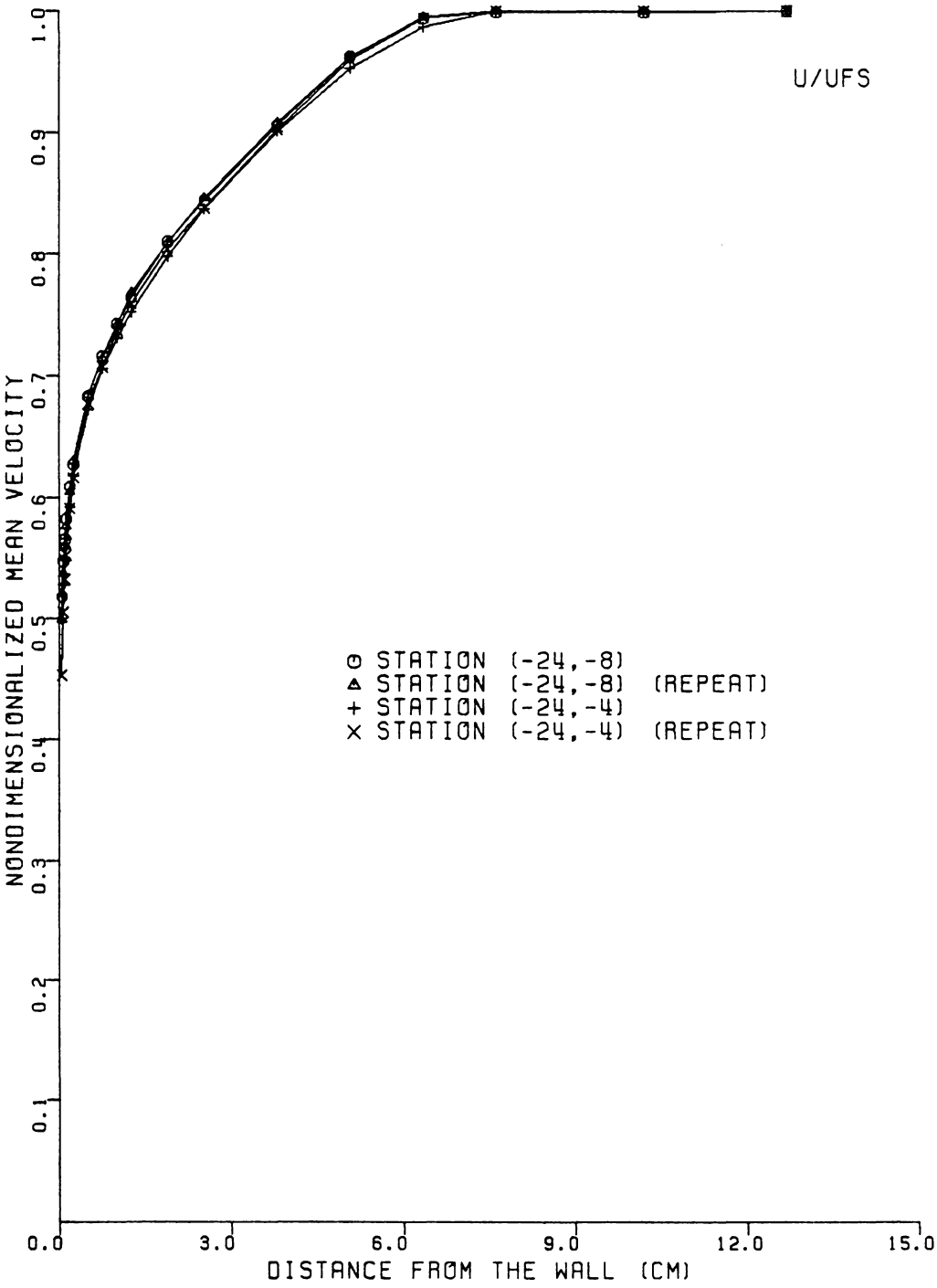

FIGURE 7.55. REPEATABILITY IN MEAN VELOCITY ALONG THE INITIAL CONDITION PLANE

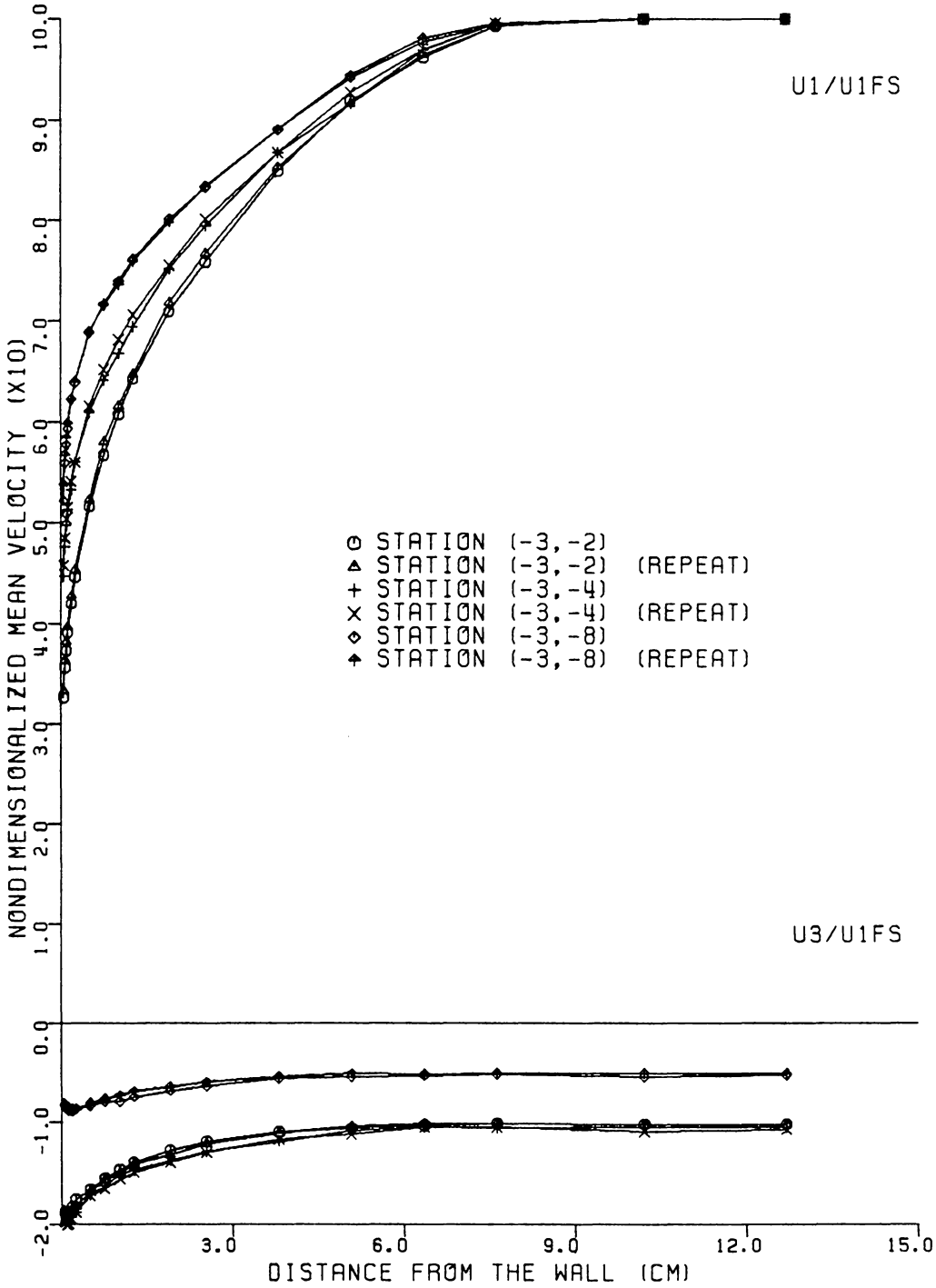

FIGURE 7.56. REPEATABILITY IN 3DTBL MEAN VELOCITY PROFILES

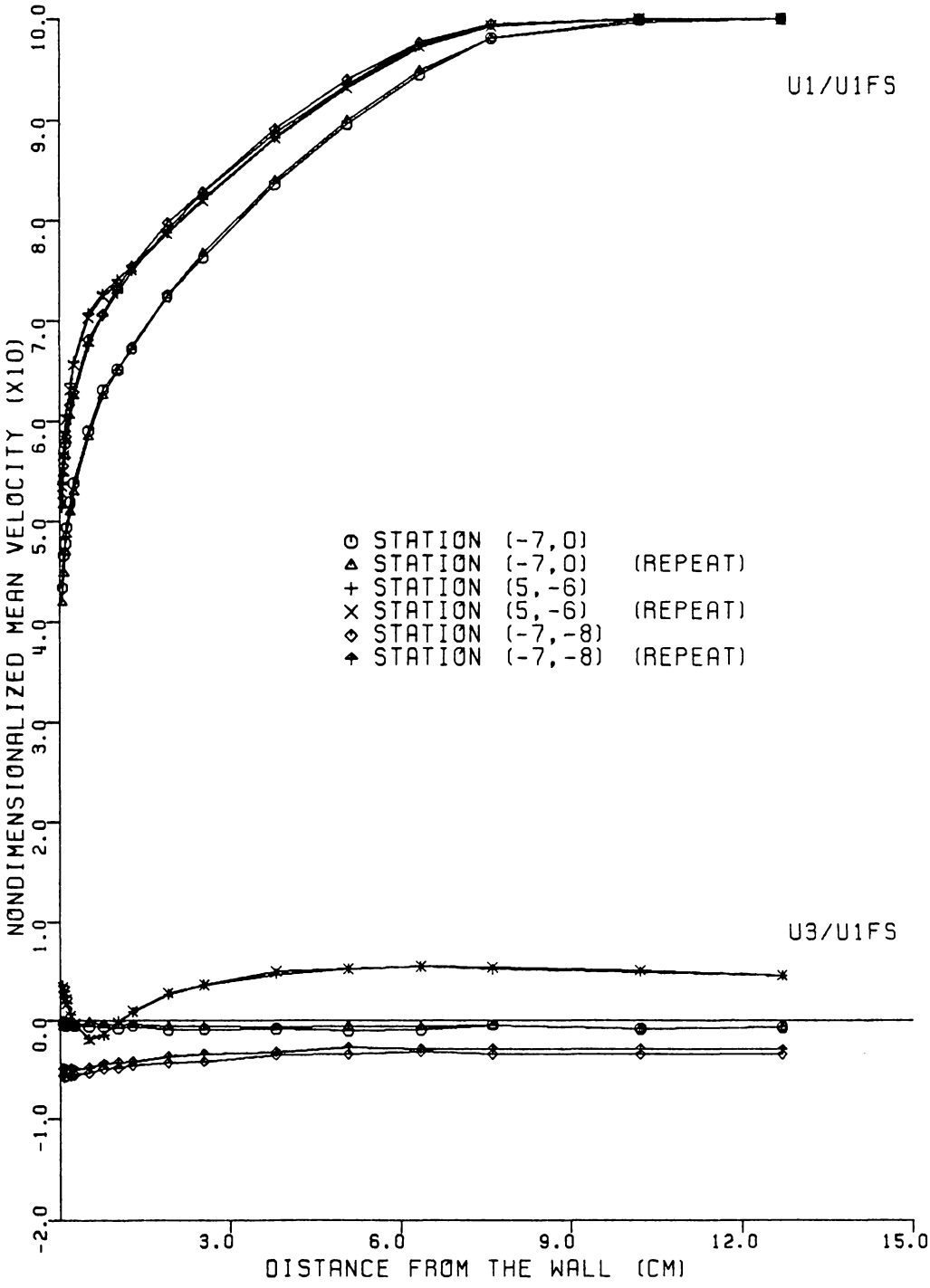

FIGURE 7.57. REPEATABILITY IN 3DTBL MEAN VELOCITY PROFILES

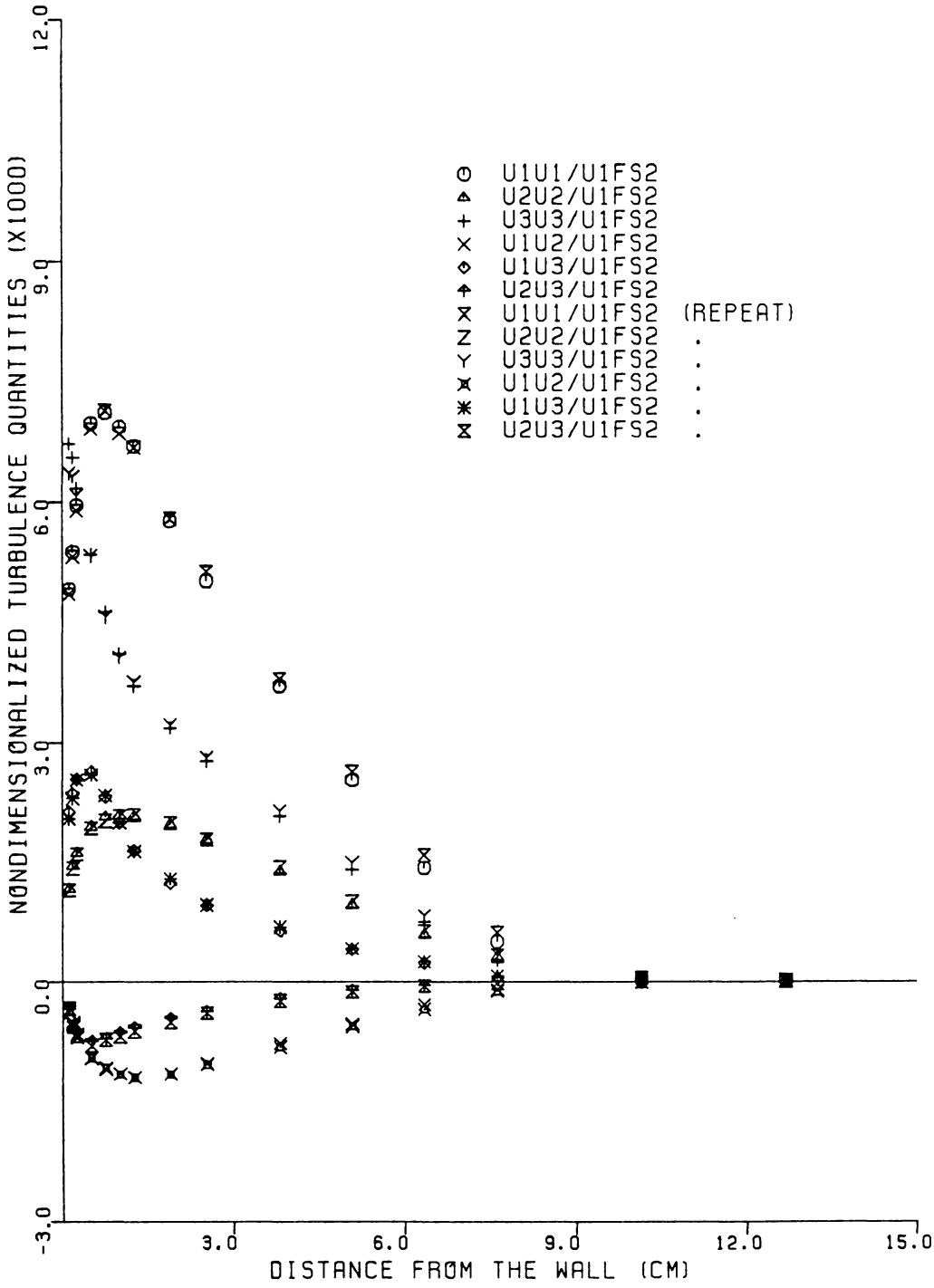

FIGURE 7.58. REPEATABILITY IN REYNOLDS STRESS TENSOR AT STATION (-3,-2)

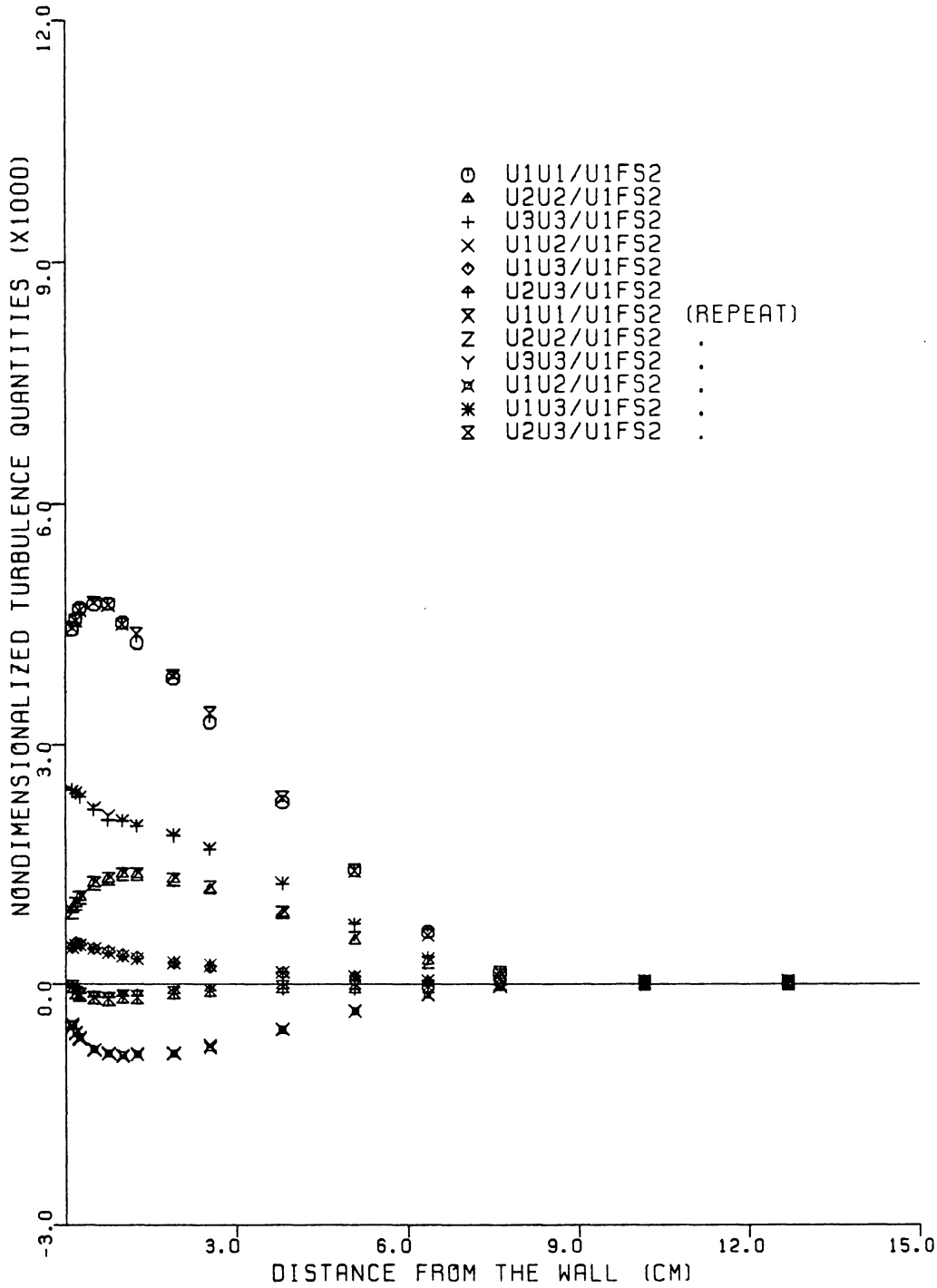

FIGURE 7.59. REPEATABILITY OF REYNOLDS STRESS TENSOR AT STATION (-7,-6)

Errors

There are various errors that can contribute to the overall uncertainty in turbulence measurements as discussed in Elsenaar and Boelsma [32]. Many of these have been discussed in earlier sections.

The more significant errors in the turbulence measurements were identified with the uncertainties in yaw parameter, k^2, the yaw angle α, and the degree of linearization which is indicated by the uncertainty in estimated slope, B. Using the results in Chapter V, these uncertainties gave errors in the turbulent stresses of approximately ±5%. This error estimate was based on a sensitivity study made on the matched sensor response equations. As discussed earlier, additional errors can be identified with the matched sensor response equations when they are used to calculate stresses from probes with asymmetric sensor yaw parameters. The largest errors occurred in the $\overline{uv}$ and $\overline{uw}$ stresses for the cases studied. Since the calibration results in Chapter V (Table 5.2) indicated some yaw parameter asymmetry in the sx-array, a modest increase in uncertainty in the $\overline{vw}$ stress was expected.

Probe misalignment errors resulting from small $\overline{U}_2$ components of velocity as shown in Fig. 3.14 and errors related to the turbulence intensity of the flow can be corrected as discussed in Chapter II. The former errors were in effect corrected by including probe misalignment in the sensor response equations derived in Chapter IV. For the intensity levels encountered in this 3DTBL flow however, no intensity-related corrections appeared to be necessary.

The flow field related errors such as interference of the probe with the local flow and the influence of the local velocity gradients on

the probe's response were difficult to quality due to their nature. Sandborn [53] showed that sizeable errors in turbulent stresses can result when large velocity gradients exist along the length of a wire. While the turbulence results were expected to be influenced by all the local velocity gradients, the effect of normal gradients would tend to be less severe in a 75-100 mm (3-4 in.) thick boundary layer as measured in this study. This may not be the case for the effects of local cross-stream pressure gradients. Such an effect is perhaps implied in the results of Fig. 7.52. The effect of the probe's intrusion on the flow are twofold. First, the probe can affect the flow locally at the 'point' of measurement and, second, the probe stem and supporting material can effect the curvature of the freestream streamlines which can alter the pressure field that drives the flow. The former effect was identified as a possible cause of the behavior in the $\overline{U}_2$ velocity near the wall shown in Figs. 7.13-7.16.

Estimates of Uncertainty

On the basis of these results and the level of repeatability in probe positioning, flow conditions, etc. implied in Figs. 7.55-7.57, the overall uncertainty in the mean velocity was estimated at approximately ± 0.5% at the outer region of the boundary layer increasing to up to ±2% at the wall. The uncertainty in the flow angle measurement was estimated at $\pm 0.5^{o}$ for both the inner and outer regions. The effects of turbulence on the magnitude of the mean velocity measured by the single film were not significant, typically being less than 1% as was shown in Tables 7.1 and 7.2.

The overall uncertainty in the turbulent stresses in the sensor coordinate system, was estimated at ±8% with the exception of the $\overline{vw}$ stress where the uncertainty was estimated at ±12%. These estimates were based on the repeatability in the measurements, the comparisons with redundant stresses, and on the uncertainty in the independent variables β, k^2, α, that were identified with causing the more significant errors in these stresses in the matched sensor response sensitivity studies.

In an attempt to approach an N^{th} order uncertainty estimate as discussed by Moffat [143], turbulence data was taken with a calibrated DISA 55D35 RMS voltmeter [47] and compared to the results obtained with the calibrated DISA 55B25 turbulence processor [43]. The sx-array was used in its position 1 and the measurements of $\overline{uu}$ stress, and $\overline{(v + w)^2}$ and $\overline{u(v + w)}$ turbulence quantities (see Chapter IV) were taken with both instruments. The comparisons are presented in Table 7.12. With only a few exceptions, the turbulence processor and RMS meter results for these quantities agreed to within 5%. It is noted that the RMS measurements of $\overline{uu}$ and $\overline{(v + w)^2}$ were not completely independent since they required measurements of the combinations $(e_a + e_b)$ and $(e_a - e_b)$, which were taken from the turbulence processor. However, the $\overline{u(v + w)}$ measurements could be taken independently by the RMS meter.

Table 7.11 Comparison of Turbulence Quantities Using a DISA 55B25 Turbulence Processor and a DISA 55D35 RMS Voltmeter

	Turbulence Processor			RMS Meter		
y	$\overline{uu}/\bar{U}^2_{FS}$	$\overline{(v+w)^2}/\bar{U}^2_{FS}$	$\overline{u(v+w)}/\bar{U}^2_{FS}$	$\overline{uu}/\bar{U}^2_{FS}$ (a)	$\overline{(v+w)^2}/\bar{U}^2_{FS}$ (b)	$\overline{u(v+w)}/\bar{U}^2_{FS}$ (c)
(cm)	($X10^3$)	($X10^3$)	($X10^4$)	($X10^3$)	($X10^3$)	($X10^4$)
0.127	4.83	3.30	-4.90	4.64	3.24	-4.68
0.190	5.08	3.36	-6.03	4.86	3.31	-5.66
0.254	5.27	3.43	-6.26	5.00	3.32	-6.49
0.508	5.58	3.48	-8.90	5.65	3.43	-8.67
0.762	5.52	3.51	-9.35	5.42	3.44	-9.13
1.016	5.22	3.48	-10.1	5.20	3.41	-10.0
1.270	4.96	3.43	-9.65	4.78	3.37	-9.95
1.905	4.34	3.35	-9.35	4.32	3.34	-9.58
2.540	3.89	3.20	-8.60	3.87	3.17	-8.30
3.810	2.97	2.70	-6.33	3.02	2.64	-5.81
5.080	2.09	1.97	-5.13	2.05	1.93	-4.90
6.350	1.06	1.16	-2.58	1.07	1.13	-2.49
7.620	0.08	0.14	-0.17	0.07	0.14	-1.40
10.160	0.02	0.03	-0.02	0.02	0.03	-0.02
12.700	0.01	0.03	-0.01	0.01	0.03	-0.02

(a) Required $(e_a + e_b)$ from turbulence processor.

(b) Required $(e_a - e_b)$ from turbulence processor.

(c) Obtained directly from RMS meters.

VIII. SUMMARY AND CLOSING

Summary

A pressure-driven 3DTBL flow upstream and around a junction vortex was experimentally studied and is offered for use as a benchmark flow for testing and evaluating the predictive ability of state-of-the-art 3DTBL codes.

The pressure-driven flow was generated by a streamlined cylinder placed normal to a flat surface. The 3DTBL flow develops from a collateral, nominally 2D upstream flow as a result of curvature of the freestream streamlines imposed by the body. The collateral character of the far upstream flow quickly changes when significant curvature of the freestream streamlines begins. The 3DTBL flow is characterized by a turning of the local velocity vectors within the boundary layer where the upstream flow experiences unilateral skewing of up to 30^{o} with some slight bilateral skewing of its inner layers in the local regions of the downstream flow. In addition to skewing of the boundary layer, the plane of symmetry flow experiences steep adverse pressure gradients with flow separation ahead of the body's leading edge with a junction vortex system developing around the body.

The documentation of the 3DTBL flow includes:

1) upstream initial conditions along a plane with measured
   a) mean velocity field,
   b) Reynolds stress tensor field including,
   c) the turbulent kinetic energy field;

2) freestream velocity or edge conditions measured from the initial plane extending downstream to the 3DTBL flow regions and wall static pressure field measurements;

3) measurements in the 3DTBL of

   a) mean velocity field,

   b) Reynolds stress tensor field,

   c) wall shear stress magnitude by a Preston tube,

   d) limiting wall streamline directions from oil streak flow visualizations, and

   e) earlier direct force wall shear measurements of both magnitude and direction.

Mean velocity magnitude and direction were measured with a single hot film probe. Measurements of the complete Reynolds stress tensor were made with three hot film x-array probes used in the crossflow mode.

Flow conditions, skin friction coefficients, and limiting wall streamline directions are summarized in Table 7.8. Three components of the mean velocity and Reynolds stress tensor results are tabulated in Appendix G. The edge conditions are given in Tables 7.5 and 7.6 and the wall static pressure coefficient distribution with a pressure gradient map are presented in Appendix H.

The Preston tube wall shear magnitudes were obtained using Patel's calibration equations summarized in Eqs. 7.8-7.10. Each Preston tube meausrement was corrected for local cross-stream pressure gradient using a first order static pressure correction. The corrected and uncorrected values of wall shear are tabulated in Table 7.9. The corrected wall

shear values are generally within 4% of the uncorrected values. Two extreme cases occur at stations (-3,-2) and (-3,0) near flow separation where the differences are 13 and 20%, respectively. In Table 7.10, the correction is shown to give a more symmetric response for the Preston tube as it is yawed with respect to the local wall shear direction.

The Preston tube wall shear magnitudes are compared to the earlier direct force wall shear measurements of McAllister in Table 7.9. The uncorrected Preston tube values generally fall within 10% of the direct force values and the corrected values are within 8% of the direct force wall shear results.

Turbulence data were taken along 4 planes at 14 stations. At the outer regions of the boundary layer, the turbulent stress profiles converge and decrease in value toward the freestream. The freestream turbulence intensity was slightly less than 0.6%. In the boundary layer, the turbulence intensity levels (based on local mean velocity) were generally below 20%.

The $\overline{u_1u_2}$ stress is shown to be the dominant shear stress at stations identified with collateral or near collateral flow. A growth in the magnitude of the $\overline{u_1u_3}$ and $\overline{u_2u_3}$ shear stresses occurs as the secondary flow developes in response to the transverse pressure gradients following freestream streamline curvature. The results suggest that the gradient $\partial(\overline{u_1u_3})/\partial x_3$, which is usually neglected in the x_1-momentum equation in a boundary layer analysis, may be signficiant near flow separation. Consequently, it may be necessary to model the $\overline{u_1u_3}$ stress as well as the $\overline{u_1u_2}$ and $\overline{u_2u_3}$ shear stresses in a 3DTBL calculation of this kind of flow.

The shear stress/TKE magnitudes are consistent with those reported by Dechow and Elsenaar and Boelsma.

Along the plane of symmetry, where the flow encounters a steep adverse pressure gradient before separating, there is a growth in the normal stresses, with the $\overline{u_1 u_1}$ stress increasing most rapidly. This results in an increase in the TKE of the flow along this plane.

Off the plane of symmetry and downstream of the leading edge, an additional extremum in the Reynolds stress profiles occurs which develops with the flow. This change in shape of the stress profiles, from one to two extrema, appears as the transverse pressure gradient changes direction. The location of the extremum nearer the wall generally falls within the y range of the boundary layer where turning of the mean velocity vectors approaching the wall changes from a monotone increasing to a monotone decreasing character. At one station, the $\overline{u_1 u_3}$ and $\overline{u_2 u_3}$ stresses change sign in this region.

In the development of this standard test case, a great emphasis was placed on the accuracy and precision of the measurements as well as the quality of the flow upstream of the body. Further, a thorough examination was made of response analyses and different cooling laws.

As part of this overall effort, the following studies were made:

1) A 2D wind tunnel calibration (Chapter VI) which involved,
   a) sensitivity studies of the spanwise nonuniformities to various upstream screen-filter cloth combinations,
   b) 2D momentum integral study along the tunnel centerline, and the

c) effect of spanwise nonuniformities on the mean 3DTBL flow field.

2) Extensive studies on the repeatability in edge condition measurements, wall shear stresses, mean velocity and Reynolds stress profiles in the usptream and downstream regions of the flow were made (Chapter VII).

3) An examination was made of the degree of symmetry in the initial and edge conditions, mean velocity field, and $\overline{uu}$ stress field (Chapter VII).

4) A calibration technique was developed to determine the individual yaw characteristics of each sensor regardless of the probe configuration (Chapter V). This method replaced the conventional approach described by Jorgensen which could not be applied to all the sensors used in this study. The cooling laws of Hinze, and Davies and Bruun were studied using both linear and nonlinear response equations for each cooling law. The yaw parameters k^2 and m determined by this new method were compared to results obtained by a more conventional method.

5) A detailed hot wire/film analysis was developed for arbitrary sensor orientation to the flow (Chapter IV) which allows

a) the correction of mean velocity for turbulence where comparisons were made to several existing correction formulas,

b) misalignment of the sensor with the local streamline direction,

c) the use of an arbitrary cooling law for calculating turbulence, and the

d) the calculation of redundant stresses from the slant x-array.

e) The analysis yields a precise defintion of the conditions required for a matched sensors in an x-array probe, and also shows the effects of deviations from the matched sensor conditions.

f) Finally, the analysis yields geometric guidelines for constructing x-array probes.

6) The generalized response equation developed here was compared to the response equations of Bruun and Champagne et al. (Appendix C).

7) Various sensor response sensitivity studies include,

a) sensitivity to flow misalignment (Chapter IV and Appendix E),

b) Reynolds stress sensitivity to the cooling laws of Hinze, and Davies and Bruun (Chapter VII), and

c) Reynolds stress sensitivity to sensor mismatch (Chapter VII).

8) A comparison was made of redundant stresses measured by the slant x-array with those measured by the horizontal and vertical x-arrays (Chapter VII).

9) A comparison of nine measurements of mean velocity was made using the various x-array probes and the single film probe, with and without turbulence correction (Chapter VII).

10) Comparisons of x-array measured turbulent streamwise intensity were made with measurements from both a single hot film and a single hot wire probe (Chapter VII).

11) Finally, comparisons of turbulent streamwise intensity obtained with and without linearizing circuitry were made (Chapter VII).

In the tunnel calibraton studies, the measured spanwise nonuniformities in mean velocity along a far field and the test section plane are consistent in magnitude with those reported by other investigators. Modest changes in these nonuniformities do not appear to significantly influence the pressure-drive 3DTBL flow. A momentum integral study along the center plane of the tunnel indicated a nominally two-dimensional flow of good quality.

The nominally 2D initial condition data of mean velocity and Reynolds stress tensor can be used to initiate a 3DTBL calculation, with the upstream initial condition plane showing no apparent influence of the body. The computer analyst must resolve the question of real world spanwise nonuniformities along the initial condition plane. Such nonuniformities have been confirmed to exist in other carefully studied nominally two-dimensional flows and are not unique to this flow.

The 3DTBL flow shows a good degree of symmetry in edge condition, mean velocity field, and $\overline{uu}$ stress field at the stations examined. Generally, the data shows good repeatability in edge condition, wall shear stress, mean velocity and Reynolds stresses.

The calibration method developed for the x-array probe sensors, gives yaw parameters k^2 and m for both a nonlinear and linearized re-

sponse that are consistent in magnitude with reported values. Probe asymmetries in both of these yaw parameters were confirmed to exist to some degree in the three x-arrays probes calibrated for this study. The calibration method developed uses a family of calibration curves to determine the unique yaw parameter for each sensor in a selected yaw interval. For those sensors that could be treated by the conventional approach, the results between the new method and the conventional approach are in good agreement.

For the conditions studied, the cooling laws of Hinze, and Davies and Bruun were essentially equivalent in the values of the function f and its first derivative, f', but gave considerably different values for the second derivative, f". The f" values of the Davies and Bruun law are as much as 40% higher than the values of the Hinze law. This second derivative term is involved in the second and higher order fluctuating velocity correlations in the sensor response equation. Hence, the difference in f" may be important in high intensity flows where these higher order correlations should be considered. In this nominally low intensity flow, these higher order terms are properly neglected in the stress measurements. Both laws give very similiar Reynolds stresses for this case.

This second derivative cooling law function term, f", is also involved in the mean velocity turbulence correction. It was convenient to include these terms in the turbulence correction for the mean flow to gain some indication of the effects of these terms. As might be expected for this low intensity flow, only small differences were observed in these corrections between the two cooling laws studied, with the

Davies and Bruun law giving slightly smaller corrections.

The generalized mean velocity correction for turbulence developed here is consistent with several reported correction formulas for a normal sensor. This generalized turbulence correction was applied to the mean velocities measured by the individual sensors of the vertical, slant, horizontal, and single film probes. For this flow, the turbulence correction decreased monotonically with increasing roll angle, γ_x, of the sensor plane. It is emphasized that no generalization can be made of such behavior for other flows since turbulence corrections depend on the individual flow field. Generally, turbulence effects on the calculated mean velocity magnitudes were not significant in this flow.

The sensor response equations of Bruun and Champagne et al. were obtained as special cases of the generalized response equation developed in this study.

Considerable analytical work was done in formulating the x-array response. In a prescribed plane, matched sensors requires not only equal velocity sensitivities but an equivalence in the sensors' yaw characteristics as well. The matched sensor assumptions are not required for the horizontal and vertical x-arrays when the general response equations, which involve all three voltage fluctuation combinations, are used to compute their stresses. The slant x-array response equations however, require the complete set of matched sensor assumptions which are necessary to obtain the $\overline{vw}$ stress. In addition to the $\overline{vw}$ stress, it is possible to measure the TKE, and the $\overline{uv}$ and $\overline{uw}$ stresses. The accuracy in these redundant stresses depends on the

magnitude of the probe asymmetries and also on the magnitudes of the Reynolds stresses themselves. Electronically matching the velocity sensitivities of the sensors gives only partially or 'quasi' matched sensors which alone is not sufficient to obtain a solvable system of equations. For a quasi-matched probe one has to deal with only yaw parameter asymmetries. When an average value of the yaw parameter k^2 was used for quasi-matched sensors, the matched sensor response equations gave slant x-array values of $\overline{uv}$, $\overline{uw}$, and TKE that agreed reasonably well with those of the matched horizontal and vertical x-arrays at the data stations considered. However, errors of up to 20% in $\overline{uw}$ and up to 10% in $\overline{uv}$ stresses were identified with using these match sensor equations for probes inherently asymmetric in k^2.

The x-array, single film, and single wire measurements of mean velocity magnitude were in very good agreement. The $\overline{uu}$ stresses from the single film obtained with and without linearizers were also in good agreement at the stations where these comparisons are made. The compared x-array film and single wire measurements of $\overline{uu}$ stress for two extreme flow conditions fell within an approximately 7% range of values.

Closing

The results in this study should allow a good test of the predictive ability of any existing 3DTBL code. The specification of turbulence data on the intial plane should permit the testing of several intermediate and higher order turbulence models. The measured initial plane condition will circumvent having to perform any additional 2DTBL

flow calculation required to match some measured condition at some downstream station to initiate a 3DTBL calculation. Further, the measured edge condition eliminates the need to assume a freestream potential flow to sustain the calculation.

The various studies and comparisons made should give the computational fluid dynamicist a reasonably good indication of what may be considered an acceptable or successful simulation of this standard test case flow. It is hoped that this work will also facilitate computational efforts in further developing turbulence models. Finally, the recent Stanford Conference on Complex Turbulent Flows noted a clear deficiency in the number of experimentally studied flows with the kind of complete documentation that could be of value in modeling turbulence. More well documented experiments are needed not only to evaluate computed results but also to gain a better understanding of complex turbulent flows. Advances in this area will require a collaboration of both theoretical and experimental efforts.

REFERENCES

1. Kline, S. J., B. J. Cantwell, and G. M. Lilley, 1980-1981 AFOSR-HTTM-Stanford Conference on Complex Turbulent Flows, Vols. I, II, III, Stanford University, 1981.

2. Fernholz, H. H., and E. Krause, "Three Dimensional Turbulent Boundary Layers," IUTAM Symposium, Berlin, Germany, 1982.

3. Bradshaw, P., "Complex Turbulent Flows," Journal of Fluids Engineering, Vol. 97, June 1975, pp. 146-154.

4. Muller, U. R., "Comparison of Three-Dimensional Turbulent Boundary-Layer Calculations with Experiment," IUTAM Symposium, Berlin, 1982, pp. 309-324.

5. van den Berg, B., and A. Elsenaar, "Measurements in a Three-Dimensional Incompressible Turbulent Boundary Layer in an Adverse Pressure Gradient Under Infinite Swept Wing Conditions," NRL TR 72092 U, 1972.

6. Boussinesq, J., "Essai sur la theorie des eaux courantes," Mem. Pres. Acad. Sci., Paris, Vol. 23, 1877, pp. 46.

7. Prandtl, L., "Uber die ausgebildete Turbulenz," Z. Angew. Math. Mech., Vol. 5, 1925, pp. 136-139.

8. Schlichting, H., Boundary Layer Theory, McGrall Hill, New York, 1979.

9. Maise, G., and H. McDonald, "Mixing Length and Kinematic Eddy Viscosity in a Compressible Boundary Layer," AIAA Journal, Vol. 6, No. 1, January 1968, pp. 73-80.

10. Pletcher, R. H., "Prediction of Turbulent Boundary Layers at Low Reynolds Number," AIAA Journal, May 1976, pp. 696.

11. Pletcher, R. H., "On a Finite-Difference Solution for a Constant Property Turbulent Boundary Layer," AIAA Journal, Vol. 7, No. 2, February 1969.

12. van Driest, E. R., "On Turbulent Flow Near a Wall," Journal of Aeronautical Sciences, November 1965, pp. 1007-1011.

13. Launder, B. E., "Turbulence Models: Present Status and Future Prospects," Proceedings of the Lockheed-Georgia Company Viscous Flow Symposium, June 22-23, 1976, pp. 415-445.

14. Bradshaw, P., D. Ferriss, and N. Atwell, "Calculation of Boundary Layer Development Using the Turbulent Energy Equation," Journal of Fluid Mechanics, Vol. 28, Part 3, 1967, pp. 593-616.

15. Bradshaw, P., "Calculation of Boundary-Layer Development Using the Turbulent Energy Equation," NPL Aero Report 1287, January 1969.

16. Bradshaw, P., and D. H. Ferriss, "The Response of a Retarded Equilibrium Turbulent Boundary Layer to the Sudden Removal of Pressure Gradient," NPL Aero Report 1145, March 1965.

17. Harsha, P. T., "Prediction of Free Turbulent Mixing Using a Turbulent Kinetic Energy Method," Proceedings - Conference on Free Turbulent Shear Flows, NASA SP 321, Langley Research Cntr., July 1972, pp. 463-521.

18. Hanjalic', K. and B. E. Launder, "A Reynold's Stress Model of Turbulence and Its Application to Thin Shear Flows," Journal of Fluid Mechanics, Vol. 52, Part 4, 1972, pp. 609-638.

19. Harlow, F., and Nakayama, P., "Turbulence Transport Equations," Physics of Fluids, November 1967, pp. 2323.

20. Mellor, G. L., and H. J. Herring, "A Survey of Mean Turbulent Field Closure Models," AIAA Journal, Vol. 11, No. 5, May 1973.

21. Hanjalic', K. and B. E. Launder, "Contribution Towards a Reynolds Stress Closure for Low Reynolds Number Turbulence," Journal of Fluid Mechanics, Vol. 74, Part 4, 1976, pp. 593-610.

22. Klebanoff, P. S., "Characteristics of Turbulence in a Boundary Layer with Zero Pressure Gradient," NACA Rep. 1247, 1955.

23. McMahon, H., J. Hubbartt, and L. Kubendran, "Mean Velocities and Reynolds Stresses in a Juncture Flow," NASA Contract Report 3605, GRANT NAG 1-40, August 1982.

24. McMahon, H., J. Hubbartt, and L. R. Kubendran, "Mean Velocities and Reynolds Stresses Upstream of a Simulated Wing-Fuselag Juncture," NASA Contractor Report 3695, GRANT NAG 1-40, June 1983.

25. Fulachier, L., E. Arzoumanian, and R. Dumas, "Effect on a Developed Turbulent Boundary Layer of a Sudden Local Wall Motion," IUTAM Symposium, Berlin, Germany, 1982, pp. 188-198.

26. Lofdahl, L., and L. Larsson, "Measurements of Reynolds-Stress Profiles in the Stern Region of a Ship Model," IUTAM Symposium, Berlin, Germany, 1982, pp. 66-78.

27. McAllister, J. E., "Near-Wall Similarity in Two- and Three-Dimensional Turbulent Boundary Layers," Dissertation, Mechanical Engineering, Virginia Polytechnic Institute and State University, Blacksburg, Virginia, December 1979.

28. Johnston, J. P., "Experimental Studies in Three-Dimensional Turbulent Boundary Layers," Stanford University, Thermosco. Div. Report MD-34, 1976.

29. Fernholz, H., "Three Dimensional Turbulent Boundary Layers: A Report on EUROMECH 33," Journal of Fluid Mechanics, Vol. 58, Part 1, 1973, pp. 177-186.

30. Fannelop, T. K., and P. A. Krogstad, "Three-Dimensional Turbulent Boundary Layers in External Flows: A Report on Euromech 60," Journal of Fluid Mechanics, Vol. 71, Part 4, 1975, pp. 815-826.

31. Fernholz, H. H., and J. D. Vagt, "Turbulence Measurements in an Adverse-Pressure-Gradient Three-Dimensional Turbulent Boundary Layer along a Circular Cylinder," Journal Fluid of Mechanics, Vol. 111, 1981, pp. 233.

32. Elsenaar, A., and S. H. Boelsma, "Measurements of the Reynolds Stress Tensor in a Three-Dimensional Turbulent Boundary Layer Under Infinite Swept-Wing Conditions," National Aerospace Laboratory, NRL, The Netherlands, NRL TR 74095 U.

33. Bissonnette, L. R., "An Experimental Study of the Development of a Three-Dimensional Turbulent Boundary Layer Under Rapidly Changing Rate of Strain," Prinston University, Aeronautical Engineering, Ph.D. Dissertation, 1970.

34. Bissonnette, L. R., and G. L. Mellor, "Experiments on the Behavior of an Axisymmetric Turbulent Boundary Layer with Sudden Circumferential Strain," Journal of Fluid Mechanics, Vol. 63, Part 2, 1974, pp. 369-413.

35. Dechow, R., "Mittlere Geschwindigkeit und Reynoldsscher Spannungstensor in der dreidimensionalen turbulenten Wandgrenzschicht vor einem stehenden zylinder," dissertation, Universitat (TH) Karlsruhe, 1977.

36. Dechow, R., and K. O. Felsch, "Measurements of the Mean Velocity and Reynolds Stress Tensor in a Three-Dimensional Turbulent Boundary Layer Induced by a Cylinder Standing on a Flat Wall," Symposium on Turbulent Shear Flows, Pennsylvania State University, University Park, Pennsylvania, 1977, pp. 9.11-9.20.

37. Lohmann, R. P., "The Response of a Developed Turbulent Boundary Layer to Local Transverse Surface Motion," ASME Paper 76-FE-3, 1976.

38. Bradshaw, P., and M. G. Terrell, "The Response of a Turbulent Boundary Layer on an 'Infinite' Swept Wing to the Sudden Removal of Pressure Gradient," NPL Aero Report 1305, 1969.

39. Müller, U. R., "Measurement of the Reynolds Stresses and the Mean-Flow Field in a Three-Dimensional Pressure-Driven Boundary Layer," Journal of Fluid Mechanics, Vol. 119, 1982, pp. 121-153.

40. Müller, U., and E. Krause, "Measurements of Mean Velocity and Reynolds Stresses in an Incompressible Three-Dimensional Turbulent Boundary Layer," 2nd Symp. Turbulent Shear Flows, Imperial College, London, pp. 15.36-15.41.

41. Bradshaw, P., and R. F. Johnson, "Turbulence Measurements with Hot Wire Anemometers," National Physics Laboratory, Notes on Applied Science, No. 33, 1963.

42. Rasmussen, C. G., "Measurement of Turbulence Characteristics," DISA Information, No. 3, January 1966, pp. 9-20.

43. DISA Instruction and Service Manual for the Type 52B25 Turbulence Processor.

44. DISA Instruction and Service Manual for the Type 55D26 Signal Conditioner.

45. DISA Instruction and Service Manual for the Type 55M25 Linearizer.

46. DISA Instruction and Service Manual for the Type 55M System with 55M10 CTA Standard Bridge.

47. DISA Instruction and Service Manual for Type 55D35 RMS Voltmeter.

48. Tennekes, H., and J. L.Lumley A First Course in Turbulence, MIT Press, 1978.

49. Jorgensen, F. E., "Directional Sensitivity of Wire and Fiber-Film Probes," DISA Information, No. 11, May 1971, pp. 31-37.

50. Corrsin, S., Turbulence: Experimental Methods, Handbuch Der Physik, Vol. 8, Part 2, Berlin, Springer, 1963, pp. 524-590.

51. Gessner, F. B., and G. L. Moller, "Response Behaviour of Hot Wires in Shear Flow," Journal of Fluid Mechanics, Vol. 47, Part 3, 1971, pp. 449-468.

52. Vagt, J. D., "Hot-Wire Probes in Low Speed Flows," Prog. Aerospace Sci., Vol. 18, 1979, pp. 271-323.

53. Sandborn, V. A., "Effect of Velocity Gradients on Measurements of Turbulent Shear Stress," AIAA Journal, Vol. 14, No. 3, March 1976, pp. 400-402.

54. Hinze, J. O., Turbulence, McGraw-Hill, 1975.

55. Comte-Bellot, G., "Hot-Wire Anemometry," Annual Review of Fluid Mechanics, Vol. 8, 1976, pp. 209-231.

56. Heskestad, G., "Hot-Wire Measurements in a Plane Turbulent Jet," Trans. ASME E, Journal of Applied Mechanics, Vol. 32, 1965, pp. 721.

57. Bruun, H. H., "Hot Wire Data Corrections in Low and in High Turbulence Intensity Flows," Journal of Scientific Instruments, Vol. 5, 1972, pp. 812-818.

58. Müller, U. R., "On the Accuracy of Turbulence Measurements with Inclined Hot Wires," Journal of Fluid Mechanics, Vol. 119, 1982, pp. 155-172.

59. Champagne, F. H., and C. A. Sleicher, "Turbulence Measurements with Inclined Wires Part 2. Hot Wire Response Equations," Journal of Fluid Mechanics, Vol. 28, 1967, pp. 177-182.

60. Rose, W. G., "Some Corrections to the Linearized Response of a Constant-Temperature Hot-Wire Anemometer Operated in a Low-Speed Flow," Journal of Applied Mechanics, Vol. 29, September 1962, pp. 554-558.

61. Turner, J. T., "Non-Linearity Corrections for the Response of a Hot-Wire Anemometer in Highly Turbulent Flows," Proc. of the Symp. on Instr. and Data Proc. for Ind. Aero., 10.1, NPL, 1968.

62. Guitton, D. E., "Correction of Hot Wire Data for High Intensity Turbulence, Longitudinal Cooling and Probe Interference," Mech. Eng. Research Lab., McGill University, Report 68-6, 1968.

63. Kristensen, H. S., "Hot-Wire Measurements in Turbulent Flows," Fluid Mechanic Department, Technical University of Denmark, Published by DISA Information, November 1973.

64. Klatt, F., "A Study of Systematic Errors in Measurements with the Constant-Temperature Anemometer in High-Turbulent Flows With and Without Hot-Wire Signal Linearization," DISA Information, No. 14, March 1973, pp. 25-28.

65. Moussa, Z. M., and S. Eskinazi, "Directional Mean Flow Measurements Using a Single Inclined Hot Wire," Physics of Fluids, Vol. 18, No. 3, March 1975, pp. 298-305.

66. Tutu, N. K., and R. Chevray, "Cross-Wire Anemometry in High Intensity Turbulence," Journal of Fluid Mechanics, Vol. 71, Part 4, 1975, pp. 785-800.

67. Rodi, W., "A New Method of Analyzing Hot-Wire Signals in Highly Turbulent Flow and Its Evaluation in a Round Jet," DISA Information, No. 17, February 1975, pp. 9-18.

68. Acrivlellis, M., "Hot-Wire Measurements in Flows of Low and High Turbulence Intensity," DISA Information, No. 22, December 1977, pp. 15-20.

69. Acrivlellis, M., "Finding the Spatial Flow Field by Means of Hot-Wire Anemometry," DISA Information, No. 22, December 1977, pp. 21-28.

70. Acrivlellis, M., "An Improved Method for Determining the Flow Field of Multidimensional Flows of any Turbulence Intensity," DISA Information, No. 23, September 1978, pp. 11-16.

71. Bartenwerfer, M., "Remarks on Hot-Wire Anemometry Using 'Squared Signals'," DISA Information, No. 24, May 1979.

72. Thinh, N. V., "On Some Measurements Made by Means of a Hot Wire in a Turbulent Flow Near a Wall," DISA Information, No. 7, January 1969, pp. 13-18.

73. Pierce, F. J., and C. I. Ezekwe, "Turbulent Stress Tensors in a Three-Dimensional Boundary Layer," Report VPI-E-75-1, Virginia Polytechnic Institute and State University, Blacksburg, Virginia.

74. Siuru, W. D., and E. Logan, Jr., "Use of a Slanting Hot-Wire to Make Measurements in an Artificially Roughened Tube," DISA Information, No. 21, April 1977.

75. Hoffmeister, M., "Using a Single Hot-Wire Probe in Three-Dimensional Turbulent Flow Fields," DISA Information, No. 13, May 1972, pp. 26-28.

76. DeGrande, G., and P. Kool, "An Improved Experimental Method to Determine the Complete Reynolds Stress Tensor with a Single Rotating Slanting Hot Wire," Journal Physics E. Scientific Instruments Vol. 14, 1981.

77. Frota, M. N., and R. J. Moffat, "Effect of Combined Roll and Pitch Angles on Triple Wire Measurements of Mean and Turbulence Structure," DISA Information, No. 28, pp. 15-23.

78. Frota, M. N., R. J. Moffat, and S. Honami, "Flow Disturbance Induced by the DISA Triaxial Hot-Wire Probe 55P91," DISA Information, No. 28, February 1983, pp. 24-26.

79. Gaulier, C., "Measurement of Air Velocity by Means of a Triple Hot-Wire Probe," DISA Information, No. 21, April 1977, pp. 16-20.

80. Gourdon, C., J. Costes, and S. Domenech, "Triple Hot-Film Probe Calibration in Water," DISA Information, No. 26, February 1981.

81. Zank, I., "Sources of Errors and Running Calibration of Three-Dimensional Hot-Film Anemometers Especially Near the Sea Surface," DISA Information, No. 26, February 1981.

82. Rey, C., and C. Beguier, "On the Use of a Three Parallel Wire Probe," DISA Information, No. 21, April 1977, pp. 11-15.

83. Groton, C. A., and B. Lakshminarayana, "A Method of Measuring the Three-Dimensional Mean Flow and Turbulence Quantities Inside a Rotating Turbo-Machinery Passage," Journal of Engineering for Power, Trans. ASME, April 1976, pp. 137-146.

84. Lakshminarayana, B., "Three Sensor Hot Wire/Film Technique for Three Dimensional Mean and Turbulence Flow Field Measurement," TSI Quarterly, Vol. VIII, Issue 1, January-March 1982.

85. Klatt, F., "The X Hot-Wire Probe in a Plane Flow Field," DISA Information, No. 8, July 1969, pp. 3-12.

86. Delleur, J. W., "Flow Direction Measurement by Hot-Wire Anemometry," Proceedings ASCE, Vol. 92, No. EM4, August 1966, pp. 45-69.

87. Taslim, M. E., S. J. Kline, and R. J. Moffat, "Calibration of Hot Wires for Velocity Fluctuations," Rep. TMC-4, Thermosciences Division, Dept. of Mech. Eng. Stanford University, August 1978.

88. Young, M. F., "Calibration of Hot-Wires and Hot-Films for Velocity Fluctuations," Thermosciences Division, Dept. of Mech. Eng., Stanford University, March 1976.

89. Mojola, O. O., "A Hot-Wire Method for Three-Dimensional Shear Flows," DISA Information, No. 16, July 1974, pp. 11-14.

90. Bruun, H. H., "Interpretation of X-Hot-Wire Signals," DISA Information, No. 18, September 1975, pp. 5-10.

91. Andreas, E. L., "Analysis of Crossed Hot-Film Velocity Data," DISA Information, No. 24, May 1979, pp. 15-23.

92. Gessner, F. B., "A Method of Measuring Reynolds Stresses with a Constant-Current Hot Wire Anemometer," ASME Paper No. 64-WA/FE-34.

93. Duerson, S. H., Jr., "Measurements of the Reynolds Stress Tensor in a Three-Dimensional Turbulent Boundary Layer," MS Thesis, Mechanical Engineering, Virginia Polytechnic Institute and State University, Blacksburg, Virginia, June 1972.

94. Pierce, F. J., and S. H. Duerson, Jr., "Measurements of the Reynolds Stress Tensor in a Three-Dimensional Turbulent Boundary Layer," Int. TR No. 4, AROD Project 6858E, U.S. Army Research Office, Durham.

95. Wyngaard, J. C., "Turbulence Structure with Hot Wires," Journal of Scientific Instruments Vol. 1, 1968, pp. 1105-1108.

96. Jerome, F. E., D. E. Guitton, and R. P. Patel, "Experimental Study of Thermal Wake Interference Between Closely Spaced Wires of a X-Type Hot-Wire Probe," Aeronautical Quarterly, Vol. 22, 1971, pp. 119-126,

97. Davies, P. O. A. L., and M. J. Fisher, "Heat Transfer From Electrically Heated Cylinders," Proceedings Royal Society, A280, 1964, pp. 486-527.

98. Davis, M. R., "Heat Transfer From Hot Wire and Film Anemometer Probes," Inst. of Sound and Vibration Research, The University, Southampton, UK, Int. Summer School of Heat and Mass Transfer in Turbulent Boundary Layers, Herzeg Novi, September 1968.

99. Collis, D. C., and M. J. Williams, "Two-Dimensional Convection from Heated Wires at Low Reynolds Numbers," Journal of Fluid Mechanics, Vol. 6, 1959, pp. 357-384.

100. Sandborn, V. A., and J. C. Laurence, "Heat Loss from Yawed Hot Wires at Subsonic Mach Numbers," NACA Rep. TN 3563, 1955.

101. King, L. V., "On the Convection of Heat from Small Cylinders in a Stream of Fluid: Determination of the Convection Constants of Small Platinum Wires with Applications to Hot-Wire Anemometry," Phiolosophical Transactions, A214, 1914, pp. 373-432.

102. Minner, G. L., and R. W. Fox, "Measurement of Flow Magnitude and Direction by Hot Wire Anemometry," NASA Technical Memorandum NASA TMX-52967, Technical Paper-Symposium on Flow, May 1971.

103. Friehe, C. A., and W. H. Schwarz, "Deviations from the Cosine Law for Yawed Cylindrical Anemometer Sensors," Journal of Applied Mechanics, Vol. 35E, December 1968, pp. 655-662.

104. Davies, P. O. A. L., and H. H. Bruun, "The Performance of a Yawed Hot Wire," Proc. of Symp. on Inst. and Data Proc. for Ind. Aero., 10.1, NPL, 1968.

105. Elsner, J., and W. R. Gundlach, "Some Remarks on the Thermal Equilibrium Equation of Hot-Wire Probes," DISA Information, No. 14, 1973, pp. 21-24.

106. Bruun, H. H., "Interpretation of a Hot Wire Signal Using a Universal Calibration Law," Journal of Physics E. Scientific Instruments, Vol. 4, 1971, pp. 225-231.

107. Mojola, O. O., "The Effects of Orientation of Hot-Wire Probe Body in Turbulent Shear Flow," DISA Information, No. 23, September 1978, pp. 24-27.

108. Rosenberg, R. E., "A Three Dimensional Hot-Wire Anemometry Technique Employing a Single Wire Probe," ARL Report No. 71-0039, March 1971.

109. Kjellström, B., and S. Hedberg, "Calibration of a DISA Hot-Wire Anemometer and Measurements in a Circular Channel for Confirmation of the Calibration, DISA Information, No. 9, 1970, pp. 8-21.

110. Rasmussen, K. R., S. E. Larsen, and F. E. Jorgensen, "Study of Flow Deformation Around Wind-Vane Mounted Three-Dimensional Hot-Wire Probes," DISA Information, No. 26, February 1981, pp. 27-34.

111. Hoffmann, J. A., "Errors in X-Wire Measurements Due to Wire Angle and Residual Cooling," ISA ASI 74257, 1974, pp. 287-290.

112. Horvatin, M., "A Contribution to the Calibration of Hot-Wire Dual Probes," DISA Information, No. 10, October 1970, pp. 22-24.

113. Champagne, F. H., C. A. Sleicher, and O. H. Wehrmann, "Turbulence Measurements with Inclined Wires Part 1. Heat Transfer Experiments with Inclined Hot-Wires," Journal of Fluid Mechanics, Vol. 28, 1967, pp. 153-175.

114. Acrivlellis, M., "Flow Field Dependence on Hot-Wire Probe Cooling Law and Probe Adjustment," DISA Information, No. 23, September 1978, pp. 17-23.

115. Webster, C. A. G., "A Note on the Sensitivity to Yaw of a Hot-Wire Anemometer," Journal of Fluid Mechanics, Vol. 13, Part 2, 1962, pp. 307-312.

116. Dahm, M., and C. G. Rasmussen, "Effect of Wire Mounting System on Hot-Wire Probe Characteristics," DISA Information, No. 7, January 1979, pp. 19-24.

117. Frota, M. N., and R. J. Moffat, "Effect of Combined Roll and Pitch Angles on Triple Hot-Wire Measurements of Mean and Turbulence Structure," DISA Information, No. 28, 1983, pp. 15-23.

118. Hoole, B. J., and J. R. Calvert, "The Use of a Hot-Wire Anemometer in Turbulent Flow," Journal Royal Aeronautical Society, Vol. 71, 1967, pp. 511-513.

119. Rosenberg, R. E., "Some New Aspects on Hot-Wire Anemometry Leading to a Special Calibration Method for Hot-Wire Probes," ARL Report 71-0038, March 1971.

120. Gilmore, D. C., "The Probe Interference Effect of Hot-Wire Anemometers," Mech. Eng. Research Lab., McGill University, Report TN67-3, 1967.

121. Sears, W. R., "The Boundary Layer of Yawed Cylinders," Journal of Aeronautical Sciences, Vol. 15, January 1948, pp. 49-52.

122. Fujita, H., and L. S. G. Kovasznay, "Measurements of Reynolds Stress by a Single Rotated Hot Wire Anemometer," Review Scientific Instruments, Vol. 39, No. 9, September 1968, pp. 1351-1355.

123. Norman, B., "Hot-Wire Anemometer Calibration at High Subsonic Speeds," DISA Information, No. 5, 1967, pp. 5-19.

124. Comte-Bellot, G., A. Strohl, and E. Alcaraz, "On Aerodynamic Disturbance Caused by Single Hot-Wire Probes," Journal of Applied Mechanics, Vol. 38, Trans. ASME 93, Ser. E, 1971, pp. 767-774.

125. Pierce, F. J., and J. E. McAllister, "Near-Wall Similarity in a Pressure-Driven Three-Dimensional Turbulent Boundary Layer," Report VPI-80.32, Mechanical Engineering, Virginia Polytechnic Institute and State University, Blacksburg, Virginia, September 1980.

126. Nielsen, P. E., and C. G. Rasmussen, "Measurement of Amplitude and Phase Characteristics," DISA Informatum, No. 4, December 1966, pp. 17-24.

127. Anderson, O. K., "Time Resolution Power in Correlation Measurements with DISA Type 55A01 Hot-Wire and Hot Film Anemometers," DISA Information, No. 4, 1966, pp. 3-16.

128. Corrsin, S., Turbulence: Experimental Methods, Handbuck Den. Physik., Vol. 8, Part 2, Berlin, Springer, 1963, pp. 524-590.

129. Freymuth, P., and L. M. Fingerson, "Electronic Testing of Frequency Response for Thermal Anemometers," TSI Incorporated.

130. Bellhouse, B. F., and C. G. Rasmussen, "Low-Frequency Characteristics of Hot-Film Anemometers," DISA Information, No. 6, February 1968, pp. 3-10.

131. DISA Instruction and Service Manual for the Type 55D31 Digital Voltmeter.

132. DANA Instruction and Service Manual for the Type 5100 Digital Multimeter.

133. Instruction and Service Manual for the Datametric Model 1400 Electronic Manometer.

134. Instruction and Service Manual for the Gould Type 590 Pressure Transducer.

135. Wills, J. A. B., "The Correction of Hot-Wire Readings for Proximity to a Solid Boundary," Journal of Fluid Mechanics, Vol. 13, Part 3, 1962.

136. Oka, S., and Z. Kostic, "Influence of Wall-Proximity on Hot-Wire Velocity Measurement," DISA Information, No. 13, May 1972, pp. 29-33.

137. Vagt, J. D., and H. H. Fernholz, "A Discussion of Probe Effects and Improved Measuring Techniques in the Near-Wall Region of an Incompressible Three-Dimensional Turbulent Boundary Layer," AGARD, Conference Proceedings, No. 271.

138. Ugural, A. C., and S. K. Fenster, Advanced Strength and Applied Elasticity, Elsevier North-Holland Publishing Company, New York, 1975.

139. Hojstrup, J., K. Rasmussen, and S. E. Larsen, "Dynamic Calibration of Temperature Wires in Moving Air," DISA Information, No. 21, April 1977, Letter to the Editor.

140. Bruun, H. H., "A Note on Static and Dynamic Calibration of Constant-Temperature Hot-Wire Probes," Journal of Fluid Mechanics, Vol. 76, Part 1, 1976, pp. 145-155.

141. Hanson, A. R., "Vortex Shedding from Yawed Cylinders," AIAA Journal, Vol. 4, No. 4, 1966, pp. 738-740.

142. Kline, S. J., and F. A. McClintock, "Describing Uncertainties in Single-Sample Experiments," Mechanical Engineering, 1953, pp. 3.

143. Moffat, R. J., "Contributions to the Theory of Single-Sample Uncertainty Analysis," ASME Trans., Vol. 104, June 1982, pp. 250-260.

144. de Brederode, V., and P. Bradshaw, "Influence of the Side Walls on the Turbulent Centre-Plane Boundary Layer in a Square Duct," Imperial College Aero Report 74-06, May 1974.

145. de Bray, B. G., "Some Investigations into the Spanwise Non-Uniformity of Nomially Two-Dimensional Incompressible Boundary Layers Downstream of Gauze Screens," Aeronautical Research Council R&M No. 3578, July 1976.

146. Bradshaw, P., "The Effect of Wind-Tunnel Screens on Nominally Two-Dimensional Boundary Layers," Journal of Fluid Mechnics, Vol. 22, Part 4, 1965.

147. Furuya, Y., and H. Osaka, "The Spanwise Non-Uniformity of Nominally Two-Dimensional Turbulent Boundary Layer (1st Report Characteristics of Spanwise Velocity Distribution)," JSME Bulletin, Vol. 18, No. 121, July 1975.

148. Furuya, Y., I. Nakamura, H. Osaka, and H. Honda, "The Spanwise Non-Uniformity of Nominally Two-Dimensional Turbulent Boundary Layer (2nd Report Wall Shear Stress and Flow Field)," JSME Bulletin, Vol. 18, No. 121, July 1975.

149. Favre, A., and J. Gaviglio, "Turbulence et Perturbations dans la limite d'une Plaque Plane," AGARD Report 278, April 1980.

150. Kovasynay, S. G., "Turbulence Measurements," Applied Mechanics Review, Vol. 12, No. 6, June 1969, pp. 375-380.

151. Coles., D., "The Young Person's Guide to the Data," Proceedings Computation of Turbulent Boundary Layers - 1968, AFOSR-IFP-Stanford Conference, Vol. II, pp. 1-45.

152. NPL Staff, "On the Measurement of Local Surface Friction on a Flat Plate by Means of Preston Tubes," Aeronautical Research Council R & M 3185, 1955.

153. Patel, V. C., "Calibration of the Preston Tube and Limitations on Its Use in Pressure Gradients," Journal of Fluid Mechanics, Vol. 23, Part 1, 1965, pp. 185-208.

154. White, F. M., Viscous Fluid Flow, McGraw Hill, New York, 1974.

155. Fitts, D. O., "A Study of Two- and Three-Dimensional Turbulent Boundary Layers Data Sets Using Momentum Integral Techniques," MS Thesis, Mechanical Engineering, Virginia Polytechnic Institute and State University, Blacksburg, Virginia, March 1982.

156. Pierce, F. J., "The Turbulent Flow at the Plane of Symmetry of a Collateral Three-Dimensional Boundary Layer," Journal of Basic Engineering, Trans. ASME, Paper No. 63-AHGT-3, 1963.

157. Johnson, L. W., and R. D. Reiss, Numerical Analysis, 2nd ed., Addison-Wesley Publishing Company, Reading, Massachusetts, 1982.

158. Frost, W., and T. H. Moulden, Handbook of Turbulence, Vol. 1, Plenum Press, 1977.

159. Butter, T. L., and J. W. Wagner, "Application of a Three-Sensor Hot-Wire Probe for Incompressible Flow," AIAA Journal, Vol. 21, No. 5, pp. 726-732.

160. Irwin, H. P. A. H., "The Longitudinal Cooling Correction for Wires Inclined to the Prongs and Some Turbulence Measurements in Fully Developed Pipe Flow," Mechanical Engineering Research Laboratory, McGill University, Montreal, Lab, TN 72-1, 1971.

161. TSI, "Hot-Wire vs. Hot-Film: The Virtues of Both," TSI Quarterly IV, No. 3, 1978.

162. Doebelin, E. O., Measurement Systems, McGrawHill, 1975.

163. Mellor, G. L., "Incompressible, Turbulent Boundary Layers with Arbitrary Pressure Gradients and Divergent or Convergent Cross Flows," AIAA Journal, Vol. 5, No. 9, 1967.

164. Schubauer, G. B., and P. S. Klebanoff, NACA Adv. Conf. Rept. No. 5K27, Wartime Report W-86, 1946.

165. Johnston, J. P., "Measurements in a Three-Dimensional Turbulent Boundary Layer Induced by a Swept, Forward-Facing Step, Journal of Fluid Mechanics, Vol. 42, Part 4, 1970, pp. 823-844.

166. Klebanoff, P. S., and Z. W. Diehl, "Some Featues of Artificially Thickened Fully Developed Turbulent Boundary Layer with Zero Pressure Gradient," NACA Rep. 1110, 1952.

167. Vagt, J. D., "Experimental Techniques in Three-Dimensional Turbulent Boundary Layers," IUTAM Symposium, Berlin, Germany, 1982.

Appendix A

A Derivation of the First and Second Order Equations for $Q(\theta - \alpha)$ and $Q(\theta - \alpha)^2$

In this section, expressions are developed for $Q(\theta - \alpha)$ and $Q(\theta - \alpha)^2$ that are required in Eq. 4.31.

The unit vector in the direction of the instantaneous velocity vector $\underline{Q}(t)$ can be expressed as

$$\hat{q}(t) = \frac{\overline{U} + u}{Q} \hat{e}_x + \frac{\overline{V} + v}{Q} \hat{e}_y + \frac{\overline{W} + w}{Q} \hat{e}_z \tag{A1}$$

where $Q = |\underline{Q}(t)|$. In Chapter IV, the unit vector along the sensor was given in Eq. 4.19 as

$$\hat{\ell}(\alpha, \gamma_x) = \sin \alpha \, \hat{e}_x + \cos \alpha \cos \gamma_x \, \hat{e}_y + \cos \alpha \sin \gamma_x \, \hat{e}_z \, . \tag{A2}$$

Forming the dot product of these two unit vectors

$$\hat{q}(t) \cdot \hat{\ell}(\alpha, \gamma_x) = \cos (90 - \theta) = \sin \theta$$

from Fig. 4.1 and hence,

$$\sin \theta = \left(\frac{\overline{U} + u}{Q}\right) \sin \alpha + \left(\frac{\overline{V} + v}{Q}\right) \cos \alpha \cos \gamma_x$$

$$+ \left(\frac{\overline{W} + w}{Q}\right) \cos \alpha \sin \gamma_x \, . \tag{A3}$$

To obtain approximations for the terms $Q(\theta - \alpha)$ and $Q(\theta - \alpha)^2$ appearing in Eq. 4.31, consider a Taylor series expansion of sin θ about the angle α:

$$\sin \theta = \sin \alpha + (\theta - \alpha) \cos \alpha - \frac{1}{2} (\theta - \alpha)^2 \sin \alpha$$

$$- \frac{1}{6} (\theta - \alpha)^3 \cos \alpha + \frac{1}{24} (\theta - \alpha)^4 \sin \alpha + O(\theta - \alpha)^5 + \cdots . \quad (A4)$$

Solving for $(\theta - \alpha)$ in Eq. A4 yields

$$(\theta - \alpha) = \frac{\sin \theta}{\cos \alpha} - \tan \alpha + \frac{1}{2} (\theta - \alpha)^2 \tan \alpha + \frac{1}{6} (\theta - \alpha)^3$$

$$- \frac{1}{24} (\theta - \alpha)^4 \tan \alpha + \cdots , \quad (A5)$$

and squaring this equation gives

$$(\theta - \alpha)^2 = \left[\frac{\sin \theta}{\cos \alpha} - \tan \alpha\right]^2 + \left[\frac{\sin \theta}{\cos \alpha} - \tan \alpha\right] \left[(\theta - \alpha)^2 \tan \alpha\right.$$

$$\left. + \frac{1}{3} (\theta - \alpha)^3 - \frac{1}{2} (\theta - \alpha)^4 \tan \alpha\right] + \frac{1}{4} (\theta - \alpha)^4 \tan^2 \alpha + \cdots . \quad (A6)$$

The procedure used to approximate the difference, $(\theta - \alpha)$, is similar to the Fixed Point Method [157]. This method is iterative and involves the use of an initial estimate of $(\theta - \alpha)$ in Eq. A5 to obtain an better approximation. Since only one iteration will be performed, an initial estimate will be carefully chosen that will give the best results. Consider the first order approximation

$$(\theta - \alpha)_1 = \frac{\sin \theta}{\cos \alpha} - \tan \alpha. \tag{A7}$$

Substituting the expression for sin θ, given in Eq. A3, in Eq. A7 yields

$$(\theta - \alpha)_1 = \left(\frac{\overline{U} + u}{Q} - 1\right) \tan \alpha + \left(\frac{\overline{V} + v}{Q}\right) \cos \gamma_x + \left(\frac{\overline{W} + w}{Q}\right) \sin \gamma_x \,. \tag{A8}$$

Equation A8 is a first order approximation to $(\theta - \alpha)$ obtained by neglecting terms of $O(\theta - \alpha)^2$ in Eq. A5. The equation pair, Eq. A5 and A8, could be used in an iterative sequence to obtain a better estimate of $(\theta - \alpha)$. An improved estimate can be obtained, however, by replacing the initial estimate, Eq. A7, by the second order approximation from Eq. A5 where

$$(\theta - \alpha)_2 = \frac{\sin \theta}{\cos \alpha} - \tan \alpha + \frac{1}{2} (\theta - \alpha)^2 \tan \alpha \,. \tag{A9}$$

Solving the quadratic for

$$(\theta - \alpha)_2 = \frac{1 \pm \left[1 - 2\tan \alpha \left(\frac{\sin \theta}{\tan \alpha} - \tan \alpha\right)\right]^{1/2}}{\tan \alpha}$$

and using Eq. A7 one obtains

$$(\theta - \alpha)_2 = \frac{1 - \left[1 - 2(\theta - \alpha)_1 \tan \alpha\right]^{1/2}}{\tan \alpha}, \tag{A10}$$

where minus sign is chosen since

$$\lim_{\theta \to \alpha} (\theta - \alpha) = 0 ,$$

is required.

This second approximation, Eq. A10, can be transformed into a more useful form by expanding the square root term. This gives

$$(\theta - \alpha)_2 = (\theta - \alpha)_1 \left[1 + \frac{1}{2} (\theta - \alpha)_1 \tan \alpha + \frac{1}{2} (\theta - \alpha)_1^2 \tan^2 \alpha \right.$$

$$\left. + \frac{5}{8} (\theta - \alpha)_1^3 \tan^3 \alpha + \frac{7}{8} (\theta - \alpha)_1^4 \tan^4 \alpha \right] + O(\theta - \alpha)_1^6 + \cdots . \tag{A11}$$

The higher order powers of $(\theta - \alpha)_2$ that are required in Eq. A5 are obtained from Eq. A11:

$$(\theta - \alpha)_2^2 = (\theta - \alpha)_1^2 \left[1 + (\theta - \alpha)_1 \tan \alpha + \frac{5}{4} (\theta - \alpha)_1^2 \tan^2 \alpha \right.$$

$$\left. + \frac{7}{4} (\theta - \alpha)_1^3 \tan^3 \alpha + \frac{21}{8} (\theta - \alpha)_1^4 \tan^4 \alpha \right] + O(\theta - \alpha)_1^7 + \cdots , \tag{A12}$$

$$(\theta - \alpha)_2^3 = (\theta - \alpha)_1^3 \left[1 + \frac{3}{2} (\theta - \alpha)_1 \tan \alpha + \frac{9}{4} (\theta - \alpha)_1^2 \tan^2 \alpha \right.$$

$$\left. + \frac{7}{4} (\theta - \alpha)_1^3 \tan^3 \alpha \right] + O(\theta - \alpha)_1^7 + \cdots , \tag{A13}$$

$$(\theta - \alpha)_2^4 = (\theta - \alpha)_1^4 \left[1 + 2(\theta - \alpha)_1 \tan \alpha + \frac{7}{2} (\theta - \alpha)_1^2 \tan^2 \alpha\right]$$

$$+ O(\theta - \alpha)_1^7 + \cdots . \tag{A14}$$

The bracketed terms in Eqs. A11 - A14 represent the corrections to the first order approximation, $(\theta - \alpha)_1$. Substitution of these equations into Eq. A5 gives a better estimate of $(\theta - \alpha)$, namely

$$(\theta - \alpha) = (\theta - \alpha)_1 \left[1 + \left(\frac{1}{2} \tan \alpha\right) (\theta - \alpha)_1 + \left(\frac{1}{2} \tan^2 \alpha + \frac{1}{6}\right) (\theta - \alpha)_1^2\right.$$

$$+ \left(\frac{5}{8} \tan^3 \alpha + \frac{5}{24} \tan \alpha\right) (\theta - \alpha)_1^3$$

$$\left. + \left(\frac{7}{8} \tan^4 \alpha + \frac{7}{24} \tan^2 \alpha\right) (\theta - \alpha)_1^4\right] + \cdots . \tag{A15}$$

Finally, squaring Eq. A15 will give for Eq. A6

$$(\theta - \alpha)^2 = (\theta - \alpha)_1^2 \left[1 + (\theta - \alpha)_1 \tan \alpha + \left(\frac{5}{4} \tan^2 \alpha + \frac{1}{3}\right) (\theta - \alpha)_1^2\right.$$

$$+ \left(\frac{7}{4} \tan^3 \alpha + \frac{7}{12} \tan \alpha\right) (\theta - \alpha)_1^3$$

$$\left. + \left(\frac{21}{8} \tan^4 \alpha + \frac{23}{24} \tan^2 \alpha + \frac{1}{36}\right) (\theta - \alpha)_1^4\right] + \cdots . \tag{A16}$$

Table A1 compares values of $(\theta - \alpha)$ and $(\theta - \alpha)^2$ obtained by the different approximations, Eqs. A7, A11, A12, A15, and A16 where a range of $(\theta - \alpha)$ differences is tested at $\alpha = 45^\circ$. The results show that Eqs.

Table A1. Relative Errors in $(\theta - \alpha)$ and $(\theta - \alpha)^2$ Using Different Processing Equations

	Relative Errors					
$(\theta - \alpha)$		$(\theta - \alpha)$			$(\theta - \alpha)^2$	
Degrees	EQ.A7	EQ.A11	EQ.A15	$(EQ.A7)^2$	EQ.A12	EQ.A16
-20	0.153	-0.006	0.018	0.328	0.003	0.058
-15	0.119	-0.007	0.005	0.252	-0.012	0.015
-10	0.082	-0.004	0.001	0.171	-0.008	0.003
-5	0.042	-0.001	0.000	0.086	-0.002	0.000
0	0.000	0.000	0.000	0.000	0.000	0.000
5	-0.045	-0.001	0.000	-0.008	-0.003	0.000
10	-0.092	-0.006	-0.001	-0.176	-0.012	-0.003
15	-0.142	-0.015	-0.005	-0.236	-0.031	-0.012
20	-0.193	-0.032	-0.016	-0.349	-0.064	-0.035

A15 and A16 provide a good estimate of Eqs. A5 and A6, respectively, and are accurate for angular differences of up to $\pm 15^{o}$.

The adequacy of the limits of the approximations given by Eqs. A15 and A16 for this application can be determined by relating the turbulence intensity, $\sqrt{\overline{u^2}}$, to a corresponding difference $(\theta - \alpha)$. Consider the case shown in Fig. A1 where $\overline{V} = \overline{W} = 0$. For this case, the sensor is aligned and a deviation from the angle α is due only to the superimposed velocity fluctuations on the mean, and this difference approaches zero as u, v, and w approach zero. If it is assumed that the aligned sensor experiences fluctuations only in its plane then, from Fig. A1,

$$\tan (\theta - \alpha) = \frac{v}{\overline{U}} \left[1 + \frac{u}{\overline{U}}\right]^{-1} .$$

Expanding this equation to second order and solving for $(\theta - \alpha)$ gives

$$(\theta - \alpha) = \tan^{-1} \left[\frac{v}{\overline{U}} - \frac{vu}{\overline{U}^2}\right] . \tag{A17}$$

A series expansion of the right side of Eq. A17 and time averaging yields the rough approximation

$$\overline{(\theta - \alpha)} \simeq 0 \frac{\overline{vu}}{\overline{U}^2} \simeq 0 \frac{\overline{u^2}}{\overline{U}^2} . \tag{A18}$$

For $\sqrt{\frac{\overline{u^2}}{\overline{U}^2}} = 0.60$, the corresponding deviation $\overline{(\theta - \alpha)} \simeq 21^{o}$. Thus, the fundamental approximations give results which are well within the limits associated with this application.

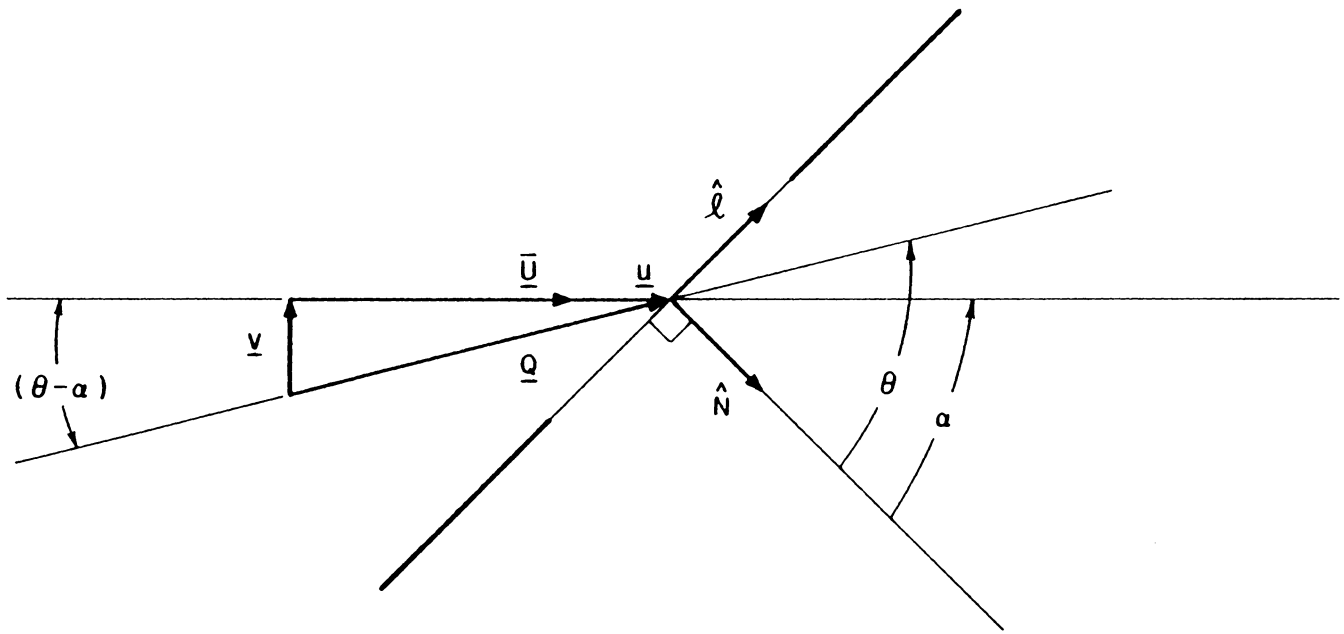

Figure A1. Definition of $(\theta - \alpha)$ for an Aligned Sensor in the uv Plane Neglecting w Components Normal to the Plane

The terms $Q(\theta - \alpha)$ and $Q(\theta - \alpha)^2$ appearing in Eq. 4.31 will be approximated by Eqs. A15 and A16, respectively. Utilizing the first equation,

$$Q(\theta - \alpha) = Q(\theta - \alpha)_1 + Q(\theta - \alpha)_1^2 \left[\frac{1}{2} \tan \alpha\right] + Q(\theta - \alpha)_1^3 \cdot \left[\frac{1}{2} \tan^2 \alpha + \frac{1}{6}\right] + Q(\theta - \alpha)_1^4 \left[\frac{5}{8} \tan^3 \alpha + \frac{5}{24} \tan \alpha\right] + Q(\theta - \alpha)_1^5 \left[\frac{7}{8} \tan^4 \alpha + \frac{7}{24} \tan^2 \alpha\right] + \cdots , \quad \text{(A19)}$$

and the second equation,

$$Q(\theta - \alpha)^2 = Q(\theta - \alpha)_1^2 + Q(\theta - \alpha)_1^3 \tan \alpha + Q(\theta - \alpha)_1^4 \left[\frac{5}{4} \tan^2 \alpha + \frac{1}{3}\right] + Q(\theta - \alpha)_1^5 \left[\frac{7}{4} \tan^3 \alpha + \frac{7}{12} \tan \alpha\right] + Q(\theta - \alpha)_1^6 \left[\frac{21}{8} \tan^4 \alpha + \frac{23}{24} \tan^2 \alpha + \frac{1}{36}\right] + \cdots . \quad \text{(A20)}$$

The remaining task involves deriving expressions for the $Q(\theta - \alpha)_1$, $Q(\theta - \alpha)_1^2$, $Q(\theta - \alpha)_1^3$, $Q(\theta - \alpha)_1^4$, $Q(\theta - \alpha)_1^5$, and $Q(\theta - \alpha)_1^6$ terms appearing in Eqs. A19 and A20. For the first term, equation A8 can be rewritten as

$$Q(\theta - \alpha)_1 = \overline{U}^* \left(\frac{\overline{U}}{\overline{U}^*} + \frac{u}{\overline{U}^*} - \frac{Q}{\overline{U}^*}\right) \tan \alpha + \overline{U}^* \left(\frac{\overline{V}}{\overline{U}^*} + \frac{v}{\overline{U}^*}\right) \cos \gamma_x$$

$$+ \overline{U}^* \left(\frac{\overline{W}}{\overline{U}^*} + \frac{w}{\overline{U}^*}\right) \sin \gamma_x \, . \tag{A21}$$

Substituting the expression for Q from Appendix B into Eq. A21 and rearranging yields

$$Q(\theta - \alpha)_1 = \overline{U}^* \left\{ \frac{\overline{U}}{\overline{U}^*} \tan \alpha + \frac{\overline{V}}{\overline{U}^*} \cos \gamma_x + \frac{\overline{W}}{\overline{U}^*} \sin \gamma_x - \tan \alpha \right.$$

$$+ \frac{u}{\overline{U}^*} \left(\tan \alpha - \frac{\overline{U}}{\overline{U}^*} \tan \alpha\right) + \frac{v}{\overline{U}^*} \left(\cos \gamma_x - \frac{\overline{V}}{\overline{U}^*} \tan \alpha\right)$$

$$+ \frac{w}{\overline{U}^*} \left(\sin \gamma_x - \frac{\overline{W}}{\overline{U}^*} \tan \alpha\right) - \frac{1}{2} \tan \alpha \left[\frac{u^2}{\overline{U}^{*2}} \left(1 - \frac{\overline{U}^2}{\overline{U}^{*2}}\right) \right.$$

$$+ \frac{v^2}{\overline{U}^*} \left(1 - \frac{\overline{V}^2}{\overline{U}^{*2}}\right) + \frac{w^2}{\overline{U}^{*2}} \left(1 - \frac{\overline{W}^2}{\overline{U}^{*2}}\right) - 2 \frac{uv}{\overline{U}^{*2}} \left(\frac{\overline{UV}}{\overline{U}^{*2}}\right)$$

$$\left. \left. - 2 \frac{uw}{\overline{U}^{*2}} \left(\frac{\overline{UW}}{\overline{U}^{*2}}\right) - 2 \frac{vw}{\overline{U}^{*2}} \left(\frac{\overline{VW}}{\overline{U}^{*2}}\right) \right] \right\} \, . \tag{A22}$$

For convenience, let

$$b_o = \frac{\overline{U}}{\overline{U}^*} \tan \alpha + \frac{\overline{V}}{\overline{U}^*} \cos \gamma_x + \frac{\overline{W}}{\overline{U}^*} \sin \gamma_x - \tan \alpha \, , \tag{A23a}$$

$$b_u = \tan \alpha - \frac{\overline{U}}{\overline{U}^*} \tan \alpha \, , \tag{A23b}$$

$$b_v = \cos \gamma_x - \frac{\overline{V}}{\overline{U}^*} \tan \alpha \, , \tag{A23c}$$

$$b_w = \sin \gamma_x \, \frac{\overline{W}}{\overline{U}^*} \tan \alpha \, , \tag{A23d}$$

$$b_{uu} = -\frac{1}{2}\left(1 - \frac{\overline{U}^2}{\overline{U^*}^2}\right) \tan \alpha \,, \tag{A23e}$$

$$b_{vv} = -\frac{1}{2}\left(1 - \frac{\overline{V}^2}{\overline{U^*}^2}\right) \tan \alpha \,, \tag{A23f}$$

$$b_{ww} = -\frac{1}{2}\left(1 - \frac{\overline{W}^2}{\overline{U^*}^2}\right) \tan \alpha \,, \tag{A23g}$$

$$b_{uv} = \frac{\overline{UV}}{\overline{U^*}^2} \tan \alpha \,, \tag{A23h}$$

$$b_{uw} = \frac{\overline{UW}}{\overline{U^*}^2} \tan \alpha \,, \tag{A23i}$$

and

$$b_{vw} = \frac{\overline{VW}}{\overline{U^*}^2} \tan \alpha \,. \tag{A23j}$$

Rewritting Eq. A22 using the definitions above gives

$$\begin{aligned} Q(\theta - \alpha)_1 = \overline{U^*} \Big\{ & b_o + b_u \frac{u}{\overline{U^*}} + b_v \frac{v}{\overline{U^*}} + b_w \frac{w}{\overline{U^*}} \\ & + b_{uu} \frac{u^2}{\overline{U^*}^2} + b_{vv} \frac{v^2}{\overline{U^*}^2} + b_{ww} \frac{w^2}{\overline{U^*}^2} \\ & + b_{uv} \frac{uv}{\overline{U^*}^2} + b_{uw} \frac{uw}{\overline{U^*}^2} + b_{vw} \frac{vw}{\overline{U^*}^2} \Big\} \,. \end{aligned} \tag{A24}$$

The remaining terms are more conveniently determined by considering the general product

$$Q(\theta - \alpha)_1^s = Q^{1-s} \{Q(\theta - \alpha)_1\}^s, \quad s = 0,1,2, \ldots . \tag{A25}$$

Substituting Eq. A24 into A25 yields

$$Q(\theta - \alpha)_1^s = Q^{1-s} \overline{U}^{*s} \left\{b_o + b_u \frac{u}{\overline{U}^*} + b_v \frac{v}{\overline{U}^*} + b_w \frac{w}{\overline{U}^*} + b_{uu} \frac{u^2}{\overline{U}^{*2}}\right.$$

$$\left. + b_{vv} \frac{v^2}{\overline{U}^{*2}} + b_{ww} \frac{w^2}{\overline{U}^{*2}} + b_{uv} \frac{uv}{\overline{U}^{*2}} + b_{uw} \frac{uw}{\overline{U}^{*2}} + b_{vw} \frac{vw}{\overline{U}^{*2}} \right\}^s . \tag{A26}$$

Expanding the expression in the braces to second order gives

$$Q(\theta - \alpha)_1^s = Q^{1-s} \overline{U}^{*s} \left\{b_o^s + s b_o^{s-1} \left[b_u \frac{u}{\overline{U}^*} + b_v \frac{v}{\overline{U}^*} + \right.\right.$$

$$+ b_w \frac{w}{\overline{U}^*} + b_{uu} \frac{u^2}{\overline{U}^{*2}} + b_{vv} \frac{v^2}{\overline{U}^{*2}} + b_{ww} \frac{w^2}{\overline{U}^{*2}} + b_{uv} \frac{uv}{\overline{U}^{*2}}$$

$$\left. + b_{uw} \frac{uw}{\overline{U}^{*2}} + b_{vw} \frac{vw}{\overline{U}^{*2}}\right] + \frac{s(s-1)}{2!} b_o^{s-2} \left[b_u^2 \frac{u^2}{\overline{U}^{*2}}\right.$$

$$+ b_v^2 \frac{v^2}{\overline{U}^{*2}} + b_w^2 \frac{w^2}{\overline{U}^{*2}} + 2b_u b_v \frac{uv}{\overline{U}^{*2}} + 2b_u b_w \frac{uw}{\overline{U}^{*2}}$$

$$\left.\left. + 2b_v b_w \frac{vw}{\overline{U}^{*2}}\right]\right\} .$$

Collecting terms involving similar fluctuating quantities yields

$$Q(\theta - \alpha)_1^s = Q^{1-s}\,\overline{U}^{*s}\,\{b_o^s + sb_o^{s-1}\,b_u\,\frac{u}{\overline{U}^*} + sb_o^{s-1}\,b_v\,\frac{v}{\overline{U}^*}$$

$$+ sb_o^{s-1}\,b_w\,\frac{w}{\overline{U}^*} + \frac{u^2}{\overline{U}^{*2}}\,[sb_o^{s-1}\,b_{uu} + \frac{s(s-1)}{2}\,b_o^{s-2}\,b_u^2]$$

$$+ \frac{v^2}{\overline{U}^{*2}}\,[sb_o^{s-1}\,b_{vv} + \frac{s(s-1)}{2}\,b_o^{s-2}\,b_v^2]$$

$$+ \frac{w^2}{\overline{U}^{*2}}\,[sb_o^{s-1}\,b_{ww} + \frac{s(s-1)}{2}\,b_o^{s-2}\,b_w^2]$$

$$+ \frac{uv}{\overline{U}^{*2}}\,[sb_o^{s-1}\,b_{uv} + s(s-1)\,b_o^{s-2}\,b_u b_v] + \frac{uw}{\overline{U}^{*2}}\,[sb_o^{s-1}\,b_{uw}$$

$$+ s(s-1)\,b_o^{s-2}\,b_u b_w] + \frac{vw}{\overline{U}^{*2}}\,[sb_o^{s-1}\,b_{vw}$$

$$+ s(s-1)b_o^{s-2}\,b_v b_w]\}\,. \qquad \text{(A27)}$$

The expanded form of the Q^{1-s} terms is obtained from Appendix B where

$$Q^{1-s} = \overline{U}^{*1-s}\,\{1 + (1-s)\,[\frac{u\overline{U} + v\overline{V} + w\overline{W}}{\overline{U}^{*2}}]$$

$$+ \frac{u^2}{\overline{U}^{*2}}\,[\frac{(1-s)}{2} + \frac{(s+1)(s-1)}{2}\,\frac{\overline{U}^2}{\overline{U}^{*2}}]$$

$$+ \frac{v^2}{\overline{U}^{*2}}\,[\frac{1-s}{2} + \frac{(s+1)(s-1)}{2}\,\frac{\overline{V}^2}{\overline{U}^{*2}}]$$

$$+ \frac{w^2}{\overline{U}^{*2}}\,[\frac{1-s}{2} + \frac{(s+1)(s-1)}{2}\,\frac{\overline{W}^2}{\overline{U}^{*2}}]$$

$$+ (s+1)(s-1)\,[\frac{uv\,\overline{UV} + uw\,\overline{UW} + vw\,\overline{VW}}{\overline{U}^{*4}}]\}\,. \qquad \text{(A28)}$$

The general product shown in Eq. A25 is formed by substituting Eq. A28 into A27 as

$$Q(\theta - \alpha)_1^s = \overline{U}^* \{b_o^s + sb_o^{s-1} b_u \frac{u}{\overline{U}^*} + sb_o^{s-1} b_v \frac{v}{\overline{U}^*}$$

$$+ sb_o^{s-1} b_w \frac{w}{\overline{U}^*} + \frac{u^2}{\overline{U}^{*2}} \left[sb_o^{s-1} b_{uu} + \frac{s(s-1)}{2} b_o^{s-2} b_u^2\right]$$

$$+ \frac{v^2}{\overline{U}^{*2}} \left[sb_o^{s-1} b_{vv} + \frac{s(s-1)}{2} b_o^{s-2} b_v^2\right]$$

$$+ \frac{w^2}{\overline{U}^{*2}} \left[sb_o^{s-1} b_{ww} + \frac{s(s-1)}{2} b_o^{s-2} b_w^2\right]$$

$$+ \frac{uv}{\overline{U}^{*2}} \left[sb_o^{s-1} b_{uv} + s(s-1) b_o^{s-2} b_u b_v\right] + \frac{uw}{\overline{U}^{*2}} \left[sb_o^{s-1} b_{uw}\right.$$

$$\left. + s(s-1) b_o^{s-2} b_u b_w\right] + \frac{vw}{\overline{U}^{*2}} \left[sb_o^{s-1} b_{vw} + s(s-1) b_o^{s-2} b_v b_w\right]$$

$$+ (1-s) b_o^s \left[\frac{u\overline{U} + v\overline{V} + w\overline{W}}{\overline{U}^{*2}}\right] + s(1-s) b_o^{s-1} b_u \left[\frac{u^2\overline{U} + uv\overline{V} + uw\overline{W}}{\overline{U}^{*3}}\right]$$

$$+ s(1-s) b_o^{s-1} b_v \left[\frac{uv\overline{U} + v^2\overline{V} + vw\overline{W}}{\overline{U}^{*3}}\right]$$

$$+ s(1-s) b_o^{s-1} b_w \left[\frac{uw\overline{U} + vw\overline{V} + w^2\overline{W}}{\overline{U}^{*3}}\right]$$

$$+ \frac{u^2}{\overline{U}^{*2}} \left[\frac{b_o^s (1-s)}{2} + \frac{b_o^s (s+1)(s-1)}{2} \frac{\overline{U}^2}{\overline{U}^{*2}}\right]$$

$$+ \frac{v^2}{\overline{U}^{*2}} \left[\frac{b_o^s (1-s)}{2} + \frac{b_o^s (s+1)(s-1)}{2} \frac{\overline{V}^2}{\overline{U}^{*2}}\right] +$$

$$+ \frac{w^2}{\overline{U}^{*2}} \left[\frac{b_o^s(1 - s)}{2} + \frac{b_o^s(s + 1)(s - 1)}{2} \frac{\overline{W}^2}{\overline{U}^{*2}}\right]$$

$$+ b_o^s (s + 1)(s - 1) \left[\frac{uv\overline{UV} + uw\overline{UW} + vw\overline{VW}}{\overline{U}^{*4}}\right]\} .$$

Finally, re-arranging gives the general form:

$$Q(\theta - \alpha)_1^s = \overline{U}^* \{b_o^s + \frac{u}{\overline{U}^*} \left[sb_o^{s-1} b_u + (1 - s)b_o^s \frac{\overline{U}}{\overline{U}^*}\right]$$

$$+ \frac{v}{\overline{U}^*} \left[sb_o^{s-1} b_v + (1 - s) b_o^s \frac{\overline{V}}{\overline{U}^*}\right] + \frac{w}{\overline{U}^*} \left[sb_o^{s-1} b_w + (1 - s) b_o^s \frac{\overline{W}}{\overline{U}^*}\right]$$

$$+ \frac{u^2}{\overline{U}^{*2}} \left[sb_o^{s-1} b_{uu} + \frac{s(s - 1)}{2} b_o^{s-2} b_u^2 + s(1 - s)b_o^{s-1} b_u \frac{\overline{U}}{\overline{U}^*}\right.$$

$$\left. + \frac{b_o^s (1 - s)}{2} + \frac{b_o^s (s + 1)(s - 1)}{2} \frac{\overline{U}^2}{\overline{U}^{*2}}\right] + \frac{v^2}{\overline{U}^{*2}} \left[sb_o^{s-1} b_{vv}\right.$$

$$\left. + \frac{s(s - 1)}{2} b_o^{s-2} b_v^2 + s(1 - s) b_o^{s-1} b_v \frac{\overline{V}}{\overline{U}^*} + \frac{b_o^s (1 - s)}{2}\right.$$

$$\left. \frac{b_o^s (s + 1)(s - 1)}{2} \frac{\overline{V}^2}{\overline{U}^{*2}}\right] + \frac{w^2}{\overline{U}^{*2}} \left[sb_o^{s-1} b_{ww} + \frac{s(s - 1)}{2} b_o^{s-2} b_w^2\right.$$

$$\left. + s(1 - s)b_o^{s-1} b_w \frac{\overline{W}}{\overline{U}^*} + \frac{b_o^s (1 - s)}{2} + \frac{b_o^s (s + 1)(s - 1)}{2} \frac{\overline{W}^2}{\overline{U}^{*2}}\right]$$

$$+ \frac{uv}{\overline{U}^{*2}} \left[sb_o^{s-1} b_{uv} + s(s - 1)b_o^{s-2} b_u b_v + s(1 - s)b_o^{s-1} b_u \frac{\overline{V}}{\overline{U}^*}\right.$$

$$\left. + s(1 - s)b_o^{s-1} b_v \frac{\overline{U}}{\overline{U}^*} + b_o^s (s + 1)(s - 1) \frac{\overline{UV}}{\overline{U}^{*2}}\right]$$

$$+ \frac{uw}{\overline{U}^{*2}} \left[sb_o^{s-1} b_{uw} + s(s - 1) b_o^{s-2} b_u b_w + s(1 - s)b_o^{s-1} b_u \frac{\overline{W}}{\overline{U}^*} +\right.$$

$$+ s(1 - s)\, b_o^{s-1}\, b_w \frac{\overline{U}}{\overline{U}^*} + b_o^s\, (s + 1)(s - 1) \frac{\overline{UW}}{\overline{U}^{*2}}]$$

$$+ \frac{\overline{vw}}{\overline{U}^{*2}} [sb_o^{s-1}\, b_{vw} + s(s - 1)b_o^{s-2}\, b_v b_w + s(1 - s)b_o^{s-1}\, b_v \frac{\overline{W}}{\overline{U}^*}$$

$$+ s(1 - s)\, b_o^{s-1}\, b_w \frac{\overline{V}}{\overline{U}^*} + b_o^s\, (s + 1)(s - 1) \frac{\overline{VW}}{\overline{U}^{*2}}]\} \quad . \tag{A29}$$

At this point, it is convenient to introduce the following notation:

$$C_s^u = sb_o^{s-1}\, b_u - (s - 1)\, b_o^s \frac{\overline{U}}{\overline{U}^*} \, , \tag{A30a}$$

$$C_s^v = sb_o^{s-1}\, b_v - (s - 1)\, b_o^s \frac{\overline{V}}{\overline{U}^*} \, , \tag{A30b}$$

$$C_s^w = sb_o^{s-1}\, b_w - (s - 1)\, b_o^s \frac{\overline{W}}{\overline{U}^*} \, , \tag{A30c}$$

$$C_s^{uu} = sb_o^{s-1}\, b_{uu} + \frac{s(s - 1)}{2}\, b_o^{s-2}\, b_u^2 - s(s - 1)\, b_o^{s-1}\, b_u \frac{\overline{U}}{\overline{U}^*}$$

$$- \frac{b_o^s\, (s - 1)}{2} + \frac{b_o^s\, (s + 1)(s - 1)}{2} \frac{\overline{U}^2}{\overline{U}^{*2}} \, , \tag{A30d}$$

$$C_s^{vv} = sb_o^{s-1} b_{vv} + \frac{s(s - 1)}{2}\, b_o^{s-2}\, b_v^2 - s(s - 1)b_o^{s-1}\, b_v \frac{\overline{V}}{\overline{U}^*}$$

$$- \frac{b_o^s\, (s - 1)}{2} + \frac{b_o^s\, (s + 1)(s - 1)}{2} \frac{\overline{V}^2}{\overline{U}^{*2}} \, , \tag{A30e}$$

$$C_s^{ww} = sb_o^{s-1}\, b_{ww} + \frac{s(s - 1)}{2}\, b_o^{s-2}\, b_w^2 - s(s-1)\, b_o^{s-1}\, b_w \frac{\overline{W}}{\overline{U}^*}$$

$$- \frac{b_o^s\, (s - 1)}{2} + \frac{b_o^s\, (s + 1)(s - 1)}{2} \frac{\overline{W}^2}{\overline{U}^{*2}} \, , \tag{A30f}$$

$$C_s^{uv} = sb_o^{s-1} b_{uv} + s(s-1)b_o^{s-2} b_u b_v - s(s-1)b_o^{s-1} b_u \frac{\overline{V}}{\overline{U}^*}$$

$$- s(s-1) b_o^{s-1} b_v \frac{\overline{U}}{\overline{U}^*} + b_o^s (s+1)(s-1) \frac{\overline{UV}}{\overline{U}^{*2}} , \qquad \text{(A30g)}$$

$$C_s^{uw} = sb_o^{s-1} b_{uw} + s(s-1) b_o^{s-2} b_u b_w - s(s-1) b_o^{s-1} b_u \frac{\overline{W}}{\overline{U}^*}$$

$$- s(s-1) b_o^{s-1} b_w \frac{\overline{U}}{\overline{U}^*} + b_o^s (s+1)(s-1) \frac{\overline{UW}}{\overline{U}^{*2}} , \qquad \text{(A30h)}$$

and

$$C_s^{vw} = sb_o^{s-1} b_{vw} + s(s-1) b_o^{s-2} b_v b_w - s(s-1) b_o^{s-1} b_v \frac{\overline{W}}{\overline{U}^*}$$

$$- s(s-1) b_o^{s-1} bw \frac{\overline{V}}{\overline{U}^*} + b_o^s (s+1)(s-1) \frac{\overline{VW}}{\overline{U}^{*2}} . \qquad \text{(A30i)}$$

By these definitions, a more compact form of Eq. A29 results,

$$Q(\theta - \alpha)_1^s = \overline{U}^* \left\{ b_o^s + \frac{u}{\overline{U}^*} C_s^u + \frac{v}{\overline{U}^*} C_s^v + \frac{w}{\overline{U}^*} C_s^w \right.$$

$$+ \frac{u^2}{\overline{U}^{*2}} C_s^{uu} + \frac{v^2}{\overline{U}^{*2}} C_s^{vv} + \frac{w^2}{\overline{U}^{*2}} C_s^{ww}$$

$$\left. + \frac{uv}{\overline{U}^{*2}} C_s^{uv} + \frac{uw}{\overline{U}^{*2}} C_s^{uv} + \frac{vw}{\overline{U}^{*2}} C_s^{vw} \right\} . \qquad \text{(A31)}$$

In matrix notation,

$$Q(\theta - \alpha)_1^s = \overline{U}^* \left[b_o^s + \underline{C}_s^T \underline{V} \right] , \qquad \text{(A32a)}$$

where

$$\underline{C}_s^T = \{C_s^u \; C_s^v \; C_s^w \; C_s^{uu} \; C_s^{vv} \; C_s^{ww} \; C_s^{uv} \; C_s^{uw} \; C_s^{vw}\} \; , \tag{A32b}$$

$$\underline{V}^T = \{\frac{u}{U^*} \; \frac{v}{U^*} \; \frac{w}{U^*} \; \frac{u^2}{U^{*2}} \; \frac{v^2}{U^{*2}} \; \frac{w^2}{U^{*2}} \; \frac{uv}{U^{*2}} \; \frac{uw}{U^{*2}} \; \frac{vw}{U^{*2}} \} \; . \tag{A32c}$$

The final expression for $Q\,(\theta - \alpha)$ is obtained by substituting Eq. A32 with s = 1, 2, 3, 4, and 5, into Eq. A19 where one obtains

$$\begin{aligned} Q\,(\theta - \alpha) = \overline{U}^* \; \{ & b_o + b_o^2 \, \frac{1}{2} \tan \alpha + b_o^3 \, (\frac{1}{2} \tan^2 \alpha + \frac{1}{6}) \\ & + b_o^4 \, (\frac{5}{8} \tan^3 \alpha + \frac{5}{24} \tan \alpha) + b_o^5 \, (\frac{7}{8} \tan^4 \alpha + \frac{7}{24} \tan^2 \alpha) \\ & + \underline{C}_1^T \, \underline{V} + \frac{1}{2} \tan \alpha \, \underline{C}_2^T \, \underline{V} + (\frac{1}{2} \tan^2 \alpha + \frac{1}{6}) \, \underline{C}_3^T \, \underline{V} \\ & + (\frac{5}{8} \tan^3 \alpha + \frac{5}{24} \tan \alpha) \, \underline{C}_4^T \, \underline{V} + (\frac{7}{8} \tan^4 \alpha + \frac{7}{24} \tan^2 \alpha) \, \underline{C}_5^T \, \underline{V} \} . \end{aligned} \tag{A33}$$

Similarily, $Q\,(\theta - \alpha)^2$ is determined by inserting Eq. A32 with s = 2, 3, 4, 5, and 6, respectively, into Eq. A20,

$$\begin{aligned} Q\,(\theta - \alpha)^2 = \overline{U}^* \; \{ & b_o^2 + b_o^3 \tan \alpha + b_o^4 \, (\frac{5}{4} \tan^2 \alpha + \frac{1}{3}) \\ & + b_o^5 \, (\frac{7}{4} \tan^3 \alpha + \frac{7}{12} \tan \alpha) + b_o^6 \, (\frac{21}{8} \tan^4 \alpha + \frac{23}{24} \tan^2 \alpha + \frac{1}{36}) \\ & + \underline{C}_2^T \, \underline{V} + \tan \alpha \, \underline{C}_3^T \, \underline{V} + (\frac{5}{4} \tan^2 \alpha + \frac{1}{3}) \, \underline{C}_4^T \, \underline{V} \end{aligned}$$

$$+ \left(\frac{7}{4}\tan^3\alpha + \frac{7}{12}\tan\alpha\right)\underline{C}_5^T\underline{V} +$$

$$+ \left(\frac{21}{8}\tan^4\alpha + \frac{23}{24}\tan^2\alpha + \frac{1}{36}\right)\underline{C}_6^T\underline{V}\Big\} . \qquad \text{(A34)}$$

For perfect probe alignment,

$$\underline{C}_3^T = \underline{C}_4^T = \underline{C}_5^T = \underline{C}_6^T = 0 ,$$

and

$$\underline{C}_1^T = \{0 \quad b_v \quad b_w \quad 0 \quad b_{vv} \quad b_{ww} \quad 0 \quad 0 \quad 0 \quad 0\} ,$$

$$\underline{C}_2^T = \{0 \quad 0 \quad 0 \quad 0 \quad b_v^2 \quad b_w^2 \quad 0 \quad 0 \quad 2_{bv}\, b_w\} ,$$

where from Eqs. A23,

$$b_v = \cos\gamma_x$$

$$b_w = \sin\gamma_x$$

$$b_{vv} = -\frac{1}{2}\tan\alpha$$

and

$$b_{ww} = -\frac{1}{2}\tan\alpha .$$

Appendix B

In this section expressions are developed for powers of $\frac{\overline{U}}{\overline{U}^*}$ and Q which are needed in the derivation of the sensor response analysis and in Appendix A. These expressions are derived from the binomial series expansion

$$(1 + \chi)^r = 1 + r\chi + \frac{r(r-1)}{2!}\chi^2 + \cdots + r(r-1)\cdots\frac{(r-s+1)}{s!}\chi^s \,. \tag{B1}$$

Determination of $\left(\frac{\overline{U}}{\overline{U}^*}\right)^p$

Referring to Eq.4.9,

$$\overline{U}^* = \overline{U}\left\{1 + \frac{\overline{V}^2 + \overline{W}^2}{\overline{U}^2}\right\}^{1/2} \tag{B2}$$

and in general one can write

$$\overline{U}^{*p} = \overline{U}^p\left\{1 + \frac{\overline{V}^2 + \overline{W}^2}{\overline{U}^2}\right\}^{p/2} \,.$$

Expanding this equation in a series via Eq. B1 yields

$$\overline{U}^{*p} = \overline{U}^p\left\{1 + \frac{p}{2}\left(\frac{\overline{V}^2 + \overline{W}^2}{\overline{U}^2}\right) + \frac{p(p-2)}{8}\left(\frac{\overline{V}^2 + \overline{W}^2}{\overline{U}^2}\right)^2 + \cdots\right\} \,,$$

which can be written to fourth order as

$$\left(\frac{\overline{U}^*}{\overline{U}}\right)^p = \left\{1 + \frac{p}{2}\left(\frac{\overline{V}^2 + \overline{W}^2}{\overline{U}^2}\right) + \frac{p\,(p-2)}{8}\left(\frac{\overline{V}^4 + 2\overline{V}^2\,\overline{W}^2 + \overline{W}^4}{\overline{U}^4}\right)\right\}, \qquad \text{(B3)}$$

with the restriction that

$$\frac{\overline{V}^2 + \overline{W}^2}{\overline{U}^2} < 1 . \qquad \text{(B4)}$$

For $p = -1$, for example, Eq. B3 becomes

$$\frac{\overline{U}}{\overline{U}^*} = \left\{1 - \frac{1}{2}\left(\frac{\overline{V}^2 + \overline{W}^2}{\overline{U}^2}\right) + \frac{3}{8}\left(\frac{\overline{V}^4 + 2\overline{V}^2\,\overline{W}^2 + \overline{W}^4}{\overline{U}^4}\right)\right\}. \qquad \text{(B5)}$$

For a perfectly aligned probe, $\overline{V} = \overline{W} = 0$, and Eq. B5 reduces to

$$\overline{U}^* = \overline{U} . \qquad \text{(B6)}$$

Determination of Q^p

Referring to Eq. 4.5,

$$Q = \left\{(\overline{U} + u)^2 + (\overline{V} + v)^2 + (\overline{W} + w)^2\right\}^{1/2} . \qquad \text{(B7)}$$

Simplifying Eq. B7 and inserting Eq. B2 provides the basis for a general relation

$$Q^p = \overline{U}^{*p}\left\{1 + 2\left(\frac{\overline{U}u + \overline{V}v + \overline{W}w}{\overline{U}^{*2}}\right) + \frac{u^2 + v^2 + w^2}{\overline{U}^{*2}}\right\}^{p/2} . \qquad \text{(B8)}$$

Expanding Eq. B8 in the series given by Eq. B1 gives

$$Q = \overline{U}^{*}\left\{1 + \frac{p}{2}\left(2\,\frac{\overline{U}u + \overline{V}v + \overline{W}w}{\overline{U}^{*2}} + \frac{u^2 + v^2 + w^2}{\overline{U}^{*2}}\right)\right.$$

$$+ \frac{p\,(p-2)}{8}\left(2\,\frac{\overline{U}u + \overline{V}v + \overline{W}w}{\overline{U}^{*2}} + \frac{u^2 + v^2 + w^2}{\overline{U}^{*2}}\right)^2$$

$$\left. + \frac{p\,(p-2)(p-4)}{48}\left(2\,\frac{\overline{U}u + \overline{V}v + \overline{W}w}{\overline{U}^{*2}} + \frac{u^2 + v^2 + w^2}{\overline{U}^{*2}}\right)^3 + \cdots\right\} .$$

An order of magnitude comparison, assuming $\frac{\overline{U}}{\overline{U}^{*}} = O(1)$ and $O\left(\frac{u}{\overline{U}^{*}}\right) = O\left(\frac{v}{\overline{U}^{*}}\right) = O\left(\frac{\overline{V}^2}{\overline{U}^{*2}}\right) = O\left(\frac{\overline{W}^2}{\overline{U}^{*2}}\right)$ gives to $O\left(\frac{u^3}{\overline{U}^{*2}}\right)$

$$Q^p = \overline{U}^{*p}\left\{1 + p\,\frac{u\overline{U} + v\overline{V} + w\overline{W}}{\overline{U}^{*2}} + \frac{u^2}{\overline{U}^{*2}}\left[\frac{p}{2} + \frac{p\,(p-2)}{2}\,\frac{\overline{U}^2}{\overline{U}^{*2}}\right]\right.$$

$$+ \frac{v^2}{\overline{U}^{*2}}\left[\frac{p}{2} + \frac{p\,(p-2)}{2}\,\frac{\overline{V}^2}{\overline{U}^{*2}}\right] + \frac{w^2}{\overline{U}^{*2}}\left[\frac{p}{2} + \frac{p\,(p-2)}{2}\,\frac{\overline{W}^2}{\overline{U}^{*2}}\right]$$

$$+ \frac{p\,(p-2)}{2}\left[\frac{2uv\overline{UV} + 2uw\overline{UW} + 2vw\overline{VW}}{\overline{U}^{*4}}\right.$$

$$\left.\left. + \frac{u^3\,\overline{U} + uv^2\,\overline{U} + uw^2\,\overline{U}}{\overline{U}^{*4}} + \frac{p\,(p-2)\,(p-4)}{6}\left[\frac{u^3\,\overline{U}^3}{\overline{U}^{*6}}\right]\right\} , \qquad \text{(B9)}$$

with the restrictions that

$$2\,\frac{u\overline{U} + v\overline{V} + w\overline{W}}{\overline{U}^{*2}} + \frac{u^2 + v^2 + w^2}{\overline{U}^{*2}} < 1 . \qquad \text{(B10)}$$

To illustrate the utility of Eq. B9, let p = 1. With this substitution Eq. B9 becomes

$$Q = \overline{U}^{*} \left\{1 + \frac{u\overline{U} + v\overline{V} + w\overline{W}}{\overline{U}^{*2}} + \frac{1}{2}\frac{u^2}{\overline{U}^{*2}}\left[1 - \frac{\overline{U}^{2}}{\overline{U}^{*2}}\right]\right.$$

$$+ \frac{1}{2}\frac{v^2}{\overline{U}^{*2}}\left[1 - \frac{\overline{V}^{2}}{\overline{U}^{*2}}\right] + \frac{1}{2}\frac{w^2}{\overline{U}^{*2}}\left[1 - \frac{\overline{W}^{2}}{\overline{U}^{*2}}\right]$$

$$- \frac{1}{2}\left[\frac{2uvUV + 2uwUW + 2vwVW + u^3\overline{U} + uv^2\overline{U} + uw^2\overline{U}}{\overline{U}^{*4}}\right]$$

$$\left. + \frac{1}{2}\frac{u^3\overline{U}^{3}}{\overline{U}^{*6}}\right\} . \qquad \text{(B11)}$$

A further simplification results when the probe is aligned to the flow. In this case Eq. B11 becomes

$$Q = \overline{U}\left\{1 + \frac{u}{\overline{U}} + \frac{1}{2}\left[\frac{v^2}{\overline{U}^{2}} + \frac{w^2}{\overline{U}^{2}}\right] - \frac{1}{2}\left[\frac{uv^2}{\overline{U}^{2}} + \frac{uw^2}{\overline{U}^{3}}\right]\right\} . \qquad \text{(B12)}$$

Appendix C

A Comparison of the Sensor Response Equations

The generalized response equation derived in Chapter IV provides the opportunity to further study and compare the present results with some of the existing response analyses. For these comparisons the two detailed analyses of Bruun [57] and Champagne et al., [59] were studied.

Bruun [57] derived two response equations, one using the Hinze [54] cooling law (Eq. 2.6) and the other using the Davies and Bruun [104] law (Eq. 2.7). Briefly, his derivation uses the expression for $\cos\theta$ obtained from the geometry shown in Fig. C1 where

$$\cos^2\theta = 1 - \left(\frac{Q_T}{Q}\right)^2 . \tag{C1}$$

The tangential component, Q_T, is obtained by the inner product

$$Q_T = \underline{Q}\,(t) \cdot \hat{\ell} , \tag{C2}$$

where $\hat{\ell}$ is a unit vector which defines the direction of the hot wire. Since an expression for the effective cooling velocity is required, one can write

$$U_e(t) = Q(t)\,\cos^m\,(\theta(t)) \tag{C3}$$

or

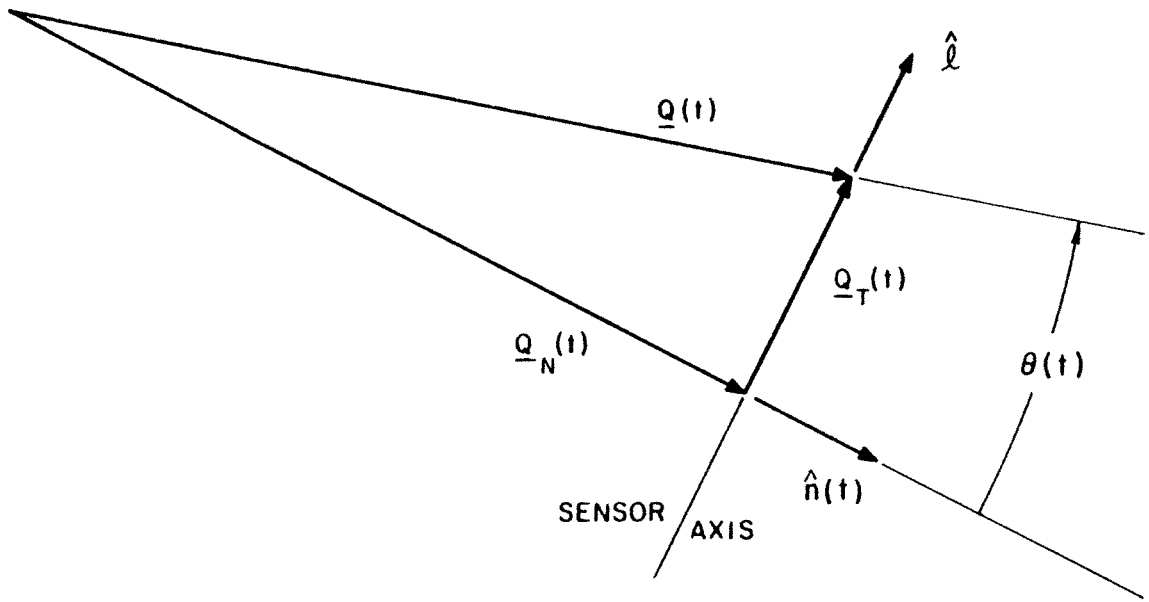

Figure C1. Instantaneous Plane Geometry Used for Bruun's [57] Sensor Response Analysis

$$U_e = Q\left[1 - \left(\frac{\underline{Q}(t)\cdot\hat{\ell}}{Q}\right)^2\right]^{m/2} \tag{C4}$$

from Eqs. C1-C3. Series expansions are subsequently performed for a wire in the xz plane exposed to the velocity components $\overline{U}$ + u, v, and w.

The response equation using the cooling law of Hinze [54], given in Eq. 2.6, is constructed from the above series expansions by setting m = 2, multiplying by this quantity $(1 - k^2)$, adding k^2, and taking the square root of the resulting expression. In essence, the square root in

$$U_e = Q\left[(1 - k^2)\cos^2\theta + k^2\right]^{1/2}, \tag{C5}$$

which is equivalent to Eq. 2.6, is expanded to obtain the final result.

Bruun's [57] approach can be extended to accommodate an arbitrary positioning of the sensor plane. In doing so the following response equations were obtained:

for the effective cooling velocity given by Eq. C3,

$$Q\cos^m\theta = \overline{U}\cos^m\alpha\left\{1 + \frac{u}{\overline{U}} + \frac{v}{\overline{U}}\left\{-m\tan\alpha\cos\gamma_x\right\}\right.$$

$$\left. + \frac{w}{\overline{U}}\left\{-m\tan\alpha\sin\gamma_x\right\} + \frac{1}{2}\frac{vv}{\overline{U}^2}\left\{1 + m\left(\tan^2\alpha - \cos^2\gamma_x\right) + \right.\right.$$

$$+ m\,(m-2)\,\tan^2\alpha\,\cos^2\gamma_x\} + \frac{1}{2}\frac{ww}{\overline{U}^2}\{1 + m(\tan^2\alpha - \sin^2\gamma_x)$$

$$+ m\,(m-2)\,\tan^2\alpha\,\sin^2\gamma_x\} + \frac{vw}{\overline{U}^2}\{\cos\gamma_x \sin\gamma_x\,[m - m(m-2)\,\tan^2\alpha]\}; \qquad (C6)$$

for the effective cooling velocity given by Eq. C5,

$$Q\{(1-k^2)\cos^2\theta + k^2\}^{1/2} = \overline{U}\{(1-k^2)\cos^2\alpha + k^2\}^{1/2}\{1 + \frac{u}{\overline{U}}$$

$$+ \frac{v}{\overline{U}}\{-\hat{m}\tan\alpha\cos\gamma_x\} + \frac{w}{\overline{U}}\{-\hat{m}\tan\alpha\sin\gamma_x\} + \frac{1}{2}\frac{vv}{\overline{U}^2}\{1$$

$$+ \hat{m}\,(\tan^2\alpha - \cos^2\gamma_x) - \hat{m}^2\tan^2\alpha\cos^2\gamma_x\} + \frac{1}{2}\frac{ww}{\overline{U}^2}\{1$$

$$+ \hat{m}\,(\tan^2\alpha - \sin^2\gamma_x) + \hat{m}^2\tan^2\alpha\sin^2\gamma_x\}$$

$$+ \frac{vw}{\overline{U}^2}\{-\cos\gamma_x\sin\gamma_x\,[\hat{m} + \hat{m}^2\tan^2\alpha]\} \qquad (C7a)$$

where

$$\hat{m} = \frac{(1-k^2)\cos^2\alpha}{(1-k^2)\cos^2\alpha + k^2}\,. \qquad (C7b)$$

In Eqs. C6 and C7, the notation adopted in Chapter IV is used. The apparent similarity between the two response equations using the different cooling laws is discussed in detail by Bruun and further discussions are presented in Chapter II. It is easily shown that the exact relations given by Eqs. C6 and C7 follow from the general theory

of an aligned sensor, presented in Chapter IV, when appropriate expressions for f, f', and f'' are inserted into Eq. 4.32.

In the final comparison, the response equation developed by Champagne et al. [59] is used. A characteristic feature in their result (written here for low intensity turbulence)

$$\overline{U}_e = \overline{U}\cos\alpha\left\{\left[1 + \frac{1}{2}k^2\tan^2\alpha - \frac{1}{8}k^4\tan^4\alpha\right]\right.$$

$$+ \frac{u}{\overline{U}}\left[1 + \frac{1}{2}k^2\tan^2\alpha - \frac{1}{8}k^4\tan^4\alpha\right]$$

$$\left. + \frac{v}{\overline{U}}\left[\tan\alpha - k^2\tan\alpha\left(1 + \frac{1}{2}\tan^2\alpha\right) + \frac{1}{2}k^4\tan^3\alpha\left(1 + \frac{3}{4}\tan^2\alpha\right)\right]\right\} \tag{C8}$$

was in the treatment of k^2 in which the fourth order terms resulted from a square root expansion of an effective cooling velocity. A closer look reveals that the velocity coefficients are actually series expansions of the cooling law function (Eq. 2.6) and its first derivative. This is shown by writing f and f', Eqs. 4.50 and 4.51, respectively, in the form

$$f(\alpha,k^2) = \cos\alpha\left[1 + k^2\tan^2\alpha\right]^{1/2},$$

$$f'(\alpha,k^2) = \cos\alpha\tan\alpha\,(k^2 - 1)\left[1 + k^2\tan^2\alpha\right]^{-1/2}.$$

A series expansion of the first expression yields,

$$f(\alpha,k^2) \simeq \cos\alpha\left[1 + \frac{1}{2}(k^2\tan^2\alpha) - \frac{1}{8}(k^2\tan^2\alpha)^2 + \ldots\right], \tag{C9}$$

which is equivalent to the first two coefficients appearing in Eq. C8. Similarily, the derivative of f is approximately

$$f'(\alpha,k^2) \simeq \cos\alpha \tan\alpha (k^2 - 1) \left[1 - \frac{1}{2}(k^2 \tan^2\alpha) + \frac{3}{8}(k^2 \tan^2\alpha)^2 + \ldots\right],$$

which becomes to fourth order in k,

$$f'(\alpha,k^2) \simeq \cos\alpha \left[-\tan\alpha + k^2 \tan\alpha \left(1 + \frac{1}{2}\tan^2\alpha\right) - \frac{1}{2}k^4 \tan^3\alpha \left(1 + \frac{3}{4}\tan^2\alpha\right)\right]. \quad (C10)$$

Thus, Eq. C8 can be rewritten as

$$\overline{U}_e = \overline{U}\left\{f + \frac{u}{\overline{U}} f - \frac{v}{\overline{U}} f'\right\}, \quad (C11)$$

which represents a first order response of a sensor in the xz plane where $\gamma_x = -\pi/2$ per Eq. 4.32.

Summarizing, a considerable simplification and versatility of the response equations is possible by the generalized theory presented in Chapter IV. This would be especially convenient when a yaw dependent cooling law parameter is considered since the more complicated expressions for describing the effective cooling velocity, i.e. those involving series expansions with a yaw dependent parameter, that would

result from the more common approach where yaw parameters appear explicitly in the response equation such as in Eq. C8, are avoided. Moreover, greater accuracy is provided by the present equation since the exact functional forms f, f', f'' ... are used instead of series expansions of these functions, which can give only an approximate representation.

APPENDIX D

A Study of the Influence of Turbulence and Pitch Angle on the Flow Angle Measurements of a Single Horizontal Sensor

Utilizing the angular sensitivity of a sensor to determine the mean flow direction involves a search in which the symmetry of the sensor's response to yaw angle is used. This technique, described in Chapter III, does not require calibrations per se, if one assumes a symmetric flow-angle response of the sensor. A voltage trace of an inclining element as it sweeps by the normal, maximum voltage position (or the parallel, minimum voltage position) approximates a cosine function whereby the relative mean flow direction can be found directly. Of primary concern is the extent to which this measurement may be influenced by the presence of turbulence and pitch angles.

For the purpose of studying such effects, a single sensor is placed parallel to the xz plane in two positions. In the first position, $\gamma_x = \pi/2$ and $\alpha = \alpha_o$, and $\gamma_x = -\pi/2$ and $\alpha = \alpha_o$ in the second position. According to Eq. 4.44 and assuming symmetric flow-angle characteristics, the difference

$$\frac{\overline{E}_2 - \overline{E}_1}{B_o \overline{U}^*} = S_o\left(\alpha_o, -\frac{\pi}{2}, \overline{\psi}_z^*, \overline{\psi}_y\right) - S_o\left(\alpha_o, \frac{\pi}{2}, \overline{\psi}_z^*, \overline{\psi}_y\right)$$

$$+ \frac{\overline{uu}}{\overline{U}^{*2}}\left\{S_{uu}\left(\alpha_o, -\frac{\pi}{2}, \overline{\psi}_z, \overline{\psi}_y\right) - S_{uu}\left(\alpha_o, \frac{\pi}{2}, \overline{\psi}_z^*, \overline{\psi}_y\right)\right\}$$

$$+ \frac{\overline{vv}}{\overline{U}^{*2}}\left\{S_{vv}\left(\alpha_o, -\frac{\pi}{2}, \overline{\psi}_z^*, \overline{\psi}_y\right) - S_{vv}\left(\alpha_o, \frac{\pi}{2}, \overline{\psi}_z^*, \overline{\psi}_y\right)\right\}$$

$$+ \frac{\overline{ww}}{\overline{U}^{*2}} \left\{ S_{ww}\left(\alpha_o, -\frac{\pi}{2}, \overline{\psi}_z^*, \overline{\psi}_y\right) - S_{ww}\left(\alpha_o, \frac{\pi}{2}, \overline{\psi}_z^*, \overline{\psi}_y\right) \right\} +$$

$$+ \frac{\overline{uv}}{\overline{U}^{*2}} \left\{ S_{uv}\left(\alpha_o, -\frac{\pi}{2}, \overline{\psi}_z^*, \overline{\psi}_y\right) - S_{uv}\left(\alpha_o, \frac{\pi}{2}, \overline{\psi}_z^*, \overline{\psi}_y\right) \right\}$$

$$+ \frac{\overline{uw}}{\overline{U}^{*2}} \left\{ S_{uw}\left(\alpha_o, -\frac{\pi}{2}, \overline{\psi}_z^*, \overline{\psi}_y\right) - S_{uw}\left(\alpha_o, \frac{\pi}{2}, \overline{\psi}_z^*, \overline{\psi}_y\right) \right\}$$

$$+ \frac{\overline{vw}}{\overline{U}^{*2}} \left\{ S_{vw}\left(\alpha_o, -\frac{\pi}{2}, \overline{\psi}_z^*, \overline{\psi}_y\right) - S_{vw}\left(\alpha_o, \frac{\pi}{2}, \overline{\psi}_z^*, \overline{\psi}_y\right) \right\} \qquad \text{(D1)}$$

will be zero for the perfect alignment ($\overline{\psi}_y = \overline{\psi}_z^* = 0$) of the sensor in both positions which suggests no influence on the angle measurement due to the higher order terms that remained after time averaging. For this case, the effects are symmetric and cancel in the difference. Equations 4.33-4.42 give the dependence of the subscripted S terms appearing in Eq. D1.

To consider the effects of pitch relative to the tunnel floor on the angle measurement, a partial misalignment of the sensor is established by setting $\overline{\psi}_y = 0$ in Eq. D1 with $\overline{\psi}_z^* \neq 0$. Referring to Eqs. 4.33-4.42 and Eqs. A23 and A30 in Appendix A, only the terms containing the odd powers of $b_w = \pm 1$ will experience a sign change as the sensor is placed from the first position to the second. Therefore, only the C_s^{uw} and C_s^{vw} terms contribute to the difference

$$\frac{\overline{E}_2 - \overline{E}_1}{B_o \overline{U}^*} = \frac{\overline{uw}}{\overline{U}^{*2}} \left\{ S_{uw}\left(\alpha_o, -\frac{\pi}{2}, \overline{\psi}_z^*, 0\right) - S_{uw}\left(\alpha_o, \frac{\pi}{2}, \overline{\psi}_z^*, 0\right) \right\}$$

$$+ \frac{\overline{vw}}{\overline{U}^{*2}} \left\{ S_{vw}\left(\alpha_o, -\frac{\pi}{2}, \overline{\psi}_z^*, 0\right) - S_{vw}\left(\alpha_o, \frac{\pi}{2}, \overline{\psi}_z^*, 0\right) \right\} . \qquad \text{(D2)}$$

Substitution of Eqs. 4.40 and 4.41 into Eq. D2 yields

$$\frac{\overline{E}_2 - \overline{E}_1}{B_o \overline{U}^*} = \frac{\overline{uw}}{\overline{U}^{*2}} \{0\} + \frac{\overline{vw}}{\overline{U}^{*2}} \{0\} = 0 \, . \tag{D3}$$

Thus, based on the response given in Eq. 4.44 and assuming a symmetric flow-angle response of the sensor, it appears that this method of measuring the flow yaw angle is unaffected by the presence of turbulence and pitch angle when a single horizontal sensor is used as described above.

Appendix E

An Evaluation of the X-Array Response for Planar Misalignment

The accuracy of the x-array response equations, Eqs. 4.69-4.71, is evaluated under the effects of misalignment occurring in the plane of the sensors. For this study a geometrically perfect vx-array is used.

In Eqs. 4.69-4.71, the turbulent stress coefficients contain the 'S' terms, defined in Eqs. 4.33-4.42, which incorporate the effects of probe misalignment. For misalignment occuring in the xy plane alone, $\overline{\psi}_y = 0$, and Eqs. 4.69-4.71 become

$$\overline{(e_a + e_b)^2} = A^{+2}\overline{uu} + B^{+2}\overline{vv} + 2A^{+}B^{+}\overline{uv} \,, \tag{E1}$$

$$\overline{(e_a - e_b)^2} = A^{-2}\overline{uu} + B^{-2}\overline{vv} + 2A^{-}B^{-}\overline{uv} \,, \tag{E2}$$

$$\overline{(e_a + e_b)(e_a - e_b)} = A^{+}A^{-}\overline{uu} + B^{+}B^{-}\overline{vv} + (A^{+}B^{-} + A^{-}B^{+})\overline{uv} \tag{E3}$$

where the $A^{\pm}$ and $B^{\pm}$ terms are of the form given by Eqs. 4.66 and 4.67 with $\overline{\psi}_y = 0$.

An ideal case can be constructed, following Bruun [90], to serve as a model for the purpose of testing the response equations, Eqs. E1-E3. Consider the situation illustrated in Fig. E1, where it is implied that the instantaneous and mean planes lie parallel to the xy plane and velocity fluctuation, w, acting normal to this plane is assumed to be negligible. Thus, for the instantaneous velocity one obtains

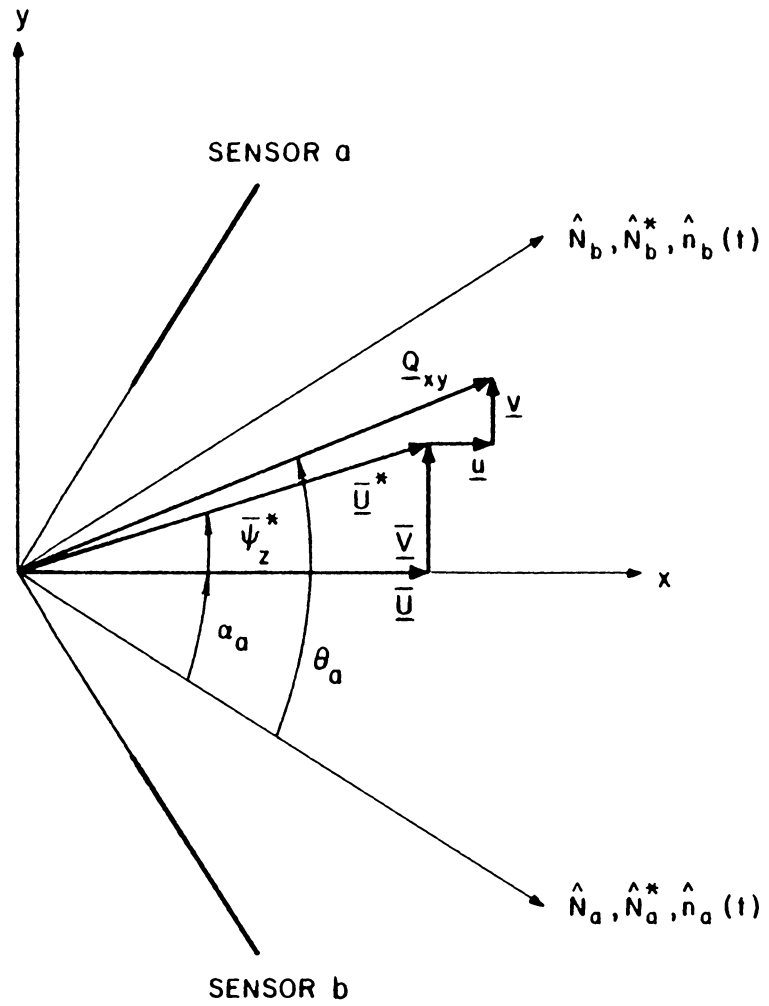

Figure E1. Misaligned Vertical X-Array Neglecting W Components Normal to the Plane of the Sensors

$$Q = \{Q_{xy}^2 + w^2\}^{1/2} = Q_{xy}\{1 + \frac{1}{2}\frac{w^2}{Q_{xy}^2} + \cdots\} ,$$

and it is assumed that

$$Q \doteq Q_{xy} . \tag{E4}$$

Referring to Eq. 4.30, the instantaneous voltage response can be written as

$$E - E_o = Q\, B_o f(\theta, P(\theta)) .$$

For the case of normal component cooling for each sensor,

$$E_a - E_{o,a} = QB_{o,a}\cos\theta_a = B_{o,a}(U\cos\alpha_a - V\sin\alpha_a) , \tag{E5}$$

$$E_b - E_{o,b} = QB_{o,b}\cos\theta_b = B_{o,b}(U\cos\alpha_b + V\sin\alpha_b) . \tag{E6}$$

The sensor's response to the fluctuating velocities follows from Eqs. E5 and E6 where

$$e_a = B_{o,a}\{u\cos\alpha_a - v\sin\alpha_a\} \tag{E7}$$

for sensor a and

$$e_b = B_{o,b}\{u\cos\alpha_b + v\sin\alpha_b\} \tag{E8}$$

for sensor b, which are exactly equal to Eqs. 4.60 and 4.61 for the ideal cosine (normal component) cooling of a geometrically perfect vx - probe aligned to the flow.

Proceding in the same manner as in Chapter IV, the sum and difference combinations of Eqs. E7 and E8 are obtained where for this case $A^{\pm}$ and $B^{\pm}$ in Eqs. 4.60 and 4.61 are replaced by the ideal coefficients $A_I^{\pm}$ and $B_I^{\pm}$, respectively. When $\alpha_a = \alpha_b = \alpha_o$ and $B_{o,a} = B_{o,b} = B_o$, the sensors become matched. Consistent with earlier discussions, this gives $A_I^- = B_I^+ = 0$ and

$$A_I^+ = 2B_o \cos\alpha_o \ , \tag{E9}$$

$$B_I^- = -2B_o \sin\alpha_o \ , \tag{E10}$$

which in turn yields

$$\overline{(e_a + e_b)^2} = A_I^{+2} \ \overline{uu} \ , \tag{E11}$$

$$\overline{(e_a - e_b)^2} = B_I^{-2} \ \overline{vv} \ , \tag{E12}$$

and

$$\overline{(e_a + e_b)(e_a - e_b)} = A_I^+ B_I^- \ \overline{uv} \ . \tag{E13}$$

The coefficients appearing in Eqs. E11-E13 and defined in Eqs. E9 and E10 are constant in that they are independent of the misalignment

angle, $\overline{\psi}_z^*$. Direct comparisons can be made of the coefficients of the Reynolds stresses appearing in Eqs. E1-E3, for the case of the normal component cooling of a misaligned sensor pair with the ideal coefficients in Eqs. E11-E13. Table E1 gives results for $\alpha_o = 45^o$ and for a range of $\overline{\psi}_z^*$ values, where the real coefficients are nondimensionalized by A_I^{+2}. Thus, in comparing the real and ideal cases, one would expect real coefficients in Table E1 to have magnitudes near either 1 or 0 depending on the stress. For the present method of evaluation, Eqs. E1-E3 gives reasonably accurate results when compared to the ideal case. For $\overline{\psi}_z^*$ angles ranging from $0\text{-}10^o$, the coefficients deviate less than 3% from the true values and less than 5% in the range $0\text{-}15^o$. For large misalignment, larger errors are shown to propagate to the subsidiary coefficients. The results given in Table E1 are consistent with those reported by Bruun [90].

Table E1. Influence of Misalignment on the Reynolds Stress Coefficients* of a Perfect Vertical X-Array with Normal Component Cooling of the Sensors at $\alpha_a = \alpha_b = 45^o$

	$\overline{(e_a + e_b)^2}$			$\overline{(e_a - e_b)^2}$			$\overline{(e_a + e_b)(e_a - e_b)}$		
$\overline{\psi_z}^*$	$\overline{uu}$	$\overline{vv}$	$\overline{uv}$	$\overline{uu}$	$\overline{vv}$	$\overline{uv}$	$\overline{uu}$	$\overline{vv}$	$\overline{uv}$
0.0	1.000	0.000	0.000	0.000	1.000	0.000	0.000	0.000	-1.000
5.0	1.000	0.000	0.001	0.000	1.007	0.000	0.000	-0.001	-1.003
10.0	1.000	0.000	0.010	0.000	1.027	-0.003	0.001	-0.005	-1.013
15.0	0.991	0.000	0.041	0.000	1.047	-0.009	0.004	-0.021	-1.019
20.0	0.967	0.003	0.115	0.000	1.044	-0.007	0.003	-0.060	-1.005
25.0	0.921	0.013	0.223	0.000	0.960	0.029	-0.014	-0.114	-0.942

* The coefficients are nondimensionalized by A_I^{+2}.

APPENDIX F

Standard Test Case Mean Velocity Results

Without Turbulence Corrections

TABLE F1. STANDARD TEST CASE MEAN VELOCITY PROFILES AT STATION (-24,8)

REU (1/M) = 1.34E 06
KINEMATIC VISC. (SQ-M/S) = 1.67E-05
DENSITY (KG/CUBIC METER) = 1.10E 00
OMEGA (DEG) = 0.1
UFS (M/S) = 2.41E 01
U1FS (M/S) = 2.41E 01

Y (CM)	BETA (DEG)	U (M/S)	U1 (M/S)	U3 (M/S)	U/UFS	U1/U1FS	U3/U1FS
0.051	0.0	1.25E 01	1.25E 01	-2.18E-02	5.18E-01	5.18E-01	-9.04E-04
0.076	-0.1	1.31E 01	1.31E 01	-0.00E-01	5.44E-01	5.44E-01	0.00E-01
0.102	0.0	1.36E 01	1.36E 01	-2.38E-02	5.65E-01	5.65E-01	-9.86E-04
0.127	0.0	1.40E 01	1.40E 01	-2.44E-02	5.79E-01	5.79E-01	-1.01E-03
0.190	0.1	1.47E 01	1.47E 01	-5.12E-02	6.08E-01	6.08E-01	-2.12E-03
0.254	0.0	1.51E 01	1.51E 01	-2.64E-02	6.27E-01	6.27E-01	-1.09E-03
0.508	0.1	1.64E 01	1.64E 01	-5.74E-02	6.81E-01	6.81E-01	-2.38E-03
0.762	0.1	1.74E 01	1.74E 01	-6.06E-02	7.19E-01	7.19E-01	-2.51E-03
1.016	0.3	1.79E 01	1.79E 01	-1.25E-01	7.41E-01	7.41E-01	-5.17E-03
1.270	0.4	1.85E 01	1.85E 01	-1.61E-01	7.66E-01	7.66E-01	-6.69E-03
1.905	0.4	1.95E 01	1.95E 01	-1.70E-01	8.08E-01	8.08E-01	-7.05E-03
2.540	0.2	2.05E 01	2.05E 01	-1.07E-01	8.49E-01	8.49E-01	-4.45E-03
3.810	0.4	2.20E 01	2.20E 01	-1.92E-01	9.12E-01	9.12E-01	-7.96E-03
5.080	0.2	2.32E 01	2.32E 01	-1.22E-01	9.62E-01	9.62E-01	-5.04E-03
6.350	0.2	2.40E 01	2.40E 01	-1.26E-01	9.95E-01	9.95E-01	-5.21E-03
7.620	0.1	2.41E 01	2.41E 01	-8.42E-02	1.00E 00	1.00E 00	-3.49E-03
10.160	0.0	2.41E 01	2.41E 01	-4.21E-02	9.99E-01	9.99E-01	-1.74E-03
12.700	0.0	2.41E 01	2.41E 01	-4.21E-02	1.00E 00	1.00E 00	-1.75E-03

TABLE F2. STANDARD TEST CASE MEAN VELOCITY PROFILES AT STATION (-24,4)

REU (1/M) = 1.34E 06
KINEMATIC VISC. (SQ-M/S) = 1.67E-05
DENSITY (KG/CUBIC METER) = 1.10E 00
OMEGA (DEG) = 0.1
UFS (M/S) = 2.40E 01
U1FS (M/S) = 2.40E 01

Y (CM)	BETA (DEG)	U (M/S)	U1 (M/S)	U3 (M/S)	U/UFS	U1/U1FS	U3/U1FS
0.051	0.2	1.26E 01	1.26E 01	-6.57E-02	5.22E-01	5.22E-01	-2.73E-03
0.076	0.1	1.33E 01	1.33E 01	-4.63E-02	5.52E-01	5.52E-01	-1.93E-03
0.102	0.1	1.37E 01	1.37E 01	-4.79E-02	5.71E-01	5.71E-01	-1.99E-03
0.127	-0.1	1.39E 01	1.39E 01	-0.00E-01	5.80E-01	5.80E-01	0.00E-01
0.190	0.1	1.46E 01	1.46E 01	-5.09E-02	6.06E-01	6.06E-01	-2.12E-03
0.254	0.1	1.51E 01	1.51E 01	-5.28E-02	6.29E-01	6.29E-01	-2.20E-03
0.508	0.1	1.65E 01	1.65E 01	-5.75E-02	6.85E-01	6.85E-01	-2.39E-03
0.762	0.2	1.72E 01	1.72E 01	-9.01E-02	7.16E-01	7.16E-01	-3.75E-03
1.016	0.2	1.78E 01	1.78E 01	-9.31E-02	7.40E-01	7.40E-01	-3.88E-03
1.270	0.2	1.85E 01	1.85E 01	-9.67E-02	7.68E-01	7.68E-01	-4.02E-03
1.905	0.2	1.96E 01	1.96E 01	-1.03E-01	8.15E-01	8.15E-01	-4.27E-03
2.540	0.4	2.05E 01	2.05E 01	-1.79E-01	8.53E-01	8.53E-01	-7.45E-03
3.810	0.4	2.21E 01	2.21E 01	-1.93E-01	9.18E-01	9.18E-01	-8.01E-03
5.080	0.2	2.32E 01	2.32E 01	-1.22E-01	9.67E-01	9.67E-01	-5.06E-03
6.350	0.1	2.40E 01	2.40E 01	-8.38E-02	9.99E-01	9.99E-01	-3.49E-03
7.620	0.1	2.42E 01	2.42E 01	-8.43E-02	1.01E 00	1.01E 00	-3.51E-03
10.160	0.1	2.41E 01	2.41E 01	-8.41E-02	1.00E 00	1.00E 00	-3.50E-03
12.700	0.0	2.40E 01	2.40E 01	-4.20E-02	1.00E 00	1.00E 00	-1.75E-03

TABLE F3. STANDARD TEST CASE MEAN VELOCITY PROFILES AT STATION (-24,0)

REU (1/M) = 1.34E 06
KINEMATIC VISC. (SQ-M/S) = 1.67E-05
DENSITY (KG/CUBIC METER) = 1.10E 00
OMEGA (DEG) = 0.2
UFS (M/S) = 2.41E 01
U1FS (M/S) = 2.41E 01

Y (CM)	BETA (DEG)	U (M/S)	U1 (M/S)	U3 (M/S)	U/UFS	U1/U1FS	U3/U1FS
0.051	-0.4	1.18E 01	1.18E 01	4.11E-02	4.90E-01	4.90E-01	1.71E-03
0.076	-0.1	1.24E 01	1.24E 01	-2.16E-02	5.14E-01	5.14E-01	-8.97E-04
0.102	-0.1	1.29E 01	1.29E 01	-2.26E-02	5.37E-01	5.37E-01	-9.37E-04
0.127	-0.2	1.33E 01	1.33E 01	-0.00E-01	5.55E-01	5.55E-01	0.00E-01
0.190	-0.1	1.39E 01	1.39E 01	-2.43E-02	5.79E-01	5.79E-01	-1.01E-03
0.254	-0.4	1.44E 01	1.44E 01	5.01E-02	5.97E-01	5.97E-01	2.08E-03
0.508	-0.3	1.57E 01	1.57E 01	2.74E-02	6.51E-01	6.51E-01	1.14E-03
0.762	-0.1	1.63E 01	1.63E 01	-2.85E-02	6.78E-01	6.78E-01	-1.18E-03
1.016	-0.1	1.71E 01	1.71E 01	-2.99E-02	7.12E-01	7.12E-01	-1.24E-03
1.270	0.0	1.78E 01	1.78E 01	-6.20E-02	7.38E-01	7.38E-01	-2.58E-03
1.905	-0.2	1.87E 01	1.87E 01	-0.00E-01	7.77E-01	7.77E-01	0.00E-01
2.540	-0.2	1.95E 01	1.95E 01	-0.00E-01	8.12E-01	8.12E-01	0.00E-01
3.810	-0.1	2.12E 01	2.12E 01	-3.69E-02	8.79E-01	8.79E-01	-1.53E-03
5.080	-0.1	2.26E 01	2.26E 01	-3.94E-02	9.38E-01	9.38E-01	-1.64E-03
6.350	0.0	2.37E 01	2.37E 01	-8.26E-02	9.83E-01	9.83E-01	-3.43E-03
7.620	-0.1	2.40E 01	2.40E 01	-4.20E-02	9.99E-01	9.99E-01	-1.74E-03
10.160	0.0	2.41E 01	2.41E 01	-8.41E-02	1.00E 00	1.00E 00	-3.50E-03
12.700	0.0	2.41E 01	2.41E 01	-8.40E-02	1.00E 00	1.00E 00	-3.49E-03

TABLE F4. STANDARD TEST CASE MEAN VELOCITY PROFILES AT STATION (-24,-4)

REU (1/M) = 1.34E 06
KINEMATIC VISC. (SQ-M/S) = 1.67E-05
DENSITY (KG/CUBIC METER) = 1.10E 00
OMEGA (DEG) = 0.1
UFS (M/S) = 2.41E 01
U1FS (M/S) = 2.41E 01

Y (CM)	BETA (DEG)	U (M/S)	U1 (M/S)	U3 (M/S)	U/UFS	U1/U1FS	U3/U1FS
0.051	-0.3	1.20E 01	1.20E 01	4.20E-02	5.00E-01	5.00E-01	1.75E-03
0.076	-0.5	1.27E 01	1.27E 01	8.87E-02	5.28E-01	5.28E-01	3.69E-03
0.102	-0.5	1.32E 01	1.32E 01	9.23E-02	5.50E-01	5.50E-01	3.84E-03
0.127	-0.5	1.36E 01	1.36E 01	9.51E-02	5.66E-01	5.66E-01	3.95E-03
0.190	-0.5	1.42E 01	1.42E 01	9.94E-02	5.92E-01	5.92E-01	4.13E-03
0.254	-0.6	1.49E 01	1.49E 01	1.30E-01	6.18E-01	6.18E-01	5.40E-03
0.508	-0.5	1.62E 01	1.62E 01	1.13E-01	6.72E-01	6.72E-01	4.69E-03
0.762	-0.3	1.70E 01	1.70E 01	5.93E-02	7.06E-01	7.06E-01	2.46E-03
1.016	-0.5	1.76E 01	1.76E 01	1.23E-01	7.32E-01	7.31E-01	5.11E-03
1.270	-0.5	1.81E 01	1.81E 01	1.26E-01	7.52E-01	7.52E-01	5.25E-03
1.905	-0.4	1.92E 01	1.92E 01	1.01E-01	7.98E-01	7.98E-01	4.18E-03
2.540	-0.3	2.01E 01	2.01E 01	7.03E-02	8.37E-01	8.37E-01	2.92E-03
3.810	-0.2	2.17E 01	2.17E 01	3.78E-02	9.01E-01	9.01E-01	1.57E-03
5.080	-0.2	2.29E 01	2.29E 01	4.00E-02	9.53E-01	9.53E-01	1.66E-03
6.350	-0.2	2.38E 01	2.38E 01	4.15E-02	9.87E-01	9.87E-01	1.72E-03
7.620	0.0	2.41E 01	2.41E 01	-4.21E-02	1.00E 00	1.00E 00	-1.75E-03
10.160	0.1	2.41E 01	2.41E 01	-8.41E-02	1.00E 00	1.00E 00	-3.50E-03
12.700	0.0	2.41E 01	2.41E 01	-4.20E-02	1.00E 00	1.00E 00	-1.75E-03

TABLE F5. STANDARD TEST CASE MEAN VELOCITY PROFILES AT STATION (-24,-8)

REU (1/M) = 1.34E 06
KINEMATIC VISC. (SQ-M/S) = 1.67E-05
DENSITY (KG/CUBIC METER) = 1.10E 00
OMEGA (DEG) = 0.2
UFS (M/S) = 2.41E 01
U1FS (M/S) = 2.41E 01

Y (CM)	BETA (DEG)	U (M/S)	U1 (M/S)	U3 (M/S)	U/UFS	U1/U1FS	U3/U1FS
0.051	-0.4	1.25E 01	1.25E 01	4.36E-02	5.18E-01	5.18E-01	1.81E-03
0.076	-0.3	1.32E 01	1.32E 01	2.30E-02	5.47E-01	5.47E-01	9.54E-04
0.102	-0.3	1.36E 01	1.36E 01	2.38E-02	5.65E-01	5.65E-01	9.85E-04
0.127	-0.4	1.41E 01	1.41E 01	4.91E-02	5.82E-01	5.82E-01	2.03E-03
0.190	-0.4	1.47E 01	1.47E 01	5.13E-02	6.09E-01	6.09E-01	2.13E-03
0.254	-0.3	1.51E 01	1.51E 01	2.64E-02	6.27E-01	6.27E-01	1.09E-03
0.508	-0.4	1.65E 01	1.65E 01	5.75E-02	6.83E-01	6.83E-01	2.38E-03
0.762	-0.3	1.73E 01	1.73E 01	3.01E-02	7.16E-01	7.16E-01	1.25E-03
1.016	-0.4	1.79E 01	1.79E 01	6.25E-02	7.42E-01	7.42E-01	2.59E-03
1.270	-0.4	1.84E 01	1.84E 01	6.43E-02	7.64E-01	7.64E-01	2.67E-03
1.905	-0.4	1.95E 01	1.95E 01	6.82E-02	8.10E-01	8.10E-01	2.83E-03
2.540	-0.3	2.04E 01	2.04E 01	3.55E-02	8.44E-01	8.44E-01	1.47E-03
3.810	-0.4	2.19E 01	2.19E 01	7.63E-02	9.06E-01	9.06E-01	3.16E-03
5.080	-0.4	2.32E 01	2.32E 01	8.10E-02	9.62E-01	9.62E-01	3.36E-03
6.350	-0.2	2.40E 01	2.40E 01	-0.00E-01	9.94E-01	9.94E-01	0.00E-01
7.620	0.0	2.41E 01	2.41E 01	-8.41E-02	9.99E-01	9.99E-01	-3.49E-03
10.160	0.0	2.41E 01	2.41E 01	-8.41E-02	9.99E-01	9.99E-01	-3.49E-03
12.700	0.0	2.41E 01	2.41E 01	-8.42E-02	1.00E 00	1.00E 00	-3.49E-03

TABLE F6. STANDARD TEST CASE MEAN VELOCITY PROFILES AT STATION (-7,0)

REU (1/M) = 1.34E 06
KINEMATIC VISC. (SQ-M/S) = 1.67E-05
DENSITY (KG/CUBIC METER) = 1.10E 00
CF = 1.94E-03
OMEGA (DEG) = 0.4
UFS (M/S) = 2.25E 01
U1FS (M/S) = 2.25E 01

Y (CM)	BETA (DEG)	U (M/S)	U1 (M/S)	U3 (M/S)	U/UFS	U1/U1FS	U3/U1FS
0.051	0.0	9.75E 00	9.75E 00	-6.81E-02	4.34E-01	4.34E-01	-3.03E-03
0.076	-0.2	1.05E 01	1.05E 01	-3.66E-02	4.67E-01	4.67E-01	-1.63E-03
0.102	0.3	1.07E 01	1.07E 01	-1.31E-01	4.78E-01	4.78E-01	-5.84E-03
0.127	0.2	1.11E 01	1.11E 01	-1.16E-01	4.94E-01	4.94E-01	-5.18E-03
0.190	0.0	1.17E 01	1.17E 01	-8.14E-02	5.19E-01	5.19E-01	-3.62E-03
0.254	0.2	1.21E 01	1.21E 01	-1.27E-01	5.38E-01	5.38E-01	-5.64E-03
0.508	0.2	1.33E 01	1.33E 01	-1.39E-01	5.90E-01	5.90E-01	-6.18E-03
0.762	0.2	1.42E 01	1.42E 01	-1.49E-01	6.31E-01	6.31E-01	-6.61E-03
1.016	0.3	1.46E 01	1.46E 01	-1.79E-01	6.51E-01	6.51E-01	-7.95E-03
1.270	0.1	1.51E 01	1.51E 01	-1.32E-01	6.72E-01	6.72E-01	-5.87E-03
1.905	0.4	1.63E 01	1.63E 01	-2.27E-01	7.25E-01	7.25E-01	-1.01E-02
2.540	0.3	1.71E 01	1.71E 01	-2.09E-01	7.63E-01	7.63E-01	-9.32E-03
3.810	0.2	1.88E 01	1.88E 01	-1.97E-01	8.36E-01	8.36E-01	-8.75E-03
5.080	0.3	2.01E 01	2.01E 01	-2.46E-01	8.96E-01	8.96E-01	-1.09E-02
6.350	0.2	2.12E 01	2.12E 01	-2.22E-01	9.45E-01	9.45E-01	-9.90E-03
7.620	-0.1	2.20E 01	2.20E 01	-1.15E-01	9.81E-01	9.81E-01	-5.14E-03
10.160	0.1	2.24E 01	2.24E 01	-1.96E-01	9.99E-01	9.99E-01	-8.71E-03
12.700	0.0	2.25E 01	2.25E 01	-1.57E-01	1.00E 00	1.00E 00	-6.98E-03

TABLE F7. STANDARD TEST CASE MEAN VELOCITY PROFILES AT STATION (-5,0)

REU (1/M) = 1.34E 06
KINEMATIC VISC. (SQ-M/S) = 1.66E-05
DENSITY (KG/CUBIC METER) = 1.11E 00
CF = 1.54E-03
OMEGA (DEG) = 0.1
UFS (M/S) = 2.17E 01
U1FS (M/S) = 2.17E 01

Y (CM)	BETA (DEG)	U (M/S)	U1 (M/S)	U3 (M/S)	U/UFS	U1/U1FS	U3/U1FS
0.051	0.4	7.83E 00	7.83E 00	-6.83E-02	3.61E-01	3.61E-01	-3.15E-03
0.076	0.6	8.63E 00	8.63E 00	-1.05E-01	3.98E-01	3.98E-01	-4.86E-03
0.102	0.2	9.00E 00	9.00E 00	-4.71E-02	4.15E-01	4.15E-01	-2.17E-03
0.127	0.3	9.34E 00	9.34E 00	-6.52E-02	4.31E-01	4.31E-01	-3.01E-03
0.190	0.3	9.77E 00	9.77E 00	-6.82E-02	4.50E-01	4.50E-01	-3.14E-03
0.254	0.4	1.03E 01	1.03E 01	-8.96E-02	4.73E-01	4.73E-01	-4.13E-03
0.508	0.4	1.15E 01	1.15E 01	-1.00E-01	5.30E-01	5.30E-01	-4.62E-03
0.762	0.2	1.25E 01	1.25E 01	-6.55E-02	5.77E-01	5.77E-01	-3.02E-03
1.016	0.3	1.37E 01	1.37E 01	-9.53E-02	6.29E-01	6.29E-01	-4.39E-03
1.270	0.4	1.43E 01	1.43E 01	-1.25E-01	6.59E-01	6.59E-01	-5.75E-03
1.905	0.3	1.56E 01	1.56E 01	-1.09E-01	7.19E-01	7.19E-01	-5.02E-03
2.540	0.1	1.66E 01	1.66E 01	-5.79E-02	7.64E-01	7.64E-01	-2.67E-03
3.810	0.2	1.82E 01	1.82E 01	-9.55E-02	8.41E-01	8.41E-01	-4.40E-03
5.080	0.2	1.96E 01	1.96E 01	-1.03E-01	9.03E-01	9.03E-01	-4.73E-03
6.350	0.2	2.07E 01	2.07E 01	-1.08E-01	9.55E-01	9.55E-01	-5.00E-03
7.620	0.1	2.14E 01	2.14E 01	-7.48E-02	9.87E-01	9.87E-01	-3.45E-03
10.160	0.1	2.17E 01	2.17E 01	-7.56E-02	9.99E-01	9.99E-01	-3.49E-03
12.700	0.0	2.17E 01	2.17E 01	-3.79E-02	1.00E 00	1.00E 00	-1.75E-03

TABLE F8. STANDARD TEST CASE MEAN VELOCITY PROFILES AT STATION (-3,0)

REU (1/M) = 1.34E 06
KINEMATIC VISC. (SQ-M/S) = 1.68E-05
DENSITY (KG/CUBIC METER) = 1.10E 00
CF = 7.05E-04
OMEGA (DEG) = 0.0
UFS (M/S) = 1.94E 01
U1FS (M/S) = 1.94E 01

Y (CM)	BETA (DEG)	U (M/S)	U1 (M/S)	U3 (M/S)	U/UFS	U1/U1FS	U3/U1FS
0.051	1.3	4.03E 00	4.03E 00	-9.14E-02	2.08E-01	2.07E-01	-4.71E-03
0.076	0.7	4.67E 00	4.67E 00	-5.71E-02	2.40E-01	2.40E-01	-2.94E-03
0.102	0.5	5.10E 00	5.10E 00	-4.45E-02	2.62E-01	2.62E-01	-2.29E-03
0.127	0.5	5.31E 00	5.31E 00	-4.63E-02	2.73E-01	2.73E-01	-2.39E-03
0.190	0.9	5.92E 00	5.92E 00	-9.30E-02	3.05E-01	3.05E-01	-4.79E-03
0.254	1.2	6.47E 00	6.47E 00	-1.35E-01	3.33E-01	3.33E-01	-6.97E-03
0.508	1.0	8.27E 00	8.27E 00	-1.44E-01	4.26E-01	4.26E-01	-7.43E-03
0.762	0.9	9.58E 00	9.58E 00	-1.50E-01	4.93E-01	4.93E-01	-7.75E-03
1.016	0.7	1.08E 01	1.08E 01	-1.32E-01	5.56E-01	5.56E-01	-6.79E-03
1.270	0.4	1.17E 01	1.17E 01	-8.20E-02	6.05E-01	6.05E-01	-4.22E-03
1.905	0.7	1.34E 01	1.34E 01	-1.64E-01	6.89E-01	6.89E-01	-8.42E-03
2.540	0.4	1.46E 01	1.46E 01	-1.02E-01	7.52E-01	7.52E-01	-5.25E-03
3.810	0.4	1.63E 01	1.63E 01	-1.14E-01	8.38E-01	8.38E-01	-5.85E-03
5.080	0.4	1.76E 01	1.76E 01	-1.23E-01	9.06E-01	9.06E-01	-6.32E-03
6.350	0.3	1.87E 01	1.87E 01	-9.79E-02	9.62E-01	9.62E-01	-5.04E-03
7.620	0.1	1.94E 01	1.94E 01	-3.38E-02	9.97E-01	9.97E-01	-1.74E-03
10.160	0.2	1.95E 01	1.95E 01	-6.81E-02	1.00E 00	1.00E 00	-3.51E-03
12.700	0.0	1.94E 01	1.94E 01	-0.00E-01	1.00E 00	1.00E 00	0.00E-01

TABLE F9. STANDARD TEST CASE MEAN VELOCITY PROFILES AT STATION (-3,-2)

REU (1/M) = 1.34E 06
KINEMATIC VISC. (SQ-M/S) = 1.68E-05
DENSITY (KG/CUBIC METER) = 1.10E 00
CF = 1.57E-03
OMEGA (DEG) = 5.8
UFS (M/S) = 2.10E 01
U1FS (M/S) = 2.09E 01

Y (CM)	BETA (DEG)	U (M/S)	U1 (M/S)	U3 (M/S)	U/UFS	U1/U1FS	U3/U1FS
0.051	24.2	7.89E 00	6.83E 00	-3.94E 00	3.75E-01	3.26E-01	-1.88E-01
0.076	22.6	8.47E 00	7.45E 00	-4.03E 00	4.02E-01	3.56E-01	-1.92E-01
0.102	21.2	8.77E 00	7.82E 00	-3.98E 00	4.17E-01	3.73E-01	-1.90E-01
0.127	19.9	9.08E 00	8.18E 00	-3.94E 00	4.32E-01	3.91E-01	-1.88E-01
0.190	17.7	9.60E 00	8.80E 00	-3.83E 00	4.56E-01	4.20E-01	-1.83E-01
0.254	15.7	1.00E 01	9.33E 00	-3.67E 00	4.76E-01	4.46E-01	-1.76E-01
0.508	12.0	1.13E 01	1.08E 01	-3.47E 00	5.39E-01	5.16E-01	-1.66E-01
0.762	9.5	1.23E 01	1.19E 01	-3.25E 00	5.85E-01	5.67E-01	-1.55E-01
1.016	7.8	1.31E 01	1.27E 01	-3.07E 00	6.21E-01	6.07E-01	-1.47E-01
1.270	6.5	1.37E 01	1.34E 01	-2.93E 00	6.53E-01	6.42E-01	-1.40E-01
1.905	4.4	1.51E 01	1.49E 01	-2.67E 00	7.17E-01	7.09E-01	-1.28E-01
2.540	3.1	1.61E 01	1.59E 01	-2.49E 00	7.64E-01	7.58E-01	-1.19E-01
3.810	1.6	1.79E 01	1.78E 01	-2.31E 00	8.52E-01	8.49E-01	-1.10E-01
5.080	0.8	1.94E 01	1.92E 01	-2.23E 00	9.20E-01	9.19E-01	-1.06E-01
6.350	0.3	2.02E 01	2.01E 01	-2.15E 00	9.62E-01	9.62E-01	-1.03E-01
7.620	0.0	2.09E 01	2.08E 01	-2.11E 00	9.93E-01	9.93E-01	-1.01E-01
10.160	0.0	2.10E 01	2.09E 01	-2.13E 00	1.00E 00	1.00E 00	-1.02E-01
12.700	0.0	2.10E 01	2.09E 01	-2.13E 00	1.00E 00	1.00E 00	-1.02E-01

TABLE F10. STANDARD TEST CASE MEAN VELOCITY PROFILES AT STATION (-7,-4)

REU (1/M) = 1.34E 06
KINEMATIC VISC. (SQ-M/S) = 1.68E-05
DENSITY (KG/CUBIC METER) = 1.10E 00
CF = 2.19E-03
OMEGA (DEG) = 2.1
UFS (M/S) = 2.31E 01
U1FS (M/S) = 2.31E 01

Y (CM)	BETA (DEG)	U (M/S)	U1 (M/S)	U3 (M/S)	U/UFS	U1/U1FS	U3/U1FS
0.051	5.5	1.10E 01	1.09E 01	-1.46E 00	4.78E-01	4.74E-01	-6.33E-02
0.076	4.8	1.17E 01	1.17E 01	-1.41E 00	5.09E-01	5.05E-01	-6.12E-02
0.102	4.7	1.22E 01	1.21E 01	-1.44E 00	5.29E-01	5.25E-01	-6.26E-02
0.127	4.5	1.25E 01	1.24E 01	-1.43E 00	5.41E-01	5.38E-01	-6.22E-02
0.190	4.0	1.30E 01	1.29E 01	-1.38E 00	5.63E-01	5.61E-01	-5.99E-02
0.254	3.8	1.35E 01	1.34E 01	-1.39E 00	5.85E-01	5.82E-01	-6.01E-02
0.508	2.9	1.46E 01	1.46E 01	-1.27E 00	6.34E-01	6.32E-01	-5.53E-02
0.762	2.5	1.54E 01	1.53E 01	-1.23E 00	6.67E-01	6.65E-01	-5.35E-02
1.016	2.0	1.59E 01	1.59E 01	-1.14E 00	6.91E-01	6.90E-01	-4.95E-02
1.270	1.9	1.65E 01	1.64E 01	-1.15E 00	7.14E-01	7.13E-01	-4.98E-02
1.905	1.5	1.76E 01	1.75E 01	-1.10E 00	7.62E-01	7.61E-01	-4.79E-02
2.540	1.1	1.85E 01	1.85E 01	-1.03E 00	8.03E-01	8.02E-01	-4.49E-02
3.810	0.6	2.01E 01	2.01E 01	-9.46E-01	8.71E-01	8.70E-01	-4.11E-02
5.080	0.3	2.13E 01	2.13E 01	-8.92E-01	9.23E-01	9.23E-01	-3.87E-02
6.350	0.1	2.23E 01	2.23E 01	-8.55E-01	9.65E-01	9.65E-01	-3.71E-02
7.620	0.0	2.28E 01	2.28E 01	-8.35E-01	9.88E-01	9.88E-01	-3.62E-02
10.160	0.1	2.30E 01	2.30E 01	-8.83E-01	9.97E-01	9.97E-01	-3.83E-02
12.700	0.0	2.31E 01	2.31E 01	-8.45E-01	1.00E 00	1.00E 00	-3.67E-02

TABLE F11. STANDARD TEST CASE MEAN VELOCITY PROFILES AT STATION (-3,-4)

REU (1/M) = 1.34E 06
KINEMATIC VISC. (SQ-M/S) = 1.68E-05
DENSITY (KG/CUBIC METER) = 1.10E 00
CF = 2.37E-03
OMEGA (DEG) = 6.0
UFS (M/S) = 2.30E 01
U1FS (M/S) = 2.28E 01

Y (CM)	BETA (DEG)	U (M/S)	U1 (M/S)	U3 (M/S)	U/UFS	U1/U1FS	U3/U1FS
0.051	16.6	1.10E 01	1.02E 01	-4.24E 00	4.81E-01	4.47E-01	-1.86E-01
0.076	16.2	1.17E 01	1.09E 01	-4.44E 00	5.12E-01	4.76E-01	-1.94E-01
0.102	15.2	1.22E 01	1.14E 01	-4.41E 00	5.32E-01	4.98E-01	-1.93E-01
0.127	14.5	1.25E 01	1.17E 01	-4.38E 00	5.45E-01	5.13E-01	-1.92E-01
0.190	13.5	1.29E 01	1.22E 01	-4.31E 00	5.62E-01	5.33E-01	-1.89E-01
0.254	12.5	1.35E 01	1.28E 01	-4.28E 00	5.88E-01	5.60E-01	-1.88E-01
0.508	9.7	1.44E 01	1.39E 01	-3.91E 00	6.29E-01	6.09E-01	-1.71E-01
0.762	8.2	1.51E 01	1.46E 01	-3.70E 00	6.57E-01	6.41E-01	-1.62E-01
1.016	6.8	1.56E 01	1.52E 01	-3.46E 00	6.80E-01	6.67E-01	-1.51E-01
1.270	6.0	1.62E 01	1.58E 01	-3.37E 00	7.05E-01	6.94E-01	-1.47E-01
1.905	4.4	1.74E 01	1.72E 01	-3.15E 00	7.60E-01	7.51E-01	-1.38E-01
2.540	3.2	1.84E 01	1.81E 01	-2.94E 00	8.00E-01	7.94E-01	-1.29E-01
3.810	1.8	2.00E 01	1.98E 01	-2.71E 00	8.71E-01	8.67E-01	-1.19E-01
5.080	0.7	2.11E 01	2.09E 01	-2.46E 00	9.17E-01	9.16E-01	-1.08E-01
6.350	0.2	2.23E 01	2.21E 01	-2.40E 00	9.69E-01	9.69E-01	-1.05E-01
7.620	0.1	2.29E 01	2.27E 01	-2.43E 00	9.96E-01	9.96E-01	-1.06E-01
10.160	0.0	2.30E 01	2.28E 01	-2.40E 00	1.00E 00	1.00E 00	-1.05E-01
12.700	0.0	2.30E 01	2.28E 01	-2.40E 00	1.00E 00	1.00E 00	-1.05E-01

TABLE F12. STANDARD TEST CASE MEAN VELOCITY PROFILES AT STATION (-7,-6)

REU (1/M) = 1.34E 06
KINEMATIC VISC. (SQ-M/S) = 1.68E-05
DENSITY (KG/CUBIC METER) = 1.10E 00
CF = 2.36E-03
OMEGA (DEG) = 2.0
UFS (M/S) = 2.38E 01
U1FS (M/S) = 2.38E 01

Y (CM)	BETA (DEG)	U (M/S)	U1 (M/S)	U3 (M/S)	U/UFS	U1/U1FS	U3/U1FS
0.051	4.5	1.21E 01	1.20E 01	-1.37E 00	5.09E-01	5.06E-01	-5.76E-02
0.076	4.4	1.27E 01	1.27E 01	-1.42E 00	5.36E-01	5.33E-01	-5.98E-02
0.102	4.0	1.31E 01	1.31E 01	-1.37E 00	5.53E-01	5.50E-01	-5.78E-02
0.127	3.9	1.34E 01	1.34E 01	-1.38E 00	5.66E-01	5.63E-01	-5.82E-02
0.190	3.7	1.40E 01	1.39E 01	-1.39E 00	5.89E-01	5.86E-01	-5.85E-02
0.254	3.4	1.45E 01	1.44E 01	-1.36E 00	6.10E-01	6.07E-01	-5.74E-02
0.508	2.6	1.56E 01	1.56E 01	-1.25E 00	6.57E-01	6.56E-01	-5.28E-02
0.762	2.1	1.64E 01	1.64E 01	-1.17E 00	6.91E-01	6.90E-01	-4.94E-02
1.016	1.7	1.70E 01	1.70E 01	-1.10E 00	7.16E-01	7.15E-01	-4.62E-02
1.270	1.5	1.75E 01	1.75E 01	-1.07E 00	7.38E-01	7.37E-01	-4.51E-02
1.905	1.2	1.85E 01	1.85E 01	-1.03E 00	7.79E-01	7.78E-01	-4.35E-02
2.540	0.8	1.95E 01	1.95E 01	-9.54E-01	8.22E-01	8.21E-01	-4.02E-02
3.810	0.4	2.10E 01	2.10E 01	-8.81E-01	8.85E-01	8.85E-01	-3.71E-02
5.080	0.2	2.22E 01	2.22E 01	-8.54E-01	9.35E-01	9.35E-01	-3.59E-02
6.350	0.0	2.32E 01	2.32E 01	-8.11E-01	9.78E-01	9.78E-01	-3.42E-02
7.620	-0.1	2.36E 01	2.36E 01	-7.82E-01	9.92E-01	9.92E-01	-3.29E-02
10.160	-0.1	2.37E 01	2.37E 01	-7.87E-01	9.99E-01	9.99E-01	-3.31E-02
12.700	0.0	2.38E 01	2.38E 01	-8.30E-01	1.00E 00	1.00E 00	-3.49E-02

TABLE F13. STANDARD TEST CASE MEAN VELOCITY PROFILES AT STATION (-3,-6)

REU (1/M) = 1.34E 06
KINEMATIC VISC. (SQ-M/S) = 1.67E-05
DENSITY (KG/CUBIC METER) = 1.10E 00
CF = 2.58E-03
OMEGA (DEG) = 4.3
UFS (M/S) = 2.39E 01
U1FS (M/S) = 2.38E 01

Y (CM)	BETA (DEG)	U (M/S)	U1 (M/S)	U3 (M/S)	U/UFS	U1/U1FS	U3/U1FS
0.051	9.8	1.26E 01	1.22E 01	-3.06E 00	5.26E-01	5.11E-01	-1.28E-01
0.076	9.5	1.32E 01	1.29E 01	-3.16E 00	5.54E-01	5.39E-01	-1.32E-01
0.102	9.1	1.37E 01	1.33E 01	-3.17E 00	5.73E-01	5.59E-01	-1.33E-01
0.127	8.9	1.40E 01	1.36E 01	-3.19E 00	5.84E-01	5.71E-01	-1.34E-01
0.190	8.2	1.45E 01	1.41E 01	-3.14E 00	6.06E-01	5.93E-01	-1.32E-01
0.254	7.9	1.49E 01	1.46E 01	-3.15E 00	6.24E-01	6.11E-01	-1.32E-01
0.508	6.3	1.60E 01	1.57E 01	-2.94E 00	6.68E-01	6.59E-01	-1.23E-01
0.762	5.3	1.68E 01	1.65E 01	-2.80E 00	7.02E-01	6.94E-01	-1.17E-01
1.016	4.5	1.74E 01	1.71E 01	-2.65E 00	7.26E-01	7.19E-01	-1.11E-01
1.270	3.8	1.79E 01	1.77E 01	-2.52E 00	7.48E-01	7.42E-01	-1.06E-01
1.905	2.9	1.88E 01	1.87E 01	-2.36E 00	7.87E-01	7.83E-01	-9.89E-02
2.540	2.1	1.98E 01	1.96E 01	-2.20E 00	8.27E-01	8.24E-01	-9.24E-02
3.810	1.1	2.12E 01	2.11E 01	-1.99E 00	8.87E-01	8.85E-01	-8.37E-02
5.080	0.5	2.24E 01	2.23E 01	-1.88E 00	9.38E-01	9.37E-01	-7.87E-02
6.350	0.1	2.34E 01	2.33E 01	-1.79E 00	9.77E-01	9.77E-01	-7.52E-02
7.620	0.0	2.38E 01	2.37E 01	-1.78E 00	9.95E-01	9.95E-01	-7.48E-02
10.160	0.0	2.39E 01	2.38E 01	-1.79E 00	1.00E 00	1.00E 00	-7.52E-02
12.700	0.0	2.39E 01	2.38E 01	-1.79E 00	1.00E 00	1.00E 00	-7.52E-02

TABLE F14. STANDARD TEST CASE MEAN VELOCITY PROFILES AT STATION (1,-6)

REU (1/M) = 1.34E 06
KINEMATIC VISC. (SQ-M/S) = 1.67E-05
DENSITY (KG/CUBIC METER) = 1.10E 00
CF = 3.19E-03
OMEGA (DEG) = 4.5
UFS (M/S) = 2.67E 01
U1FS (M/S) = 2.66E 01

Y (CM)	BETA (DEG)	U (M/S)	U1 (M/S)	U3 (M/S)	U/UFS	U1/U1FS	U3/U1FS
0.051	7.6	1.58E 01	1.54E 01	-3.30E 00	5.90E-01	5.79E-01	-1.24E-01
0.076	8.4	1.67E 01	1.63E 01	-3.72E 00	6.24E-01	6.10E-01	-1.40E-01
0.102	8.7	1.72E 01	1.67E 01	-3.93E 00	6.44E-01	6.29E-01	-1.47E-01
0.127	8.8	1.75E 01	1.71E 01	-4.03E 00	6.56E-01	6.41E-01	-1.51E-01
0.190	8.8	1.81E 01	1.76E 01	-4.16E 00	6.77E-01	6.61E-01	-1.56E-01
0.254	8.5	1.84E 01	1.80E 01	-4.15E 00	6.90E-01	6.75E-01	-1.56E-01
0.508	7.2	1.93E 01	1.89E 01	-3.91E 00	7.22E-01	7.10E-01	-1.47E-01
0.762	5.8	1.99E 01	1.95E 01	-3.55E 00	7.43E-01	7.33E-01	-1.33E-01
1.016	4.8	2.02E 01	2.00E 01	-3.27E 00	7.58E-01	7.50E-01	-1.23E-01
1.270	4.0	2.07E 01	2.05E 01	-3.06E 00	7.75E-01	7.69E-01	-1.15E-01
1.905	2.8	2.16E 01	2.14E 01	-2.75E 00	8.09E-01	8.05E-01	-1.03E-01
2.540	1.7	2.24E 01	2.23E 01	-2.42E 00	8.39E-01	8.37E-01	-9.09E-02
3.810	0.6	2.40E 01	2.39E 01	-2.13E 00	8.97E-01	8.96E-01	-8.00E-02
5.080	-0.1	2.53E 01	2.52E 01	-1.94E 00	9.46E-01	9.46E-01	-7.28E-02
6.350	-0.3	2.63E 01	2.62E 01	-1.92E 00	9.83E-01	9.83E-01	-7.22E-02
7.620	-0.4	2.67E 01	2.67E 01	-1.91E 00	1.00E 00	1.00E 00	-7.18E-02
10.160	-0.1	2.68E 01	2.68E 01	-2.06E 00	1.00E 00	1.00E 00	-7.73E-02
12.700	0.0	2.67E 01	2.66E 01	-2.10E 00	1.00E 00	1.00E 00	-7.87E-02

TABLE F15. STANDARD TEST CASE MEAN VELOCITY PROFILES AT STATION (3,-6)

REU (1/M) = 1.34E 06
KINEMATIC VISC. (SQ-M/S) = 1.68E-05
DENSITY (KG/CUBIC METER) = 1.10E 00
CF = 3.13E-03
OMEGA (DEG) = 1.0
UFS (M/S) = 2.75E 01
U1FS (M/S) = 2.75E 01

Y (CM)	BETA (DEG)	U (M/S)	U1 (M/S)	U3 (M/S)	U/UFS	U1/U1FS	U3/U1FS
0.051	3.0	1.65E 01	1.65E 01	-1.15E 00	6.00E-01	5.99E-01	-4.19E-02
0.076	4.0	1.73E 01	1.72E 01	-1.50E 00	6.28E-01	6.26E-01	-5.47E-02
0.102	4.6	1.78E 01	1.77E 01	-1.73E 00	6.47E-01	6.44E-01	-6.31E-02
0.127	5.2	1.82E 01	1.81E 01	-1.97E 00	6.62E-01	6.59E-01	-7.16E-02
0.190	6.0	1.88E 01	1.86E 01	-2.29E 00	6.82E-01	6.77E-01	-8.32E-02
0.254	6.4	1.92E 01	1.91E 01	-2.48E 00	7.00E-01	6.94E-01	-9.02E-02
0.508	6.1	2.02E 01	2.00E 01	-2.49E 00	7.35E-01	7.29E-01	-9.08E-02
0.762	4.8	2.07E 01	2.06E 01	-2.10E 00	7.55E-01	7.51E-01	-7.63E-02
1.016	3.7	2.12E 01	2.11E 01	-1.73E 00	7.70E-01	7.68E-01	-6.31E-02
1.270	2.7	2.15E 01	2.14E 01	-1.39E 00	7.81E-01	7.80E-01	-5.04E-02
1.905	1.4	2.24E 01	2.24E 01	-9.40E-01	8.17E-01	8.16E-01	-3.42E-02
2.540	0.8	2.34E 01	2.33E 01	-7.34E-01	8.50E-01	8.50E-01	-2.67E-02
3.810	-0.1	2.49E 01	2.49E 01	-3.91E-01	9.07E-01	9.07E-01	-1.42E-02
5.080	-0.5	2.64E 01	2.64E 01	-2.30E-01	9.60E-01	9.60E-01	-8.38E-03
6.350	-0.6	2.70E 01	2.70E 01	-1.89E-01	9.84E-01	9.85E-01	-6.87E-03
7.620	-0.6	2.74E 01	2.74E 01	-1.91E-01	9.98E-01	9.98E-01	-6.97E-03
10.160	-0.3	2.76E 01	2.76E 01	-3.37E-01	1.00E 00	1.00E 00	-1.23E-02
12.700	0.0	2.75E 01	2.75E 01	-4.80E-01	1.00E 00	1.00E 00	-1.75E-02

TABLE F16. STANDARD TEST CASE MEAN VELOCITY PROFILES AT STATION (5,-6)

REU (1/M) = 1.34E 06
KINEMATIC VISC. (SQ-M/S) = 1.67E-05
DENSITY (KG/CUBIC METER) = 1.10E 00
CF = 2.58E-03
OMEGA (DEG) = -2.6
UFS (M/S) = 2.65E 01
U1FS (M/S) = 2.65E 01

Y (CM)	BETA (DEG)	U (M/S)	U1 (M/S)	U3 (M/S)	U/UFS	U1/U1FS	U3/U1FS
0.051	-1.1	1.43E 01	1.42E 01	9.20E-01	5.38E-01	5.37E-01	3.48E-02
0.076	-0.4	1.51E 01	1.50E 01	7.88E-01	5.68E-01	5.68E-01	2.98E-02
0.102	0.3	1.56E 01	1.56E 01	6.27E-01	5.89E-01	5.89E-01	2.37E-02
0.127	0.9	1.60E 01	1.60E 01	4.76E-01	6.05E-01	6.06E-01	1.80E-02
0.190	2.1	1.69E 01	1.69E 01	1.47E-01	6.36E-01	6.37E-01	5.56E-03
0.254	2.9	1.75E 01	1.75E 01	-9.14E-02	6.58E-01	6.59E-01	-3.45E-03
0.508	4.1	1.87E 01	1.87E 01	-4.91E-01	7.07E-01	7.08E-01	-1.85E-02
0.762	3.8	1.93E 01	1.93E 01	-4.03E-01	7.27E-01	7.27E-01	-1.52E-02
1.016	2.7	1.96E 01	1.96E 01	-3.43E-02	7.41E-01	7.41E-01	-1.29E-03
1.270	2.0	2.00E 01	2.00E 01	2.09E-01	7.55E-01	7.55E-01	7.91E-03
1.905	0.7	2.09E 01	2.09E 01	6.93E-01	7.88E-01	7.88E-01	2.62E-02
2.540	0.1	2.18E 01	2.18E 01	9.50E-01	8.22E-01	8.22E-01	3.59E-02
3.810	-0.4	2.34E 01	2.34E 01	1.23E 00	8.83E-01	8.83E-01	4.63E-02
5.080	-0.6	2.48E 01	2.47E 01	1.38E 00	9.35E-01	9.35E-01	5.23E-02
6.350	-0.6	2.58E 01	2.58E 01	1.44E 00	9.75E-01	9.74E-01	5.45E-02
7.620	-0.4	2.64E 01	2.63E 01	1.38E 00	9.95E-01	9.95E-01	5.21E-02
10.160	-0.2	2.65E 01	2.65E 01	1.30E 00	1.00E 00	1.00E 00	4.90E-02
12.700	0.0	2.65E 01	2.65E 01	1.20E 00	1.00E 00	1.00E 00	4.54E-02

TABLE F17. STANDARD TEST CASE MEAN VELOCITY PROFILES AT STATION (-7,-8)

REU (1/M) = 1.34E 06
KINEMATIC VISC. (SQ-M/S) = 1.68E-05
DENSITY (KG/CUBIC METER) = 1.10E 00
CF = 2.42E-03
OMEGA (DEG) = 2.0
UFS (M/S) = 2.39E 01
U1FS (M/S) = 2.39E 01

Y (CM)	BETA (DEG)	U (M/S)	U1 (M/S)	U3 (M/S)	U/UFS	U1/U1FS	U3/U1FS
0.051	4.1	1.26E 01	1.25E 01	-1.34E 00	5.26E-01	5.23E-01	-5.59E-02
0.076	4.0	1.33E 01	1.33E 01	-1.39E 00	5.58E-01	5.55E-01	-5.83E-02
0.102	3.7	1.38E 01	1.38E 01	-1.37E 00	5.78E-01	5.76E-01	-5.75E-02
0.127	3.6	1.40E 01	1.39E 01	-1.37E 00	5.86E-01	5.84E-01	-5.72E-02
0.190	3.2	1.48E 01	1.47E 01	-1.34E 00	6.18E-01	6.16E-01	-5.61E-02
0.254	3.0	1.51E 01	1.50E 01	-1.31E 00	6.31E-01	6.29E-01	-5.50E-02
0.508	2.5	1.63E 01	1.63E 01	-1.28E 00	6.83E-01	6.81E-01	-5.36E-02
0.762	2.0	1.69E 01	1.69E 01	-1.18E 00	7.08E-01	7.07E-01	-4.94E-02
1.016	1.8	1.75E 01	1.75E 01	-1.16E 00	7.34E-01	7.33E-01	-4.87E-02
1.270	1.5	1.80E 01	1.80E 01	-1.10E 00	7.55E-01	7.54E-01	-4.61E-02
1.905	1.1	1.91E 01	1.90E 01	-1.03E 00	7.98E-01	7.98E-01	-4.32E-02
2.540	0.9	1.98E 01	1.98E 01	-1.00E 00	8.29E-01	8.29E-01	-4.20E-02
3.810	0.3	2.13E 01	2.13E 01	-8.54E-01	8.91E-01	8.91E-01	-3.58E-02
5.080	0.1	2.25E 01	2.24E 01	-8.23E-01	9.40E-01	9.40E-01	-3.45E-02
6.350	-0.1	2.33E 01	2.33E 01	-7.74E-01	9.77E-01	9.77E-01	-3.24E-02
7.620	0.0	2.38E 01	2.38E 01	-8.30E-01	9.95E-01	9.95E-01	-3.47E-02
10.160	0.0	2.39E 01	2.39E 01	-8.34E-01	1.00E 00	1.00E 00	-3.49E-02
12.700	0.0	2.39E 01	2.39E 01	-8.34E-01	1.00E 00	1.00E 00	-3.49E-02

TABLE F18. STANDARD TEST CASE MEAN VELOCITY PROFILES AT STATION (-3,-8)

REU (1/M) = 1.34E 06
KINEMATIC VISC. (SQ-M/S) = 1.67E-05
DENSITY (KG/CUBIC METER) = 1.10E 00
CF = 2.62E-03
OMEGA (DEG) = 3.0
UFS (M/S) = 2.46E 01
U1FS (M/S) = 2.46E 01

Y (CM)	BETA (DEG)	U (M/S)	U1 (M/S)	U3 (M/S)	U/UFS	U1/U1FS	U3/U1FS
0.051	5.9	1.30E 01	1.28E 01	-2.01E 00	5.28E-01	5.22E-01	-8.17E-02
0.076	5.7	1.39E 01	1.37E 01	-2.10E 00	5.64E-01	5.59E-01	-8.55E-02
0.102	5.5	1.44E 01	1.42E 01	-2.12E 00	5.83E-01	5.77E-01	-8.63E-02
0.127	5.4	1.48E 01	1.46E 01	-2.15E 00	5.99E-01	5.93E-01	-8.76E-02
0.190	5.1	1.54E 01	1.53E 01	-2.18E 00	6.27E-01	6.22E-01	-8.85E-02
0.254	4.7	1.58E 01	1.57E 01	-2.12E 00	6.43E-01	6.38E-01	-8.63E-02
0.508	3.9	1.70E 01	1.69E 01	-2.05E 00	6.92E-01	6.88E-01	-8.33E-02
0.762	3.3	1.77E 01	1.76E 01	-1.94E 00	7.19E-01	7.16E-01	-7.90E-02
1.016	3.1	1.83E 01	1.82E 01	-1.94E 00	7.42E-01	7.39E-01	-7.90E-02
1.270	2.6	1.88E 01	1.87E 01	-1.83E 00	7.63E-01	7.61E-01	-7.46E-02
1.905	1.9	1.98E 01	1.97E 01	-1.69E 00	8.02E-01	8.01E-01	-6.86E-02
2.540	1.4	2.06E 01	2.05E 01	-1.58E 00	8.34E-01	8.33E-01	-6.41E-02
3.810	0.6	2.19E 01	2.19E 01	-1.38E 00	8.91E-01	8.90E-01	-5.60E-02
5.080	0.3	2.32E 01	2.32E 01	-1.34E 00	9.42E-01	9.42E-01	-5.43E-02
6.350	0.1	2.41E 01	2.41E 01	-1.30E 00	9.78E-01	9.78E-01	-5.30E-02
7.620	0.0	2.45E 01	2.44E 01	-1.28E 00	9.94E-01	9.94E-01	-5.21E-02
10.160	0.1	2.46E 01	2.46E 01	-1.33E 00	1.00E 00	1.00E 00	-5.42E-02
12.700	0.0	2.46E 01	2.46E 01	-1.29E 00	1.00E 00	1.00E 00	-5.24E-02

TABLE F19. STANDARD TEST CASE MEAN VELOCITY PROFILES AT STATION (1,-8)

REU (1/M) = 1.34E 06
KINEMATIC VISC. (SQ-M/S) = 1.67E-05
DENSITY (KG/CUBIC METER) = 1.10E 00
CF = 2.90E-03
OMEGA (DEG) = 2.4
UFS (M/S) = 2.59E 01
U1FS (M/S) = 2.58E 01

Y (CM)	BETA (DEG)	U (M/S)	U1 (M/S)	U3 (M/S)	U/UFS	U1/U1FS	U3/U1FS
0.051	3.4	1.47E 01	1.46E 01	-1.49E 00	5.69E-01	5.67E-01	-5.76E-02
0.076	3.5	1.56E 01	1.56E 01	-1.61E 00	6.05E-01	6.02E-01	-6.22E-02
0.102	3.7	1.61E 01	1.60E 01	-1.71E 00	6.22E-01	6.19E-01	-6.62E-02
0.127	3.9	1.65E 01	1.64E 01	-1.81E 00	6.37E-01	6.33E-01	-6.99E-02
0.190	3.8	1.71E 01	1.70E 01	-1.85E 00	6.61E-01	6.58E-01	-7.15E-02
0.254	4.0	1.75E 01	1.74E 01	-1.95E 00	6.76E-01	6.72E-01	-7.54E-02
0.508	3.5	1.85E 01	1.84E 01	-1.90E 00	7.16E-01	7.12E-01	-7.36E-02
0.762	3.1	1.92E 01	1.91E 01	-1.84E 00	7.42E-01	7.39E-01	-7.11E-02
1.016	2.6	1.97E 01	1.96E 01	-1.72E 00	7.62E-01	7.59E-01	-6.64E-02
1.270	2.2	2.00E 01	2.00E 01	-1.61E 00	7.75E-01	7.73E-01	-6.22E-02
1.905	1.5	2.10E 01	2.10E 01	-1.43E 00	8.12E-01	8.11E-01	-5.53E-02
2.540	1.0	2.18E 01	2.18E 01	-1.29E 00	8.43E-01	8.42E-01	-5.00E-02
3.810	0.5	2.34E 01	2.34E 01	-1.18E 00	9.04E-01	9.04E-01	-4.58E-02
5.080	0.1	2.45E 01	2.45E 01	-1.07E 00	9.48E-01	9.48E-01	-4.14E-02
6.350	0.0	2.55E 01	2.54E 01	-1.07E 00	9.85E-01	9.85E-01	-4.13E-02
7.620	0.0	2.58E 01	2.58E 01	-1.08E 00	9.99E-01	9.99E-01	-4.19E-02
10.160	0.0	2.58E 01	2.58E 01	-1.08E 00	9.99E-01	9.99E-01	-4.19E-02
12.700	0.0	2.59E 01	2.58E 01	-1.08E 00	1.00E 00	1.00E 00	-4.19E-02

TABLE F20. STANDARD TEST CASE MEAN VELOCITY PROFILES AT STATION (5,-8)

REU (1/M) = 1.34E 06
KINEMATIC VISC. (SQ-M/S) = 1.67E-05
DENSITY (KG/CUBIC METER) = 1.10E 00
CF = 2.72E-03
OMEGA (DEG) = -1.0
UFS (M/S) = 2.60E 01
U1FS (M/S) = 2.60E 01

Y (CM)	BETA (DEG)	U (M/S)	U1 (M/S)	U3 (M/S)	U/UFS	U1/U1FS	U3/U1FS
0.051	-2.0	1.43E 01	1.42E 01	7.46E-01	5.49E-01	5.49E-01	2.88E-02
0.076	-1.7	1.50E 01	1.50E 01	7.05E-01	5.77E-01	5.76E-01	2.72E-02
0.102	-1.3	1.54E 01	1.54E 01	6.18E-01	5.93E-01	5.93E-01	2.38E-02
0.127	-0.9	1.58E 01	1.58E 01	5.23E-01	6.07E-01	6.07E-01	2.01E-02
0.190	-0.5	1.65E 01	1.65E 01	4.32E-01	6.36E-01	6.36E-01	1.66E-02
0.254	0.0	1.71E 01	1.71E 01	2.98E-01	6.57E-01	6.57E-01	1.15E-02
0.508	0.8	1.83E 01	1.83E 01	6.38E-02	7.04E-01	7.04E-01	2.46E-03
0.762	0.9	1.89E 01	1.89E 01	3.30E-02	7.29E-01	7.29E-01	1.27E-03
1.016	0.8	1.94E 01	1.94E 01	6.78E-02	7.48E-01	7.48E-01	2.61E-03
1.270	0.6	1.99E 01	1.99E 01	1.39E-01	7.66E-01	7.66E-01	5.35E-03
1.905	0.3	2.09E 01	2.09E 01	2.55E-01	8.05E-01	8.05E-01	9.83E-03
2.540	0.0	2.17E 01	2.17E 01	3.79E-01	8.36E-01	8.36E-01	1.46E-02
3.810	-0.1	2.33E 01	2.33E 01	4.47E-01	8.97E-01	8.97E-01	1.72E-02
5.080	-0.2	2.45E 01	2.45E 01	5.13E-01	9.44E-01	9.44E-01	1.98E-02
6.350	-0.2	2.54E 01	2.54E 01	5.32E-01	9.79E-01	9.79E-01	2.05E-02
7.620	-0.2	2.59E 01	2.59E 01	5.42E-01	9.98E-01	9.98E-01	2.09E-02
10.160	0.0	2.60E 01	2.60E 01	4.53E-01	1.00E 00	1.00E 00	1.75E-02
12.700	0.0	2.60E 01	2.60E 01	4.53E-01	1.00E 00	1.00E 00	1.75E-02

APPENDIX G

Standard Test Case Mean Velocity and Reynolds

Stress Tensor Results

Mean Velocities Corrected for Turbulence

TABLE G1. STANDARD TEST CASE MEAN VELOCITY AND REYNOLDS STRESS PROFILES AT STATION (-24,8)

REU = 1.34D+06 (1/M)
KINEMATIC VISC. = 1.67D-05 (SQ-M/S)
DENSITY = 1.10D+00 (KG/CUBIC METER)
OMEGA = 0.1 DEG.
UFS= 2.41D+01 M/S
U1FS = 2.41D+01 M/S

NONDIMENSIONALIZED MEAN VELOCITY NONDIMENSIONALIZED REYNOLDS STRESS TENSOR

LABORATORY COORDINATE SYSTEM

Y (CM)	BETA (DEG)	PSIZ* (DEG)	U1/U1FS	U2/U1FS	U3/U1FS	U1U1/U1FS2	U2U2/U1FS2	U3U3/U1FS2	U1U2/U1FS2	U1U3/U1FS2	U2U3/U1FS2
0.127	0.0	1.1	5.78D-01	1.11D-02	-1.01D-03	4.55D-03	9.90D-04	2.22D-03	-5.55D-04	1.38D-04	1.26D-04
0.190	0.1	0.7	6.07D-01	7.41D-03	-2.12D-03	4.67D-03	1.04D-03	2.16D-03	-6.45D-04	1.23D-04	1.01D-04
0.254	0.0	0.6	6.26D-01	6.55D-03	-1.09D-03	4.75D-03	1.09D-03	2.07D-03	-7.07D-04	1.42D-04	9.10D-05
0.508	0.1	0.3	6.81D-01	3.56D-03	-2.38D-03	4.75D-03	1.21D-03	1.92D-03	-7.92D-04	9.31D-05	5.17D-05
0.762	0.1	0.1	7.19D-01	1.25D-03	-2.51D-03	4.63D-03	1.23D-03	1.90D-03	-8.21D-04	9.74D-05	3.23D-05
1.016	0.3	0.1	7.40D-01	1.29D-03	-5.17D-03	4.30D-03	1.21D-03	1.84D-03	-8.11D-04	1.10D-04	2.14D-05
1.270	0.4	0.1	7.66D-01	1.34D-03	-6.68D-03	4.04D-03	1.20D-03	1.79D-03	-7.85D-04	1.55D-04	-1.05D-06
1.905	0.4	0.0	8.08D-01	0.00D-01	-7.05D-03	3.38D-03	1.13D-03	1.68D-03	-7.31D-04	1.50D-04	-1.70D-05
2.540	0.2	0.0	8.48D-01	0.00D-01	-4.44D-03	2.93D-03	1.03D-03	1.49D-03	-6.21D-04	1.03D-04	-1.21D-05
3.810	0.4	0.0	9.12D-01	0.00D-01	-7.96D-03	1.98D-03	7.38D-04	1.03D-03	-4.47D-04	8.20D-05	-5.15D-05
5.080	0.2	0.1	9.62D-01	1.68D-03	-5.04D-03	9.83D-04	4.37D-04	4.87D-04	-2.42D-04	3.45D-05	-5.42D-05
6.350	0.2	0.1	9.95D-01	1.74D-03	-5.21D-03	2.63D-04	1.66D-04	1.45D-04	-5.37D-05	6.41D-06	-2.51D-05
7.620	0.1	0.1	1.00D+00	1.75D-03	-3.49D-03	5.23D-05	5.42D-05	4.31D-05	-5.96D-06	8.46D-06	-5.90D-06
10.160	0.0	0.1	9.99D-01	1.74D-03	-1.74D-03	3.05D-05	1.66D-05	2.57D-05	-9.21D-07	9.73D-06	1.04D-06
12.700	0.0	0.1	1.00D+00	1.75D-03	-1.75D-03	2.81D-05	1.54D-05	2.46D-05	-1.35D-06	1.02D-05	1.16D-06

SENSOR COORDINATE SYSTEM

Y (CM)	BETA (DEG)	PSIZ* (DEG)	Q/UFS	U/UFS	UU/UFS2	VV/UFS2	WW/UFS2	UV/UFS2	UW/UFS2	VW/UFS2
0.127	0.0	1.1	5.78D-01	5.78D-01	4.55D-03	9.90D-04	2.21D-03	-5.55D-04	1.34D-04	1.27D-04
0.190	0.1	0.7	6.07D-01	6.07D-01	4.67D-03	1.04D-03	2.16D-03	-6.45D-04	1.14D-04	1.03D-04
0.254	0.0	0.6	6.26D-01	6.26D-01	4.75D-03	1.09D-03	2.07D-03	-7.07D-04	1.37D-04	9.22D-05
0.508	0.1	0.3	6.81D-01	6.81D-01	4.75D-03	1.21D-03	1.92D-03	-7.91D-04	8.32D-05	5.45D-05
0.762	0.1	0.1	7.19D-01	7.19D-01	4.63D-03	1.23D-03	1.90D-03	-8.21D-04	8.79D-05	3.52D-05
1.016	0.3	0.1	7.40D-01	7.40D-01	4.31D-03	1.21D-03	1.84D-03	-8.10D-04	9.25D-05	2.71D-05
1.270	0.4	0.1	7.66D-01	7.66D-01	4.04D-03	1.20D-03	1.79D-03	-7.85D-04	1.35D-04	5.80D-06
1.905	0.4	0.0	8.08D-01	8.08D-01	3.38D-03	1.13D-03	1.68D-03	-7.31D-04	1.35D-04	-1.07D-05
2.540	0.2	0.0	8.48D-01	8.48D-01	2.93D-03	1.03D-03	1.49D-03	-6.22D-04	9.59D-05	-8.85D-06
3.810	0.4	0.0	9.12D-01	9.12D-01	1.98D-03	7.38D-04	1.03D-03	-4.47D-04	7.38D-05	-4.76D-05
5.080	0.2	0.1	9.62D-01	9.62D-01	9.83D-04	4.37D-04	4.86D-04	-2.42D-04	3.19D-05	-5.29D-05
6.350	0.2	0.1	9.95D-01	9.95D-01	2.63D-04	1.66D-04	1.45D-04	-5.38D-05	5.79D-06	-2.49D-05
7.620	0.1	0.1	1.00D+00	1.00D+00	5.23D-05	5.42D-05	4.30D-05	-5.98D-06	8.43D-06	-5.88D-06
10.160	0.0	0.1	9.99D-01	9.99D-01	3.05D-05	1.66D-05	2.57D-05	-9.19D-07	9.72D-06	1.05D-06
12.700	0.0	0.1	1.00D+00	1.00D+00	2.81D-05	1.54D-05	2.46D-05	-1.35D-06	1.02D-05	1.16D-06

TABLE G2. STANDARD TEST CASE MEAN VELOCITY AND REYNOLDS STRESS PROFILES AT STATION (-24,0)

REU = 1.34D+06 (1/M)
KINEMATIC VISC. = 1.67D-05 (SQ-M/S)
DENSITY = 1.10D+00 (KG/CUBIC METER)
OMEGA = 0.2 DEG.
UFS= 2.41D+01 M/S
U1FS = 2.41D+01 M/S

NONDIMENSIONALIZED MEAN VELOCITY NONDIMENSIONALIZED REYNOLDS STRESS TENSOR

LABORATORY COORDINATE SYSTEM

Y (CM)	BETA (DEG)	PSIZ* (DEG)	U1/U1FS	U2/U1FS	U3/U1FS	U1U1/U1FS2	U2U2/U1FS2	U3U3/U1FS2	U1U2/U1FS2	U1U3/U1FS2	U2U3/U1FS2
0.127	-0.2	0.8	5.54D-01	7.73D-03	0.00D-01	4.16D-03	9.53D-04	2.03D-03	-5.50D-04	9.95D-05	9.09D-05
0.190	-0.1	0.5	5.78D-01	5.04D-03	-1.01D-03	4.28D-03	1.03D-03	1.98D-03	-6.43D-04	1.17D-04	3.73D-05
0.254	-0.4	0.3	5.96D-01	3.12D-03	2.08D-03	4.36D-03	1.07D-03	1.93D-03	-7.05D-04	9.46D-05	5.84D-05
0.508	-0.3	0.1	6.50D-01	1.14D-03	1.14D-03	4.36D-03	1.18D-03	1.84D-03	-7.95D-04	5.96D-05	2.51D-05
0.762	-0.1	0.0	6.77D-01	0.00D-01	-1.18D-03	4.20D-03	1.22D-03	1.79D-03	-8.16D-04	2.49D-05	1.04D-05
1.016	-0.1	-0.1	7.12D-01	-1.24D-03	-1.24D-03	3.98D-03	1.23D-03	1.76D-03	-8.06D-04	2.44D-05	-1.49D-05
1.270	0.0	0.0	7.37D-01	0.00D-01	-2.57D-03	3.72D-03	1.21D-03	1.72D-03	-7.86D-04	5.59D-05	-6.37D-07
1.905	-0.2	-0.1	7.77D-01	-1.36D-03	0.00D-01	3.25D-03	1.16D-03	1.62D-03	-7.28D-04	3.38D-05	-1.21D-05
2.540	-0.2	0.0	8.11D-01	0.00D-01	0.00D-01	2.87D-03	1.07D-03	1.50D-03	-6.69D-04	3.28D-05	-7.56D-06
3.810	-0.1	0.0	8.79D-01	0.00D-01	-1.53D-03	2.12D-03	7.94D-04	1.12D-03	-4.89D-04	2.16D-05	-1.90D-05
5.080	-0.1	0.0	9.37D-01	0.00D-01	-1.64D-03	1.27D-03	4.78D-04	6.39D-04	-2.71D-04	1.17D-05	-1.09D-05
6.350	0.0	0.0	9.83D-01	0.00D-01	-3.43D-03	4.63D-04	1.99D-04	2.24D-04	-8.09D-05	-1.91D-06	-1.01D-05
7.620	-0.1	0.1	9.99D-01	1.74D-03	-1.74D-03	7.81D-05	6.27D-05	5.50D-05	-9.49D-06	9.63D-06	2.17D-06
10.160	0.0	0.1	1.00D+00	1.75D-03	-3.50D-03	3.10D-05	1.99D-05	2.59D-05	-2.10D-06	1.12D-05	-5.19D-10
12.700	0.0	-0.1	1.00D+00	-1.75D-03	-3.49D-03	2.94D-05	1.74D-05	2.47D-05	-1.95D-06	1.22D-05	-7.46D-07

SENSOR COORDINATE SYSTEM

Y (CM)	BETA (DEG)	PSIZ* (DEG)	Q/UFS	U/UFS	UU/UFS2	VV/UFS2	WW/UFS2	UV/UFS2	UW/UFS2	VW/UFS2
0.127	-0.2	0.8	5.54D-01	5.54D-01	4.16D-03	9.53D-04	2.03D-03	-5.50D-04	9.95D-05	9.09D-05
0.190	-0.1	0.5	5.78D-01	5.78D-01	4.28D-03	1.03D-03	1.98D-03	-6.43D-04	1.13D-04	3.84D-05
0.254	-0.4	0.3	5.96D-01	5.96D-01	4.36D-03	1.07D-03	1.93D-03	-7.05D-04	1.03D-04	5.59D-05
0.508	-0.3	0.1	6.50D-01	6.50D-01	4.36D-03	1.18D-03	1.84D-03	-7.95D-04	6.40D-05	2.37D-05
0.762	-0.1	0.0	6.77D-01	6.77D-01	4.20D-03	1.22D-03	1.79D-03	-8.16D-04	2.07D-05	1.19D-05
1.016	-0.1	-0.1	7.12D-01	7.12D-01	3.98D-03	1.23D-03	1.76D-03	-8.06D-04	2.05D-05	-1.35D-05
1.270	0.0	0.0	7.37D-01	7.37D-01	3.72D-03	1.21D-03	1.72D-03	-7.86D-04	4.89D-05	2.11D-06
1.905	-0.2	-0.1	7.77D-01	7.77D-01	3.25D-03	1.16D-03	1.62D-03	-7.28D-04	3.38D-05	-1.21D-05
2.540	-0.2	0.0	8.11D-01	8.11D-01	2.87D-03	1.07D-03	1.50D-03	-6.69D-04	3.28D-05	-7.56D-06
3.810	-0.1	0.0	8.79D-01	8.79D-01	2.12D-03	7.94D-04	1.12D-03	-4.89D-04	1.98D-05	-1.82D-05
5.080	-0.1	0.0	9.37D-01	9.37D-01	1.27D-03	4.78D-04	6.39D-04	-2.71D-04	1.06D-05	-1.04D-05
6.350	0.0	0.0	9.83D-01	9.83D-01	4.63D-04	1.99D-04	2.24D-04	-8.09D-05	-2.74D-06	-9.85D-06
7.620	-0.1	0.1	9.99D-01	9.99D-01	7.81D-05	6.27D-05	5.50D-05	-9.48D-06	9.59D-06	2.18D-06
10.160	0.0	0.1	1.00D+00	1.00D+00	3.11D-05	1.99D-05	2.58D-05	-2.10D-06	1.12D-05	6.82D-09
12.700	0.0	-0.1	1.00D+00	1.00D+00	2.95D-05	1.74D-05	2.47D-05	-1.95D-06	1.22D-05	-7.39D-07

TABLE G3. STANDARD TEST CASE MEAN VELOCITY AND REYNOLDS STRESS PROFILES AT STATION (-24,-4)

REU = 1.34D+06 (1/M)
KINEMATIC VISC. = 1.67D-05 (SQ-M/S)
DENSITY = 1.10D+00 (KG/CUBIC METER)
OMEGA = 0.1 DEG.
UFS= 2.41D+01 M/S
U1FS = 2.41D+01 M/S

NONDIMENSIONALIZED MEAN VELOCITY NONDIMENSIONALIZED REYNOLDS STRESS TENSOR

LABORATORY COORDINATE SYSTEM

Y (CM)	BETA (DEG)	PSIZ* (DEG)	U1/U1FS	U2/U1FS	U3/U1FS	U1U1/U1FS2	U2U2/U1FS2	U3U3/U1FS2	U1U2/U1FS2	U1U3/U1FS2	U2U3/U1FS2
0.127	-0.5	0.9	5.65D-01	8.88D-03	3.94D-03	4.74D-03	1.03D-03	2.35D-03	-6.47D-04	2.81D-05	7.04D-05
0.190	-0.5	0.6	5.91D-01	6.18D-03	4.12D-03	4.86D-03	1.08D-03	2.19D-03	-6.98D-04	4.83D-05	6.94D-05
0.254	-0.6	0.5	6.17D-01	5.39D-03	5.39D-03	4.86D-03	1.13D-03	2.11D-03	-7.45D-04	5.17D-05	5.70D-05
0.508	-0.5	0.3	6.71D-01	3.51D-03	4.68D-03	4.74D-03	1.23D-03	1.93D-03	-8.45D-04	7.37D-05	3.45D-05
0.762	-0.3	0.2	7.05D-01	2.46D-03	2.46D-03	4.50D-03	1.28D-03	1.83D-03	-8.72D-04	8.82D-05	1.12D-05
1.016	-0.5	0.1	7.31D-01	1.28D-03	5.10D-03	4.25D-03	1.30D-03	1.82D-03	-8.73D-04	9.03D-05	6.32D-06
1.270	-0.5	0.1	7.51D-01	1.31D-03	5.24D-03	4.03D-03	1.30D-03	1.75D-03	-8.59D-04	7.20D-05	9.79D-06
1.905	-0.4	0.1	7.97D-01	1.39D-03	4.17D-03	3.49D-03	1.22D-03	1.64D-03	-8.11D-04	9.71D-05	1.20D-05
2.540	-0.3	0.1	8.36D-01	1.46D-03	2.92D-03	2.96D-03	1.10D-03	1.51D-03	-7.01D-04	9.15D-05	1.25D-06
3.810	-0.2	0.0	9.00D-01	0.00D-01	1.57D-03	2.11D-03	8.02D-04	1.05D-03	-4.97D-04	4.85D-05	7.41D-06
5.080	-0.2	0.0	9.53D-01	0.00D-01	1.66D-03	1.06D-03	4.38D-04	5.40D-04	-2.41D-04	3.16D-05	-1.05D-05
6.350	-0.2	0.0	9.87D-01	0.00D-01	1.72D-03	2.85D-04	1.48D-04	1.69D-04	-5.24D-05	1.03D-06	-1.24D-05
7.620	0.0	0.1	1.00D+00	1.75D-03	-1.75D-03	6.21D-05	4.76D-05	4.61D-05	-5.98D-06	1.19D-05	-2.33D-06
10.160	0.1	0.0	1.00D+00	0.00D-01	-3.50D-03	3.07D-05	1.92D-05	2.59D-05	-1.99D-06	1.12D-05	-8.01D-08
12.700	0.0	0.1	1.00D+00	1.75D-03	-1.75D-03	2.91D-05	1.67D-05	2.48D-05	1.13D-06	1.17D-05	6.14D-07

SENSOR COORDINATE SYSTEM

Y (CM)	BETA (DEG)	PSIZ* (DEG)	Q/UFS	U/UFS	UU/UFS2	VV/UFS2	WW/UFS2	UV/UFS2	UW/UFS2	VW/UFS2
0.127	-0.5	0.9	5.65D-01	5.65D-01	4.74D-03	1.03D-03	2.35D-03	-6.48D-04	4.48D-05	6.59D-05
0.190	-0.5	0.6	5.91D-01	5.91D-01	4.86D-03	1.08D-03	2.19D-03	-6.98D-04	6.70D-05	6.45D-05
0.254	-0.6	0.5	6.17D-01	6.17D-01	4.86D-03	1.13D-03	2.11D-03	-7.45D-04	7.58D-05	5.05D-05
0.508	-0.5	0.3	6.71D-01	6.71D-01	4.74D-03	1.23D-03	1.93D-03	-8.45D-04	9.33D-05	2.86D-05
0.762	-0.3	0.2	7.05D-01	7.05D-01	4.50D-03	1.28D-03	1.83D-03	-8.72D-04	9.75D-05	8.14D-06
1.016	-0.5	0.1	7.31D-01	7.31D-01	4.25D-03	1.30D-03	1.82D-03	-8.73D-04	1.07D-04	2.28D-07
1.270	-0.5	0.1	7.51D-01	7.51D-01	4.02D-03	1.30D-03	1.76D-03	-8.59D-04	8.79D-05	3.79D-06
1.905	-0.4	0.1	7.97D-01	7.97D-01	3.49D-03	1.22D-03	1.64D-03	-8.11D-04	1.07D-04	7.74D-06
2.540	-0.3	0.1	8.36D-01	8.36D-01	2.96D-03	1.10D-03	1.51D-03	-7.01D-04	9.66D-05	-1.20D-06
3.810	-0.2	0.0	9.00D-01	9.00D-01	2.11D-03	8.02D-04	1.05D-03	-4.97D-04	5.03D-05	6.54D-06
5.080	-0.2	0.0	9.53D-01	9.53D-01	1.06D-03	4.38D-04	5.40D-04	-2.41D-04	3.25D-05	-1.09D-05
6.350	-0.2	0.0	9.87D-01	9.87D-01	2.85D-04	1.48D-04	1.69D-04	-5.24D-05	1.24D-06	-1.25D-05
7.620	0.0	0.1	1.00D+00	1.00D+00	6.21D-05	4.76D-05	4.61D-05	-5.98D-06	1.18D-05	-2.32D-06
10.160	0.1	0.0	1.00D+00	1.00D+00	3.08D-05	1.92D-05	2.59D-05	-1.99D-06	1.12D-05	-7.32D-08
12.700	0.0	0.1	1.00D+00	1.00D+00	2.91D-05	1.67D-05	2.47D-05	1.13D-06	1.17D-05	6.12D-07

TABLE G4. STANDARD TEST CASE MEAN VELOCITY AND REYNOLDS STRESS PROFILES AT STATION (-24,-8)

REU = 1.34D+06 (1/M)
KINEMATIC VISC. = 1.67D-05 (SQ-M/S)
DENSITY = 1.10D+00 (KG/CUBIC METER)
OMEGA = 0.2 DEG.
UFS= 2.41D+01 M/S
U1FS = 2.41D+01 M/S

NONDIMENSIONALIZED MEAN VELOCITY NONDIMENSIONALIZED REYNOLDS STRESS TENSOR

LABORATORY COORDINATE SYSTEM

Y (CM)	BETA (DEG)	PSIZ* (DEG)	U1/U1FS	U2/U1FS	U3/U1FS	U1U1/U1FS2	U2U2/U1FS2	U3U3/U1FS2	U1U2/U1FS2	U1U3/U1FS2	U2U3/U1FS2
0.127	-0.4	1.1	5.81D-01	1.12D-02	2.03D-03	4.53D-03	9.85D-04	2.19D-03	-5.79D-04	9.77D-05	9.54D-05
0.190	-0.4	0.7	6.08D-01	7.43D-03	2.12D-03	4.61D-03	1.06D-03	2.12D-03	-6.64D-04	4.86D-05	7.93D-05
0.254	-0.3	0.6	6.26D-01	6.55D-03	1.09D-03	4.69D-03	1.09D-03	2.04D-03	-7.30D-04	4.22D-05	5.25D-05
0.508	-0.4	0.3	6.82D-01	3.57D-03	2.38D-03	4.73D-03	1.21D-03	1.93D-03	-8.48D-04	1.20D-05	3.16D-05
0.762	-0.3	0.2	7.15D-01	2.50D-03	1.25D-03	4.53D-03	1.25D-03	1.86D-03	-8.70D-04	-1.21D-05	1.25D-05
1.016	-0.4	0.3	7.41D-01	3.88D-03	2.59D-03	4.20D-03	1.26D-03	1.80D-03	-8.42D-04	-1.15D-05	2.09D-05
1.270	-0.4	0.2	7.63D-01	2.66D-03	2.66D-03	3.98D-03	1.24D-03	1.75D-03	-8.26D-04	-1.12D-05	1.37D-05
1.905	-0.4	0.1	8.09D-01	1.41D-03	2.82D-03	3.38D-03	1.16D-03	1.61D-03	-7.68D-04	-2.03D-05	7.19D-06
2.540	-0.3	0.1	8.43D-01	1.47D-03	1.47D-03	2.86D-03	1.03D-03	1.45D-03	-6.84D-04	-2.74D-05	-1.12D-05
3.810	-0.4	0.1	9.06D-01	1.58D-03	3.16D-03	1.92D-03	7.42D-04	9.78D-04	-4.74D-04	-2.78D-05	5.89D-06
5.080	-0.4	0.0	9.62D-01	0.00D-01	3.36D-03	1.02D-03	4.08D-04	4.95D-04	-2.21D-04	-2.60D-05	2.43D-05
6.350	-0.2	0.0	9.94D-01	0.00D-01	0.00D-01	2.19D-04	1.34D-04	1.29D-04	-4.12D-05	-3.58D-06	1.55D-05
7.620	0.0	0.0	9.99D-01	0.00D-01	-3.49D-03	5.50D-05	4.64D-05	4.16D-05	-4.40D-06	1.05D-05	4.60D-06
10.160	0.0	0.0	9.99D-01	0.00D-01	-3.49D-03	3.15D-05	1.77D-05	2.59D-05	-1.41D-06	1.17D-05	-2.04D-07
12.700	0.0	0.2	1.00D+00	3.49D-03	-3.49D-03	2.86D-05	1.59D-05	2.48D-05	-1.32D-06	1.12D-05	-1.25D-06

SENSOR COORDINATE SYSTEM

Y (CM)	BETA (DEG)	PSIZ* (DEG)	Q/UFS	U/UFS	UU/UFS2	VV/UFS2	WW/UFS2	UV/UFS2	UW/UFS2	VW/UFS2
0.127	-0.4	1.1	5.82D-01	5.81D-01	4.53D-03	9.85D-04	2.19D-03	-5.79D-04	1.06D-04	9.34D-05
0.190	-0.4	0.7	6.08D-01	6.08D-01	4.61D-03	1.06D-03	2.12D-03	-6.65D-04	5.73D-05	7.70D-05
0.254	-0.3	0.6	6.26D-01	6.26D-01	4.69D-03	1.09D-03	2.04D-03	-7.30D-04	4.68D-05	5.12D-05
0.508	-0.4	0.3	6.82D-01	6.82D-01	4.73D-03	1.21D-03	1.93D-03	-8.48D-04	2.18D-05	2.86D-05
0.762	-0.3	0.2	7.15D-01	7.15D-01	4.53D-03	1.25D-03	1.86D-03	-8.70D-04	-7.42D-06	1.10D-05
1.016	-0.4	0.3	7.41D-01	7.41D-01	4.20D-03	1.26D-03	1.80D-03	-8.42D-04	-3.14D-06	1.80D-05
1.270	-0.4	0.2	7.63D-01	7.63D-01	3.98D-03	1.24D-03	1.75D-03	-8.26D-04	-3.46D-06	1.08D-05
1.905	-0.4	0.1	8.09D-01	8.09D-01	3.38D-03	1.16D-03	1.61D-03	-7.68D-04	-1.41D-05	4.51D-06
2.540	-0.3	0.1	8.43D-01	8.43D-01	2.86D-03	1.03D-03	1.45D-03	-6.84D-04	-2.49D-05	-1.24D-05
3.810	-0.4	0.1	9.06D-01	9.06D-01	1.92D-03	7.42D-04	9.77D-04	-4.74D-04	-2.45D-05	4.23D-06
5.080	-0.4	0.0	9.62D-01	9.62D-01	1.02D-03	4.08D-04	4.94D-04	-2.21D-04	-2.42D-05	2.35D-05
6.350	-0.2	0.0	9.94D-01	9.94D-01	2.19D-04	1.34D-04	1.29D-04	-4.12D-05	-3.58D-06	1.55D-05
7.620	0.0	0.0	9.99D-01	9.99D-01	5.51D-05	4.64D-05	4.16D-05	-4.38D-06	1.04D-05	4.62D-06
10.160	0.0	0.0	9.99D-01	9.99D-01	3.15D-05	1.77D-05	2.58D-05	-1.41D-06	1.17D-05	-1.99D-07
12.700	0.0	0.2	1.00D+00	1.00D+00	2.87D-05	1.59D-05	2.47D-05	-1.32D-06	1.12D-05	-1.24D-06

TABLE G5. STANDARD TEST CASE MEAN VELOCITY AND REYNOLDS STRESS PROFILES AT STATION (-7,0)

REU = 1.34D+06 (1/M)
KINEMATIC VISC. = 1.67D-05 (SQ-M/S)
DENSITY = 1.10D+00 (KG/CUBIC METER)
CF = 1.95D-03
OMEGA = 0.4 DEG.
UFS= 2.25D+01 M/S
U1FS = 2.25D+01 M/S

NONDIMENSIONALIZED MEAN VELOCITY NONDIMENSIONALIZED REYNOLDS STRESS TENSOR

LABORATORY COORDINATE SYSTEM

Y (CM)	BETA (DEG)	PSIZ* (DEG)	U1/U1FS	U2/U1FS	U3/U1FS	U1U1/U1FS2	U2U2/U1FS2	U3U3/U1FS2	U1U2/U1FS2	U1U3/U1FS2	U2U3/U1FS2
0.127	0.2	1.1	4.93D-01	9.47D-03	-5.16D-03	5.52D-03	1.01D-03	2.52D-03	-5.36D-04	8.98D-05	8.30D-05
0.190	0.0	0.8	5.18D-01	7.23D-03	-3.61D-03	5.61D-03	1.15D-03	2.48D-03	-6.70D-04	4.02D-05	3.17D-05
0.254	0.2	0.6	5.37D-01	5.62D-03	-5.62D-03	5.80D-03	1.23D-03	2.46D-03	-7.55D-04	8.07D-05	2.47D-05
0.508	0.2	0.4	5.89D-01	4.11D-03	-6.17D-03	6.08D-03	1.42D-03	2.36D-03	-9.09D-04	2.67D-05	-1.53D-05
0.762	0.2	0.3	6.30D-01	3.30D-03	-6.60D-03	5.94D-03	1.47D-03	2.31D-03	-9.64D-04	1.93D-05	-2.65D-05
1.016	0.3	0.3	6.49D-01	3.40D-03	-7.93D-03	5.66D-03	1.53D-03	2.22D-03	-9.89D-04	1.60D-05	-4.88D-05
1.270	0.1	0.3	6.71D-01	3.52D-03	-5.86D-03	5.33D-03	1.55D-03	2.21D-03	-9.84D-04	4.59D-05	-5.49D-05
1.905	0.4	0.4	7.23D-01	5.05D-03	-1.01D-02	4.69D-03	1.49D-03	2.10D-03	-9.64D-04	5.31D-05	-6.93D-05
2.540	0.3	0.5	7.62D-01	6.65D-03	-9.31D-03	4.09D-03	1.40D-03	1.95D-03	-8.96D-04	4.61D-05	-5.77D-05
3.810	0.2	0.6	8.35D-01	8.74D-03	-8.74D-03	3.08D-03	1.16D-03	1.57D-03	-7.48D-04	6.51D-06	-2.60D-05
5.080	0.3	0.6	8.95D-01	9.38D-03	-1.09D-02	2.14D-03	8.43D-04	1.13D-03	-5.20D-04	1.15D-05	-4.03D-05
6.350	0.2	0.7	9.45D-01	1.15D-02	-9.90D-03	1.19D-03	5.12D-04	5.38D-04	-3.09D-04	1.13D-05	-4.80D-05
7.620	-0.1	0.8	9.81D-01	1.37D-02	-5.14D-03	3.65D-04	2.45D-05	2.06D-04	-1.03D-05	-1.20D-05	2.11D-05
10.160	0.1	0.9	9.99D-01	1.57D-02	-8.72D-03	3.86D-05	3.60D-05	3.66D-05	-9.75D-07	5.76D-06	-3.67D-06
12.700	0.0	1.1	1.00D+00	1.92D-02	-6.98D-03	2.88D-05	1.80D-05	3.13D-05	-1.10D-06	6.18D-06	3.90D-07

SENSOR COORDINATE SYSTEM

Y (CM)	BETA (DEG)	PSIZ* (DEG)	Q/UFS	U/UFS	UU/UFS2	VV/UFS2	WW/UFS2	UV/UFS2	UW/UFS2	VW/UFS2
0.127	0.2	1.1	4.93D-01	4.93D-01	5.52D-03	1.01D-03	2.52D-03	-5.35D-04	5.84D-05	8.86D-05
0.190	0.0	0.8	5.18D-01	5.18D-01	5.61D-03	1.15D-03	2.47D-03	-6.70D-04	1.83D-05	3.64D-05
0.254	0.2	0.6	5.37D-01	5.37D-01	5.80D-03	1.23D-03	2.46D-03	-7.55D-04	4.58D-05	3.26D-05
0.508	0.2	0.4	5.89D-01	5.89D-01	6.08D-03	1.42D-03	2.36D-03	-9.09D-04	-1.23D-05	-5.77D-06
0.762	0.2	0.3	6.30D-01	6.30D-01	5.94D-03	1.47D-03	2.31D-03	-9.64D-04	-1.87D-05	-1.64D-05
1.016	0.3	0.3	6.49D-01	6.49D-01	5.66D-03	1.52D-03	2.22D-03	-9.90D-04	-2.60D-05	-3.67D-05
1.270	0.1	0.3	6.71D-01	6.71D-01	5.33D-03	1.55D-03	2.21D-03	-9.85D-04	1.87D-05	-4.63D-05
1.905	0.4	0.4	7.24D-01	7.24D-01	4.69D-03	1.49D-03	2.10D-03	-9.65D-04	1.69D-05	-5.58D-05
2.540	0.3	0.5	7.62D-01	7.62D-01	4.09D-03	1.40D-03	1.95D-03	-8.96D-04	2.00D-05	-4.68D-05
3.810	0.2	0.6	8.35D-01	8.35D-01	3.08D-03	1.16D-03	1.57D-03	-7.48D-04	-9.28D-06	-1.82D-05
5.080	0.3	0.6	8.96D-01	8.95D-01	2.14D-03	8.43D-04	1.13D-03	-5.21D-04	-9.08D-07	-3.39D-05
6.350	0.2	0.7	9.45D-01	9.45D-01	1.19D-03	5.12D-04	5.37D-04	-3.09D-04	4.48D-06	-4.48D-05
7.620	-0.1	0.8	9.81D-01	9.81D-01	3.65D-04	2.45D-05	2.06D-04	-1.02D-05	-1.28D-05	2.12D-05
10.160	0.1	0.9	9.99D-01	9.99D-01	3.87D-05	3.60D-05	3.65D-05	-1.01D-06	5.74D-06	-3.66D-06
12.700	0.0	1.1	1.00D+00	1.00D+00	2.89D-05	1.80D-05	3.12D-05	-1.10D-06	6.20D-06	3.98D-07

TABLE G6. STANDARD TEST CASE MEAN VELOCITY AND REYNOLDS STRESS PROFILES AT STATION (-5,0)

REU = 1.34D+06 (1/M)
KINEMATIC VISC. = 1.66D-05 (SQ-M/S)
DENSITY = 1.11D+00 (KG/CUBIC METER)
CF = 1.54D-03
OMEGA = 0.1 DEG.
UFS= 2.17D+01 M/S
U1FS = 2.17D+01 M/S

NONDIMENSIONALIZED MEAN VELOCITY NONDIMENSIONALIZED REYNOLDS STRESS TENSOR

LABORATORY COORDINATE SYSTEM

Y (CM)	BETA (DEG)	PSIZ* (DEG)	U1/U1FS	U2/U1FS	U3/U1FS	U1U1/U1FS2	U2U2/U1FS2	U3U3/U1FS2	U1U2/U1FS2	U1U3/U1FS2	U2U3/U1FS2
0.127	0.3	0.6	4.29D-01	4.50D-03	-3.00D-03	6.59D-03	1.09D-03	2.75D-03	-5.29D-04	5.28D-05	4.15D-05
0.190	0.3	0.2	4.49D-01	1.57D-03	-3.14D-03	6.83D-03	1.25D-03	2.75D-03	-6.61D-04	4.86D-05	-6.02D-06
0.254	0.4	0.1	4.72D-01	8.24D-04	-4.12D-03	7.08D-03	1.36D-03	2.71D-03	-7.75D-04	8.06D-05	-5.55D-06
0.508	0.4	-0.1	5.29D-01	-9.23D-04	-4.61D-03	7.32D-03	1.58D-03	2.62D-03	-9.54D-04	5.24D-05	-2.20D-05
0.762	0.2	-0.1	5.76D-01	-1.00D-03	-3.01D-03	7.17D-03	1.66D-03	2.53D-03	-1.03D-03	-2.42D-05	-2.68D-05
1.016	0.3	0.0	6.28D-01	0.00D-01	-4.39D-03	6.68D-03	1.66D-03	2.49D-03	-1.05D-03	-1.99D-05	-6.15D-05
1.270	0.4	0.3	6.58D-01	3.45D-03	-5.74D-03	6.39D-03	1.71D-03	2.41D-03	-1.06D-03	1.39D-06	-9.70D-05
1.905	0.3	0.2	7.18D-01	2.51D-03	-5.01D-03	5.41D-03	1.64D-03	2.30D-03	-1.03D-03	3.97D-06	-8.20D-05
2.540	0.1	0.2	7.63D-01	2.67D-03	-2.67D-03	4.71D-03	1.55D-03	2.12D-03	-9.62D-04	1.10D-05	-6.50D-05
3.810	0.2	0.4	8.40D-01	5.87D-03	-4.40D-03	3.54D-03	1.25D-03	1.71D-03	-7.68D-04	-1.41D-05	-2.67D-05
5.080	0.2	0.5	9.03D-01	7.88D-03	-4.73D-03	2.44D-03	9.21D-04	1.16D-03	-5.65D-04	1.85D-05	2.21D-05
6.350	0.2	0.6	9.54D-01	1.00D-02	-5.00D-03	1.36D-03	5.69D-04	6.22D-04	-3.25D-04	-1.27D-05	6.90D-06
7.620	0.1	0.8	9.87D-01	1.38D-02	-3.45D-03	4.20D-04	2.93D-04	2.14D-04	-1.18D-04	-6.58D-06	1.17D-06
10.160	0.1	1.1	9.99D-01	1.92D-02	-3.49D-03	3.59D-05	4.22D-05	3.32D-05	-5.37D-07	4.18D-06	-6.97D-07
12.700	0.0	1.4	1.00D+00	2.44D-02	-1.75D-03	2.46D-05	2.04D-05	2.63D-05	-1.15D-06	2.87D-06	-2.19D-06

SENSOR COORDINATE SYSTEM

Y (CM)	BETA (DEG)	PSIZ* (DEG)	Q/UFS	U/UFS	UU/UFS2	VV/UFS2	WW/UFS2	UV/UFS2	UW/UFS2	VW/UFS2
0.127	0.3	0.6	4.29D-01	4.29D-01	6.59D-03	1.09D-03	2.75D-03	-5.29D-04	2.60D-05	4.52D-05
0.190	0.3	0.2	4.49D-01	4.49D-01	6.83D-03	1.25D-03	2.75D-03	-6.61D-04	2.01D-05	-1.40D-06
0.254	0.4	0.1	4.72D-01	4.72D-01	7.08D-03	1.36D-03	2.70D-03	-7.75D-04	4.34D-05	1.22D-06
0.508	0.4	-0.1	5.29D-01	5.29D-01	7.32D-03	1.58D-03	2.61D-03	-9.54D-04	1.14D-05	-1.37D-05
0.762	0.2	-0.1	5.76D-01	5.76D-01	7.17D-03	1.66D-03	2.53D-03	-1.03D-03	-4.85D-05	-2.14D-05
1.016	0.3	0.0	6.28D-01	6.28D-01	6.68D-03	1.66D-03	2.49D-03	-1.05D-03	-4.92D-05	-5.41D-05
1.270	0.4	0.3	6.58D-01	6.58D-01	6.39D-03	1.71D-03	2.41D-03	-1.06D-03	-3.34D-05	-8.77D-05
1.905	0.3	0.2	7.18D-01	7.18D-01	5.41D-03	1.64D-03	2.30D-03	-1.03D-03	-1.77D-05	-7.48D-05
2.540	0.1	0.2	7.63D-01	7.63D-01	4.71D-03	1.55D-03	2.12D-03	-9.62D-04	2.02D-06	-6.16D-05
3.810	0.2	0.4	8.40D-01	8.40D-01	3.54D-03	1.25D-03	1.71D-03	-7.68D-04	-2.37D-05	-2.26D-05
5.080	0.2	0.5	9.03D-01	9.03D-01	2.44D-03	9.21D-04	1.16D-03	-5.65D-04	1.18D-05	2.50D-05
6.350	0.2	0.6	9.55D-01	9.54D-01	1.36D-03	5.69D-04	6.23D-04	-3.25D-04	-1.65D-05	8.60D-06
7.620	0.1	0.8	9.87D-01	9.87D-01	4.20D-04	2.93D-04	2.14D-04	-1.18D-04	-7.30D-06	1.58D-06
10.160	0.1	1.1	9.99D-01	9.99D-01	3.59D-05	4.22D-05	3.32D-05	-5.39D-07	4.17D-06	-6.95D-07
12.700	0.0	1.4	1.00D+00	1.00D+00	2.46D-05	2.04D-05	2.63D-05	-1.16D-06	2.87D-06	-2.19D-06

TABLE G7. STANDARD TEST CASE MEAN VELOCITY AND REYNOLDS STRESS PROFILES AT STATION (-3,0)

REU = 1.34D+06 (1/M)
KINEMATIC VISC. = 1.68D-05 (SQ-M/S)
DENSITY = 1.10D+00 (KG/CUBIC METER)
CF = 7.05D-04
OMEGA = 0.0 DEG.
UFS= 1.94D+01 M/S
U1FS = 1.94D+01 M/S

NONDIMENSIONALIZED MEAN VELOCITY NONDIMENSIONALIZED REYNOLDS STRESS TENSOR

LABORATORY COORDINATE SYSTEM

Y (CM)	BETA (DEG)	PSIZ* (DEG)	U1/U1FS	U2/U1FS	U3/U1FS	U1U1/U1FS2	U2U2/U1FS2	U3U3/U1FS2	U1U2/U1FS2	U1U3/U1FS2	U2U3/U1FS2
0.127	0.5	0.8	2.71D-01	3.78D-03	-2.36D-03	1.15D-02	1.31D-03	3.43D-03	-5.19D-04	4.03D-04	2.24D-05
0.190	0.9	0.1	3.02D-01	5.27D-04	-4.74D-03	1.23D-02	1.65D-03	3.59D-03	-8.18D-04	5.48D-04	-3.90D-05
0.254	1.2	0.1	3.30D-01	5.76D-04	-6.92D-03	1.26D-02	1.90D-03	3.66D-03	-1.02D-03	5.18D-04	-7.60D-05
0.508	1.0	0.0	4.23D-01	0.00D-01	-7.38D-03	1.31D-02	2.31D-03	3.73D-03	-1.35D-03	1.82D-04	-1.09D-04
0.762	0.9	0.2	4.91D-01	1.71D-03	-7.71D-03	1.21D-02	2.52D-03	3.49D-03	-1.46D-03	2.13D-04	-1.46D-04
1.016	0.7	0.4	5.54D-01	3.87D-03	-6.77D-03	1.10D-02	2.48D-03	3.34D-03	-1.54D-03	1.75D-04	-1.51D-04
1.270	0.4	0.2	6.03D-01	2.10D-03	-4.21D-03	1.02D-02	2.45D-03	3.17D-03	-1.48D-03	6.68D-05	-1.30D-04
1.905	0.7	0.1	6.88D-01	1.20D-03	-8.40D-03	8.38D-03	2.32D-03	2.88D-03	-1.32D-03	1.36D-04	-1.39D-04
2.540	0.4	-0.3	7.51D-01	-3.93D-03	-5.24D-03	7.21D-03	2.13D-03	2.62D-03	-1.24D-03	1.46D-04	-1.57D-04
3.810	0.4	-0.6	8.38D-01	-8.77D-03	-5.85D-03	5.03D-03	1.69D-03	2.07D-03	-9.97D-04	6.95D-05	-1.12D-04
5.080	0.4	-1.0	9.05D-01	-1.58D-02	-6.32D-03	3.54D-03	1.23D-03	1.43D-03	-7.14D-04	5.59D-05	-3.73D-05
6.350	0.3	-1.1	9.62D-01	-1.85D-02	-5.04D-03	2.13D-03	7.89D-04	7.69D-04	-4.35D-04	-1.86D-05	-4.91D-05
7.620	0.1	-0.9	9.97D-01	-1.57D-02	-1.74D-03	8.02D-04	4.04D-04	3.32D-04	-1.76D-04	-1.34D-05	2.77D-05
10.160	0.2	0.1	1.00D+00	1.75D-03	-3.51D-03	5.12D-05	5.94D-05	3.58D-05	-3.67D-06	-5.98D-07	2.04D-05
12.700	0.0	1.4	1.00D+00	2.44D-02	0.00D-01	3.55D-05	2.28D-05	3.41D-05	-1.49D-06	-7.32D-06	3.75D-06

SENSOR COORDINATE SYSTEM

Y (CM)	BETA (DEG)	PSIZ* (DEG)	Q/UFS	U/UFS	UU/UFS2	VV/UFS2	WW/UFS2	UV/UFS2	UW/UFS2	VW/UFS2
0.127	0.5	0.8	2.71D-01	2.71D-01	1.15D-02	1.31D-03	3.43D-03	-5.19D-04	3.33D-04	2.70D-05
0.190	0.9	0.1	3.02D-01	3.02D-01	1.23D-02	1.65D-03	3.57D-03	-8.19D-04	4.10D-04	-2.61D-05
0.254	1.2	0.1	3.30D-01	3.30D-01	1.26D-02	1.90D-03	3.64D-03	-1.02D-03	3.31D-04	-5.47D-05
0.508	1.0	0.0	4.23D-01	4.23D-01	1.31D-02	2.31D-03	3.73D-03	-1.35D-03	1.77D-05	-8.55D-05
0.762	0.9	0.2	4.91D-01	4.91D-01	1.21D-02	2.52D-03	3.48D-03	-1.46D-03	7.77D-05	-1.23D-04
1.016	0.7	0.4	5.54D-01	5.54D-01	1.10D-02	2.48D-03	3.34D-03	-1.54D-03	8.10D-05	-1.32D-04
1.270	0.4	0.2	6.03D-01	6.03D-01	1.02D-02	2.45D-03	3.17D-03	-1.48D-03	1.79D-05	-1.20D-04
1.905	0.7	0.1	6.88D-01	6.88D-01	8.38D-03	2.32D-03	2.88D-03	-1.32D-03	6.91D-05	-1.22D-04
2.540	0.4	-0.3	7.51D-01	7.51D-01	7.21D-03	2.13D-03	2.62D-03	-1.24D-03	1.14D-04	-1.49D-04
3.810	0.4	-0.6	8.38D-01	8.38D-01	5.03D-03	1.69D-03	2.07D-03	-9.98D-04	4.88D-05	-1.05D-04
5.080	0.4	-1.0	9.05D-01	9.05D-01	3.54D-03	1.23D-03	1.43D-03	-7.14D-04	4.12D-05	-3.23D-05
6.350	0.3	-1.1	9.62D-01	9.62D-01	2.13D-03	7.89D-04	7.69D-04	-4.35D-04	-2.58D-05	-4.68D-05
7.620	0.1	-0.9	9.97D-01	9.97D-01	8.02D-04	4.04D-04	3.32D-04	-1.76D-04	-1.42D-05	2.80D-05
10.160	0.2	0.1	1.00D+00	1.00D+00	5.12D-05	5.94D-05	3.58D-05	-3.60D-06	-6.52D-07	2.05D-05
12.700	0.0	1.4	1.00D+00	1.00D+00	3.55D-05	2.28D-05	3.41D-05	-1.49D-06	-7.32D-06	3.75D-06

TABLE G8. STANDARD TEST CASE MEAN VELOCITY AND REYNOLDS STRESS PROFILES AT STATION (-3,-2)

REU = 1.34D+06 (1/M)
KINEMATIC VISC. = 1.68D-05 (SQ-M/S)
DENSITY = 1.10D+00 (KG/CUBIC METER)
CF = 1.57D-03
OMEGA = 5.8 DEG.
UFS= 2.10D+01 M/S
U1FS = 2.09D+01 M/S

NONDIMENSIONALIZED MEAN VELOCITY NONDIMENSIONALIZED REYNOLDS STRESS TENSOR

LABORATORY COORDINATE SYSTEM

Y (CM)	BETA (DEG)	PSIZ* (DEG)	U1/U1FS	U2/U1FS	U3/U1FS	U1U1/U1FS2	U2U2/U1FS2	U3U3/U1FS2	U1U2/U1FS2	U1U3/U1FS2	U2U3/U1FS2
0.127	19.9	1.2	3.90D-01	9.05D-03	-1.87D-01	4.92D-03	1.18D-03	6.73D-03	-3.90D-04	2.14D-03	-3.47D-04
0.190	17.7	0.9	4.19D-01	7.18D-03	-1.82D-01	5.38D-03	1.47D-03	6.56D-03	-5.35D-04	2.37D-03	-5.78D-04
0.254	15.7	0.7	4.44D-01	5.83D-03	-1.75D-01	5.96D-03	1.63D-03	6.17D-03	-7.10D-04	2.55D-03	-6.36D-04
0.508	12.0	0.6	5.14D-01	5.65D-03	-1.65D-01	6.98D-03	1.96D-03	5.35D-03	-9.70D-04	2.64D-03	-7.55D-04
0.762	9.5	0.7	5.66D-01	7.17D-03	-1.55D-01	7.12D-03	2.08D-03	4.63D-03	-1.11D-03	2.33D-03	-7.15D-04
1.016	7.8	0.9	6.06D-01	9.79D-03	-1.47D-01	6.94D-03	2.10D-03	4.10D-03	-1.17D-03	2.01D-03	-6.46D-04
1.270	6.5	0.9	6.40D-01	1.03D-02	-1.40D-01	6.70D-03	2.08D-03	3.71D-03	-1.21D-03	1.66D-03	-5.83D-04
1.905	4.4	0.8	7.08D-01	1.00D-02	-1.27D-01	5.77D-03	1.99D-03	3.18D-03	-1.17D-03	1.25D-03	-4.63D-04
2.540	3.1	0.6	7.57D-01	8.03D-03	-1.19D-01	5.02D-03	1.80D-03	2.78D-03	-1.04D-03	9.79D-04	-3.72D-04
3.810	1.6	0.4	8.49D-01	5.98D-03	-1.10D-01	3.71D-03	1.40D-03	2.09D-03	-7.79D-04	6.46D-04	-2.19D-04
5.080	0.8	0.3	9.19D-01	4.84D-03	-1.06D-01	2.54D-03	9.86D-04	1.43D-03	-5.39D-04	4.06D-04	-1.04D-04
6.350	0.3	0.2	9.62D-01	3.38D-03	-1.03D-01	1.45D-03	5.95D-04	7.62D-04	-2.92D-04	2.35D-04	-4.81D-05
7.620	0.0	0.3	9.93D-01	5.23D-03	-1.01D-01	5.09D-04	3.18D-04	2.73D-04	-9.80D-05	4.76D-05	9.78D-06
10.160	0.0	0.8	1.00D+00	1.40D-02	-1.02D-01	4.99D-05	4.17D-05	4.58D-05	1.88D-07	-9.84D-06	3.10D-07
12.700	0.0	1.7	1.00D+00	2.98D-02	-1.02D-01	2.34D-05	1.72D-05	2.54D-05	1.46D-06	1.53D-06	1.28D-06

SENSOR COORDINATE SYSTEM

Y (CM)	BETA (DEG)	PSIZ* (DEG)	Q/UFS	U/UFS	UU/UFS2	VV/UFS2	WW/UFS2	UV/UFS2	UW/UFS2	VW/UFS2
0.127	19.9	1.2	4.30D-01	4.30D-01	6.86D-03	1.17D-03	4.66D-03	-4.97D-04	2.02D-03	-1.42D-04
0.190	17.7	0.9	4.55D-01	4.55D-01	7.23D-03	1.46D-03	4.59D-03	-7.14D-04	2.03D-03	-3.14D-04
0.254	15.7	0.7	4.75D-01	4.75D-01	7.65D-03	1.62D-03	4.35D-03	-8.84D-04	1.92D-03	-3.28D-04
0.508	12.0	0.6	5.37D-01	5.37D-01	8.28D-03	1.94D-03	3.93D-03	-1.14D-03	1.65D-03	-4.18D-04
0.762	9.5	0.7	5.84D-01	5.84D-01	8.05D-03	2.06D-03	3.58D-03	-1.25D-03	1.36D-03	-3.92D-04
1.016	7.8	0.9	6.20D-01	6.20D-01	7.62D-03	2.08D-03	3.31D-03	-1.28D-03	1.13D-03	-3.49D-04
1.270	6.5	0.9	6.52D-01	6.52D-01	7.19D-03	2.06D-03	3.12D-03	-1.30D-03	8.82D-04	-3.08D-04
1.905	4.4	0.8	7.16D-01	7.16D-01	6.06D-03	1.97D-03	2.80D-03	-1.22D-03	7.14D-04	-2.46D-04
2.540	3.1	0.6	7.63D-01	7.63D-01	5.21D-03	1.79D-03	2.51D-03	-1.08D-03	5.84D-04	-2.04D-04
3.810	1.6	0.4	8.52D-01	8.52D-01	3.81D-03	1.39D-03	1.93D-03	-7.93D-04	4.12D-04	-1.15D-04
5.080	0.8	0.3	9.20D-01	9.20D-01	2.60D-03	9.76D-04	1.34D-03	-5.42D-04	2.65D-04	-4.05D-05
6.350	0.3	0.2	9.62D-01	9.62D-01	1.48D-03	5.89D-04	7.13D-04	-2.92D-04	1.55D-04	-1.66D-05
7.620	0.0	0.3	9.93D-01	9.93D-01	5.10D-04	3.15D-04	2.63D-04	-9.56D-05	2.27D-05	1.94D-05
10.160	0.0	0.8	1.00D+00	1.00D+00	4.74D-05	4.13D-05	4.74D-05	2.16D-07	-9.95D-06	2.86D-07
12.700	0.0	1.7	1.00D+00	1.00D+00	2.35D-05	1.71D-05	2.48D-05	1.57D-06	1.68D-06	1.12D-06

TABLE G9. STANDARD TEST CASE MEAN VELOCITY AND REYNOLDS STRESS PROFILES AT STATION (-3,-4)

REU = 1.34D+06 (1/M)
KINEMATIC VISC. = 1.68D-05 (SQ-M/S)
DENSITY = 1.10D+00 (KG/CUBIC METER)
CF = 2.37D-03
OMEGA = 6.0 DEG.
UFS= 2.30D+01 M/S
U1FS = 2.28D+01 M/S

NONDIMENSIONALIZED MEAN VELOCITY NONDIMENSIONALIZED REYNOLDS STRESS TENSOR

LABORATORY COORDINATE SYSTEM

Y (CM)	BETA (DEG)	PSIZ* (DEG)	U1/U1FS	U2/U1FS	U3/U1FS	U1U1/U1FS2	U2U2/U1FS2	U3U3/U1FS2	U1U2/U1FS2	U1U3/U1FS2	U2U3/U1FS2
0.127	14.5	1.1	5.13D-01	1.05D-02	-1.92D-01	3.67D-03	9.73D-04	3.65D-03	-4.22D-04	1.04D-03	-2.91D-04
0.190	13.5	0.8	5.32D-01	7.88D-03	-1.88D-01	3.80D-03	1.15D-03	3.68D-03	-5.02D-04	1.14D-03	-4.05D-04
0.254	12.5	0.6	5.60D-01	6.18D-03	-1.87D-01	3.93D-03	1.25D-03	3.66D-03	-5.82D-04	1.23D-03	-5.16D-04
0.508	9.7	0.4	6.08D-01	4.41D-03	-1.71D-01	4.60D-03	1.49D-03	3.42D-03	-8.01D-04	1.38D-03	-5.58D-04
0.762	8.2	0.4	6.40D-01	4.61D-03	-1.62D-01	4.69D-03	1.60D-03	3.21D-03	-9.16D-04	1.33D-03	-5.82D-04
1.016	6.8	0.5	6.66D-01	5.96D-03	-1.51D-01	4.70D-03	1.69D-03	3.00D-03	-9.59D-04	1.19D-03	-5.35D-04
1.270	6.0	0.5	6.93D-01	6.18D-03	-1.47D-01	4.58D-03	1.71D-03	2.86D-03	-9.91D-04	1.10D-03	-4.96D-04
1.905	4.4	0.6	7.51D-01	7.99D-03	-1.38D-01	4.23D-03	1.64D-03	2.59D-03	-9.71D-04	9.08D-04	-4.09D-04
2.540	3.2	0.6	7.93D-01	8.41D-03	-1.28D-01	3.75D-03	1.54D-03	2.35D-03	-9.16D-04	7.91D-04	-3.22D-04
3.810	1.8	0.7	8.67D-01	1.07D-02	-1.19D-01	2.83D-03	1.20D-03	1.82D-03	-7.17D-04	5.17D-04	-1.54D-04
5.080	0.7	0.6	9.16D-01	9.66D-03	-1.08D-01	1.93D-03	8.36D-04	1.19D-03	-4.85D-04	3.30D-04	-9.51D-05
6.350	0.2	0.6	9.69D-01	1.02D-02	-1.05D-01	1.07D-03	4.89D-04	6.60D-04	-2.47D-04	1.76D-04	-5.02D-05
7.620	0.1	0.8	9.96D-01	1.40D-02	-1.06D-01	3.68D-04	2.13D-04	2.08D-04	-6.62D-05	5.31D-05	-3.40D-05
10.160	0.0	1.0	1.00D+00	1.76D-02	-1.05D-01	3.56D-05	3.41D-05	3.67D-05	-1.65D-06	3.78D-06	-3.56D-06
12.700	0.0	1.4	1.00D+00	2.46D-02	-1.05D-01	2.53D-05	1.92D-05	2.94D-05	-1.48D-06	5.55D-06	-2.44D-06

SENSOR COORDINATE SYSTEM

Y (CM)	BETA (DEG)	PSIZ* (DEG)	Q/UFS	U/UFS	UU/UFS2	VV/UFS2	WW/UFS2	UV/UFS2	UW/UFS2	VW/UFS2
0.127	14.5	1.1	5.44D-01	5.44D-01	4.30D-03	9.63D-04	2.93D-03	-4.91D-04	7.74D-04	-1.24D-04
0.190	13.5	0.8	5.62D-01	5.61D-01	4.45D-03	1.14D-03	2.94D-03	-6.02D-04	8.42D-04	-2.12D-04
0.254	12.5	0.6	5.87D-01	5.87D-01	4.59D-03	1.23D-03	2.91D-03	-7.08D-04	8.95D-04	-3.01D-04
0.508	9.7	0.4	6.28D-01	6.28D-01	5.17D-03	1.47D-03	2.76D-03	-9.12D-04	8.58D-04	-3.17D-04
0.762	8.2	0.4	6.56D-01	6.56D-01	5.17D-03	1.58D-03	2.64D-03	-1.02D-03	8.08D-04	-3.36D-04
1.016	6.8	0.5	6.79D-01	6.79D-01	5.08D-03	1.67D-03	2.54D-03	-1.04D-03	6.94D-04	-3.06D-04
1.270	6.0	0.5	7.04D-01	7.04D-01	4.90D-03	1.69D-03	2.46D-03	-1.06D-03	6.50D-04	-2.77D-04
1.905	4.4	0.6	7.59D-01	7.59D-01	4.45D-03	1.62D-03	2.30D-03	-1.02D-03	5.53D-04	-2.25D-04
2.540	3.2	0.6	7.99D-01	7.99D-01	3.92D-03	1.52D-03	2.12D-03	-9.45D-04	5.24D-04	-1.69D-04
3.810	1.8	0.7	8.70D-01	8.70D-01	2.91D-03	1.19D-03	1.68D-03	-7.23D-04	3.59D-04	-5.47D-05
5.080	0.7	0.6	9.17D-01	9.17D-01	1.97D-03	8.27D-04	1.11D-03	-4.88D-04	2.34D-04	-3.74D-05
6.350	0.2	0.6	9.69D-01	9.69D-01	1.09D-03	4.84D-04	6.21D-04	-2.48D-04	1.26D-04	-2.30D-05
7.620	0.1	0.8	9.96D-01	9.96D-01	3.73D-04	2.11D-04	1.96D-04	-6.87D-05	3.46D-05	-2.64D-05
10.160	0.0	1.0	1.00D+00	1.00D+00	3.60D-05	3.37D-05	3.55D-05	-1.99D-06	3.77D-06	-3.33D-06
12.700	0.0	1.4	1.00D+00	1.00D+00	2.62D-05	1.90D-05	2.79D-05	-1.71D-06	5.79D-06	-2.25D-06

TABLE G10. STANDARD TEST CASE MEAN VELOCITY AND REYNOLDS STRESS PROFILES AT STATION (-7,-6)

REU = 1.34D+06 (1/M)
KINEMATIC VISC. = 1.68D-05 (SQ-M/S)
DENSITY = 1.10D+00 (KG/CUBIC METER)
CF = 2.36D-03
OMEGA = 2.0 DEG.
UFS= 2.38D+01 M/S
U1FS = 2.38D+01 M/S

NONDIMENSIONALIZED MEAN VELOCITY NONDIMENSIONALIZED REYNOLDS STRESS TENSOR

LABORATORY COORDINATE SYSTEM

Y (CM)	BETA (DEG)	PSIZ* (DEG)	U1/U1FS	U2/U1FS	U3/U1FS	U1U1/U1FS2	U2U2/U1FS2	U3U3/U1FS2	U1U2/U1FS2	U1U3/U1FS2	U2U3/U1FS2
0.127	3.9	0.8	5.62D-01	7.89D-03	-5.81D-02	4.44D-03	9.60D-04	2.44D-03	-5.33D-04	4.64D-04	-4.80D-05
0.190	3.7	0.4	5.85D-01	4.11D-03	-5.84D-02	4.56D-03	1.04D-03	2.40D-03	-6.25D-04	5.27D-04	-1.03D-04
0.254	3.4	0.4	6.06D-01	4.25D-03	-5.73D-02	4.70D-03	1.11D-03	2.36D-03	-6.90D-04	5.00D-04	-1.22D-04
0.508	2.6	0.0	6.55D-01	0.00D-01	-5.27D-02	4.75D-03	1.28D-03	2.20D-03	-8.31D-04	4.49D-04	-1.59D-04
0.762	2.1	0.0	6.89D-01	0.00D-01	-4.94D-02	4.76D-03	1.34D-03	2.07D-03	-8.81D-04	4.19D-04	-1.71D-04
1.016	1.7	0.1	7.14D-01	1.25D-03	-4.61D-02	4.52D-03	1.40D-03	2.06D-03	-9.08D-04	3.69D-04	-1.54D-04
1.270	1.5	0.0	7.36D-01	0.00D-01	-4.50D-02	4.27D-03	1.39D-03	1.99D-03	-8.92D-04	3.44D-04	-1.46D-04
1.905	1.2	0.2	7.77D-01	2.72D-03	-4.35D-02	3.83D-03	1.34D-03	1.88D-03	-8.67D-04	2.71D-04	-1.17D-04
2.540	0.8	0.2	8.20D-01	2.87D-03	-4.01D-02	3.28D-03	1.21D-03	1.70D-03	-7.73D-04	2.21D-04	-8.43D-05
3.810	0.4	0.2	8.84D-01	3.09D-03	-3.71D-02	2.29D-03	9.11D-04	1.28D-03	-5.65D-04	1.44D-04	-5.89D-05
5.080	0.2	0.2	9.35D-01	3.27D-03	-3.59D-02	1.45D-03	5.56D-04	7.70D-04	-3.36D-04	9.41D-05	-6.50D-05
6.350	0.0	0.3	9.78D-01	5.12D-03	-3.41D-02	6.64D-04	2.98D-04	3.45D-04	-1.36D-04	3.20D-05	-2.63D-05
7.620	-0.1	0.4	9.92D-01	6.93D-03	-3.29D-02	1.51D-04	1.10D-04	1.12D-04	-2.16D-05	-1.69D-06	-8.36D-06
10.160	-0.1	0.5	9.99D-01	8.72D-03	-3.31D-02	3.52D-05	2.46D-05	3.84D-05	-2.67D-06	-1.88D-06	6.63D-06
12.700	0.0	0.6	1.00D+00	1.05D-02	-3.49D-02	2.93D-05	1.88D-05	3.48D-05	-2.14D-06	-2.03D-06	5.54D-07

SENSOR COORDINATE SYSTEM

Y (CM)	BETA (DEG)	PSIZ* (DEG)	Q/UFS	U/UFS	UU/UFS2	VV/UFS2	WW/UFS2	UV/UFS2	UW/UFS2	VW/UFS2
0.127	3.9	0.8	5.65D-01	5.65D-01	4.51D-03	9.59D-04	2.36D-03	-5.35D-04	2.49D-04	7.08D-06
0.190	3.7	0.4	5.88D-01	5.88D-01	4.64D-03	1.04D-03	2.32D-03	-6.31D-04	3.03D-04	-4.03D-05
0.254	3.4	0.4	6.09D-01	6.09D-01	4.76D-03	1.11D-03	2.29D-03	-6.97D-04	2.72D-04	-5.63D-05
0.508	2.6	0.0	6.56D-01	6.56D-01	4.80D-03	1.28D-03	2.15D-03	-8.40D-04	2.39D-04	-9.18D-05
0.762	2.1	0.0	6.90D-01	6.90D-01	4.80D-03	1.34D-03	2.02D-03	-8.90D-04	2.22D-04	-1.07D-04
1.016	1.7	0.1	7.15D-01	7.15D-01	4.55D-03	1.39D-03	2.02D-03	-9.15D-04	2.07D-04	-9.51D-05
1.270	1.5	0.0	7.37D-01	7.37D-01	4.30D-03	1.39D-03	1.95D-03	-8.98D-04	2.01D-04	-9.14D-05
1.905	1.2	0.2	7.78D-01	7.78D-01	3.85D-03	1.34D-03	1.85D-03	-8.71D-04	1.60D-04	-6.84D-05
2.540	0.8	0.2	8.21D-01	8.21D-01	3.29D-03	1.21D-03	1.68D-03	-7.75D-04	1.43D-04	-4.64D-05
3.810	0.4	0.2	8.84D-01	8.84D-01	2.30D-03	9.10D-04	1.27D-03	-5.66D-04	1.01D-04	-3.51D-05
5.080	0.2	0.2	9.35D-01	9.35D-01	1.45D-03	5.55D-04	7.62D-04	-3.38D-04	6.77D-05	-5.20D-05
6.350	0.0	0.3	9.78D-01	9.78D-01	6.65D-04	2.97D-04	3.43D-04	-1.36D-04	2.08D-05	-2.16D-05
7.620	-0.1	0.4	9.92D-01	9.92D-01	1.50D-04	1.10D-04	1.12D-04	-2.19D-05	-2.95D-06	-7.63D-06
10.160	-0.1	0.5	9.99D-01	9.99D-01	3.50D-05	2.46D-05	3.84D-05	-2.45D-06	-1.77D-06	6.71D-06
12.700	0.0	0.6	1.00D+00	1.00D+00	2.92D-05	1.88D-05	3.49D-05	-2.12D-06	-1.83D-06	6.27D-07

TABLE G11. STANDARD TEST CASE MEAN VELOCITY AND REYNOLDS STRESS PROFILES AT STATION (-3,-6)

REU = 1.34D+06 (1/M)
KINEMATIC VISC. = 1.67D-05 (SQ-M/S)
DENSITY = 1.10D+00 (KG/CUBIC METER)
CF = 2.58D-03
OMEGA = 4.3 DEG.
UFS= 2.39D+01 M/S
U1FS = 2.38D+01 M/S

NONDIMENSIONALIZED MEAN VELOCITY NONDIMENSIONALIZED REYNOLDS STRESS TENSOR

LABORATORY COORDINATE SYSTEM

Y (CM)	BETA (DEG)	PSIZ* (DEG)	U1/U1FS	U2/U1FS	U3/U1FS	U1U1/U1FS2	U2U2/U1FS2	U3U3/U1FS2	U1U2/U1FS2	U1U3/U1FS2	U2U3/U1FS2
0.127	8.9	0.9	5.70D-01	9.19D-03	-1.34D-01	3.83D-03	9.02D-04	2.75D-03	-4.89D-04	7.03D-04	-1.46D-04
0.190	8.2	0.5	5.93D-01	5.30D-03	-1.31D-01	3.90D-03	1.00D-03	2.73D-03	-5.68D-04	7.47D-04	-2.34D-04
0.254	7.9	0.4	6.11D-01	4.36D-03	-1.32D-01	3.94D-03	1.08D-03	2.66D-03	-6.30D-04	8.04D-04	-2.84D-04
0.508	6.3	0.2	6.58D-01	2.34D-03	-1.23D-01	4.26D-03	1.28D-03	2.51D-03	-7.78D-04	8.20D-04	-3.54D-04
0.762	5.3	0.2	6.93D-01	2.45D-03	-1.17D-01	4.30D-03	1.36D-03	2.42D-03	-8.63D-04	7.73D-04	-3.33D-04
1.016	4.5	0.1	7.18D-01	1.27D-03	-1.11D-01	4.25D-03	1.42D-03	2.34D-03	-8.83D-04	6.78D-04	-3.08D-04
1.270	3.8	0.1	7.41D-01	1.31D-03	-1.06D-01	4.11D-03	1.40D-03	2.26D-03	-8.95D-04	6.40D-04	-2.70D-04
1.905	2.9	0.2	7.82D-01	2.75D-03	-9.88D-02	3.67D-03	1.36D-03	2.08D-03	-8.32D-04	5.05D-04	-2.37D-04
2.540	2.1	0.3	8.23D-01	4.34D-03	-9.23D-02	3.26D-03	1.25D-03	1.89D-03	-7.99D-04	4.38D-04	-1.82D-04
3.810	1.1	0.3	8.85D-01	4.65D-03	-8.36D-02	2.35D-03	9.51D-04	1.41D-03	-5.83D-04	2.84D-04	-1.26D-04
5.080	0.5	0.4	9.37D-01	6.56D-03	-7.87D-02	1.47D-03	6.19D-04	8.22D-04	-3.73D-04	1.70D-04	-8.60D-05
6.350	0.1	0.4	9.77D-01	6.84D-03	-7.52D-02	6.30D-04	3.38D-04	3.73D-04	-1.39D-04	4.51D-05	-4.54D-05
7.620	0.0	0.5	9.95D-01	8.71D-03	-7.48D-02	1.27D-04	1.41D-04	9.96D-05	-3.69D-05	3.66D-06	-2.75D-05
10.160	0.0	0.7	1.00D+00	1.23D-02	-7.52D-02	3.36D-05	2.50D-05	3.82D-05	-1.46D-06	1.78D-06	3.36D-07
12.700	0.0	0.9	1.00D+00	1.58D-02	-7.52D-02	3.12D-05	1.79D-05	3.64D-05	-1.57D-06	1.21D-06	2.14D-07

SENSOR COORDINATE SYSTEM

Y (CM)	BETA (DEG)	PSIZ* (DEG)	Q/UFS	U/UFS	UU/UFS2	VV/UFS2	WW/UFS2	UV/UFS2	UW/UFS2	VW/UFS2
0.127	8.9	0.9	5.84D-01	5.84D-01	4.06D-03	8.97D-04	2.48D-03	-5.06D-04	3.87D-04	-2.99D-05
0.190	8.2	0.5	6.05D-01	6.05D-01	4.14D-03	9.97D-04	2.45D-03	-6.02D-04	4.25D-04	-1.04D-04
0.254	7.9	0.4	6.23D-01	6.23D-01	4.19D-03	1.07D-03	2.38D-03	-6.72D-04	4.67D-04	-1.43D-04
0.508	6.3	0.2	6.68D-01	6.68D-01	4.47D-03	1.27D-03	2.26D-03	-8.25D-04	4.45D-04	-2.04D-04
0.762	5.3	0.2	7.01D-01	7.01D-01	4.47D-03	1.35D-03	2.21D-03	-9.01D-04	4.20D-04	-1.83D-04
1.016	4.5	0.1	7.25D-01	7.25D-01	4.39D-03	1.41D-03	2.17D-03	-9.15D-04	3.56D-04	-1.68D-04
1.270	3.8	0.1	7.47D-01	7.47D-01	4.22D-03	1.39D-03	2.10D-03	-9.19D-04	3.55D-04	-1.41D-04
1.905	2.9	0.2	7.86D-01	7.86D-01	3.75D-03	1.35D-03	1.97D-03	-8.51D-04	2.90D-04	-1.30D-04
2.540	2.1	0.3	8.26D-01	8.26D-01	3.32D-03	1.24D-03	1.80D-03	-8.10D-04	2.74D-04	-9.09D-05
3.810	1.1	0.3	8.86D-01	8.86D-01	2.38D-03	9.45D-04	1.36D-03	-5.89D-04	1.90D-04	-7.03D-05
5.080	0.5	0.4	9.37D-01	9.37D-01	1.48D-03	6.16D-04	7.94D-04	-3.77D-04	1.13D-04	-5.42D-05
6.350	0.1	0.4	9.77D-01	9.77D-01	6.32D-04	3.36D-04	3.65D-04	-1.42D-04	2.47D-05	-3.44D-05
7.620	0.0	0.5	9.95D-01	9.95D-01	1.27D-04	1.40D-04	9.86D-05	-3.86D-05	1.52D-06	-2.45D-05
10.160	0.0	0.7	1.00D+00	1.00D+00	3.37D-05	2.48D-05	3.77D-05	-1.42D-06	2.09D-06	4.42D-07
12.700	0.0	0.9	1.00D+00	1.00D+00	3.12D-05	1.78D-05	3.60D-05	-1.55D-06	1.57D-06	3.29D-07

TABLE G12. STANDARD TEST CASE MEAN VELOCITY AND REYNOLDS STRESS PROFILES AT STATION (1,-6)

REU = 1.34D+06 (1/M)
KINEMATIC VISC. = 1.67D-05 (SQ-M/S)
DENSITY = 1.10D+00 (KG/CUBIC METER)
CF = 3.19D-03
OMEGA = 4.5 DEG.
UFS= 2.67D+01 M/S
U1FS = 2.66D+01 M/S

NONDIMENSIONALIZED MEAN VELOCITY NONDIMENSIONALIZED REYNOLDS STRESS TENSOR

LABORATORY COORDINATE SYSTEM

Y (CM)	BETA (DEG)	PSIZ* (DEG)	U1/U1FS	U2/U1FS	U3/U1FS	U1U1/U1FS2	U2U2/U1FS2	U3U3/U1FS2	U1U2/U1FS2	U1U3/U1FS2	U2U3/U1FS2
0.127	8.8	0.8	6.40D-01	9.18D-03	-1.51D-01	2.61D-03	6.60D-04	2.05D-03	-3.70D-04	2.62D-04	-6.01D-05
0.190	8.8	0.7	6.60D-01	8.29D-03	-1.56D-01	2.34D-03	6.74D-04	2.16D-03	-4.00D-04	3.21D-04	-1.49D-04
0.254	8.5	0.6	6.74D-01	7.25D-03	-1.56D-01	2.27D-03	7.43D-04	2.23D-03	-4.31D-04	3.63D-04	-2.11D-04
0.508	7.2	0.7	7.09D-01	8.84D-03	-1.47D-01	2.39D-03	1.01D-03	2.23D-03	-6.07D-04	4.31D-04	-3.59D-04
0.762	5.8	0.8	7.32D-01	1.04D-02	-1.33D-01	2.60D-03	1.19D-03	2.10D-03	-7.51D-04	4.41D-04	-3.53D-04
1.016	4.8	0.8	7.49D-01	1.06D-02	-1.23D-01	2.69D-03	1.25D-03	2.03D-03	-8.21D-04	4.08D-04	-3.29D-04
1.270	4.0	0.8	7.68D-01	1.08D-02	-1.15D-01	2.74D-03	1.27D-03	1.96D-03	-8.19D-04	3.88D-04	-3.07D-04
1.905	2.8	0.8	8.04D-01	1.13D-02	-1.03D-01	2.59D-03	1.23D-03	1.81D-03	-8.08D-04	3.22D-04	-2.51D-04
2.540	1.7	0.7	8.36D-01	1.03D-02	-9.08D-02	2.36D-03	1.16D-03	1.62D-03	-7.58D-04	2.90D-04	-1.91D-04
3.810	0.6	0.6	8.96D-01	9.42D-03	-8.00D-02	1.76D-03	8.83D-04	1.27D-03	-5.75D-04	2.04D-04	-1.16D-04
5.080	-0.1	0.4	9.46D-01	6.62D-03	-7.28D-02	1.15D-03	5.73D-04	8.03D-04	-3.39D-04	1.34D-04	-4.34D-05
6.350	-0.3	0.3	9.83D-01	5.16D-03	-7.22D-02	5.84D-04	2.94D-04	4.08D-04	-1.58D-04	6.85D-05	-1.60D-05
7.620	-0.4	0.1	1.00D+00	1.75D-03	-7.18D-02	1.94D-04	1.15D-04	1.43D-04	-3.73D-05	1.83D-05	-8.23D-06
10.160	-0.1	0.1	1.00D+00	1.76D-03	-7.73D-02	4.75D-05	2.75D-05	4.97D-05	-3.41D-06	8.76D-06	2.38D-07
12.700	0.0	0.3	1.00D+00	5.25D-03	-7.87D-02	2.67D-05	2.46D-05	3.13D-05	5.13D-06	7.43D-06	1.74D-06

SENSOR COORDINATE SYSTEM

Y (CM)	BETA (DEG)	PSIZ* (DEG)	Q/UFS	U/UFS	UU/UFS2	VV/UFS2	WW/UFS2	UV/UFS2	UW/UFS2	VW/UFS2
0.127	8.8	0.8	6.56D-01	6.56D-01	2.68D-03	6.56D-04	1.95D-03	-3.72D-04	1.07D-04	2.66D-05
0.190	8.8	0.7	6.76D-01	6.76D-01	2.46D-03	6.70D-04	2.02D-03	-4.21D-04	2.46D-04	-5.32D-05
0.254	8.5	0.6	6.90D-01	6.90D-01	2.42D-03	7.39D-04	2.06D-03	-4.64D-04	3.14D-04	-1.08D-04
0.508	7.2	0.7	7.22D-01	7.22D-01	2.54D-03	1.01D-03	2.05D-03	-6.64D-04	3.61D-04	-2.27D-04
0.762	5.8	0.8	7.42D-01	7.42D-01	2.72D-03	1.19D-03	1.95D-03	-7.98D-04	3.23D-04	-2.12D-04
1.016	4.8	0.8	7.57D-01	7.57D-01	2.79D-03	1.25D-03	1.91D-03	-8.58D-04	2.79D-04	-1.90D-04
1.270	4.0	0.8	7.74D-01	7.74D-01	2.82D-03	1.27D-03	1.85D-03	-8.50D-04	2.54D-04	-1.81D-04
1.905	2.8	0.8	8.09D-01	8.08D-01	2.64D-03	1.23D-03	1.73D-03	-8.29D-04	2.13D-04	-1.46D-04
2.540	1.7	0.7	8.38D-01	8.38D-01	2.40D-03	1.16D-03	1.56D-03	-7.69D-04	2.02D-04	-1.07D-04
3.810	0.6	0.6	8.97D-01	8.97D-01	1.78D-03	8.78D-04	1.23D-03	-5.79D-04	1.57D-04	-6.38D-05
5.080	-0.1	0.4	9.46D-01	9.46D-01	1.16D-03	5.70D-04	7.80D-04	-3.39D-04	1.05D-04	-1.72D-05
6.350	-0.3	0.3	9.83D-01	9.83D-01	5.90D-04	2.92D-04	3.97D-04	-1.58D-04	5.45D-05	-4.32D-06
7.620	-0.4	0.1	1.00D+00	1.00D+00	1.95D-04	1.14D-04	1.40D-04	-3.76D-05	1.44D-05	-5.50D-06
10.160	-0.1	0.1	1.00D+00	1.00D+00	4.85D-05	2.73D-05	4.81D-05	-3.36D-06	8.78D-06	4.96D-07
12.700	0.0	0.3	1.00D+00	1.00D+00	2.77D-05	2.44D-05	2.99D-05	5.21D-06	7.65D-06	1.33D-06

TABLE G13. STANDARD TEST CASE MEAN VELOCITY AND REYNOLDS STRESS PROFILES AT STATION (3,-6)

REU = 1.34D+06 (1/M)
KINEMATIC VISC. = 1.68D-05 (SQ-M/S)
DENSITY = 1.10D+00 (KG/CUBIC METER)
CF = 3.13D-03
OMEGA = 1.0 DEG.
UFS= 2.75D+01 M/S
U1FS = 2.75D+01 M/S

NONDIMENSIONALIZED MEAN VELOCITY NONDIMENSIONALIZED REYNOLDS STRESS TENSOR

LABORATORY COORDINATE SYSTEM

Y (CM)	BETA (DEG)	PSIZ* (DEG)	U1/U1FS	U2/U1FS	U3/U1FS	U1U1/U1FS2	U2U2/U1FS2	U3U3/U1FS2	U1U2/U1FS2	U1U3/U1FS2	U2U3/U1FS2
0.127	5.2	0.9	6.58D-01	1.04D-02	-7.15D-02	2.87D-03	7.43D-04	1.97D-03	-4.10D-04	-9.50D-06	2.10D-05
0.190	6.0	0.8	6.77D-01	9.52D-03	-8.31D-02	2.57D-03	6.90D-04	2.06D-03	-4.10D-04	1.07D-04	-1.88D-05
0.254	6.4	0.7	6.94D-01	8.55D-03	-9.01D-02	2.35D-03	7.13D-04	2.16D-03	-4.08D-04	1.80D-04	-7.89D-05
0.508	6.1	1.0	7.28D-01	1.28D-02	-9.07D-02	2.14D-03	9.41D-04	2.35D-03	-5.09D-04	2.75D-04	-3.12D-04
0.762	4.8	1.2	7.50D-01	1.58D-02	-7.62D-02	2.32D-03	1.18D-03	2.21D-03	-7.01D-04	2.94D-04	-3.66D-04
1.016	3.7	1.4	7.67D-01	1.88D-02	-6.30D-02	2.55D-03	1.29D-03	2.02D-03	-8.09D-04	1.84D-04	-3.14D-04
1.270	2.7	1.5	7.79D-01	2.04D-02	-5.04D-02	2.64D-03	1.33D-03	1.89D-03	-8.63D-04	9.54D-05	-2.48D-04
1.905	1.4	1.4	8.15D-01	1.99D-02	-3.42D-02	2.55D-03	1.30D-03	1.65D-03	-8.35D-04	4.20D-05	-1.55D-04
2.540	0.8	1.3	8.49D-01	1.93D-02	-2.67D-02	2.31D-03	1.18D-03	1.49D-03	-7.81D-04	5.73D-05	-1.22D-04
3.810	-0.1	0.9	9.06D-01	1.42D-02	-1.42D-02	1.70D-03	8.88D-04	1.15D-03	-6.00D-04	4.50D-05	-5.78D-05
5.080	-0.5	0.6	9.60D-01	1.01D-02	-8.38D-03	1.12D-03	5.99D-04	7.54D-04	-3.64D-04	2.85D-05	1.29D-05
6.350	-0.6	0.3	9.84D-01	5.15D-03	-6.87D-03	5.89D-04	2.97D-04	3.66D-04	-1.66D-04	1.21D-05	3.19D-07
7.620	-0.6	0.1	9.98D-01	1.74D-03	-6.97D-03	1.64D-04	1.27D-04	1.03D-04	-4.81D-05	6.08D-06	-2.60D-06
10.160	-0.3	-0.1	1.00D+00	-1.75D-03	-1.23D-02	3.07D-05	3.35D-05	3.27D-05	-7.76D-06	7.35D-06	1.98D-06
12.700	0.0	-0.2	1.00D+00	-3.49D-03	-1.75D-02	2.56D-05	2.64D-05	2.92D-05	-5.88D-06	6.50D-06	1.63D-06

SENSOR COORDINATE SYSTEM

Y (CM)	BETA (DEG)	PSIZ* (DEG)	Q/UFS	U/UFS	UU/UFS2	VV/UFS2	WW/UFS2	UV/UFS2	UW/UFS2	VW/UFS2
0.127	5.2	0.9	6.62D-01	6.62D-01	2.85D-03	7.42D-04	1.98D-03	-4.05D-04	-1.05D-04	6.51D-05
0.190	6.0	0.8	6.82D-01	6.82D-01	2.58D-03	6.90D-04	2.04D-03	-4.10D-04	4.23D-05	3.14D-05
0.254	6.4	0.7	7.00D-01	7.00D-01	2.39D-03	7.13D-04	2.11D-03	-4.15D-04	1.49D-04	-2.57D-05
0.508	6.1	1.0	7.34D-01	7.34D-01	2.21D-03	9.41D-04	2.28D-03	-5.44D-04	2.91D-04	-2.47D-04
0.762	4.8	1.2	7.54D-01	7.54D-01	2.37D-03	1.18D-03	2.15D-03	-7.34D-04	2.77D-04	-2.93D-04
1.016	3.7	1.4	7.69D-01	7.69D-01	2.57D-03	1.29D-03	1.99D-03	-8.32D-04	1.39D-04	-2.46D-04
1.270	2.7	1.5	7.80D-01	7.80D-01	2.64D-03	1.33D-03	1.88D-03	-8.77D-04	4.65D-05	-1.92D-04
1.905	1.4	1.4	8.16D-01	8.16D-01	2.55D-03	1.30D-03	1.65D-03	-8.41D-04	4.44D-06	-1.20D-04
2.540	0.8	1.3	8.49D-01	8.49D-01	2.31D-03	1.18D-03	1.49D-03	-7.85D-04	3.14D-05	-9.76D-05
3.810	-0.1	0.9	9.06D-01	9.06D-01	1.70D-03	8.88D-04	1.15D-03	-6.00D-04	3.64D-05	-4.83D-05
5.080	-0.5	0.6	9.60D-01	9.60D-01	1.12D-03	5.99D-04	7.53D-04	-3.64D-04	2.53D-05	1.61D-05
6.350	-0.6	0.3	9.84D-01	9.84D-01	5.89D-04	2.97D-04	3.65D-04	-1.66D-04	1.05D-05	1.48D-06
7.620	-0.6	0.1	9.98D-01	9.98D-01	1.64D-04	1.27D-04	1.02D-04	-4.81D-05	5.65D-06	-2.26D-06
10.160	-0.3	-0.1	1.00D+00	1.00D+00	3.08D-05	3.35D-05	3.25D-05	-7.73D-06	7.37D-06	2.07D-06
12.700	0.0	-0.2	1.00D+00	1.00D+00	2.58D-05	2.64D-05	2.89D-05	-5.85D-06	6.56D-06	1.73D-06

TABLE G14. STANDARD TEST CASE MEAN VELOCITY AND REYNOLDS STRESS PROFILES AT STATION (5,-6)

REU = 1.34D+06 (1/M)
KINEMATIC VISC. = 1.67D-05 (SQ-M/S)
DENSITY = 1.10D+00 (KG/CUBIC METER)
CF = 2.58D-03
OMEGA = -2.6 DEG.
UFS= 2.65D+01 M/S
U1FS = 2.65D+01 M/S

NONDIMENSIONALIZED MEAN VELOCITY NONDIMENSIONALIZED REYNOLDS STRESS TENSOR

LABORATORY COORDINATE SYSTEM

Y (CM)	BETA (DEG)	PSIZ* (DEG)	U1/U1FS	U2/U1FS	U3/U1FS	U1U1/U1FS2	U2U2/U1FS2	U3U3/U1FS2	U1U2/U1FS2	U1U3/U1FS2	U2U3/U1FS2
0.127	0.9	0.8	6.05D-01	8.45D-03	1.79D-02	3.46D-03	9.85D-04	2.37D-03	-5.10D-04	-3.25D-04	1.32D-04
0.190	2.1	0.7	6.36D-01	7.77D-03	5.55D-03	3.36D-03	9.54D-04	2.41D-03	-5.43D-04	-2.52D-04	1.42D-04
0.254	2.9	0.6	6.58D-01	6.89D-03	-3.45D-03	3.25D-03	9.23D-04	2.39D-03	-5.39D-04	-1.51D-04	9.20D-05
0.508	4.1	0.9	7.07D-01	1.11D-02	-1.85D-02	2.74D-03	1.03D-03	2.54D-03	-5.16D-04	1.54D-04	-1.07D-04
0.762	3.8	1.1	7.26D-01	1.39D-02	-1.52D-02	2.63D-03	1.25D-03	2.62D-03	-6.06D-04	2.27D-04	-2.46D-04
1.016	2.7	1.4	7.40D-01	1.81D-02	-1.29D-03	2.77D-03	1.40D-03	2.64D-03	-7.26D-04	2.31D-04	-2.90D-04
1.270	2.0	1.6	7.54D-01	2.11D-02	7.90D-03	2.93D-03	1.49D-03	2.43D-03	-8.25D-04	1.13D-04	-2.90D-04
1.905	0.7	1.8	7.87D-01	2.47D-02	2.61D-02	2.98D-03	1.45D-03	1.99D-03	-8.99D-04	-6.82D-05	-2.21D-04
2.540	0.1	1.7	8.21D-01	2.44D-02	3.58D-02	2.63D-03	1.30D-03	1.59D-03	-8.57D-04	-1.29D-04	-1.27D-04
3.810	-0.4	1.3	8.82D-01	2.00D-02	4.62D-02	1.97D-03	9.51D-04	1.19D-03	-6.14D-04	-9.55D-05	2.46D-05
5.080	-0.6	0.8	9.34D-01	1.31D-02	5.22D-02	1.29D-03	6.26D-04	7.92D-04	-3.91D-04	-6.59D-05	5.00D-05
6.350	-0.6	0.5	9.74D-01	8.51D-03	5.44D-02	6.49D-04	3.28D-04	4.13D-04	-1.81D-04	-3.78D-05	2.56D-05
7.620	-0.4	0.2	9.95D-01	3.48D-03	5.21D-02	1.61D-04	1.36D-04	1.38D-04	-4.71D-05	-2.59D-06	4.05D-06
10.160	-0.2	-0.3	1.00D+00	-5.25D-03	4.90D-02	3.28D-05	2.77D-05	3.27D-05	-4.11D-06	6.27D-06	1.44D-06
12.700	0.0	-0.5	1.00D+00	-8.74D-03	4.54D-02	2.84D-05	2.16D-05	3.04D-05	-3.79D-06	6.32D-06	1.53D-06

SENSOR COORDINATE SYSTEM

Y (CM)	BETA (DEG)	PSIZ* (DEG)	Q/UFS	U/UFS	UU/UFS2	VV/UFS2	WW/UFS2	UV/UFS2	UW/UFS2	VW/UFS2
0.127	0.9	0.8	6.04D-01	6.04D-01	3.47D-03	9.83D-04	2.35D-03	-5.13D-04	-2.92D-04	1.16D-04
0.190	2.1	0.7	6.36D-01	6.36D-01	3.36D-03	9.52D-04	2.40D-03	-5.43D-04	-2.43D-04	1.37D-04
0.254	2.9	0.6	6.58D-01	6.58D-01	3.25D-03	9.21D-04	2.39D-03	-5.37D-04	-1.55D-04	9.46D-05
0.508	4.1	0.9	7.06D-01	7.06D-01	2.74D-03	1.03D-03	2.53D-03	-5.18D-04	1.48D-04	-9.34D-05
0.762	3.8	1.1	7.26D-01	7.26D-01	2.63D-03	1.25D-03	2.60D-03	-6.09D-04	2.26D-04	-2.33D-04
1.016	2.7	1.4	7.40D-01	7.39D-01	2.76D-03	1.40D-03	2.63D-03	-7.25D-04	2.30D-04	-2.88D-04
1.270	2.0	1.6	7.54D-01	7.53D-01	2.92D-03	1.48D-03	2.42D-03	-8.21D-04	1.18D-04	-2.98D-04
1.905	0.7	1.8	7.87D-01	7.87D-01	2.98D-03	1.44D-03	1.98D-03	-8.89D-04	-3.52D-05	-2.50D-04
2.540	0.1	1.7	8.21D-01	8.21D-01	2.64D-03	1.29D-03	1.58D-03	-8.49D-04	-8.29D-05	-1.64D-04
3.810	-0.4	1.3	8.83D-01	8.82D-01	1.97D-03	9.49D-04	1.18D-03	-6.13D-04	-5.42D-05	-7.53D-06
5.080	-0.6	0.8	9.35D-01	9.35D-01	1.30D-03	6.24D-04	7.85D-04	-3.92D-04	-3.75D-05	2.81D-05
6.350	-0.6	0.5	9.74D-01	9.74D-01	6.51D-04	3.27D-04	4.09D-04	-1.82D-04	-2.44D-05	1.55D-05
7.620	-0.4	0.2	9.95D-01	9.95D-01	1.61D-04	1.36D-04	1.38D-04	-4.72D-05	-1.37D-06	1.57D-06
10.160	-0.2	-0.3	1.00D+00	1.00D+00	3.22D-05	2.76D-05	3.33D-05	-4.16D-06	6.24D-06	1.23D-06
12.700	0.0	-0.5	1.00D+00	1.00D+00	2.78D-05	2.16D-05	3.09D-05	-3.85D-06	6.19D-06	1.35D-06

APPENDIX H

Wall Static Pressure Distribution and Pressure Gradient Map for the Forward Half of the Teardrop Flow

TABLE H1. WALL STATIC PRESSURE DISTRIBUTION IN THE FORWARD HALF OF THE TEARDROP 3DTBL FLOW.
CP=2(PWALL-PATM)/(RHO(U1**2))

REU (1/M) = 1.34E 06
U1 (M/S) = 2.24E 01
DENSITY (KG/CUBIC METER) = 1.11E 00
AMBIENT TEMP. (K) = 3.00E 02
BAROMETRIC PRES. (KPA) = 9.51E 01

STATION			STATION			STATION			STATION		
X	Z	CP	X	Z	CP	X	Z	CP	X	Z	CP
-7.0	10.0	-1.35	-7.0	9.5	-1.34	-7.0	9.0	-1.36	-7.0	8.5	-1.35
-6.5	10.0	-1.35	-6.5	9.5	-1.35	-6.5	9.0	-1.35	-6.5	8.5	-1.35
-6.0	10.0	-1.35	-6.0	9.5	-1.35	-6.0	9.0	-1.36	-6.0	8.5	-1.34
-5.5	10.0	-1.35	-5.5	9.5	-1.35	-5.5	9.0	-1.36	-5.5	8.5	-1.35
-5.0	10.0	-1.37	-5.0	9.5	-1.36	-5.0	9.0	-1.37	-5.0	8.5	-1.36
-4.5	10.0	-1.36	-4.5	9.5	-1.36	-4.5	9.0	-1.37	-4.5	8.5	-1.36
-4.0	10.0	-1.37	-4.0	9.5	-1.37	-4.0	9.0	-1.38	-4.0	8.5	-1.37
-3.5	10.0	-1.37	-3.5	9.5	-1.37	-3.5	9.0	-1.38	-3.5	8.5	-1.37
-3.0	10.0	-1.39	-3.0	9.5	-1.38	-3.0	9.0	-1.40	-3.0	8.5	-1.39
-2.5	10.0	-1.39	-2.5	9.5	-1.39	-2.5	9.0	-1.40	-2.5	8.5	-1.40
-2.0	10.0	-1.40	-2.0	9.5	-1.40	-2.0	9.0	-1.42	-2.0	8.5	-1.41
-1.5	10.0	-1.40	-1.5	9.5	-1.41	-1.5	9.0	-1.42	-1.5	8.5	-1.42
-1.0	10.0	-1.41	-1.0	9.5	-1.42	-1.0	9.0	-1.43	-1.0	8.5	-1.43
-0.5	10.0	-1.42	-0.5	9.5	-1.42	-0.5	9.0	-1.45	-0.5	8.5	-1.45
0.0	10.0	-1.42	0.0	9.5	-1.44	0.0	9.0	-1.46	0.0	8.5	-1.46
0.5	10.0	-1.43	0.5	9.5	-1.44	0.5	9.0	-1.47	0.5	8.5	-1.47
1.0	10.0	-1.44	1.0	9.5	-1.46	1.0	9.0	-1.48	1.0	8.5	-1.48
2.0	10.0	-1.46	2.0	9.5	-1.47	2.0	9.0	-1.50	2.0	8.5	-1.51
3.0	10.0	-1.46	3.0	9.5	-1.48	3.0	9.0	-1.50	3.0	8.5	-1.51
4.0	10.0	-1.45	4.0	9.5	-1.47	4.0	9.0	-1.51	4.0	8.5	-1.51
5.0	10.0	-1.45	5.0	9.5	-1.47	5.0	9.0	-1.49	5.0	8.5	-1.50

TABLE H1 CONTINUED

REU (1/M) = 1.34E 06
UI (M/S) = 2.24E 01
DENSITY (KG/CUBIC METER) = 1.11E 00
AMBIENT TEMP. (K) = 3.00E 02
BAROMETRIC PRES. (KPA) = 9.51E 01

STATION			STATION			STATION			STATION		
X	Z	CP	X	Z	CP	X	Z	CP	X	Z	CP
-7.0	8.0	-1.33	-7.0	7.5	-1.32	-7.0	7.0	-1.33	-7.0	6.5	-1.32
-6.5	8.0	-1.33	-6.5	7.5	-1.32	-6.5	7.0	-1.33	-6.5	6.5	-1.32
-6.0	8.0	-1.33	-6.0	7.5	-1.32	-6.0	7.0	-1.34	-6.0	6.5	-1.31
-5.5	8.0	-1.33	-5.5	7.5	-1.33	-5.5	7.0	-1.33	-5.5	6.5	-1.31
-5.0	8.0	-1.34	-5.0	7.5	-1.33	-5.0	7.0	-1.34	-5.0	6.5	-1.33
-4.5	8.0	-1.34	-4.5	7.5	-1.34	-4.5	7.0	-1.34	-4.5	6.5	-1.33
-4.0	8.0	-1.35	-4.0	7.5	-1.35	-4.0	7.0	-1.35	-4.0	6.5	-1.33
-3.5	8.0	-1.36	-3.5	7.5	-1.35	-3.5	7.0	-1.36	-3.5	6.5	-1.35
-3.0	8.0	-1.37	-3.0	7.5	-1.36	-3.0	7.0	-1.38	-3.0	6.5	-1.36
-2.5	8.0	-1.39	-2.5	7.5	-1.38	-2.5	7.0	-1.38	-2.5	6.5	-1.38
-2.0	8.0	-1.40	-2.0	7.5	-1.40	-2.0	7.0	-1.41	-2.0	6.5	-1.39
-1.5	8.0	-1.41	-1.5	7.5	-1.41	-1.5	7.0	-1.42	-1.5	6.5	-1.42
-1.0	8.0	-1.43	-1.0	7.5	-1.43	-1.0	7.0	-1.44	-1.0	6.5	-1.44
-0.5	8.0	-1.44	-0.5	7.5	-1.44	-0.5	7.0	-1.46	-0.5	6.5	-1.47
0.0	8.0	-1.46	0.0	7.5	-1.47	0.0	7.0	-1.50	0.0	6.5	-1.50
0.5	8.0	-1.47	0.5	7.5	-1.47	0.5	7.0	-1.51	0.5	6.5	-1.52
1.0	8.0	-1.49	1.0	7.5	-1.50	1.0	7.0	-1.53	1.0	6.5	-1.56
2.0	8.0	-1.51	2.0	7.5	-1.53	2.0	7.0	-1.58	2.0	6.5	-1.60
3.0	8.0	-1.52	3.0	7.5	-1.54	3.0	7.0	-1.58	3.0	6.5	-1.62
4.0	8.0	-1.51	4.0	7.5	-1.53	4.0	7.0	-1.58	4.0	6.5	-1.60
5.0	8.0	-1.50	5.0	7.5	-1.52	5.0	7.0	-1.55	5.0	6.5	-1.57

TABLE H1 CONTINUED

REU (1/M) = 1.34E 06
UI (M/S) = 2.24E 01
DENSITY (KG/CUBIC METER) = 1.11E 00
AMBIENT TEMP. (K) = 3.00E 02
BAROMETRIC PRES. (KPA) = 9.51E 01

STATION			STATION			STATION			STATION		
X	Z	CP	X	Z	CP	X	Z	CP	X	Z	CP
-7.0	6.0	-1.30	-7.0	5.5	-1.29	-7.0	5.0	-1.30	-7.0	4.5	-1.28
-6.5	6.0	-1.30	-6.5	5.5	-1.29	-6.5	5.0	-1.29	-6.5	4.5	-1.27
-6.0	6.0	-1.30	-6.0	5.5	-1.29	-6.0	5.0	-1.29	-6.0	4.5	-1.28
-5.5	6.0	-1.30	-5.5	5.5	-1.29	-5.5	5.0	-1.29	-5.5	4.5	-1.26
-5.0	6.0	-1.31	-5.0	5.5	-1.29	-5.0	5.0	-1.29	-5.0	4.5	-1.28
-4.5	6.0	-1.31	-4.5	5.5	-1.30	-4.5	5.0	-1.29	-4.5	4.5	-1.27
-4.0	6.0	-1.32	-4.0	5.5	-1.30	-4.0	5.0	-1.29	-4.0	4.5	-1.27
-3.5	6.0	-1.32	-3.5	5.5	-1.31	-3.5	5.0	-1.31	-3.5	4.5	-1.27
-3.0	6.0	-1.35	-3.0	5.5	-1.32	-3.0	5.0	-1.32	-3.0	4.5	-1.29
-2.5	6.0	-1.36	-2.5	5.5	-1.34	-2.5	5.0	-1.33	-2.5	4.5	-1.31
-2.0	6.0	-1.38	-2.0	5.5	-1.37	-2.0	5.0	-1.36	-2.0	4.5	-1.33
-1.5	6.0	-1.40	-1.5	5.5	-1.39	-1.5	5.0	-1.39	-1.5	4.5	-1.37
-1.0	6.0	-1.43	-1.0	5.5	-1.42	-1.0	5.0	-1.44	-1.0	4.5	-1.42
-0.5	6.0	-1.47	-0.5	5.5	-1.47	-0.5	5.0	-1.49	-0.5	4.5	-1.48
0.0	6.0	-1.50	0.0	5.5	-1.52	0.0	5.0	-1.55	0.0	4.5	-1.56
0.5	6.0	-1.53	0.5	5.5	-1.55	0.5	5.0	-1.61	0.5	4.5	-1.65
1.0	6.0	-1.57	1.0	5.5	-1.61	1.0	5.0	-1.67	1.0	4.5	-1.74
2.0	6.0	-1.62	2.0	5.5	-1.68	2.0	5.0	-1.78	2.0	4.5	-1.87
3.0	6.0	-1.64	3.0	5.5	-1.69	3.0	5.0	-1.78	3.0	4.5	-1.89
4.0	6.0	-1.61	4.0	5.5	-1.66	4.0	5.0	-1.74	4.0	4.5	-1.79
5.0	6.0	-1.58	5.0	5.5	-1.62	5.0	5.0	-1.66	5.0	4.5	-1.70

TABLE H1 CONTINUED

REU (1/M) = 1.34E 06
UI (M/S) = 2.24E 01
DENSITY (KG/CUBIC METER) = 1.11E 00
AMBIENT TEMP. (K) = 3.00E 02
BAROMETRIC PRES. (KPA) = 9.51E 01

STATION			STATION			STATION			STATION		
X	Z	CP	X	Z	CP	X	Z	CP	X	Z	CP
-7.0	4.0	-1.26	-7.0	3.5	-1.25	-7.0	3.0	-1.26	-4.5	2.5	-1.18
-6.5	4.0	-1.26	-6.5	3.5	-1.25	-6.5	3.0	-1.24	-4.0	2.5	-1.16
-6.0	4.0	-1.25	-6.0	3.5	-1.24	-6.0	3.0	-1.23	-3.5	2.5	-1.15
-5.5	4.0	-1.24	-5.5	3.5	-1.23	-5.5	3.0	-1.23	-3.0	2.5	-1.15
-5.0	4.0	-1.24	-5.0	3.5	-1.22	-5.0	3.0	-1.21	-2.5	2.5	-1.14
-4.5	4.0	-1.24	-4.5	3.5	-1.22	-4.5	3.0	-1.20	-2.0	2.5	-1.15
-4.0	4.0	-1.24	-4.0	3.5	-1.21	-4.0	3.0	-1.20	-1.5	2.5	-1.20
-3.5	4.0	-1.24	-3.5	3.5	-1.21	-3.5	3.0	-1.19	-1.0	2.5	-1.31
-3.0	4.0	-1.26	-3.0	3.5	-1.22	-3.0	3.0	-1.19	-0.5	2.5	-1.48
-2.5	4.0	-1.27	-2.5	3.5	-1.23	-2.5	3.0	-1.19	0.0	2.5	-1.60
-2.0	4.0	-1.29	-2.0	3.5	-1.25	-2.0	3.0	-1.21	-7.0	2.0	-1.23
-1.5	4.0	-1.33	-1.5	3.5	-1.29	-1.5	3.0	-1.26	-6.5	2.0	-1.21
-1.0	4.0	-1.39	-1.0	3.5	-1.36	-1.0	3.0	-1.33	-6.0	2.0	-1.20
-0.5	4.0	-1.47	-0.5	3.5	-1.47	-0.5	3.0	-1.50	-5.5	2.0	-1.18
0.0	4.0	-1.58	0.0	3.5	-1.63	0.0	3.0	-1.69	-5.0	2.0	-1.17
0.5	4.0	-1.70	0.5	3.5	-1.80	0.5	3.0	-1.87	-4.5	2.0	-1.15
1.0	4.0	-1.84	1.0	3.5	-1.96	-7.0	2.5	-1.24	-4.0	2.0	-1.13
2.0	4.0	-2.00	2.0	3.5	-2.15	-6.5	2.5	-1.23	-3.5	2.0	-1.11
3.0	4.0	-1.97	3.0	3.5	-2.08	-6.0	2.5	-1.21	-3.0	2.0	-1.10
4.0	4.0	-1.83	4.0	3.5	-1.87	-5.5	2.5	-1.20	-2.5	2.0	-1.10
5.0	4.0	-1.70	5.0	3.5	-1.72	-5.0	2.5	-1.20	-2.0	2.0	-1.10

TABLE H1 CONTINUED

REU (1/M) = 1.34E 06
UI (M/S) = 2.24E 01
DENSITY (KG/CUBIC METER) = 1.11E 00
AMBIENT TEMP. (K) = 3.00E 02
BAROMETRIC PRES. (KPA) = 9.51E 01

STATION			STATION			STATION			STATION		
X	Z	CP	X	Z	CP	X	Z	CP	X	Z	CP
-1.5	2.0	-1.14	-4.5	1.0	-1.13	-5.0	-0.0	-1.14	-5.5	-1.0	-1.18
-1.0	2.0	-1.27	-4.0	1.0	-1.11	-4.5	-0.0	-1.11	-5.0	-1.0	-1.16
-0.5	2.0	-1.35	-3.5	1.0	-1.08	-4.0	-0.0	-1.08	-4.5	-1.0	-1.13
-7.0	1.5	-1.22	-3.0	1.0	-1.06	-3.5	-0.0	-1.05	-4.0	-1.0	-1.11
-6.5	1.5	-1.21	-2.5	1.0	-1.03	-3.0	-0.0	-1.01	-3.5	-1.0	-1.08
-6.0	1.5	-1.19	-2.0	1.0	-1.01	-2.5	-0.0	-0.97	-3.0	-1.0	-1.05
-5.5	1.5	-1.17	-7.0	0.5	-1.22	-2.0	-0.0	-0.94	-2.5	-1.0	-1.03
-5.0	1.5	-1.15	-6.5	0.5	-1.20	-7.0	-0.5	-1.21	-2.0	-1.0	-1.00
-4.5	1.5	-1.14	-6.0	0.5	-1.18	-6.5	-0.5	-1.20	-7.0	-1.5	-1.23
-4.0	1.5	-1.11	-5.5	0.5	-1.17	-6.0	-0.5	-1.19	-6.5	-1.5	-1.22
-3.5	1.5	-1.09	-5.0	0.5	-1.15	-5.5	-0.5	-1.16	-6.0	-1.5	-1.19
-3.0	1.5	-1.07	-4.5	0.5	-1.12	-5.0	-0.5	-1.14	-5.5	-1.5	-1.18
-2.5	1.5	-1.06	-4.0	0.5	-1.09	-4.5	-0.5	-1.12	-5.0	-1.5	-1.17
-2.0	1.5	-1.05	-3.5	0.5	-1.07	-4.0	-0.5	-1.09	-4.5	-1.5	-1.15
-1.5	1.5	-1.09	-3.0	0.5	-1.03	-3.5	-0.5	-1.05	-4.0	-1.5	-1.12
-1.0	1.5	-1.19	-2.5	0.5	-1.01	-3.0	-0.5	-1.02	-3.5	-1.5	-1.10
-7.0	1.0	-1.23	-2.0	0.5	-0.97	-2.5	-0.5	-0.98	-3.0	-1.5	-1.08
-6.5	1.0	-1.21	-7.0	-0.0	-1.21	-2.0	-0.5	-0.95	-2.5	-1.5	-1.07
-6.0	1.0	-1.19	-6.5	-0.0	-1.20	-7.0	-1.0	-1.23	-2.0	-1.5	-1.05
-5.5	1.0	-1.18	-6.0	-0.0	-1.18	-6.5	-1.0	-1.22	-1.5	-1.5	-1.07
-5.0	1.0	-1.16	-5.5	-0.0	-1.16	-6.0	-1.0	-1.20	-1.0	-1.5	-1.17

TABLE H1 CONTINUED

REU (1/M) = 1.34E 06
UI (M/S) = 2.24E 01
DENSITY (KG/CUBIC METER) = 1.11E 00
AMBIENT TEMP. (K) = 3.00E 02
BAROMETRIC PRES. (KPA) = 9.51E 01

STATION			STATION			STATION			STATION		
X	Z	CP	X	Z	CP	X	Z	CP	X	Z	CP
-7.0	-2.0	-1.23	-3.5	-2.5	-1.15	-0.5	-3.0	-1.47	3.0	-3.5	-2.09
-6.5	-2.0	-1.22	-3.0	-2.5	-1.14	0.0	-3.0	-1.68	4.0	-3.5	-1.90
-6.0	-2.0	-1.21	-2.5	-2.5	-1.14	0.5	-3.0	-1.85	5.0	-3.5	-1.74
-5.5	-2.0	-1.18	-2.0	-2.5	-1.15	-7.0	-3.5	-1.27	-7.0	-4.0	-1.27
-5.0	-2.0	-1.17	-1.5	-2.5	-1.18	-6.5	-3.5	-1.25	-6.5	-4.0	-1.26
-4.5	-2.0	-1.16	-1.0	-2.5	-1.28	-6.0	-3.5	-1.24	-6.0	-4.0	-1.25
-4.0	-2.0	-1.14	-0.5	-2.5	-1.47	-5.5	-3.5	-1.24	-5.5	-4.0	-1.25
-3.5	-2.0	-1.12	0.0	-2.5	-1.60	-5.0	-3.5	-1.24	-5.0	-4.0	-1.25
-3.0	-2.0	-1.11	-7.0	-3.0	-1.26	-4.5	-3.5	-1.23	-4.5	-4.0	-1.24
-2.5	-2.0	-1.10	-6.5	-3.0	-1.25	-4.0	-3.5	-1.22	-4.0	-4.0	-1.24
-2.0	-2.0	-1.09	-6.0	-3.0	-1.24	-3.5	-3.5	-1.22	-3.5	-4.0	-1.24
-1.5	-2.0	-1.13	-5.5	-3.0	-1.23	-3.0	-3.5	-1.22	-3.0	-4.0	-1.25
-1.0	-2.0	-1.27	-5.0	-3.0	-1.22	-2.5	-3.5	-1.24	-2.5	-4.0	-1.27
-0.5	-2.0	-1.33	-4.5	-3.0	-1.21	-2.0	-3.5	-1.26	-2.0	-4.0	-1.29
-7.0	-2.5	-1.23	-4.0	-3.0	-1.20	-1.5	-3.5	-1.30	-1.5	-4.0	-1.33
-6.5	-2.5	-1.23	-3.5	-3.0	-1.20	-1.0	-3.5	-1.37	-1.0	-4.0	-1.39
-6.0	-2.5	-1.22	-3.0	-3.0	-1.20	-0.5	-3.5	-1.48	-0.5	-4.0	-1.47
-5.5	-2.5	-1.20	-2.5	-3.0	-1.21	0.0	-3.5	-1.62	0.0	-4.0	-1.57
-5.0	-2.5	-1.19	-2.0	-3.0	-1.23	0.5	-3.5	-1.81	0.5	-4.0	-1.69
-4.5	-2.5	-1.18	-1.5	-3.0	-1.26	1.0	-3.5	-1.93	1.0	-4.0	-1.82
-4.0	-2.5	-1.16	-1.0	-3.0	-1.33	2.0	-3.5	-2.13	2.0	-4.0	-2.00

TABLE H1 CONTINUED

REU (1/M) = 1.34E 06
UI (M/S) = 2.24E 01
DENSITY (KG/CUBIC METER) = 1.11E 00
AMBIENT TEMP. (K) = 3.00E 02
BAROMETRIC PRES. (KPA) = 9.51E 01

STATION			STATION			STATION			STATION		
X	Z	CP	X	Z	CP	X	Z	CP	X	Z	CP
3.0	-4.0	-1.97	3.0	-4.5	-1.87	3.0	-5.0	-1.79	3.0	-5.5	-1.70
4.0	-4.0	-1.84	4.0	-4.5	-1.79	4.0	-5.0	-1.73	4.0	-5.5	-1.68
5.0	-4.0	-1.71	5.0	-4.5	-1.70	5.0	-5.0	-1.67	5.0	-5.5	-1.63
-7.0	-4.5	-1.27	-7.0	-5.0	-1.30	-7.0	-5.5	-1.30	-7.0	-6.0	-1.30
-6.5	-4.5	-1.27	-6.5	-5.0	-1.29	-6.5	-5.5	-1.30	-6.5	-6.0	-1.30
-6.0	-4.5	-1.27	-6.0	-5.0	-1.29	-6.0	-5.5	-1.30	-6.0	-6.0	-1.30
-5.5	-4.5	-1.26	-5.5	-5.0	-1.29	-5.5	-5.5	-1.30	-5.5	-6.0	-1.30
-5.0	-4.5	-1.26	-5.0	-5.0	-1.30	-5.0	-5.5	-1.31	-5.0	-6.0	-1.31
-4.5	-4.5	-1.26	-4.5	-5.0	-1.30	-4.5	-5.5	-1.30	-4.5	-6.0	-1.31
-4.0	-4.5	-1.27	-4.0	-5.0	-1.30	-4.0	-5.5	-1.31	-4.0	-6.0	-1.32
-3.5	-4.5	-1.27	-3.5	-5.0	-1.31	-3.5	-5.5	-1.32	-3.5	-6.0	-1.32
-3.0	-4.5	-1.28	-3.0	-5.0	-1.32	-3.0	-5.5	-1.34	-3.0	-6.0	-1.35
-2.5	-4.5	-1.30	-2.5	-5.0	-1.34	-2.5	-5.5	-1.35	-2.5	-6.0	-1.36
-2.0	-4.5	-1.33	-2.0	-5.0	-1.36	-2.0	-5.5	-1.37	-2.0	-6.0	-1.37
-1.5	-4.5	-1.36	-1.5	-5.0	-1.39	-1.5	-5.5	-1.39	-1.5	-6.0	-1.40
-1.0	-4.5	-1.40	-1.0	-5.0	-1.43	-1.0	-5.5	-1.44	-1.0	-6.0	-1.43
-0.5	-4.5	-1.47	-0.5	-5.0	-1.48	-0.5	-5.5	-1.47	-0.5	-6.0	-1.46
0.0	-4.5	-1.55	0.0	-5.0	-1.54	0.0	-5.5	-1.52	0.0	-6.0	-1.50
0.5	-4.5	-1.63	0.5	-5.0	-1.61	0.5	-5.5	-1.57	0.5	-6.0	-1.53
1.0	-4.5	-1.71	1.0	-5.0	-1.66	1.0	-5.5	-1.61	1.0	-6.0	-1.57
2.0	-4.5	-1.86	2.0	-5.0	-1.75	2.0	-5.5	-1.68	2.0	-6.0	-1.63

TABLE H1 CONTINUED

REU (1/M) = 1.34E 06
UI (M/S) = 2.24E 01
DENSITY (KG/CUBIC METER) = 1.11E 00
AMBIENT TEMP. (K) = 3.00E 02
BAROMETRIC PRES. (KPA) = 9.51E 01

STATION			STATION			STATION			STATION		
X	Z	CP	X	Z	CP	X	Z	CP	X	Z	CP
3.0	-6.0	-1.64	3.0	-6.5	-1.60	3.0	-7.0	-1.59	3.0	-7.5	-1.56
4.0	-6.0	-1.63	4.0	-6.5	-1.59	4.0	-7.0	-1.58	4.0	-7.5	-1.55
5.0	-6.0	-1.59	5.0	-6.5	-1.57	5.0	-7.0	-1.56	5.0	-7.5	-1.54
-7.0	-6.5	-1.31	-7.0	-7.0	-1.33	-7.0	-7.5	-1.34	-7.0	-8.0	-1.33
-6.5	-6.5	-1.31	-6.5	-7.0	-1.33	-6.5	-7.5	-1.33	-6.5	-8.0	-1.33
-6.0	-6.5	-1.31	-6.0	-7.0	-1.33	-6.0	-7.5	-1.34	-6.0	-8.0	-1.33
-5.5	-6.5	-1.31	-5.5	-7.0	-1.34	-5.5	-7.5	-1.34	-5.5	-8.0	-1.34
-5.0	-6.5	-1.32	-5.0	-7.0	-1.34	-5.0	-7.5	-1.35	-5.0	-8.0	-1.34
-4.5	-6.5	-1.32	-4.5	-7.0	-1.34	-4.5	-7.5	-1.34	-4.5	-8.0	-1.35
-4.0	-6.5	-1.33	-4.0	-7.0	-1.36	-4.0	-7.5	-1.36	-4.0	-8.0	-1.36
-3.5	-6.5	-1.34	-3.5	-7.0	-1.36	-3.5	-7.5	-1.36	-3.5	-8.0	-1.36
-3.0	-6.5	-1.35	-3.0	-7.0	-1.37	-3.0	-7.5	-1.38	-3.0	-8.0	-1.38
-2.5	-6.5	-1.37	-2.5	-7.0	-1.39	-2.5	-7.5	-1.39	-2.5	-8.0	-1.39
-2.0	-6.5	-1.39	-2.0	-7.0	-1.41	-2.0	-7.5	-1.40	-2.0	-8.0	-1.40
-1.5	-6.5	-1.41	-1.5	-7.0	-1.43	-1.5	-7.5	-1.42	-1.5	-8.0	-1.41
-1.0	-6.5	-1.43	-1.0	-7.0	-1.45	-1.0	-7.5	-1.44	-1.0	-8.0	-1.43
-0.5	-6.5	-1.46	-0.5	-7.0	-1.46	-0.5	-7.5	-1.46	-0.5	-8.0	-1.45
0.0	-6.5	-1.49	0.0	-7.0	-1.49	0.0	-7.5	-1.48	0.0	-8.0	-1.46
0.5	-6.5	-1.52	0.5	-7.0	-1.52	0.5	-7.5	-1.49	0.5	-8.0	-1.47
1.0	-6.5	-1.54	1.0	-7.0	-1.54	1.0	-7.5	-1.52	1.0	-8.0	-1.49
2.0	-6.5	-1.59	2.0	-7.0	-1.57	2.0	-7.5	-1.55	2.0	-8.0	-1.52

TABLE H1 CONTINUED

REU (1/M) = 1.34E 06
UI (M/S) = 2.24E 01
DENSITY (KG/CUBIC METER) = 1.11E 00
AMBIENT TEMP. (K) = 3.00E 02
BAROMETRIC PRES. (KPA) = 9.51E 01

STATION			STATION			STATION			STATION		
X	Z	CP	X	Z	CP	X	Z	CP	X	Z	CP
3.0	-8.0	-1.53	3.0	-8.5	-1.51	3.0	-9.0	-1.51	3.0	-9.5	-1.49
4.0	-8.0	-1.52	4.0	-8.5	-1.51	4.0	-9.0	-1.50	4.0	-9.5	-1.49
5.0	-8.0	-1.51	5.0	-8.5	-1.50	5.0	-9.0	-1.51	5.0	-9.5	-1.49
-7.0	-8.5	-1.34	-7.0	-9.0	-1.35	-7.0	-9.5	-1.35	-7.0	-10.0	-1.35
-6.5	-8.5	-1.34	-6.5	-9.0	-1.36	-6.5	-9.5	-1.35	-6.5	-10.0	-1.35
-6.0	-8.5	-1.34	-6.0	-9.0	-1.36	-6.0	-9.5	-1.35	-6.0	-10.0	-1.35
-5.5	-8.5	-1.34	-5.5	-9.0	-1.36	-5.5	-9.5	-1.36	-5.5	-10.0	-1.35
-5.0	-8.5	-1.35	-5.0	-9.0	-1.37	-5.0	-9.5	-1.37	-5.0	-10.0	-1.37
-4.5	-8.5	-1.36	-4.5	-9.0	-1.38	-4.5	-9.5	-1.37	-4.5	-10.0	-1.37
-4.0	-8.5	-1.36	-4.0	-9.0	-1.38	-4.0	-9.5	-1.38	-4.0	-10.0	-1.37
-3.5	-8.5	-1.37	-3.5	-9.0	-1.39	-3.5	-9.5	-1.38	-3.5	-10.0	-1.38
-3.0	-8.5	-1.38	-3.0	-9.0	-1.39	-3.0	-9.5	-1.40	-3.0	-10.0	-1.39
-2.5	-8.5	-1.39	-2.5	-9.0	-1.41	-2.5	-9.5	-1.40	-2.5	-10.0	-1.39
-2.0	-8.5	-1.40	-2.0	-9.0	-1.42	-2.0	-9.5	-1.41	-2.0	-10.0	-1.40
-1.5	-8.5	-1.41	-1.5	-9.0	-1.43	-1.5	-9.5	-1.42	-1.5	-10.0	-1.40
-1.0	-8.5	-1.43	-1.0	-9.0	-1.44	-1.0	-9.5	-1.43	-1.0	-10.0	-1.42
-0.5	-8.5	-1.44	-0.5	-9.0	-1.45	-0.5	-9.5	-1.44	-0.5	-10.0	-1.43
0.0	-8.5	-1.46	0.0	-9.0	-1.46	0.0	-9.5	-1.45	0.0	-10.0	-1.44
0.5	-8.5	-1.47	0.5	-9.0	-1.47	0.5	-9.5	-1.46	0.5	-10.0	-1.44
1.0	-8.5	-1.48	1.0	-9.0	-1.48	1.0	-9.5	-1.47	1.0	-10.0	-1.45
2.0	-8.5	-1.50	2.0	-9.0	-1.50	2.0	-9.5	-1.48	2.0	-10.0	-1.46

TABLE H1 CONTINUED

REU (1/M) = 1.34E 06
UI (M/S) = 2.24E 01
DENSITY (KG/CUBIC METER) = 1.11E 00
AMBIENT TEMP. (K) = 3.00E 02
BAROMETRIC PRES. (KPA) = 9.51E 01

STATION			STATION			STATION			STATION		
X	Z	CP	X	Z	CP	X	Z	CP	X	Z	CP
3.0	-10.0	-1.47	4.0	-10.5	-1.45	5.0	-11.0	-1.46	-7.0	-12.0	-1.37
4.0	-10.0	-1.46	5.0	-10.5	-1.46	-7.0	-11.5	-1.37	-6.5	-12.0	-1.36
5.0	-10.0	-1.46	-7.0	-11.0	-1.37	-6.5	-11.5	-1.37	-6.0	-12.0	-1.37
-7.0	-10.5	-1.35	-6.5	-11.0	-1.37	-6.0	-11.5	-1.37	-5.5	-12.0	-1.36
-6.5	-10.5	-1.36	-6.0	-11.0	-1.37	-5.5	-11.5	-1.37	-5.0	-12.0	-1.38
-6.0	-10.5	-1.36	-5.5	-11.0	-1.38	-5.0	-11.5	-1.38	-4.5	-12.0	-1.38
-5.5	-10.5	-1.35	-5.0	-11.0	-1.38	-4.5	-11.5	-1.38	-4.0	-12.0	-1.38
-5.0	-10.5	-1.37	-4.5	-11.0	-1.39	-4.0	-11.5	-1.38	-3.5	-12.0	-1.38
-4.5	-10.5	-1.37	-4.0	-11.0	-1.39	-3.5	-11.5	-1.39	-3.0	-12.0	-1.40
-4.0	-10.5	-1.38	-3.5	-11.0	-1.40	-3.0	-11.5	-1.40	-2.5	-12.0	-1.39
-3.5	-10.5	-1.38	-3.0	-11.0	-1.40	-2.5	-11.5	-1.40	-2.0	-12.0	-1.40
-3.0	-10.5	-1.39	-2.5	-11.0	-1.41	-2.0	-11.5	-1.40	-1.5	-12.0	-1.40
-2.5	-10.5	-1.40	-2.0	-11.0	-1.41	-1.5	-11.5	-1.42	-1.0	-12.0	-1.41
-2.0	-10.5	-1.40	-1.5	-11.0	-1.42	-1.0	-11.5	-1.42	-0.5	-12.0	-1.41
-1.5	-10.5	-1.41	-1.0	-11.0	-1.43	-0.5	-11.5	-1.42	0.0	-12.0	-1.42
-1.0	-10.5	-1.41	-0.5	-11.0	-1.43	0.0	-11.5	-1.42	0.5	-12.0	-1.42
-0.5	-10.5	-1.42	0.0	-11.0	-1.44	0.5	-11.5	-1.43	1.0	-12.0	-1.43
0.0	-10.5	-1.43	0.5	-11.0	-1.44	1.0	-11.5	-1.44	2.0	-12.0	-1.44
0.5	-10.5	-1.43	1.0	-11.0	-1.45	2.0	-11.5	-1.45	3.0	-12.0	-1.44
1.0	-10.5	-1.44	2.0	-11.0	-1.46	3.0	-11.5	-1.45	4.0	-12.0	-1.43
2.0	-10.5	-1.45	3.0	-11.0	-1.46	4.0	-11.5	-1.44	5.0	-12.0	-1.44
3.0	-10.5	-1.46	4.0	-11.0	-1.46	5.0	-11.5	-1.44			

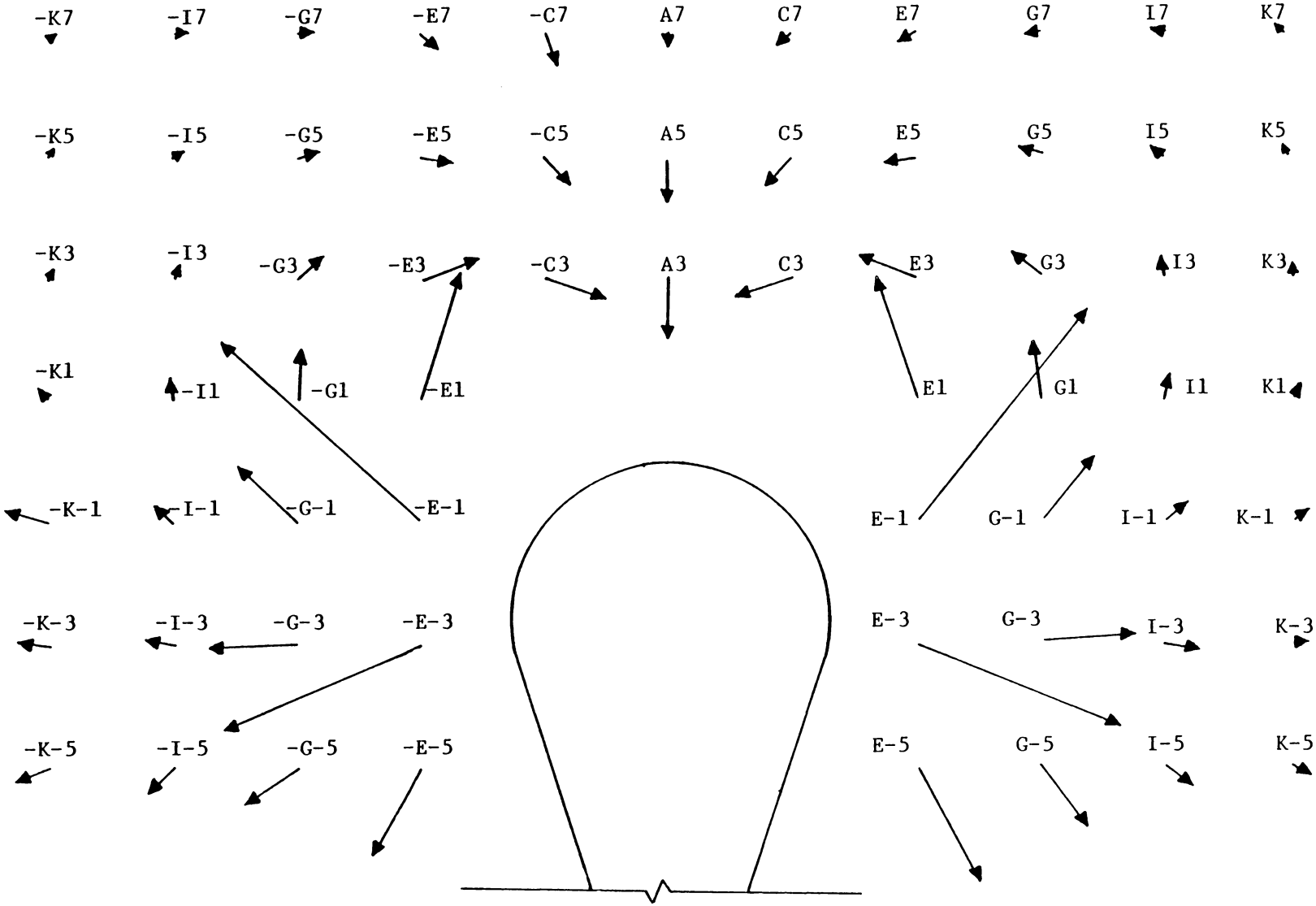

Figure H1. Wall Pressure Gradient Map for the Forward Half of the Teardrop Flow (Taken from McAllister [27])

The vita has been removed from the scanned document